Multi-Component Metal-Organic Frameworks

Cadman, Laura

Award date:
2017

Awarding institution:
University of Bath

Multi-Component Metal-Organic Frameworks

Laura Kathryn Cadman

A thesis submitted for the degree of Doctor of Philosophy
University of Bath
Department of Chemistry

May 2017

For my parents, Paul and Denise, whose support allowed me to embark on this journey, and for Jonny, whose love and belief in me enabled me to complete it.

Contents

Acknowledgements

I would like to thank Professor Andrew Burrows and Dr Mary Mahon for their supervision and guidance throughout my PhD.

Special thanks go to my colleagues Dr William Gee, Dr Sebastien Rochat, Harina Amer Hamzah and Jane Knichal for their support and comradery.

Thanks also go to Dr John Lowe and Dr Catherine Lyall for assistance with NMR spectroscopy measurements, Professor Aron Walsh, Jessica Bristow and Dr Pascaline Patureau for their collaborations and Dr Floriana Tuna for assistance with EPR spectroscopy studies. Additional thanks go to EPSRC for financial support.

Declaration of Work Done in Conjunction with Others

Single crystal structure refinements which contain complex disorder were carried out with the assistance of Dr Mary Mahon (Chapters 2, 3 and 4).

The work carried out in Chapter 2 entitled Computational modelling (Sections 2.2.9 and 2.3.3) were carried out by Professor Aron Walsh and Jessica Bristow.

EPR spectroscopy measurements presented in Chapter 4 were conducted by Dr Floriana Tuna, National EPR facility, University of Manchester.

SEM/EDX spectroscopy measurements presented in Chapter 5 were made with the assistance of Dr Philip Fletcher, Microscopy and Analysis Suite, University of Bath. Florescence spectroscopy analysis also presented in Chapter 5 was undertaken together with Dr Pascaline Patureau, University of Bath.

Abstract

The synthesis of metal-organic frameworks (MOFs) with new structures and multi-functional pore environments is an area of growing research interest. One route to forming materials of this kind is through the synthesis of multi-component MOFs, which may include multiple organic ligand types or metals in the framework. This thesis presents new examples of multi-component MOFs which aim to demonstrate how this approach affects the properties of the resulting frameworks.

Chapter 1 details the terminology surrounding metal-organic frameworks and includes a review of the literature. The overall aims of the thesis are presented at the end of this chapter.

A series of mixed-ligand MOFs are presented in Chapter 2, combining multiple organic ligands which perform the same structural role within the framework but contain different functionalities. X-ray diffraction studies revealed that the pore size and geometry of the products can be systematically altered through compositional control.

Chapter 3 is an investigation into defect formation through the systematic inclusion of a dicarboxylate ligand into frameworks based on tricarboxylate ligands. X-ray diffraction and gas adsorption studies on the mixed-ligand products show them to be isostructural to the single ligand analogues and contain defects which induce porosity into an otherwise non-porous system.

The preparation of zinc-based anionic MOFs which contain viologen cations in their pores are detailed in Chapter 4. A reduction of the viologen counter-ions from the dication (yellow) to the radical cation (blue) was observed with heating or irradiation. Stability of the viologen radical cations within the MOFs was investigated through electron paramagnetic spectroscopy and was shown to be dependent on the framework topology.

Finally, Chapter 5 describes the synthesis and characterisation of a range of mixed-lanthanide core-shell MOFs, containing gadolinium, terbium and europium. These materials exhibit different emission properties than those of an isostructural framework containing randomly distributed lanthanide centres.

1. Introduction

1.1 Terminology

There have been varied and sometimes conflicting definitions of co-ordination polymers and metal-organic frameworks (MOFs) within the literature. Their hybrid nature, combining inorganic coordination chemistry and organic synthesis, has led to their prevalence in multiple fields and resulted in a diversified terminology. Recently, IUPAC guidelines have been released on the definition and description of these commonly used terms.[1, 2]

The IUPAC definition of a co-ordination polymer is a co-ordination compound with repeating units in one, two or three dimensions.[1] This is the most general term for co-ordination compounds containing metal ions and bridging organic linkers, and therefore this is an umbrella term which is further subdivided into distinct classifications of compounds. Co-ordination polymers which extend in two or three dimensions are part of the co-ordination network subset. Co-ordination networks are defined as one-dimensional repeating co-ordination units which are cross-linked into two or three dimensions.[1]

Metal-organic frameworks, often abbreviated to MOFs, are a type of co-ordination network (and therefore co-ordination polymer) which contain potential voids.[1] MOFs should have a robust nature, with strong bonding present in the framework, have a well-defined structure and contain linking units formed from organic molecules which can often be further modified through organic synthesis.[3] An example of a MOF is given in Figure 1.1 and is that of $[Zr_6O_4(OH)_4(bdc)_6]$, the so-called UiO-66 structure (bdc = 1,4-benzenedicarboxylate). UiO-66 is formed from $Zr_6O_6(CO_2)_{12}$ inorganic co-ordination nodes known as secondary building units (SBUs) which are linked together by the bdc ligands to form a three-dimensional porous network.

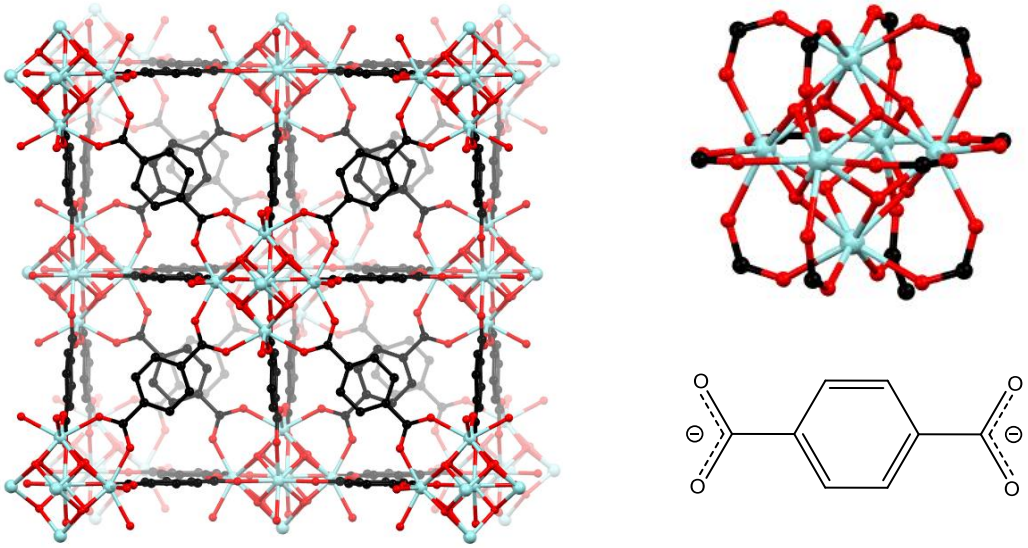

Figure 1.1 The structure of $[Zr_6O_4(OH)_4(bdc)_6]$, UiO-66. The framework structure is shown alongside the $Zr_6O_6(CO_2)_{12}$ clusters and the ligand structure.[4]

An overview of the terms used to describe this class of materials and their relation to one another, is shown in Figure 1.2. The MOF category can be further subdivided to group together MOFs with similar properties or structural features, such as porous MOFs (MOFs which contain voids) or anionic MOFs (MOFs whose framework holds an overall negative charge). Three examples of subsets of the MOF family are given in Figure 1.2.

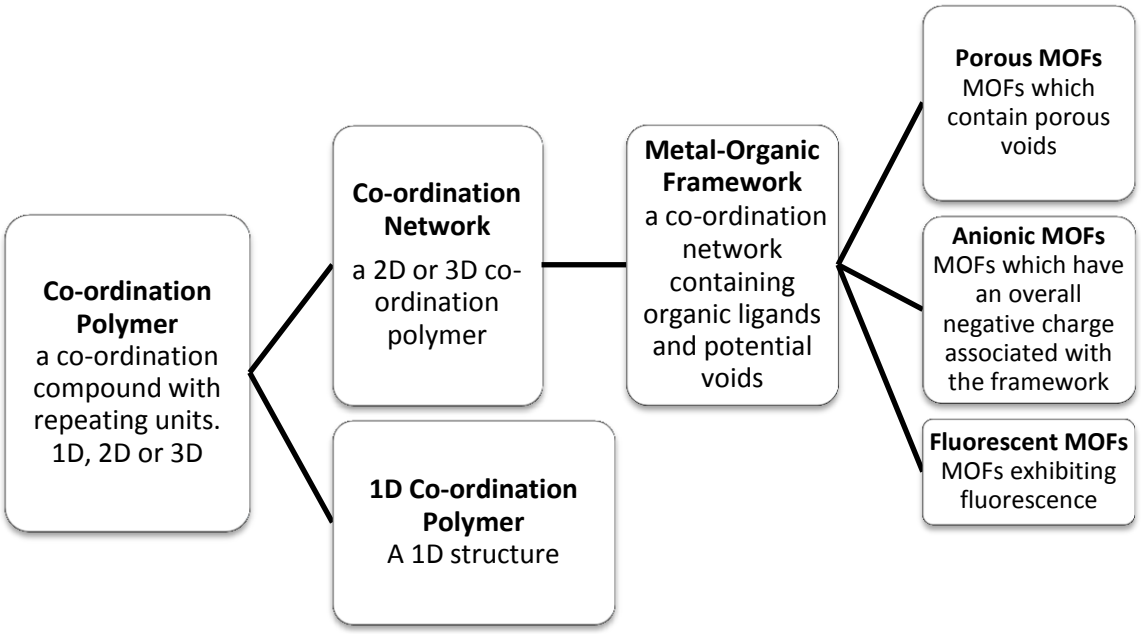

Figure 1.2 A hierarchy of terms used to describe metal and organic containing co-ordination compounds. The subset of MOFs shows types of frameworks displaying similarities in their structure or properties and are not mutually exclusive.

It is generally agreed that porosity is a key feature of MOFs, and one reason for the significant attention they have received.[2] A review of the literature shows that most descriptions of MOFs include porosity, or potential for porosity, as a defining factor.[5, 6] Whilst the IUPAC recommended definition of a MOF states that they should contain potential voids, there has been some debate in the literature as to whether proven porosity is necessary to fulfil the definition of a MOF.[2] Proven porosity is reached when a MOF remains structurally stable upon the removal of guest or solvent molecules from the pores. Many MOFs exhibit a flexible nature resulting in changes to the porosity of the material which are dependent upon external factors such as temperature or pressure.[1] This makes establishing proven porosity more complex. It has also been noted that a widespread reporting of proven porosity, for example through gas adsorption studies, would be difficult to enforce.[2]

Many MOFs have a robust nature which is exemplified in their relatively high thermal stability, with temperatures of 250 ^{o}C to 500 ^{o}C typically being reached before framework collapse is accomplished.[7] MOFs which display high chemical stability have been more difficult to attain due

to the susceptibility of the metal-ligand bonds to replacement from competing ligands or solvent molecules.[7]

The ability to vary both the metal centre and organic ligands within the framework has led to thousands of MOF structures being prepared and studied over recent years.[7] Organic ligands used in MOF synthesis range from charged species such as dicarboxylates and phosphates to neutral electron donors such as N-heterocycles or cyano-based ligands. These ligands in turn can be modified through organic synthesis reactions adding to the breadth of diversity of structures produced. Examples of some organic molecules used in MOF synthesis are given in Figure 1.3.

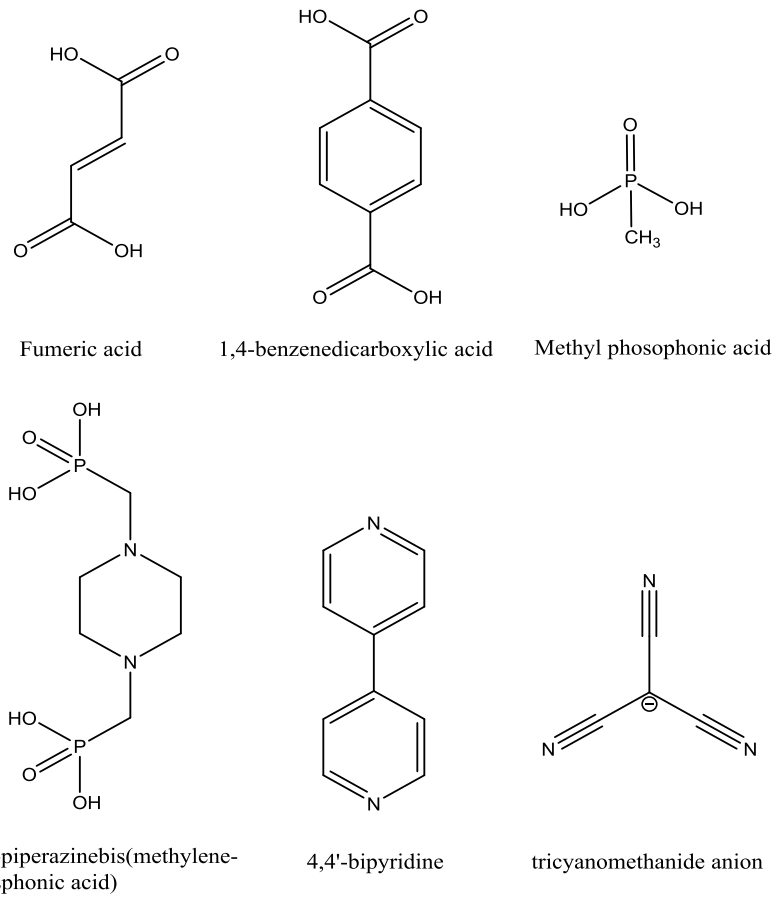

Figure 1.3 Examples of dicarboxylic acids, phosphonic acids, nitrogen-donor N-heterocycles and cyano-based molecules used in the synthesis of MOFs.

The overall structure of a MOF is often complex and is therefore described through a bottom-up approach. This begins by stating the ligand and metal type, describing possible co-ordination modes of the ligands and is followed by a description of the co-ordination environment of the inorganic aggregates which form the nodes of the structure. These are referred to as secondary building units (SBUs) a concept derived from zeolite chemistry. SBUs are formed from metal ions and co-ordinating groups from the ligands. They are often presented through geometric

representations (Figure 1.4).[3] Depending upon the co-ordination of the metal centres and the geometry of the organic ligands, SBUs of different geometries can be formed.[5]

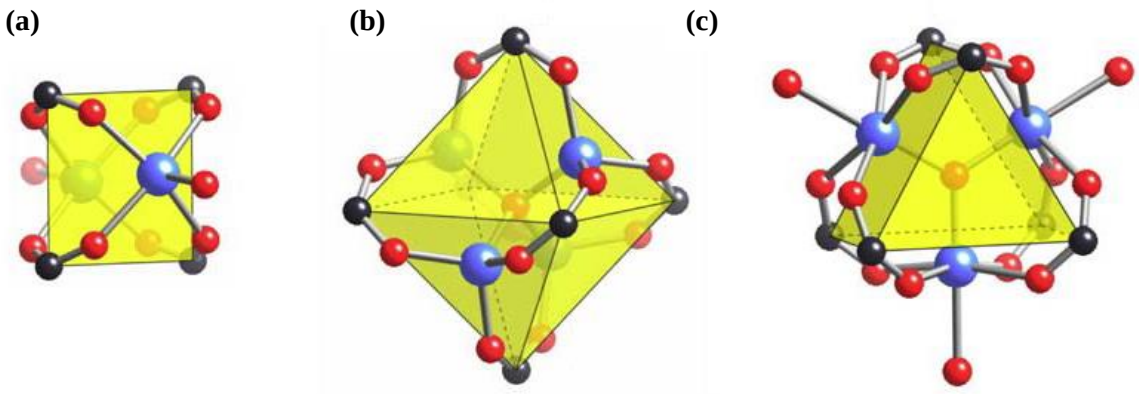

Figure 1.4 Examples of secondary building units (SBUs) commonly occurring in MOFs showing the geometric representations used to describe them. **(a)** a square ‘‘paddlewheel’’ **(b)** an octahedral geometry and **(c)** a trigonal prismatic oxo-centered trimer.[3]

The SBUs are linked together by the organic ligands to form the multidimensional framework of the MOF. The network topologies of MOFs are described through three letter codes assigned by the RCSR (Reticular Chemical Structure Resource). This classification of MOFs based on their ligand and metal types, SBU and net geometries allows the clear communication of often complex structures as well as the direct comparison between MOF structures to be achieved.[8] An example is given in Figure 1.5 showing the ligand structure, SBU geometry and network present in $[Zn_4O(bdc)_3]$ MOF-5.[9] This MOF has an octahedral SBU, $[Zn_4O(CO_2)_6]$, formed from four oxo-centred zinc ions which are bridged by six carboxylate groups. The SBUs are linked by the rod-like bdc linkers to form a **pcu** primitive cubic net.

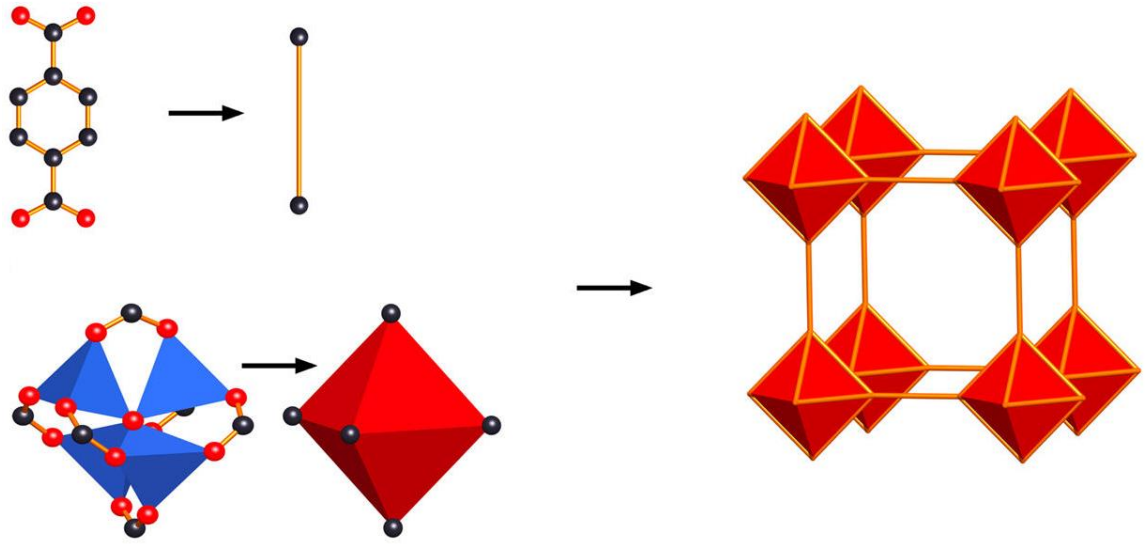

Figure 1.5 The components of $[Zn_4O(bdc)_3]$ MOF-5 showing the rod-like ligand, octahedral SBU formed from $[Zn_4O(CO_2)_6]$ and the cubic net.[10]

The regular repeating units have resulted in an assumption that crystallinity is a criterion for compounds being classified as MOFs.[2, 3, 6] Inherent crystallinity is not a recommendation made by IUPAC, which instead recognises the possibility for the retention of the basic structure and connectivity of a MOF without long range periodicity. More recently, amorphous frameworks have gained attention after being historically overlooked within the field due to the difficulty in structurally characterising these compounds.[11] The lack of long range periodicity means crystallographic techniques are not suitable for the characterisation of amorphous compounds. However, the application of other analysis methods such as Raman spectroscopy is aiding the expansion of amorphous MOF studies.[11]

Much has been made of the possibility for design in MOF chemistry, suggesting that predetermined structures and topologies can be accessed through a careful selection of ligands and metal ions. Although the term 'design' is widely reported there is an important distinction to be made between design and predictability.[12] The process of design infers that a specific form which fulfils an intended function can be created and assumes that the designer has creative freedom over the design.[12] Neither of these definitions of design can be completely fulfilled through the synthesis of MOF structures. Often the constructions of MOFs presented as being designed are structures which were intended, but not guaranteed. Whilst very reliable predictions are possible, the design of MOFs where the outcome is beyond all doubt is still beyond reach. Arguably, this is fortuitous as many unexpected structures have proven to be of great interest.[13] A lack of freedom exists in the creative process of synthetic chemistry, with limiting factors such as the stability of building units and solubility meaning that at best chemists are selecting outcomes from a set of given options, rather than a pure design of the outcome itself.[12]

Reticular synthesis is an example of predictable MOF synthesis, in which the rigidity of the building units (organic ligands) and directionality of the metal-ligand bonding are exploited to assemble products of a predetermined structure.[3,10] This allows systematic alterations to be made to a MOF to alter its functionality or dimensions whilst maintaining its overall network topology. Series of MOFs formed through this process are referred to as isoreticular structures, indicating a commonality in their framework geometries. Following on from the example of network topology in Figure 1.5, it can be shown how reticular synthesis based around MOF-5 can be used to form an isoreticular series of MOFs. As previously described, MOF-5 has octahedral $[Zn_4O(CO_2)_6]$ SBUs which are linked through the organic ligand (1,4-benzenedicarboxylate) to give a **pcu** cubic network. Yaghi and co-workers targeted extended structures based around the topology of MOF-5 by selecting organic ligands which kept similar attributes to 1,4-benzenedicarboxylate in order to form the same framework topology, but were extended in order to alter the dimensions of the resulting framework.[9] Sixteen linear dicarboxylate ligands were selected and were reacted under similar solvothermal conditions to that used to form MOF-5. This resulted in sixteen MOFs being formed, all of which retained the octahedral SBU and **pcu** cubic network of MOF-5 but differed in their framework dimensions and pore sizes (Figure 1.6). This series of MOFs is referred to as the IRMOF-series.

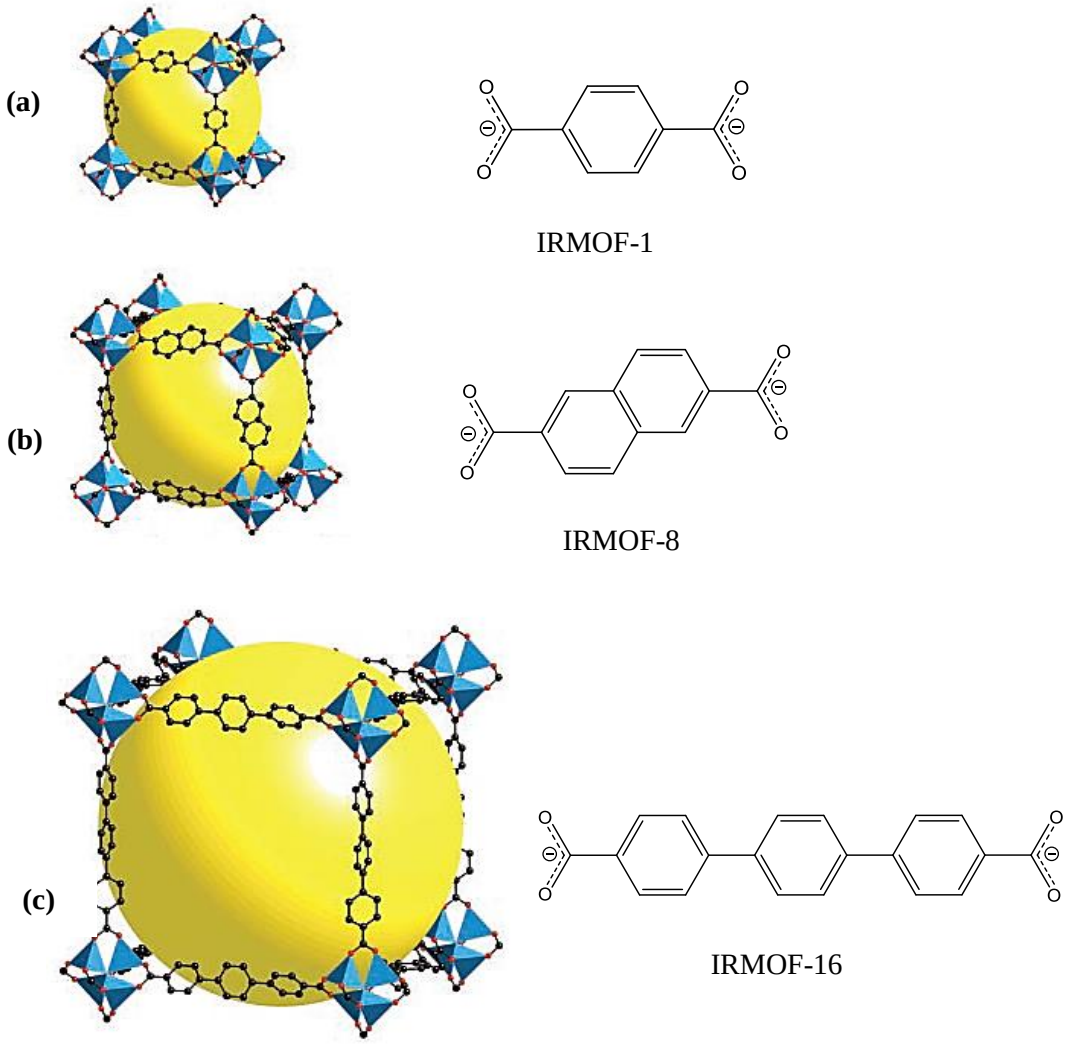

Figure 1.6 Members of the IRMOF series, showing their framework topology and relative pore size represented by the yellow spheres. The dicarboxylate ligand structure is shown below each corresponding framework. **(a)** IRMOF-1 (also called MOF-5) containing 1,4-benzenedicarboxylate ligands **(b)** IRMOF-8 containing 1,4'-naphthalenedicarboxylate ligands and **(c)** IRMOF-16 containing 1,1',4',1"-terphenyl-4,4"-dicarboxylate ligands.[9]

Sequentially extending ligands in length, such as in the IRMOF series described above, can lead to the formation of frameworks which are interpenetrated. Interpenetration, sometimes referred to as catenation, is the interweaving of multiple identical but independent frameworks with one another. The process occurs during self-assembly of the structure and is dependent upon the topology of the framework and lattice size.[14] The degree of interpenetration refers to the number of nets which are interwoven. A schematic representation of two fold interpenetration is given in Figure 1.7.

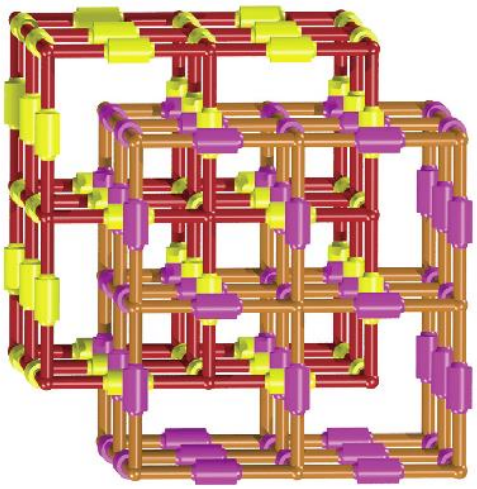

Figure 1.7 A schematic representation showing two identical, independent networks with two-fold interpenetration.[14]

Four of the structures formed as part of the IRMOF series discussed display interpenetrating networks, including IRMOF-15 which is formed from the 1,1',4',1''-terphenyl-4,4''-dicarboxylate ligand.[9] Interpenetration affects the size and shape of pores in the resulting structures, and control of its occurrence has been achieved through a number of methods. Yaghi and co-workers employed dilution to control framework formation in the IRMOF series. The concentration of reactants were reduced during framework synthesis, and IRMOF-16 was obtained, the non-interpenetrating equivalent of IRMOF-15 (Figure 1.6).[9]

Other methods of interpenetration control include the modification of the organic ligand to include sterically bulky functionalities. Telfer and co-workers demonstrated this method in an IRMOF-based structure $[Zn_4O(L)_3]$ (L = biphenyl-4,4'-dicarboxylic acid ligands).[15] When the ligand is modified with a hydroxyl group the MOF synthesis produces a doubly interpenetrated structure. However, when the hydroxyl group is protected by the sterically encumbered 2-nitrobenzyl moiety the reaction synthesis gives an open, non-interpenetrated isoreticular structure (Figure 1.8).

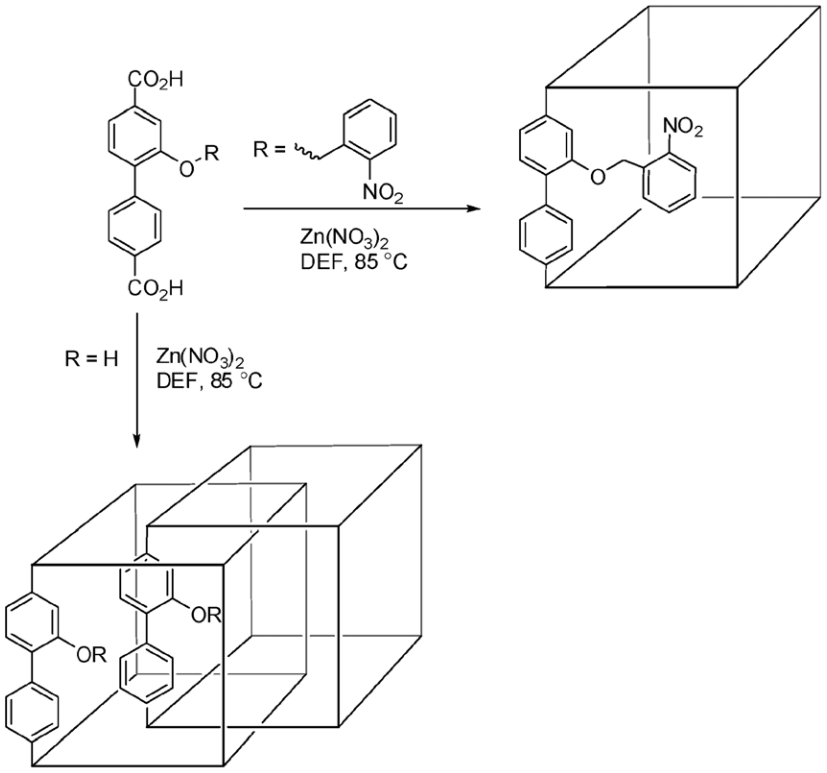

Figure 1.8 Schematic representation of interpenetration control in the $[Zn_4O(L)_3]$ system. The biphenyl dicarboxylate ligand containing a hydroxyl side arm leads to formation of an interpenetrated structure whilst modification of the hydroxyl group to include the bulky nitrobenzyl moiety leads to a non-interpenetrating structure.[15]

A post-synthetic photolytic reaction on the $[Zn_4O(L)_3]$ non-interpenetrated product allowed the cleavage of the O-R bond on the ligand, removing the nitrobenzyl moiety and allowing the non-interpenetrated hydroxyl functionalised structure to be achieved (Figure 1.9).[15] The reaction was achieved through irradiation of the MOF with a 355 nm laser light and a conversion of 50–100 % could be achieved dependent upon the size of the crystals being irradiated.

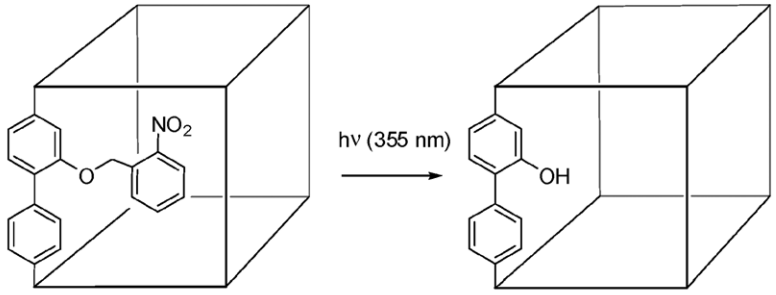

Figure 1.9 Schematic representation of the post-synthetic photolytic reaction of the $[Zn_4O(L)]$ non-interpenetrated product.[15]

Whilst interpenetration of a structure limits its porosity, it can produce structures which have a favourable pore size for gas adsorption or separations. This has been widely studied with the adsorption of CO_2 by interpenetrated MOFs. Zaworotko and co-workers reported two structures of $[Cu(dpa)_2(SiF_6)]$ (dpa = 4,4'–dipyridylacetylene), both displaying the same framework structure but with one being non-interpenetrated and the other displaying two-fold interpenetration.[16] A gas adsorption study on both materials revealed that the interpenetrated structure had a higher CO_2 adsorption than the non-interpenetrated structure, with uptakes of 238 mg/g and 81.3 mg/g respectively.[17] This increase in CO_2 adsorption with interpenetration is thought to be due to stronger interactions between the framework and CO_2 molecules as the interpenetrated structure has small, compact pores.

1.2 Synthesis of MOFs

There are several approaches to MOF synthesis, however all involve self-assembly methods. Most typical synthetic routes involve one step reactions in which the product is precipitated from a solution of dissolved precursors.[3] Convectional heating methods are perhaps the most common, in which organic and inorganic building blocks are combined along with a solvent in a sealed vial or autoclave and heated, often above the boiling point of the solvent used (solvothermal methods), for a given period of time. As many ligands employed are anionic, the solvent used must be basic enough to deprotonate the acid precursor. Advantages of convectional heating methods for MOF synthesis include the relatively low temperatures employed (with a typical range from room temperature to 200 ^{o}C) and scalability, with many systems showing successful increases to industrial scale production levels.[18] Similar reactions in solvent are also reported at room temperature and often require the addition of a base to achieve deprotonation and generate the ligand anions. Differences in the solubility of the organic ligand and inorganic precursors can be an obstacle to such synthetic methods, but have been overcome through careful solvent selection, combining multiple solvents which are miscible with one another and satisfy the required solubility conditions of the ligand and metal components.[19]

An attempt to reduce the timescales of MOF synthesis (typically hours or days) in order to make the materials more attractive for industrial application has seen the development of microwave assisted synthesis of MOFs. This is similar to the convectional heating approach, however the use of microwave heating allows a specific and rapid heating to be used, resulting in much lower reaction times.[20] For example, in the preparation of MOF-5 (see Section 1.1) crystals begin to form after 15-30 minutes under microwave heating compared to 12-24 hours under convection heating.[21] Microwave assisted synthesis is often reported as forming smaller crystals in comparison to the same systems being prepared under typical convectional heating conditions. The microwave preparation of MOF-5 gives crystals of 20-25 μm dimensions compared to 500 μm through the convectional heating synthesis.[21] Often MOFs are prepared through convectional heating methods in order to undergo structural analysis, such as single crystal X-ray diffraction, whilst their preparation through microwave assisted heating is then used for a more rapid production.

Another synthetic method which can reduce reaction times of MOF synthesis is that of grinding. Grinding also allows solvent free synthesis or the use of only small quantities of solvent (10-100 μL) and can be carried out in a pestle and mortar or in a ball mill.[22] Ball mills are vessels which contain a ball bearing. Upon addition of the reactants the vessel is sealed and shaken in rapid side-to-side or rotation motions which cause the ball bearing to impact the contents and vessel walls, or grind in a friction motion along the vessel walls. The kinetic energy from this grinding motion causes heating and a collision of reactant particles resulting in the formation of the MOF product.[22] Both amorphous[11] and crystalline[23] MOFs being synthesised through ball mill methods are known.

The desirability for highly crystalline products, particularly single crystals which are suitable for single crystal X-ray diffraction analysis, has led to some reports favouring solvent diffusion methods of synthesis over the more typical solvothermal routes described above. These techniques are similar to those used to grow crystals of inorganic salts. Typically slow diffusion methods involve dissolving the organic and inorganic components of the system in two separate solvents, which are miscible but have differing densities. The resulting solutions are then layered, with the higher density solvent forming the bottom layer. The two solutions are left to slowly combine over time. The slow rate at which the precursors are combined aims to increase the nucleation time and allow single crystals to form.[3] These methods are often successful in forming crystalline products which can be analysed through single crystal X-ray diffraction methods and have typical crystallisation times ranging from weeks to months.

1.3 Gas adsorption studies of MOFs

1.3.1 Activation methods

One of the main reasons MOFs have continued to gain increasing attention is due to their porosity. The porosity of a material can be classified into three categories. Microporous materials contain pores with a diameter of less than 2 nm, mesoporous materials with pore diameters ranging from 2-50 nm and macroporous materials which are those with pore diameters of greater than 50 nm. MOFs have been shown to display a range of pore sizes from microporous to mesoporous. Some MOFs with exceptionally high porosity have been termed as having ultrahigh porosity, exceeding the porosity of many zeolite compounds.[7] There is also a wide range of pore geometries including one-dimensional channels and three-dimensional cavities.[24]

In order for MOFs to be utilised in gas storage, the guest-free form of the MOF must first be accessed. After synthesis, MOFs typically contain solvent guest molecules within the pores. The removal of these guest molecules is known as activation, and if successful leads to the guest-free structures in which the pores are empty.[25] This is often a difficult and challenging process, as not all MOF structures have been found to be stable in the absence of guest molecules. The ability for a MOF to maintain often large, empty cavities in its guest free form is referred to as exhibiting permanent porosity.[26] Several activation methods have been developed, perhaps the most common of which is that of heating under vacuum. This method is possible due to the relatively high thermal stability of most reported MOFs. An example of successful activation through this method is that of $[Zr_6O_4(OH)_4(bdc)_6]$, UiO-66 (where bdc is 1,4-benzenedicarboxylate). UiO-66 is thermally stable up to 540 ^oC and is activated by heating at 300 ^oC under vacuum for 1 hour.[4] The experimentally measured surface area of 1187 m^2/g matches that of the calculated surface area from the crystal structure, confirming that the removal of all guest molecules has successfully been achieved.[4]

Another commonly used method of activation is that of solvent exchange.[25] The solvent within the pores of the MOF is exchanged with a solvent of lower boiling point, such as chloroform, by repeated replacement of the solvent over multiple days.[25] Activation is then achieved through heating under vacuum as in the previous method but the removal of a lower boiling point solvent allows milder conditions to be used. It is a particularly useful technique if the structure originally contains solvents of high boiling point, such as *N*,*N*-dimethylformamide, DMF, which is commonly used in MOF synthesis, or if the MOF has a lower thermal stability than the boiling point of the solvent in the pores. Solvent exchange methods have been shown to achieve measured surface area values closer to those predicted from crystal structure or simulation data compared to activation carried out on samples which haven't undergone solvent exchange. An example of this is for $[Zn_4O(bdc\text{-}NH_2)_3]$ (IRMOF-3, bdc-NH_2 = 2-amino-1,4-benzenedicarboxylate).[27] Samples of IRMOF-3 were activated through heating at 110 ^oC under vacuum or through solvent exchange, exchanging DMF in the pores for chloroform, and heating at 25 ^oC under vacuum. The sample

which did not undergo solvent exchange had a measured surface area of 10 m^2/g whilst the sample undergoing solvent exchange activation had a measured surface area of 1800 m^2/g.[27] This example shows how solvent exchange can lead to more successful evacuation of the pores at lower heating temperatures compared to activation occurring without solvent exchange.

An extension of the solvent exchange method is activation with supercritical CO_2. This method is useful in cases where solvent exchange is unsuccessful or leads to framework collapse as it offers a milder route to activation through which the liquid to gas phase transformation within the pores is avoided.[28] The MOF first undergoes a solvent exchange with a solvent miscible with supercritical CO_2. Excess solvent is removed and the MOF is then cooled to 2-10 ^oC before a further solvent exchange with liquid CO_2 in a supercritical dryer. The MOF is finally heated in a chamber to the supercritical temperature and pressure of CO_2 and the dryer slowly vented to achieve the activated MOF.[28] Another technique aiming to avoid the liquid to gas phase transition of solvent activation is that of freeze-drying.[25] In this method the sample undergoes solvent exchange with a solvent (often benzene) and is then frozen to 0 ^oC and warmed to room temperature. This cooling and heating cycle is repeated multiple times and on the last heating cycle is also placed under vacuum and held at a temperature and pressure below the triple point of the solvent. As it warms, the benzene sublimes (converting from a solid to gas).[25]

1.3.2 Surface area measurements

Once activated, MOFs can undergo gas adsorption studies to determine their surface area. This is usually done through the measurement of nitrogen adsorption isotherms from which the surface area can be calculated. Adsorption can occur through physisorption or chemisorption. In physisorption weak Van der Waals' forces exist between the adsorbate (gas) and the surface of the solid. In chemisorption the interactions between adsorbate and solid surface involve the formation of a chemical bond. Physisorption allows reversible adsorption and desorption to occur making it of interest to the study of MOFs for further applications.

During the adsorption experiment, a known amount of the adsorbate (typically nitrogen gas) is introduced to an evacuated chamber holding the adsorbent (MOF) at constant temperature (the standard being 77 K for nitrogen adsorption). A reduction in the pressure of the chamber occurs as the gas is adsorbed onto the surface of the MOF until equilibrium is reached.[29] The amount of gas adsorbed at this equilibrium pressure can then be measured. Successive amounts of gas are admitted into the chamber in this manner to build up a series of data points. These results are displayed in graphical form plotting amount of gas adsorbed (mol/g) against the equilibrium relative pressure (p/p^0, where p^0 is the saturation pressure after which no further adsorption is achieved).[29] These graphical representations of adsorption data are called isotherms.

Six main types of isotherms have been identified by IUPAC and are used to classify particular pore structures or adsorption behaviours. Further additions of isotherm types have been made in recent years and these are discussed in Section 3.1.2. For clarity, the original six isotherm types are presented here in Figure 1.10.[29]

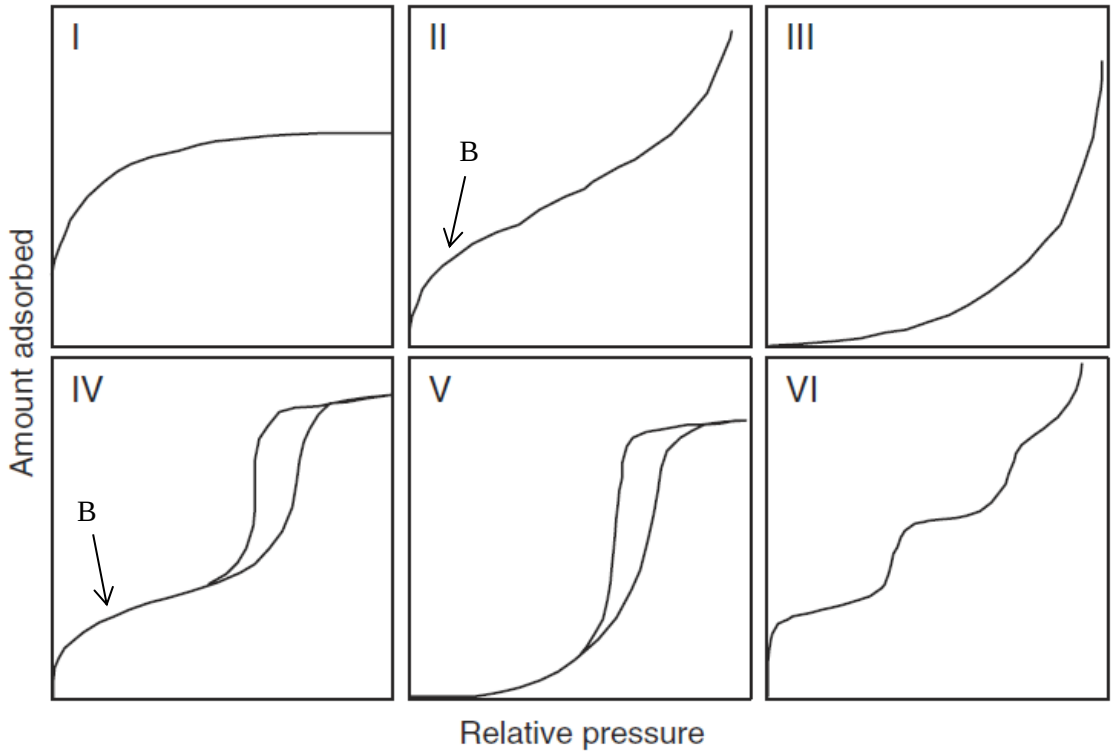

Figure 1.10 Types of adsorption isotherm as classified by IUPAC recommendations.[29, 30] Point B in type II and IV isotherms indicates the point at which monolayer coverage is achieved.

Materials displaying type I isotherms are typical of microporous solids. The amount of gas adsorbed approaches a limiting amount at low relative pressure, indicating small accessible micropores. The type II isotherm indicates a non-porous material. Point B indicates the point at which monolayer coverage (surface coverage with the gas adsorbate one atom thick) is achieved. The progressive increase is due to multilayer formation of the adsorbate on the surface of the non-porous material, which is unrestricted and continues without reaching a limit to a high relative pressure. Type III isotherms also occur for non-porous solids. In this case there is no point B, and therefore no point at which monolayer coverage is achieved. This is because materials exhibiting type III isotherms have weak adsorbate-adsorbent interactions, and the gas molecules cluster at the most favourable sites on the surface.

Type IV isotherms have a distinctive S-shaped curve. The first stage at low relative pressure is similar to that of type II isotherms, with a steep uptake followed by a plateau indicating monolayer coverage (point B). Type IV isotherms can be indicative of mesoporous materials or some

microporous solids. Following the monolayer coverage a steep uptake in adsorbate can be seen followed by a limit at high relative pressure. This behaviour is typical of capillary condensation. Capillary condensation occurs when the gas in the pores of the adsorbent condense into liquid below the saturation pressure of the bulk liquid.[29] Capillary condensation can be described by thinking of the pores within the material in question being cylindrical in shape with open ends.[30] After monolayer formation of the gas on the surfaces of the pores, multi-layer formation begins to occur until the equilibrium vapour pressure within the cylindrical pores increases to the point at which it is equal to the saturation vapour pressure of the gas. At this point spontaneous condensation occurs.[30] A schematic depiction of capillary condensation is given in Figure 1.11.

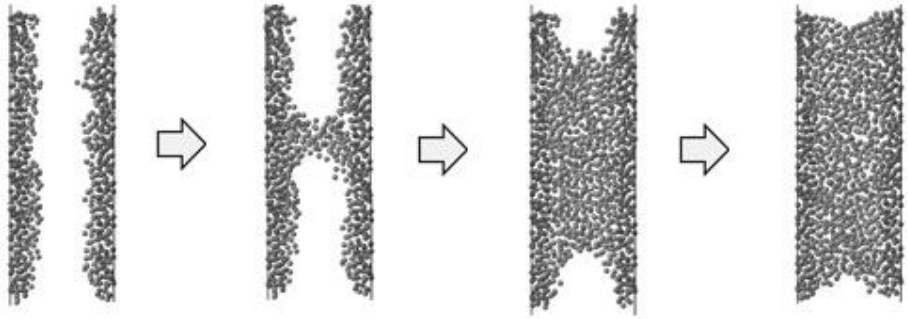

Figure 1.11 Schematic representation of capillary condensation mechanism for pore filling.[31]

Pore filling through capillary condensation can be identified by a difference in the adsorption and desorption isotherms known as hysteresis. Desorption of the condensed gas within the pores occurs at a lower relative pressure in comparison to the adsorption of the gas, resulting in the observed hysteresis loop (refer to Figure 1.10). Type V isotherms also display hysteresis loops and are typical of water adsorption in hydrophobic mesoporous materials. At low pressure the isotherm is similar to that of the type III isotherm – indicating weak adsorbate-adsorbent interactions. With increasing pressure the water molecules cluster in the mesopores and instead of the multilayer formation observed in type III materials, capillary condensation occurs.

The final classification is type VI isotherms, which are often referred to as layering isotherms. They represent a layer by layer adsorption typical of uniform non-porous materials. Each step in the isotherm represents a new layer formation.[29] The interpretation of isotherms can be difficult and in reality compounds are rarely homogeneous in their pore types, having a range of pore sizes and geometries.[32]

The standard method for calculating the surface areas of MOFs from nitrogen adsorption isotherms is the Brunauer–Emmett–Teller (BET) method. The BET method of surface area calculation determines the amount of gas required to cover the external and accessible internal pores. It

assumes that adsorption occurs through monolayer followed by multilayer adsorption. The BET equation is given below (Equation 1.1).[33]

$$\frac{1}{X\left(\left(\frac{p}{p^0}\right)-1\right)} = \frac{C-1}{X_m C}\left(\frac{p}{p^0}\right) + \frac{1}{X_m C}$$

Equation 1.1 Brunauer–Emmett–Teller equation

X is the amount of gas adsorbed at relative pressure p/p^0, X_m is the amount of gas required to form a monolayer and C is the BET constant. The value of C is related to the heat of adsorption of the first layer of molecules, E_1, and therefore provides information on the strength of the adsorbate-adsorbent interactions (Equation 1.2).[34]

$$C = \exp\left(\frac{E_1 - E_L}{RT}\right)$$

Equation 1.2 The BET constant, C. E_1 is the heat of adsorption for the first layer of adsorbed molecules, and E_L is the heat of adsorption for subsequent layers of adsorbed molecules.

To calculate the BET surface area of a material, the adsorption isotherm must first be converted into a BET plot. This is a plot of $1/(X((p/p^0)-1))$ versus p/p^0. The plot is normally linear in the low pressure region (p/p^0 typically 0.05 to 0.30) which is equivalent to the monolayer coverage region.[34] From this linear plot the slope and intercept can be obtained, which are derived from Equation 1.1 and given in Equation 1.3.

$$\text{slope} = \frac{C-1}{X_m C} \qquad \text{intercept} = \frac{1}{X_m C}$$

Equation 1.3 Slope and intercept of the BET plot

From the relationship of the slope and intercept equations, the values of the monolayer coverage, X_m, and the BET constant, C, can be calculated (Equation 1.4).

$$X_m = \frac{1}{s+i} \qquad C = \frac{s}{i} + 1$$

Equation 1.4 Calculation of monolayer coverage, X_m and the BET constant C from the slope s and intercept i of the BET plot.

The surface area can now be calculated using Equation 1.5.

$$S = \frac{X_m N_A A_M}{M}$$

Equation 1.5 Surface area calculation using the BET method

N_A is Avagadro's number, M is the molecular weight of the adsorbate gas and A_M is the average area the adsorbate gas occupies in the monolayer coverage (cross-sectional area) which can be calculated from the gas's density.[34] For nitrogen gas the value of A_M is 0.162 nm^2 assuming close packing of the molecules.[29]

The BET method of surface area calculation relies on a number of assumptions, many of which have been criticised.[29, 33] One basic assumption is that the compounds studied have homogeneous surface areas, in other words that the adsorption sites on the surfaces are all equivalent. The BET method also assumes that after a certain vapour pressure, the formation of a monolayer is complete and subsequent molecules are stacked on top of this first layer to form multiple layers.[34] In reality, the formation a monolayer prior to multilayer formation does not occur. Instead it is likely that adsorption of gas molecules onto already adsorbed molecules occurs whilst monolayer formation is incomplete.[33] Another assumption of the BET method is that molecules in all layers except the first have heat of adsorption and condensation values equivalent to those of the bulk liquid. This is more likely to be true for layers far away from the surface of the adsorbent than it is for layers close to the first monolayer on the adsorbent.[33]

Despite these and other assumptions the BET method for surface area calculation has been highly successful for nonporous and mesoporous solids.[29] In the case of microporous solids, the application of the BET method can be misleading.[35] This is because the adsorption in microporous materials occurs through a pore filling rather than a multi-layer process. This can result in difficulty obtaining the linear section of the BET plot corresponding to monolayer formation. In these cases, the surface area calculated by BET methods can still be used, but should be regarded as an apparent surface area, rather than a realistic surface area which can be useful for fingerprinting the surface areas of microporous materials.[29] Reported surface areas of MOFs typically range from 1,000 m^2g^{-1} to 7,000 m^2g^{-1}.[7]

1.4 Properties and applications

1.4.1 Adsorption

The range of pores available to MOF chemists, often with high surface areas, makes them ideal candidates for gas storage.[7, 37] The adsorption of hydrogen by MOFs has gained particular attention. Hydrogen is a potential energy source and an effective and safe storage mechanism is required to ensure its use is feasible. Currently hydrogen gas is stored in compressed systems which is energetically costly and requires the use of heavy pressurised cylinders.[36] An alternative storage mechanism is therefore sought which could operate under ambient pressures.

Amongst the MOFs displaying the highest hydrogen uptake is $[Zn_4O(btb)_2]$, MOF-177 (btb = 1,3,5-tris(4-carboxyphenyl)benzene) which has shown an uptake of 7.6 wt% (percentage by mass) at 77 K and 70 bar.[38] Although the aim is find materials which can effectively store hydrogen at ambient conditions this is still a distance from being achieved and measurements at increased pressure or low temperature are useful indicators of the adsorption performance of a material.[38] MOF-177 has a high surface area of 4500 m^2/g, and there is evidence of a positive correlation between the surface area of a MOF and its gas uptake ability. Nevertheless, pore size is not always an indicator of hydrogen storage ability, and cases of MOFs containing small pores whilst exhibiting high uptakes have been found. This is exemplified in the case of $[Cu_3(btc)_2]$, HKUST-1 which contains multiple pore types (Figure 1.12). Upon the adsorption of hydrogen, the smaller pores are filled prior to the larger pores.[38] It is thought that stronger interactions between the framework and the H_2 molecules within the smaller pores contribute to this effect. Smaller pores have interactions between multiple pore walls and the same H_2 molecule, enhancing the binding in comparison to the larger pores which form interactions between only one pore wall and the hydrogen molecule.[38]

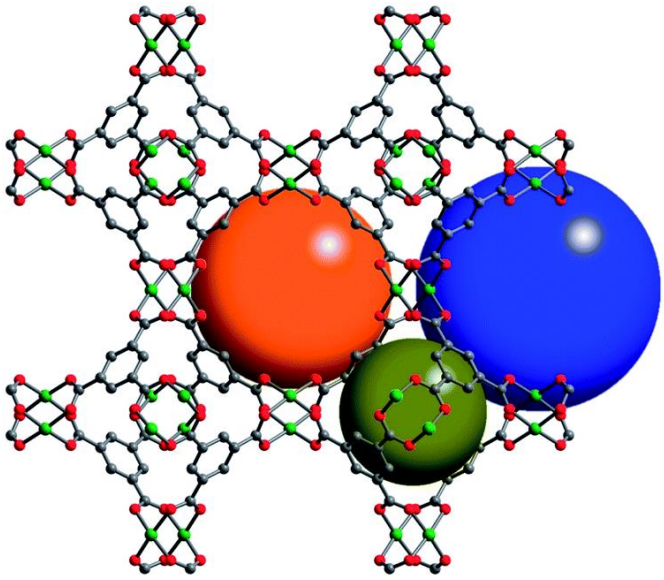

Figure 1.12 Framework of $[Cu_3(btc)_2]$, HKUST-1 showing the three distinctive pore types with diameters of approximately 5 Å (green), 11 Å (orange), and 13.5 Å (blue).[39]

The adsorption of CO_2 by MOFs has been widely studied due to the drive to reduce rising CO_2 levels in the atmosphere.[26] Carbon dioxide adsorption in MOFs has been found to be improved by the presence of open metal sites in the framework.[40] Open metal sites are the unsaturated co-ordination sites of metal centres in the framework, and can be accessed through the removal of terminally bound solvent molecules on metal centres. This occurs during the activation process, when the solvent in the pores is also removed. Open metal sites provide charge-dense binding sites for the adsorbed CO_2 molecules, increasing the affinity for CO_2 uptake.[40] An example can be seen in $[Cr_3O(H_2O)_2F(BDC)_3]$, MIL-101, a chromium-based MOF containing terminal H_2O molecules.[41] A CO_2 uptake of 40 wt% at 50 bar and 304 K was recorded for this activated material.[40] The presence of open metal sites in a framework can also increase selective adsorption of CO_2 in a mixture of gases, such as a CO_2/N_2 mixture. The open metal site has a greater affinity for the polarisable CO_2 molecules over the N_2 molecules, leading to selective adsorption. This was found to be the case in MIL-101 which demonstrated a high CO_2 selectivity over N_2, as can be seen in Figure 1.13.

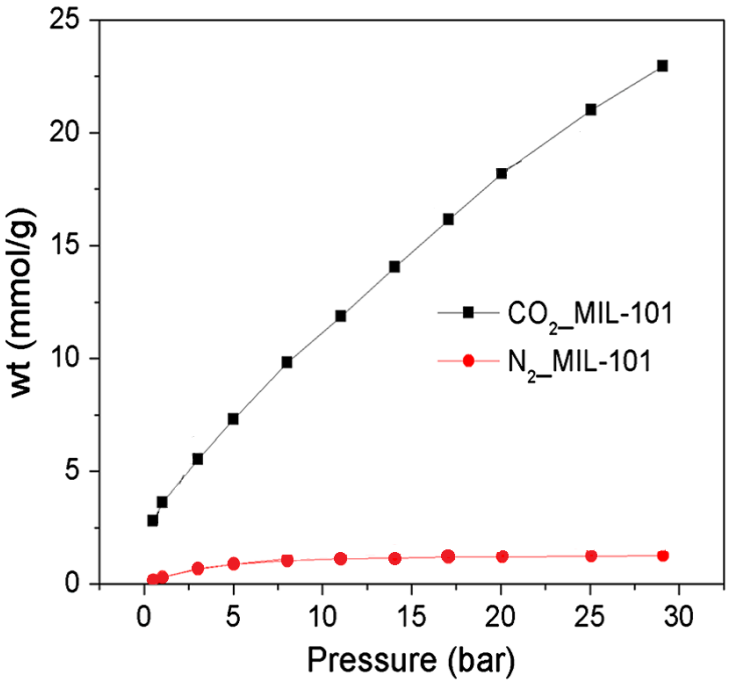

Figure 1.13 CO_2 and N_2 adsorption of activated MIL-101 at 298 K.[42]

Removal of harmful gases such as CO_2 from the atmosphere by adsorption is not the only way MOFs can be used to capture hazardous materials. Harmful compounds such as organic pollutants or heavy metals can also be adsorbed into the pores of MOFs allowing them to be removed from liquid mixtures. $[Fe_3O(bdc)_3(DMF)_3][FeCl_4]$, MOF-235, has been used to adsorb organic dyes from aqueous solutions.[43, 44] The dyes adsorbed include the anionic dye methyl orange and the cationic dye methylene blue (Figure 1.14). Both dyes are known to be toxic and are widely used in the textile and pharmaceutical industries.

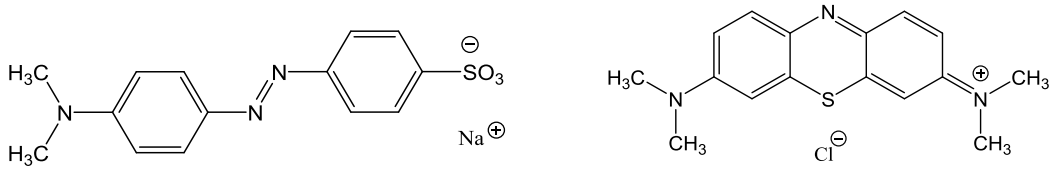

methyl orange **methylene blue**

Figure 1.14 Structures of the Methyl Orange and Methylene Blue organic dyes.[44]

MOF-235 is itself a cationic framework, holding a +1 charge per unit formula $[Fe_3O(bdc)_3(DMF)_3]^+$. It is charge balanced through the presence of $FeCl_4^-$ anions within the pores of the framework. The adsorption capacity of MOF-235 for the methyl orange has been shown to be 477 mg/g and for methylene blue 187 mg/g. The unusual ability for the MOF to adsorb both anionic and cationic dyes has been proposed to be due to electrostatic interactions between the dye and the adsorbent, with anionic dye molecules interacting with the cationic framework, and cationic dye molecules interacting with $FeCl_4^-$ anions within the pores of the framework.[44]

The growth of the nuclear industry to support an increasing global energy demand raises the challenge of radionuclide extraction from water streams. Lin and co-workers have shown that modifications to the ligands in $[Zr_6O_4(OH)_4(L)_6]$ (L = dicarboxylate ligand) to contain diethoxyphosphorylurea moieties have shown promise in the adsorption of uranium from aqueous solution.[45] The $[Zr_6O_4(OH)_4(L)_6]$ frameworks have a UiO-68 topology, with open pores which can include guest molecules up to 10 Å in diameter. Three MOFs were formed, two containing phosphorylurea groups and one without phosphorylurea groups as a control. The structures of ligands used are given in Figure 1.15.

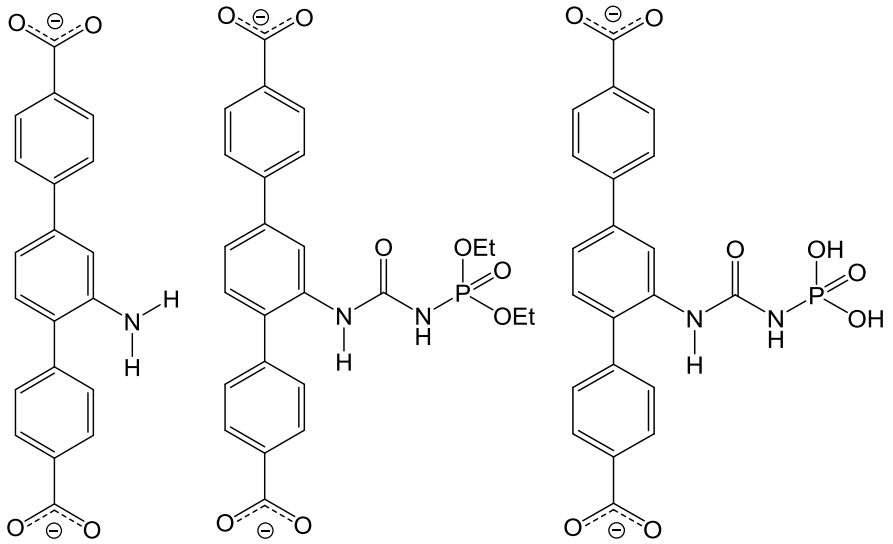

Figure 1.15 Structures of the ligands used to form MOFs isoreticular to UiO68 for the extraction of uranium from solution.[45]

Each MOF was formed by combining the ligand with zirconium chloride and benzoic acid in DMF and heating the solution at 70 ^{o}C for 3 days. Once formed the MOFs were placed in aqueous solutions of uranyl acetate ($UO_2(CH_3COO)_2$) and shaken at room temperature for 1 hour. The solutions were then centrifuged and the MOFs were analysed for uranium content. MOFs containing the ligands with phosphorylurea groups displayed a near quantitative uptake of uranium from the solutions whist the MOF without the phosphorylurea group showed no uranium uptake.[45] This study shows the potential for phosphorylurea containing MOFs to be used to extract radio nuclei such as uranium from solution.

1.4.2 Catalysis

MOFs have been widely investigated for their potential as heterogeneous catalysts. Heterogeneous catalysts are particularly attractive as they are easily recoverable post-reaction. They are widely used in industry and currently the inorganic porous materials, zeolites, are the most commonly used catalysts in industry.[46] MOFs have some potential advantages over zeolites, such as their high surface areas, tuneable pore sizes and wide variety of organic ligands.[47] These features have led to the exploration of MOFs as potential heterogeneous catalysts.

Many metal ions play key roles within catalytic reactions. The exploitation of metal ions within MOFs for catalysis has therefore become one of the most common approaches to using MOFs as heterogeneous catalysts. Many MOFs contain metal ions with weakly bound solvent molecules which can be easily removed upon heating (see Section 1.4.1). The removal of these solvent molecules leaves unco-ordinated metal sites which can act as catalytic sites.[47] $[Cr_3X(H_2O)_2O(bdc)_3]$, MIL-101 (X = F, OH, bdc = 1,4-benzenedicarboxylate) is a chromium-based MOF with octahedral SBUs containing water molecules. Upon heating under vacuum the water molecules can be removed, leaving unsaturated chromium sites within the framework. MIL-101 containing these unsaturated sites has been shown to be an effective catalyst for the cyanosilylation of benzaldehyde, with a 98.5 % product yield after 3 hours (Figure 1.16).[48] The high porosity and thermal stability of MIL-101 makes it an attractive candidate for catalytic study.

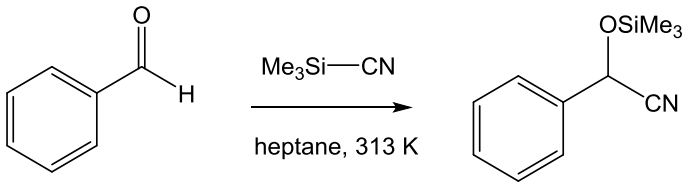

Figure 1.16 A schematic representation of the cyanosilylation of benzaldehyde.

It is not only metal sites within MOFs which can be exploited for catalysis, catalytically active organic ligands can also be incorporated into the framework.[47] This has been well demonstrated by Kitagawa and co-workers who incorporated free radical sites within the pores of a MOF through the inclusion of the dpio (4,7-bis(4-pyridyl)-1,1,3,3-tetramethylisoindolin-2-yloxy) ligand containing a pyrroline nitroxide stable radical (Figure 1.17).[49] The resulting MOF, $[Cu(dpio)_2(SiF_6)]$, was used in the catalytic conversion of multiple alcohols to ketones or aldehydes. Alcohols employed include benzyl alcohol, substituted benzyl alcohols and aliphatic alcohols a selection of which are shown in Figure 1.17.

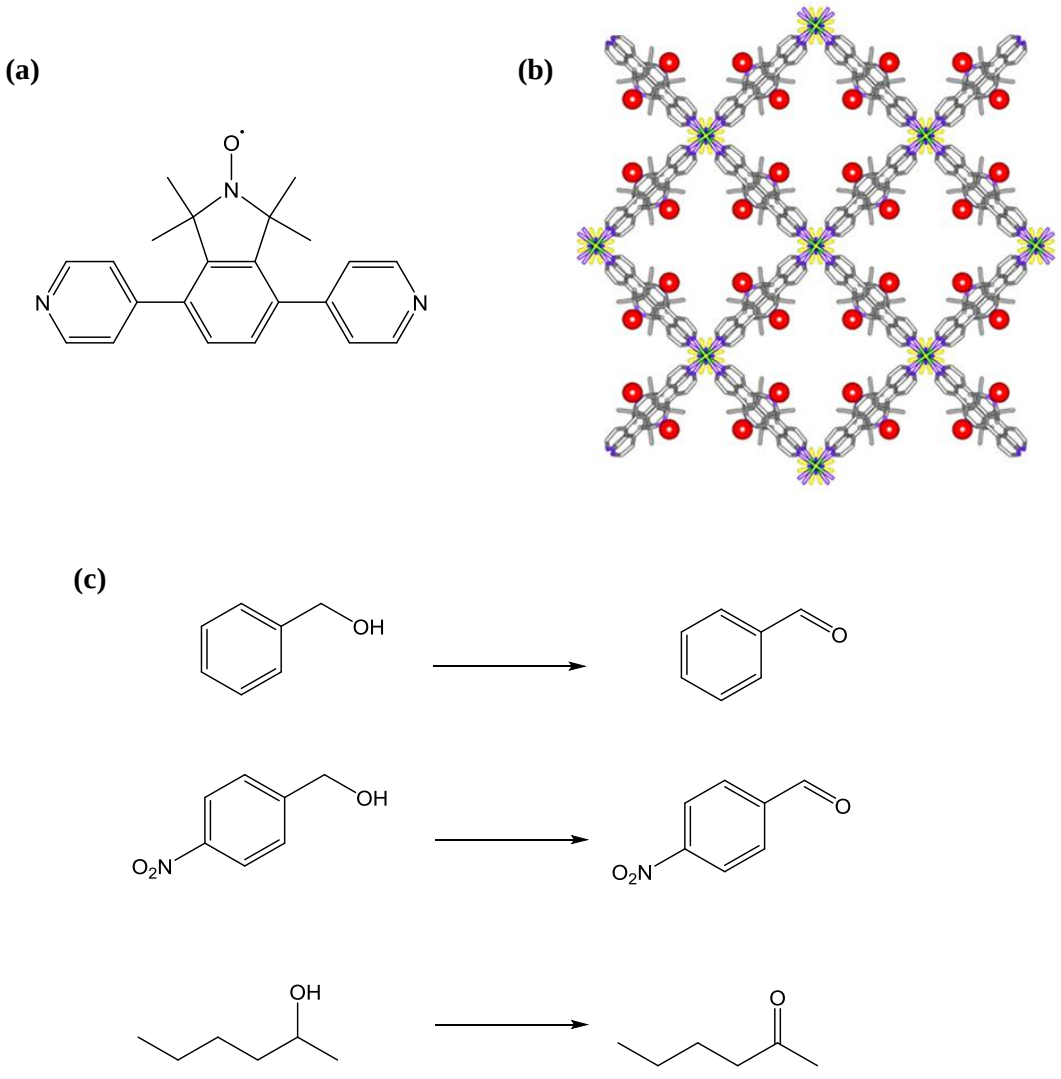

Figure 1.17 (a) Structure of the dpio ligand **(b)** crystal structure of $[Cu(dpio)_2(SiF_6)]$ viewed along the *c* axis, with oxygen atoms of the pyrroline nitroxide radical shown as red spheres and **(c)** examples of the catalysed oxidation reactions performed.[49]

The high surface areas of many MOFs mean that catalytically active compounds can be encapsulated within the pores of the framework. The heteropolyanion compounds $[PW_{11}CoO_{39}]^{5-}$ and $[PW_{11}TiO_{40}]^{5-}$ are known oxidation catalysts and were incorporated into the pores of MIL-101, $[Cr_3F(H_2O)_2O(bdc)_3]$.[50] Catalytic activity of the resulting host-guest compounds were tested on the oxidation of alkenes in the presence of H_2O_2 and O_2 and were shown to behave as heterogeneous catalysts, with no leaching of the catalyst during the reaction. This demonstrates the potential for MOFs to act as an effective inorganic matrix for catalytic guest molecules.[50]

1.4.3 Flexible MOFs

Unlike other inorganic porous materials such as zeolites, many MOFs exhibit framework flexibility and dynamic behaviour.[51] There are several possible reasons for framework flexibility in MOFs, including the use of flexible organic ligands, the multiple possible co-ordination modes and geometries of metal ions and interpenetrating nets which can move relative to one another. Flexibility can arise from an expansion or shrinkage of the framework, an opening or closing of pores within the structure or by bond formation or cleavage.[52] These behaviours often occur in response to external stimuli such as temperature, pressure or the presence of guest molecules within the framework.

Several types of framework flexibility can be classed as guest-induced responses, where reversible structural changes occur in response to the adsorption of a type of guest molecule including breathing, swelling and linker rotation. Breathing is a type of framework flexibility in which the adsorption or desorption of a guest molecule causes displacement of the atoms within the framework resulting in a change in the unit cell volume. This is accompanied by a change in the unit cell shape and the crystallographic space group.[53] Many MOFs displaying breathing behaviour have a 'wine-rack' type topology, in which adsorption or desorption of the guest results in the increase of one crystal dimension and an overall reduction in unit cell volume.[54] Such behaviour is termed non-linear compressibility.[55] $[Zn_2(bdc)_2(dabco)]$, DMOF-1, is an example of a MOF which displays the wine-rack motif and undergoes breathing flexibility upon adsorption of guest molecules within its pore (Figure 1.18). In its guest-free state (containing no guest molecules within the pore) DMOF-1 has a square grid topology and crystallises in a tetragonal space group. Upon adsorption of benzene guest molecules into the pores the framework undergoes a structural transition, resulting in a rhomboidal grid topology, reduced unit cell volume and a change from tetragonal to orthorhombic space group.[56]

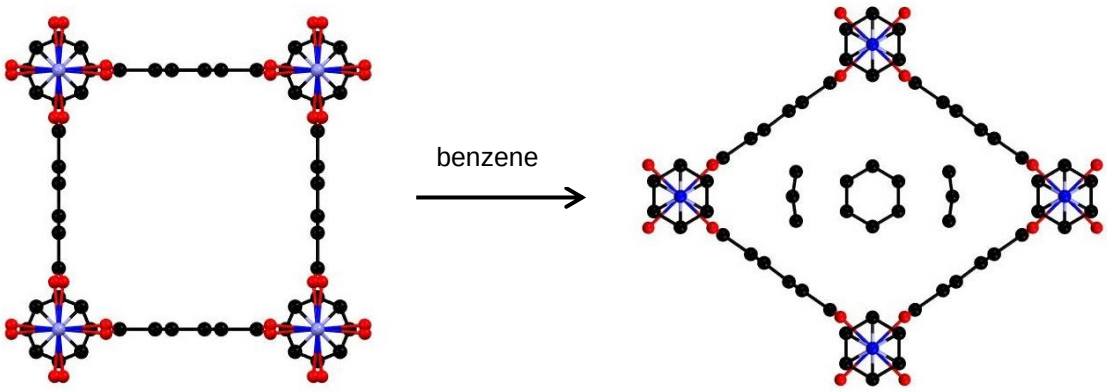

Figure 1.18 The breathing behaviour of $[Zn_2(bdc)_2(dabco)]$, DMOF-1, showing the guest free framework (left) and the change of the pore shape and size upon adsorption of benzene molecules (right).[56]

The flexible behaviour of swelling is characterised by the enlargement of the unit cell of the MOF upon adsorption of a guest molecule. However, unlike the breathing phenomenon there is no change to the unit cell shape or crystallographic space group of the MOF upon the swelling behaviour.[53] A MOF displaying characteristic swelling behaviour is $[Fe_3O(MeOH)(bdc)_3]CH_3CO_2$, MIL-88 (Figure 1.19).[57] Upon adsorption of polar guest molecules, such as ethanol, methanol and water, the pores of MIL-88 expand. This is demonstrated in an increase of the unit cell parameters upon adsorption of the guest molecules, with the *a*-axis increasing from 9.26 Å in the guest-free, dried form to 13.07 Å upon ethanol adsorption, 13.78 Å upon methanol adsorption and 13.87 Å in the hydrated form.[57] The formation of hydrogen bonds between solvent molecules and the framework are thought to aid the expansion of the pore channels, which occurs through a rotation of both the metal trimeric SBU and the bdc ligand (Figure 1.19).

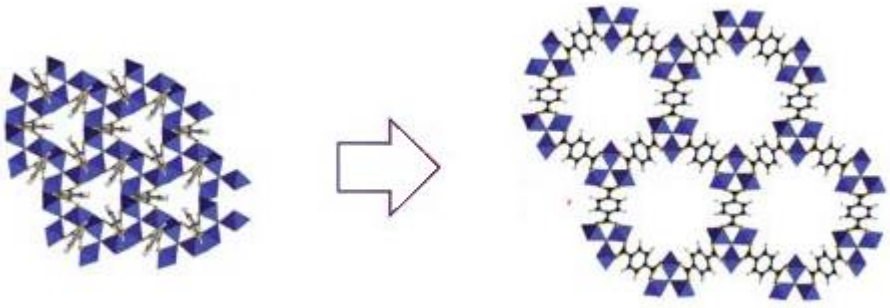

Figure 1.19 View of closed, guest-free (left) and solvent included, open (right) forms of $[Fe_3O(MeOH)(bdc)_3]$, MIL-88. Metal trimeric SBU, carbon atoms, and hydrogen atoms are in blue, black, and gray, respectively. Guest molecules and hydrogen atoms are omitted for clarity.[58]

Linker rotation is another guest-induced flexibility, in which the rotation of the ligand can induce a change to the accessible pore size.[53] This complex type of framework flexibility can be

demonstrated through the example of $[Cd_2(pzdc)_2(BHE\text{-}bpd)]$ (pzdc = 2,3-pyrazinedicarboxylate and BHE-bpb = 2,5-bis(2-hydroxyethoxy)-1,4-bis(4-pyridyl)benzene).[59] The alkyloxy-functionalised pyridyl ligands within the framework contain OH-groups which interact with neighbouring pyridyl ligands effectively causing a gating of the pore, blocking guest-molecules from being adsorbed. However, polar molecules interact with the metal centres of the framework, resulting in a rotation of the gating ligands and allowing adsorption to occur (Figure 1.20). MOFs which exhibit this type of flexibility can therefore selectivity adsorb polar over non-polar molecules.

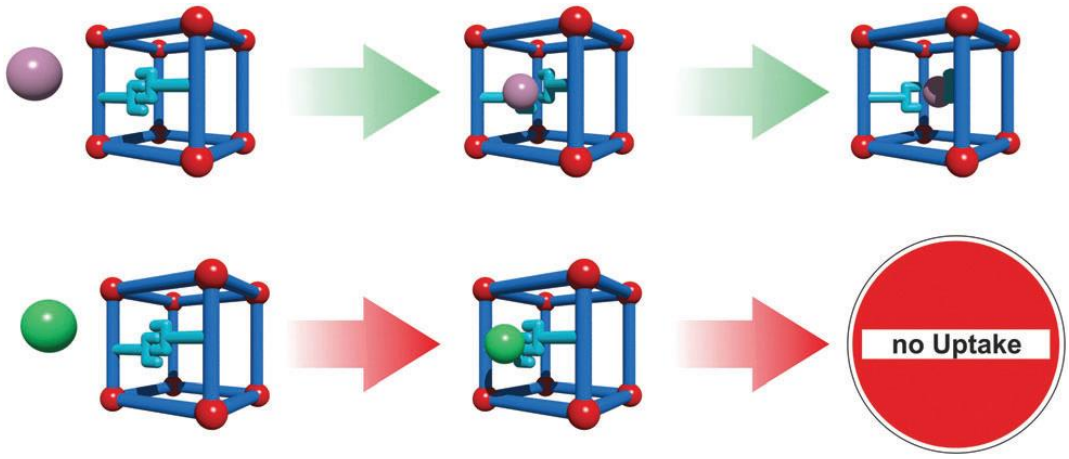

Figure 1.20 Schematic representation of the linker rotation mechanism in $[Cd_2(pzdc)_2(BHE\text{-}bpd)]$. The purple sphere represents a polar guest molecule, whilst the green sphere represents a non-polar molecule. Interaction of the polar molecule with the framework results in a rotation of the gating ligands and adsorption into the pores. Non-polar molecules are not adsorbed into the pores.[53]

Not all flexible behaviours are guest-induced, and many MOFs exhibit reversible structural transformations upon the presence of other external stimuli such as temperature, pressure and light. Thermal expansion is a similar flexible behaviour to that of swelling, with an increase (or in the case of negative thermal expansion, decrease) in the unit cell volume upon heating of the MOF.[53, 55] Increasingly, high pressure studies are being conducted on MOFs which show pronounced phase-transitions under increased pressure.[55] High pressure studies of $[Zn_4O(bdc)_3]$, MOF-5, have shown that an initial increase in pore volume occurs with applied pressure, caused by pressure-induced solvent inclusion into the pores. Further increases to the applied pressure cause decreases to pore volume as the solvent is squeezed out of the pores and an eventual amorphisation of the material.[60] Photoresponsive reversible structural transformations are also known in some MOFs, perhaps the most common of which include photoresponsive moieties on the linkers, often incorporating an azobenzene moiety into the framework.[55] PCN-123, $[Zn_4O(L)_3]$ (where L is 2-(phenyldiazenyl)terephthalate) undergoes a *trans* to *cis* isomerisation of its azobenzene containing

ligand upon irradiation by UV light (Figure 1.21).[61] A decrease in the accessible pore volume results from the conformational shift of the ligand within the pore (Figure 1.21). This was demonstrated through CO_2 adsorption studies on the *trans* and *cis* forms of the structure. A 53.9 % reduction in CO_2 adsorption occurred when the structure moves from its *trans* to its *cis* form. The main adsorption sites for CO_2 molecules are around the metal centres. In the cis form of PCN-123 the azobenzene moiety shifts to a closer proximity to the zinc centres, preventing CO_2 adsorption at these preferential sites.[61]

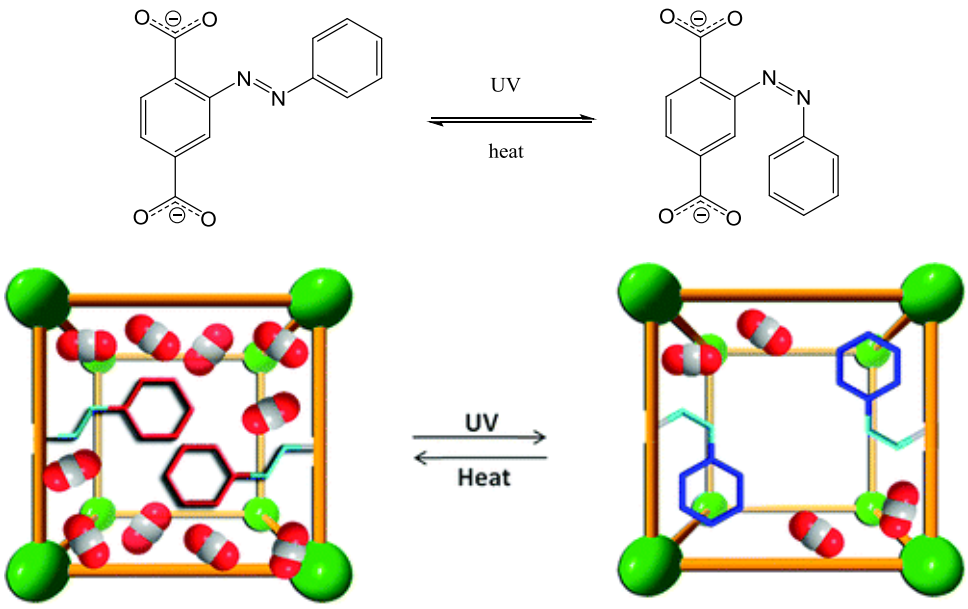

Figure 1.21 Schematic representation of the *trans* to *cis* isomerism of the phenyldiazenyl) terephthalate ligand (top) and within the PCN-123 framework, showing the relative CO_2 adsorption of each conformation (bottom).[61]

The number of flexible MOFs being reported is increasing and a characterisation of their properties has shown an increased understanding of their unusual and interesting behaviours. Potential applications in controlled and selective adsorptions have emerged, with similarities to some biological macromolecules such as enzymes which selectively adsorb and perform chemical transformations on substrates.[51,53]

1.4.4 Biomedical applications

The multifunctional nature of MOFs, owing to the ability to tune and adapt the metal and organic components, has made them attractive materials in the biomedical field. As with all compounds studied for biomedical application, toxicology and chemical stability are important considerations for the MOFs studied, and current research is in its infancy with respect to clinical application.[62]

However, progress has been seen for MOFs used in biomedical applications including drug delivery and biosensing.

The high surface areas of MOFs have shown potential for bioactive compounds to be adsorbed into the pores of frameworks and undergo slow or controlled release. Ibuprofen delivery has been studied with a number of MOFs,[47] with highly porous structures such as MIL-101 (see Section 1.4.1) showing possible loadings of up to 1.4g of ibuprofen per 1g of activated MIL-101.[63]

Due to the ability to modify and (to some extent) design organic ligands within MOFs, bioactive components have the potential to be incorporated into the framework of the MOF. The iron chelator drug, deferiprone has been shown to be successfully incorporated into the framework of zinc-based MOFs (Figure 1.22).[64] Deferiprone is used to treat disorders involving haemosiderosis (iron overload) but once in the body, it can be metabolised to an inactive form. Its inclusion into a robust framework may offer a solution to this problem, reducing the metabolism of the drug and offering an effective delivery method.

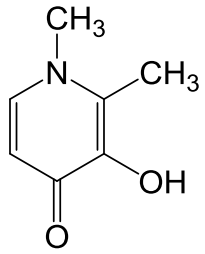

Figure 1.22 The structure of deferiprone.

The solvothermal reaction of deferiprone with zinc nitrate and 1,4-benzenedicarboxylic acid (H_2bdc) in various solvent mixtures yielded two MOF compounds, $[Zn_3(bdc)_2(dfp)_2]\cdot 2DMF$ and $[Zn_3(bdc)_2(dfp)_2(H_2O)_2]$. [64] In both MOFs, the deferiprone acts as a linker, co-ordinating to zinc metal centres through the ketone oxygen and the deprotonated hydroxyl group. Release of the deferiprone is achieved through treatment of the framework with acid, causing the framework to decompose.

A more recent application of MOFs is as biosensors. Biosensors typically allow the detection of a biological compound through the production of a signal, often luminescence based. Whilst organic components of MOFs can be luminescent, they tend to absorb light in the UV-visible range. MOFs containing *f*-block metals have been attractive as luminescent sensors due to their visible colour ranges and often long lasting luminescence. A lanthanide-containing MOF has been shown to be an effective sensor for anthrax, by detecting low levels of dipicolinic acid which forms 15 % of anthrax spores by mass.[65] The MOF prepared was $[Eu(bdc)_{1.5}(H_2O)_2]$. This was then coated with a silica shell that was further modified by the addition of silylated Tb-EDTA groups (Tb-ethylenediaminetetraacetic acid) which is a known dipicolinic acid sensor (Figure 1.23). Tb-EDTA

alone is non-emissive, but the formation of Tb-EDTA complexed to dipicolinic acid displays emission typical of Tb^{3+}. The fluorescence of the modified MOF was then monitored in the absence and presence of dipicolinic acid, with an excitation wavelength of 278 nm. In the absence of the dipicolinic acid only emission from the europium ions was detected, as the Tb-EDTA moiety is non-emissive. In the presence of dipicolinic acid, emission from the terbium ions was detected, confirming the formation of the Tb-EDTA-dipicolinate complex. At low concentrations, monitoring of the Eu^{3+}:Tb^{3+} emission intensity showed a linear relationship to the concentration of dipicolinic acid. This relationship levelled off with increasing dipicolinic acid as the Tb-EDTA sites become saturated.[65]

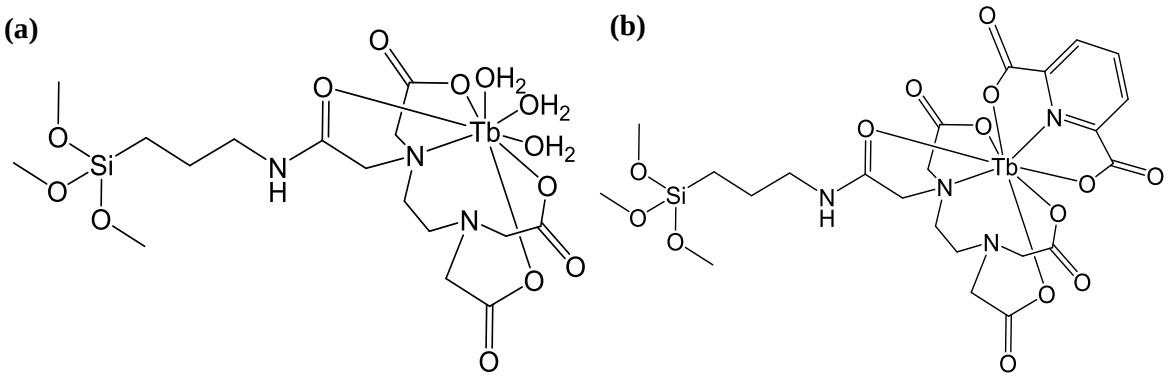

Figure 1.23 (a) The silylated Tb-EDTA modified group attached to silica coated MOFs (colourless) and **(b)** the complex formed upon binding of dipicolinic acid (green).

1.5 Multi-Component MOFs

MOFs that contain two or more organic ligands or metals which perform the same structural role within the framework are classed as multi-component MOFs (MC-MOFs).[66] MC-MOFs allow structurally similar MOFs that have varied compositions to be formed. The potential to adjust or control the relative amount of each component, either organic ligands or metals, within the structure can lead to a change in the resulting properties of the MOF, leading to some degree of property tailoring.

MC-MOFs can be formed through direct synthesis, in which the multiple components are combined during the synthesis of the MOF, or post-synthetically, in which a MOF is initially synthesised prior to undergoing a solid-state reaction to form a new, modified MOF.[66] There are multiple types of MC-MOFs, each with distinctive features, which will be outlined in this section.

1.5.1 Mixed-ligand/multivariate MOFs

MOFs which contain multiple organic ligands performing the same structural role within the framework, with similar lengths and donor groups, are known as mixed-ligand or multivariate MOFs. The formation of a mixed-ligand MOF does not alter the topology of the framework with respect to its single-ligand analogue and the ligands are randomly distributed throughout the framework.

Yaghi and co-workers showed that multiple functionalities could be incorporated into one structure through the direct synthesis of a multivariate MOF.[67] The single ligand structure of $[Zn_4O(bdc)_3]$, MOF-5, was modified by including multiple ligands of similar length to 1,4-benzenedicarboxylate (bdc) but with altered functionalities at various positions around the phenyl ring of the ligand, into the reaction mixture. The resulting structures contained between two and eight ligands, depending upon the number of ligands present in the reaction mixture (Figure 1.24).

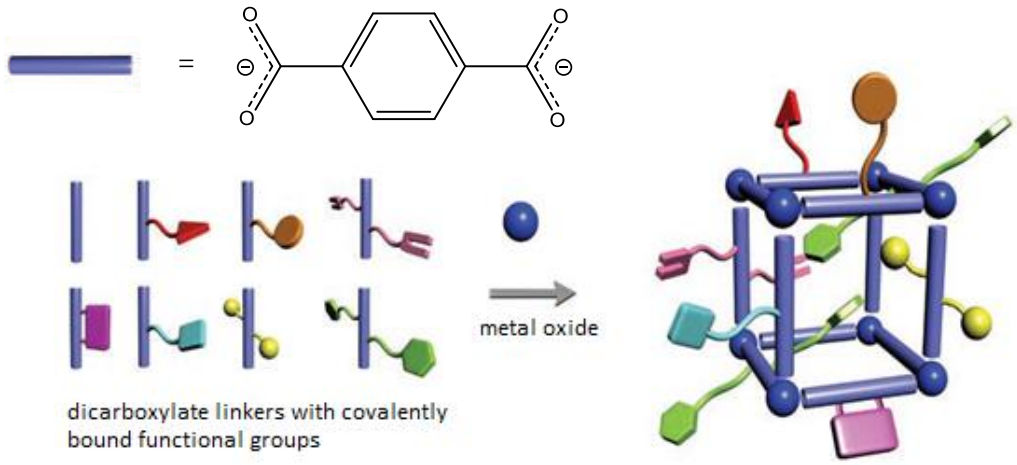

Figure 1.24 Pictorial representation of the formation of the mixed-ligand-MOF-5 structure, in which eight different dicarboxylate ligands are incorporated into one framework.[67]

Complex pore environments can therefore be formed, containing multiple functionalities, the composition of which can often be controlled through the ratio of ligands in the synthetic procedure. This can lead to new or combined properties in the resulting MOFs, an example of which is seen in the mixed-ligand modification of [Al(OH)(bdc)], CAU-10. A mixed-ligand MOF retaining the topology of CAU-10 was formed through the combination of H_2bdc and H_2bdc-Br (H_2bdc-Br = 2-bromo-1,4-dicarboxylic acid) in the reaction mixture. This resulted in the formation of the mixed-ligand structure [Al(OH)$(bdc)_{0.8}$$(bdc\text{-}Br)_{0.2}$].[68] The mixed-ligand MOF had modified adsorption properties in comparison to its single-ligand parent structures. The single ligand compounds [Al(OH)(bdc)] and [Al(OH)(bdc-Br)] have CO_2 adsorption uptakes of 10.6 and 3.6 % respectively when measured at 298 K and 1 bar. The mixed-ligand compound [Al(OH)$(bdc)_{0.8}$$(bdc\text{-}Br)_{0.2}$] has a CO_2 adsorption uptake of 8.1 % at 298 K and 1 bar (Figure 1.25).[68] This shows how the adsorption properties of MOFs can be systematically modified through the formation of mixed-ligand compounds.

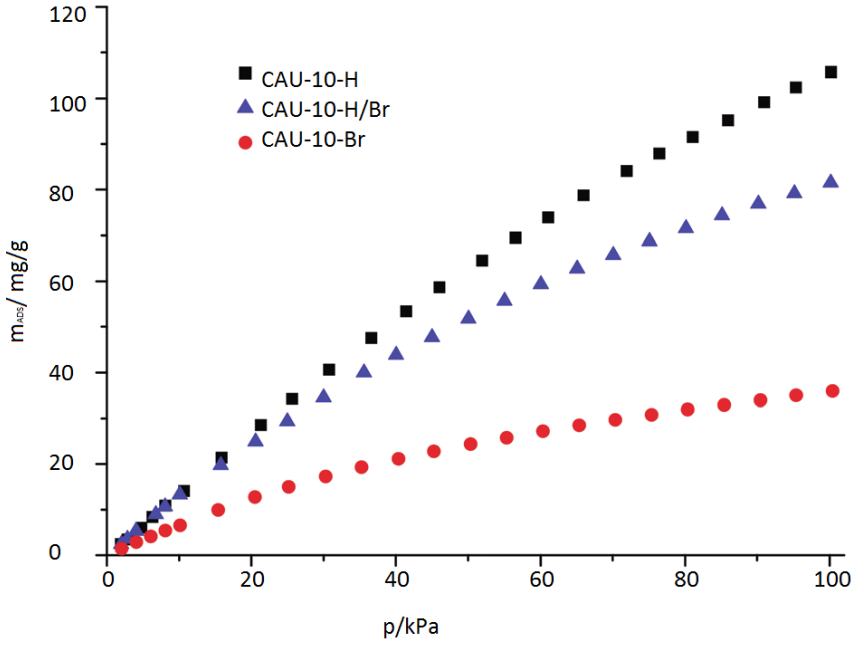

Figure 1.25 Adsorption isotherms of CO_2 for [Al(OH)(bdc)] (CAU-10-H), [Al(OH)(bdc-Br)] (CAU-10-Br) and [Al(OH)$(bdc)_{0.8}$$(bdc\text{-}Br)_{0.2}$] (CAU-10-H/Br).[68]

Multivariate MOFs can also be formed through post-synthetic modification (PSM). This process is often utilised for the inclusion of bulky substituents into a mixed-ligand MOF, which may be difficult to incorporate through direct synthesis due to unfavourable steric interactions. Numerous reports of PSM reactions on amine-containing MOFs have been reported, due to a wide range of available reactants with which they are able to react. Reaction of a number of amine groups within the framework, but not all available amine groups, will lead to the formation of a mixed-ligand MOF. An example of such a reaction is given in Figure 1.26, in which the amine group present on

the bdc-NH_2 (2-amino-1,4-benzenedicarboxylate) ligand of IRMOF-3, [Zn_4O(bdc-NH_2)$_3$] is reacted with acetic anhydrides to form an acetyl functionalised ligand.[69]

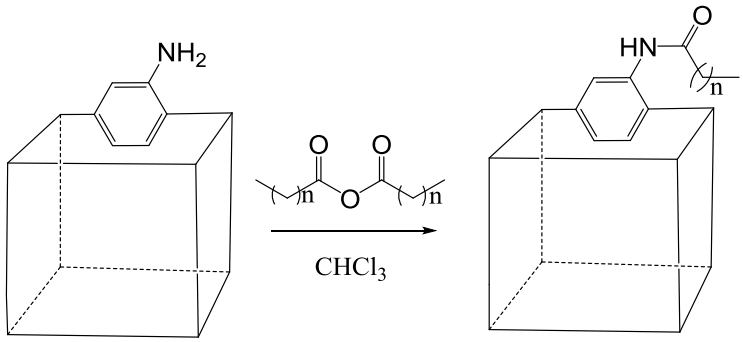

Figure 1.26 Schematic representation of the PSM reaction performed on the amine group of IRMOF-3, [Zn_4O(bdc-NH_2)$_3$] to form the acylated product.[69]

The reaction of the amine group on the bdc-NH_2 ligand to give the acylated ligand occurred at a conversion rate which varied depending on the chain length of the reactant used (greater than 85 % for n = 1 and 10 % for n = 18), forming mixed-ligand products which contain both bdc-NH_2 and bdc-NHCO$(CH_2)_n(CH_3)$ ligands.[69]

1.5.2 Core-shell MOFs

Core-shell MOFs form when one MOF grows epitaxially on the surface of a different MOF. This gives a layered-type system in which the core and outer layer of the crystals are not the same.[66] In order for core-shell MOFs to form, the lattice parameters of the two MOFs need to be similar. The denotation of a core-shell MOF is often expressed in the form MOF-2@MOF-1, where MOF-1 forms the core of the structure and MOF-2 forms the outer layer. Core-shell MOFs are typically synthesised through post-synthetic methods.

An example of a core-shell MOF was prepared based around the structures of MOF-5, [$Zn_4O(bdc)_3$] and IRMOF-3, [Zn_4O(bdc-NH_2)$_3$]. This core-shell MOF is denoted as MOF-5@IRMOF-3@MOF-5 in which the core is colourless MOF-5, the first layer is orange IRMOF-3 and the outer layer is colourless MOF-5 (Figure 1.27).[70] The core-shell MOF is prepared first by synthesising MOF-5, which after washing is placed in a solution containing the reactants to form IRMOF-3. After solvothermal reaction, the IRMOF-3 layer grows epitaxially onto the surface of the MOF-5 crystals, forming IRMOF-3@MOF-5 as an intermediate. This process is then repeated, placing the IRMOF-3@MOF-5 structure into a solution of the reactants required to form MOF-5 in order to generate the third layer.[70]

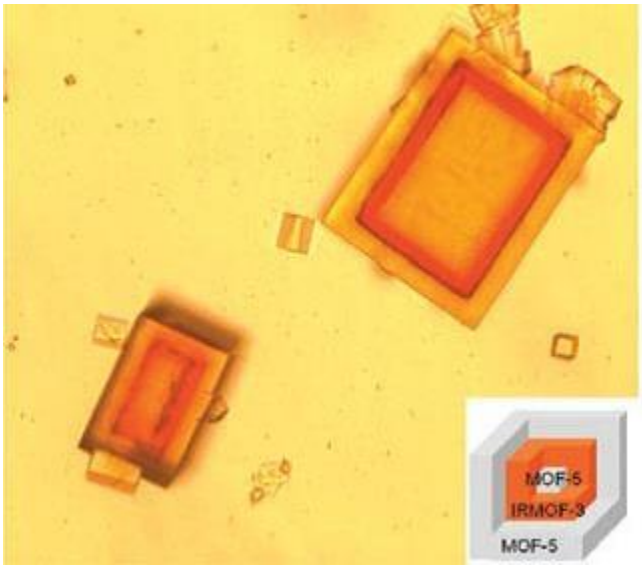

Figure 1.27 Crystals of MOF-5@IRMOF-3@MOF-5 as viewed down a microscope, alongside a pictorial representation of the core-shell structure of the MOF.[70]

By modifying compounds through this method new materials with the combined properties of both the shell(s) and the core can be formed. It is can be an effective route to forming complex materials with multiple properties in a controlled manner.

1.5.3 Surface modified MOFs

Surface modified MOFs are formed through post-synthetic modification on the surface of a crystal to form a type of core-shell MOF.[66] A main difference between surface modified and core-shell MOFs is the thickness of the outer layer, which is much thinner in surface modified MOFs due to the limited ability of the reactants to penetrate the surface of the crystal. This has been explored through the incorporation of fluorescent groups onto the surfaces of MOFs, in order to demonstrate its success.

Kitagawa and co-workers have shown how the association-dissociation equilibrium of metal-ligand coordination bonds present in MOFs can be exploited to achieve surface modification.[71] In solution, ligand substitution around the metal ions may occur with ligands present in the solution or even solvent molecules. Surfaces of MOFs are particularly vulnerable to this and therefore solutions of competing ligands can be used to cause ligand exchange at the surface interfaces of MOFs.[71] The study by Kitagawa began with $[Zn_2(bdc)_2(dabco)]$ (DMOF-1). DMOF-1 contains two types of ligand, bdc (1,4-benzenedicarboxylate) and dabco (1,4-diazabicyclo[2.2.2]octane). Due to its rectangular prism morphology, the crystals of DMOF-1 have a total of six faces, four faces of which are terminated by carboxylate ligands and two faces by dabco ligands. The fluorescent dye chosen to perform the surface modification reaction contained a carboxylate group (Figure 1.28).

Crystals of DMOF-1 were immersed in a DMF solution of the fluorescent dye, and left for 3 hours at 45 ^{o}C. A control batch using the dye without the carboxylate group was also reacted. After this time, both samples were washed with DMF multiple times before collecting fluorescence spectra. The sample treated with the control dye showed no fluorescence indicating no dye present in the sample. The sample treated with the carboxylate containing dye showed fluorescence on four of its surfaces when excited at 635 nm. This indicates that the carboxylate dye had undergone a ligand exchange reaction on DMOF-1. The presence of the dye on four of the faces of the crystals suggests that it has exchanged with the bdc ligands, but not the dabco ligands.

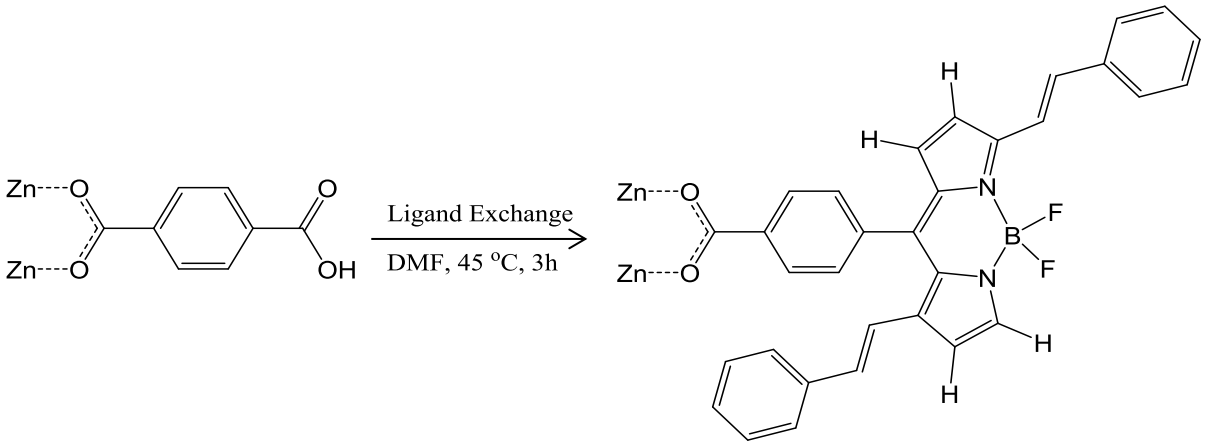

Figure 1.28 Schematic representation of the ligand exchange reaction in DMOF-1. The terminal carboxylate ligands are replaced with boron dipyrromethene fluorescent dyes, such as the one shown.[71]

1.5.4 Mixed-metal MOFs

As well as containing multiple ligands which perform the same structural role, multi-component MOFs can also contain multiple types of metal centre. These can be synthesised by either direct synthesis, combining different metal sources with the organic ligand components in the synthetic step, or post-synthetically, by synthesising a MOF with one type of metal centre and performing an exchange reaction to replace some of the metal centres for a second, different metal type.[66]

Often metals combined in mixed-metal MOFs have the same oxidation state as one another. An example of this is a series of MOFs with the general formula $[M_2L_2]$, L = bis(carboxyphenyl)-1,2,4-triazole, M = Co^{2+}, Cu^{2+} and Zn^{2+}.[72] Homonuclear species containing one of the metals were first synthesised and then heteronuclear species containing Co/Cu, Co/Zn and Cu/Zn combinations were formed. Crystallographic analysis revealed all species, homonuclear and heteronuclear were isoreticular to one another. The frameworks contain paddlewheel motifs, in which two metal centres are bridged by four carboxylate groups from the bis(carboxyphenyl)-1,2,4-triazole ligands. The paddlewheel motifs are linked by axially co-ordinating ligands which coordinate through the nitrogen atoms of the triazole moiety (Figure 1.29).

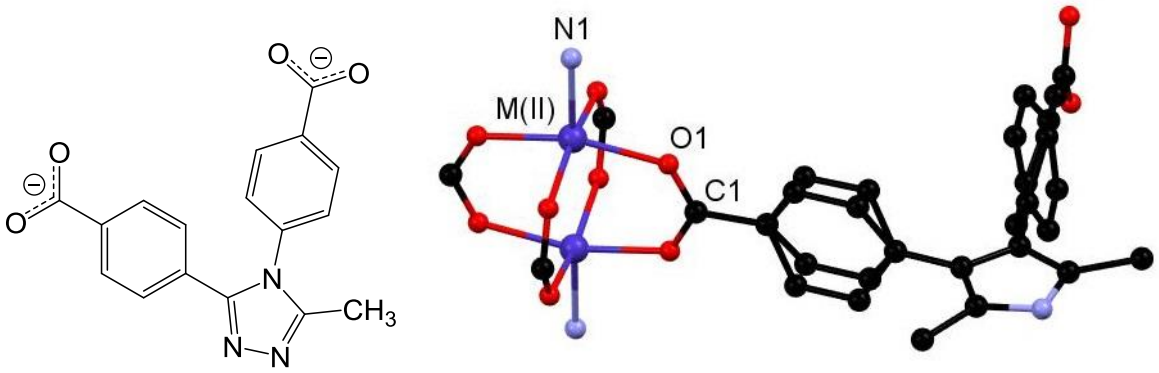

Figure 1.29 The structure of the bis(carboxyphenyl)-1,2,4-triazole ligand (left) and a fragment of the crystal structure showing the paddlewheel motif of the MOFs formed. Carbon atoms are shown in black, oxygen in red, nitrogen in blue and the M(II) metal centres (Cu, Co or Zn) in purple. The phenyl rings of the ligand are disordered over two positions.[72]

The mixed-metal MOFs were formed through direct synthesis, with both metal salts being combined with the ligand during synthesis. Confirmation of a mixed-metal species was given by electron dispersive X-ray (EDX) spectroscopic analysis, which showed that both metal centres were present in a single crystal, confirming that the product was not a mixture of two homonuclear species. This example demonstrates the propensity for MOFs to include multiple metal species of similar oxidation state, despite differences in the size and coordination behaviour of the metal centres.

In some cases, metals of differing oxidation states can be combined in the same MOF. These are often referred to as mixed-valence state MOFs. HKUST-1, $[Cu_3(btc)_2]$, has been shown to undergo a reduction reaction post-synthetically, whereby in the presence of hydroquinone reducing agent some of the Cu^{2+} centres in HKUST-1 are reduced to give a mixture of Cu^{2+} and Cu^{+} centres.[73] This post-synthetic reaction yields a new mixed-valence MOF with an altered structure to that of HKUST-1. It has been structurally characterised as $[Cu^{I}Cu^{II}(btc)(H_2O)]\cdot 2H_2O$ and consists of two interpenetrating three-dimensional nets. Two distinct co-ordination environments are present, one containing Cu^{2+} ions in a paddlewheel motif, and one containing Cu^{+} ions in a macrocyclic arrangement (Figure 1.30).

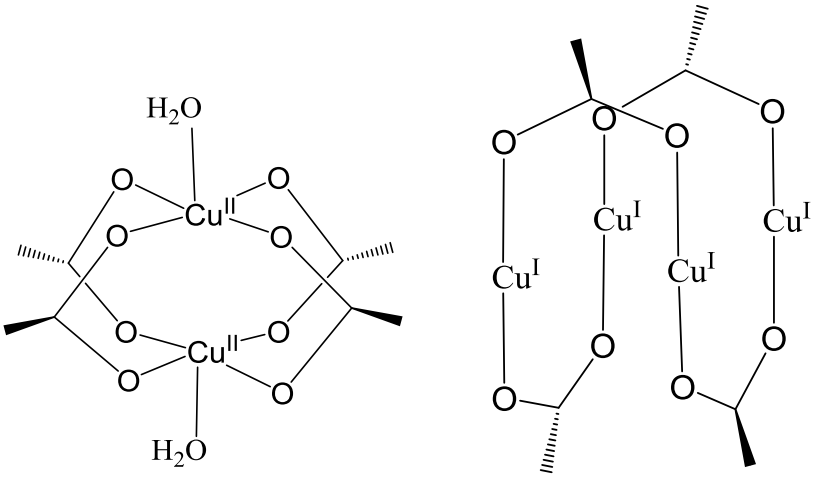

Figure 1.30 Structural representations of the Cu^{2+} and Cu^{+} co-ordination environments in $[Cu^{I}Cu^{II}(btc)(H_2O)]\cdot 2H_2O$.[73]

The mixed-valence MOF shows an increased stability towards moisture relative to the starting HKUST-1 MOF.[73] HKUST-1 readily shows signs of structure disintegration when immersed in water for short periods of time, however the mixed-valence MOF showed structural stability when in water and heated to 50 ^{o}C for 24 hours. The Cu-O bonds in the mixed valence MOF are more shielded due to its interpenetrating structure, compared to the non-interpenetrating large, open pore structure of HKUST-1. It also has lower porosity than HKUST-1 with every second pore containing Cu^{+} co-ordinating moieties making them less accessible to water molecules (Figure 1.31). The metal-oxygen bonds are prone to hydrolysis in the presence of H_2O causing the framework to collapse.

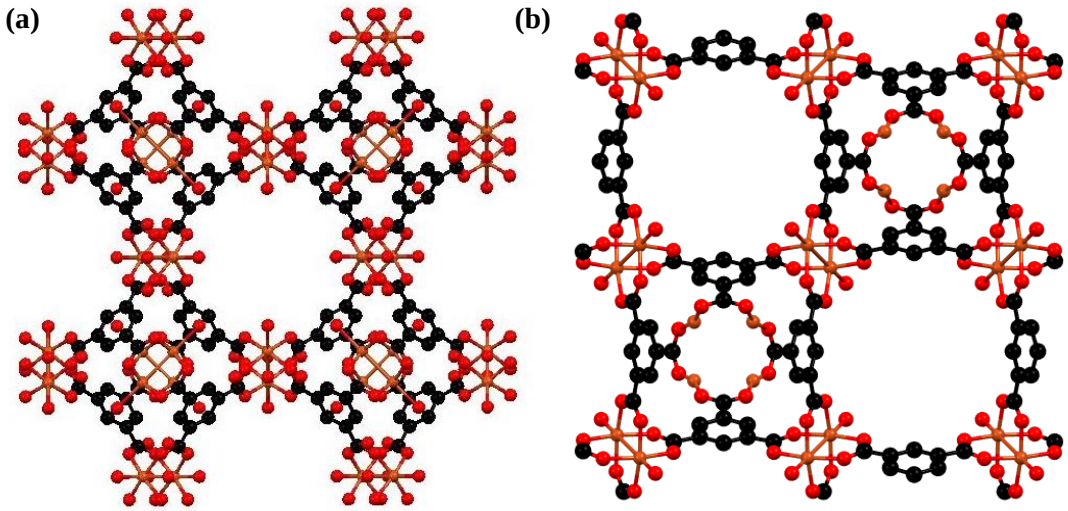

Figure 1.31 Crystal structures of $[Cu_3(btc)_2]$, HKUST-1 **(a)** and $[Cu^{I}Cu^{II}(btc)(H_2O)]\cdot 2H_2O$ **(b)**. Copper atoms are shown in orange, oxygen in red and carbon in black. Hydrogen atoms and solvent molecules have been omitted from both structures.[73]

1.6 Outlook: the future of MOF chemistry

The large number of MOF structures and the great structural diversity they display is evidence of the level of ongoing research in this area. Increasingly MOFs have been shown to have potential applications across a breadth of fields as has been discussed in previous sections of this chapter. To date, much research has focussed on relatively simple MOF structures.[74] Whilst the ability to control or predict MOF structures from their respective building blocks has been a great advance in MOF chemistry, there remain challenges within the field. One such challenge is that of introducing heterogeneity into MOF structures whilst retaining crystallinity.[75] Heterogeneity can be achieved by the combination of multiple building blocks within one framework (as discussed in Section 1.5) but can also include deviation from order in other ways, such as defects and multiple pore environments. Pushing the boundaries of heterogeneity in MOFs has the potential to propel the field into new arenas.[7, 74]

Analysis of compounds with complex heterogeneity is challenging due to the lack of experimental techniques available to determine the ordering of multiple functionalities within a structure.[76] In a study by Yaghi and co-workers, solid state NMR and molecular modelling techniques were combined to map the distribution of functionalities in multi-functional MOFs. Multivariate MOFs were synthesised based around the structure of MOF-5 (see Section 1.1) by combining two or three benzenedicarboxylate ligands which had been modified with different functional groups around the phenyl ring. Different arrangements of functionalities throughout the resulting structures were found depending on the combination of ligands used. Ligands which were able to form preferential interactions with each other were located in clusters throughout the crystal, whilst those which formed preferential interactions with a different ligand type in the structure were arranged in an alternating manner. Ligands which formed no preferential interactions were randomly distributed throughout the structure. Studies such as these demonstrate how the randomness of heterogeneous structures can be evaded to instead form periodic frameworks through careful building block choices.[76, 77]

A recent study by Telfer and co-workers demonstrates how ligand choices can lead to complex, periodic structures being formed.[77] The MOF $[Zn_4O(btb)_{4/3}(bdc)_{1/2}(bpdc)_{1/2}]$ (btb = benzene-1,3,5-tribenzoate, bdc = 1,4-benzenedicarboxylate and bpdc = 4,4'-biphenyldicarboxylate) containing three topologically distinct ligands, is known as a quaternary MOF. The pores of the MOF were then shown to be systematically modified through ligand exchange reactions with carefully selected modified ligands. The modified ligands (shown in Figure 1.32) were chosen to retain the conformation and crystallographic symmetry exhibited by their unmodified counterparts. A range of isoreticular MOFs dubbed programmed-pore MOFs were formed through this method, in which pore functionality and size of the resulting structures was modified and controlled.

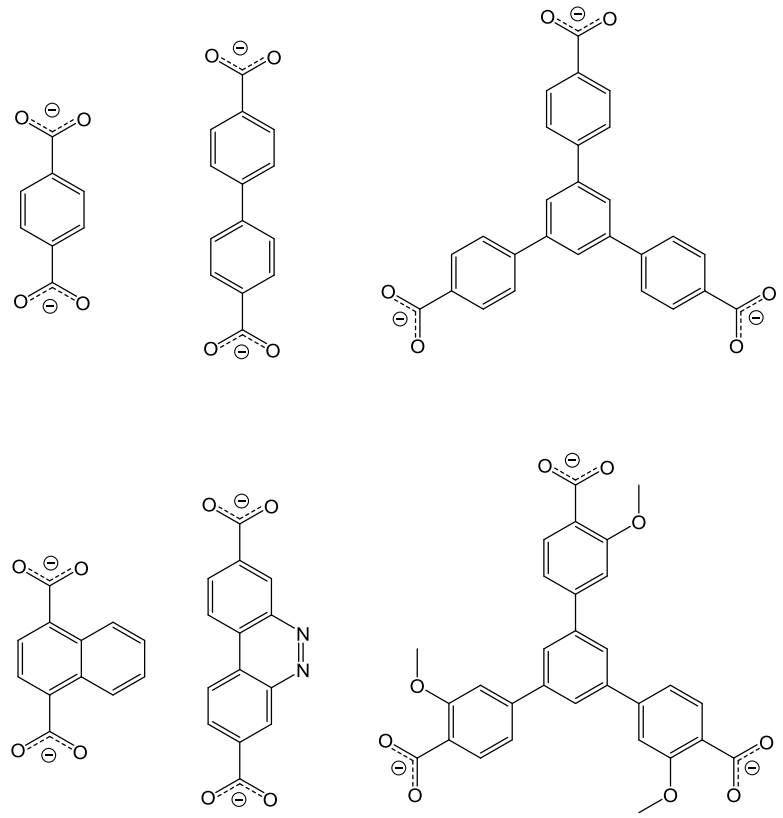

Figure 1.32 Structures of the bdc, bpdc and btb ligands forming the $[Zn_4O(btb)_{4/3}(bdc)_{1/2}(bpdc)_{1/2}]$ MOF (top) and their modified counterparts used in ligand exchange reactions to form programmed-pore analogues of $[Zn_4O(btb)_{4/3}(bdc)_{1/2}(bpdc)_{1/2}]$ (bottom).[77]

Complex functional structures of this nature are evocative of biological macromolecules. The programmable-pore MOFs described above took their inspiration from enzymes, in which active sites arise from the spatial arrangement of multiple functionalities in a confined zone.[77]

MOFs which exhibit altered properties upon the inclusion of guest molecules within their pores have been reported. These materials exhibit emergent properties which are not characteristic to either host or guest individually, but arise upon their combination to form a new material referred to as a guest@MOF structure.[78] An example can be seen in the inclusion of the guest molecule 7,7,8,8-tetracyanoquinododimethane (TCNQ) into the HKUST-1 framework (see Section 1.4). Neither TCNQ or HKUST-1 exhibit electrical conductivity individually, however the TCNQ@HKUST-1 material shows an electrical conductivity of 7 S m^{-1}.[79] Further research is needed in this area, investigating the emergent properties of host-guest inclusion MOFs.

There has been a focus to date on the use of symmetric ligands in MOF synthesis.[46] A greater exploration of asymmetric ligands, either in respect to their geometry, functional group position or type of co-ordinating groups, may yield new and interesting MOF architectures. In a similar manner, a lack of order within the structure of MOFs through the presence of defects can impart

new and interesting properties. The study of unintentional defects as well as purposeful defect inclusion in MOFs is revealing how, in many cases, defects can control the overall performance of the MOF. For example, structures which without defects have limited pore accessibility have been shown to allow the diffusion of guest molecules through their pores when defects are introduced into the structure.[80]

In summary, it is clear that MOF chemistry is continuing to grow and mature. The future of MOF chemistry is likely to lie in the formation and control of increasingly complex, heterogeneous structures.

1.7 Overall aims of this project

This thesis aims to investigate methods of producing new multi-component metal-organic frameworks and determine how their properties differ from those of their single-component analogues. Several approaches to forming multi-component MOFs are available, including the use of more than one type of organic ligand to form mixed-ligand frameworks, the inclusion of guest molecules or counter-ions into the pores of a structure or the combining of different metal centres to give mixed-metal MOFs. This thesis investigates each of these approaches, and details the effect on the structure and properties of the resulting materials.

Chapters 2 and 3 present two studies which focus on the formation of mixed-ligand MOFs. These investigations aim to determine the structural effects of systematically altering the ratio of ligands in isostructural series of frameworks. The effect on the pore size and geometry of the resulting materials is presented.

Chapter 4 details the inclusion of radical cations into the pores of anionic frameworks. This approach aims to investigate how different MOF topologies affect the stability of the radical counter-ions.

A mixed-metal study is presented in Chapter 5, detailing the synthesis of mixed-lanthanide MOFs through two methods, with an aim to investigate the effect of the distribution of lanthanide centres within the structure on the emission of the resulting material.

1.8 References

1. S. R. Batten, N. R. Champness, X.M. Chen, J. Garcia-Martinez, S. Kitagawa, L. Öhrström, M. O'Keeffe, M. P. Suh and J. Reedijk, *Pure Appl. Chem.*, 2013, 85, 1715-1724
2. S. R. Batten, N. R. Champness, X.M. Chen, J. Garcia-Martinez, S. Kitagawa, L. Öhrström, M. O'Keeffe, M. P. Suh and J. Reedijk, *Cryst. Eng. Comm.*, 2012, 14, 3001-3004
3. J. L. C. Rowsell and O. M. Yaghi, *Microporous Mesoporous Mater.*, 2004, 73, 3-14
4. S.Jakobsen. J. H. Cavka, U. Olsbye, N. Guillou, C. Lamberti, S. Bordiga and K. P. Lillerud, *J. Am. Chem. Soc*, 2008, 130, 13850–13851
5. D. J. Tranchemontagne, J. L. Mendoza-Cortes, M. O'Keeffe and O. M. Yaghi, *Chem. Soc. Rev.*, 2009, 38, 1257-1283
6. H. Garcia, A. Corma, and F. X. Llabres i Xamena, *Chem. Rev.*, 2010, 110, 4606–4655
7. H. Furukawa, K. E. Cordova, M. O'Keeffe and O. M. Yaghi, *Science*, 2013, 341, 1230444-1 - 120044-12
8. L. Öhrström, *Crystals*, 2015, 5, 154-162
9. M. Eddaoudi, J. Kim, N. Rosi, D. Vodak, J. Wachter, M. O'Keeffe and O. M. Yaghi, *Science*, 2002, 295, 469-472
10. M. Li, D. Li, M. O'Keeffe and O. M. Yaghi, *Chemical Rev.*, 2014, 114, 1343-1370
11. T. D. Bennett and A. K. Cheetham, *Acc. Chem. Res.*, 2014, 47, 1555-1562
12. M. Jansen and J. C. Schon, *Angew. Chem. Int. Ed.*, 2006, 45, 3406-3412
13. R. Robson, *Dalton Trans.*, 2008, 5113-5131
14. A. Ferguson, L. Liu, S. J. Tapperwijn, D. Perl, F. X. Coudert, S. Van Cleuvenbergen, T. Verbiest, M. A. van der Veen and S. G. Telfer, *Nat. Chem.*, 2016, 8, 250-257
15. R. K. Deshpande, G. I. Waterhouse, G. B. Jameson and S. G. Telfer, *Chem. Commun.*, 2012, 48, 1574-1576
16. P. Nugent, Y. Belmabkhout, S. D. Burd, A. J. Cairns, R. Luebke, K. Forrest, T. Pham, S. Ma, B. Space, L. Wojtas, M. Eddaoudi and M. J. Zaworotko, *Nature*, 2013, 495, 80-84
17. N. Sikdar, T. K. Maji and R Haldara, *Mater. Today* 2015, 18, 97-116
18. D. Shen. Q. M. Wang, M. Bulow , M. L. Lau, S. Deng,ulow, F. R. Fitch, N. O. Lemcoff and J. Semanscin, *Microporous Mesoporous Mater.*, 2002, 55, 217–230
19. M. J. Rosseinsky, *Microporous and Mesoporous Mater.*, 2004, 73, 15-30
20. J. Klinowski, F. A. Paz, P. Silva and J. Rocha, *Dalton Trans.*, 2011, 40, 321-330
21. J. S. Choi, W. J. Son, J. Kim and W. S. Ahn, *Microporous and Mesoporous Mater.*, 2008, 116, 727-731
22. A. L. Garay, A. Pichon and S. L. James, *Chem. Soc. Rev.*, 2007, 36, 846-855
23. W. Yuan, A. L. Garay, A. Pichon, R. Clowes, C. D. Wood, A. I. Cooper and S. L. James, *Cryst. Eng. Comm.*, 2010, 12, 4063-4065
24. S. Kitagawa, R. Kitaura and S. Noro, *Angew. Chem. Int. Ed.*, 2004, 43, 2334-2375
25. J. E. Mondloch, O. Karagiaridi, O. K. Farha and J. T. Hupp, *Cryst. Eng. Comm.*, 2013, 15, 9258-9264
26. S. Li and F. Huo, *Nanoscale*, 2015, 7, 7482-7501
27. O. K. F. Andrew P. Nelson, Karen L. Mulfort, and Joseph T. Hupp, *J. Am. Chem. Soc*, 2009, 131, 458–460.
28. A. J. Howarth, A. W. Peters, N. A. Vermeulen, T. C. Wang, J. T. Hupp and O. K. Farha, *Chem. Mater.*, 2017, 29, 26-39.
29. M. Thommes, K. Kaneko, A. V. Neimark, J. P. Olivier, F. Rodriguez-Reinoso, J. Rouquerol and K. S. W. Sing, *Pure Appl. Chem.*, 2015, 87,1051-1069
30. T. Horikawa, D. D. Do and D. Nicholson, *Adv. Colloid Interface Sci.*, 2011, 169, 40-58
31. K. Yamashita, K. Kashiwagi, A. Agrawal and H. Daiguji, *Mol. Phys.*, 2016, 115, 328-342
32. P. B. Balbuena. and K. E. Gubbins, *Langmuir* 1993, 9, 1801-1814
33. J. E. Shields, S. Lowell, M. A. Thomas and M. Thommes, *Characterization of Porous Solids and Powders: Surface Area, Pore Size and Density*, Kluwer Academic Publishers, Dordrecht, The Netherlands 2004
34. G. Fagerlund, *Mat. Constr*, 1973, 6, 239-245
35. K. S. Walton and R. Q. Snurr, *J. Am. Chem. Soc.*, 2007, 129, 8552-8556
36. L. J. Murray, M. Dinca and J. R. Long, *Chem. Soc. Rev.*, 2009, 38, 1294-1314
37. M. Mani-Biswas and T. Cagin, *Comp.Theor. Chem.*, 2012, 987, 42-56

38. D. Zhao, D. Yuan and H.-C. Zhou, *Energ. Environ. Sci.*, 2008, 1, 222-235
39. J. A. Mason, M. Veenstra and J. R. Long, *Chem. Sci.*, 2014, 5, 32-51
40. Z. Zhang, Y. Zhao, Q. Gong, Z. Li and J. Li, *Chem. Commun.*, 2013, 49, 653-661
41. Y. F. Chen, R. Babarao, S. I. Sandler and J. W. Jiang, *Langmuir*, 2010, 26, 8743-8750
42. P. Li, J. Chen, W. Feng and X. Wang, *J. Iran. Chem. Soc.*, 2013, 11, 741-749
43. N. A. Khan, Z. Hasan and S. H. Jhung, *J. Hazard. Mater.*, 2013, 244-245, 444-456
44. E. Haque, J. W. Jun and S. H. Jhung, *J. Hazard. Mater.*, 2011, 185, 507-511
45. M. Carboni, C. W. Abney, S. Liu and W. Lin, *Chem. Sci.*, 2013, 4, 2396-2402
46. F. A. Paz, J. Klinowski, S. M. Vilela, J. P. Tome, J. A. Cavaleiro and J. Rocha, *Chem. Soc. Rev.*, 2012, 41, 1088-1110
47. B. Li, H. M. Wen, Y. Cui, W. Zhou, G. Qian and B. Chen, *Adv. Mater.*, 2016, 28, 8819-8860
48. A. Henschel, K. Gedrich, R. Kraehnert and S. Kaskel, *Chem. Commun.*, 2008, 4192-4194
49. L. Li, R. Matsuda, I. Tanaka, H. Sato, P. Kanoo, H. J. Jeon, M. L. Foo, A. Wakamiya, Y. Murata and S. Kitagawa, *J. Am. Chem. Soc.*, 2014, 136, 7543-7546
50. N. Maksimchuk, M. Timofeeva, M. Melgunov, A. Shmakov, Y. Chesalov, D. Dybtsev, V. Fedin and O. Kholdeeva, *J. Catal.*, 2008, 257, 315-323
51. Z. Chang, D. H. Yang, J. Xu, T. L. Hu and X. H. Bu, *Adv. Mater.*, 2015, 27, 5432-5441
52. A. J. Fletcher, K. M. Thomas and M. J. Rosseinsky, *J. Solid State Chem.*, 2005, 178, 2491-2510
53. A. Schneemann, V. Bon, I. Schwedler, I. Senkovska, S. Kaskel and R. A. Fischer, *Chem. Soc. Rev.*, 2014, 43, 6062-6096
54. E. L. Harty, A. R. Ha, M. R. Warren, A. L. Thompson, D. R. Allan, A. L. Goodwin and N. P. Funnell, *Chemical Commun.*, 2015, 51, 10608-10611
55. F.X. Coudert, *Chem. Mater.*, 2015, 27, 1905-1916
56. D. N. Dybtsev, H. Chun and K. Kim, *Angew. Chem. Int. Ed.*, 2004, 43, 5033-5036
57. C. S. Caroline Mellot-Draznieks, Suzy Surble, Nathalie Audebrand and Gerard Fe, *J. Am. Chem. Soc*, 2005, 127, 16273-16278
58. C. Mellot-Draznieks, *J. Mater. Chem.*, 2007, 17, 4348-4358
59. P. Horcajada, F. Salles, S. Wuttke, T. Devic, D. Heurtaux, G. Maurin, A. Vimont, M. Daturi, O. David, E. Magnier, N. Stock, Y. Filinchuk, D. Popov, C. Riekel, G. Ferey and C. Serre, *J. Am. Chem. Soc.*, 2011, 133, 17839-17847
60. A. J. Graham, D. R. Allan, A. Muszkiewicz, C. A. Morrison and S. A. Moggach, *Angew. Chem. Int. Ed.*, 2011, 50, 11138-11141
61. J. Park, D. Yuan, K. T. Pham, J. R. Li, A. Yakovenko and H. C. Zhou, *J. Am. Chem. Soc.*, 2012, 134, 99-102
62. M. Giménez-Marqués, T. Hidalgo, C. Serre and P. Horcajada, *Coord. Chem. Rev.*, 2016, 307, 342-360
63. P. Horcajada, C. Serre, M. Vallet-Regi, M. Sebban, F. Taulelle and G. Ferey, *Angew. Chem. Int. Ed.*, 2006, 45, 5974-5978
64. A. D. Burrows, M. Jurcic, L. L. Keenan, R. A. Lane, M. F. Mahon, M. R. Warren, H. Nowell, M. Paradowski and J. Spencer, *Chemical Commun.*, 2013, 49, 11260-11262
65. K. M. L. Taylor, W. J. Rieter, and W. Lin, *J. Am. Chem. Soc*, 2007, 129, 9852-9853
66. A. D. Burrows, *Cryst. Eng. Comm.*, 2011, 13, 3623-3642
67. H. Deng, C. J. Doonan, H. Furukawa, R. B. Ferreira, J. Towne, C. B. Knobler, B. Wang and O. M. Yaghi, *Science*, 2010, 327, 846-850
68. H. Reinsch, S. Waitschat and N. Stock, *Dalton Trans.*, 2013, 42, 4840-4847
69. Z. Wang and S. M. Cohen, *Chemical Soc. Rev.*, 2009, 38, 1315-1329
70. K. Koh, A. G. Wong-Foy and A. J. Matzger, *Chemical Commun*, 2009, 6162-6164
71. M. Kondo, S. Furukawa, K. Hirai and S. Kitagawa, *Angew. Chem. Int. Ed.*, 2010, 49, 5327-5330
72. K. Kobalz, M. Kobalz, J. Mollmer, U. Junghans, M. Lange, J. Bergmann, S. Dietrich, M. Wecks, R. Glaser and H. Krautscheid, *Inorg. Chem.*, 2016, 55, 6938-6948
73. A. Ahmed, C. M. Robertson, A. Steiner, T. Whittles, A. Ho, V. Dhanak and H. Zhang, *RSC Adv.*, 2016, 6, 8902-8905
74. N. R. Champness, *Dalton Trans.*, 2011, 40, 10311-10315

75. H. Furukawa, U. Muller and O. M. Yaghi, *Angew. Chem. Int. Ed.*, 2015, 54, 3417-3430
76. X. Kong, H. Deng, F. Yan, J. Kim, J. A. Swisher, B. Smit, O. M. Yaghi and J. A. Reimer, *Science*, 2013, 341, 882-885
77. L. Liu, K. Konstas, M. R. Hill and S. G. Telfer, *J. Am. Chem. Soc.*, 2013, 135, 17731-17734
78. M. D. Allendorf, M. E. Foster, F. Leonard, V. Stavila, P. L. Feng, F. P. Doty, K. Leong, E. Y. Ma, S. R. Johnston and A. A. Talin, *J. Phys. Chem. Lett.*, 2015, 6, 1182-1195
79. A. Centrone. A. A. Talin, A. C. Ford, M. E. Foster, V. Stavila, P. Haney, R. A. Kinney, V. Szalai, F. El Gabaly, H. P. Yoon, F. Léonard and M. D. Allendorf, *Science*, 2014, 343, 66-69
80. D. S. Sholl and R. P. Lively, *J. Phys. Chem. Lett.*, 2015, 6, 3437-3444

2. Compositional control of pore geometry in multivariate metal-organic frameworks (MOFs)

2.1 Introduction

The concept of property tailoring in MOFs refers to the ability to control a particular structural or chemical property of a MOF through rational design. One particular area of interest is the design and control of pore size and geometry. The wide range of pore types, sizes and geometries of MOFs are attractive for applications such as sensing[1], molecular sieving[2], gas storage[3-5] and hazardous material capture.[6] Such interest largely stems from the capacity of many MOFs to selectively absorb guest molecules within the pore.[7] Therefore the ability to control the pore geometry or size within a system is particularly attractive as successful property tailoring of this kind allows MOF systems the potential to be tuned to the requirements of a specific guest or application.

Pore size control has been demonstrated through ligand extension methods by Yaghi, in the formation of the isoreticular series of IRMOF structures (see Section 1.1).[8] The general formula of these MOFs is $[Zn_4OL_3]$ where L is a linear dicarboxylate. All members of the IRMOF series have a similar topology, containing oxide-centred tetrahedra, Zn_4O, which are linked by linear dicarboxylates to form a 3-dimensional cubic grid (Figure 2.1). By extending the length of the ligand, MOFs with larger pore sizes are formed whilst retaining the overall topology of the IRMOF system.

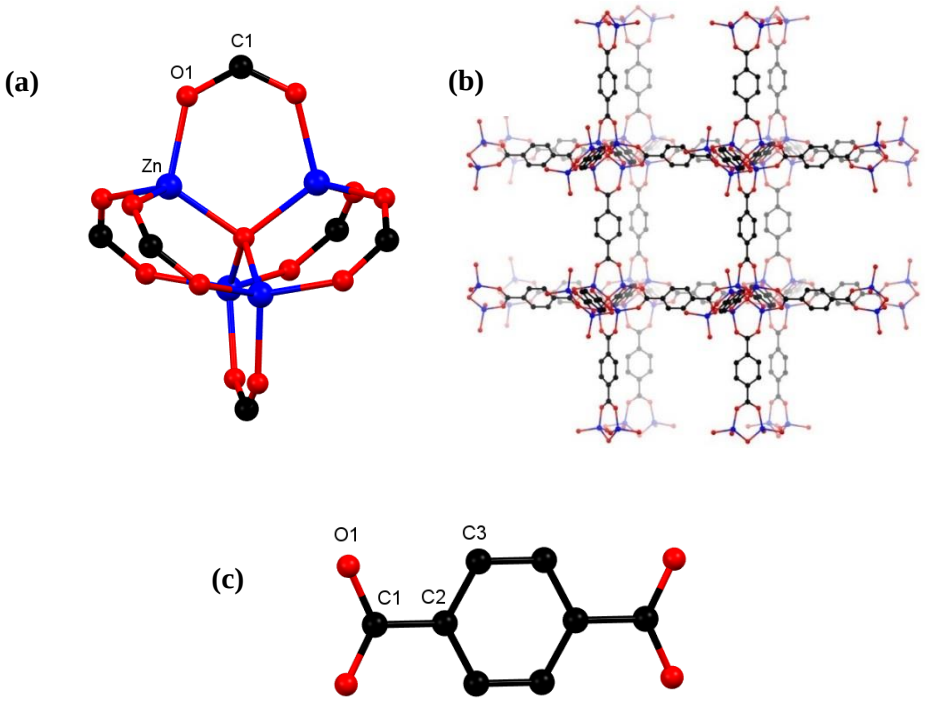

Figure 2.1 Structure of IRMOF-1[8] showing **(a)** the Zn_4O moiety, **(b)** the 3-dimensional network with cubic grid topology and **(c)** the 1,4-benzenedicarboxylate ligand structure. Hydrogen atoms are omitted for clarity.

Calculations of the free percentage volume in each IRMOF crystal structure show an incremental increase from 79.2 % in $[Zn_4O(bdc)_3]$, IRMOF-1 (bdc = 1,4-benzenedicarboxylate), to 91.1 % in $[Zn_4O(tpdc)_3]$, IRMOF-16 (tpdc = 1,1',4',1''-terphenyl-4,4''-dicarboxylate) (Figure 2.2). A decrease in pore size can also be achieved with respect to IRMOF-1 through the addition of a substituent onto the ligand which projects into the pores. This can be seen in the case of IRMOF-5 which contains 2,5-bis(pentyloxy)benzene-1,4-dicarboxylate ligands, similar in length to the bdc ligand in IRMOF-1 but with long chain pentyloxy groups at the 2 and 5 positions on the benzene ring (Figure 2.2). This results in a free percentage volume of 55.8 % for IRMOF-5, significantly lower than the 79.2 % of IRMOF-1.

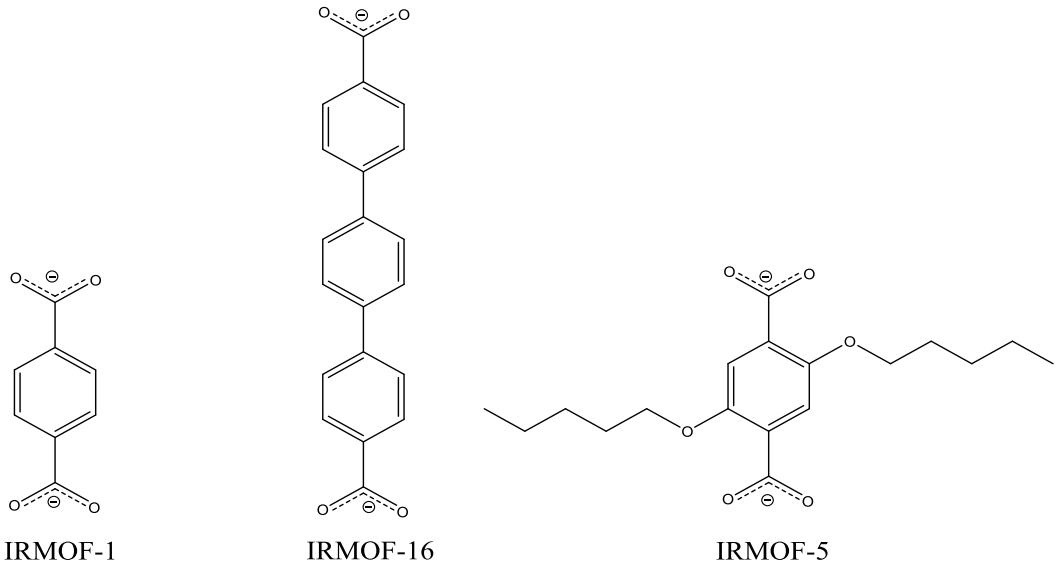

Figure 2.2 The dicarboxylate ligands used to form members of the IRMOF series. The dicarboxylate ligands are 1,4-benzenedicarboxylic acid for IRMOF-1, 1,1',4',1''-terphenyl-4,4''-dicarboxylic acid benzene for IRMOF-16 and 2,5-bis(pentyloxy)benzene-1,4-dicarboxylic acid for IRMOF-5.[8]

A similar ligand extension method to that of the IRMOF series is demonstrated in the isoreticular series based around $[Mg_2L]$, MOF-74 where L is a dioxidoterephthalate ligand.[9] In this system the dioxidoterephthalate ligand contains one disubstituted benzene ring and the MOF displays one-dimensional hexagonal pores (Figure 2.3). Extension of the ligand to contain up to 11 benzene rings gives oligoparaxylene ligands which can be used to form isoreticular MOFs to IRMOF-74. The extended ligands are substituted with hexyl side chains in order to ensure their solubility during the MOF synthesis. The pore apertures of this series range from 14 to 98 Å, increasing with increasing ligand length. All structures are non-interpenetrating and contain one-dimensional hexagonal channels (Figure 2.3).

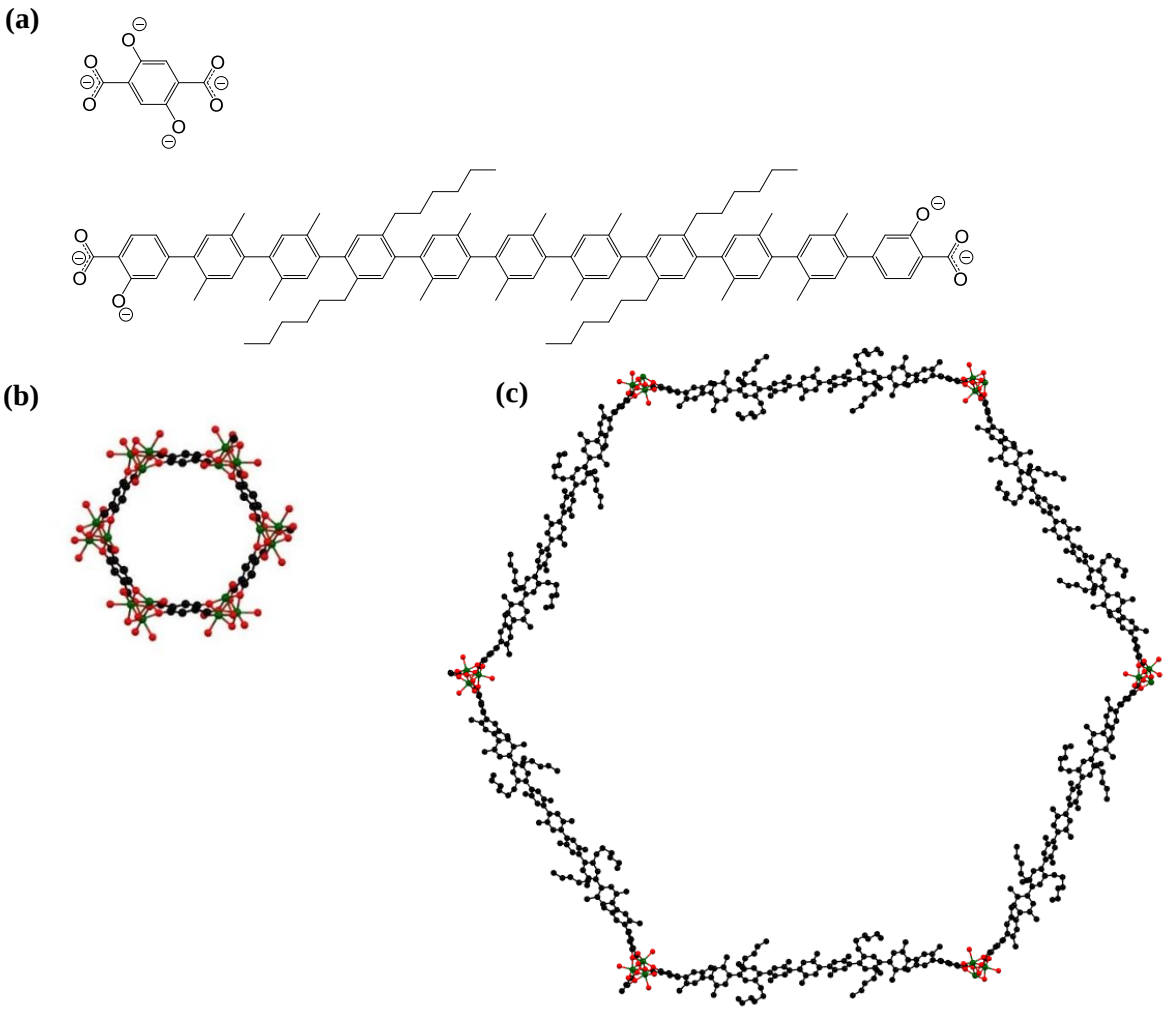

Figure 2.3 (a) The dioxidoterephthalate ligand in IRMOF-74 and the extended oligoparaxylene ligand containing eleven phenylene rings and hexyl side chains **(b)** crystal structure of IRMOF-74 showing the hexagonal pores and **(c)** pore structure containing the extended ligand containing 11 phenylene rings.[9] Hydrogen atoms have been omitted for clarity. Magnesium atoms are shown in green, oxygen in red and carbon in black.

Ligand extension methods of pore expansion such as the ones described above often require complex ligand synthesis which can be undesirable for applications. Therefore other methods of pore size control have been sought. One such method has been demonstrated in the MOF systems of the formula [Cd(bdc-NH_2)(bpy)] (bdc-NH_2 = 2-amino-1,4-benzenedicarboxylate, bpy = 4,4'-bipyridine). These systems have the same formula but different topologies and pore environments (Figure 2.4).[1] By altering reaction conditions such as concentration and time, three different products were formed. Different solvent inclusions and structural perturbations lead to the three unique structures with differing pore geometries and sizes ranging from non-porous (interpenetrating) to micro and mesoporous structures.

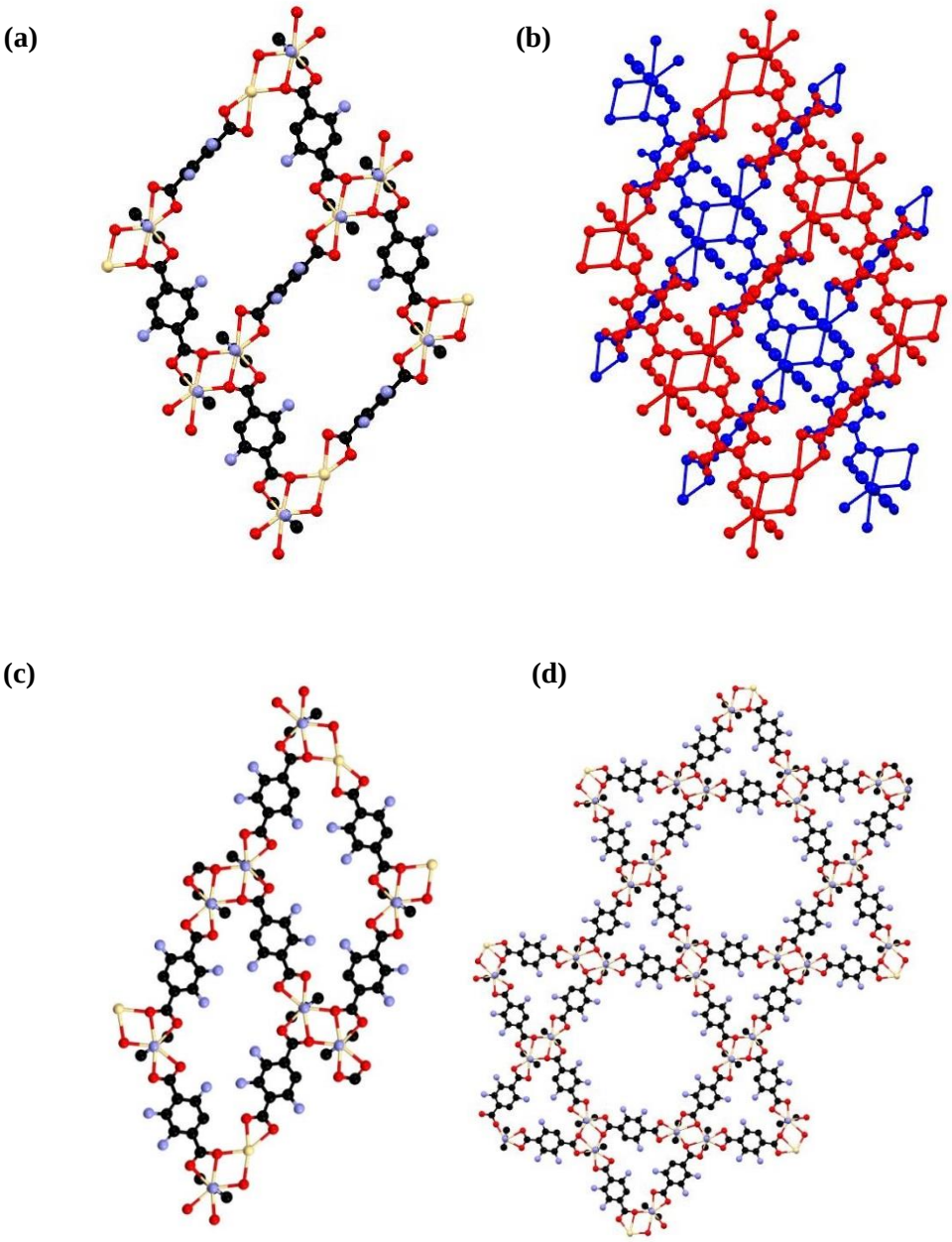

Figure 2.4 Structures of [Cd(bdc-NH_2)(bpy)]. **(a)** The interpenetrating structure showing pore topology, **(b)** the two nets of the interpenetrating structure in blue and red, **(c)** the microporous structure and **(d)** the mesoporous structure.[1] In all structures the amino group is disordered on the bdc-NH_2 ligand. In **(a)** the amino group is disordered over two available positions of the ring whilst in **(b)** and **(c)** it is disordered over three available positions. Cadmium atoms are shown in yellow, oxygen in red, carbon in black and nitrogen in blue. All hydrogens are omitted for clarity.

Pore size alterations can also occur in MOFs that exhibit framework flexibility. Such MOFs can undergo structural transformations in response to external stimuli, such as a change in the guest molecules, temperature or pressure. An example of this behaviour is seen in the flexible system [Al(OH)(bdc)], MIL-53 which undergoes pore compression or expansion depending on the size of the guest molecules included within the structure.[10] When water molecules are present within the framework, the structure displays a narrow, rhomboidal pore. This is due to attractive forces

between the water molecules and the framework which hold the structure in this narrow form. Upon removal of the guest molecules the attractive forces are removed, and the pores expand to give the open form of the MOF (Figure 2.5).

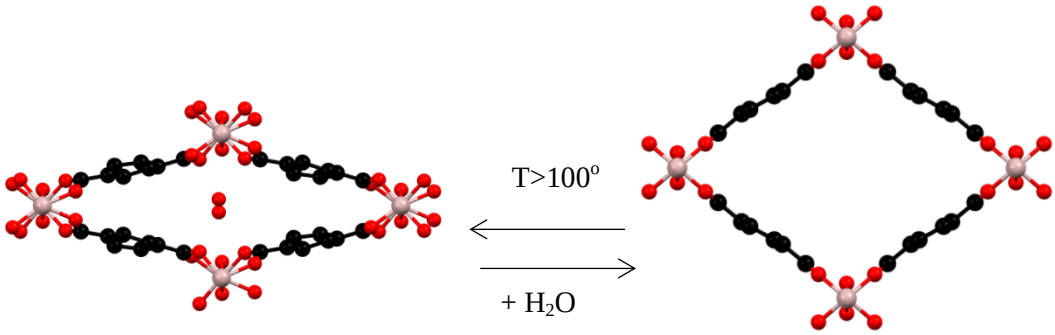

Figure 2.5 Pore shapes of MIL-53 upon adsorption and desorption of water into the pores.[10] Aluminium atoms are shown in pink, oxygen in red and carbon in black. Hydrogen atoms are omitted for clarity.

2.1.1 The structure and properties of DMOF-1

DMOF-1 is a zinc-based pillared MOF of the formula $[Zn_2(bdc)_2(dabco)]\cdot 1.4DMF\cdot 0.5H_2O$[11] where bdc is 1,4-benzenedicarboxylate and dabco is 1,4-diazabicyclo[2.2.2]octane. The SBU contains two zinc centres which are bridged by four dicarboxylate groups in a paddlewheel arrangement. The SBUs are linked together by the bdc linkers forming two-dimensional sheets, which are in turn linked together in a three-dimensional grid by dabco ligands (Figure 2.6). DMOF-1 has square pores; however the dicarboxylate ligands are distorted resulting in them being bent away from a linear square grid arrangement, instead alternating in and out of the pore (Figure 2.6).

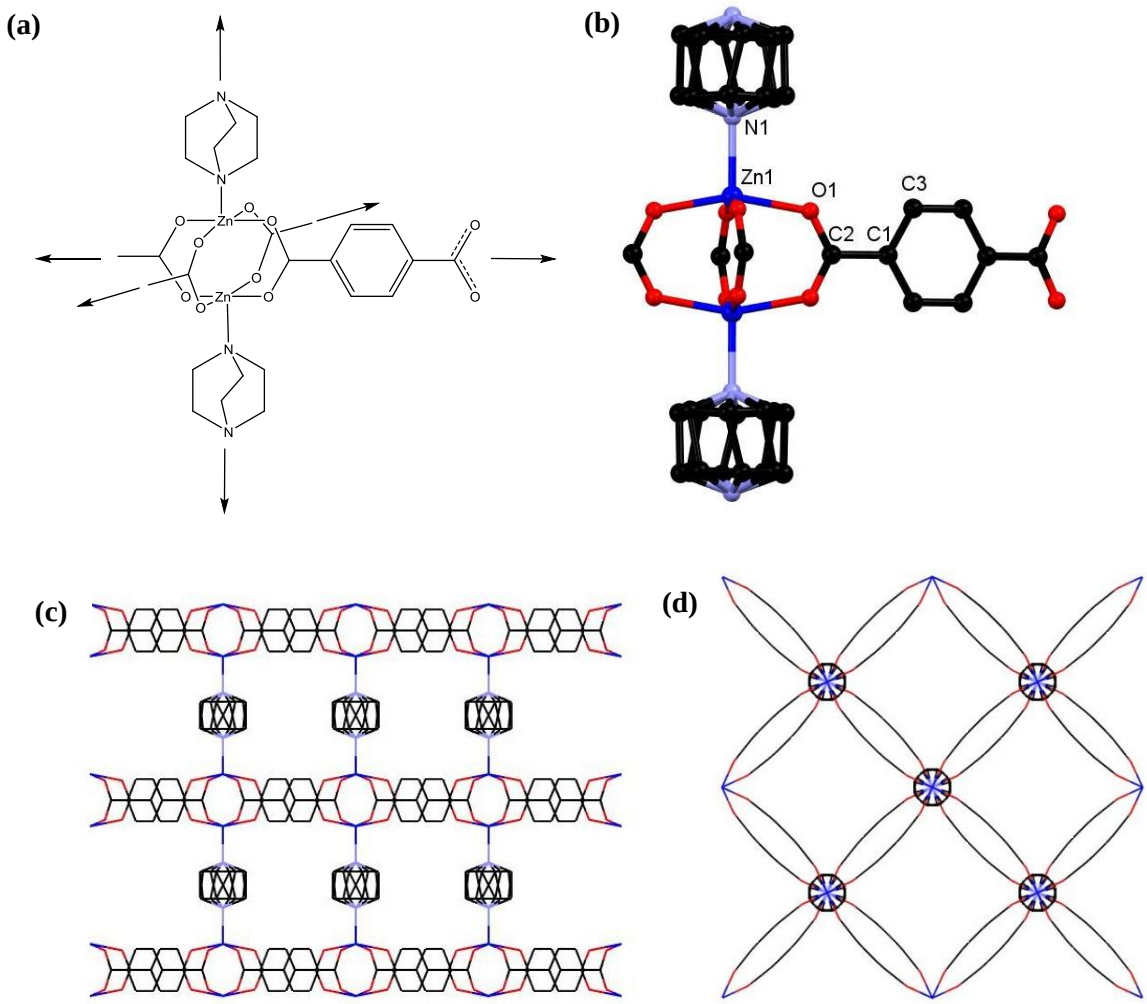

Figure 2.6 (a) A schematic representation and **(b)** the crystallographic structure of the paddlewheel motif in $[Zn_2(bdc)_2(dabco)]\cdot 1.4DMF\cdot 0.5H_2O$. The dabco moiety is disordered. **(c)** View of the 3-dimensional grid down the *a*-axis and **(d)** *c*-axis. All hydrogen atoms and solvent molecules have been removed for clarity.[11]

DMOF-1 is a flexible MOF, undergoing pore geometry and size alterations with changes of the guest molecules within the pores. This flexibility is largely due to its paddlewheel motif, which imparts elasticity to the framework.[12] When synthesised, DMOF-1 contains DMF and H_2O molecules within its pores. In this solvated form, the DMOF-1 displays a cubic grid framework with open square pores. Upon exchange of the DMF/H_2O solvent occupying the pores for benzene

molecules, a contraction of the pore occurs.[11] This contraction results in the formation of a compressed structure in which the overall topology of the framework remains the same as the DMF/H_2O containing framework but in which the pore shape and size is altered from the cubic grid to a rhomboidal grid (Figure 2.7). This behaviour is accompanied by a loss in the ligand distortion, with the rhomboidal or narrow pore form exhibiting ligands which are directly overlaid when viewed along the pillared axis of the framework (Figure 2.7). The pore contraction is reversible upon the removal of the benzene guest and is often referred to as a breathing phenomenon.

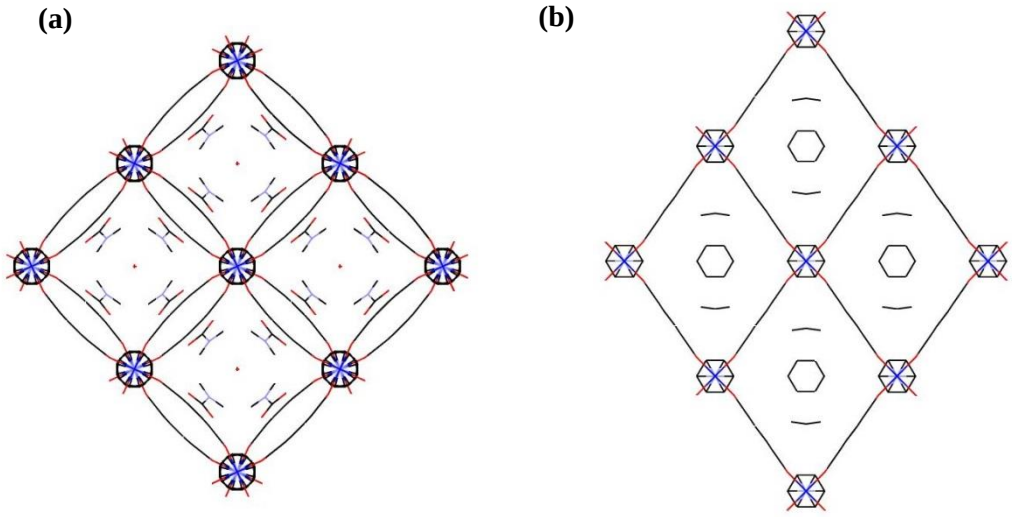

Figure 2.7 The pore shapes and geometries of DMOF-1 **(a)** with DMF and H_2O solvent occupying the pores viewed down the *c*-axis and **(b)** with benzene molecules within the pores viewed down the *a*-axis. Hydrogen atoms are omitted for clarity.[11]

The pore size and geometry of DMOF-1 type structures have been modulated by post-synthetic modification (PSM) methods, taking advantage of the framework's inherent flexibility.[13] The amino-functionalised framework $[Zn_2(bdc\text{-}NH_2)_2(dabco)]\cdot nDMF$, DMOF-1-$NH_2$ has undergone PSM with reactions targeting the amino groups within the framework to form amide functionalised ligands of varying chain length (Figure 2.8).

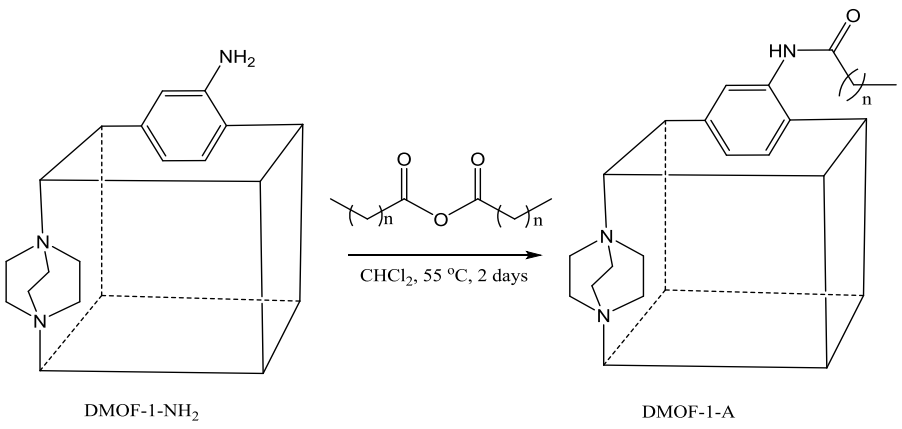

Figure 2.8 Schematic depiction of the PSM reaction on DMOF-1-NH_2 to give amide functionalised DMOF-1-A structures of varying chain length, *n*.[13]

A structural analysis of the products found that those containing shorter alkyl chains gave rise to stabilised narrow pore structures in which rhomboidal pores were present, whilst products containing longer chains stabilised the open, square pore form of the MOF. Mid-length alkyl chains (n = 2,3) lead to structures that could switch between narrow and open pore forms giving rise to breathing. Therefore by varying the alkyl chain length via PSM, some control over the pore geometry and shape of the MOF could be achieved. Weak chain-chain interactions such as van der Waals' interactions and steric interactions are possible explanations for this observed behaviour.

Pore shape and geometry changes in DMOF-1 structures have also been observed upon modification of the benzenedicarboxylate ligand. The addition of a functional group at the ortho-position of the benzene ring can give rise to a characteristic pore shape (square or rhomboidal) and size (open or narrow) for a given DMOF-1 type framework. The observed pore geometries for functionalised DMOF-1 type structures of the form $[Zn_2(bdc\text{-}X)_2(dabco)]\cdot nDMF$ (bdc-X = bdc-Br or bdc-NH_2) are shown in Figure 2.9. The addition of a bromo group at the ortho position on the ligand results in the framework $[Zn_2(bdc\text{-}Br)_2(dabco)]\cdot 4.4DMF$ which has rhomboidal, narrow pores in its solvated form. Addition of an amino group at the ortho position, in $[Zn_2(bdc\text{-}NH_2)_2(dabco)]\cdot nDMF$ results in a framework with square, open pores in its solvated form, similar to that of the unfunctionalised DMOF-1. However, instead of having distorted ligands as in DMOF-1, the DMOF-1-NH_2 structure has ligands in an overlaying arrangement.

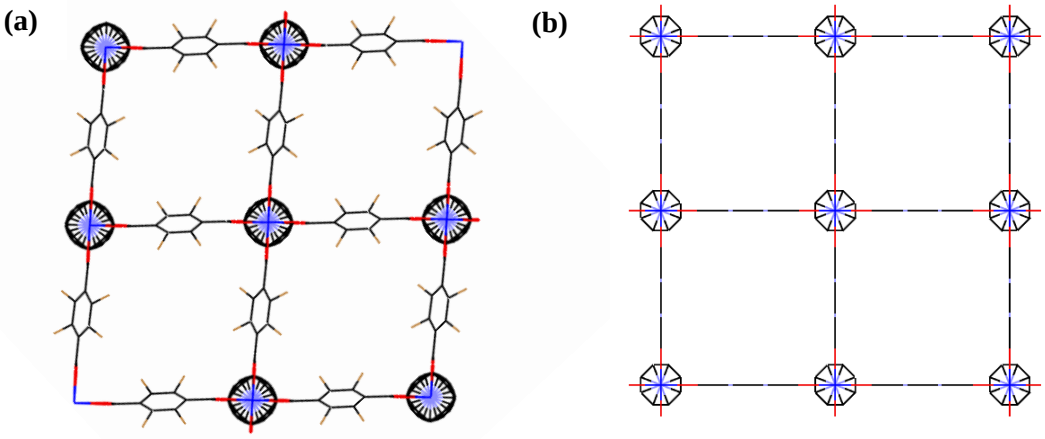

Figure 2.9 Pore geometry of **(a)** $[Zn_2(bdc\text{-}Br)_2(dabco)]\cdot 4.4DMF$[14] and **(b)** $[Zn_2(bdc\text{-}NH_2)_2(dabco)]\cdot nDMF$.[15] Both structures are viewed down the *c*-axis and all hydrogen atoms are omitted for clarity.

2.2 Compositional control of pore geometry through non-covalent interactions

2.2.1 Aims and objectives

With the addition of functional groups onto the dicarboxylate ligand in DMOF-1 giving pore shape and size variations, a multivariate MOF investigation was undertaken to investigate the possibility of tailoring pore geometry and size through compositional control. Systems based around the DMOF-1 structure containing two types of benzenedicarboxylate ligands, each performing the same structural role within the framework, were investigated. For each system, one ligand contains a hydrogen atom at the ortho-position on the benzene ring (unfunctionalised) and one ligand contains a different functional group on the ortho-position on the benzene ring (functionalised).

The ratios of unfunctionalised to functionalised ligand within the system were varied systematically to produce a series of mixed-ligand MOFs. This approach allowed the effect of functional group content on the framework structure to be investigated. Firstly, two systems which contain halide substituents on the benzenedicarboxylate ligands were investigated to assess the effect on the pore geometry and shape with varying halide content. These contain the 1,4-benzenedicarboxylate (bdc) ligand and either 2-bromo-1,4-benzenedicarboxylate (bdc-Br) or 2-iodo-1,4-benzenedicarboxylate (bdc-I) ligands. Two further systems were investigated as a comparison to the halogenated series containing nitro and amino functionalised ligands. These systems contain 1,4-benzenedicarboxylate (bdc) and 2-nitro-1,4-benzenedicarboxylate (bdc-NO_2) or 2-amino-1,4-benzenedicarboxylate (bdc-NH_2) respectively.

Following on from these studies, systems which contain two different functionalised ligands, replacing the unfunctionalised ligand entirely, were investigated, containing varying amounts of bdc-Br/bdc-I and bdc-NO_2/bdc-NH_2.

In all systems, the composition of the structures and any ligand preferences were investigated through ^{1}H NMR spectroscopy. The topology and structure of resulting products were studied through powder X-ray diffraction and single crystal X-ray diffraction studies. This work is also enhanced by collaboration with Jessica Bristow and Aron Walsh who provided computational studies to accompany the experimental work.

2.2.2 Synthesis and characterisation of $[Zn_2(bdc)_{2-x}(bdc\text{-}Br)_x(dabco)]\cdot nDMF$

In order to investigate the effects of varying the 2-bromo-1,4-dicarboxylate (bdc-Br): 1,4-benzenedicarboxylate (bdc) ratio within the DMOF-1 type structure, a series of mixed ligand compounds were prepared. As $[Zn_2(bdc\text{-}Br)_2(dabco)]\cdot 4.4DMF$, DMOF-1-Br, is known to present rhomboidal, narrow pores, the mixed-ligand products were investigated to assess the effect on the pore geometry and shape by varying bdc-Br content within the framework. Reactions of $Zn(NO_3)_2\cdot 6H_2O$ with dabco and mixtures of H_2bdc and H_2bdc-Br were carried out in DMF at 120 °C for three days. By varying the ratio of the dicarboxylic acids H_2bdc:H_2bdc-Br in the reaction mixture, a range of crystalline products was formed all of which gave colourless block crystals. Reaction mixtures containing 89:11, 81:19, 70:30, 50:50, 39:61, 27:73, 19:81 and 10:90 ratios of H_2bdc:H_2bdc-Br were prepared. The products of all eight reactions were soaked and washed in fresh DMF three times over three days to ensure any unreacted starting materials were removed.

In order to determine the composition of the products ^{1}H NMR spectra were recorded on acid-digested samples of the MOFs which had been dried at 120 ^{o}C for 15 minutes using a d_6-DMSO/DCl mixture. ^{1}H NMR spectra carried out on *ca.* 5 mg of each sample prepared in this way are referred to as the bulk NMR spectra. All of the products showed the presence of both dicarboxylate ligands. An example of a bulk NMR spectrum is shown in Figure 2.10.

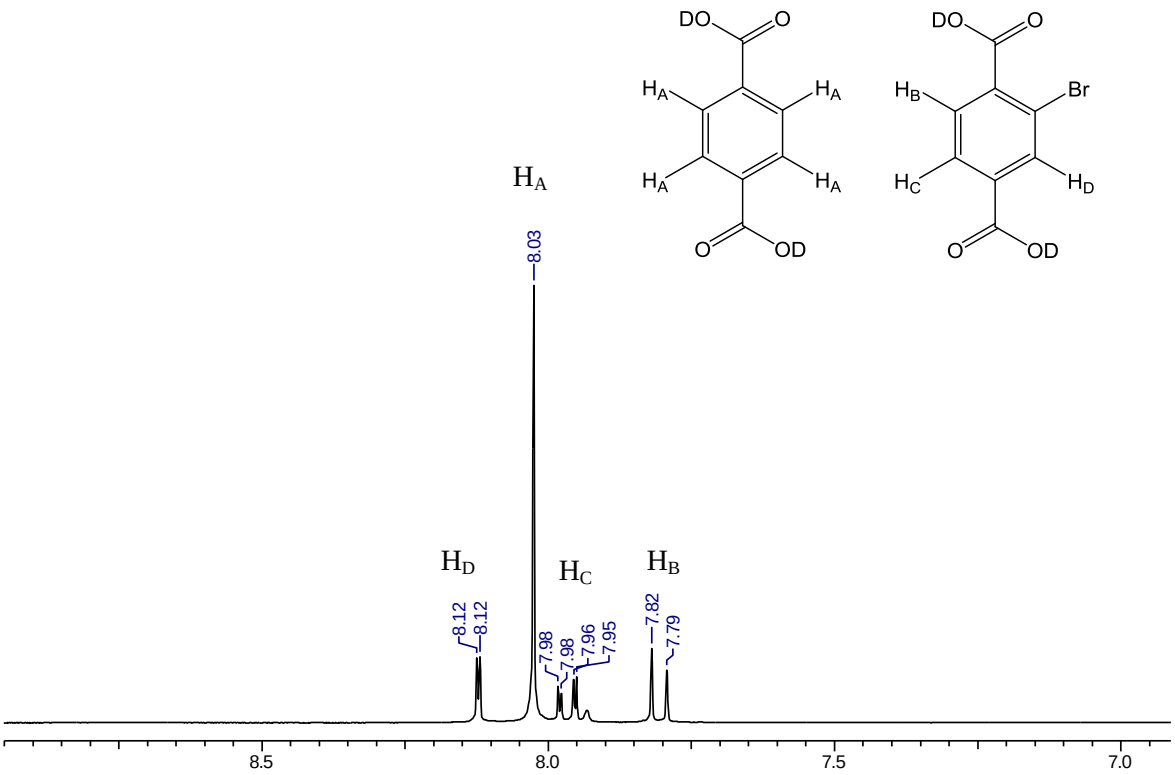

Figure 2.10 ^{1}H NMR spectrum of the acid-digested product formed from a reaction mixture containing 27 % H_2bdc and 73 % H_2bdc-Br. The structures of the two deuterated dicarboxylic acids are also shown.

The peak at δ 8.03 ppm corresponds to the four aromatic protons of D_2bdc (in its acid form following MOF digestion). The peaks at δ 8.12 ppm, δ 7.97 ppm and δ 7.81 ppm, correspond to the three aromatic protons of D_2bdc-Br with each resonance representing one proton. The unlabelled peak at δ 7.93 ppm corresponds to the DMF solvent present in the sample. ^{1}H NMR spectra of all products are shown in Figure 2.11.

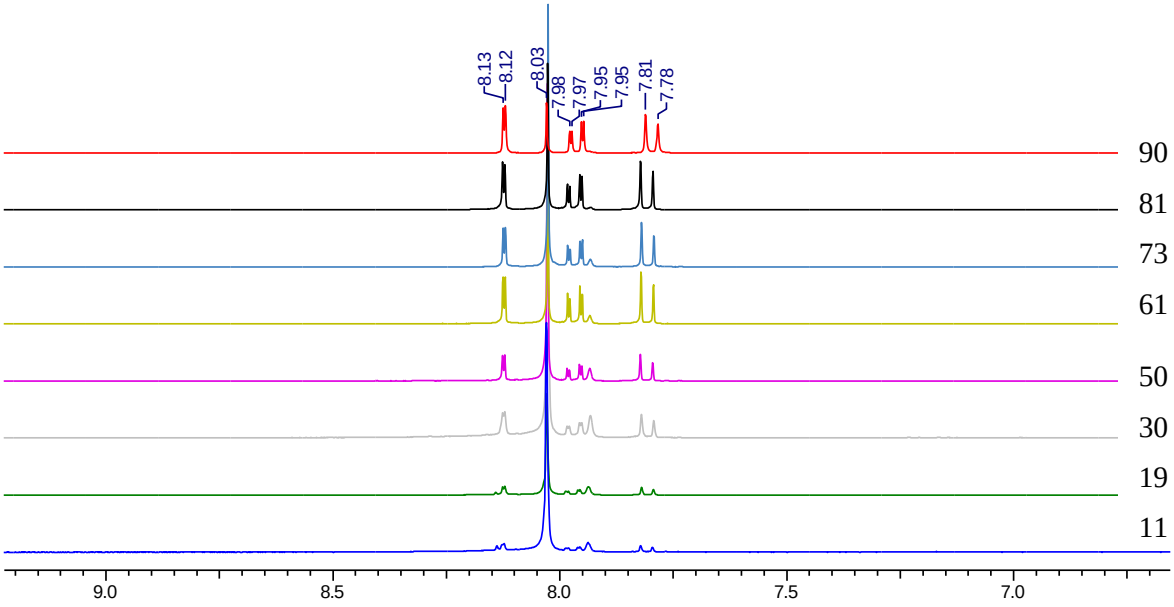

Figure 2.11 ^{1}H NMR spectra of acid-digested products formed from varying ratios of H_2bdc:H_2bdc-Br. The percentage of H_2bdc-Br used in the reaction mixture is shown alongside the corresponding spectrum.

Although both ligands are present in the bulk NMR spectra this alone does not confirm the formation of mixed-ligand products, as the formation of a discrete mixture of two single ligand frameworks, $[Zn_2(bdc)_2(dabco)]$ and $[Zn_2(bdc\text{-}Br)_2(dabco)]$ could also explain these results. Therefore, in addition to studying bulk samples, ^{1}H NMR spectra were also recorded on individual acid digested crystals of the products from the reactions containing 30, 61 and 90% H_2bdc-Br. An individual crystal was selected in each case using a microscope and digested in a d_6-DMSO/DCl mixture, in a similar manner to that of the bulk samples.

The ^{1}H NMR spectra of digested individual crystals showed the presence of both dicarboxylic acids, indicating that each crystal contains both dicarboxylate ligands and therefore are truly mixed-ligand species. An example of an individual crystal ^{1}H NMR spectrum of a crystal taken from the reaction mixture containing 10 % H_2bdc and 90 % H_2bdc-Br is given in Figure 2.12.

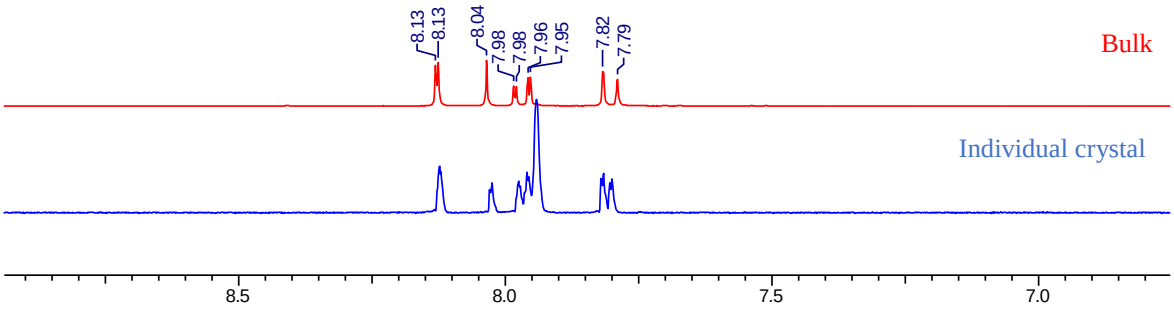

Figure 2.12 ^{1}H NMR spectra of acid digested bulk and individual crystal samples from a reaction mixture containing 10 % H_2bdc and 90 % H_2bdc-Br.

Both the singlet associated with the D_2bdc species at δ 8.03 ppm and the peaks associated with the D_2bdc-Br species at δ 8.12 ppm, δ 7.96 ppm and δ 7.82 ppm are present in the spectrum. The peak at δ 7.94 ppm originates from the DMF solvent present in the sample. The products formed can therefore be confirmed to be mixed-ligand species. Analysis of the integrated ^{1}H NMR spectra shown in Figure 2.12 determined a bdc:bdc-Br content of 15:85 from the bulk and 11:89 from the individual crystal sample. This similarity in composition from both bulk and individual crystal samples suggests little compositional variation is present within this product.

This analysis of the integrated ^{1}H NMR spectra taken of both bulk and individual crystal samples was extended to all products. In order to standardise this process, integrals from the peaks at δ 8.12 ppm and δ 8.03 ppm were compared for all products and the percentage of D_2bdc-Br present in the digestion mixtures are shown in Figure 2.13. The integration shows that there is no apparent ligand preference in the products, with similar ratios of the D_2bdc:D_2bdc-Br dicarboxylic acids present in the acid digested samples to those of the corresponding reaction mixtures.

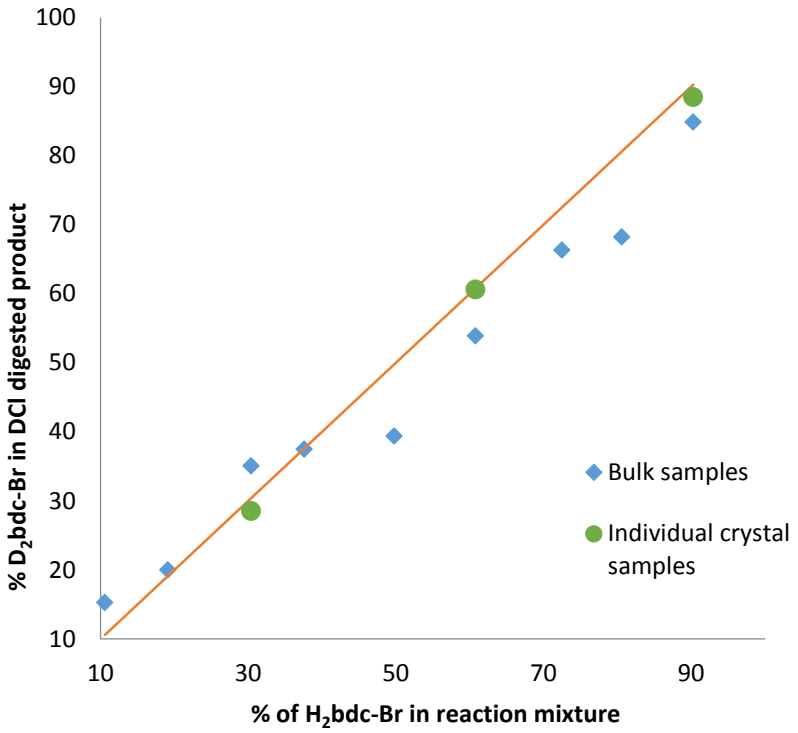

Figure 2.13 A plot of the percentage D_2bdc-Br content in the acid digested products against the percentage of H_2bdc-Br in the reaction mixture.

Bulk and individual crystal samples from the same product show similar D_2bdc:D_2bdc-Br ratios to one another, with a variation in D_2bdc-Br content from 3 % to 7 % indicating that there is little compositional variation within each sample. The ligand ratios determined from ^{1}H NMR spectra of the bulk samples are therefore considered to be representative of the product composition which are given in Table 2.1.

Table 2.1 Experimental percentages of H_2bdc-Br and the corresponding average percentage of bdc-Br in the products as determined through ^{1}H NMR studies. Corresponding product formulae excluding guest solvent are also given.

% H_2bdc-Br in reaction mixture	**Average % bdc-Br in product**	**Average Product Formula (as determined through ^{1}H NMR studies)**
11	15	$[Zn_2(bdc)_{1.7}(bdc\text{-}Br)_{0.3}(dabco)]$
19	20	$[Zn_2(bdc)_{1.44}(bdc\text{-}Br)_{0.56}(dabco)]$
30	35	$[Zn_2(bdc)_{1.36}(bdc\text{-}Br)_{0.64}(dabco)]$
50	39	$[Zn_2(bdc)_{1.2}(bdc\text{-}Br)_{0.8}(dabco)]$
61	54	$[Zn_2(bdc)_{0.8}(bdc\text{-}Br)_{1.2}(dabco)]$
73	66	$[Zn_2(bdc)_{0.67}(bdc\text{-}Br)_{1.33}(dabco)]$
81	68	$[Zn_2(bdc)_{0.5}(bdc\text{-}Br)_{1.5}(dabco)]$
90	85	$[Zn_2(bdc)_{0.3}(bdc\text{-}Br)_{1.7}(dabco)]$

All products were analysed by powder X-ray diffraction and gave powder XRD patterns containing the same general features as one another, suggesting all compounds possess similar framework topologies. A comparison to powder traces generated from single crystal data for the single ligand structures $[Zn_2(bdc)_2(dabco)]\cdot 1.4DMF\cdot 0.5H_2O$[11, 14] and $[Zn_2(bdc\text{-}Br)_2(dabco)]\cdot 4.4DMF$[14] show similarities to the powder patterns obtained for the mixed ligand structures confirming the formation of the DMOF-1 type topology. The formula of the products can therefore be described as $[Zn_2(bdc)_{2-x}(bdc\text{-}Br)_x(dabco)]\cdot nDMF$.

A closer inspection of the product powder diffraction patterns reveals the presence of two unique phases, which can be identified through differences in their peak positions (Figure 2.14).

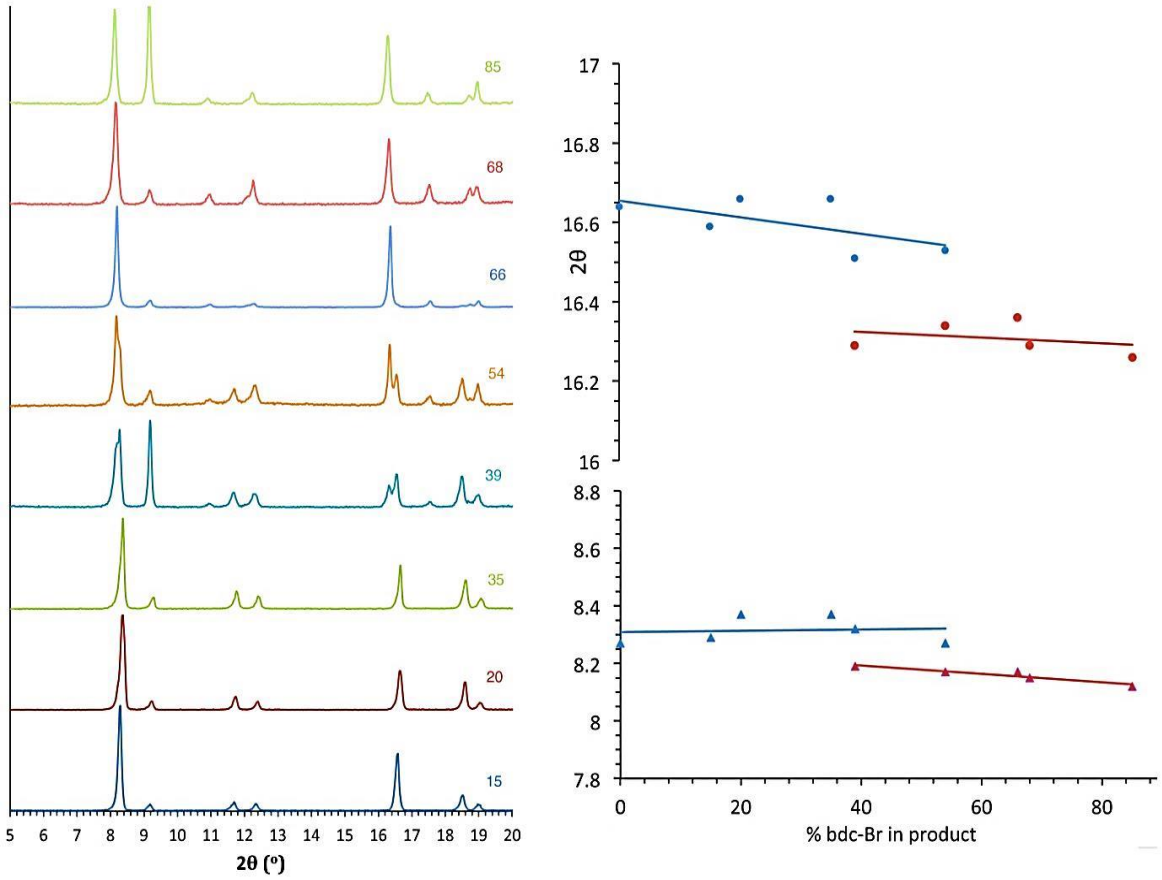

Figure 2.14 PXRD patterns of products with the number shown against each powder pattern the % bdc-Br in the sample. The plot of 2θ against % bdc-Br shows the key peaks which shift with the change in pore topology.

Above a bdc-Br content of 54%, peaks at 2θ 8.3° and 16.7° shift to lower values of 2θ 8.2° and 16.3°. A plot of the 2θ positions for these reflections is given in Figure 2.14 to demonstrate this peak shift. Such changes in peak positions are indicative of a change in the unit cell parameters. These subtle alterations in the PXRD patterns suggest that the products with higher bdc-Br content contain structural differences (concurrent with altered unit cell parameters) to those with lower bdc-Br content. The PXRD patterns from the samples with 39% and 54% bdc-Br contain peaks at both 2θ 16.7° and 16.3° and have broad shoulders on the peaks at 2θ 8.3° (Figure 2.14). The

presence of both peak positions in the PXRD patterns for these samples suggests the presence of both different phases of these products.

In order to investigate the structural differences between the two phases identified from powder diffraction analysis, single crystal X-ray diffraction was carried out on selected products. Four of the ligand ratios used yielded crystals that were suitable for single crystal X-ray diffraction, and these compounds were structurally characterised as $[Zn_2(bdc)(bdc\text{-}Br)(dabco)]\cdot 2.1DMF$ **1a**, $[Zn_2(bdc)_{0.8}(bdc\text{-}Br)_{1.2}(dabco)]\cdot DMF$ **1b**, $[Zn_2(bdc)_{0.4}(bdc\text{-}Br)_{1.6}(dabco)]\cdot 2.5DMF$ **1c** and $[Zn_2(bdc)_{0.3}(bdc\text{-}Br)_{1.7}(dabco)]$ **1d**. The samples analysed by single crystal X-ray diffraction were freshly prepared samples of $[Zn_2(bdc)_{2-x}(bdc\text{-}Br)_x(dabco)]\cdot nDMF$ synthesised by an MChem project student, Naomi Stubbs. In all structures, **1a-1d**, the bdc and bdc-Br ligand occupancies were attributed based on the ^1H NMR spectroscopy analysis of the bulk products.

Structure description of $[Zn_2(bdc)(bdc\text{-}Br)(dabco)]\cdot 2.1DMF$ **1a**

The solvent content of **1a** was determined through thermogravimetric analysis, which found a percentage mass loss of 26.5 % between 130 – 203 ^oC equating to 2.1 DMF molecules per unit formula (Figure 2.15). The thermogravimetric analysis was completed on a different batch of the product than that from which the single crystal was obtained, and therefore the solvent content attributed to **1a** is included as a guide only. Crystallographically, 0.25 DMF molecules were modelled per asymmetric unit, equating to one DMF molecule per unit formula. Although some solvent electron density was present which could not be modelled due to disorder, analysis from PLATON revealed that any residual solvent was minimal and therefore did not merit treatment with SQUEEZE.

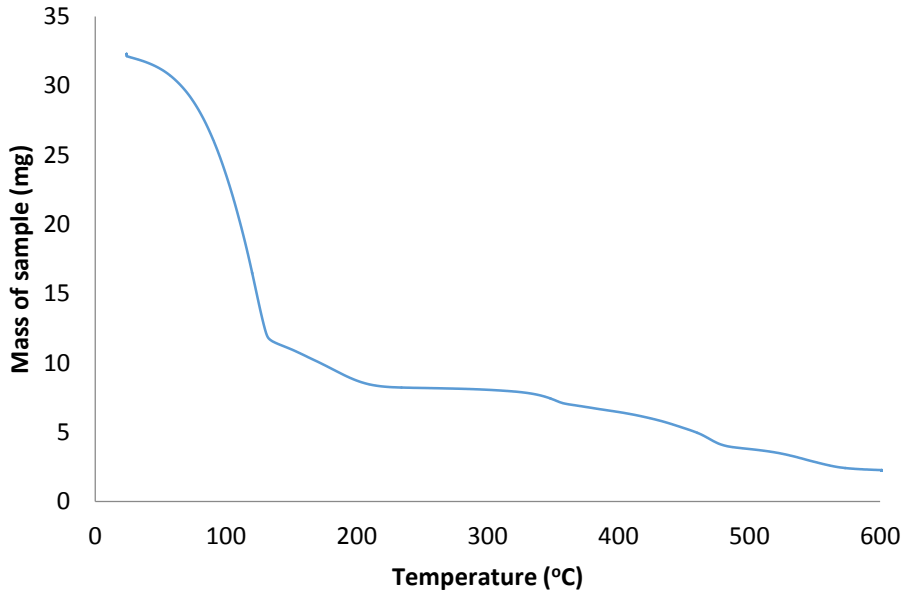

Figure 2.15 TGA of $[Zn_2(bdc\text{-}Br)_{1.36}(bdc)_{0.64}(dabco)]\cdot 2.1DMF$ (freshly made **1a**).

The asymmetric unit of **1a** comprises of two zinc atoms at 25% occupancy each, half a dicarboxylate ligand, one quarter of a dabco ligand and one DMF guest in the pore at 25% occupancy (Figure 2.16).

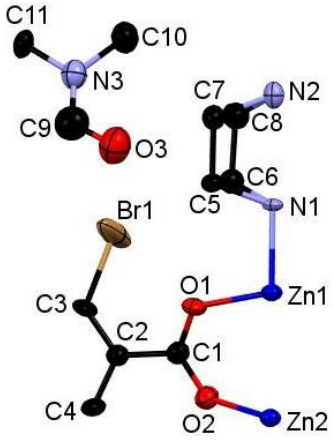

Figure 2.16 Asymmetric unit of $[Zn_2(bdc)(bdc\text{-}Br)(dabco)]\cdot 2.1DMF$ **1a** with a calculated ellipsoid probability of 40 %. Hydrogen atoms have been omitted for clarity.

N1 and N2 from the dabco present in the asymmetric unit are located on a 4-fold rotation axis and are assigned a site occupancy of 25 %. This necessarily results in symmetry related disorder of the dabco carbons (Figure 2.17). In order to model this disorder, the occupancy of C5-C8 was attributed as 37.5 % based on the electron density, giving an overall total of 6 carbons and 2 nitrogens per dabco moiety. Geometrical restraints were also employed to C-C and N-C distances within the dabco to achieve a chemically sensible convergence.

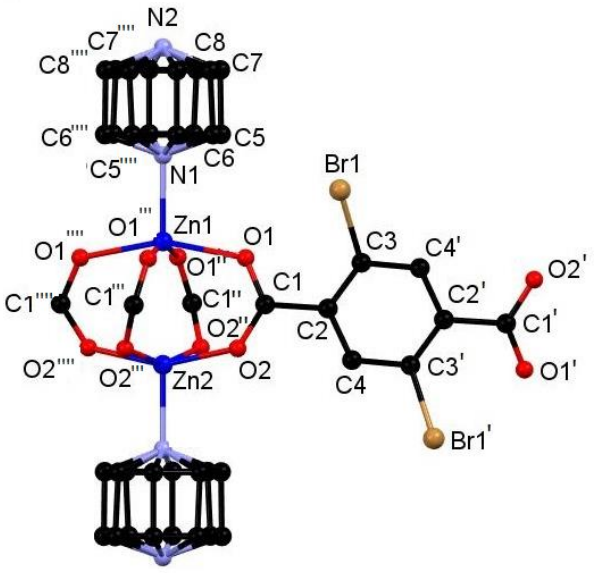

Figure 2.17 Part of the structure of $[Zn_2(bdc)(bdc\text{-}Br)(dabco)]\cdot 2.1DMF$ **1a.** Primed, double primed, triple and quadruple primed labelled atoms are related to those in the ASU by the ½ – *y*, *x* – ½, – *z* – ½, *y*, ½ – *x*, *z*, ½ –*x*, ½ – *y*, *z* and ½ –*y*, *x*, *z* symmetry operations respectively. Hydrogen atoms have been omitted for clarity.

The bromine substituent on the bdc-Br ligand is attached to C3 in the asymmetric unit and crystallographic symmetry necessarily means that this is disordered over two positions on the ligand. As the site-occupancy of Br1 25 %, and it is disordered over two positions, the total bromine content of the framework is 50 %.

The SBU of **1a** can be described as a paddlewheel motif, in which two zinc atoms are bridged by four carboxylate groups from four different bdc-Br ligands. These SBU's are then linked by the dicarboxylate ligands forming a two-dimensional sheet. The zinc ions are axially co-ordinated to the nitrogen atoms from the dabco moieties which connect the two-dimensional sheets into a three-dimensional grid (Figure 2.18).

1a crystallises in the tetragonal space group *P*4/*ncc* and displays a distorted square grid topology similar to that observed in the solvated DMOF-1 structure. The dicarboxylate linkers are bent, arching away from a linear arrangement and causing a distortion to the regular square grid topology of the framework. These distortions alternate into and out of the pore between each layer of the framework leading to square channels throughout the structure.

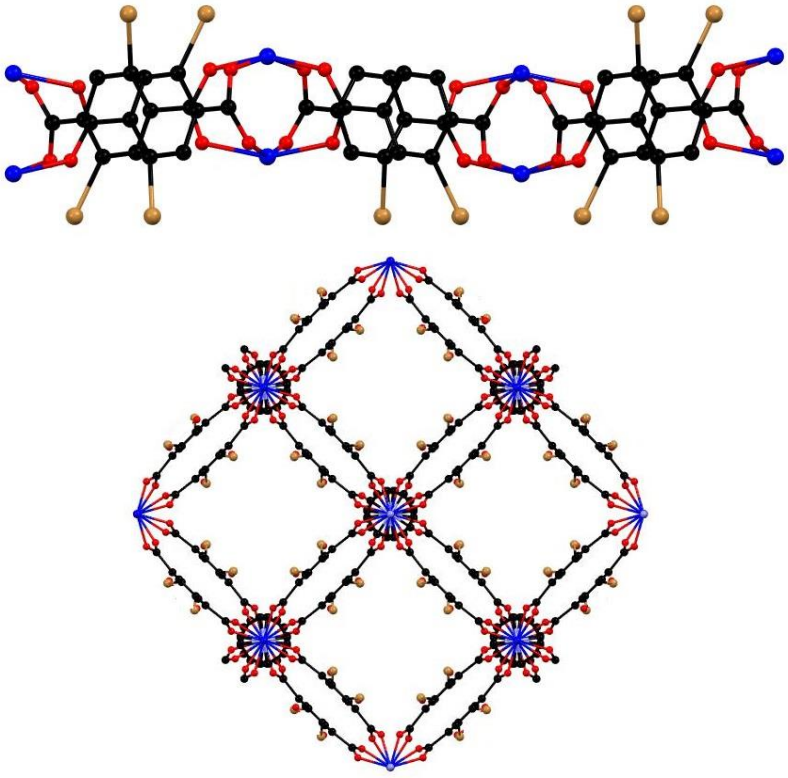

Figure 2.18 Part of the structure of $[Zn_2(bdc)(bdc\text{-}Br)(dabco)]\cdot 2.1DMF$ **1a** showing **(a)** the two-dimensional layers of paddlewheel SBUs connected by dicarboxylate ligands viewed down the *a*-axis and **(b)** the square pores over multiple layers viewed down the *c*-axis. Hydrogen atoms and solvent molecules have been omitted for clarity.

Structure description of $[Zn_2(bdc)_{0.8}(bdc\text{-}Br)_{1.2}(dabco)]\cdot DMF$ **1b**

The asymmetric unit of **1b** contains two zinc ions with an occupancy of 25 % each, half a bdc-Br ligand, one quarter of a dabco moiety and a DMF solvent molecule with an occupancy of 25 % (Figure 2.19). The overall structure of **1b** is very similar to that of **1a**, with the two structures displaying a similar connectivity and topology.

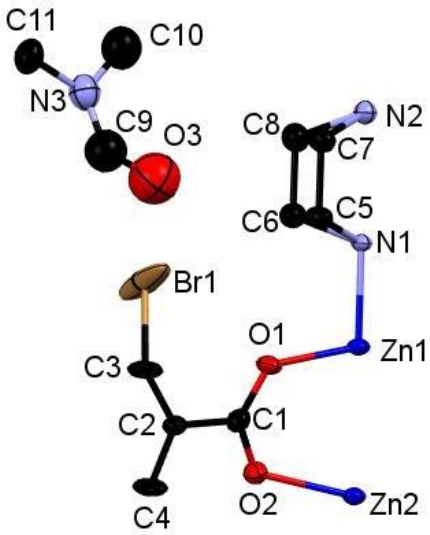

Figure 2.19 Asymmetric unit of $[Zn_2(bdc)_{0.8}(bdc\text{-}Br)_{1.2}(dabco)]\cdot DMF$ **1b** with a calculated ellipsoid probability of 40 %. Hydrogen atoms have been omitted for clarity.

The dabco moiety of **1b** displays similar disorder to that observed in **1a**, with N1 and N2 located on four-fold rotation axis resulting in symmetry related disorder of the dabco carbons. Both N1 and N2 have attributed site occupancy of 25 %. The dabco disorder was treated in a similar manner to that of **1a** with the occupancy of C5-C8 attributed as 37.5 % based on the electron density, giving an overall total of 6 carbons and 2 nitrogens per dabco moiety. Geometrical restraints were applied to N-C and C-C bond lengths to achieve a chemically sensible convergence. The bromine atom within **1b** has site occupancy of 30 % and is attached to C3 in the asymmetric unit. Crystallographic symmetry results in the bromine being disordered over two positions on the ligand, through a two-fold rotation axis, making the total bromine content 60 % per formula unit.

In a similar manner to **1a**, **1b** also crystallises space group *P*4/*ncc* (Table 2.2). It exhibits an overall distorted square grid topology similar to that observed in **1a** and the solvated DMOF-1 structure. Thermogravimetric analysis was not completed for **1b** but residual electron density was present in the pores of the structure. Analysis with PLATON revealed that this was minimal and therefore did not merit treatment with SQUEEZE.

Table 2.2 Crystal data and structure refinement for $[Zn_2(bdc)(bdc\text{-}Br)(dabco)]\cdot 2.1DMF$ **1a** and $[Zn_2(bdc)_{0.8}(bdc\text{-}Br)_{1.2}(dabco)]\cdot DMF$ **1b**

Identification code	**1a**	**1b**
Empirical formula	$C_{25}H_{26}BrN_3O_9Zn_2$	$C_{25}H_{25.8}O_9N_3Br_{1.2}Zn_2$
Formula weight	723.14	738.92
Temperature/K	150.15	150(2)
Crystal system	tetragonal	tetragonal
Space group	*P*4/*ncc*	*P*4/*ncc*
a/Å	14.9880(4)	14.9760(4)
b/Å	14.9880(4)	14.9760(4)
c/Å	19.2400(5)	19.2380(6)
α/°	90	90
β/°	90	90
γ/°	90	90
Volume/Å^3	4322.1(3)	4314.7(3)
Z	4	4
ρ_{calc}g/cm^3	1.111	1.138
μ/mm^{-1}	2.071	2.260
F(000)	1456.0	1483.0
Crystal size/mm^3	0.25 × 0.18 × 0.13	0.25 × 0.18 × 0.13
Radiation	Mo*K*α (λ = 0.71073)	Mo*K*α (λ = 0.71073)
2θ range for data collection/°	8.6 to 50.038	7.414 to 50.052
Index ranges	$-17 \le h \le 17$, $-17 \le k \le 17$, $-22 \le l \le 22$	$-17 \le h \le 16$, $-14 \le k \le 17$, $-22 \le l \le 22$
Reflections collected	71851	20056
Independent reflections	1901 [R_{int} = 0.0967, R_{sigma} = 0.0173]	1904 [R_{int} = 0.0561, R_{sigma} = 0.0276]
Data/restraints/parameters	1901/73/162	1904/78/162
Goodness-of-fit on F^2	1.160	1.129
Final *R* indexes [$I>=2\sigma(I)$]	R_1 = 0.0917, wR_2 = 0.2620	R_1 = 0.0967, wR_2 = 0.2472
Final *R* indexes [all data]	R_1 = 0.1212, wR_2 = 0.2795	R_1 = 0.1109, wR_2 = 0.2558
Largest diff. peak/hole / e Å^{-3}	1.02/-0.78	1.34/-1.22

Structure description of $[Zn_2(bdc)_{0.4}(bdc\text{-}Br)_{1.6}(dabco)]\cdot 2.5DMF$ **1c**

The solvent content of **1c** was determined through thermogravimetric analysis which indicates a percentage mass loss of 28.9 % between 120 – 200 ^{o}C (Figure 2.20). This corresponds to a solvent loss of 2.5 molecules of DMF per pair of zinc atoms.

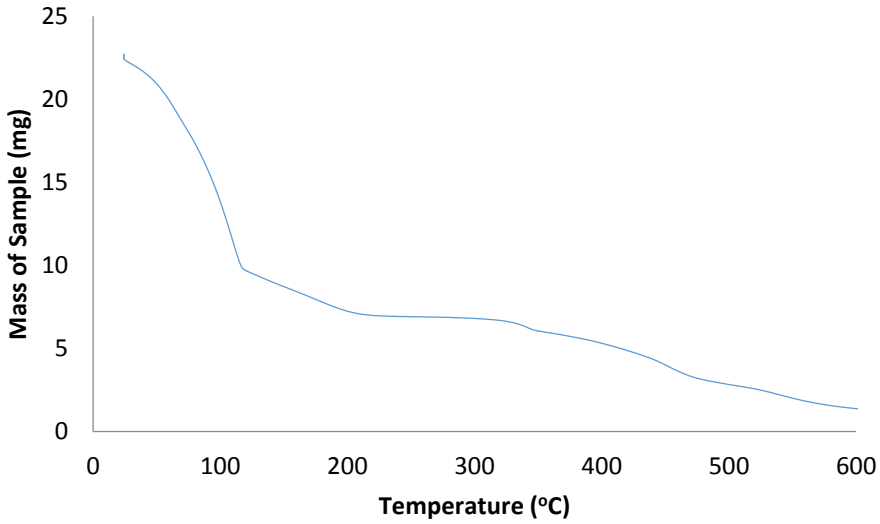

Figure 2.20 TGA of $[Zn_2(bdc)_{0.4}(bdc\text{-}Br)_{1.6}(dabco)]\cdot 2.5DMF$ **1c**.

The thermogravimetric analysis was conducted on a different batch of **1c** to that of the single crystal X-ray diffraction analysis, and therefore the solvent content is a guide only. Crystallographically no solvent could be modelled within the structure of **1c**, although disordered solvent electron density was present within the pores but could not be modelled due to disorder. Analysis by PLATON indicated this did not merit treatment with the SQUEEZE algorithm.

The asymmetric unit of **1c** contains one zinc atom at 25 % occupancy, one quarter of a dabco moiety and one quarter of the dicarboxylate ligand. The dicarboxylate ligand displays disorder, with C3 and Br1 atoms disordered over two positions in the asymmetric unit (Figure 2.21).

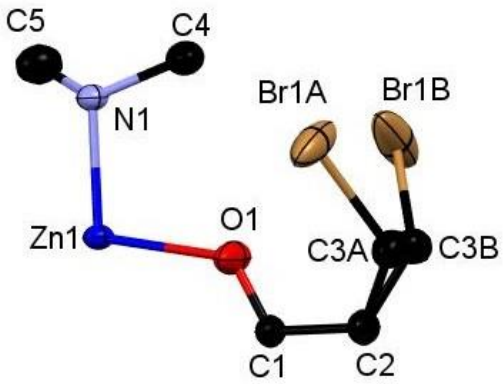

Figure 2.21 Asymmetric unit of $[Zn_2(bdc)_{0.4}(bdc\text{-}Br)_{1.6}(dabco)]\cdot 2.5DMF$ **1c** with calculated ellipsoid probability of 40 %. Hydrogen atoms have been omitted for clarity.

The disordered dicarboxylate ligand is modelled by attributing the site occupancy of C3A and C3B at 50 % based on electron density. The bdc and bdc-Br ligands are disordered over the same sites, with the symmetry related atoms of the ligands generated through an inversion centre, two-fold rotation axis and a mirror plane perpendicular to the *a*-axis. The bromine substituent of bdc-Br is disordered over the two sites Br1A and Br1B with site occupancies of 15 % and 5 % respectively. Overall, through symmetry generation of a whole dicarboxylate ligand the bromine is disordered across all available positions of each ring and the total bromine content of the framework is 80 % (Figure 2.22). Disordered hydrogen atoms could not be located reliably on the ring and were omitted from the model.

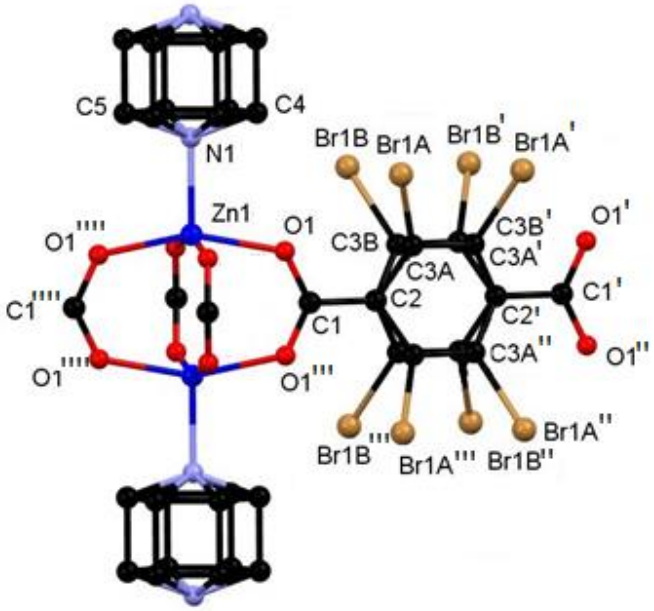

Figure 2.22 Part of the structure of $[Zn_2(bdc)_{0.4}(bdc\text{-}Br)_{1.6}(dabco)]\cdot 2.5DMF$ **1c**. Primed, double primed, triple primed and quadruple primed atoms are related to the asymmetric unit by the *x*, ½ – *y*, ½ – *z*, – *x*, ½ – *y*, ½ - *z*, –*x*, *y*, *z* and *x*, 1 – *y*, – *z* symmetry operations respectively. Hydrogen atoms are omitted for clarity.

N1 from the dabco moiety in the asymmetric unit is located on a two-fold rotation axis and both N1 and C5 are located on a mirror plane perpendicular to the *c*-axis. This results in symmetry related disorder of the dabco moiety. In order to model the disorder present in the dabco, the occupancy of N1, C4 and C5 was attributed at 25 %, 50 % and 25 % respectively, resulting in a total of 6 carbons and two nitrogens per dabco moiety. N1, C4 and C5 are also located about an inversion centre, generating the entire dabco moiety (Figure 2.22). Atomic displacement parameter restraints were employed for C4 and C5.

The SBU of **1c** can be described as a paddlewheel motif, in which two zinc atoms are bridged by four carboxylate groups from four different dicarboxylate ligands. These SBU's are then linked by the dicarboxylate ligands and dabco moieties to form three-dimensional grid in a similar manner to **1a**.

1c crystallises in the orthorhombic space group *Ammm* and displays a rhomboidal grid topology (Figure 2.23). The dicarboxylate linkers can be described as linear resulting in regular rhomboidal channels throughout the structure.

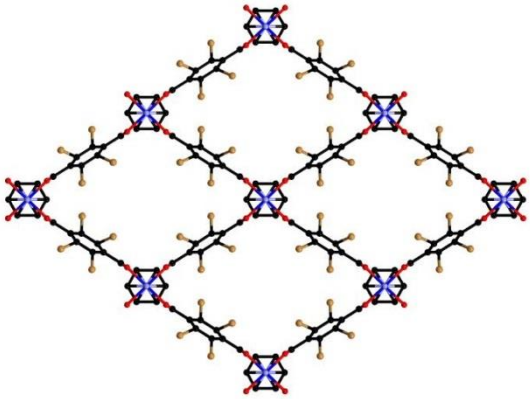

Figure 2.23 The rhomboidal pores of $[Zn_2(bdc)_{0.4}(bdc\text{-}Br)_{1.6}(dabco)]\cdot 2.5DMF$ **1c** viewed down the *a*-axis. Hydrogen atoms are omitted for clarity.

Structure description of $[Zn_2(bdc)_{0.3}(bdc\text{-}Br)_{1.7}(dabco)]$ **1d**

The asymmetric unit of **1d** contains one zinc atom at 25 % occupancy, one quarter of a dabco moiety and one quarter of the dicarboxylate ligand. The dicarboxylate ligand displays disorder in a similar manner to that in **1c**, with C3 and Br1 atoms disordered over two positions in the asymmetric unit (Figure 2.24). Both C3A and C3B have site occupancy of 50 %.

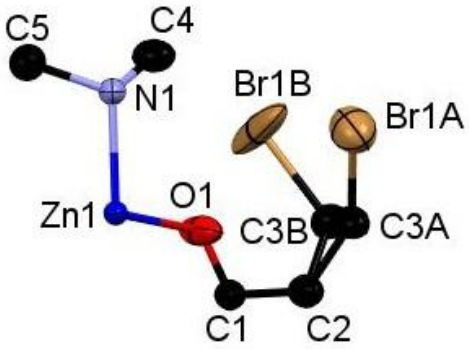

Figure 2.24 Asymmetric Unit of $[Zn_2(bdc)_{0.3}(bdc\text{-}Br)_{1.7}(dabco)]$ **1d** with an ellipsoid probability of 40 %. Hydrogen atoms are omitted for clarity.

The bromine atom of bdc-Br is disordered over two positions with a site occupancy of 16.25 % for Br1A and 5 % for Br1B based on the electron density. Symmetry generation of the whole dicarboxylate ligand through an inversion centre, two-fold rotation axis and a mirror plane perpendicular to the *a*-axis result in the bromine atom being disordered over all available positions of the two dicarboxylate rings present. The total bromine content of the framework is therefore 85 %. The dabco moiety displays similar disorder to that present in **1c** with N1 located on a two-

fold rotation axis and both N1 and C5 located on a mirror plane perpendicular to the *c*-axis. The occupancy of N1, C4 and C5 is 25 %, 50 % and 25 % respectively, resulting in a total of 6 carbons and two nitrogens per dabco moiety. Similarly to **1c** N1, C4 and C5 are also located about an inversion centre, generating the entire dabco moiety. Atomic displacement parameter restraints were employed for C4 and C5.

In a similar manner to **1c**, **1d** also crystallises in space group *Ammm* (Table 2.3) and displays a rhomboidal grid topology. Thermogravimetric analysis was not completed for **1d** but residual electron density was present in the pores of the structure. Analysis with PLATON revealed that this was minimal and therefore did not merit treatment with SQUEEZE.

Table 2.3 Crystal data and structure refinement for $[Zn_2(bdc)_{0.4}(bdc\text{-}Br)_{1.6}(dabco)]\cdot 2.5DMF$ **1c** and $[Zn_2(bdc)_{0.3}(bdc\text{-}Br)_{1.7}(dabco)]$ **1d**

Identification code	**1c**	**1d**
Empirical formula	$C_{22}H_{18.4}O_8Br_{1.6}Zn_2N_2$	$C_{22}H_{18.3}O_8Br_{1.7}Zn_2N_2$
Formula weight	697.38	705.27
Temperature/K	150.15	150.15
Crystal system	orthorhombic	orthorhombic
Space group	*Ammm*	*Ammm*
a/Å	9.6280(2)	9.6230(3)
b/Å	12.7590(2)	12.8580(6)
c/Å	17.5720(3)	17.4800(8)
α/°	90	90
β/°	90	90
γ/°	90	90
Volume/Å^3	2158.61(7)	2162.84(16)
Z	2	2
ρ_{calc}g/cm^3	1.073	1.083
μ/mm^{-1}	2.621	2.708
F(000)	689.0	696.0
Crystal size/mm^3	0.3 × 0.3 × 0.2	0.3 × 0.3 × 0.2
Radiation	Mo*K*α (λ = 0.71073)	Mo*K*α (λ = 0.71073)
2θ range for data collection/°	7.664 to 55.136	9.794 to 55.206
Index ranges	-12 ≤ *h* ≤ 12, -16 ≤ *k* ≤ 16, -22 ≤ *l* ≤ 22	-12 ≤ *h* ≤ 12, -16 ≤ *k* ≤ 16, -22 ≤ *l* ≤ 22
Reflections collected	19984	15147
Independent reflections	1399 [R_{int} = 0.0437, R_{sigma} = 0.0176]	1403 [R_{int} = 0.0752, R_{sigma} = 0.0281]
Data/restraints/parameters	1399/36/81	1403/36/81
Goodness-of-fit on F^2	1.146	1.069
Final *R* indexes [*I*>=2σ (*I*)]	R_1 = 0.0653, wR_2 = 0.1840	R_1 = 0.0735, wR_2 = 0.2074
Final *R* indexes [all data]	R_1 = 0.0697, wR_2 = 0.1897	R_1 = 0.0786, wR_2 = 0.2131
Largest diff. peak/hole / e Å^{-3}	0.98/-0.56	1.37/-0.94

Compounds **1a**-**1d** contain the expected gross DMOF-1 framework topology, consistent with PXRD results. A clear difference in the crystal structures is observed between the lower bdc-Br

content structures **1a** and **1b** which display a square grid topology framework and the higher bdc-Br content structures **1c** and **1d** which display a rhomboidal grid topology framework

The subtle changes observed in the experimental PXRD patterns from low to high bdc-Br content reflect changes in the unit cell parameters that occur with the change in pore geometry, from square pores at low bdc-Br content to rhomboidal pores at high bdc-Br content within the framework. A comparison of the frameworks of **1c** and **1d** to that of $[Zn_2(bdc\text{-}Br)_2(dabco)]\cdot 4.4DMF$[14] show that the pores in the mixed-ligand structures are compressed to a higher degree than in the single ligand parent (Table 2.4).

Table 2.4 Zn···Zn distances in single and mixed-ligand systems of $[Zn_2(bdc)_{2-x}(bdc\text{-}Br)_x(dabco)]\cdot nDMF$.

Structure	Pore shape	Shortest pore diagonal Zn···Zn (Å)
$[Zn_2(bdc)_2(dabco)]\cdot 1.4DMF\cdot 0.5H_2O$ (DMOF-1)[11]	Distorted square	15.063(2)
$[Zn_2(bdc)(bdc\text{-}Br)(dabco)]\cdot 2.1DMF$ **1a**	Distorted square	14.9880(4)
$[Zn_2(bdc)_{0.8}(bdc\text{-}Br)_{1.2}(dabco)]\cdot DMF$ **1b**	Distorted square	14.9760(4)
$[Zn_2(bdc)_{0.4}(bdc\text{-}Br)_{1.6}(dabco)]\cdot 2.5DMF$ **1c**	Rhomboidal	12.7590(2)
$[Zn_2(bdc)_{0.3}(bdc\text{-}Br)_{1.7}(dabco)]$ **1d**	Rhomboidal	12.8580(6)
$[Zn_2(bdc\text{-}Br)_2(dabco)]\cdot 4.4DMF$[14]	Rhomboidal	14.627(3)

The experimental powder XRD patterns of **1a** and **1b** show similar features to that of the powder X-ray patterns simulated from their respective single crystal structures (Figure 2.25).

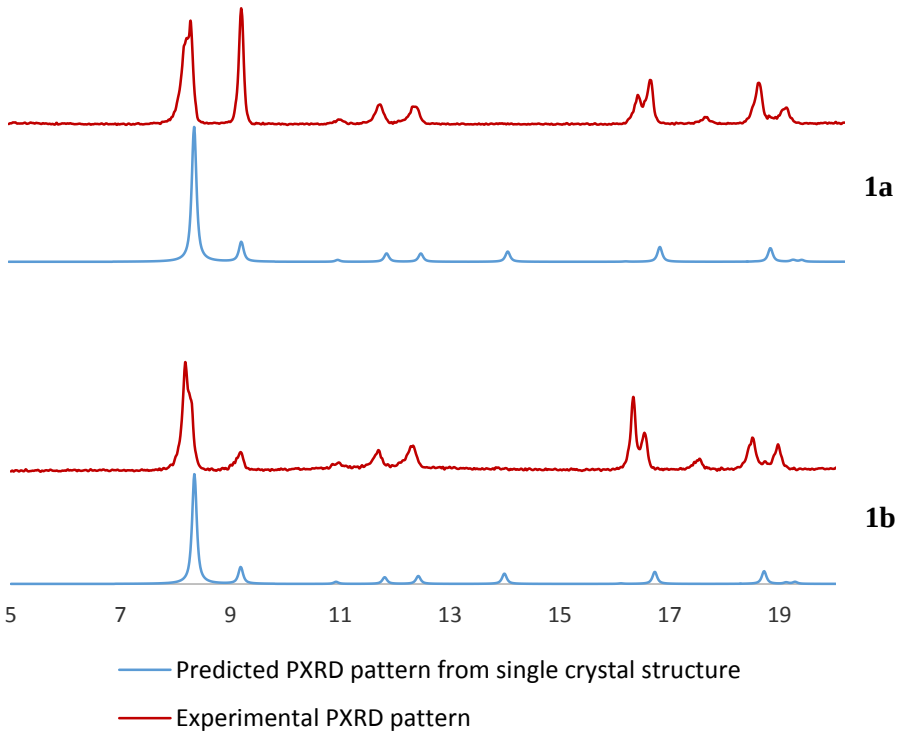

Figure 2.25 Predicted and experimental PXRD patterns of $[Zn_2(bdc)(bdc\text{-}Br)(dabco)]\cdot 2.1DMF$ **1a** (top) and $[Zn_2(bdc)_{0.8}(bdc\text{-}Br)_{1.2}(dabco)]\cdot DMF$ **1b** (bottom).

However, the experimental powder X-ray diffraction patterns of **1c** and **1d** show a number of differences in the positions of the peaks to the corresponding simulated patterns from single crystal data (Figure 2.26). Most notable is a shift in the peak at 2θ value of 8.14° in the simulated PXRD pattern from the single crystal data, to a 2θ value of 8.66° in the experimental PXRD pattern.

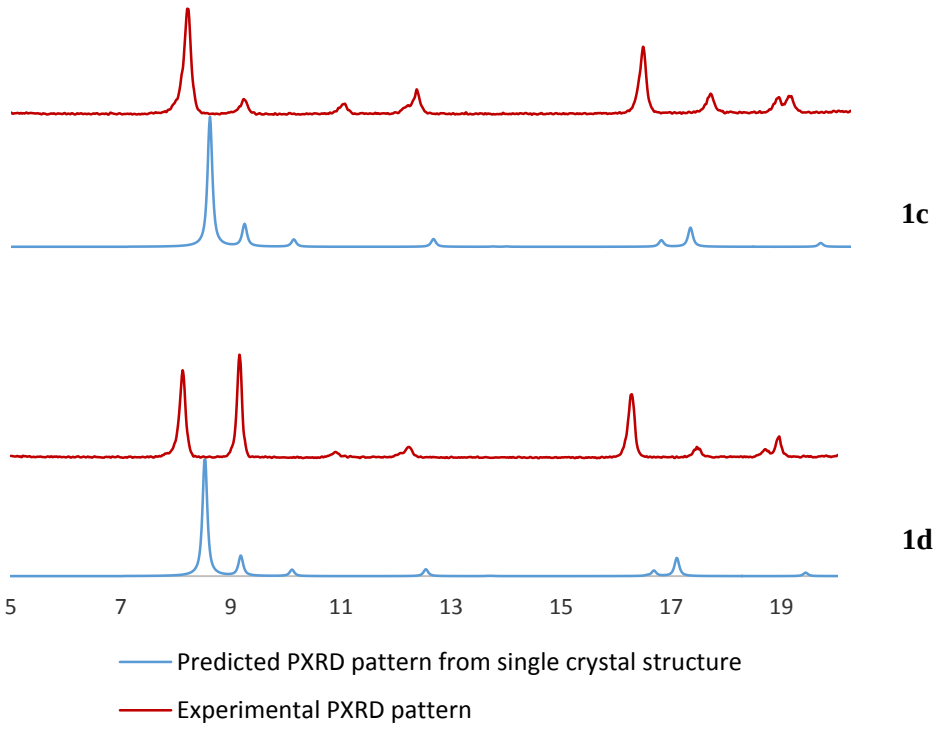

Figure 2.26 Predicted and experimental PXRD patterns of $[Zn_2(bdc)_{0.27}(bdc\text{-}Br)_{1.73}(dabco)]\cdot 2.5DMF$ **1c** (top) and $[Zn_2(bdc)_{0.3}(bdc\text{-}Br)_{1.7}(dabco)]$ **1d** (bottom).

These differences were suspected of being related to the difference in temperature at which the diffraction patterns were generated – with the experimental patterns being collected at ambient temperature and the single crystal X-ray diffraction data collected at 150 K. To test this theory, the single crystal data for **1c** was re-collected at ambient temperature (**1c'**). The overall topology of **1c'** was found to be similar to that of **1c**, crystallising in an orthorhombic space group and presenting rhomboidal pores. However, a significant change in the unit cell parameters between the structures of **1c** and **1c'** was observed (Table 2.5). A comparison of the structures of **1c** and **1c'** shows that the compression of the pores is more acute in **1c** than in **1c'** (Figure 2.27). This change in the pores accounts for the changes in unit cell parameters observed between the two structures.

Table 2.5 Unit cell parameters for $[Zn_2(bdc)_{0.27}(bdc\text{-}Br)_{1.73}(dabco)]\cdot 2.5DMF$ collected at 150 K **1c** and 298 K **1c'**.

Compound	**1c**	**1c'**
Temperature/K	150	298
Crystal system	Orthorhombic	Orthorhombic
Space group	*Ammm*	*Ammm*
a/Å	9.6280(2)	9.6342(14)
b/Å	12.7590(2)	16.488(3)
c/Å	17.5720(3)	14.229(3)
α/°	90	90
β/°	90	90
γ/°	90	90
Unit cell volume/Å^3	2158.61(7)	2260.2(8)

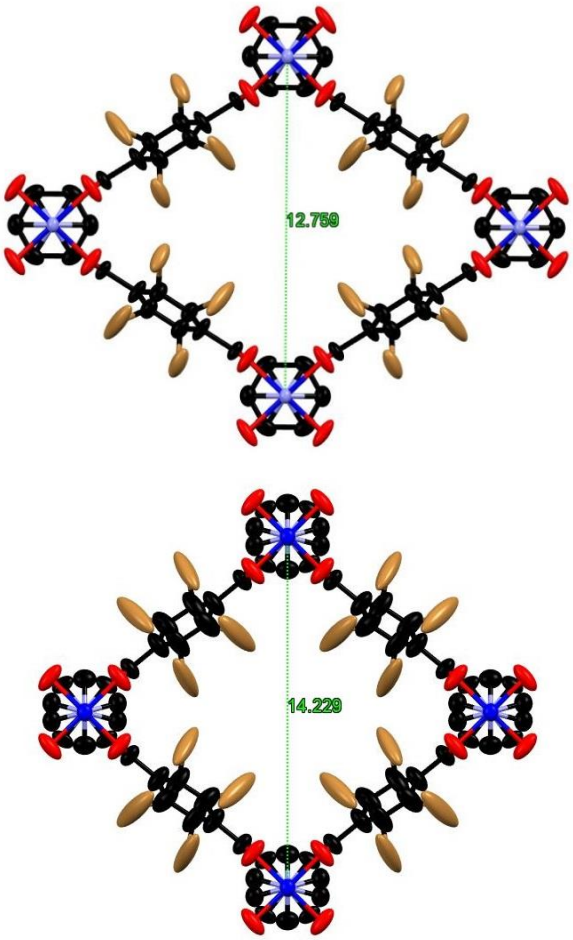

1c

1c'

Figure 2.27 Pore structures of $[Zn_2(bdc)_{0.27}(bdc\text{-}Br)_{1.73}(dabco)]\cdot 2.6DMF$ **1c** (top) and **1c'** (bottom) showing the Zn···Zn distances across the pore in Å. Ellipsoids are calculated with an ellipsoid probability of 40 %.

Whilst the structure of **1c'** is similar to that of **1c** a notable difference is present in the disorder of the dabco moieties between the two structures. In **1c'** the asymmetric unit contains one quarter of the dabco moiety, with the carbons disordered over three positions with respective site occupancies of 14 %, 30.5 % and 30.5 %. Symmetry generation of the dabco moiety through a two-fold rotation axis, mirror plane and inversion centre give a total of two nitrogen atoms and six carbon atoms.

The simulated PXRD pattern of **1c'** matches that of the experimental PXRD pattern of **1c** (Figure 2.28). This confirms that the differences in the PXRD between single crystal and experimental patterns of **1c** and **1d** are due to the difference in temperature at which the collections were carried out. After the room temperature collection, **1c'** was cooled to 150 K and data collected to determine the unit cell parameters, which matched that of **1c**.

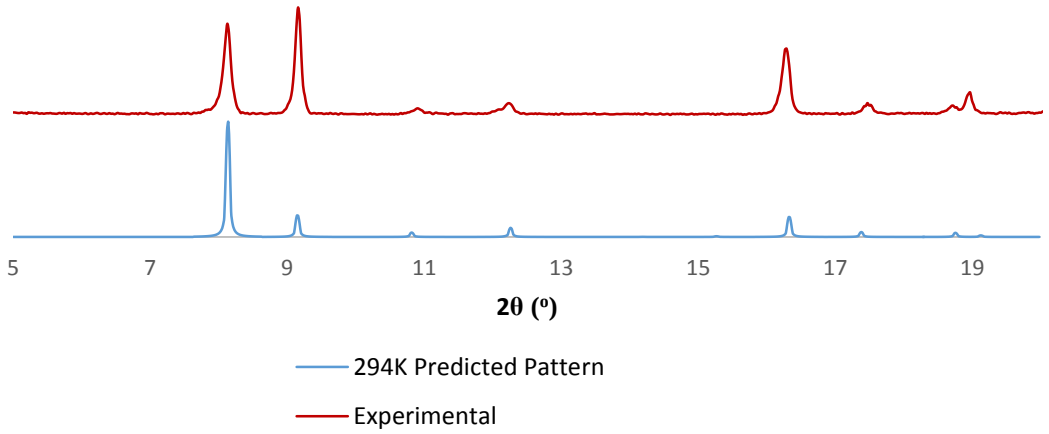

Figure 2.28 Experimental PXRD pattern of $[Zn_2(bdc)_{0.27}(bdc\text{-}Br)_{1.73}(dabco)]\cdot 2.5DMF$ **1c** compared to the predicted pattern from single crystal data collections at 298 K **1c'**.

The powder diffraction patterns of compounds containing 39 % and 85 % bdc-Br show an increase in intensity of the second reflection observed compared to the other compounds in the series (refer to Figure 2.14). This difference in relative peak intensity is largely due to differing solvent content within the pores of the structures. This was successfully demonstrated through the generation of artificial electron density within the pores of the structure of **1a.** A centroid was generated within the pore and assigned electron density. The structure was refined and the resulting calculated powder X-ray diffraction pattern showed alterations in the relative peak intensities making them more akin to that for the experimental powder diffraction pattern.

2.2.3 Synthesis and characterisation of $[Zn_2(bdc)_{2-x}(bdc\text{-}I)_x(dabco)]\cdot nDMF$

The mixed-ligand series containing bdc and bdc-I (2-iodo-1,4-dicarboxylate) ligands based around the DMOF-1 structure was investigated. This system was chosen in order to determine any effects arising from the inclusion of a larger halide group into the DMOF-1 framework. As the $[Zn_2(bdc\text{-}I)_2(dabco)]$, DMOF-1-I structure containing bdc-I ligands has not previously been reported, it was first synthesised prior to the mixed-ligand investigations. The H_2bdc-I ligand was synthesised according to a literature procedure (Scheme 2.1).[16] The reaction of the H_2bdc-I ligand with $Zn(NO_3)_2\cdot 6H_2O$ and dabco was carried out under similar conditions to that of DMOF-1. The reaction yielded colourless, needle shaped crystals which were analysed by powder X-ray diffraction. The diffraction pattern was compared to that of DMOF-1-Br (which displays rhomboidal pores) and showed similar peak positions indicating an isoreticular MOF had been formed (Figure 2.29).

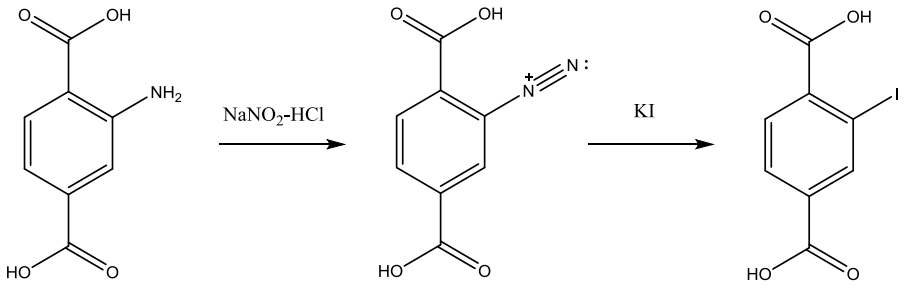

Scheme 2.1 Synthetic procedure for formation of iodoterephthalic acid, H_2bdc-I.[16]

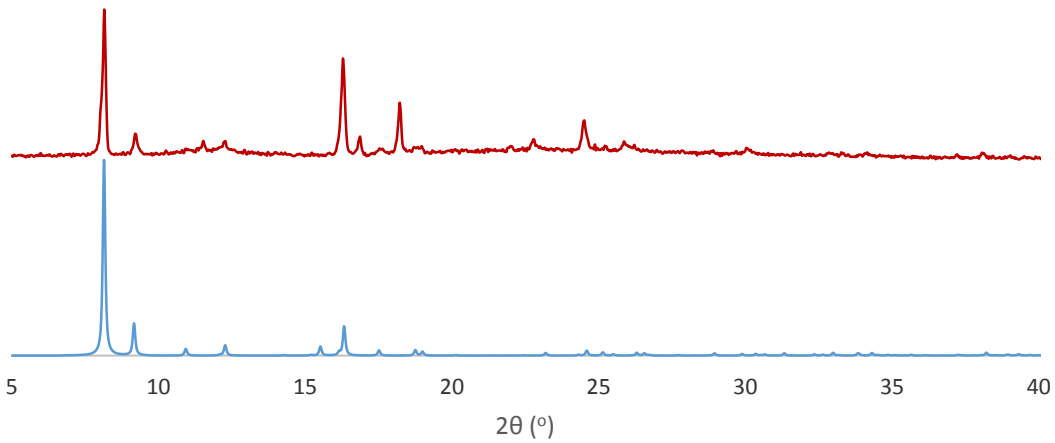

Figure 2.29 Experimental PXRD pattern of $[Zn_2(bdc\text{-}I)_2(dabco)]$ (top) compared to the predicted pattern from single crystal data of $[Zn_2(bdc\text{-}Br)_2(dabco)]$ (bottom).

Following on from the mixed ligand compounds $[Zn_2(bdc)_{2-x}(bdc\text{-}Br)_x(dabco)]\cdot nDMF$ discussed in Section 2.2.2, a similar synthetic method was employed to form mixed-ligand products containing

both 1,4-benzenedicarboxylate (bdc) and 2-iodo-1,4-dicarboxylate (bdc-I) ligands in varying ratios. Six ratios of bdc:bdc-I were used. All products gave colourless, thin needle crystals.

^{1}H NMR spectroscopy was carried out on bulk samples of dried, acid digested products (Figure 2.30). The acid digestion was completed in a d_6-DMSO/DCl mixture. All products showed the presence of both D_2bdc (singlet at δ 8.01 ppm) and D_2bdc-I (peaks at δ 8.38 ppm, δ 7.96 ppm and δ 7.74 ppm) in the digested sample.

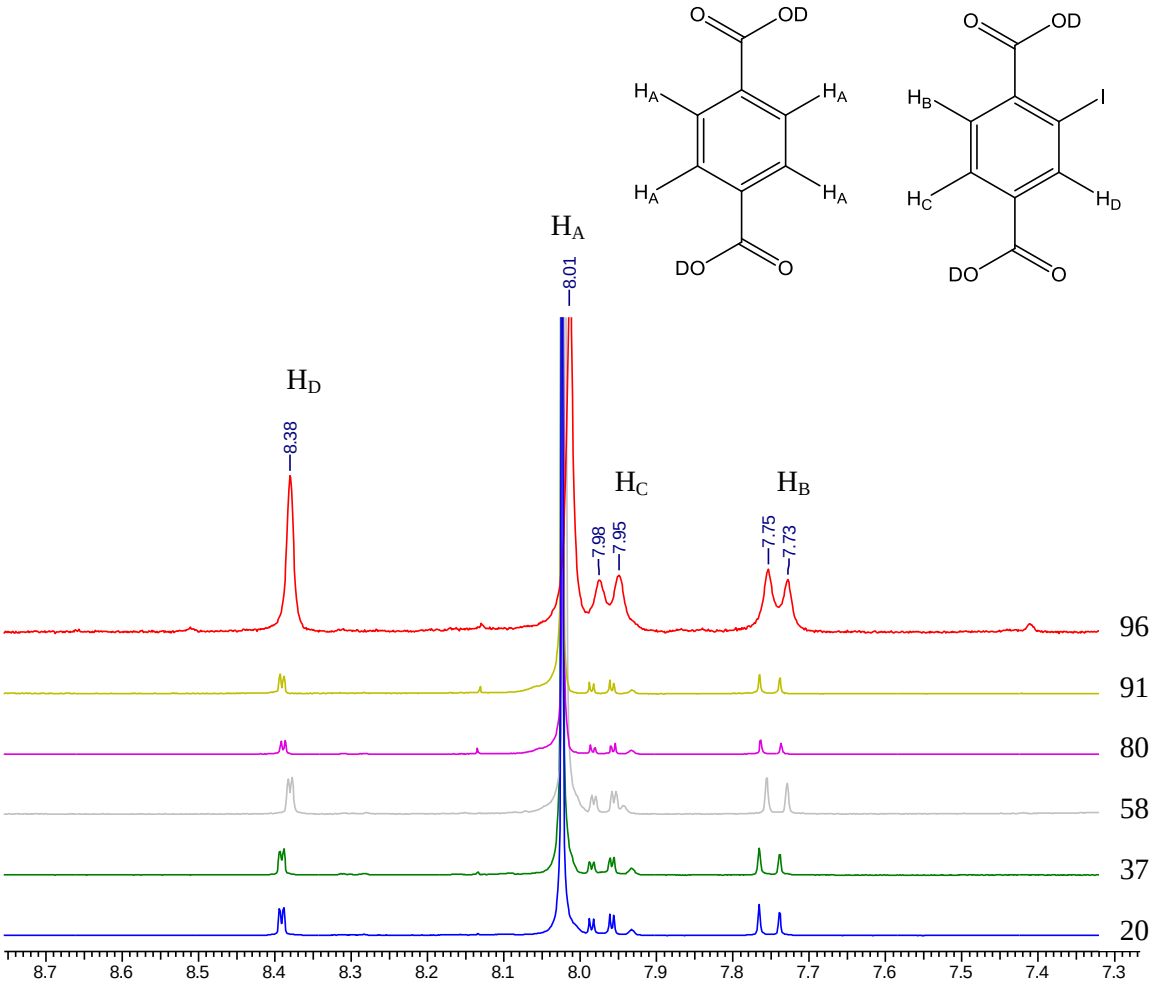

Figure 2.30 ^{1}H NMR spectra for the digested bulk samples of all products. The corresponding percentage of H_2bdc-I used in the reaction mixture is given alongside each spectrum.

Due to the small size of the crystals formed, it was not possible to conduct ^{1}H NMR spectroscopy on individual crystals. However, the homogenous appearance of the crystals formed from reaction mixtures containing both H_2bdc and H_2bdc-I, in all cases thin colourless needles, suggest that only one species is present. As the ^{1}H NMR analysis shows the presence of both ligands in all products this is consistent with the formation of mixed-ligand species.

Integral analysis of the resonances within the ^{1}H NMR spectra of the products reveals evidence of strong ligand preferences. In all products the bdc ligand is included within the framework in

preference to the bdc-I ligand, with much lower D_2bdc-I content being found in the digested sample than was present in the corresponding reaction mixture (Figure 2.31).

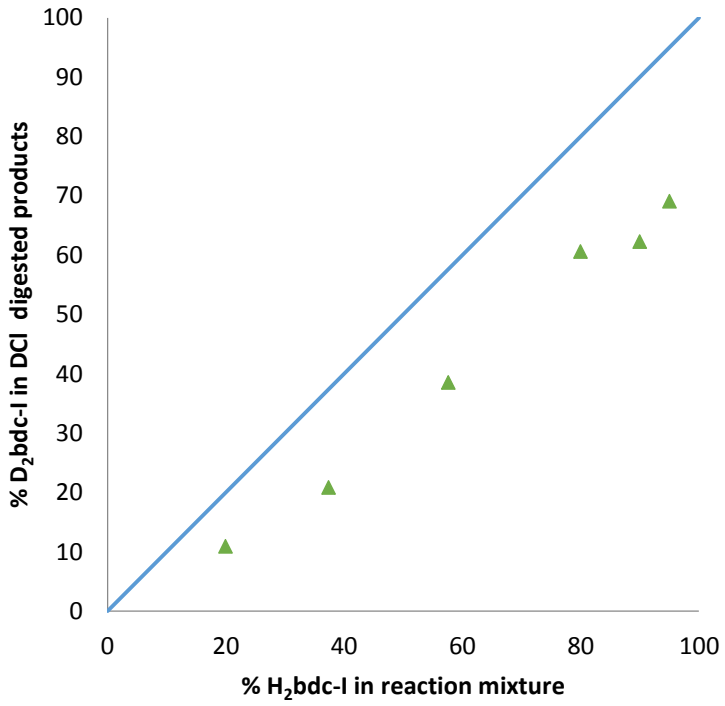

Figure 2.31 A plot of the percentage D_2bdc-I content in the acid digested products against the percentage of H_2bdc-I in the reaction mixture.

A preferential incorporation of up to 20 % more bdc into the framework than was present in the reaction mixture is found from the bulk ^{1}H NMR spectra and the determined composition of the products are given in Table 2.6.

Table 2.6 Percentages of H_2bdc-I within the reaction mixture and within the products as determined through ^{1}H NMR studies alongside the product formulae, excluding any guest solvent.

% H_2bdc-I in reaction mixture	**Average % bdc-I in product**	**Average Product Formula (as determined through ^{1}H NMR studies)**
20	11	$[Zn_2(bdc)_{1.78}(bdc\text{-}I)_{0.22}(dabco)]$
37	21	$[Zn_2(bdc)_{1.58}(bdc\text{-}I)_{0.42}(dabco)]$
58	39	$[Zn_2(bdc)_{1.23}(bdc\text{-}I)_{0.77}(dabco)]$
80	61	$[Zn_2(bdc)_{0.78}(bdc\text{-}I)_{1.22}(dabco)]$
91	62	$[Zn_2(bdc)_{0.75}(bdc\text{-}I)_{1.25}(dabco)]$
96	69	$[Zn_2(bdc)_{0.62}(bdc\text{-}I)_{1.38}(dabco)]$

A number of factors may be at play in causing preferential inclusion of a ligand into a MOF. The increased steric demand of the bdc-I ligand in comparison to the bdc ligand may limit its incorporation into the framework. This would cause the framework to incorporate higher amounts of the bdc ligand, to reduce repulsive steric interactions within the pores of the framework. Another possible explanation is that of differences in the crystallisation rates between bdc and bdc-I containing materials. A more rapid crystallisation of bdc containing moieties may lead to the formation of a framework with a higher bdc content than was present in the reaction mixture, and this has also been observed previously with $[Zn_4O(bdc)_{3-x}(bdc\text{-}I)_x]$.[17]

All mixed-ligand products were analysed by powder X-ray diffraction and similar structural trends to those found in the mixed-ligand series $[Zn_2(bdc)_{2-x}(bdc\text{-}Br)_x(dabco)]\cdot nDMF$ were observed. All compounds display powder diffraction patterns with the same gross features as those in DMOF-1, suggesting all multivariate species are isoreticular and of the form $[Zn_2(bdc)_{2-x}(bdc\text{-}I)_x(dabco)]\cdot nDMF$ (Figure 2.32).

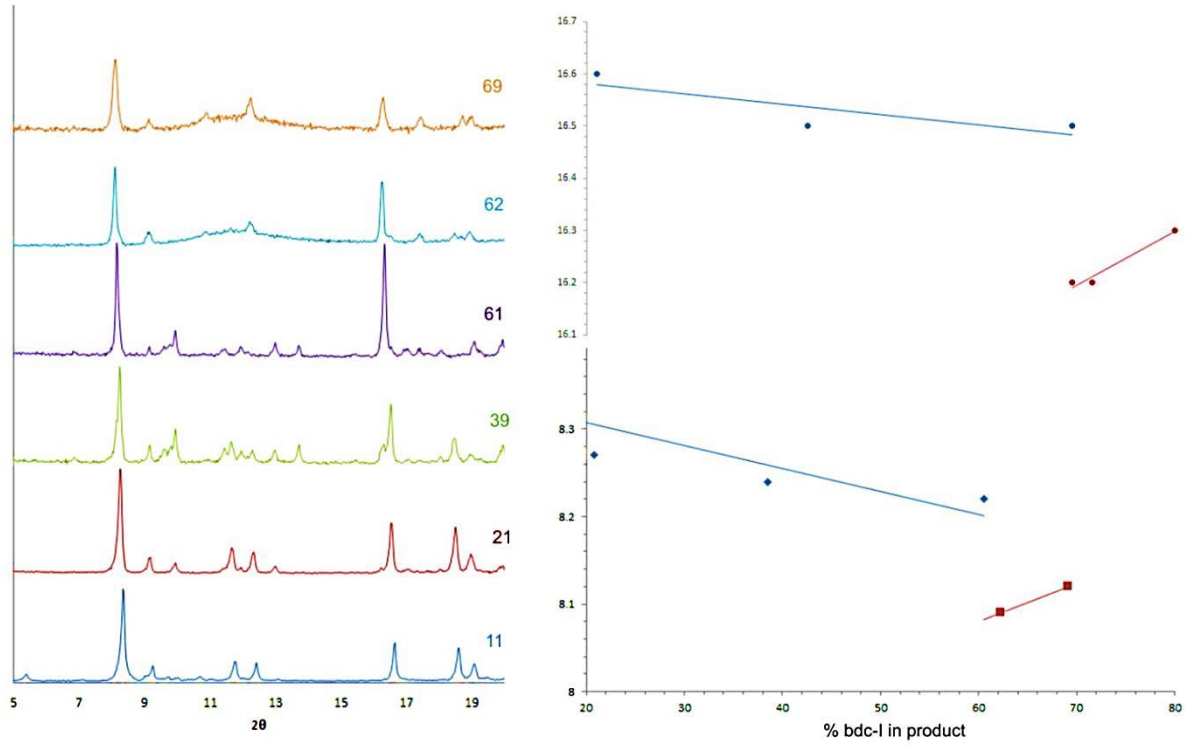

Figure 2.32 PXRD patterns of the products with the number shown against each powder pattern the % bdc-I in the sample. The plot of 2θ against % bdc-I shows the key peak which shifts with the change in pore topology.

Above a bdc-I content of 60 % in the MOF the powder diffraction patterns display a peak position shift from 2θ values of 8.3° and 16.7° to lower values of 2θ 8.2° and 16.3° suggesting the formation of a different phase. The powder diffraction patterns of the products containing 61 and 62 % bdc-I display shoulder peaks at 2θ values of 8.3° and 16.7° suggesting both phases are present in these samples. This is similar to the effect observed in the powder X-ray diffraction

patterns of the $[Zn_2(bdc)_{2-x}(bdc\text{-}Br)_x(dabco)]\cdot nDMF$ products. The $[Zn_2(bdc)_{2-x}(bdc\text{-}I)_x(dabco)]\cdot nDMF$ products with a bdc-I content of less than 60 % display peak positions comparable to those observed in the powder diffraction pattern of DMOF-1, which displays a square pore topology. However, the products with a bdc-I content of greater than 60 % display peaks with a lower 2θ value which are similar in position to those for $[Zn_2(bdc\text{-}Br)_2(dabco)]\cdot 4.4DMF$, DMOF-1-Br and $[Zn_2(bdc\text{-}I)_2(dabco)]\cdot nDMF$, DMOF-1-I which display rhomboidal pores. This suggests that varying the halogen content of either bromo or iodo functionalised dicarboxylate ligand in DMOF-1 type structures has a similar effect on the pore geometry. Both halogenated series show a phase change from open square pores to narrow rhomboidal pores with increasing halogen content in the framework.

Unfortunately the small size and needle-like nature of the $[Zn_2(bdc)_{2-x}(bdc\text{-}I)_x(dabco)]\cdot nDMF$ mixed-ligand crystals meant that single crystal X-ray diffraction was not possible for any of the compounds in this series.

2.2.4 Synthesis and characterisation of $[Zn_2(bdc)_{2-x}(bdc\text{-}NO_2)_x(dabco)]\cdot nDMF$

The DMF solvated DMOF-1-NO_2 structure, $[Zn_2(bdc\text{-}NO_2)_2(dabco)]\cdot 4.3DMF$[18] where bdc-$NO_2$ is 2-nitro-1,4-benenedicarboxylate, has a rhomboidal pore topology, similar to that of $[Zn_2(bdc\text{-}Br)_2(dabco)]\cdot 4.4DMF$, DMOF-1-Br. A mixed-ligand approach, similar to that of the $[Zn_2(bdc)_{2-x}(bdc\text{-}Br)_x(dabco)]\cdot nDMF$ and $[Zn_2(bdc)_{2-x}(bdc\text{-}I)_x(dabco)]\cdot DMF$ series, was therefore employed to investigate the effects of varying the nitro content of the frameworks of the general formula $[Zn_2(bdc)_{2-x}(bdc\text{-}NO_2)_x(dabco)]\cdot nDMF$. As with the two previous series discussed, mixed-ligand species were synthesised using a similar method to that for DMOF-1. By combining $Zn(NO_3)_2\cdot 6H_2O$ with dabco and varying ratios of H_2bdc and $H_2bdc\text{-}NO_2$ ligands, nine compounds giving colourless, block crystals were formed. The nine ratios of H_2bdc:$H_2bdc\text{-}NO_2$ ligands used were 90:10, 82:18, 70:30, 61:39, 51:49, 39:61, 30:70, 21:79 and 11:89.

^{1}H NMR spectroscopy was conducted on dried, acid digested samples of each product in a similar method to that used for $[Zn_2(bdc)_{2-x}(bdc\text{-}Br)_x(dabco)]\cdot nDMF$ compounds. All products showed the presence of both D_2bdc (δ 8.02 ppm) and $D_2bdc\text{-}NO_2$ (δ 8.38 ppm, δ 8.28 ppm and δ 7.94 ppm) in the acid digested bulk samples (Figure 2.33).

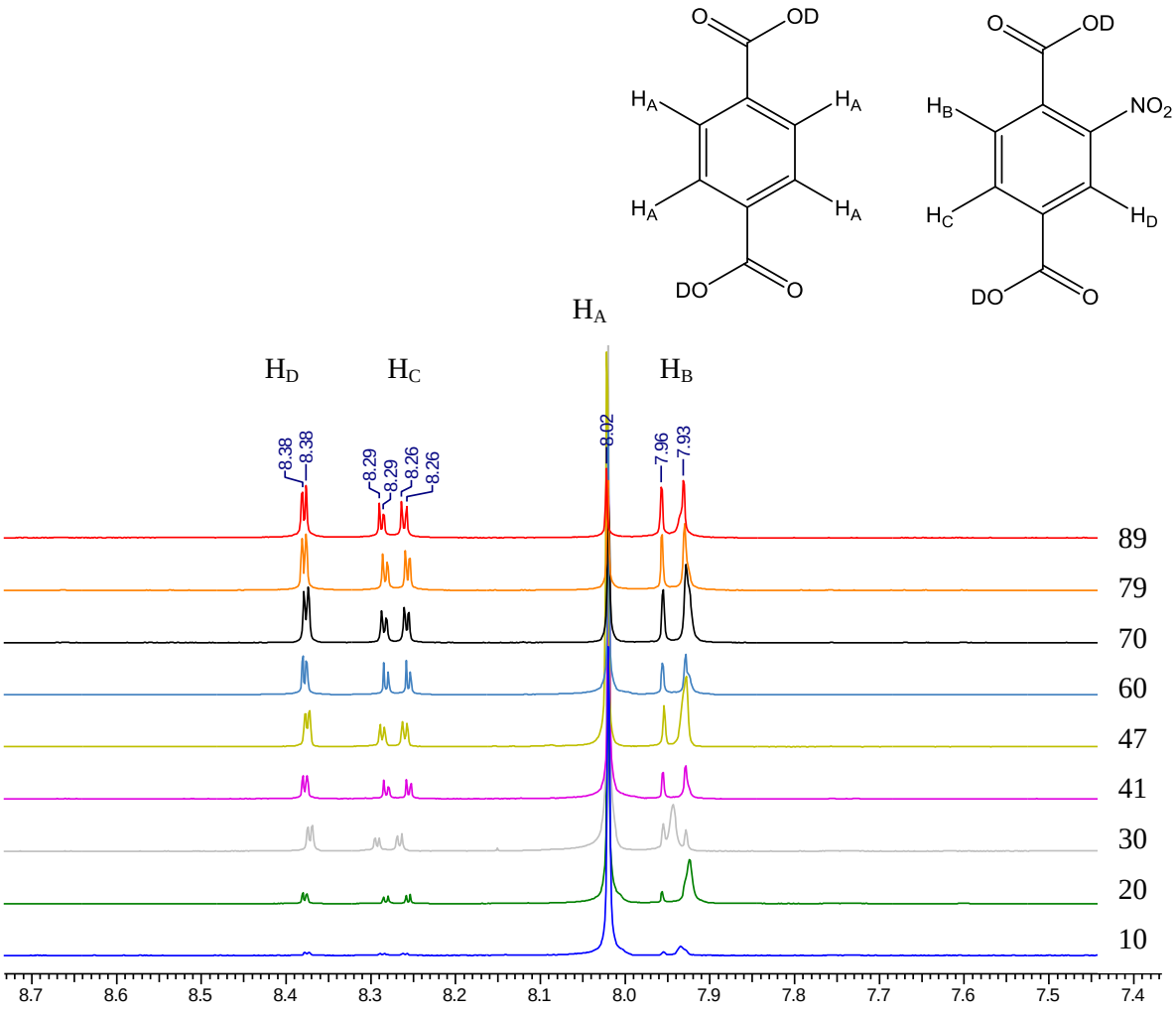

Figure 2.33 ^{1}H NMR spectra for the digested bulk samples of all products. The percentage of $H_2bdc\text{-}NO_2$ used in the reaction mixture is shown alongside the spectrum for the corresponding product.

Individual crystals of select products were also analysed by ^{1}H NMR spectroscopy. Individual crystals of products from the reaction mixtures containing 20, 47 and 79 % D_2bdc-NO_2 were selected using a microscope and digested in a d_6-DMSO/DCl mixture. The presence of both D_2bdc and D_2bdc-NO_2 in these individual acid digestions confirmed the formation of mixed-ligand species. Integral analysis of ^{1}H NMR signals from both bulk and individual crystal samples was conducted to determine the composition of the products. All bulk NMR spectra show a similar ligand ratio to that of the corresponding reaction mixture, indicating that no preferential uptake of one ligand occurs in this system (Figure 2.34).

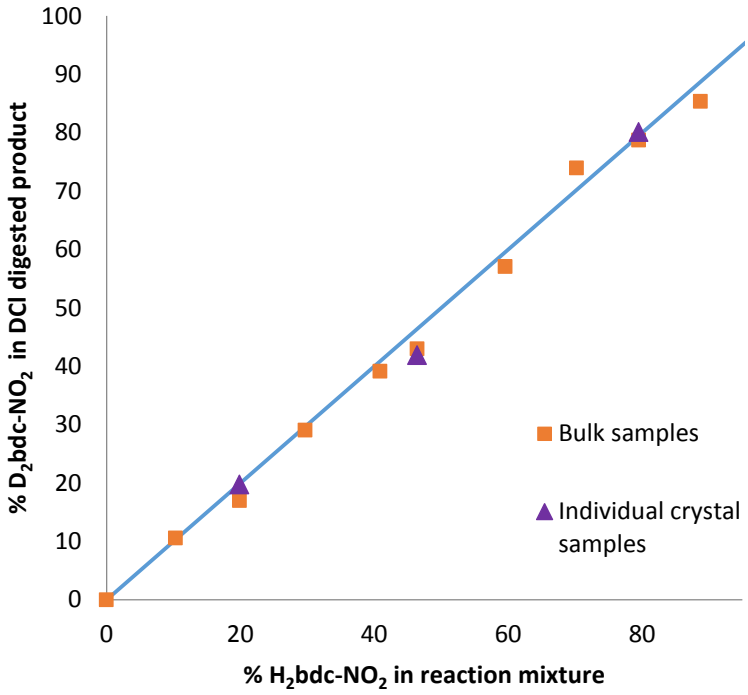

Figure 2.34 A plot of the percentage D_2bdc-NO_2 content in the acid digested products against the percentage of H_2bdc-NO_2 in the reaction mixture.

The ^{1}H NMR spectra of individual crystals show similar ratios of the two dicarboxylate ligands to that present in the corresponding bulk samples with a variation of between 1.4 % and 2.7 % in H_2bdc-NO_2 content observed. This suggests that there is little compositional variation within the bulk phase, and therefore the 'bulk integral analyses' are representative of the product compositions, which are given in Table 2.7.

Table 2.7 Experimental percentages of H_2bdc-NO_2 used to form $[Zn_2(bdc)_{2-x}(bdc\text{-}NO_2)_x(dabco)]$ products and the corresponding average percentages of H_2bdc- NO_2 found in the product. Product formulae are given, excluding any guest solvent.

% H_2bdc-NO_2 in reaction mixture	**Average % bdc-NO_2 in product**	**Average Product Formula (as determined through ^{1}H NMR studies)**
10	10	$[Zn_2(bdc)_{1.79}(bdc\text{-}NO_2)_{0.21}(dabco)]$
18	20	$[Zn_2(bdc)_{1.63}(bdc\text{-}NO_2)_{0.37}(dabco)]$
30	29	$[Zn_2(bdc)_{1.42}(bdc\text{-}NO_2)_{0.58}(dabco)]$
39	41	$[Zn_2(bdc)_{1.22}(bdc\text{-}NO_2)_{0.78}(dabco)]$
49	46	$[Zn_2(bdc)_{1.2}(bdc\text{-}NO_2)_{0.8}(dabco)]$
61	59	$[Zn_2(bdc)_{0.86}(bdc\text{-}NO_2)_{1.14}(dabco)]$
70	73	$[Zn_2(bdc)_{0.54}(bdc\text{-}NO_2)_{1.46}(dabco)]$
79	79	$[Zn_2(bdc)_{0.42}(bdc\text{-}NO_2)_{1.58}(dabco)]$
89	85	$[Zn_2(bdc)_{0.3}(bdc\text{-}NO_2)_{1.7}(dabco)]$

Powder X-ray diffraction analysis of all products reveals similar gross features to that of DMFO-1, suggesting the products are of the form $[Zn_2(bdc)_{2-x}(bdc\text{-}NO_2)_x(dabco)]\cdot nDMF$. The powder diffraction patterns of products containing less than 60 % bdc-NO_2 display peaks with 2θ values of 8.4^o and 16.7^o which are similar to those in the $[Zn_2(bdc)_2(dabco)]\cdot 1.4DMF\cdot 0.5H_2O$, DMOF-1, structure which displays square pore topology. Products which contain more than 60 % bdc-NO_2 have peaks at lower 2θ values of 8.2^o and 16.3^o compared to the low bdc-NO_2 content products. These lower peaks are similar in position to those found in $[Zn_2(bdc\text{-}NO_2)_2(dabco)]\cdot 4.3DMF$ which displays rhomboidal pores. In the sample containing 59 % bdc-NO_2, the PXRD pattern shows the presence of peaks corresponding to both square-pore and rhomboidal-pore phases of the MOF (Figure 2.35).

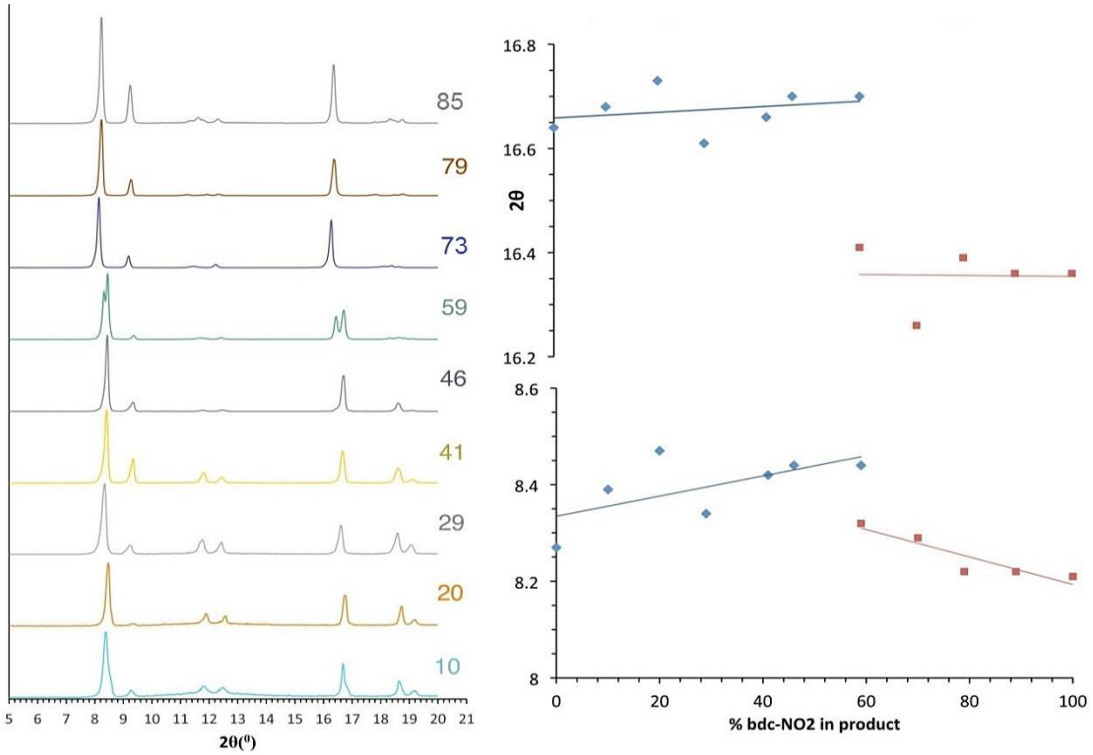

Figure 2.35 PXRD patterns of the products with the number shown against each powder pattern the % bdc-NO_2 in the sample. The plot of 2θ against % bdc-NO_2 shows the key peaks which shift with the change in pore topology.

Structure description of $[Zn_2(bdc)_{1.2}(bdc\text{-}NO_2)_{0.8}(dabco)]\cdot 2.5DMF$ **3a**

A crystal from the product containing an average of 41 % bdc-NO_2 was found to be suitable for single crystal X-ray analysis and was characterised as $[Zn_2(bdc)_{1.2}(bdc\text{-}NO_2)_{0.8}(dabco)]\cdot 2.5DMF$, **3a**. Thermogravimetric analysis of **3a** shows a percentage mass loss of 26.7 % between 120 ^oC and 208 ^oC corresponding to a solvent content of 2.5 DMF molecules per unit formula (see appendix Figure A2.2.1). Crystallographically guest solvent within the structure was diffuse and was treated with the PLATON SQUEEZE algorithm.

The asymmetric unit comprises one zinc atom with site occupancy of 25 %, a quarter of a dabco moiety and a quarter of a dicarboxylate ligand (Figure 2.36).

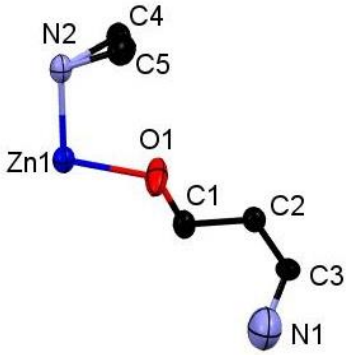

Figure 2.36 Asymmetric unit of $[Zn_2(bdc)_{1.2}(bdc\text{-}NO_2)_{0.8}(dabco)]\cdot 2.5DMF$ **3a** with an ellipsoid probability of 40 %. Hydrogen atoms are omitted for clarity.

The bdc/bdc-NO_2 ligands are disordered over the same site with O1, C1, C2 and C3 belonging to both ligands. N1, belonging to the nitro moiety of the bdc-NO_2 ligand, is attached to C3 and has a site occupancy of 15 % based on electron density. Symmetry generation of the bdc/bdc-NO_2 ligand occurs through an inversion centre, two fold rotation and mirror plane perpendicular to the *c*-axis. This necessarily results in the nitro moiety being disordered at all four available positions of the phenyl ring (Figure 2.37). A total nitro content of 60 % is therefore present in the framework.

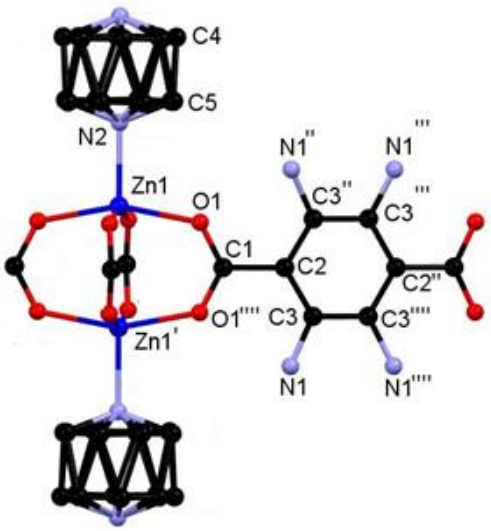

Figure 2.37 Part of the structure of $[Zn_2(bdc)_{1.2}(bdc\text{-}NO_2)_{0.8}(dabco)]\cdot 2.5DMF$ **3a.** Primed, double primed, triple primed and quadruple primed atoms are related to those in the asymmetric unit by the $-x, -y, -z$, $x, y, -z$, $½ - y, ½ - x, -z$, and $½ - y, ½ - x, z$ symmetry operations respectively. Hydrogen atoms are removed for clarity.

Although electron density was present in the expected region for the two oxygen atoms bonded to the nitro-N, they could not be located with certainty due to diffuse nature of the electron density and hence were omitted from the model.

N2 belonging to the dabco moiety is present on a four-fold rotation axis and therefore has a site occupancy of 25 %. A two-fold rotation axis is also present about which the dabco moiety is generated. This necessarily results in symmetry related disorder of both C4 and C5. To model this disorder the site occupancies of C4 and C5 were attributed to 35 % and 40 % respectively, resulting in a total of six carbon atoms in the dabco moiety. Geometric restraints were employed to N-C distances within the dabco to achieve a chemically sensible convergence.

The structure crystallises in the tetragonal space group *I*4/*mcm* (Table 2.8) displaying an overall square pore topology similar to that observed in $[Zn_2(bdc)(bdc\text{-}Br)(dabco)]\cdot nDMF$ **1a** and $[Zn_2(bdc)_{0.8}(bdc\text{-}Br)_{1.2}(dabco)]\cdot nDMF$ **1b**, which is consistent with the PXRD data (Figure 2.38).

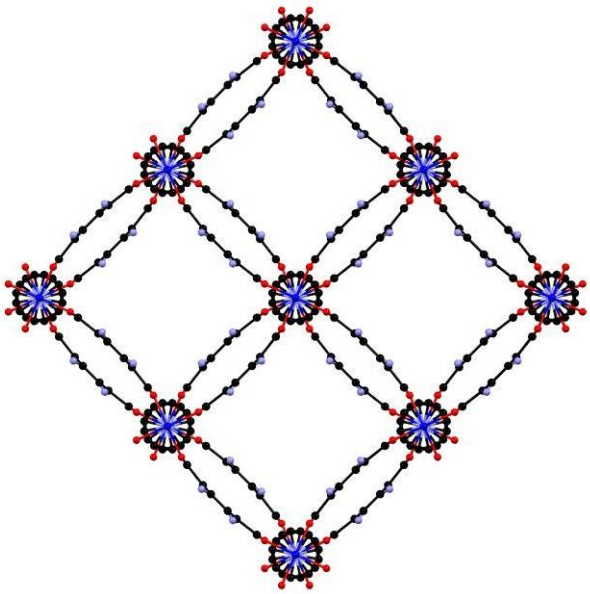

Figure 2.38 The pore structure present in $[Zn_2(bdc)_{1.2}(bdc\text{-}NO_2)_{0.8}(dabco)]\cdot 2.5DMF$ **3a** as viewed down the *c*-axis. Hydrogen atoms have been removed for clarity.

Table 2.8 Crystal data and structure refinement for $[Zn_2(bdc)_{1.2}(bdc\text{-}NO_2)_{0.8}(dabco)]\cdot 2.5DMF$ **3a**.

Identification code	**3a**
Empirical formula	$C_{29.5}H_{36.7}O_{12.1}N_{5.3}Zn_2$
Formula weight	789.88
Temperature/K	150.15
Crystal system	tetragonal
Space group	*I*4/*mcm*
a/Å	15.0210(4)
b/Å	15.0210(4)
c/Å	19.2220(8)
α/°	90
β/°	90
γ/°	90
Volume/Å^3	4337.1(3)
Z	4
ρ_{calc}g/cm^3	1.210
μ/mm^{-1}	1.160
F(000)	1630.0
Crystal size/mm^3	0.4 × 0.2 × 0.2
Radiation	Mo*K*α (λ = 0.71073)
2θ range for data collection/°	7.674 to 54.948
Index ranges	$-19 \leq h \leq 19$, $-19 \leq k \leq 18$, $-24 \leq l \leq 24$
Reflections collected	39254
Independent reflections	1356 [R_{int} = 0.1208, R_{sigma} = 0.0333]
Data/restraints/parameters	1356/21/64
Goodness-of-fit on F^2	1.071
Final *R* indexes [$I>=2\sigma(I)$]	R_1 = 0.0529, wR_2 = 0.1299
Final *R* indexes [all data]	R_1 = 0.0806, wR_2 = 0.1483
Largest diff. peak/hole / e Å^{-3}	0.45/-0.41

The predicted PXRD pattern generated from the single crystal structure of $[Zn_2(bdc)_{1.2}(bdc\text{-}NO_2)_{0.8}(dabco)]\cdot 2.5DMF$ **3a** shows a good correspondence to the experimental PXRD patterns collected (Figure 2.39).

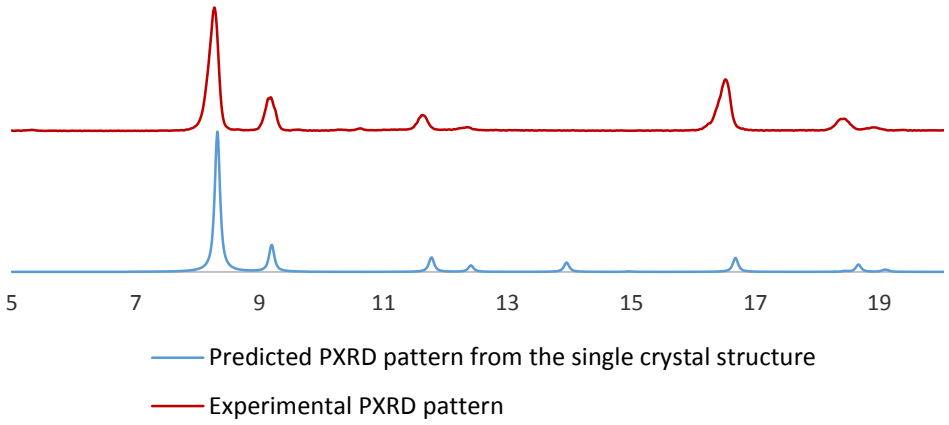

Figure 2.39 Predicted and experimental PXRD patterns of $[Zn_2(bdc)_{1.2}(bdc\text{-}NO_2)_{0.8}(dabco)]\cdot 2.5DMF$ **3a**.

Single crystal X-ray data for the compound $[Zn_2(bdc)_{0.6}(bdc\text{-}NO_2)_{1.4}(dabco)]$ **3b** (taken from the product containing an average of 73 % bdc-NO_2) was also collected, however was of poor quality and the structure suffered from extensive disorder. While the solution is not of sufficient quality to present in full, it is notable that **3b** crystallises in an orthorhombic system, similar to the rhomboidal pore structures $[Zn_2(bdc)_{0.4}(bdc\text{-}Br)_{1.6}(dabco)]DMF$ **1c** and $[Zn_2(bdc)_{0.3}(bdc\text{-}Br)_{1.7}(dabco)]$ **1d** suggesting that the rhomboidal pore form of this species is accessible (Table 2.9).

Table 2.9 unit cell parameters for $[Zn_2(bdc)_{0.6}(bdc\text{-}NO_2)_{1.4}(dabco)]\cdot n$DMF **3b**, $[Zn_2(bdc)_{0.4}(bdc\text{-}Br)_{1.6}(dabco)]\cdot$nDMF **1c** and $[Zn_2(bdc)_{0.3}(bdc\text{-}Br)_{1.7}(dabco)]\cdot$nDMF **1d**.

Compound	**3b**	**1c**	**1d**
Crystal system	Orthorhombic	Orthorhombic	Orthorhombic
Space group	*C*222	*Ammm*	*Ammm*
a/Å	12.871(9)	9.6280(2)	9.6230(3)
b/Å	17.4764(11)	12.7590(2)	12.8580(6)
c/Å	9.6458(5)	17.5720(3)	17.4800(8)
α/°, β/°, γ/°	90	90	90

The rhomboidal pore form with bdc-NO_2 present is therefore accessible in mixed-component systems with a bdc-NO_2 content of greater than 59 % within the framework, a similar content level to that of $[Zn_2(bdc)_{2-x}(bdc\text{-}Br)_x(dabco)]\cdot nDMF$ and $[Zn_2(bdc)_{2-x}(bdc\text{-}I)_x(dabco)]\cdot nDMF$.

2.2.5 Synthesis and characterisation of $[Zn_2(bdc)_{2-x}(bdc\text{-}NH_2)_x(dabco)]\cdot nDMF$

An investigation into a mixed-ligand series based around the DMOF-1 structure which contains a smaller nitrogen-containing functional group than that of the $[Zn_2(bdc)_{2-x}(bdc\text{-}NO_2)_x(dabco)]\cdot nDMF$ was undertaken. The amino-functionalised bdc-NH_2 ligand was chosen (bdc-NH_2 = 2-amino-1,4-benenedicarboxylate). The DMOF-1-NH_2 structure, $[Zn_2(bdc\text{-}NH_2)_2(dabco)]\cdot nDMF$[15] has a square pore topology, similar to that of unfunctionalised DMOF-1.

Solvothermal synthesis was carried out using a similar method to the synthesis of DMOF-1-NH_2, with varying ratios of H_2bdc and $H_2bdc\text{-}NH_2$ in the reaction mixture. Nine H_2bdc:$H_2bdc\text{-}NH_2$ ratios were employed and all products produced orange/brown block crystals.

^{1}H NMR spectroscopy was conducted on acid digested bulk samples of all products and on acid digested individual crystal samples of products from reaction mixtures containing 20, 50 and 78 % $H_2bdc\text{-}NH_2$. Bulk and individual crystal ^{1}H NMR spectra showed the presence of both D_2bdc and $D_2bdc\text{-}NH_2$ in the acid digestions indicating that mixed-ligand systems had been formed (Figure 2.40). The variation in chemical shift of $D_2bdc\text{-}NH_2$ between different samples is caused by deuteration of the amino group during the acid digestion.

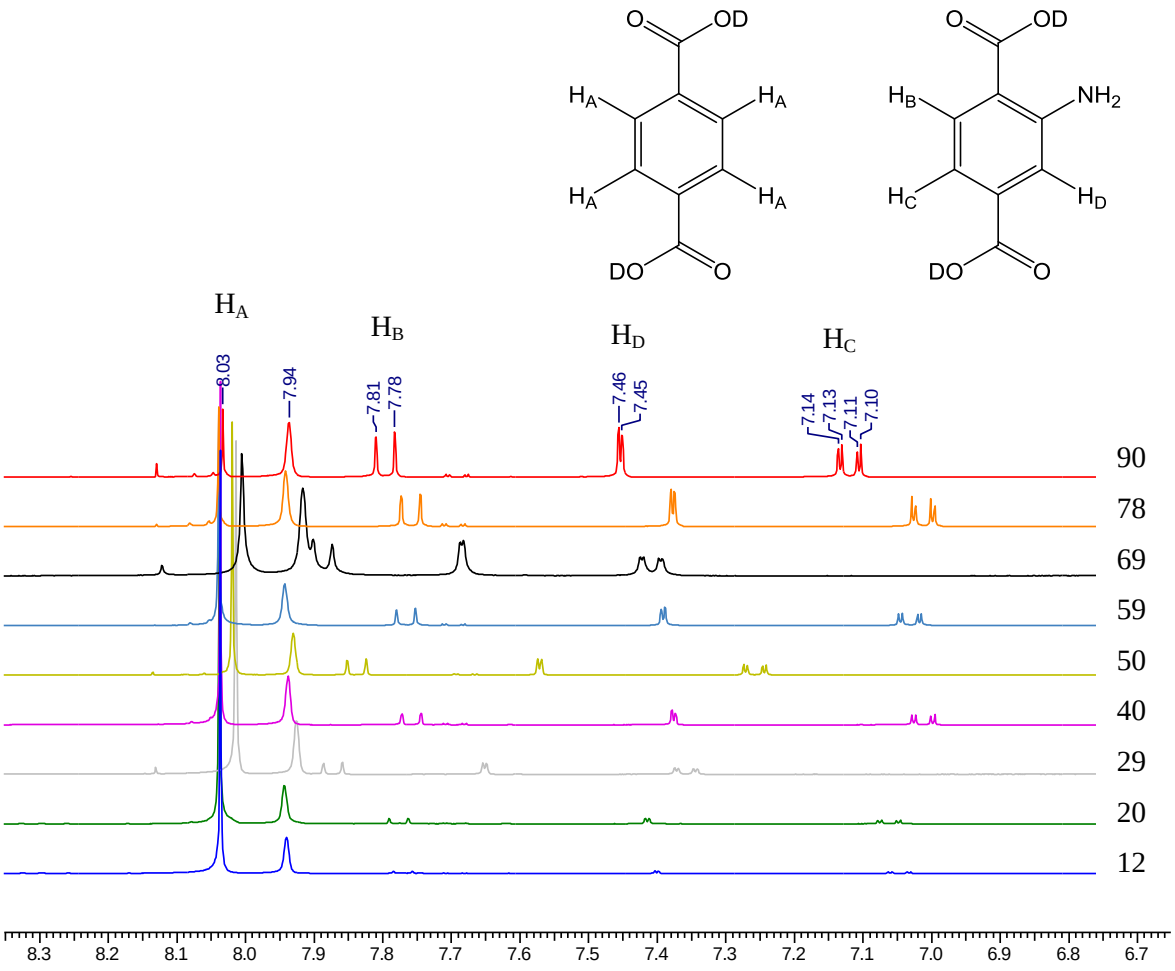

Figure 2.40 ^{1}H NMR spectra for the digested bulk samples of all products. The percentage of $H_2bdc\text{-}NH_2$ used in the reaction mixtures are shown alongside the corresponding product spectrum.

A comparison of the integral analysis between bulk and individual samples is given in Figure 2.41. Some deviation in H_2bdc-NH_2 content of the acid digestion samples from the content present in the corresponding reaction mixture is present in samples with D_2bdc-NH_2 content of 50-70 %. These deviations lie in the range of 9-12 %.

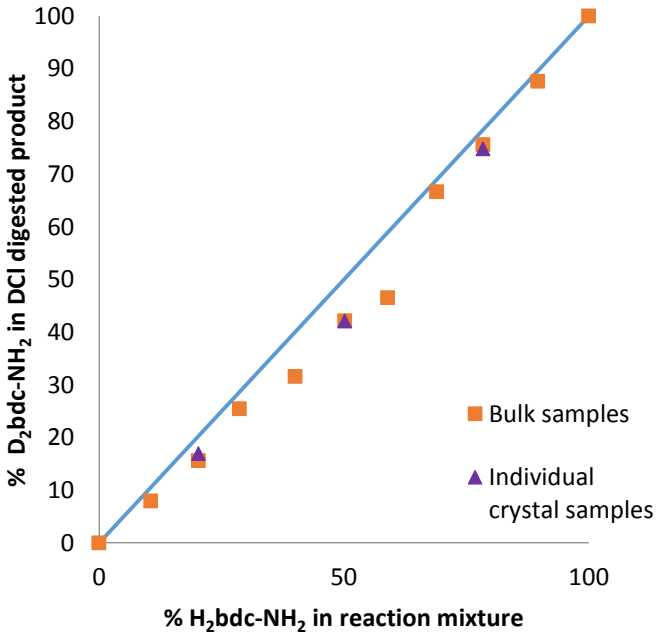

Figure 2.41 A plot of the percentage D_2bdc-NH_2 content in the acid digested products against the percentage of H_2bdc-NH_2 in the reaction mixture..

These variations in bdc-NH_2 content between product and experimental ratio are not present in all compounds and are therefore attributed to experimental anomalies. Product formulae, excluding solvent present in the pores, are given in Table 2.10.

Table 2.10 Experimental ratios of H_2bdc and H_2bdc-NH_2 used to form $[Zn_2(bdc)_{2-x}(bdc\text{-}NH_2)_x(dabco)]$ products, omitting any guest solvent from the formulae.

% H_2bdc-NH_2 in reaction mixture	**Average % H_2bdc-NH_2 in product**	**Average Product Formula (as determined through ^{1}H NMR studies)**
12	8	$[Zn_2(bdc)_{1.84}(bdc\text{-}NH_2)_{0.16}(dabco)]$
20	16	$[Zn_2(bdc)_{1.6}(bdc\text{-}NH_2)_{0.4}(dabco)]$
29	25	$[Zn_2(bdc)_{1.49}(bdc\text{-}NH_2)_{0.51}(dabco)]$
40	32	$[Zn_2(bdc)_{1.38}(bdc\text{-}NH_2)_{0.62}(dabco)]$
50	42	$[Zn_2(bdc)_{1.12}(bdc\text{-}NH_2)_{0.88}(dabco)]$
59	53	$[Zn_2(bdc)_{1.01}(bdc\text{-}NH_2)_{0.99}(dabco)]$
69	67	$[Zn_2(bdc)_{0.67}(bdc\text{-}NH_2)_{1.33}(dabco)]$
78	76	$[Zn_2(bdc)_{0.5}(bdc\text{-}NH_2)_{1.5}(dabco)]$
90	88	$[Zn_2(bdc)_{0.2}(bdc\text{-}NH_2)_{1.8}(dabco)]$

In contrast to the halogenated and nitro mixed-ligand series previously discussed, the PXRD patterns for compounds of series $[Zn_2(bdc)_{2-x}(bdc\text{-}NH_2)_x(dabco)]$ show no evidence for a transition between structures containing square and rhomboidal pores, with no peak shifts observed in this series (Figure 2.42). Instead, all of the mixed-ligand frameworks display powder diffraction patterns that correspond to the square pore form.

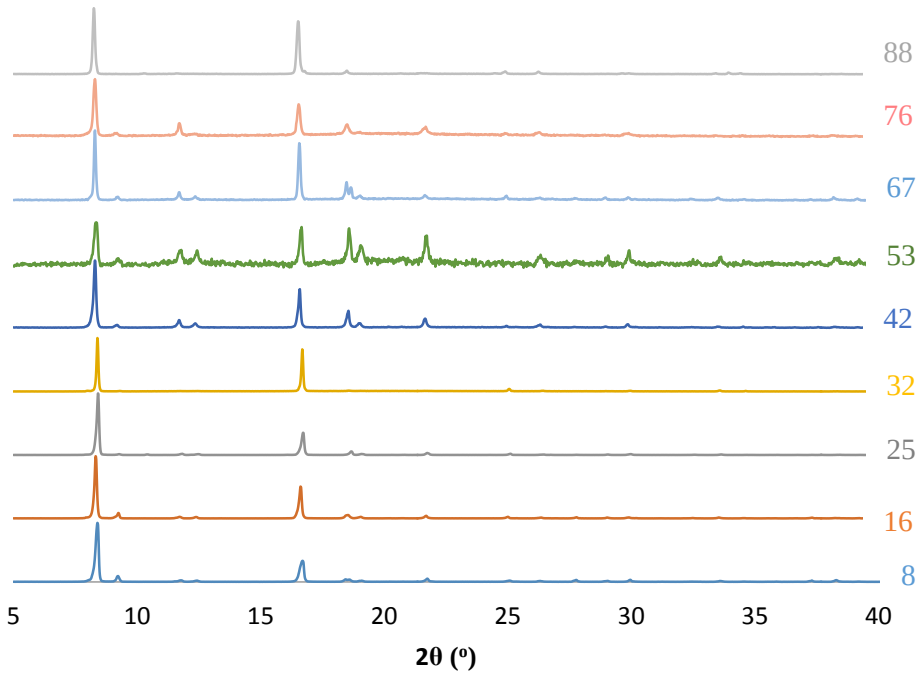

Figure 2.42 PXRD patterns of the compounds $[Zn_2(bdc)_{2-x}(bdc\text{-}NH_2)_x(dabco)]$ with the number shown against each powder pattern the % bdc-NH_2 in the sample.

Further evidence is provided by single crystal analyses completed upon $[Zn_2(bdc)_{1.6}(bdc\text{-}NH_2)_{0.4}(dabco)]\cdot 2.6DMF$ **4a** and $[Zn_2(bdc)_{0.2}(bdc\text{-}NH_2)_{1.8}(dabco)]\cdot 1.5DMF$ **4b**.

Structure description of $[Zn_2(bdc)_{1.6}(bdc\text{-}NH_2)_{0.4}(dabco)]\cdot 2.6DMF$ **4a**

Thermogravimetric analysis of **4a** shows a percentage mass loss of 31 % between 100 °C and 200 °C corresponding to 2.6 DMF solvent molecules per unit formula (see appendix Figure A2.2.2). Crystallographic evidence for some diffuse solvent was present in the lattice pores, but this could not be modelled credibly. It was therefore treated via PLATON-SQUEEZE. Based on the findings from TGA results, 2.6 molecules of DMF have been included per unit formula

The asymmetric unit of **4a** contains two zinc atoms each with site occupancy of 25 %, half a dicarboxylate ligand and half a dabco moiety (Figure 2.43).

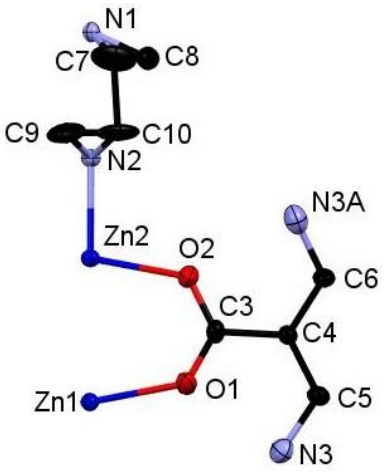

Figure 2.43 Asymmetric unit of $[Zn_2(bdc)_{1.6}(bdc\text{-}NH_2)_{0.4}(dabco)]\cdot 2.6DMF$ **4a** with ellipsoid probability of 40 %. Hydrogen atoms are removed for clarity.

The amino group present in bdc-NH_2 is disordered over two sites and attached to C5 and C6 on the benzene ring. The site occupancy of the disordered amino nitrogen atoms in the asymmetric unit is 6.5 % and 3.5 % and was informed by the ^{1}H NMR spectroscopy analysis of the bulk sample. Symmetry generation of the whole ligand through a two-fold rotation axis means that overall the amino group is disordered across all available positions of the phenyl ring and the total amino content of the framework is 20 % (Figure 2.44).

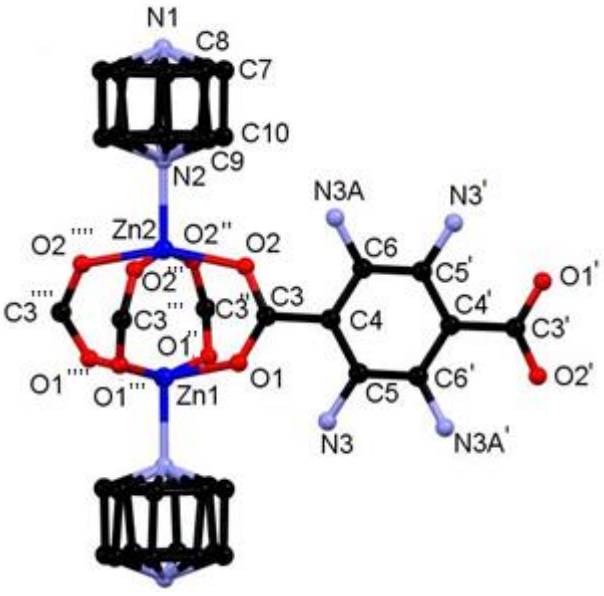

Figure 2.44 Part of the structure of $[Zn_2(bdc)_{1.6}(bdc\text{-}NH_2)_{0.4}(dabco)]\cdot 2.6DMF$ **4a** with primed and double primed atoms related to those in the asymmetric unit by the $-y, -x, \frac{1}{2}-z$, $y, \frac{1}{2}-x, z$, $\frac{1}{2}-y, x, z$ and $\frac{1}{2}-x, \frac{1}{2}-y, z$ symmetry operations respectively. Hydrogen atoms are removed for clarity.

N2 from the dabco moiety is present on a four-fold rotation axis and has a site occupancy of 25 %. The four-fold rotation axis leads to symmetry related disorder of the dabco carbons. In order to

model this disorder C7, C8, C9 and C10 were attributed site occupancies of 37.5 % each based on electron density. Symmetry generation of the dabco moiety results in a total of two nitrogen and six carbon atoms.

The overall structure of **4a** show similar connectivity and topology to that of DMOF-1, displaying paddlewheel SBUs which are connected to give a three-dimensional framework with distorted square pores (Figure 2.45).

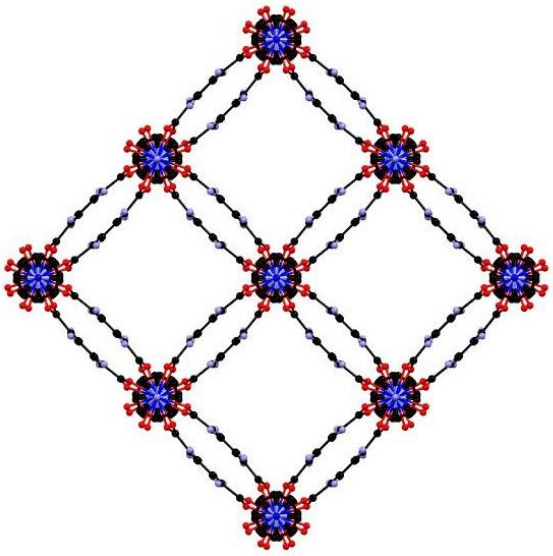

Figure 2.45 Pore structure of $[Zn_2(bdc)_{1.6}(bdc\text{-}NH_2)_{0.4}(dabco)]\cdot 2.6DMF$ **4a** with hydrogen atoms omitted.

Structure description of $[Zn_2(bdc)_{0.2}(bdc\text{-}NH_2)_{1.8}(dabco)]\cdot 1.5DMF$ **4b**

Thermogravimetric analysis of **4b** shows a percentage mass loss of 18 % between 100 ^{o}C and 200 ^{o}C corresponding to a solvent loss of 1.5 DMF molecules (see appendix Figure A2.2.3). As for **4a**, diffuse pore solvent was found crystallographically and treated *via* PLATON-SQUEEZE. 1.5 molecules of DMF have been included per metal centre in the formula for this MOF based on the TGA data.

The asymmetric unit of **4b** contains one zinc atom, one dicarboxylate ligand and half a dabco moiety (Figure 2.46). The bdc/bdc-NH_2 ligands are disordered over the same ligand site, with amino groups was found to be present on three of the four available carbons (C3, C4 and C7).

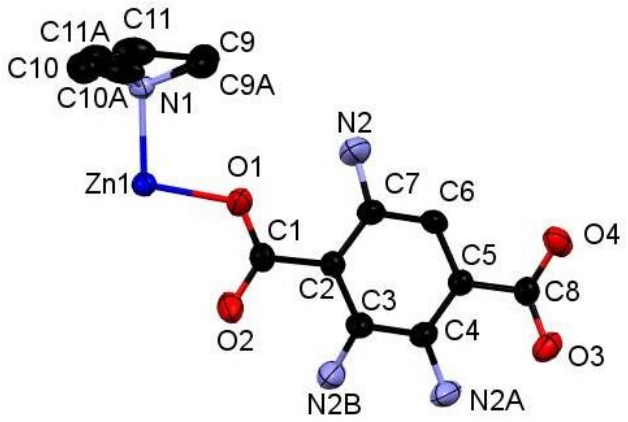

Figure 2.46 Asymmetric unit of $[Zn_2(bdc)_{0.2}(bdc\text{-}NH_2)_{1.8}(dabco)]\cdot 1.5DMF$ **4b** with ellipsoid probabilities of 40 %.

N2, N2A and N2B from the amino groups have site occupancies of 40 %, 40 % and 10 % respectively, based upon electron density. This gives a total amino content of 90 % within the framework. Geometric restraints to C-N distances pertaining to the amino nitrogens were employed to facilitate convergence.

Three carbons of the dabco unit, each disordered over two sites, are present in the asymmetric unit. This disorder was modelled by attributing the site occupancies of C9, C9A, C10, C10A, C11 and C11A to 50 %. The half dabco moiety present in the asymmetric unit lies about a two-fold rotation axis which causes the generation of the full dabco containing a total of six carbon atoms. The overall topology of **4b** is similar to that of **4a**, displaying the gross DMOF-1 structure and square pore form, despite the difference in bdc-NH_2 content between **4a** and **4b**.

Whilst a comparison to the $[Zn_2(bdc)_{2-x}(bdc\text{-}Br)_x(dabco)]\cdot nDMF$, $[Zn_2(bdc)_{2-x}(bdc\text{-}I)_x(dabco)]\cdot nDMF$ and $[Zn_2(bdc)_{2-x}(bdc\text{-}NO_2)_x(dabco)]\cdot DMF$ series might lead to the assumption that both **4a** and **4b** would crystallise in tetragonal settings, there is a change in space group from tetragonal in the case of **4a** to monoclinic in the case of **4b**. The structure of **4b** is overall very similar to that of **4a** but shows a minor deviation in the alignment of the crystal sheets as viewed along the *b*-axis. This deviation is a result of a shift in the Zn···Zn positions across the paddlewheel, causing a vertical misalignment and a distortion of the neighbouring dabco units (Figure 2.47). As this distortion is in the *a*-*b* plane, it corresponds to the β angle shifting away from the required 90° of the tetragonal species, to 94.727(2)° of the observed monoclinic species (Table 2.11).

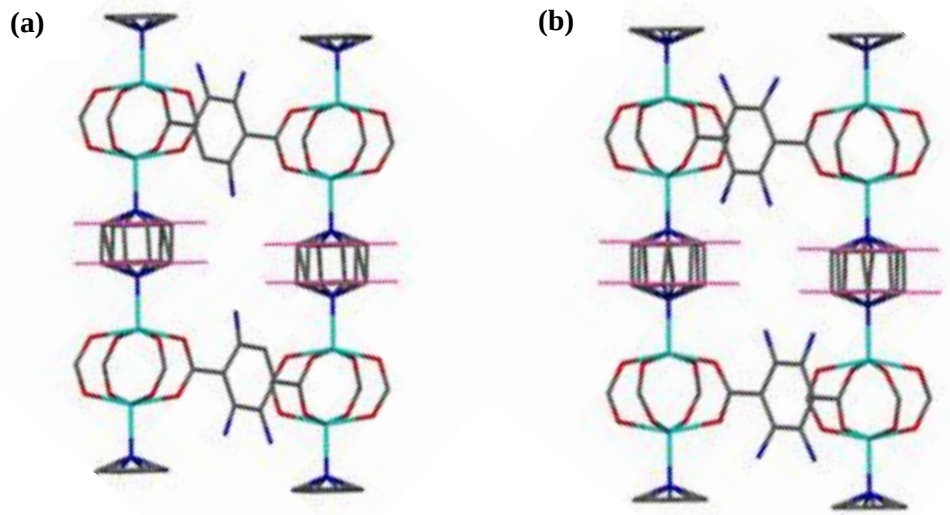

Figure 2.47 (a) View of $[Zn_2(bdc)_{0.2}(bdc\text{-}NH_2)_{1.8}(dabco)]\cdot 1.5DMF$ **4b** down the *b*-axis showing the offset nature of the neighbouring dabco ligands. **(b)** view of $[Zn_2(bdc)_{1.6}(bdc\text{-}NH_2)_{0.4}(dabco)]\cdot 2.6DMF$ **4a** down the *b*-axis showing the neighbouring dabco ligands in-line with one another. Solvent molecules and hydrogen atoms have been removed for clarity.

Table 2.11 Crystal data and structure refinement for $[Zn_2(bdc)_{1.6}(bdc\text{-}NH_2)_{0.4}(dabco)]\cdot 2.6DMF$ **4a** and $[Zn_2(bdc)_{0.2}(bdc\text{-}NH_2)_{1.8}(dabco)]\cdot 1.5DMF$ **4b**.

Identification code	**4a**	**4b**
Empirical formula	$C_{29.8}H_{38.6}N_5O_{10.6}Zn_2$	$C_{22}H_{21.8}N_{3.8}O_8Zn_2$
Formula weight	767.19	598.17
Temperature/K	150.15	150.00(10)
Crystal system	tetragonal	monoclinic
Space group	*P*4/*ncc*	*I*2/*a*
a/Å	14.9813(3)	15.3434(4)
b/Å	14.9813(3)	14.7669(3)
c/Å	19.2011(6)	19.2363(4)
α/°	90	90
β/°	90	94.7265(19)
γ/°	90	90
Volume/Å^3	4309.5(2)	4343.63(17)
Z	4	4
ρ_{calc}g/cm^3	1.182	0.915
μ/mm^{-1}	1.798	1.626
F(000)	1589.0	1218.0
Crystal size/mm^3	0.163 × 0.129 × 0.099	0.29 × 0.23 × 0.09
Radiation	Cu *K*α (λ = 1.54184)	Cu*K*α (λ = 1.54184)
2θ range for data collection/°	10.946 to 143.86	8.324 to 143.646
Index ranges	$-11 \le h \le 17$, $-18 \le k \le 11$, $-23 \le l \le 12$	$-16 \le h \le 18$, $-18 \le k \le 17$, $-23 \le l \le 21$
Reflections collected	14611	23630
Independent reflections	2088 [R_{int} = 0.0789, R_{sigma} = 0.0433]	4259 [R_{int} = 0.0526, R_{sigma} = 0.0308]
Data/restraints/parameters	2088/47/121	4259/39/208
Goodness-of-fit on F^2	1.047	1.099
Final R indexes [I>=2σ (I)]	R_1 = 0.0650, wR_2 = 0.1891	R_1 = 0.0523, wR_2 = 0.1624
Final *R* indexes [all data]	R_1 = 0.0810, wR_2 = 0.2081	R_1 = 0.0595, wR_2 = 0.1702
Largest diff. peak/hole / e Å^{-3}	2.07/-0.76	0.61/-0.57

Predicted PXRD patterns generated from the single crystal structures of $[Zn_2(bdc)_{1.6}(bdc\text{-}NH_2)_{0.4}(dabco)]\cdot 2.6DMF$ **4a** and $[Zn_2(bdc)_{0.2}(bdc\text{-}NH_2)_{1.8}(dabco)]\cdot 1.5DMF$ **4b** showed good correspondence to the experimental PXRD patterns collected (see appendix Figures A2.1.3 and A2.1.4).

A sample of $[Zn_2(bdc)_{1.6}(bdc\text{-}NH_2)_{0.4}(dabco)]\cdot 2.6DMF$ **4a** was analysed by powder X-ray diffraction after being left in DMF solution for several months. This diffraction pattern was significantly altered, indicating a new structure had formed. No peaks characteristic of **4a** were identified in the powder pattern, indicating a complete conversion to the new structure (Figure 2.48).

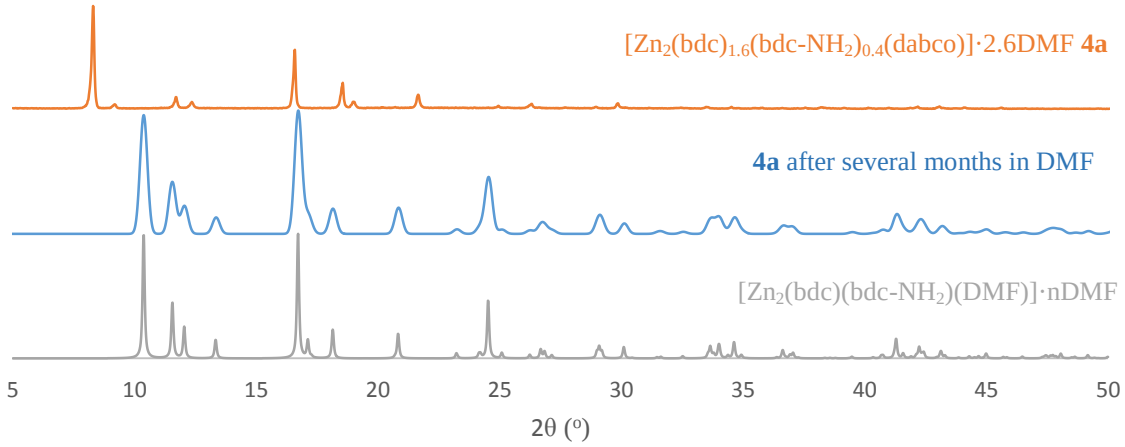

Figure 2.48 Powder X-ray diffraction patterns of $[Zn_2(bdc)_{1.6}(bdc\text{-}NH_2)_{0.4}(dabco)]\cdot 2.6DMF$ **4a** (top), **4a** after several months in DMF solution (middle) and $[Zn_2(bdc)(bdc\text{-}NH_2)(DMF)]\cdot nDMF$ (bottom).

The powder X-ray diffraction pattern is similar to that of $[Zn_2(bdc)(bdc\text{-}NH_2)(DMF)]$ which has been previously observed as a by-product in PSM reactions of $[Zn_2(bdc)(bdc\text{-}NH_2)(dabco)]$ in DMF.[19] The structure is related to that of **4a**, containing a paddlewheel zinc SBU with the pillaring dabco ligands of DMOF-1 being replaced with capping DMF molecules to form an interpenetrating two dimensional network. The co-ordinating DMF is disordered over two positions (Figure 2.49).

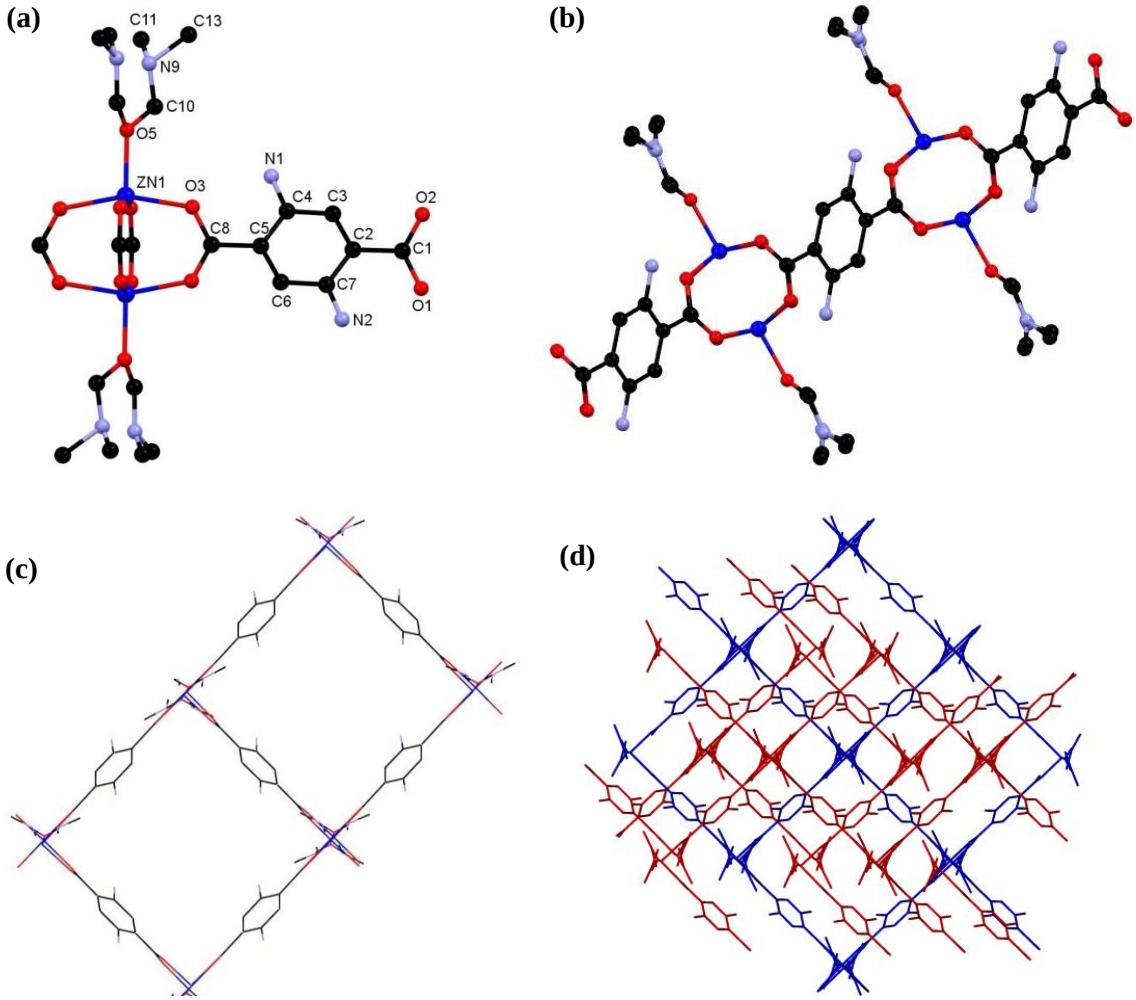

Figure 2.49 The structure of $[Zn_2(bdc)(bdc\text{-}NH_2)(DMF)]$ **(a)** showing the paddlewheel motif, **(b)** the two dimensional chains of linked zinc-dicarboxylate paddlewheel units in as viewed down the *b*-axis, **(c)** the square grid framework of the two dimensional sheets and **(d)** the interpenetration with the two nets shown in blue and red. Hydrogen atoms are omitted for clarity.[19]

2.2.6 Synthesis and characterisation of $[Zn_2(bdc\text{-}Br)_{2-x}(bdc\text{-}I)_x(dabco)]\cdot nDMF$

This mixed-ligand investigation considered the combination of two halide substituted dicarboxylate ligands by replacing all of the 1,4-benzenedicarboxylate (bdc) ligand within the framework for varying ratios of 2-bromo-1,4-benzenedicarboxylate (bdc-Br) and 2-iodo-1,4-benzenedicarboxylate (bdc-I). This system was chosen to determine if the pore shape of the products is similar to that of both single ligand systems, $[Zn_2(bdc\text{-}Br)_2(dabco)]\cdot 4.4DMF$ and $[Zn_2(bdc\text{-}I)_2(dabco)]\cdot nDMF$. The presence of a preferential ligand uptake was also studied due to the preferential inclusion of bdc over bdcI in the $[Zn_2(bdc)_{2-x}(bdc\text{-}I)_x(dabco)]\cdot nDMF$ system.

A similar synthetic approach was used as for the previous mixed-ligand structures discussed in this chapter. Three mixed-ligand products were formed all of which yielded small, colourless block crystals. As with the previous $[Zn_2(bdc)_{2-x}(bdc\text{-}X)_x(dabco)]\cdot nDMF$ series discussed (where X = Br, I, NO_2 or NH_2), the composition of these products was identified through ^1H NMR spectroscopy on bulk samples. The products were dried and digested in a d_6-DMSO/DCl mixture. All spectra showed the presence of both D_2bdc-Br and D_2bdc-I (Figure 2.50). The peaks at δ 8.13 ppm and δ 7.81 ppm correspond to the D_2bdc-Br protons, whilst the peaks at δ 8.40 ppm and δ 7.75 ppm correspond to the D_2bdc-I protons. There is an overlap of the remaining D_2bdc-Br and D_2bdc-I peaks at δ 7.96-7.99 ppm. The peak at δ 7.94 ppm originates from the DMF solvent present in the sample.

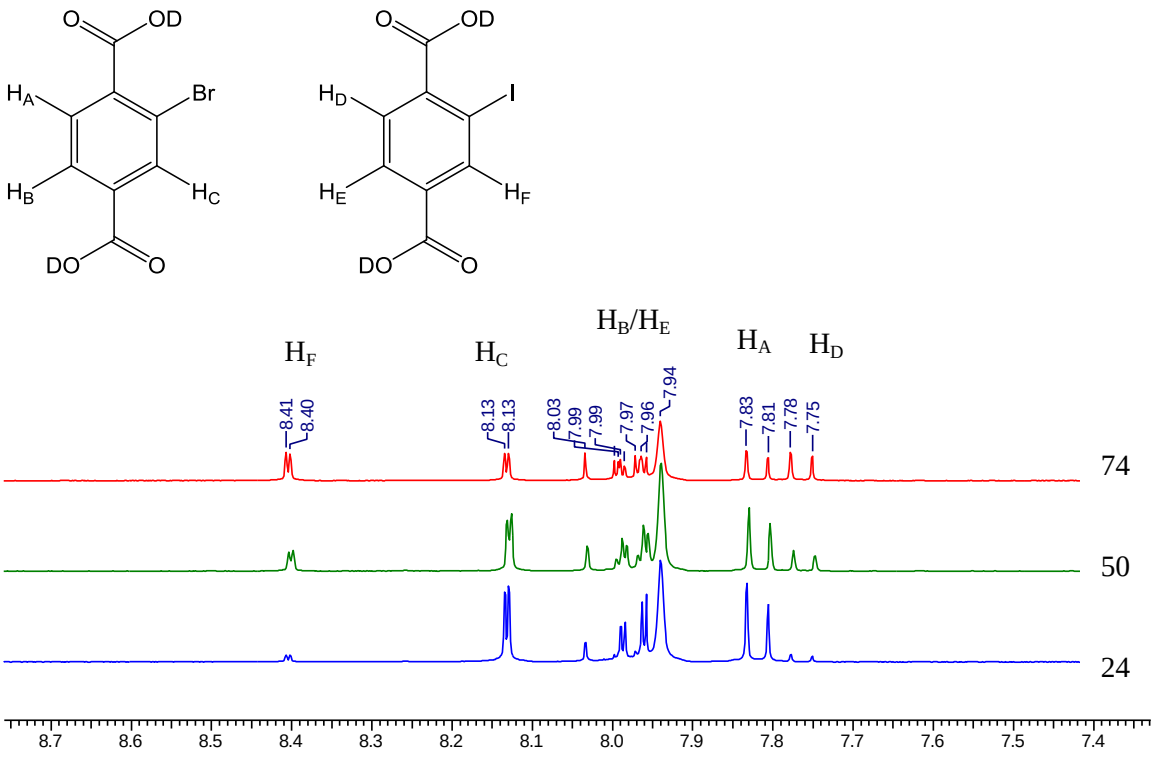

Figure 2.50 ^1H NMR spectra for the digested bulk samples of all products. The percentage of H_2bdc-I used for each reaction is shown alongside the corresponding product spectrum.

The crystals from this series were too small to facilitate undertaking ^{1}H NMR spectroscopy on individual crystals. However, an analysis of the integrals from the bulk NMR spectra shows that the bromide functionalised ligand was preferentially included in the framework. The percentage of D_2bdc-I calculated from the integral analysis of the products was much lower than the amount of H_2bdc-I used in the corresponding reaction mixtures, resulting in between 14 % and 24 % more D_2bdc-Br in the digestion compared to the amount present in the reaction mixture (Figure 2.51).

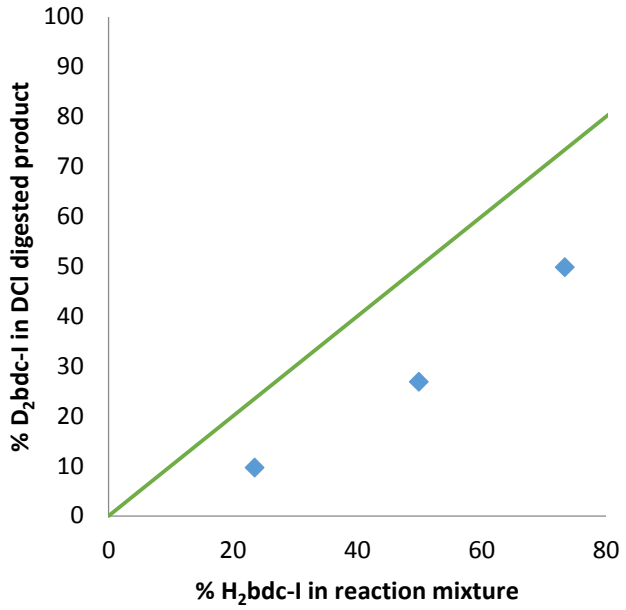

Figure 2.51 A plot of the percentage D_2bdc-I content in the acid digested products against the percentage of H_2bdc-I in the reaction mixture..

This is a similar trend to that seen in as seen in the $[Zn_2(bdc)_{2-x}(bdc\text{-}I)_x(dabco)]\cdot nDMF$ series, where the bdc ligand was preferentially included in the framework to similar levels over the bdc-I. A discussion of why the preferential inclusion of bdc over bdc-I may occur in the $[Zn_2(bdc)_{2-x}(bdc\text{-}I)_x(dabco)]\cdot DMF$ compounds was given in Section 2.2.3. It is likely that similar factors, such as steric interactions or a difference in crystallisation rates, are responsible for the preferred inclusion of bdc-Br over that of bdc-I in these products. The determined compositions of the products are given in Table 2.12.

Table 2.12 Experimental amounts H_2bdc-I used to form $[Zn_2(bdc\text{-}Br)_{2-x}(bdc\text{-}I)_x(dabco)]$ products and the amount of bdc-I in the product as determined through ^{1}H NMR spectroscopy studies. The product composition excluding any guest solvent is also given.

% H_2bdc-I in reaction mixture	**Average % bdc-I in product**	**Average Product Formula (as determined through ^{1}H NMR studies)**
24	10	$[Zn_2(bdc\text{-}Br)_{1.81}(bdc\text{-}I)_{0.19}(dabco)]$
50	27	$[Zn_2(bdc\text{-}Br)_{1.4}(bdc\text{-}I)_{0.6}(dabco)]$

74	50	$[Zn_2(bdc\text{-}Br)_{1.01}(bdc\text{-}I)_{0.99}(dabco)]$

PXRD analysis of the products showed similarities to that of DMOF-1, indicating that isoreticular structures had been formed. A comparison of the peak positions to previously synthesised DMOF-type structures showed similarities to the rhomboidal pore topology in all members of the series $[Zn_2(bdc\text{-}Br)_{2-x}(bdc\text{-}I)_x(dabco)]\cdot nDMF$. No evidence for a transition between structural types was observed (Figure 2.52). Unlike the mixed-ligand series $[Zn_2(bdc)_{2-x}(bdc\text{-}Br)_x(dabco)]\cdot nDMF$ and $[Zn_2(bdc)_{2-x}(bdc\text{-}I)_x(dabco)]\cdot nDMF$, the compounds of $[Zn_2(bdc\text{-}Br)_{2-x}(bdc\text{-}I)_x(dabco)]\cdot nDMF$ always contain 100 % halogenated ligands, but with varying ratios of bdc-Br and bdc-I. The absence of any changes in the peak positions within the PXRD patterns is suggestive of only one phase present in this series.

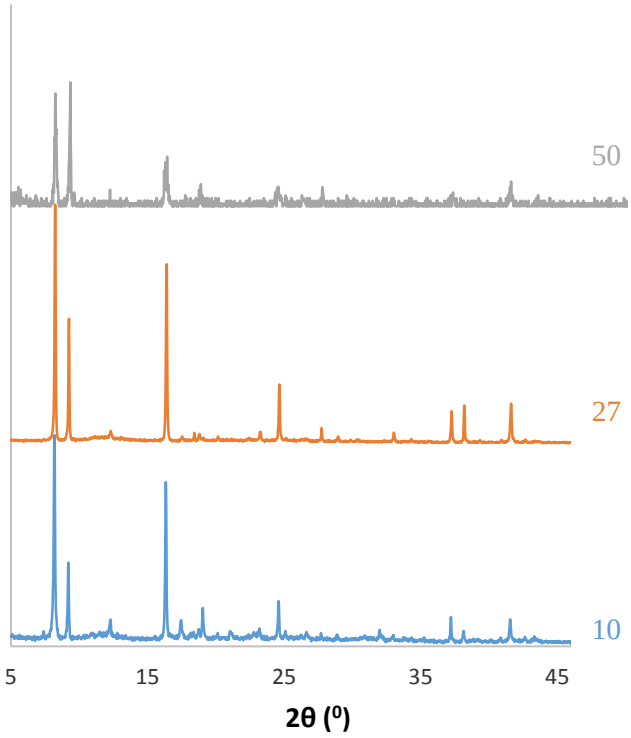

Figure 2.52 PXRD patterns of the as-synthesised compounds $[Zn_2(bdc\text{-}Br)_{2-x}(bdc\text{-}I)_x(dabco)]$ with the number shown against each powder pattern the percentage of bdc-I in the sample.

The products from a reaction mixture ratio containing 50 % H_2bdc-Br and 50 % H_2bdc-I (containing 27 % bdc-I in the product as determined through ^{1}H NMR spectroscopy) yielded crystals suitable for single crystal X-ray diffraction.

Structure description of $[Zn_2(bdc\text{-}Br)_{1.4}(bdc\text{-}I)_{0.6}(dabco)]\cdot 2.6DMF$ **5a**

The solvent content of **5a** was determined through thermogravimetric analysis of the bulk sample, which showed a percentage mass loss of 23 % between 120 ^{o}C and 200 ^{o}C (see appendix Figure A2.2.4). This corresponds to a solvent loss of 2.6 DMF molecules per unit formula. Crystallographically, guest solvent was found to be diffuse and was treated with the PLATON SQUEEZE algorithm. The asymmetric unit contains one zinc with site occupancy of 50 %, a quarter of a dabco moiety displaying positional disorder and half a dicarboxylate ligand with C3 and C4 disordered over two positions in a 65:35 ratio (Figure 2.53).

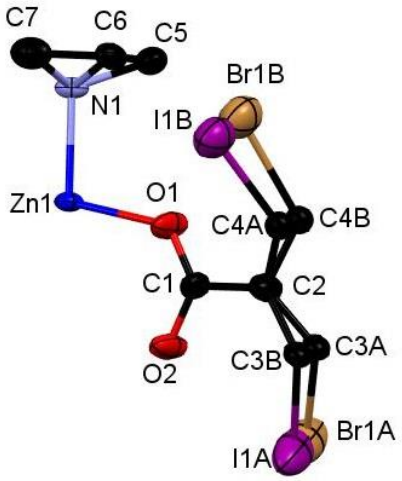

Figure 2.53 Asymmetric unit of $[Zn_2(bdc\text{-}Br)_{1.4}(bdc\text{-}I)_{0.6}(dabco)]\cdot 2.6DMF$ **5a** with ellipsoid probability of 40 %. Hydrogen atoms are removed for clarity.

The halide substituents present on the bdc-I and bdc-Br ligands are heavily disordered. Both the bromine and iodine are disordered over C3 and C4 positions of the phenyl rings in 30:5 and 12:3 ratios, respectively. The assignment of bromo and iodo substituents was informed by the ^{1}H NMR spectroscopy analysis which showed a higher percentage of bdc-Br than bdc-I in the product. The smeared electron density from the halide substituents and required atomic displacement parameter and geometric restraints of the C-Br and C-I distances to assist convergence. Symmetry generation of the whole ligand through an inversion centre results in the halide substituents being disordered over all available positions of the phenyl ring and results in a total bromine content of 70 % and iodine content of 30 % within the framework (Figure 2.54).

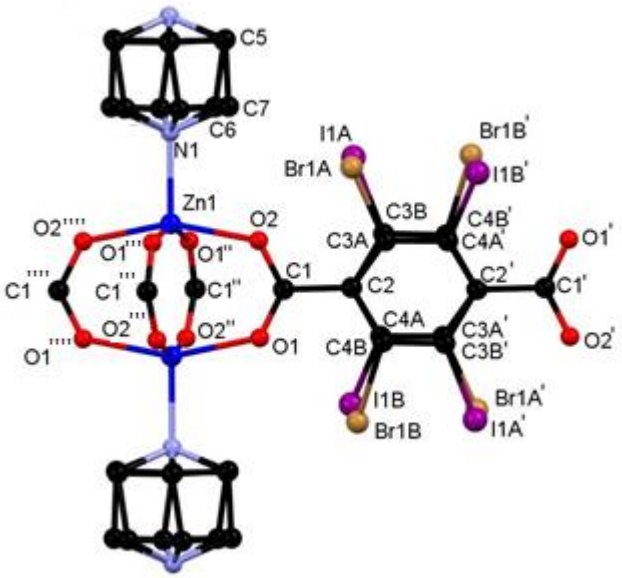

Figure 2.54 Part of the structure of $[Zn_2(bdc\text{-}Br)_{1.4}(bdc\text{-}I)_{0.6}(dabco)]\cdot 2.6DMF$ **5a** showing disorder of the carboxylate rings and the halide substituents. Primed, double primed, triple primed and quadruple primed atoms are related to those in the asymmetric unit by the $1 - x$, $1 - y$, $1 - z$, $1 - x$, $½ - y$, z, $1 - x$, y, $^3/_2 - z$ and x, $½ - y$, $^3/_2 - z$ symmetry operations respectively. Hydrogen atoms are omitted for clarity.

N1 is located on a two-fold rotation axis and necessarily has site occupancy of 50 %. This results in symmetry related disorder of the dabco in a similar manner to the other structures reported in this chapter. To model this disorder C5, C6 and C7 were modelled with a site occupancy attributed to 50 % and the entire dabco moiety is generated through the symmetry operation of two two-fold rotation axis.

The crystal structure was solved in the orthorhombic space group *Pncb* (Table 2.13) and shows the presence of rhomboidal pores, similar to those observed in $[Zn_2(bdc)_{0.4}(bdc\text{-}Br)_{1.6}(dabco)]\cdot 2.5DMF$ **1c** and $[Zn_2(bdc)_{0.3}(bdc\text{-}Br)_{1.7}(dabco)]$ **1d** (Figure 2.55).

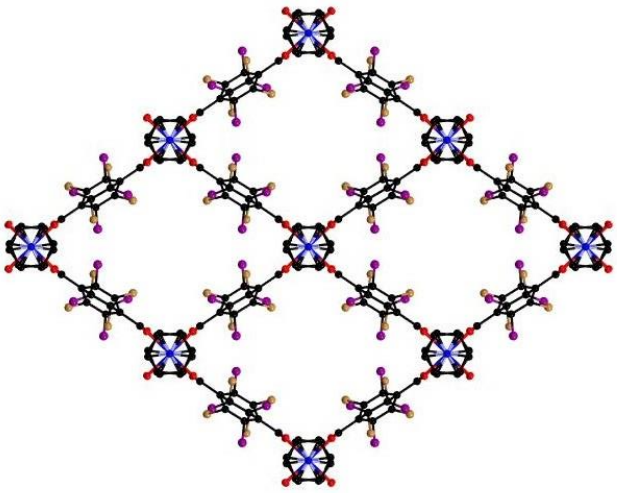

Figure 2.55 Pore structure of $[Zn_2(bdc\text{-}Br)_{1.4}(bdc\text{-}I)_{0.6}(dabco)]\cdot 2.6DMF$ **5a**. Hydrogen atoms are omitted for clarity.

Table 2.13 Crystal data and structure refinement for $[Zn_2(bdc\text{-}Br)_{1.4}(bdc\text{-}I)_{0.6}(dabco)]\cdot 2.6DMF$ **5a**.

Identification code	**5a**
Empirical formula	$C_{29.8}H_{36.2}N_{4.6}O_{10.6}Zn_2I_{0.6}Br_{1.4}$
Formula weight	947.19
Temperature/K	150.15
Crystal system	orthorhombic
Space group	*Pncb*
a/Å	9.6270(3)
b/Å	13.2670(4)
c/Å	17.2190(5)
α/°	90
β/°	90
γ/°	90
Volume/Å^3	2199.24(11)
Z	2
ρ_{calc}g/cm^3	1.430
μ/mm^{-1}	2.834
F(000)	946.0
Crystal size/mm^3	0.6 × 0.12 × 0.08
Radiation	Mo*K*α (λ = 0.71073)
2θ range for data collection/°	7.054 to 50.036
Index ranges	$-11 \leq h \leq 11$, $-15 \leq k \leq 15$, $-20 \leq l \leq 20$
Reflections collected	31992
Independent reflections	1953 [R_{int} = 0.0996, R_{sigma} = 0.0353]
Data/restraints/parameters	1953/86/128
Goodness-of-fit on F^2	1.111
Final *R* indexes [$I>=2\sigma(I)$]	R_1 = 0.0950, wR_2 = 0.2457
Final *R* indexes [all data]	R_1 = 0.1186, wR_2 = 0.2667
Largest diff. peak/hole / e Å^{-3}	1.36/-1.17

The PXRD pattern generated from the single crystal structure shows a similarity to that of the experimental PXRD pattern; however there is some apparent deviation in the peak positions with the experimental powder diffraction pattern showing peaks shifted to a lower 2θ value than those in the predicted pattern (see appendix Figure A2.1.5). This is a similar effect to that observed for **1c**, in which the peak position differences between experimental PXRD and the predicted pattern (generated from single crystal data) were found to be due to a difference in the collection temperature (Section 2.2.2). It is likely that similar effects are the cause for peak differences observed for **5a**.

2.2.7 Synthesis and characterisation of $[Zn_2(bdc\text{-}NO_2)_{2-x}(bdc\text{-}NH_2)_x(dabco)]\cdot nDMF$

Amino and nitro functionalised dicarboxylate ligands were selected to form a mixed-ligand series containing two functionalised ligands in varying ratios, in a similar method to that of the $[Zn_2(bdc\text{-}Br)_{2-x}(bdc\text{-}I)_x(dabco)]\cdot nDMF$ series. Five mixed-ligand MOFs were synthesised and produced crystals which were formed of multiple regions identified through distinct colour changes (Figure 2.56). Three regions were visibly present under the microscope; a brown region, a white region and a colourless region.

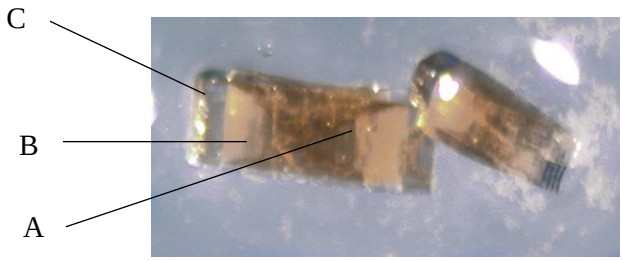

Figure 2.56 Two crystals of $[Zn_2(bdc\text{-}NO_2)_{2-x}(bdc\text{-}NH_2)_x(dabco)]$ showing the three regions, brown A, white B and colourless C.

Bulk ^1H NMR spectroscopy on dried, acid digested samples of the products show the presence of both $D_2bdc\text{-}NO_2$ and $D_2bdc\text{-}NH_2$ in all cases, with an overall ligand preference for $bdc\text{-}NO_2$ (Figure 2.57). Individual crystals were selected from samples in which the reaction mixture contained 21, 51 and 81 % $H_2bdc\text{-}NO_2$. All three of these samples gave ^1H NMR spectra with both $D_2bdc\text{-}NO_2$ and $D_2bdc\text{-}NH_2$ ligands present.

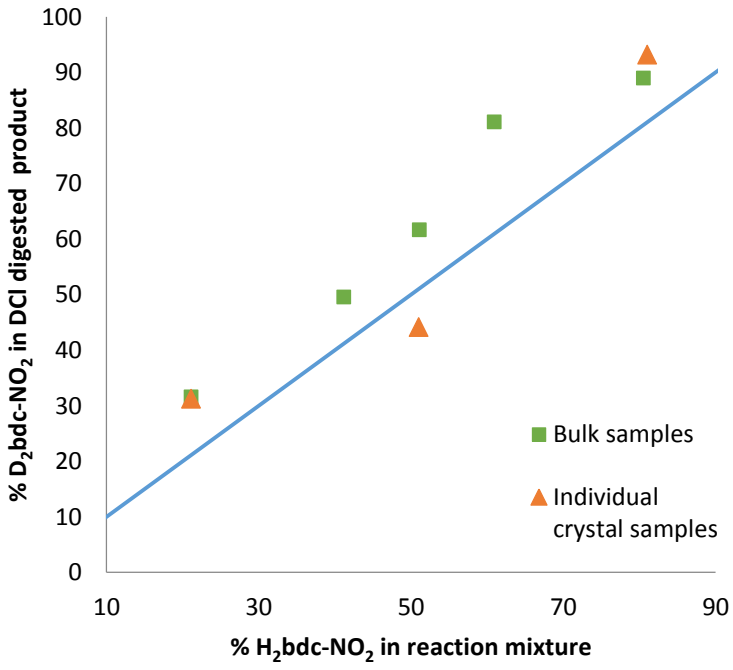

Figure 2.57 A plot of the percentage $D_2bdc\text{-}NO_2$ content in the acid digested products against the percentage of $H_2bdc\text{-}NO_2$ in the reaction mixture.

As individual crystals contain multiple regions of differing appearance, ^{1}H NMR spectroscopy of individual crystal samples could not confirm the formation of mixed-ligand species. ^{1}H NMR analysis was therefore carried out on each region of the crystals. These studies were carried out on a single batch containing a 1:1 ratio of bdc-NO_2:bdc-NH_2 in the reaction mixture. The crystals were cut along the seamlines between the regions, and same regions from multiple crystals were combined prior to ^{1}H NMR analysis. A second study was completed in which regions of one individual crystal were cut, digested and analysed by ^{1}H NMR spectroscopy (Figure 2.58).

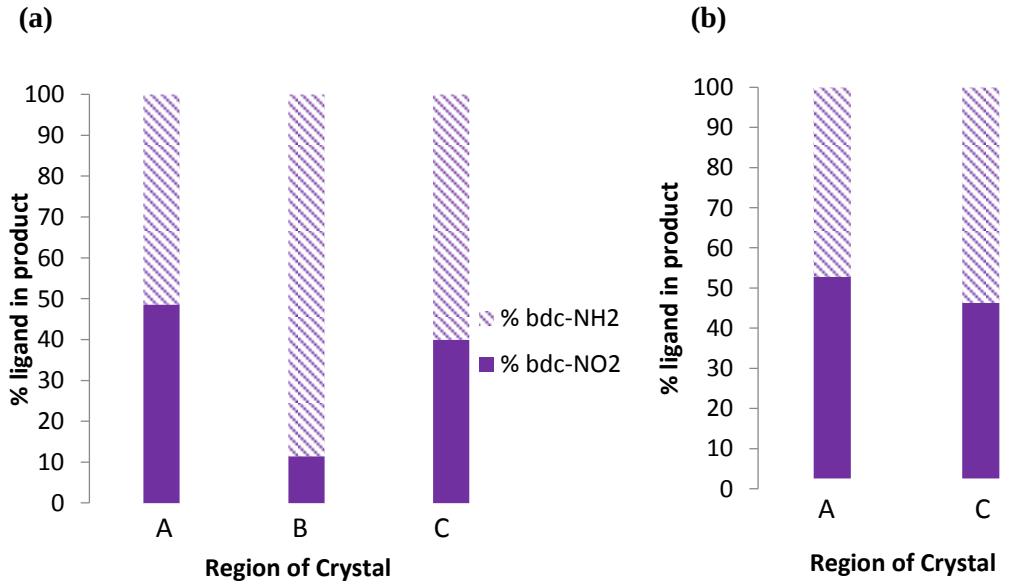

Figure 2.58 The percentage inclusion of bdc-NO_2 and bdc-NH_2 in regions A, B and C from reaction mixture containing 50 % H_2bdc-NO_2 and 50 % H_2bdc-NH_2. **(a)** Regions cut from multiple crystals from the same batch and combined prior to digestion and **(b)** regions cut from an individual crystal and digested.

For the study on the regions of one individual crystal, the digestion of region B did not produce a concentrated enough sample to be analysed by ^{1}H NMR spectroscopy. In both NMR studies all regions showed the presence of both bdc-NH_2 and bdc-NO_2 demonstrating that multivariate MOFs were formed. However, each region varied in its ligand ratio. Region A contains approximately 50 % bdc-NO_2 and region C 40 % bdc-NO_2, while region B contains a significantly different composition with only 12 % bdc-NO_2.

Such complex crystal composition could be due to a number of factors affecting the inclusion of the ligands into the framework as it grows. A difference in solubility of H_2bdc-NO_2 and H_2bdc-NH_2 is predicted, with the nitro group on H_2bdc-NO_2 causing increased solubility in polar solvents such as DMF compared to the less polar nitro containing H_2bdc-NH_2. This solubility difference may lead to a faster crystallisation rate of the product with one ligand over the other, leading to a preferential inclusion. A further factor is that of steric interactions. The reduced steric hindrance of the amino-functionalised ligand compared to that of bdc-NO_2 may lead to a favourable uptake into the framework over the bulkier, and more sterically demanding nitro-functionalised dicarboxylate

ligand. It is likely that these factors compete throughout the growth of the crystal with different effects becoming more or less prevalent in influencing the composition of the ligand ratios throughout the crystal growth, leading to the complex structures of the products observed. A difference in the pK_a values of 2-aminobenzoic acid (2.4) and the lower pK_a value of 2-nitrobenzoic acid (2.2) can be observed due to the electron withdrawing inductive effect of the nitro group on the ring. An extrapolation of this suggests that a difference in acidity of H_2bdc-NO_2 and H_2bdc-NH_2 may also be present and contribute to the preferential inclusion of one ligand over the other in the framework.

The compositions of the products were taken from the analysis of integral data from ^{1}H NMR spectra on the bulk samples (Table 2.14).

Table 2.14 Experimental ratios of H_2bdc-NO_2 used to form $[Zn_2(bdc\text{-}NO_2)_{2-x}(bdc\text{-}NH_2)_x(dabco)]$ products and the corresponding percentage H_2bdc-NO_2 determined through ^{1}H NMR studies. The formulae of the products excluding guest solvent is given.

% H_2bdc-NO_2 in reaction mixture	**Average % H_2bdc-NO_2 in product**	**Average Product Formula (as determined through ^{1}H NMR studies)**
21	32	$[Zn_2(bdc\text{-}NO_2)_{0.62}(bdc\text{-}NH_2)_{1.38}(dabco)]$
41	50	$[Zn_2(bdc\text{-}NO_2)_{0.98}(bdc\text{-}NH_2)_{1.02}(dabco)]$
51	61	$[Zn_2(bdc\text{-}NO_2)_{1.22}(bdc\text{-}NH_2)_{0.78}(dabco)]$
61	81	$[Zn_2(bdc\text{-}NO_2)_{1.62}(bdc\text{-}NH_2)_{0.38}(dabco)]$
81	89	$[Zn_2(bdc\text{-}NO_2)_{1.76}(bdc\text{-}NH_2)_{0.24}(dabco)]$

Powder X-ray diffraction was carried out on all products, showing similar features to the powder diffraction patterns to DMOF-1, suggesting the topologically similar frameworks, $[Zn_2(bdc\text{-}NO_2)_{2-x}(bdc\text{-}NH_2)_x(dabco)]\cdot nDMF$, are formed (Figure 2.59). The mixed-ligand compounds $[Zn_2(bdc\text{-}NO_2)_{2-x}(bdc\text{-}NH_2)_x(dabco)]$ have diffraction patterns which show the presence of peaks corresponding to both square and rhomboidal pore forms of the DMOF-1 topology. This is evidenced through shoulder peaks at approximately 2θ 8.3^o and 16.3^o which correspond to the peak positions observed in the rhomboidal structure of $[Zn_2(bdc\text{-}NO_2)_2(dabco)]$.

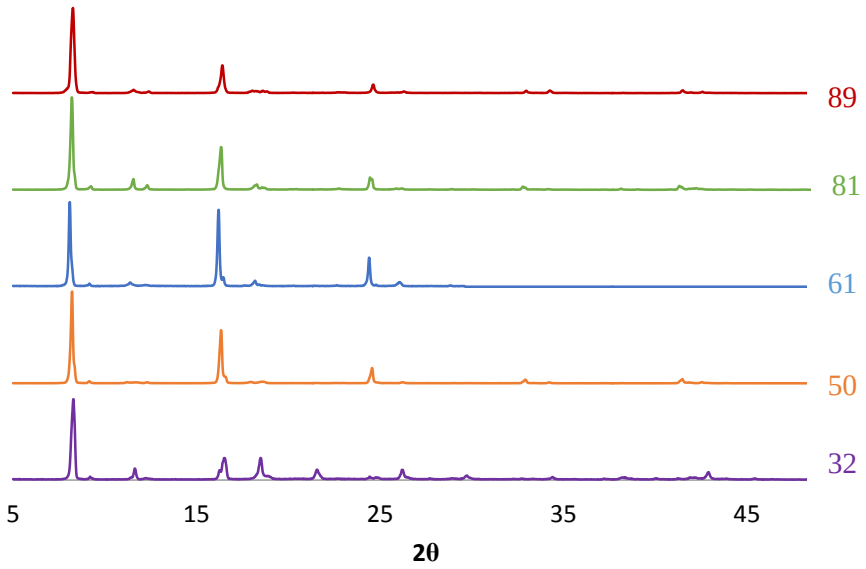

Figure 2.59 PXRD patterns of the products with the number shown against each powder pattern the % bdc-NO_2 in the sample.

As the powder X-ray diffraction patterns show an average of the bulk sample, it is not possible to know if the two pore topologies arise from different regions of the crystals (in a similar manner to a core-shell type MOF), or if the bulk samples consist of two phases, one phase containing crystals of square pore topology and another with crystals containing a rhomboidal pore topology. It is therefore also unclear at what ratio of bdc-NO_2:bdc-NH_2 ligands within the framework such transition in pore shape and size occurs.

A crystal from the sample containing an average of 61 % bdc-NO_2 was cut, exposing the three distinct regions. A fragment from the white coloured region (region B in Figure 2.56) was suitable for single crystal X-ray analysis.

Structure description of $[Zn_2(bdc\text{-}NO_2)_{0.12}(bdc\text{-}NH_2)_{0.88}(dabco)]\cdot 1.5DMF$ **6a**

The solvent content of **6a** was determined through thermogravimetric analysis conducted on the sample which revealed a percentage mass loss of 30 % during heating of 100 ^{o}C to 200 ^{o}C (see appendix Figure A2.2.5). This corresponds to a solvent loss of 1.5 DMF molecules per unit formula. Electron density of guest solvent molecules was present in the crystal structure, but was diffuse and therefore treated with the PLATON SQUEEZE algorithm.

The asymmetric unit of the crystal structure contained one quarter of a zinc atom, a quarter of the dabco ligand and a quarter of the dicarboxylate ligand which is disordered over two positions in a 50:50 ratio (Figure 2.60).

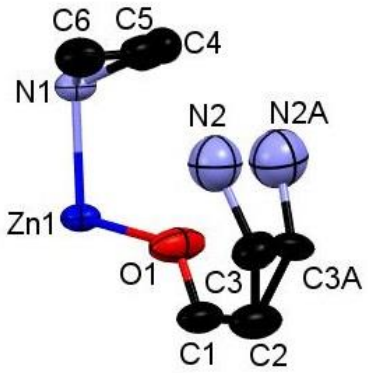

Figure 2.60 Asymmetric unit of $[Zn_2(bdc\text{-}NO_2)_{0.12}(bdc\text{-}NH_2)_{0.88}(dabco)]\cdot 1.5DMF$ **6a** with ellipsoid probability of 40 %. Hydrogen atoms are omitted for clarity.

Only the nitrogen atom from the amino and nitro substituents could be reliably located and is disordered over all available carbons of the ring, C3 and C3A in the asymmetric unit. Symmetry generation of the entire dicarboxylate ligand through inversion centre, two-fold rotation and mirror plane perpendicular to the *a*-axis results in the disorder of the amino/nitro groups over all eight available carbons of the ligands in equal ratios (Figure 2.61).

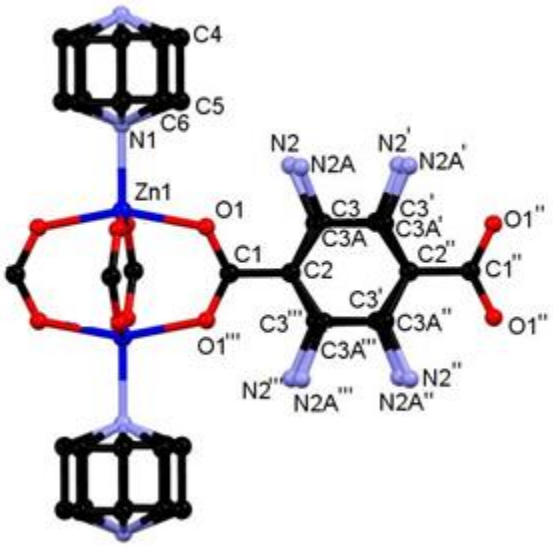

Figure 2.61 The paddlewheel unit of $[Zn_2(bdc\text{-}NO_2)_{0.12}(bdc\text{-}NH_2)_{0.88}(dabco)]\cdot 1.5DMF$ **6a**. Primed, double primed and triple primed labelled atoms are related to those in the asymmetric unit by the *x*, ½ – *y*, ½ – *z*, 1 – *x*, ½ – *y*, ½ – *z* and 1 – *x*, *y*, *z* symmetry operations respectively. Hydrogen atoms are omitted for clarity.

As only the nitrogen of the substituents on the dicarboxylate ring could be located in the crystal structure, the ratio of amino to nitro-substituted ligands in the unit formula is derived from the ^{1}H NMR spectroscopy data alone.

The dabco moiety exhibits disorder as with other structures in this chapter. N1 is located on a two-fold rotation axis and a mirror plane perpendicular to the *b*-axis. As such the site occupancy of N1 is 25 % and symmetry generation of the entire dabco moiety results in disorder of the dabco carbons, C4-C6. This disorder is modelled through the site occupancy of C4, C5 and C6 being attributed to 17.5 %, 40 % and 17.5 % respectively.

The structure crystallises in the orthorhombic space group *Ammm* (Table 2.15) and exhibits rhomboidal pores, which were indicated to be present in the powder diffraction patterns (Figure 2.62).

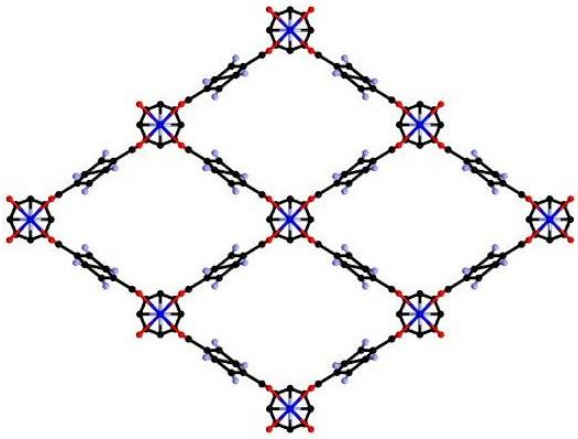

Figure 2.62 The rhomboidal pore structure of $[Zn_2(bdc\text{-}NO_2)_{0.12}(bdc\text{-}NH_2)_{0.88}(dabco)]\cdot 1.5DMF$ **6a** viewed down the *a*-axis. All hydrogen atoms have been omitted for clarity.

Table 2.15 Crystal data and structure refinement for $[Zn_2(bdc\text{-}NO_2)_{0.12}(bdc\text{-}NH_2)_{0.88}(dabco)]\cdot 1.5DMF$ **6a**.

Identification code	**6a**
Empirical formula	C3.6875 H4.5875 N0.6625 O1.5125 Zn0.25
Formula weight	98.74
Temperature	150(2) K
Wavelength	0.71073 Å
Crystal system	Orthorhombic
Space group	*Ammm*
Unit cell dimensions	a = 9.6540(4)Å α= 90°
	b = 12.7750(7)Å β = 90°
	c = 17.5580(10)Å γ = 90°
Volume	2165.43(19) Å^3
Z	16
Density (calculated)	1.211 Mg/m^3
Absorption coefficient	1.162 mm^{-1}
F(000)	815
Crystal size	0.30 x 0.20 x 0.10 mm
Theta range for data collection	3.83 to 25.02 °.
Index ranges	0<=h<=11; 0<=k<=15; 0<=l<=20
Reflections collected	1088
Independent reflections	1088 [R(int) = 0.0000]
Reflections observed (>2sigma)	920
Data Completeness	0.985
Absorption correction	Semi-empirical from equivalents
Max. and min. transmission	0.650 and 0.544
Refinement method	Full-matrix least-squares on F^2
Data / restraints / parameters	1088 / 47 / 87
Goodness-of-fit on F^2	1.117
Final R indices [I>2sigma(I)]	$R1$ = 0.0846 $wR2$ = 0.2242
R indices (all data)	$R1$ = 0.0993 $wR2$ = 0.2385
Largest diff. peak and hole	0.760 and -0.548 eÅ^{-3}

2.2.8 Structural stability of mixed-ligand products

Previous reports have shown that the DMOF-1 structure is susceptible to hydrolysis from atmospheric water leading to the collapse of the framework over time.[20] Studies into the water stability of MOFs have shown a thermodynamic effect, whereby stability of the framework can be related to the basicity of the ligands in the structure. In these cases, ligands with a higher basicity reduce the rate at which framework collapse occurs under humid conditions due to increased metal-ligand bond strength. A recent study into the hydrolysis of DMOF-1 has shown that kinetic factors are also at play in this structure. Addition of a tetra-substituted dicarboxylate ligand (2,3,5,6-tetramethyl-1,4-benzenedicarboxylate) into the framework increased the MOF's stability under humid conditions. This was found to be a result of the non-polar methyl groups shielding carboxylate groups within the pore, and therefore preventing nucleophilic attack of the metal-ligand bonds from water molecules. Studies were therefore undertaken on selected members of the mixed-ligand series presented in this chapter to determine if the addition of a functionally substituted dicarboxylate ligand affects the structural stability in air. Due to its complex composition, the $[Zn_2(bdc\text{-}NO_2)_{2-x}(bdc\text{-}NH_2)_x(dabco)]\cdot nDMF$ series was not included in this study.

DMOF-1, DMOF-1-Br and compounds $[Zn_2(bdc)(bdc\text{-}Br)(dabco)]\cdot 2.1DMF$ **1a**, $[Zn_2(bdc)_{1.5}(bdc\text{-}I)_{0.5}(dabco)]\cdot nDMF$ **2a**, $[Zn_2(bdc)_{1.2}(bdc\text{-}NO_2)_{0.8}(dabco)]\cdot 2.5DMF$ **3a**, $[Zn_2(bdc)_{1.16}(bdc\text{-}NH_2)_{0.84}(dabco)]\cdot nDMF$ **4c** and $[Zn_2(bdc\text{-}Br)_{1.4}(bdc\text{-}I)_{0.6}(dabco)]\cdot 2.6DMF$ **5a** were air dried and left open to atmospheric moisture for several weeks. The structural integrity of the samples was monitored by powder X-ray diffraction at one week intervals. These results are summarised graphically in Figure 2.63, showing the number of weeks after which structural changes began to occur. Structural changes were characterised through peak broadening, peak loss or a loss of crystallinity in the powder X-ray diffraction patterns. A similar protocol has been previously used to assess the structural stability of MOF-177.[21]

DMOF-1 showed minor changes to its PXRD pattern after 1 week at which point framework collapse was achieved. The PXRD monitoring of all mixed-ligand species showed some increase in stability in air relative to DMOF-1.

Compounds **2a**, **4c** and **5a** maintained their crystallinity for two weeks, with all samples showing only minor changes in their PXRD patterns for this time period. Powder X-ray diffraction of **3a** showed no change in the structure of the framework and maintained its crystallinity for one week.

The diffraction pattern of compound **1a** remained unchanged for over four weeks of air exposure, suggesting that the framework has considerably greater structural stability in air than DMOF-1. The powder diffraction patterns of **1a** showed a similar signal to noise ratios over time, suggesting that the bulk of the material remains crystalline for up to six weeks.

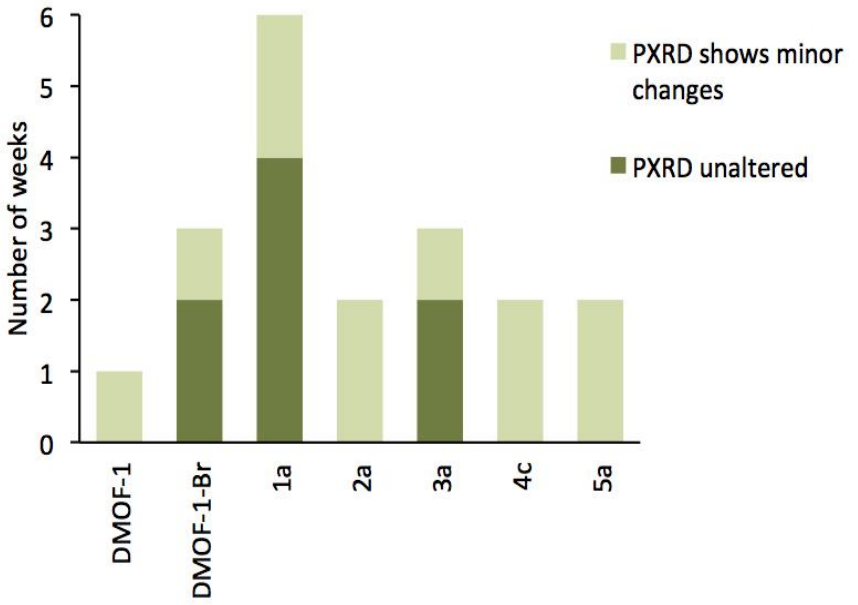

Figure 2.63 Structural stability tests of selected compounds as monitored by PXRD. Minor changes to the PXRD patterns include peak broadening and the appearance of additional peaks, while the main peaks remain present.

The stability of **1a** is significantly greater than both that of DMOF-1 and DMOF-1-Br (which shows stability in air for up to three weeks). Multivariate MOFs, such as **1a**, therefore can allow access to more air- or moisture-stable structures than those of the single-linker structures.

From the observed results it is clear that the basicity of the ligands plays little role in the stability of the resulting framework. This is apparent from **4c** which contains the substituent with the greatest electron donating effect, increasing its basicity. However, in this structure no increase in the overall stability of the framework is observed, with structural changes occurring after only 1 week of exposure to moisture.

No evidence of ligand steric effects influencing framework stability of the compounds is determined. For example, in both DMOF-1-Br and **5a** 100 % of the dicarboxylate ligands with in the frameworks contain bulky halide substituents, yet both of these compounds are less stable in air than compounds **1a** which contains a 50 % of the bdc-Br ligand within the framework.

Some explanation for this can be found in a comparison of the crystal structures of DMOF-1-Br and **1a**. The structure of DMOF-1shows a significant torsion of the dicarboxylate rings causing the halide substituents to point away from the zinc node (Figure 2.64). In the structure of **1a** the dicarboxylate rings do not twist and the bromo substituents point towards the zinc atoms (Figure 2.64). This could account for the more effective shielding of the metal-carboxylate bond from hydrolysis in **1a** compared to DMOF-1-Br.

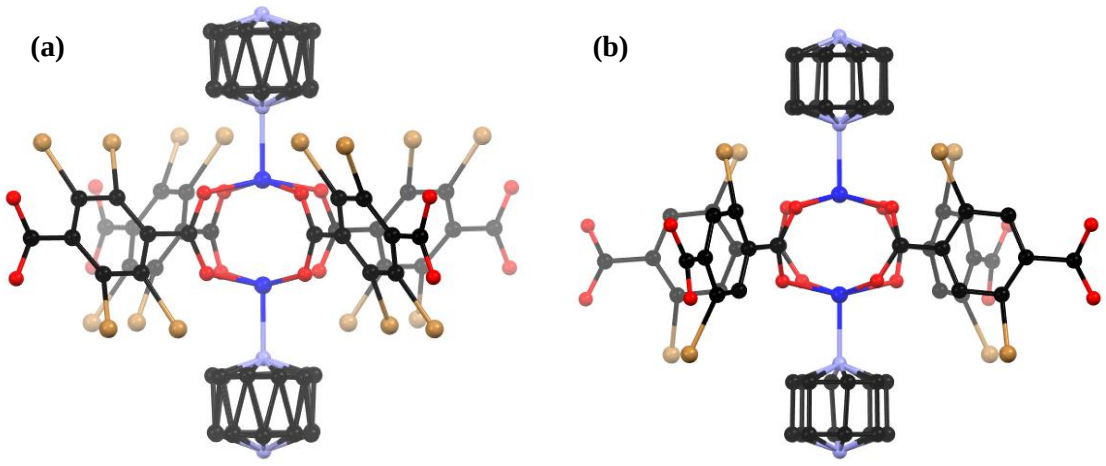

Figure 2.64 (a) The structure of DMOF-1-Br showing the twist of the dicarboxylate ring and the bromine substituents pointing away from the zinc-carboxylate bond. **(b)** the structure of **1a** showing the bromine substituent pointing towards the metal centres. In this structure the ring is not twisted. In both structures hydrogen atoms and solvent molecules are removed for clarity.

2.2.9 Computational modelling

Given the changes observed in pore geometry with composition in compounds from series $[Zn_2(bdc)_{2-x}(bdc\text{-}Br)_x(dabco)]\cdot nDMF$, $[Zn_2(bdc)_{2-x}(bdc\text{-}I)_x(dabco)]\cdot nDMF$, $[Zn_2(bdc)_{2-x}(bdc\text{-}NO_2)_x(dabco)]\cdot nDMF$ and the contrasting lack of structural changes observed in series $[Zn_2(bdc)_{2-x}(bdc\text{-}NH_2)_x(dabco)]\cdot nDMF$ and $[Zn_2(bdc\text{-}Br)_{2-x}(bdc\text{-}I)_x(dabco)]\cdot nDMF$, atomistic simulations were undertaken in order to gain insight into these observations.

The energy differences between different phases of the compounds were assessed, along with investigations into the transition between the structures. This work was carried out by Jessica Bristow and Aron Walsh and involved solid-state nudged elastic band (SS-NEB) calculations between symmetry representative structures which were performed using VASP at the DFT/PBEsol level of theory.[22-26] The saddle point in potential energy obtained between two stable polymorphs (within SS-NEB) can be used to predict the activation energy associated with the structural transformation. Full computational details can be found in Section 2.5.10.

For the series $[Zn_2(bdc)_{2-x}(bdc\text{-}Br)_x(dabco)]\cdot nDMF$ and $[Zn_2(bdc)_{2-x}(bdc\text{-}I)_x(dabco)]\cdot nDMF$, the fully halogenated frameworks, $[Zn_2(bdc\text{-}X)_2(dabco)]$, were modelled through two approaches. The first model has halogens substituted alternately on each side of neighbouring aromatic rings, resulting in 50% of the halogens within neighbouring pores. This model shall be referred to as the 'alternating pore structure' or (A) in which all pores contain one bromine substituent. The second model has halogen substitution with halogens on neighbouring rings located within the same pores. This model shall be referred to as the 'same pore structure' or (S) in which half the pores are occupied by two bromine groups and half by none (Figure 2.65). These models allow us to assess the effect of local halogen orientation and concentration, which may influence the phase stability.

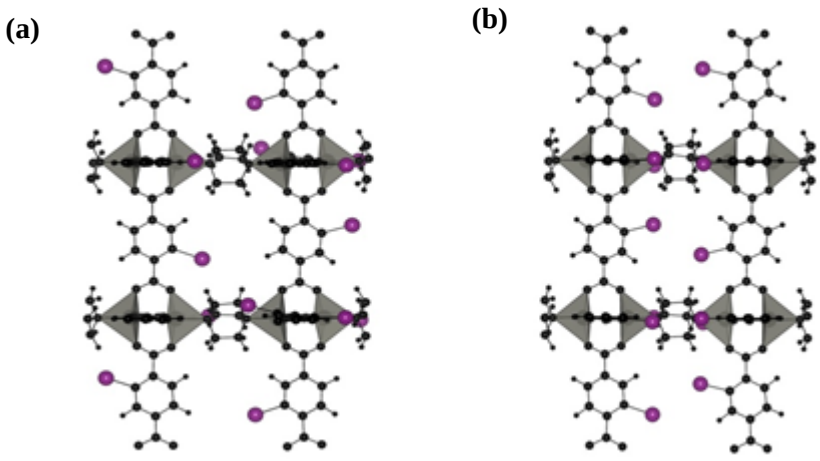

Figure 2.65 Halogen substitution positions modelled in DMOF-1. **(a)** Substitution within alternating pores (A) and **(b)** substitution in the same pore (S), with the halogen atoms shown in purple.

Three pore topologies were considered for the bromine and iodine substituted structures, and the unsubstituted $[Zn_2(bdc)_2(dabco)]$ framework; linear square, distorted square and rhomboidal. The relative energies of each topology with respect to the distorted pore structures are given in Table 2.16, with calculated activation energies for movement between each phase.

Table 2.16 Relative total energies between perfect square, distorted square and narrow pore structures in kJ $mol^{-1.}$ Note that the reported energy of each structure is relative to the distorted pore structure of DMOF-1. Activation energies reported for Transition 1 are from the distorted to perfect square, from distorted to the rhomboid pore structure for Transition 2 and from square to rhomboid pore structure for Transition 3.

Ligand	Linear square pore	Distorted square pore	Rhomboidal pore	$E_{act}(1)$ / kJ mol^{-1}	$E_{act}(2)$ / kJ mol^{-1}	$E_{act}(3)$ / kJ mol^{-1}
bdc	52.1	0	–8.2	18.5	–0.1	-
bdc-Br (A)	–34.8	0	–10.8	42.7	–0.2	37.8
bdc-Br (S)	–29.4	0	–68.5	37.4	-	14.6
bdc-I (A)	–65.7	0	–32.6	49.2	2.1	67.0
bdc-I (S)	23.0	0	–51.8	69.2	3.1	22.0

When considering the relative energies between square and rhomboid structures of the unsubstituted framework to the alternating pore structures (A) of 100% bdc-Br or 100% bdc-I, the rhomboidal pore form is the higher energy configuration. In contrast, for either the same pore structures (S) 100% bdc-Br or 100% bdc-I where there is a high concentration of Br in half of the pores, the rhomboidal form is more stable. This observation suggests that above a certain concentration of halogen within a pore, there is a thermodynamic driving force for the formation of the narrow, rhomboidal pore framework. The relative energy between the square and rhomboidal pore structures is lowest for the unsubstituted framework, while the linear square pore structure becomes less accessible with increasing halogen content. This supports the experimental observation that with increasing halogen content the square pore structure is not formed.

Potential energy profiles showing the activation energies between structures (as given in Table 2.16) for the three hypothetical structural transformations are depicted in Figure 2.66 to further evaluate the thermodynamic stabilities of each structure. Three structural transitions were considered:

Transition 1: 'Distorted square' to 'linear square' pore structure. This defines the activation energy $E_{act}(1)$ required to remove the structural distortion following solvent evacuation.

Transition 2: 'Distorted square' to 'rhomboid' pore structure. This defines the activation energy $E_{act}(2)$ for the compression of the pores observed in some mixed-ligand structures.

Transition 3: 'linear square' to 'rhomboid' pore structure. This defines activation energy $E_{act}(3)$ associated with compressing the structure from a higher symmetry square pore form. It is also associated with MOF 'breathing' and structural flexibility.

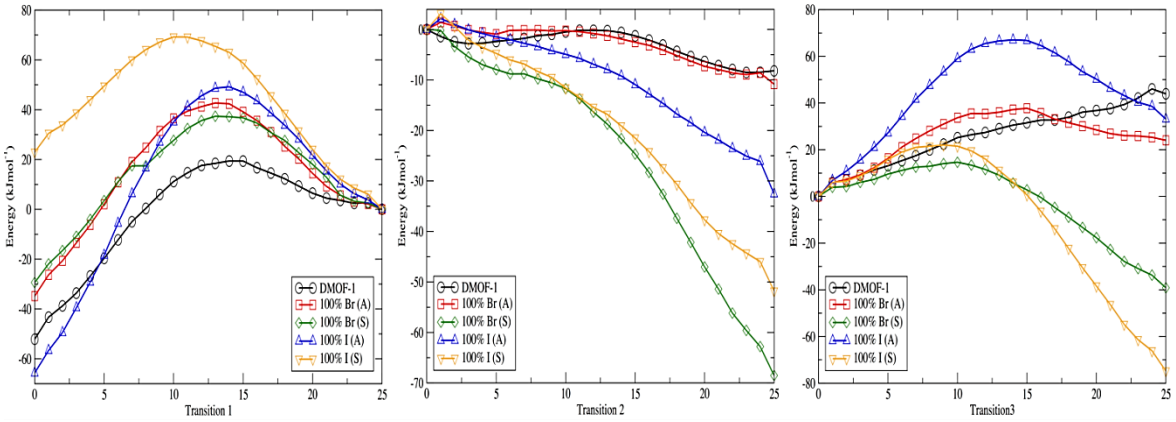

Figure 2.66 The potential energy surfaces associated with the three structural transformations with varying halide concentration, as predicted from nudged elastic band calculations (DFT/PBEsol). Structures labelled (A) have the halogens on neighbouring rings projecting into alternating pores whereas structures labelled (S) have the halogens on neighbouring rings projecting in to the same pores.

The energy profiles further support the observed behaviour of the frameworks. Each structure is locally stable and dynamic conversion between pore topologies would not be possible for structures with halogen substituents. Interestingly, for the 100% bdc structure, no activation barrier between square and rhomboid pore topology is evident. This supports the capability of the 100% bdc structure to 'breathe' with applied external stimulus such as a temperature or pressure.

Non covalent interaction (NCI) analysis allowed the visualisation of charge density within a chemical system that is not attributed to formal covalent bonding.[27-30] Two interactions were found to be of importance for the structural behaviour of the structures investigated. Firstly, attractive dispersive interactions between the carboxylate oxygen atoms and the hydrogen atoms on the dabco ligand are present. This interaction is present regardless of the substituent on the bdc ligand and could be a driving force for the structural breathing effect observed whereby the COO-Zn-COO angle changes. The calculated activation energies confirm that the structures are not interconvertible and a single pore topology is thermodynamically favorable for all systems, supporting the experimental observations of a phase change within the powder diffraction patterns.

Secondly, dispersive interactions between the halogen atom and the hydrogen atom on the dabco ligand explain why rhomboidal pore structures are observed experimentally for mixed-ligand systems at a halogen content of greater than 60 %. Figure 2.67 depicts this interaction between Br and H in the 100% bdc-Br (S) system. With increasing concentration of halogen, the number of these interactions increases and this provides the thermodynamic driving force for the observed behaviour. As the halogen-halogen distances within the pore are greater than 6 Å in series $[Zn_2(bdc)_{2-x}(bdc\text{-}Br)_x(dabco)]\cdot nDMF$, this rules out halogen-halogen interactions as a contributing factor to pore compression. Indeed, these interactions were also not evident in the NCI analysis.

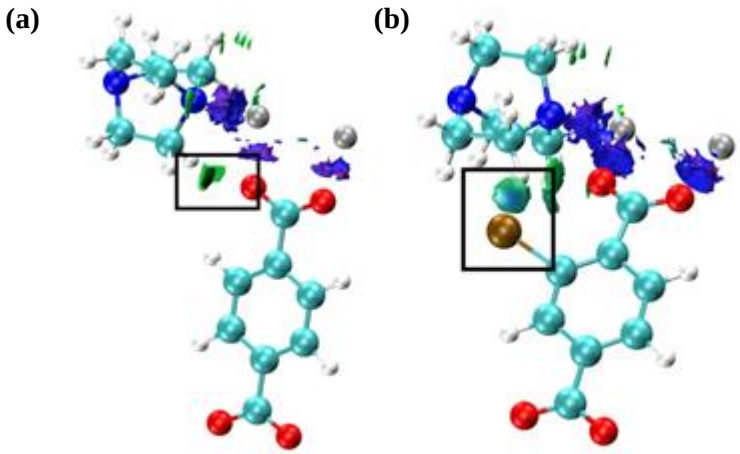

Figure 2.67 Non-covalent interactions **(a)** in DMOF-1 determined from topological analysis of DFT calculations and **(b)** between H and Br in DMOF-1-Br. The depicted density represents repulsive interactions between the paired Zn metals (blue) and attractive interactions as highlighted between the carboxylate O and Zn atoms (green). Also shown are attractive interactions between the carboxylate O and H-(dabco).

Computational analysis of both the $[Zn_2(bdc)_{2-x}(bdc\text{-}NO_2)_x(dabco)]\cdot nDMF$ and $[Zn_2(bdc)_{2-x}(bdc\text{-}NH_2)_x(dabco)]\cdot nDMF$ series offers further support for the experimental observations. At 100% concentration of both amino and nitro substituents on the aromatic ring these structures do not distort into rhomboidal geometry, but remain in a square pore topology. For the amino-containing frameworks $[Zn_2(bdc)_{2-x}(bdc\text{-}NH_2)_x(dabco)]\cdot nDMF$, only weak $H(NH_2)$-H(dabco) interactions are present that would not provide enough attractive force to drive the structure to collapse. For the case of series $[Zn_2(bdc)_{2-x}(bdc\text{-}NO_2)_x(dabco)]\cdot nDMF$, the analysis of observed pore topologies is more complex. During geometry optimisation, a rotation of the NO_2 substituent renders the non-covalent interactions diffuse and weak due to the lone pair repulsion between the $O(NO_2)$-O(carboxylate).

2.3 Compositional control of pore geometry through steric interactions

2.3.1 Aims and objectives

The formation and analysis of mixed-ligand series $[Zn_2(bdc)_{2-x}(bdc\text{-}Br)_x(dabco)]\cdot nDMF$, $[Zn_2(bdc)_{2-x}(bdc\text{-}I)_x(dabco)]\cdot nDMF$, $[Zn_2(bdc)_{2-x}(bdc\text{-}NO_2)_x(dabco)]\cdot nDMF$, $[Zn_2(bdc)_{2-x}(bdc\text{-}NH_2)_x(dabco)]\cdot nDMF$, $[Zn_2(bdc\text{-}Br)_{2-x}(bdc\text{-}I)_x(dabco)]\cdot nDMF$ and $[Zn_2(bdc\text{-}NO_2)_{2-x}(bdc\text{-}NH_2)_x(dabco)]\cdot nDMF$ demonstrate how altering functional group content within frameworks of DMOF-1 topology can impact pore shape and size of the resulting MOF. In order to extend this investigation, a seventh mixed-ligand series was prepared based around the DMOF-1 topology, combining the bdc ligand of DMOF-1 with a second, bulkier dicarboxylate ligand; 1,4-naphthalenedicarboxylate (ndc). Mixed-ligand MOFs were produced with varying bdc:ndc ratios, formed through systematically altering the ratio of H_2bdc:H_2ndc in the reaction mixture. The effect of increasing steric interactions within the pores of the framework, through the inclusion of increasing ndc content, was investigated.

The composition of the products were determined through ^{1}H NMR spectroscopy, and the structures of mixed-ligand species were investigated through a combination of powder X-ray diffraction and single crystal X-ray diffraction analysis. Computational studies accompany the experimental work which were carried out by Jessica Bristow and Aron Walsh.

2.3.2 Synthesis and characterisation of $[Zn_2(bdc)_{2-x}(ndc)_x(dabco)]\cdot nDMF$

The reaction of $Zn(NO_3)_2\cdot 6H_2O$ with dabco and mixtures of 1,4-benzenedicarboxylic acid and 1,4-naphthalene dicarboxylic acid in varying ratios in DMF at 120°C for 3 days afforded crystalline products. All products were formed in good yields of approximately 60-80% and produced colourless crystals.

Nine products were successfully synthesised by varying the ratio of H_2bdc:H_2ndc ligands in the reaction mixture. Ratios of approximately 1:9, 2:8, 3:7, 4:6, 5:5, 6:4, 7:3, 8:2 and 9:1 were used.

Compositions of all products were determined through ^{1}H NMR spectroscopy on acid digested bulk samples (samples of multiple crystals) which were dried at 120 ^{o}C for 15 minutes prior to being digested in a d_6-DMSO/DCl mixture. In order to ensure that the products were mixed-ligand systems and not a physical mixture of two single ligand systems, ^{1}H NMR spectra were also recorded on individual crystals of the products with the exception of products from reaction ratios of 1:9 and 2:8 H_2bdc:H_2ndc, as these yielded crystals too small to isolate and digest. Individual crystals were selected under the microscope and digested in a d_6-DMSO/DCl mixture. Three crystals from each product were analysed using this method to determine compositional variation within the samples.

^{1}H NMR analysis on all bulk and individual crystal samples showed the presence of both D_2ndc and D_2bdc dicarboxylic acids, and the bulk spectrum for the reaction mixture containing 50 % H_2bdc and 50 % H_2ndc is given in Figure 2.68.

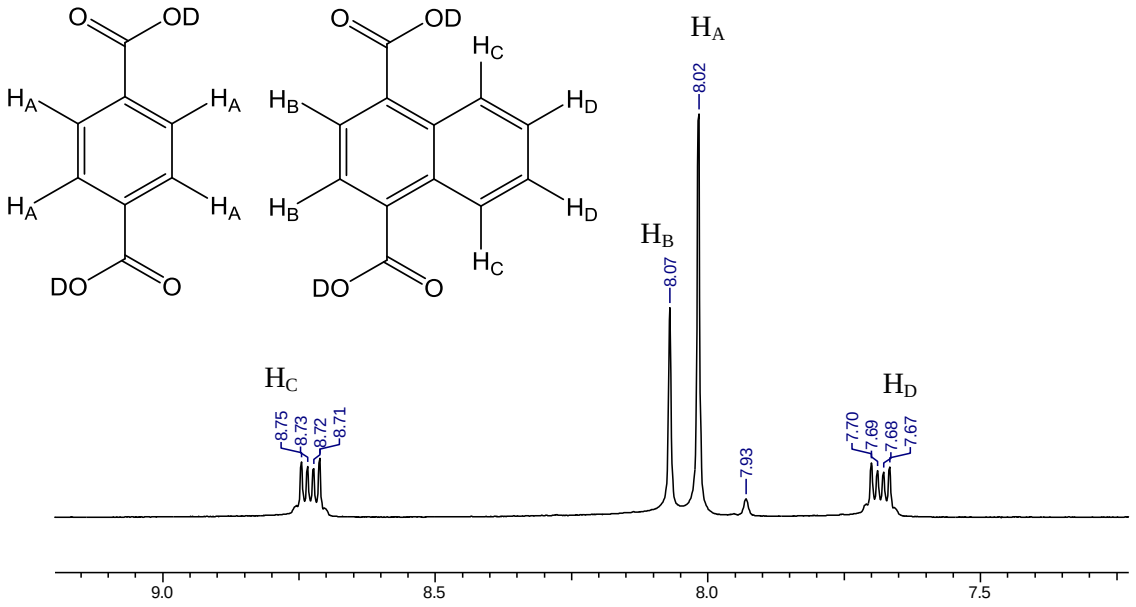

Figure 2.68 ^{1}H NMR spectrum of the acid digested product formed from the reaction mixture containing a 1:1 ratio of H_2bdc:H_2ndc. The structures of the two deuterated dicarboxylic acids are shown.

The resonance at δ 8.02 ppm corresponds to the four aromatic protons of D_2bdc. The resonances at δ 7.69 ppm, δ 8.07 ppm and δ 8.73 ppm correspond to the aromatic protons of H_2ndc. The signal at δ 7.93 ppm originates from the DMF solvent present in the sample. The presence of both dicarboxylic acids in all digestion mixtures confirms the formation of mixed-ligand products (Figure 2.69).

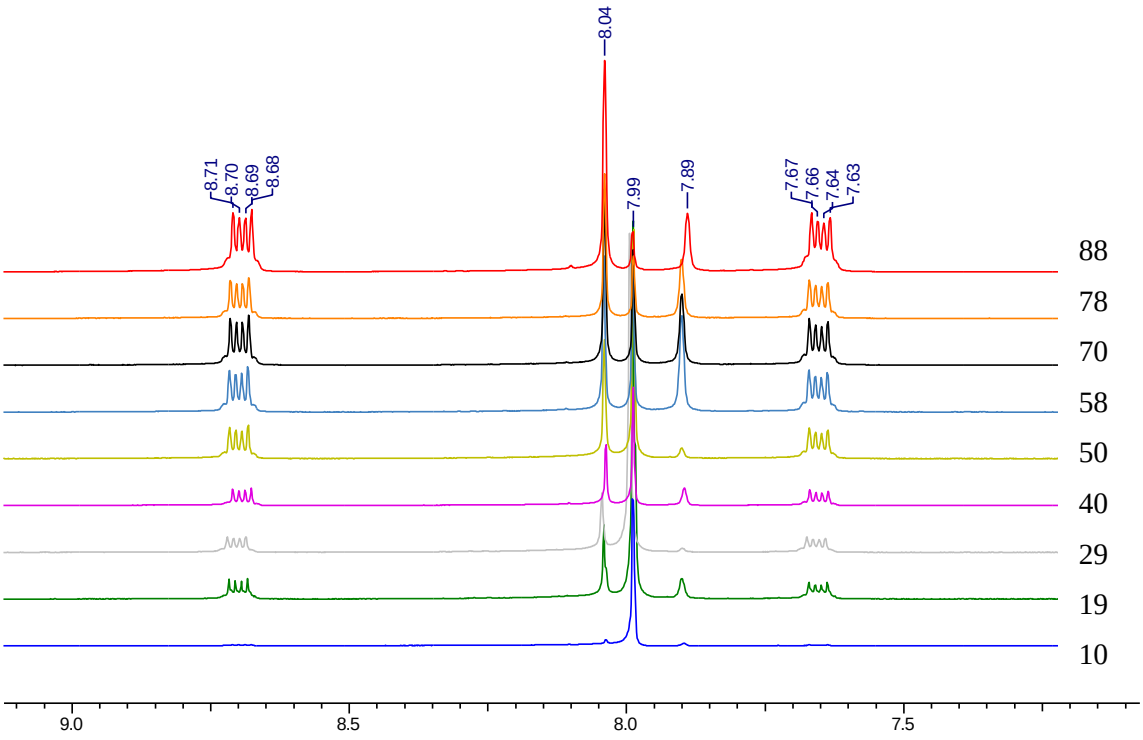

Figure 2.69 ^{1}H NMR spectra of acid digested products formed from varying ratios of H_2bdc and H_2ndc. The percentage of D_2ndc in the reaction mixture is shown alongside the corresponding spectrum.

Analysis of the integrated spectra was conducted to determine the product compositions. Similar percentages of D_2ndc were found in the digestion mixtures of all products to those of the corresponding reaction mixtures, indicating no strong ligand preferences in the formation of the products (Figure 2.70).

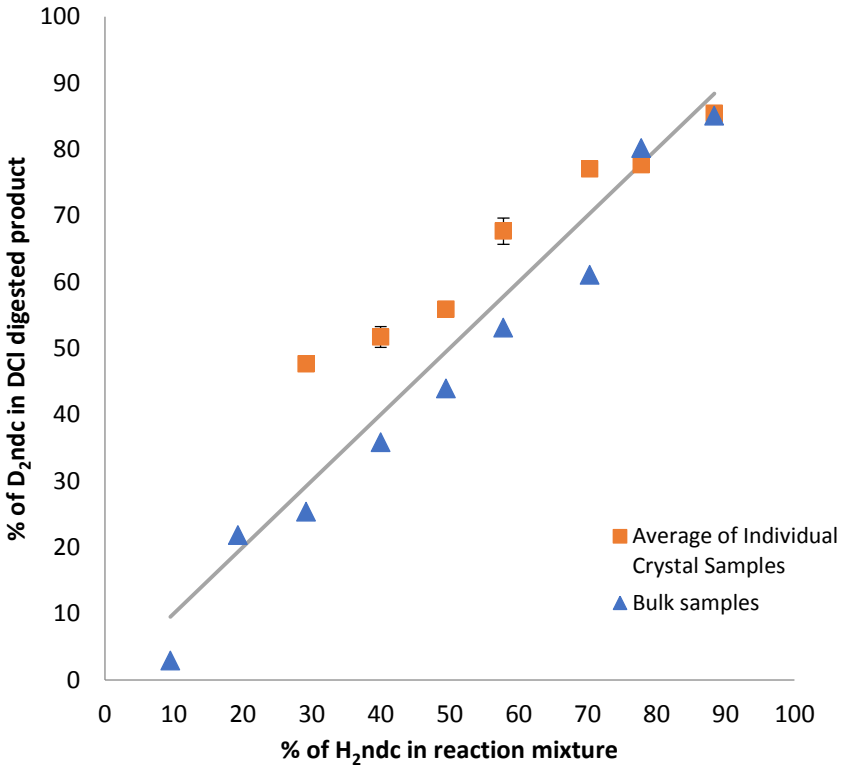

Figure 2.70 A plot of the percentage D_2ndc content in the acid digested products against the percentage of H_2ndc in the reaction mixture. Individual crystal data shown is an average of the integral analysis from the three crystals taken from each product showing standard deviation error bars where the error is greater than 1 %.

A comparison of the three individual crystal ^{1}H NMR spectra for each product showed similar D_2bdc:D_2ndc ratios were present in different crystals from the same product. This indicates that little compositional variation is present within each sample with variations in H_2ndc content of 0.4 % and 2.1 %. Final product compositions are taken from the integration on the bulk samples and can be seen in Table 2.17.

Table 2.17 Experimental ratios of H_2ndc used to form $[Zn_2(bdc)_{2-x}(ndc)_x(dabco)]$ products and the corresponding percentage of ndc in the products as determined through ^{1}H NMR studies. The formulae of the products excluding guest solvent are given.

% H_2ndc in reaction mixture	**Average % ndc in product**	**Average Product Formula (as determined through ^{1}H NMR studies)**
10	3	$[Zn_2(bdc)_{1.94}(ndc)_{0.06}(dabco)]$
19	22	$[Zn_2(bdc)_{1.56}(ndc)_{0.44}(dabco)]$
29	25	$[Zn_2(bdc)_{1.5}(ndc)_{0.5}(dabco)]$
40	36	$[Zn_2(bdc)_{1.28}(ndc)_{0.72}(dabco)]$
50	44	$[Zn_2(bdc)_{1.12}(ndc)_{0.88}(dabco)]$
58	53	$[Zn_2(bdc)_{0.94}(ndc)_{1.06}(dabco)]$
70	61	$[Zn_2(bdc)_{0.78}(ndc)_{1.22}(dabco)]$
78	80	$[Zn_2(bdc)_{0.4}(ndc)_{1.6}(dabco)]$
88	85	$[Zn_2(bdc)_{0.3}(ndc)_{1.7}(dabco)]$

Structural characterisation of all products was carried out through powder X-ray diffraction. All products gave PXRD patterns containing similar general features to one another suggesting that all mixed-ligand products possess similar framework topologies (Figure 2.71). A comparison to the powder diffraction trace generated from the single crystal structure of DMOF-1 confirms that it is topologically similar to that of the mixed-ligand products.

Much like previous mixed-ligand series discussed in Section 2.2 a shift in peak positions can be observed in the powder diffraction patterns of $[Zn_2(bdc)_{2-x}(ndc)_x(dabco)]\cdot$nDMF products with increasing ndc content. This is most noticeable for peaks at 2θ values of 8.3° and 16.6°. In low ndc content products (less than 20 % ndc content) the peak positions resemble those of DMOF-1, occurring at 2θ values of 8.3° and 16.6°, whilst in samples of ndc content between 29% and 70%, these peaks occur at lower 2θ values of 8.1° and 16.1°. A similar peak shift was observed in the powder diffraction patterns of $[Zn_2(bdc)_{2-x}(bdc\text{-}Br)_x(dabco)]\cdot$nDMF, $[Zn_2(bdc)_{2-x}(bdc\text{-}I)_x(dabco)]\cdot$DMF and $[Zn_2(bdc)_{2-x}(bdc\text{-}NO_2)_x(dabco)]\cdot$nDMF and was found to be is associated with structural changes within the frameworks, transitioning from square to rhomboidal pore forms. In contrast to previously discussed series, a second transition point is observed in the powder diffraction patterns of in products with an ndc content of greater than 70 %. In these products the peak positions are similar to low ndc content products at 2θ values of 8.3° and 16.6°. These two

peak shift transitions can be seen in the 2θ plots for the peaks at around 2θ 8° and 16° for all products given in Figure 2.71.

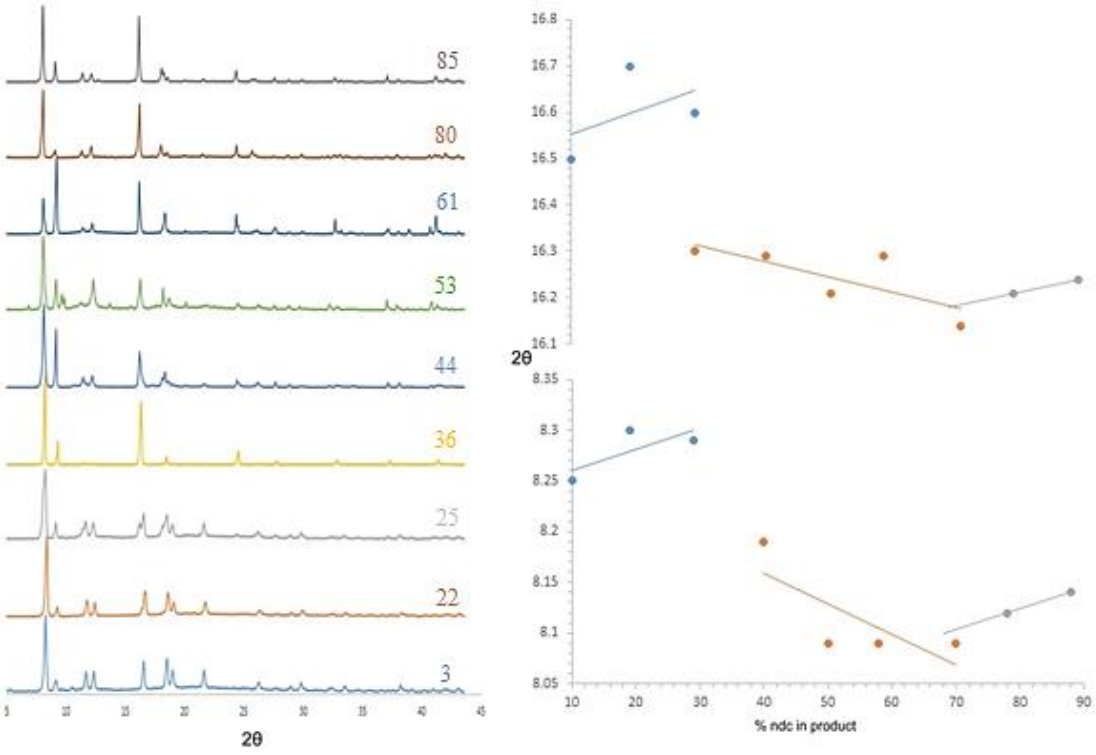

Figure 2.71 PXRD patterns of the as-synthesised compounds $[Zn_2(bdc)_{2-x}(ndc)_x(dabco)].nDMF$. The plot of 2θ against % ndc shows the key peaks which shift with the change ndc content in the framework.

A change in relative intensity of the peak at 2θ value of around 9° in products containing 44 % and 61 % ndc can be explained by differences in solvent in the pores between products. A similar effect was observed in the PXRD patterns of $[Zn_2(bdc)_{2-x}(bdc\text{-}Br)_x(dabco)]$ products (see Section 2.2.2).

Crystals from two of the products were suitable for single crystal X-ray diffraction analysis. The products are identified as $[Zn_2(bdc)_{0.94}(ndc)_{1.06}(dabco)]\cdot 2.3DMF$ **7a** and $[Zn_2(bdc)_{0.2}(ndc)_{1.8}(dabco)]\cdot 1.6DMF$ **7b**. From the powder diffraction data, we would expect **7a** to have some structural differences to **7b**, due to differences in their peak positions.

Structure description of $[Zn_2(bdc)_{0.94}(ndc)_{1.06}(dabco)]\cdot 2.3DMF$ **7a**

Thermogravimetric analysis of **7a** shows a percentage mass loss of 28 % between 115 °C and 205 °C, corresponding to a solvent loss of 2.3 DMF molecules per unit formula (see appendix Figure A2.2.6).

The asymmetric unit of **7a** consists of a quarter of a zinc atom, a quarter of a bdc/ndc ligand disordered over two sites and a quarter of a dabco moiety (Figure 2.72).

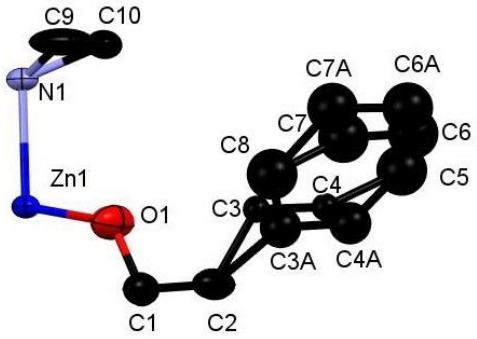

Figure 2.72 Asymmetric unit of $[Zn_2(bdc)_{1.01}(1,4\text{-ndc})_{0.99}(dabco)]\cdot 2.3DMF$ **7a** with ellipsoid probability of 40 %. Hydrogen atoms are omitted for clarity.

The phenyl ring of the dicarboxylate ligand has considerable disorder, being positioned on a mirror plane and disordered over two positions within the asymmetric unit it is further complicated by disorder due to the presence of both bdc and ndc ligands in a 50:50 ratio within the structure. At positions C3 and C4, which are disordered with C3a and C4a and are common to both bdc and ndc ligands, the atoms have a 25 % site occupancy. C5 and C8, which are only present in ndc ligands have a 12.5 % site occupancy. C6, C7, C6a and C7a are disordered both within the asymmetric unit and through symmetry and have an attributed occupancy of 6.25 %.

The dabco is disordered in a similar manner to other structures in this chapter as N1 is located on a mirror plane perpendicular to the *a*-axis and is located about an inversion centre. This leads to symmetry related disorder of C9 and C10 which is modelled by attributing the site occupancies to 50 % and 25 % respectively. Generation of the whole dabco moiety results in a total of two nitrogen atoms and six carbon atoms.

The structure of **7a** presents a framework with similar connectivity to that of DMOF-1. However, **7a** displays a rhomboidal pore structure which can be seen in Figure 2.73. The powder X-ray diffraction trace of **7a** shows a good correlation to that of the bulk experimental powder diffraction pattern (see appendix A2.1.7).

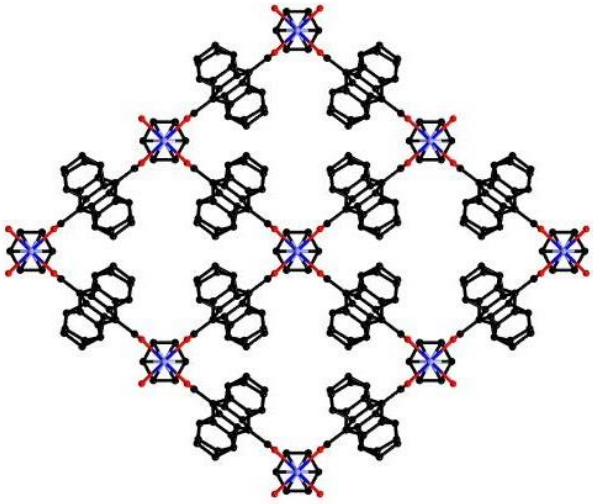

Figure 2.73 Pore structure of $[Zn_2(bdc)_{1.01}(1,4\text{-ndc})_{0.99}(dabco)]\cdot 2.3DMF$ **7a** viewed down the *c*-axis with ndc moieties disordered. Hydrogen atoms are omitted for clarity.

Structure description of $[Zn_2(bdc)_{0.2}(ndc)_{1.8}(dabco)]\cdot 1.6DMF$ **7b**

Thermogravimetric analysis of **7b** reveals a percentage mass loss of 24 % between 115 ^{o}C and 200 ^{o}C, corresponding to a solvent loss of 1.6 DMF molecules per unit formula (see appendix Figure A2.2.7).

The asymmetric unit of **7b** consists of a quarter of a zinc atom, a quarter of a bdc/ndc ligand and a quarter of a dabco moiety (Figure 2.74).

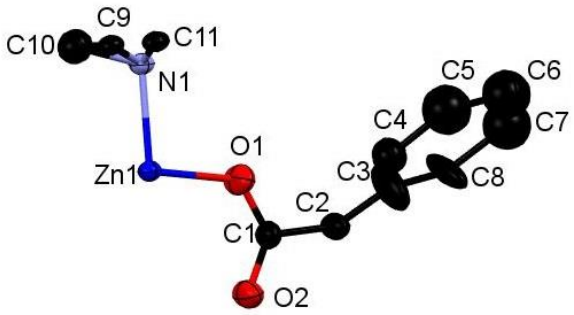

Figure 2.74 Asymmetric unit of $[Zn_2(bdc)_{0.2}(ndc)_{1.8}(dabco)]\cdot 1.6DMF$ **7b** with ellipsoid probability of 40 %. Hydrogen atoms are omitted for clarity.

C1 and C2 belong to both bdc and ndc ligands and are located on a mirror plane perpendicular to the *c*-axis. Their site occupancy is therefore 50 %. An inversion centre and two-fold rotation axes are also present about the bdc/ndc ligand resulting in symmetry related disorder of C3-C8. This disorder is modelled by attributing the site occupancies of C3 and C8 which are common to both

bdc and ndc ligands to 50 % and C4, C5, C6 and C7 which belong to only the ndc ligand to 22.5 %. Symmetry generation results in a total of 90 % ndc ligand in the structure.

N1 is located on a four-fold rotation axis resulting in symmetry related disorder of the dabco carbons. This is modelled through attributing site occupancies of C9, C10 and C11 to 25 % each. A total of six carbons are therefore present in a full dabco moiety.

The overall structure of **7b** displays the gross DMOF-1 connectivity and square pore topology (Figure 2.75). This is in contrast to **7a** which contains a lower percentage of ndc within the framework and displays rhomboidal pores. The powder diffraction pattern of **7b** shows a good match to that of the experimental bulk trace (see appendix A2.1.8).

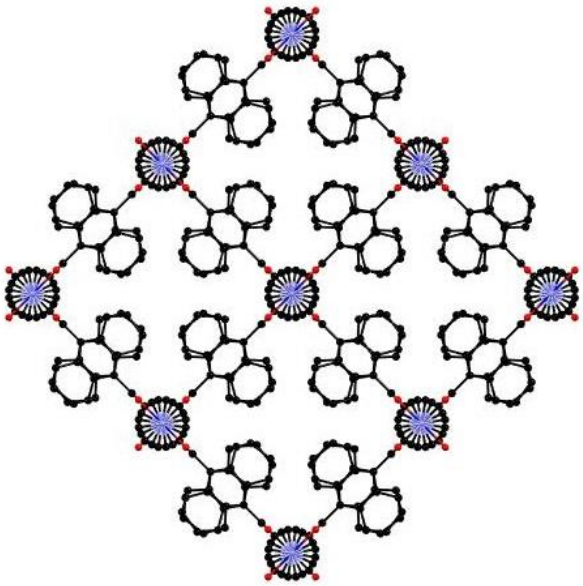

Figure 2.75 Pore structure of $[Zn_2(bdc)_{0.2}(ndc)_{1.8}(dabco)]\cdot 1.6DMF$ **7b** viewed down the *c*-axis. The ndc moieties show disorder over multiple positions. Hydrogen atoms are omitted for clarity.

These observations are consistent with the PXRD findings, and confirm that peak shifts represent a change in pore geometry of the product frameworks from the rhomboidal pores of the orthorhombic **7a** structure to the square pores of the tetragonal **7b** structure (Table 2.18). The formation of $[Zn_2(bdc)_{2-x}(ndc)_x(dabco)]$ mixed-ligand products therefore causes a pore geometry shift from square to rhomboidal to square pores with increasing ndc content.

Table 2.18 Crystal data and structure refinement for $[Zn_2(bdc)_{0.94}(ndc)_{1.06}(dabco)]\cdot 2.3DMF$ **7a** and $[Zn_2(bdc)_{0.2}(ndc)_{1.8}(dabco)]\cdot 1.6DMF$ **7b**.

Identification code	**7a**	**7b**
Empirical formula	C3.25 H2.70 N0.25 O Zn0.25	C3.65 H2.95 N0.25 O Zn0.25
Formula weight	77.6	82.66
Temperature	150(2) K	150(2) K
Wavelength	0.71073 Å	0.71073 Å
Crystal system	Orthorhombic	Tetragonal
Space group	*Cmmm*	*P4/nbm*
Unit cell dimensions	a = 13.9230(3)Å α = 90°	a = 15.4550(3)Å α= 90°
	b = 16.7920(3)Å β= 90°	b = 15.4550(3)Å β = 90°
	c = 9.6660(2)Å γ = 90°	c = 9.6660(2)Å γ = 90°
Volume	2259.86(8) $Å^3$	2308.79(8) $Å^3$
Z	16	16
Density (calculated)	0.912 Mg/m^3	0.951 Mg/m^3
Absorption coefficient	1.091 mm^{-1}	1.072 mm^{-1}
F(000)	631	674
Crystal size	0.40 x 0.30 x 0.30 mm	0.30 x 0.30 x 0.20 mm
Theta range for data collection	4.63 to 27.73 °.	3.62 to 27.49°
Index ranges	-17<=h<=18; -21<=k<=21; -12<=l<=12	-20<=h<=19; -20<=k<=19; -12<=l<=12
Reflections collected	16618	32572
Independent reflections	1457 [R(int) = 0.0385]	1397 [R(int) = 0.0596]
Reflections observed (>2sigma)	1381	872
Data Completeness	0.961	0.993
Absorption correction	Semi-empirical from equivalents	Semi-empirical from equivalents
Max. and min. transmission	0.811 and 0.758	0.83 and 0.75
Refinement method	Full-matrix least-squares on F^2	Full-matrix least-squares on F^2
Data / restraints / parameters	1457 / 75 / 80	1397 / 67 / 112
Goodness-of-fit on F^2	1.104	1.216
Final R indices [I>2sigma(I)]	$R1$ = 0.0460 $wR2$ = 0.1300	$R1$ = 0.0556 $wR2$ = 0.1547
R indices (all data)	$R1$ = 0.0483 $wR2$ = 0.1338	$R1$ = 0.0770 $wR2$ = 0.1798
Largest diff. peak and hole	0.585 and -0.558 $eÅ^{-3}$	0.373 and -0.458 $eÅ^{-3}$

2.3.3 Computational modelling

Computational modelling was used to explore the relationship between ndc ligand content in the $[Zn_2(bdc)_{2-x}(ndc)_x(dabco)]$ frameworks and the resulting pore geometry. Computational studies were conducted on $[Zn_2(bdc)_2(dabco)]$, $[Zn_2(bdc)(ndc)(dabco)]$ and $[Zn_2(ndc)_2(dabco)]$. Relative total energies of the rhomboidal and square framework topologies for frameworks with 0, 50 and 100 % ndc content are given in Table 2.19.

Table 2.19 Energy relative to the orthorhombic structure ($KJmol^{-1}$).

	Content of ndc in the structure		
	0 %	50 %	100 %
Rhomboidal Pore	52.2	-60.4	51.3
Square Pore	0.0	0.0	0.0

At 50 % ndc concentration the rhombohedral pore structure is more stable. In stark contrast, at both 0 % and 100 % ndc content the structures favour a square pore framework. This shows that the final symmetry and pore shape of the structure is dependent upon ndc concentration within the framework, confirming the observations from experimental studies.

In both structures containing 50 % and 100 % concentration of ndc, the ligand is twisted within the structure, as observed in the single crystal structure analyses. The twisting is needed to allow the side ring fused to the main body of the aromatic dicarboxylate unit to reside within the pore of the MOF. This twisting reduces destabilizing steric interactions. However, with a higher content of ndc the larger pore structure, with open square pores has a lower total energy and is therefore formed in preference to the narrow pore, rhomboidal structure. This is likely to be due to steric interactions between the increasing ndc moieties within the framework, which despite the orientation of the naphthalene rings, causes the narrow pore form to become unstable (at a ndc content of 50 % in the framework, the rhomboidal framework is observed with a lower total energy than the square pore form).

The symmetry changes observed in $[Zn_2(bdc)_{2-x}(bdc\text{-}X)_x(dabco)]\cdot nDMF$ (X=Br, I, NO_2) were found to be due to non-covalent interactions between the substituent atom and the hydrogen on the dabco (see Section 2.2.9).[31] Similar analysis was carried out on **7a** to consider possible interactions in the pore involving naphthalene groups. Whilst dispersion interactions may be present in **7a** which account for the rhomboidal pore topology at low concentrations of ndc, no significant

interaction between H(ndc)···H(dabco) is predicted in the square pore form with the non-covalent interaction (NCI) analysis approach (Figure 2.76).

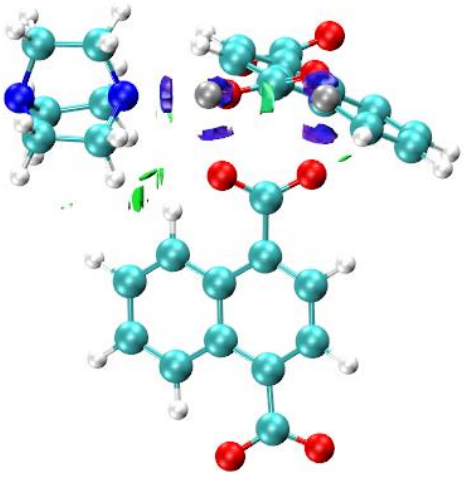

Figure 2.76 The non-covalent interactions between H and ndc in [Zn_2(bdc)(ndc)(dabco)], **7a**. Repulsive interactions between the paired Zn metals and attractive interactions between the ndc and H-dabco are shown in blue and green respectively.

A stronger dispersive interaction is observed in the rhombohedral framework when compared to the square pore form due to shorter H(ndc)···H(dabco) and H(ndc)···O(carb) distances (Figure 2.77). Therefore these non-covalent interactions can be concluded to be responsible for the initial phase change to rhomboidal symmetry, as was the case for the halogen-substituted frameworks. However, as the ndc content increases, steric interactions between the ndc groups within the framework pores dominate, and the square pore form becomes the lowest in total energy.

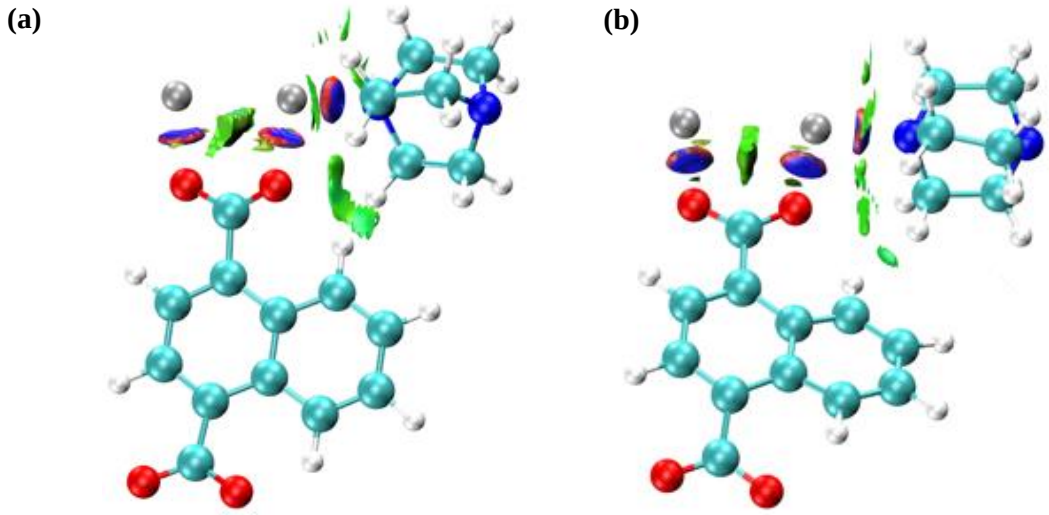

Figure 2.77 NCI analysis of [Zn_2(bdc)(ndc)(dabco)], **7a** in a **(a)** rhomboidal pore geometry and **(b)** square pore geometry. The attractive dispersive interactions between H (dabco)···H (ndc) are shown in green.

2.4 Conclusions and future work

Multivariate MOFs based on the structure of DMOF-1 and containing varying ratios of different dicarboxylate ligands have been successfully synthesised and characterised. The series $[Zn_2(bdc)_{2-x}(bdc\text{-}Br)_x(dabco)]\cdot DMF$, $[Zn_2(bdc)_{2-x}(bdc\text{-}NO_2)_x(dabco)]\cdot nDMF$, $[Zn_2(bdc)_{2-x}(bdc\text{-}NH_2)_x(dabco)]\cdot nDMF$ and $[Zn_2(bdc)_{2-x}(ndc)_x(dabco)]\cdot nDMF$ show the incorporation of ligands into the product framework in the same ratio as that present in the reaction mixture. Both series $[Zn_2(bdc)_{2-x}(bdc\text{-}I)_x(dabco)]\cdot nDMF$ and $[Zn_2(bdc\text{-}Br)_{2-x}(bdc\text{-}I)_x(dabco)]\cdot nDMF$ demonstrate a strong ligand preference with the bdc-I ligand being preferentially excluded during framework formation. Mixed-ligand products of the form $[Zn_2(bdc\ NO_2)_{2-x}(bdc\text{-}NH_2)_x(dabco)]\cdot nDMF$ present a more complex case in which crystals are formed of multiple multivariate regions differing in their composition.

The systematic approach to multivariate MOF formation has demonstrated that by variation of dicarboxylic acid ratios in the reaction mixture the pore topology of the framework can be controlled through functional group choice and concentration within the framework. For series $[Zn_2(bdc)_{2-x}(bdc\text{-}Br)_x(dabco)]\cdot nDMF$, $[Zn_2(bdc)_{2-x}(bdc\text{-}I)_x(dabco)]\cdot nDMF$ and $[Zn_2(bdc)_{2-x}(bdc\text{-}NO_2)_x(dabco)]\cdot nDMF$ experimental observations show that above a concentration of approximately 60 % of the substituted dicarboxylate ligand within the framework, a pore compression similar to that observed in solvent driven breathing phenomenon occurs. Computational studies on these series show a thermodynamic driving force for pore compression with increasing substituent concentration. This has been found to be due to non-covalent interactions between the substituent and the hydrogen atom on the dabco moiety.

For the $[Zn_2(bdc)_{2-x}(ndc)_x(dabco)]\cdot nDMF$ series inclusion of the ndc ligand has a similar effect, with the series displaying square to rhomboidal to square pore transitions as the ndc content increases. Non-covalent interactions are found to cause the initial observed structural symmetry change from square to rhomboidal pores. Above a concentration of 70 % ndc within the framework the second transition from rhomboidal to square pores is observed which is thought to be due to increased steric interactions between the naphthalene moieties within the framework.

These pore transitions are dependent upon the substituent group, as demonstrated by series $[Zn_2(bdc)_{2-x}(bdc\text{-}NH_2)_x(dabco)]\cdot nDMF$ and $[Zn_2(bdc\text{-}Br)_{2-x}(bdc\text{-}I)_x(dabco)]\cdot nDMF$ which show no pore transitions. The correlation of pore geometry to the ligand ratio opens up the possibility of pore size and shape tuning through reaction stoichiometry control without the loss of desirable properties introduced through ligand choices. Pore geometries which may only otherwise be accessed *via* solvent changes or complete substitution of the ligand can therefore be formed through the use of a multivariate approach.

The multivariate MOFs containing bromo, iodo, nitro and amino functionalities show an increased stability to air than DMOF-1. In the specific case of $[Zn_2(bdc)(bdc\text{-}Br)(dabco)]\cdot DMF$ **1a**, the compound shows enhanced stability over both $[Zn_2(bdc)_2(dabco)]\cdot 1.4DMF\cdot 0.5H_2O$, DMOF-1, and $[Zn_2(bdc\text{-}Br)_2(dabco)]\cdot 4.4DMF$, DMOF-1-Br, demonstrating that multivariate species can have properties which extend beyond the combination of the corresponding single ligand systems.

Further work could be completed on the water stability of mixed-ligand products to understand the preliminary results reported in this chapter. These studies could also be extended to the naphthalene containing products of $[Zn_2(bdc)_{2-x}(ndc)_x(dabco)]\cdot nDMF$. Further crystallographic studies could be completed, for example on the $[Zn_2(bdc\text{-}Br)_{2-x}(bdc\text{-}I)_x(dabco)]$ series with the use of a synchatron source. Crystal growth studies of the $[Zn_2(bdc\ NO_2)_{2-x}(bdc\text{-}NH_2)_x(dabco)]\cdot nDMF$ products may help to determine if specific compositions and regions form over time.

2.5 Experimental

2.5.1 General experimental details

With the exception of 2-iodo-1,4-benzenedicarboxylic acid (H_2bdc-I), starting materials and solvents were purchased from commercial sources and were used without further purification.

Powder X-ray diffraction (PXRD) patterns were recorded on a Bruker AXS D8 Advance diffractometer with copper Kα radiation of wavelength 1.5406 Å at 298 K. Samples were placed on a flat plate, and measured with a 2θ range of 5-60°. The step size was 0.024° with time per step of 0.3 s. Samples for PXRD analysis were air dried at room temperature for 1-2 minutes.

^{1}H NMR spectroscopy on bulk samples was carried out on a 300 MHz Bruker Avance Spectrometer. Samples were dried at 100 °C for 20 minutes and digested in a solution of d_6-DMSO and DCl. The digestion solution was prepared by combining 3 ml d_6-DMSO with 0.1 ml DCl (35% wt in D_2O). Each sample was dissolved in 0.4 ml of d_6-DMSO and 0.2 ml of the digestion solution. ^{1}H NMR spectroscopy on individual crystals was carried out on a 500 MHz Bruker Avance using a dual solvent suppression programme. Samples were prepared in the same way as the bulk NMR samples.

TGA experiments were carried out on a Perkin Elmer TGA 4000 Thermogravimetric Analyser. The samples were heated from 25 °C to 600 °C at a heating rate of 10 °C/min, under a flow of nitrogen (20 mL/min).

2.5.2 Synthetic procedures

H_2bdc-I was prepared according to previously reported methods.[16] Synthesis of the mixed-linker compounds were carried out using an analogous synthesis to that of DMOF-1, originally reported by Kim and co-workers.[11] In all cases syntheses were carried out using a total of approximately 0.5 mmol of the two dicarboxylic acids.

2.5.3 Synthesis of $[Zn_2(bdc)_{2-x}(bdc\text{-}Br)_x(dabco)]\cdot n$DMF,

For **1a** $Zn(NO_3)_2\cdot 6H_2O$ (0.502 mmol, 0.149 g), H_2bdc (0.404 mmol, 0.067 g), H_2bdc-Br (0.102 mmol, 0.025 g) and dabco (0.245 mmol, 0.028 g) were dissolved in 7 ml anhydrous DMF. The solution was placed in a glass vial and sealed. The sample was sonicated for 10-15 minutes to fully dissolve the reagents and heated at 120°C for 3 days. Colourless, block shaped crystals were collected and washed 2-3 times with fresh DMF.

2.5.4 Synthesis of $[Zn_2(bdc)_{2-x}(bdc\text{-}I)_x(dabco)]\cdot n$ DMF

For $[Zn_2(bdc)_{1.22}(bdc\text{-}I)_{0.78}(dabco)]$ $Zn(NO_3)_2\cdot 6H_2O$ (0.502 mmol, 0.149 g), H_2bdc (0.277 mmol, 0.046 g), H_2bdc-I (0.198 mmol, 0.056 g) and dabco (0.245 mmol, 0.028 g) were dissolved in 7 ml

anhydrous DMF. The solution was placed in a glass vial and sealed. The sample was sonicated for 10-15 minutes to fully dissolve the reagents and heated at 120°C for 3 days. Colourless, needle shaped crystals were collected and washed 2-3 times with fresh DMF.

2.5.5 Synthesis of $[Zn_2(bdc)_{2-x}(bdc\text{-}NO_2)_x(dabco)]\cdot n$DMF

For **3a** $Zn(NO_3)_2\cdot 6H_2O$ (0.502 mmol, 0.149 g), H_2bdc (0.253 mmol, 0.042 g), H_2bdc-NO_2 (0.252 mmol, 0.053 g) and dabco (0.245 mmol, 0.028 g) were dissolved in 7 ml anhydrous DMF. The solution was placed in a glass vial and sealed. The sample was sonicated for 10-15 minutes to fully dissolve the reagents and heated at 120°C for 3 days. Colourless, block shaped crystals were collected and washed 2-3 times with fresh DMF.

2.5.6 Synthesis of $[Zn_2(bdc)_{2-x}(bdc\text{-}NH_2)_x(dabco)]\cdot n$DMF

For **4a** $Zn(NO_3)_2\cdot 6H_2O$ (0.502 mmol, 0.149 g), H_2bdc (0.404 mmol, 0.067 g), H_2bdc-NH_2 (0.099 mmol, 0.018 g) and dabco (0.245 mmol, 0.028 g) were dissolved in 7 ml anhydrous DMF. The solution was placed in a glass vial and sealed. The sample was sonicated for 10-15 minutes to fully dissolve the reagents and heated at 120°C for 3 days. Orange, block shaped crystals were collected and washed 2-3 times with fresh DMF.

2.5.7 Synthesis of $[Zn_2(bdc\text{-}Br)_{2-x}(bdc\text{-}I)_x(dabco)]\cdot n$DMF

For **5a** $Zn(NO_3)_2\cdot 6H_2O$ (0.502 mmol, 0.149 g), H_2bdc-Br (0.249 mmol, 0.061 g), H_2bdc-I (0.250 mmol, 0.073 g) and dabco (0.245 mmol, 0.028 g) were dissolved in 7 ml anhydrous DMF. The solution was placed in a glass vial and sealed. The sample was sonicated for 10-15 minutes to fully dissolve the reagents and heated at 120°C for 3 days. Colourless, block shaped crystals were collected and washed 2-3 times with fresh DMF.

2.5.8 Synthesis of $[Zn_2(bdc\text{-}NO_2)_{2-x}(bdc\text{-}NH_2)_x(dabco)]\cdot n$DMF

For **6a** $Zn(NO_3)_2\cdot 6H_2O$ (0.502 mmol, 0.149 g), H_2bdc-NO_2 (0.252 mmol, 0.053 g), H_2bdc-NH_2 (0.248 mmol, 0.045 g) and dabco (0.245 mmol, 0.028 g) were dissolved in 7 ml anhydrous DMF. The solution was placed in a glass vial and sealed. The sample was sonicated for 10-15 minutes to fully dissolve the reagents and heated at 120°C for 3 days. Block shaped crystals with white, colourless and orange regions were collected and washed 2-3 times with fresh DMF.

2.5.9 Synthesis of $[Zn_2(bdc)_{2-x}(ndc)_x(dabco)]\cdot n$DMF

For **7a** $Zn(NO_3)_2\cdot 6H_2O$ (0.502 mmol, 0.149 g), H_2bdc (0.253 mmol, 0.042 g), H_2ndc (0.241 mmol, 0.052 g) and dabco (0.245 mmol, 0.028 g) were dissolved in 7 ml anhydrous DMF. The solution was placed in a glass vial and sealed. The sample was sonicated for 10-15 minutes to fully dissolve the reagents and heated at 120°C for 3 days. Block shaped crystals with white, colourless and orange regions were collected and washed 2-3 times with fresh DMF.

2.5.10 Computational methodology

Electronic structure calculations were carried out on the periodic crystals in the VASP (Vienna *ab-initio* Simulation Programme) code. The PBEsol functional was used to calculate the electronic density distribution within the systems. PBEsol is known to accurately reproduce the structural and electronic properties of solid-porous materials.[S4] Γ-point calculations were conducted on all structures due to large unit-cell lengths and sufficient sampling sizes. The quasi-Newtonian relaxation employed for structural optimization was converged to forces of 0.005 eV/Å or lower and kinetic energy cut-off of 500 eV was employed for the basis set. To model the interactions between core and shell of the atoms, projector-augmented wave (PAW) potentials were used.

To calculate the MEP (minimum energy path) for each structural transformation, SS-NEB (solid-state nudged elastic band) calculations were performed also using the VASP code. It is necessary to use the solid-state correction of the nudged elastic band model to include changes in unit-cell volume during a phase transition. The SS-NEB is a contribution to the VASP code by Henkelman *et al.* and requires single point calculations to be performed on each image generated by a linear interpolation between the two optimised initial and final structures (before and after the phase change). Forces are calculated by projecting the perpendicular component of the force acting upon each image allowing the MEP (minimum energy path) between the generated images to be calculated. The climbing image nudged elastic band (CI-NEB) profiles are reported to demonstrate the 'true' maxima of the highest energy image generated by the nudged elastic band method. The number of images are an important consideration to ensure the highest energy image structural configuration is representative of the 'true' saddle point. Considering computational expense and accuracy, 24 images were created for each calculation. The number of images chosen represents a high accuracy for plotting a MEP for such a structural transformation.

The program critic2 was used to study the chemical interactions within the non-covalent interactions (NCI) methodology. NCI index identifies interactions in a chemical system analysing the electron density (ρ) and its reduced gradient:

$$s = \frac{1}{2(3\pi^2)^{\frac{1}{3}}} \frac{|\nabla\rho|}{\rho^{\frac{4}{3}}}$$

NCIplot within VMD was then used to visualise charge density associated with non-covalent interactions such as dispersion between two non-bonded species.

2.6 References

1. H. Jiang, Y. Tatsu and Q. Xu, *J.Am. Chem. Soc.*, 2010, 132, 5586-5587
2. F. A. Paz, J. Klinowski, S. M. Vilela, J. P. Tome, J. A. Cavaleiro and J. Rocha, *Chem. Soc. Rev.*, 2012, 41, 1088-1110
3. U. Mueller, M. Schubert, F. Teich, H. Puetter, K. Schierle-Arndt and J. Pastré, *J. Mater. Chem.*, 2006, 16, 626-636
4. M. Mani-Biswas and T. Cagin, *Comp. Theor. Chem.*, 2012, 987, 42-56
5. L. J. Murray, M. Dinca and J. R. Long, *Chem. Soc. Rev.*, 2009, 38, 1294-1314
6. N. A. Khan, Z. Hasan and S. H. Jhung, *J. Hazard Mater.*, 2013, 244-245, 444-456
7. S. Kitagawa, R. Kitaura and S. Noro, *Angew. Chem. Int. Ed.*, 2004, 43, 2334-2375
8. M. Eddaoudi, J. Kim, N. Rosi, D. Vodak, J. Wachter, M. O'Keeffe and O. M. Yaghi, *Science*, 2002, 295, 469-472
9. H. Deng, S. Grunder, K. E. Cordova, C. Valente, H. Furukawa, M. Hmadeh, F. Gandara, A. C. Whalley, Z. Liu, S. Asahina, H. Kazumori, M. O'Keeffe, O. Terasaki, J. F. Stoddart and O. M. Yaghi, *Science*, 2012, 336, 1018-1023
10. P. Trens, T. K. Trung, N. Tanchoux, S. Bourrelly, S. Loera-Serna, P. L. Llewellyn, C. Serre, T. Loiseau, F. Fajula, and G. Ferey, *J. Am. Chem. Soc*, 2008, 130, 16926-16932
11. D. N. Dybtsev, H. Chun and K. Kim, *Angew. Chem. Int. Ed.*, 2004, 43, 5033-5036
12. P. Horcajada, F. Salles, S. Wuttke, T. Devic, D. Heurtaux, G. Maurin, A. Vimont, M. Daturi, O. David, E. Magnier, N. Stock, Y. Filinchuk, D. Popov, C. Riekel, G. Ferey and C. Serre, *J. Am. Chem. Soc.*, 2011, 133, 17839-17847
13. Z. Wang and S. M. Cohen, *J. Am. Chem. Soc*, 2009, 131, 16675-16677
14. K. Uemura, Y. Yamasaki, F. Onishi, H. Kita and M. Ebihara, *Inorg. Chem.*, 2010, 49, 10133-10143
15. S. Furukawa, K. Hirai, M. Kondo, M. Meilikhov, Y. Sakata, O. Sakata and S. Kitagawa, *Chem. Commun*, 2012, 48, 6472-6474
16. A. Kommreddy, M. S. Bowsher, M. R. Gunna, K. Botha and T. K. Vinod, *Tetrahedron Lett.*, 2008, 49, 4378-4382
17. A. D. Burrows, L. C. Fisher, C. Richardson and S. P. Rigby, *Chem.Commun.*, 2011, 47, 3380-3382
18. S. Henke, W. Li and A. K. Cheetham, *Chem. Sci.*, 2014, 5, 2392-2397
19. W. J. Gee, A. D Burrows and H. A. Hamzah, *Unpublished Work*.
20. H. Jasuja, N. C. Burtch, Y. G. Huang, Y. Cai and K. S. Walton, *Langmuir*, 2013, 29, 633-642
21. Deng S, *J .Phys. Chem. Lett*, 2010, 73-78
22. P. E. Blöchl, *Phys. Rev. B*, 1994, 50, 17953-17979
23. G. Henkelman and H. Jónsson, *J. Chem. Phys.*, 2000, 113, 9978-9985
24. G. Henkelman, B. P. Uberuaga and H. Jónsson, *J. Chem. Phys.*, 2000, 113, 9901-9904
25. K. Burke, J. P. Perdew, M. Ernzerhof, *Phys. Rev. Lett.*, 1996, 77, 3865-3868
26. K. J. Caspersen and E. A. Carter, *Proc. Natl. Acad. Sci.*, 2005, 102, 6738-6743
27. J. Contreras-Garcia, E. R. Johnson, S. Keinan, R. Chaudret, J. P. Piquemal, D. N. Beratan and W. Yang, *J. Chem. Theory. Comput.*, 2011, 7, 625-632
28. A. Dalke. W. Humphrey, and K. Schulten, *J. Mol. Graphics* 1996, 14, 33-38
29. A. Otero-de-la-Roza, M. A. Blanco, A. M. Pendás and V. Luaña, *Comput. Phys. Commun.*, 2009, 180, 157-166
30. A. Otero-de-la-Roza, E. R. Johnson and V. Luaña, *Comput. Phys. Commun.*, 2014, 185, 1007-1018
31. L. K. Cadman, J. K. Bristow, N. E. Stubbs, D. Tiana, M. F. Mahon, A. Walsh and A. D. Burrows, *Dalton Trans*, 2016, 45, 4316-4326

3 Porosity control through defect formation within metal-organic frameworks (MOFs)

3.1 Introduction

Whilst defects are likely to exist in the ordered structures of MOFs in a variety of ways, defect engineering is the intended inclusion of defects at either random or ordered sites within the structure. This approach provides the potential to tailor and control the pore environment of the framework.

3.1.1 Modification of MOFs through defect formation

There are two main types of defects which can exist within MOFs; point defects and extended defects, and these can be understood through an analogy with the more widely characterised defects in zeolite materials.[1] Zeolites are aluminosilicate materials based on the TO_4 tetrahedra (T = Al, Si).[2] Point defects can occur in zeolites through oxygen vacancies, leading to enhanced catalytic properties of the zeolite.[1] Similar point defects can be found in MOFs, through either metal site vacancies or ligand vacancies within the framework. Such defects can be unintentional, occurring naturally during the synthetic procedure, or can be intentional, having being induced to alter the structure and properties of the MOF.

Extended defects occur on a larger scale to point defects and are essentially imperfections within the crystal itself. In zeolites, extended defects can occur through the formation of different phases within a crystal, each of which contains a different polymorph of the zeolite material.[1] As some MOFs are known to exist in multiple polymorphs, it is possible for them to display similar extended defects as those described for zeolite materials.

Defect engineering has been shown to alter and often enhance the properties of MOFs through the formation of open metal sites, increased porosity and improved gas adsorption of the defect material. There are multiple methods to engineer defects within MOFs and the success of each is often dependent on the selected framework. One method of defect engineering is to use an acid modulator in the framework synthesis. Modulators can be used to terminate crystal growth, but if chosen correctly they can also be incorporated into the framework itself, creating missing linker sites.[3] This has been exemplified in the UiO-66 system, $[Zr_6O_4(OH)_4(bdc)_6]$ (see Section 1.1 for detail of the MOF structure) where the presence of trifluoroacetic acid (TFA) in the reaction mixture results in partial substitution of bdc ligands with trifluoroacetates (Figure 3.1).[4] The charge balance in the modified structure is achieved through replacing some of the OH^- anions with O^{2-} anions, altering the composition of the framework according to the amount of trifluoroacetate incorporated into the structure.

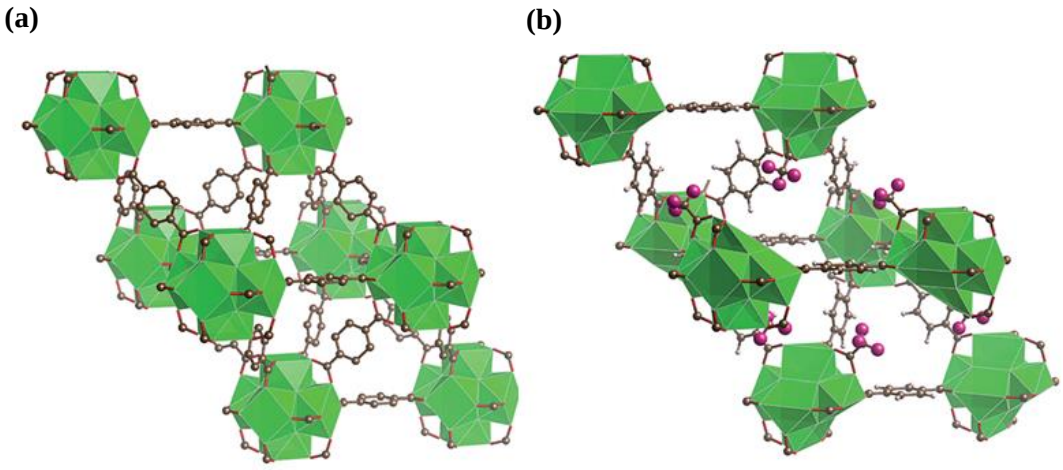

Figure 3.1 (a) Structure of UiO-66 **(b)** Structure of modified UiO-66 with TFA molecules capping the zirconium SBUs.[5]

The TFA ions can be removed by heating the MOF to 320 ^{o}C thereby creating unco-ordinated metal sites within the structure. These unco-ordinated sites, referred to as open metal sites, can affect the properties of the MOF, including increasing the reactivity of the framework in catalytic reactions. This is demonstrated in the defective UiO-66 material through its use as a catalyst in the cyclisation of citronellal (Figure 3.2). The unmodified UiO-66 has a conversion rate of 34 % over a 10 hour period for the cyclisation of citronellal. Modified UiO-66, prepared through the inclusion of 20 equivalents of TFA with respect to H_2bdc in the MOF synthesis, results in a 75 % conversion rate for the cyclisation of citronellal over a comparative period.[4]

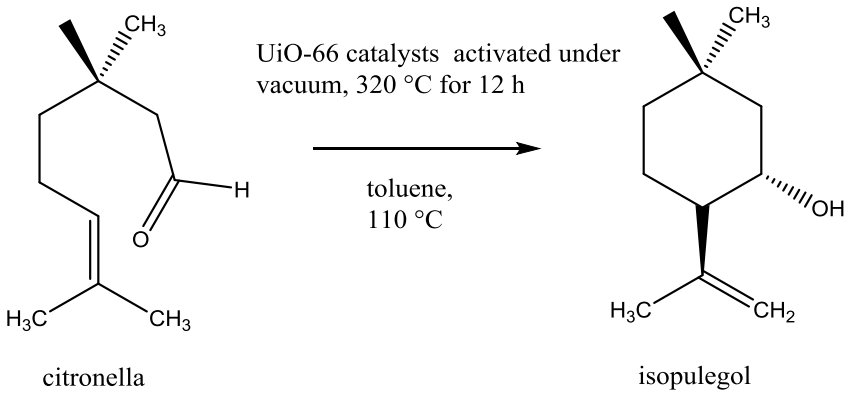

Figure 3.2 Catalytic cyclisation of citronellal by UiO-66.[4]

Treatment of MOFs with acid can also be carried out post synthetically to good effect. This approach targets the metal-carboxylate bonds within the structure, cleaving the bonds to leave unco-ordinated metal sites in the framework. $[Fe_3O(H_2O)_2F(btc)_2]\cdot nH_2O$, MIL-100(Fe) (btc = 1,3,5-benzenetricarboxylate), was treated postsynthetically with dilute solutions of TFA or perchloric acid ($HClO_4$).[6] Once treated, the products were analysed by powder X-ray diffraction

and showed no structural degradation suggesting frameworks of similar topology remained. The presence of open metal sites within the resulting structures was investigated by a comparison of CO inclusion into the pores of the unmodified and acid-modified frameworks, which was analysed by FTIR. By monitoring CO adsorption bands associated with chemisorbed CO onto metal sites, the authors revealed an increase in the number of free metal sites in the acid-modified structures. This was determined through a twofold increase in the intensity of CO-bands in the FTIR for acid-treated samples in comparison to untreated samples.

A second method of defect engineering involves ligand substitution, whereby a mixed-ligand MOF is formed through the inclusion of ligands with missing or modified co-ordination sites into the framework either during synthesis or postsynthetically. $[Cu_3(btc)_2(H_2O)_2]$, HKUST-1 has been employed in multiple defective linker studies. The structure is formed from Cu^{2+} ions arranged in a paddlewheel formation giving $Cu_2(CO_2)_4$ SBUs. The SBUs are linked by the btc linkers to give a 3-dimensional net with porous channels (see Section 1.1). Co-ordinating water molecules within the structure can be readily removed to give open metal sites. However, the microporous nature of the framework means that the adsorption abilities of HKUST-1 are limited to relatively small guest molecules, restricting its catalytic potential.[7]

Replacement of a proportion of the H_3btc tricarboxylic acid in the reaction mixture with a reduced symmetry substrate, H_2ip (isophthalic acid, Figure 3.3), results in a mixed-ligand species.[7] The mixed-ligand MOF is isostructural to HKUST-1 but contains a modified pore structure, with heterogeneous pores of both microporous and mesoporous nature.

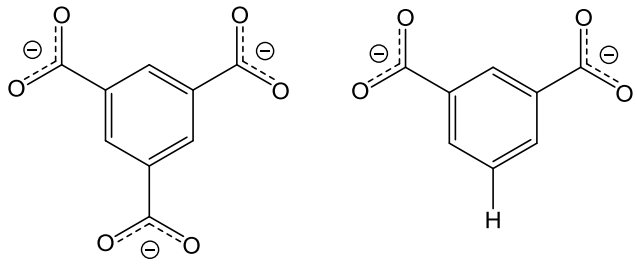

Figure 3.3 Structures of the 1,3,5-benzenetricarboxylate (btc) and isophthalate (ip) ligands used to form the defect containing MOF.

The modified pore structure of the defect material is effectively demonstrated through an increased catalytic activity in comparison to the unmodified HKUST-1. Samples of HKUST-1 and the defect material containing a btc:ip ratio of 75:25, were used as the catalytically active species for the ring-opening reaction of styrene oxide with methanol (Figure 3.4).

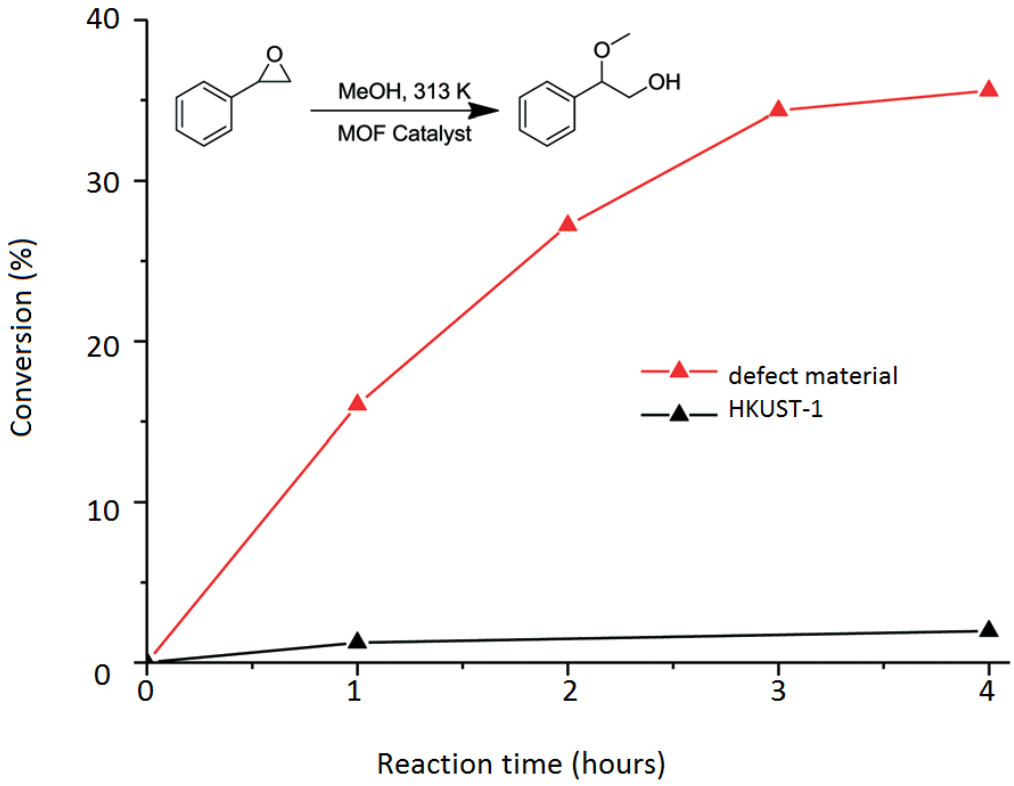

Figure 3.4 Ring opening reaction of styrene oxide to 2-methoxy-2-phenylethanol catalysed by HKUST-1 and the defect material containing a btc:ip ratio of 75:25.[7]

Both MOFs were activated by solvent exchange methods (see Section 1.3), replacing DMF by methanol and heating to 120 ^{o}C under vacuum for 24 hours in order to remove solvent molecules from the pores prior to the catalytic reaction. After 4 hours, HKUST-1 was found to have converted 1.97 % of the styrene oxide to 2-methoxy-2-phenylethanol, whilst after the same reaction time the ip-containing material had converted 35.6 %.[7] This is thought to be due to a combination of increased pore size, facilitating the movement of the reactants through the pores of the MOF, and increased numbers of open metal sites in the defect material compared to the unmodified material.

The high tolerance of HKUST-1 for modification was demonstrated by Fischer and co-workers who prepared a number of modified HKUST-1 type materials in which a reduced symmetry ligand was introduced into the structure.[8] The reduced symmetry ligands replaced one of the carboxylate groups of btc with a weaker co-ordinating group (Figure 3.5). The resulting MOFs were isostructural to HKUST-1 and reported to be of the form $[Cu_3(btc)_{2-x}(Ln)_x][X]_x$ where Ln = L_{1-4}. For L_n ligands with a reduced charge compared to btc^{3-} the inclusion of an anion into the framework as a guest in the pores was reported. The anion, X^-, was either NO_3^- or BF_4^- and originated from the copper salt used in the synthesis.

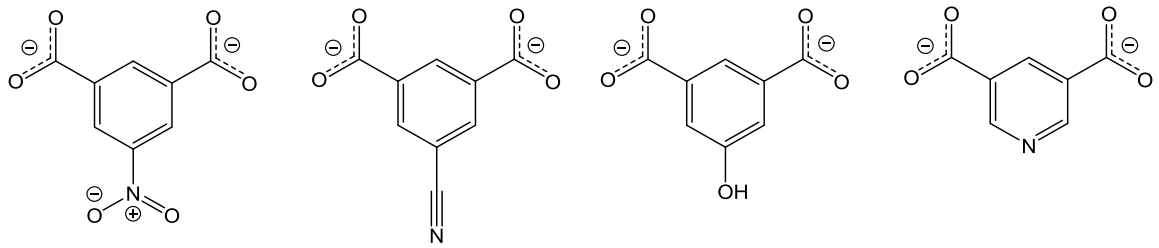

L$_1$ **L$_2$** **L$_3$** **L$_4$**

Figure 3.5 Structures of the reduced symmetry ligands L_{1-4} used to replace partial amounts of btc in HKUST-1.[8]

In a similar manner to the ip-containing material, the $[Cu_3(btc)_{2-x}(Ln)_x][X]_x$ products were found to contain mesoporous environments originating from defect sites within the materials.[8]

As well as modifying the pore environment, the defect ligand inclusion was found to alter the electronic properties of the MOF. The band gap for HKUST-1 was found to be 2.87 eV whilst in the modified frameworks $[Cu_3(btc)_{2-x}(Ln)_x][X]_x$ the band gap was found to range from 3.31 – 3.87 eV.[8] This demonstrates the potential for defect-engineered materials in tailoring both the structural and physical properties of MOFs.

3.1.2 Adsorption properties of defective MOFs

Many MOFs containing induced defects exhibit altered adsorption properties compared to their unmodified counterparts, due to the changed pore environments of the defective materials. This is commonly observed through the presence of hysteresis loops in adsorption isotherms of defective MOFs (see Section 1.3). Hysteresis is characterised by a divergence between the adsorption and desorption curves of the isotherm. When hysteresis is found to be reproducible and occurs in the multilayer region of the adsorption isotherm, it is associated with the occurrence of capillary condensation within the material. Capillary condensation is the formation of condensed liquid from the gas vapour during adsorption (see Section 1.3). It occurs due to the presence of strong van der Waals forces between vapour molecules in confined pores and can therefore be the result of network geometry effects such as pore blocking. Pore blocking effects occur in materials containing complex pore systems, such as defect materials containing multiple pores of varying size, and occur when large pores can only be accessed through narrow neck openings. Often called ink-bottle pores, the larger pores remain filled during desorption until the necks are emptied at a lower pressure, resulting in the observed hysteresis.[9]

Hysteresis loops can be catagorised into six classifications, giving information on the pore structure of the corresponding material (Figure 3.6).[9]

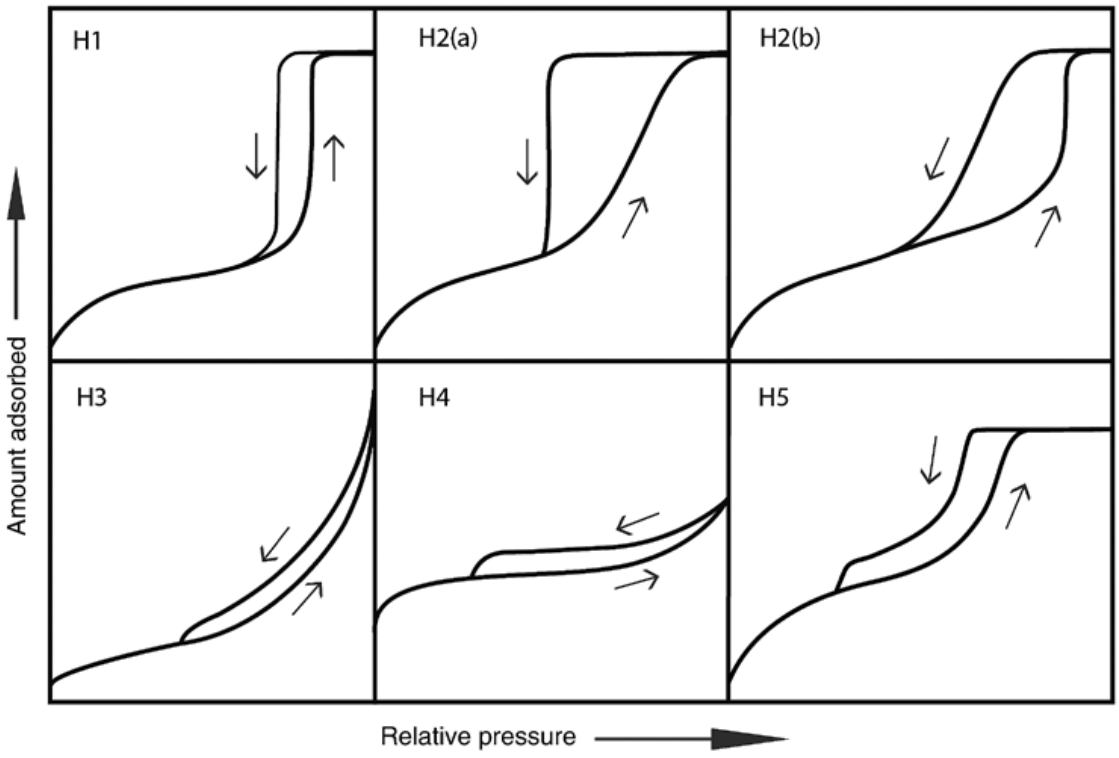

Figure 3.6 Types of hysteresis loops as classified by IUPAC.[9]

Type H1 and H2a/b hysteresis loops have a distinct plateau at high relative pressure (p/p^0). Type H1 loops are typified by a steep, narrow hysteresis loop and are displayed by materials which have mesopores of a narrow size distribution. Hysteresis loops of type H2a and H2b occur in materials containing either heterogeneous pores with ink-bottle shapes or complex pore networks. Structures with a narrow range of pore neck sizes display H2a hysteresis, whilst materials with a large pore neck size distribution display H2b hysteresis, which has a more gradual desorption curve than H1 or H2a.

Type H3 and H4 hysteresis loops are typical of materials with slit shaped pores. They have narrow hysteresis loops extending to low pressure with closure occurring at around the saturation pressure, which for N_2 gas at 77 K is p/p^0 = 0.4-0.5. The adsorption curve in H3 hysteresis is typical of a type II isotherm (see Section 1.3). H4 hysteresis is similar to that of H3, but the adsorption resembles a combination of type I and II isotherms (see Section 1.3) and has a more pronounced uptake during adsorption compared to H3 isotherms. Type H5 hysteresis is uncommon, and is displayed by materials which contain both open and partially blocked mesopores.

The effect of defect formation on adsorption properties can be seen in the example of HKUST-1 and the defect material containing btc and ip ligands (see Section 3.1.1).[7] Unmodified HKUST-1 displays a type I isotherm with no hysteresis and a BET surface area of 1690 m^2g^{-1}. The adsorption isotherm of the defect material was reported to display a composite of type I/IV isotherm behaviour with H2 hysteresis (Figure 3.7). The H2 hysteresis signifies the presence of ink bottle pores suggesting the formation of large mesopores linked by smaller openings. Interlinked mesopores generated from ligand vacancies in the defect framework and the intrinsic micropores of the material would explain this H2 hysteresis behaviour.

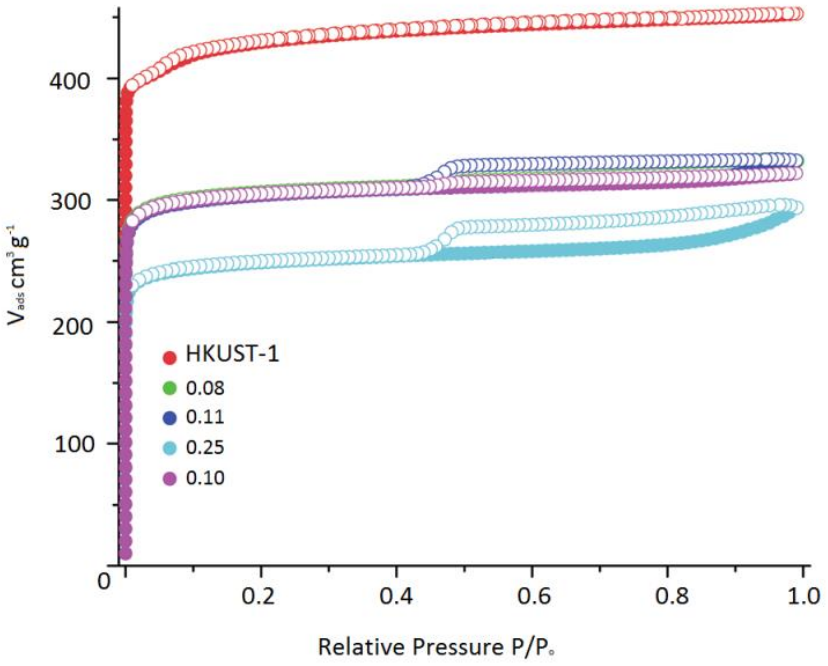

Figure 3.7 Nitrogen adsorption isotherms of HKUST-1 and defect modified materials, showing the incorporated molar ratio of ip compared to btc in the product.[7]

3.2 Aims and objectives

Due to the success of defect engineering in MOFs such as HKUST-1 using reduced symmetry ligands, an investigation into the formation of mixed-ligand MOFs combining tricarboxylate and dicarboxylate ligands was undertaken. Structures containing the tricarboxylate ligand bptc (4,3',5'-biphenyltricarboxylate) were modified through the inclusion of a second, reduced co-ordination mode ligand bpdc (4,3'-biphenyldicarboxylate) (Figure 3.8).

Two bptc containing systems were studied, $[Cd_3(bptc)_2(H_2O)_9]\cdot 5H_2O$ and $[Zn_4O(bptc)(H_2O)_2(DMF)]$. Both systems were chosen due to their straightforward synthesis and T-shaped co-ordination mode of the tricarboxylate ligand. The bptc ligand is known to have multiple possible co-ordination modes referred to as T, L and V-shaped (Figure 3.8).[10] Structures containing T-shaped co-ordination were chosen to optimise the effect of including a dicarboxylate defect ligand.

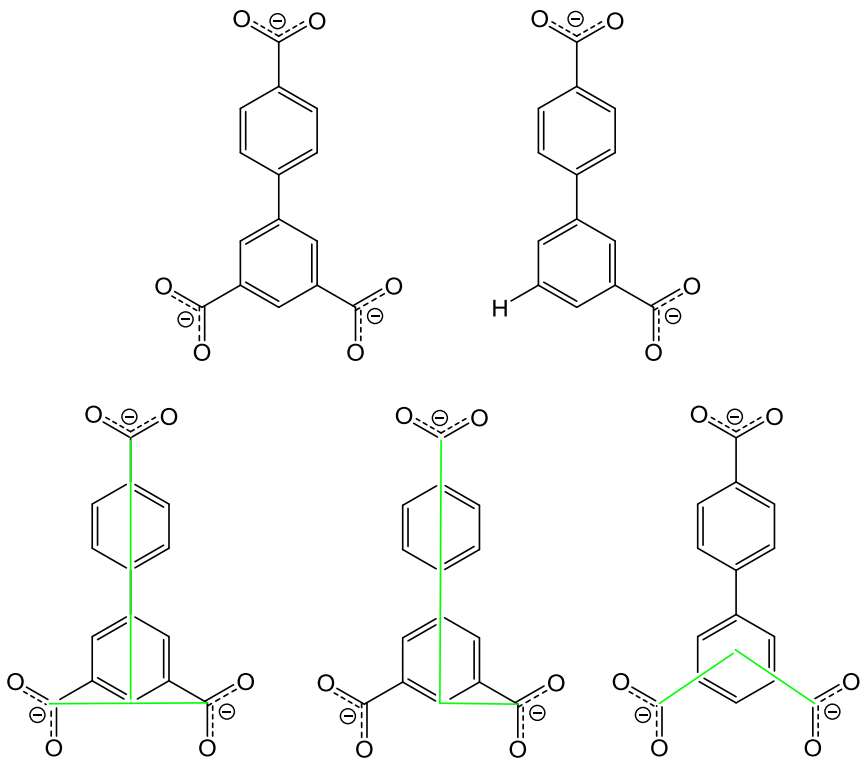

Figure 3.8 Structures of the 4,3',5'-biphenyltricarboxylate (bptc) and 4,3'-biphenyldicarboxylate (bpdc) ligands (top) and the T, L and V co-ordination modes of the bptc ligand (bottom).[10]

For each system investigated, series of mixed-ligand MOFs were synthesised by varying the ratio of H_3bptc:H_2bpdc in the reaction mixture. The composition of resulting products were analysed through ^{1}H NMR spectroscopy. In order to determine the effect of defect formation on the structure and topology of the products, powder X-ray diffraction and single crystal X-ray diffraction analysis were carried out. Where possible, defect products were subjected to gas adsorption studies to investigate the pore size of the resulting products.

3.3 Defect formation in $[Cd_3(bptc)_{1-x}(bpdc)_x(H_2O)_9][NO_3]_x \cdot nH_2O$

The structure of $[Cd_3(bptc)_2(H_2O)_9]\cdot 5H_2O$ has been reported by Zheng and co-workers.[10] The MOF is synthesised by combining cadmium nitrate with H_3bptc in a DMF/H_2O mixture and heating to 80 ^oC for 2 days. The reaction produces colourless, plank shaped crystals in a 76 % yield.

Single crystal X-ray analysis for $[Cd_3(bptc)_2(H_2O)_9]\cdot 5H_2O$[10] showed that the product crystallises in the monoclinic space group C2. The bptc ligand displays two coordination modes, with one carboxylate being unidentate and the remaining two carboxylates bidentate (Figure 3.9). The T-shaped co-ordinating bptc ligands link together cadmium centres to form a three dimensional network. The network displays interpenetration and contains one-dimensional channels which are occupied by water molecules (Figure 3.9).

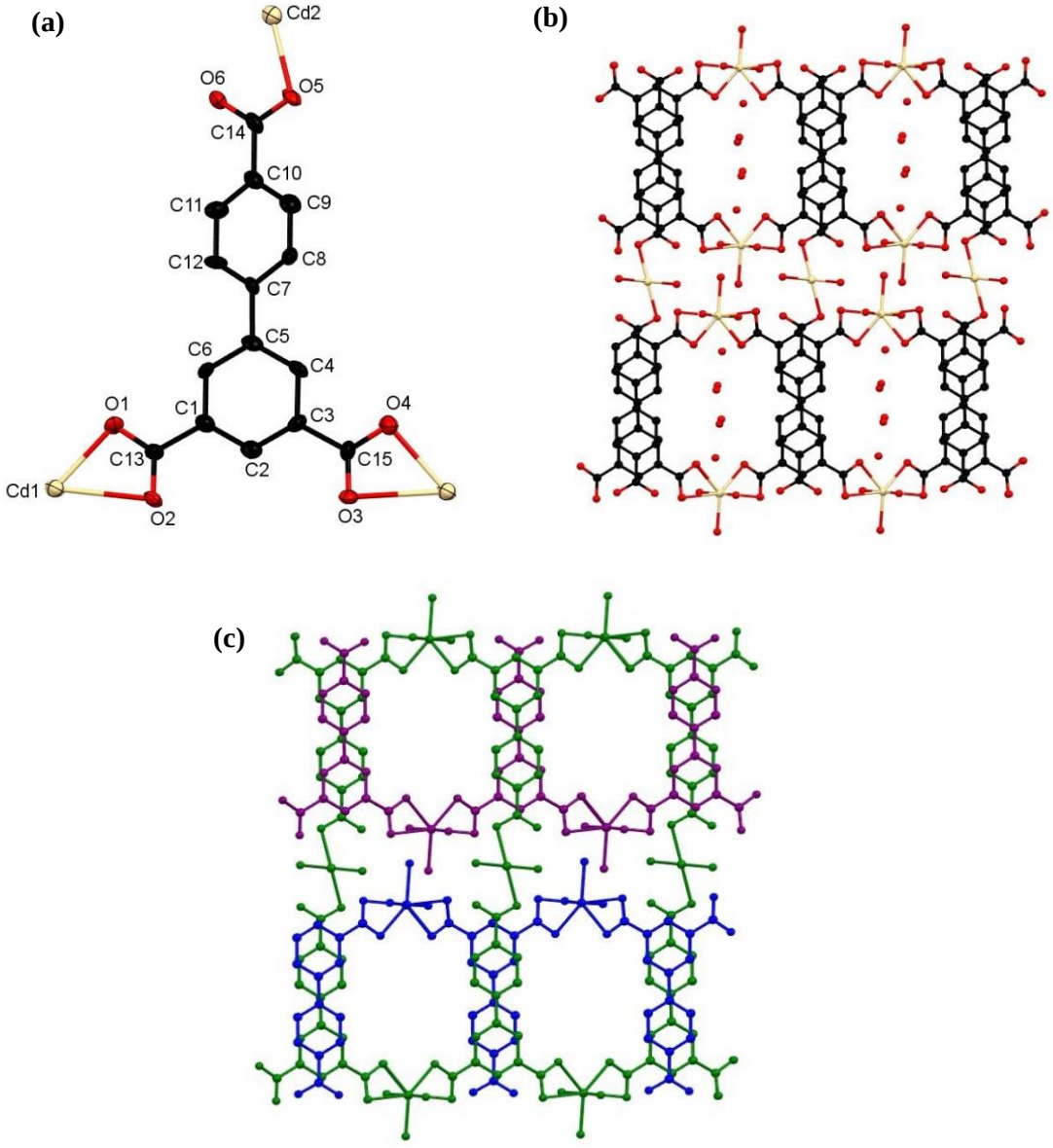

Figure 3.9 Structure of $[Cd_3(bptc)_2(H_2O)_9]\cdot 5H_2O$ showing **(a)** the co-ordination mode of the bptc ligand, with atoms belonging to the asymmetric unit labelled, **(b)** the framework structure viewed down the *b*-axis with 1D channels and **(c)** the interpenetrating framework with nets in purple, green and blue and with solvent water molecules removed. In all cases hydrogen atoms are removed for clarity.[10]

In order to investigate the effects of introducing defects into the structure of $[Cd_3(bptc)_2(H_2O)_9]\cdot 5H_2O$ a second ligand with reduced co-ordination capabilities (bpdc) was introduced into the framework. A series of mixed-ligand compounds were prepared by varying the H_3bptc:H_2bpdc ratios in the reaction mixture. Three ratios of H_3bptc:H_2bpdc were assessed, namely, 1:1, 3:7 and 2:8. A similar synthetic procedure to that for $[Cd_3(bptc)_2(H_2O)_9]\cdot 5H_2O$ was employed and the reactions were carried out in a 1:4 DMF:H_2O mixture at 80 ^oC for 2 days. All reactions produced colourless, plate-like crystals in low yields of 10-20 %.

In order to determine the composition of the products, ^1H NMR spectroscopy was carried out on acid-digested samples. Both bulk (multiple crystals) and individual crystal (one crystal selected using a microscope) samples were thus analysed. Either 2 or 3 individual crystals were each analysed per product allowing a comparison between crystals to be made. All samples were dried at 120 ^oC for 15 minutes prior to be being digested in a d_6-DMSO/DCl mixture.

The ^1H NMR spectra from bulk and individual crystal samples showed the presence of both D_3bptc and D_2bpdc confirming the formation of truly mixed-ligand species. The bulk ^1H NMR spectra are shown in Figure 3.10.

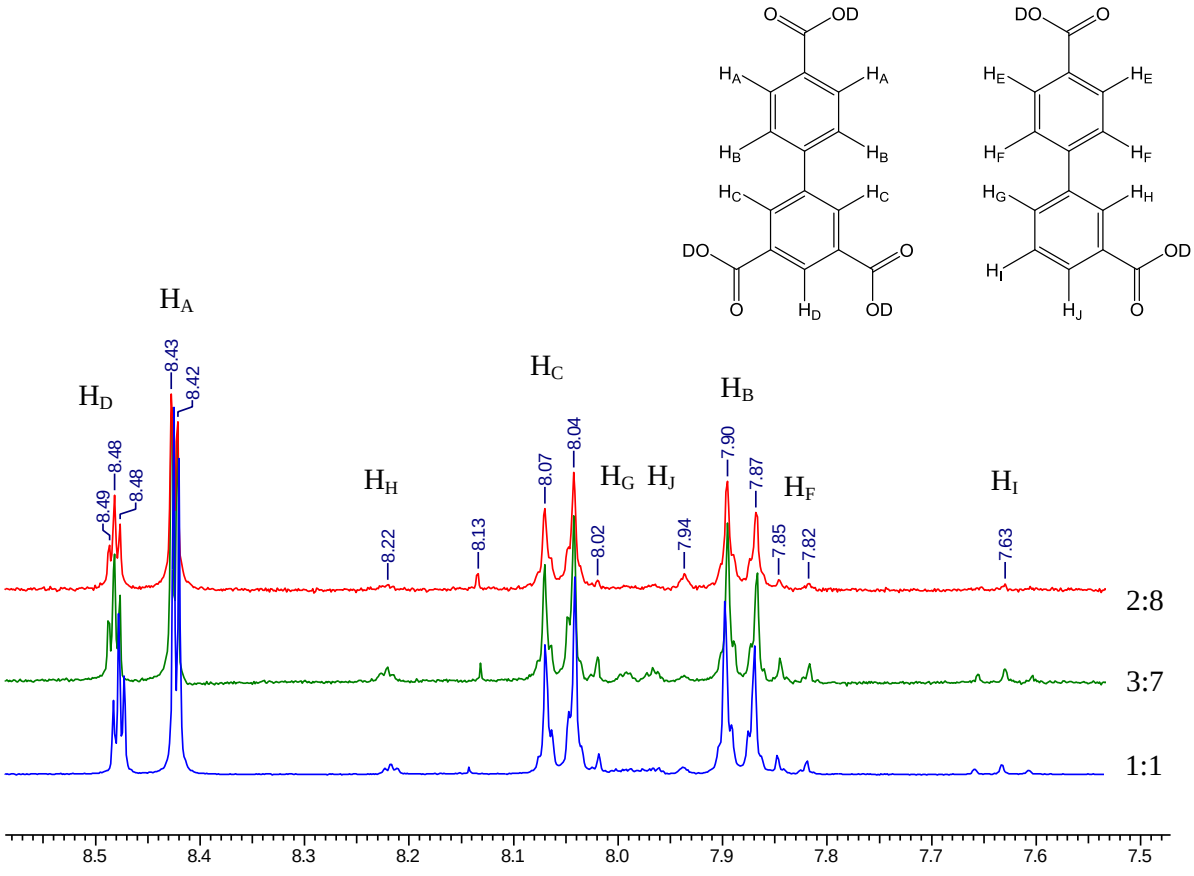

Figure 3.10 ^1H NMR spectra of acid digested products. The corresponding H_3bptc:H_2bpdc ratios used in the reaction mixtures are shown against each spectrum. Insert of the deuterated ligand structures and corresponding protons to the resonances in the spectra are shown. Protons H_E are hidden beneath resonances for protons H_C.

The resonances at δ 8.48 ppm, δ 8.43 ppm, δ 8.06 ppm and δ 7.89 ppm correspond to the aromatic protons of D_3bptc. The resonances at δ 8.22 ppm, δ 8.02 ppm, δ 8.00 ppm δ 7.84 ppm and δ 7.63 ppm correspond to the aromatic protons of D_2bpdc. The remaining protons of D_2bpdc have resonances at δ 8.05 ppm and are hidden under the δ 8.06 ppm resonances of D_3bptc. The peak at δ 7.94 ppm originates from the DMF solvent used.

Analysis of the integrals for each spectrum was undertaken to determine the product composition. The percentage of bpdc within the digestion mixtures of bulk and individual crystal samples are shown in Figure 3.11.

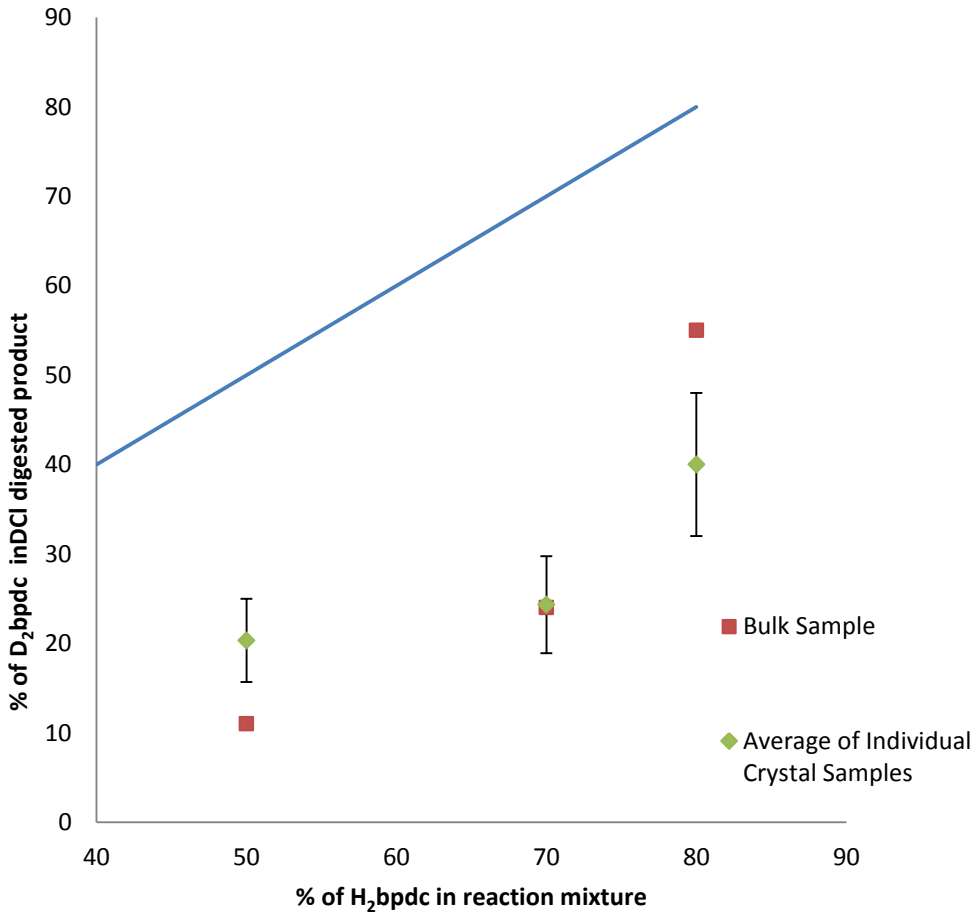

Figure 3.11 A plot of the percentage D_2bpdc content in the acid digested products against the percentage of H_2bpdc in the reaction mixture. The blue line shows the H_2bpdc content within the reaction mixtures.

The error bars on individual crystal samples have been calculated by determining the standard deviations between the two or three different crystals analysed for each sample. There is a clear ligand preference for bptc over bpdc across all samples, with all spectra showing 30-40 % more bptc ligand in the product than is present in the reaction mixture. Several effects can contribute to preferential ligand inclusion within MOFs including steric effects, relative pK_a values and solubility of the ligands. In this instance it is unlikely that steric effects or the pK_a of the acids play a decisive role in the relative uptake of the bptc and bpdc ligands into the product framework. Both ligands

have similar structures and therefore steric effects, and both have similar pK_a estimates of 3.3 ± 0.8 for H_3bptc and 4.0 ± 0.8 for H_2bpdc.[11] It is however, possible that crystallisation rates of the bptc and bpdc frameworks vary compared to one another. Such behaviour can be affected by the relative solubilities of the two products, causing the framework with lower solubility to start crystallising first. As the reaction continues uptake of the second ligand into the framework may occur, but at a reduced rate. Similar effects have been observed for other mixed-ligand frameworks.[12] Ligand solubility may also affect product composition. In some mixed-ligand frameworks, a lower solubility of one ligand is known to result in lower inclusion of that ligand into MOF products over more soluble competing ligands.[13]

The integrated resonances show a deviation between the bpdc content of the bulk and the individual crystal samples, as well as significant variation between different crystals from the same product, as seen from the error bars. This indicates that the samples are not homogenous in their composition, and that there is a variation of 4-8 % in the bpdc content of crystals within each product.

The average bpdc content calculated from integral analysis of the individual crystal samples was used to estimate the compositions of the three mixed-ligand products which are given in Table 3.1. The solvent contribution was determined through thermogravimetric analysis and will be presented in Sections 3.3.1 and 3.3.2.

Table 3.1 Percentage of H_2bpdc in the reaction mixture and resulting products, as determined from ^{1}H NMR spectra of individual crystal samples. The product formula is given in each case.

% of H_2bpdc in reaction mixture	**Average % of bpdc in product**	**Product Formula**
50	20	$[Cd_3(bptc)_{1.6}(bpdc)_{0.4}(H_2O)_9][NO_3]_{0.4}\cdot 3.8H_2O$
70	25	$[Cd_3(bptc)_{1.5}(bpdc)_{0.5}(H_2O)_9][NO_3]_{0.5}\cdot 2.9H_2O$
80	40	$[Cd_3(bptc)_{1.2}(bpdc)_{0.8}(H_2O)_9][NO_3]_{0.8}\cdot 1.9H_2O$

The formula of the mixed-ligand products includes an anion (NO_3^-) to charge balance the reduction in charge from the ligand contribution, as some of the $bptc^{3-}$ trianions are replaced with $bpdc^{2-}$ dianions. The nitrate counter-ion originates from the cadmium source, $Cd(NO_3)_2\cdot 4H_2O$. In order to confirm this is credible, the reaction using a 1:1 ratio of H_3bptc:H_2bpdc was repeated using the alternative cadmium source, $Cd(BF_4)_2$. The reaction yielded colourless crystals which were washed with a 1:4 DMF:H_2O mixture 3 times over 3 days prior to being analysed by ^{1}H NMR spectroscopy. The washed sample was dried and digested using a d_6-DMSO/DCl mixture. Integral analysis of the resonances in the ^{1}H NMR spectrum found a D_2bptc:D_2bpdc ratio of 85:15. ^{19}F

NMR spectroscopy was carried out to determine the presence of the BF_4^- anion in the product. The fluorine resonance from the free BF_4^- anion in $Cd(BF_4)_2$ occurs at δ -148.3 ppm when digested using a similar methodology to that for the mixed-ligand compound.[14] The ^{19}F NMR spectrum of the product showed a resonance at δ -148.4 ppm, indicating the presence of BF_4^- anions in the digested product along with additional resonances at δ -139.94 ppm, δ -146.47 ppm and δ -157.11 ppm (Figure 3.12). These are unassigned but may be the result of interactions between the BF_4^- anions and digested components of the MOF in solution. This gives an overall product formula of $[Cd_3(bptc)_{1.7}(bpdc)_{0.3}(H_2O)_9][BF_4]_{0.3}$.

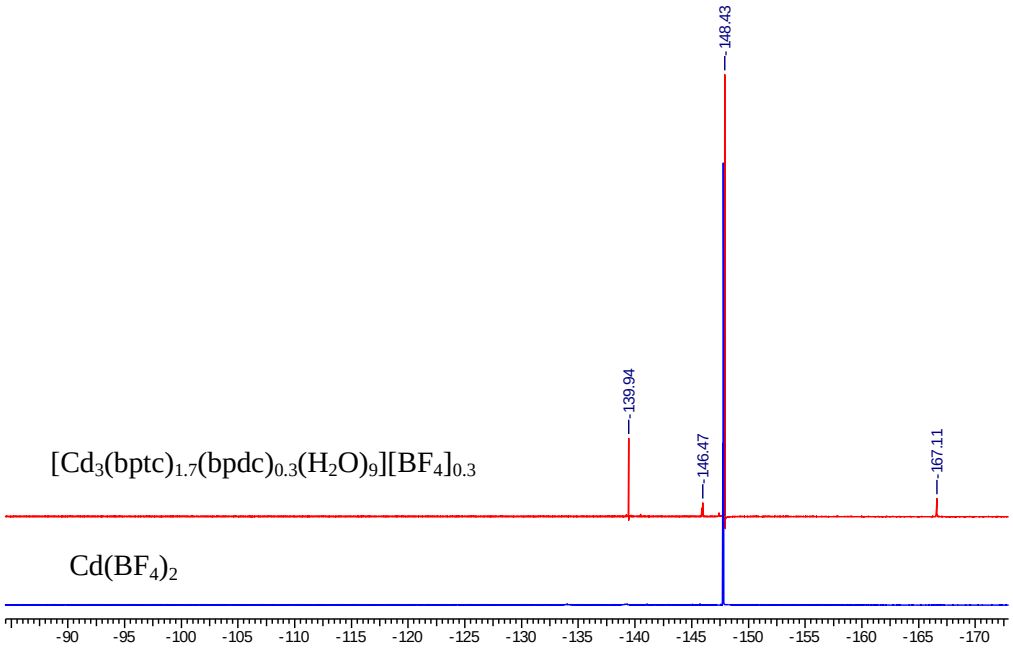

Figure 3.12 ^{19}F NMR spectra of $Cd(BF_4)_2$ and $[Cd_3(bptc)_{1.7}(bpdc)_{0.3}(H_2O)_9][BF_4]_{0.3}$.

The presence of BF_4^- in the product of $[Cd_3(bptc)_{1.7}(bpdc)_{0.3}(H_2O)_9][BF_4]_{0.3}$ supports the assertion that charge-balancing nitrate counterions are present within the mixed-ligand products $[Cd_3(bptc)_{2-x}(bpdc)_x(H_2O)_9][NO_3]_x \cdot nH_2O$ and that they originate from the cadmium source.

It is also possible that the charge balance for $[Cd_3(bptc)_{2-x}(bpdc)_x(H_2O)_9][NO_3]_x \cdot nH_2O$ products occurs via reduced cadmium ion content within the structure. This would cause metal ion vacancies in the structure leading to further defect sites. A combination of both NO_3^- counterions and reduced cadmium content is possible and will be discussed further in Section 3.3.1 and 3.3.2.

All mixed-ligand products were analysed by powder X-ray diffraction and compared to the powder diffraction trace generated from the reported single crystal structure of $[Cd_3(bptc)(H_2O)_9] \cdot 5H_2O$ (Figure 3.13).

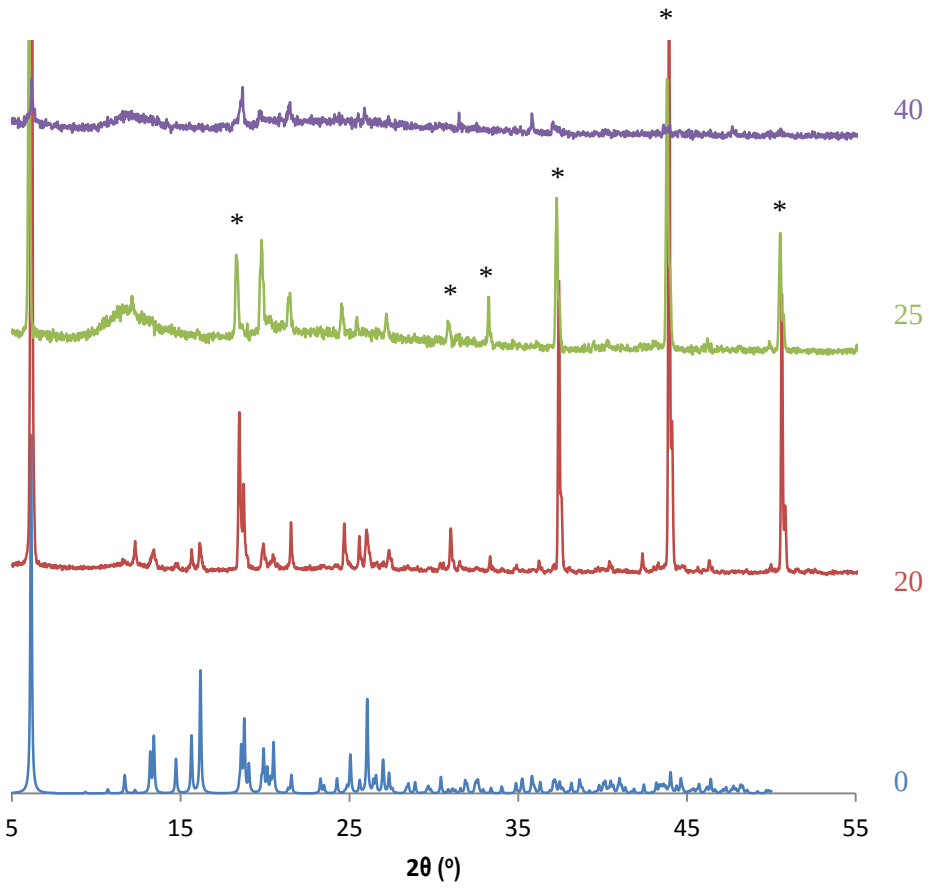

Figure 3.13 PXRD patterns of the compounds $[Cd_3(bptc)_{2-x}(bpdc)_x(H_2O)_9][NO_3]_x{\cdot}nH_2O$ with the corresponding % bpdc for each product given.

The powder diffraction pattern of $[Cd_3(bptc)_{1.6}(bpdc)_{0.4}(H_2O)_9][NO_3]_{0.4}{\cdot}3.8H_2O$ (containing 20 % bpdc) shows Bragg peaks of similar positions to those in the diffraction pattern of $[Cd_3(bptc)_2(H_2O)_9]{\cdot}5H_2O$ in the 2θ region of 5-30°. The relative intensities of these peaks vary between $[Cd_3(bptc)_2(H_2O)_9]{\cdot}5H_2O$ and the experimental pattern. This is possibly due to a difference in solvent content within the pores. For both $[Cd_3(bptc)_{1.5}(bpdc)_{0.5}(H_2O)_9][NO_3]_{0.5}{\cdot}2.9H_2O$ and $[Cd_3(bptc)_{1.2}(bpdc)_{0.8}(H_2O)_9][NO_3]_{0.8}{\cdot}1.9H_2O$ products (containing 25 and 40 % bpdc respectively) some peaks can be observed which correspond to those present in the diffraction pattern of $[Cd_3(bptc)_2(H_2O)_9]{\cdot}5H_2O$. This is most notable for peaks at 2θ values of 18.3° and 21.5°. A broad peak centred about 2θ 12° is present, which is typical of an amorphous material. There is also an increase in background noise in these products. These effects, coupled with a reduction in intensity of the peaks present, suggest that a reduction in crystallinity of the products occurs with increasing bpdc content.

Both $[Cd_3(bptc)_{1.6}(bpdc)_{0.4}(H_2O)_9][NO_3]_{0.4}{\cdot}3.8H_2O$ and $[Cd_3(bptc)_{1.5}(bpdc)_{0.5}(H_2O)_9][NO_3]_{0.5}{\cdot}2.9H_2O$ (20 and 25 % bpdc respectively) contain additional peaks not observed in the diffraction pattern of $[Cd_3(bptc)_2(H_2O)_9]{\cdot}5H_2O$. These peaks are highlighted by * in Figure 3.13. The high 2θ values and wide spacing of peaks is indicative of a crystalline compound with a small unit cell.

Attempts were made to match the unknown peaks to known compounds in the crystallographic databases, but no match could be found.

The PXRD pattern of $[Cd_3(bptc)_{1.7}(bpdc)_{0.3}(H_2O)_9][BF_4]_{0.3}$ was also collected and can be seen in Figure 3.14 alongside that of $[Cd_3(bptc)_{1.6}(bpdc)_{0.4}(H_2O)_9][NO_3]_{0.4}{\cdot}3.8H_2O$.

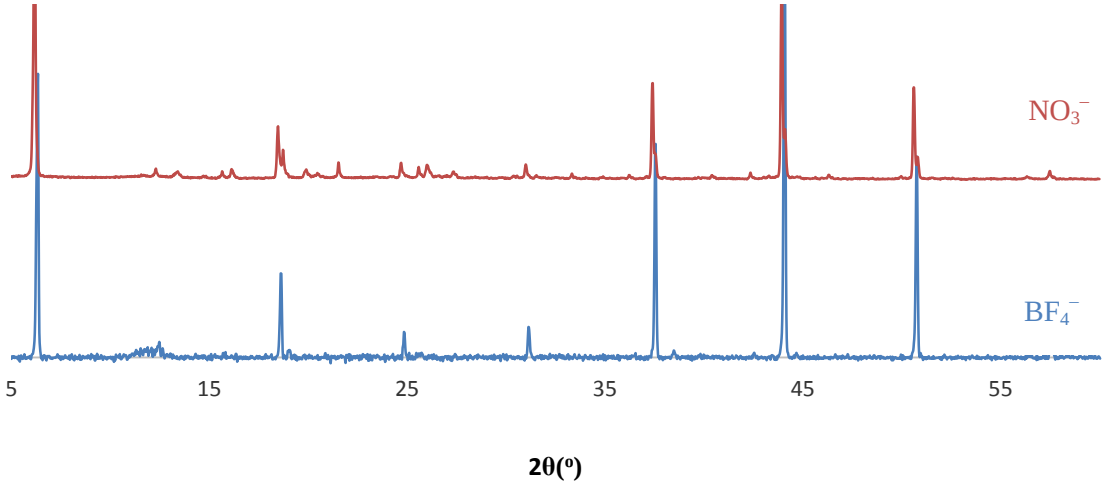

Figure 3.14 PXRD patterns of $[Cd_3(bptc)_{1.7}(bpdc)_{0.3}(H_2O)_9][BF_4]_{0.3}$ and $[Cd_3(bptc)_{1.6}(bpdc)_{0.4}(H_2O)_9][NO_3]_{0.4}{\cdot}3.8H_2O$.

The unidentified peaks in $[Cd_3(bptc)_{1.6}(bpdc)_{0.4}(H_2O)_9][NO_3]_{0.4}{\cdot}3.8H_2O$ are also found to be present in $[Cd_3(bptc)_{1.7}(bpdc)_{0.3}(H_2O)_9][BF_4]_{0.3}$**.**

3.3.1 Structure description of $[Cd_3(bptc)_{1.54}(bpdc)_{0.46}(H_2O)_9][NO_3]_{0.46}{\cdot}1.9H_2O$ **8a**

A single crystal selected from the batch containing 40 % bpdc (with an average formula of $[Cd_3(bptc)_{1.2}(bpdc)_{0.8}(H_2O)_9][NO_3]_{0.8}{\cdot}1.9H_2O$) was suitable for single crystal X-ray diffraction. Thermogravimetric analysis of the sample revealed a percentage mass loss of 19 % at 90–130 ^oC corresponding to a loss of 10.9 water molecules per unit formula (see appendix Figure A3.1.1). Nine of these water molecules co-ordinate to cadmium centres within the framework, and the remaining 1.9 water molecules are situated in the pores of the structure.

The crystal, **8a**, displayed merohedral twinning which was addressed in the data integration as a two-component twin with a ratio of 73:27. The structure crystallises in the monoclinic space group, *C*2 (Table 3.2).

Table 3.2 Crystal data for $[Cd_3(bptc)_{1.54}(bpdc)_{0.46}(H_2O)_9][NO_3]_{0.46}\cdot 1.9H_2O$ **8a**.

Identification code	**8a**
Empirical formula	$C_{29.54}H_{36.26}Cd_3O_{23.36}N_{0.46}$
Formula weight	1108.73
Temperature/K	150.00(10)
Crystal system	monoclinic
Space group	*C*2
a/Å	18.9994(8)
b/Å	7.2519(3)
c/Å	18.0681(7)
α/°	90
β/°	127.096(6)
γ/°	90
Volume/Å^3	1985.65(19)
Z	2
ρ_{calc}g/cm^3	1.854
μ/mm^{-1}	13.533
F(000)	1095.0
Crystal size/mm^3	0.22 × 0.0548 × 0.0382
Radiation	Cu*K*α (λ = 1.54184)
2θ range for data collection/°	9.354 to 144.06
Index ranges	$-23 \leq h \leq 23$, $-8 \leq k \leq 8$, $-22 \leq l \leq 22$
Reflections collected	6362
Independent reflections	6362 [R_{int} = 0.0982, R_{sigma} = 0.0360]
Data/restraints/parameters	6362/51/255
Goodness-of-fit on F^2	1.034
Final *R* indexes [$I>=2\sigma(I)$]	R_1 = 0.0599, wR_2 = 0.1578
Final *R* indexes [all data]	R_1 = 0.0625, wR_2 = 0.1595
Largest diff. peak/hole / e Å^{-3}	2.43/-1.38
Flack parameter	0.195(11)

The asymmetric unit comprises one and a half cadmium atoms, one ligand and four and a half co-ordinating water molecules (Figure 3.15). Cd1 is present with full occupancy whilst Cd2 is present with a site occupancy of 50 %.

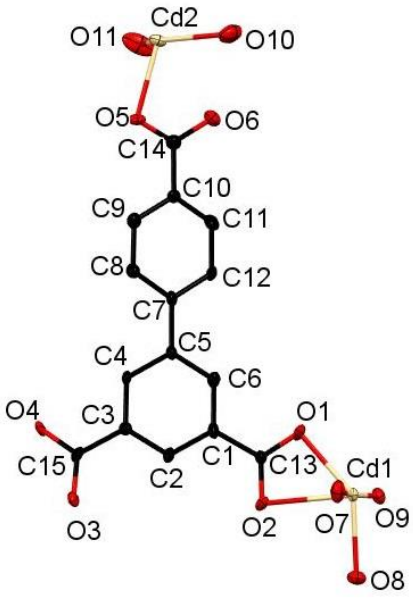

Figure 3.15 The asymmetric unit of **8a** with a calculated ellipsoid probability of 40 %.

The two cadmium atoms display different connectivities. Cd1 is seven-co-ordinate, with four co-ordinating oxygen atoms from bidentate carboxylate groups and three oxygen atoms from co-ordinating water molecules. Cd2 is sited on a two-fold rotation axis and is five coordinate, co-ordinating to two monodentate carboxylate groups and three co-ordinating water molecules. The asymmetric unit and connectivity of the structure is very similar to that of $[Cd_3(bptc)_2(H_2O)_9]\cdot 5H_2O$, with the T-shaped $Cd_{1.5}$bptc motifs linking together to form a three-dimensional interpenetrating net (Figure 3.16).

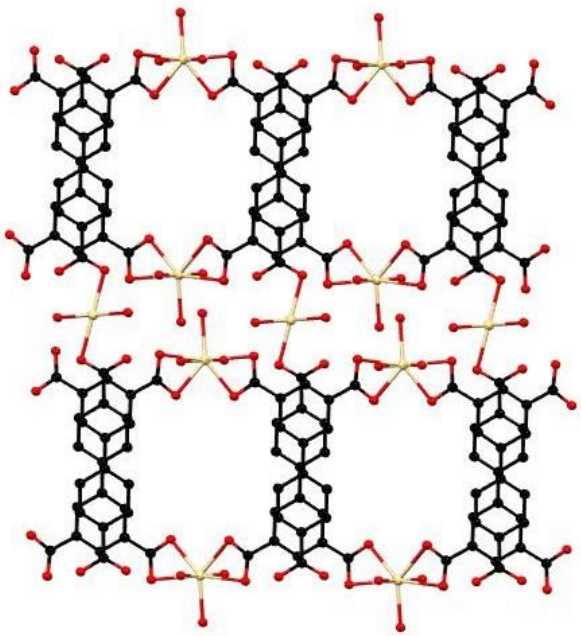

Figure 3.16 Part of the structure of **8a** viewed down the *b*-axis.

The structure of **8a** shows clear crystallographic evidence for the presence of both bptc and bpdc ligands. The O1-C13-O2 and O3-C15-O4 carboxylate groups were refined with site occupancies of 88.5 % based on electron density. This reduction in occupancy for the two carboxylate groups suggests that both bptc and bpdc ligands are present in the structure in a 77:23 ratio. The guest solvent and counter-ion could not be resolved in the crystal data and were treated with Platon SQUEEZE. Therefore the formula of **8a** was determined to be $[Cd_3(bptc)_{1.54}(bpdc)_{0.46}(H_2O)_9][NO_3]_{0.46}\cdot 1.9H_2O$, with solvent content taken from thermogravimetric analysis.

Although a crystal of **8a** was selected from the sample containing an average of 40 % bpdc as determined through ^{1}H NMR spectroscopy studies, it was found to contain only 23 % bpdc crystallographically. This suggests that the crystal selected for the single crystal study is not representative of the average batch composition. A possible explanation is that increased defects within the structure cause a reduction in crystal quality, leading lower bpdc content crystals to be selected for single crystal analysis. This would also support powder X-ray diffraction analysis of the mixed-ligand products, which highlight a reduction in crystallinity of products with increasing bpdc content.

The substitution of some tricarboxylate ligands in the framework for dicarboxylate ligands can either result in open metal sites within the structure, or partial occupancy of the cadmium centres. As there is no convincing crystallographic evidence for the reduced occupancy of cadmium centres in the structure of **8a** it is likely that the structure contains open metal sites.

Overall **8a** shows a similar topology to that of $[Cd_3(bptc)_2(H_2O)_9]\cdot 5H_2O$. Both structures crystallise in the space group *C*2 but show different unit cell parameters, most notably a lengthening of the *c*-axis and an increase of the *β*-angle in **8a** compared to that of $[Cd_3(bptc)_2(H_2O)_9]\cdot 5H_2O$ (Table 3.3).

Table 3.3 Crystal data for $[Cd_3(bptc)_{1.54}(bpdc)_{0.46}(H_2O)_9][NO_3]_{0.46}\cdot 1.9H_2O$, **8a** and $[Cd_3(bptc)_2(H_2O)_9]\cdot 5H_2O$.

Identification code	**8a**	$[Cd_3(bptc)_2(H_2O)_9]\cdot 5H_2O$
Empirical formula	$C_{29.54}H_{36.26}Cd_3O_{23.36}N_{0.46}$	$C_{30}H_{42}O_{26}Cd_3$
Formula weight	1108.73	1155. 84
Temperature/K	150	291
Crystal system	monoclinic	monoclinic
Space group	*C*2	*C*2
a/Å	18.9994(8)	18.984(3)
b/Å	7.2519(3)	7.3315(11)
c/Å	18.0681(7)	16.506(3)
α/°	90	90
β/°	127.096(6)	119.337(2)
γ/°	90	90
Volume/Å^3	1985.65(19)	2002.7(6)
Z	2	2

An overlay of the two structures demonstrates the level of similarity between their connectivities (Figure 3.17). The difference in unit cell parameters is therefore thought to originate from the gross packing and pore content.

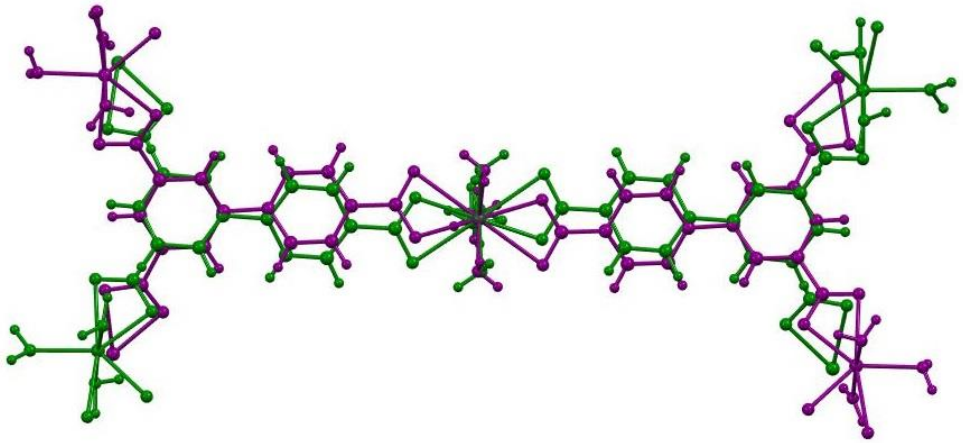

Figure 3.17 Overlay of $[Cd_3(bptc)_2(H_2O)_9]\cdot 5H_2O$ (purple) and $[Cd_3(bptc)_{1.54}(bpdc)_{0.46}(H_2O)_9][NO_3]_{0.46}\cdot 1.9H_2O$ **8a** (green) with the overlay centred around Cd2.

The powder diffraction trace generated from the single crystal data is shown alongside that of the experimental powder diffraction data in the appendix, Figure A3.2.1. A comparison of the two is made difficult by the poor crystallinity of the experimental powder diffraction pattern.

3.3.2 Structure description of $[Cd_3(bptc)_{1.8}(bpdc)_{0.2}(H_2O)_9][NO_3]_{0.2}\cdot 3.8H_2O$ **8b**

The mixed-ligand product containing 20 % bpdc (with an average formula of $[Cd_3(bptc)_{1.6}(bpdc)_{0.4}(H_2O)_9][NO_3]_{0.4}\cdot 3.8H_2O$) also gave crystals which were suitable for single crystal X-ray diffraction. Thermogravimetric analysis was completed on a sample of this product and revealed a percentage mass loss of 23 % at 80–130 ^oC corresponding to a loss of 12.8 water molecules per unit formula (see appendix Figure A3.1.2). Minus the nine water molecules which co-ordinate to cadmium centres within the framework, this indicates a presence of 3.8 water molecules as guest solvent in the pores of the structure. The sample shows no other mass loss until 400 ^oC after which a loss of 32 % occurs, corresponding to framework collapse. The final mass of the sample corresponds to 2.7 cadmium oxide moieties per unit formula.

A colourless crystal with dimensions of 0.215 mm × 0.063 mm × 0.047 mm, **8b**, was selected and analysed. It was found to display merohedral twinning. Data integration was effected to take account of the two components in a ratio of 91:09. The powder diffraction trace generated from the single crystal data shows a good agreement with the experimental powder diffraction pattern (see Appendix A3.2.2).

8b crystallises in the monoclinic space group *C*2 similarly to $[Cd_3(bptc)_2(H_2O)_9]\cdot 5H_2O$ (Table 3.4).

Table 3.4 Crystal data for $[Cd_3(bptc)_{1.8}(bpdc)_{0.2}(H_2O)_9][NO_3]_{0.2}\cdot 3.8H_2O$ **8b**

Identification code	**8b**
Empirical formula	$C_{29.8}H_{39.8}Cd_3O_{25}N_{0.2}$
Formula weight	1138.02
Temperature/K	150.15
Crystal system	monoclinic
Space group	*C*2
a/Å	18.9962(6)
b/Å	7.26700(10)
c/Å	18.0644(6)
α/°	90
β/°	127.107(5)
γ/°	90
Volume/Å^3	1988.76(14)
Z	2
ρ_{calc}g/cm^3	1.900
μ/mm^{-1}	13.560
F(000)	1128.0
Crystal size/mm^3	0.215 × 0.063 × 0.047
Radiation	Cu*K*α (λ = 1.54184)
2θ range for data collection/°	9.356 to 144.064
Index ranges	$-23 \le h \le 23$, $-8 \le k \le 8$, $-22 \le l \le 22$
Reflections collected	6960
Independent reflections	6960 [R_{int} = 0.0422, R_{sigma} = 0.0267]
Data/restraints/parameters	6960/13/252
Goodness-of-fit on F^2	1.136
Final *R* indexes [*I*>=2σ (*I*)]	R_1 = 0.0417, wR_2 = 0.1214
Final *R* indexes [all data]	R_1 = 0.0446, wR_2 = 0.1267
Largest diff. peak/hole / e Å^{-3}	1.25/-0.90
Flack parameter	-0.006(5)

The framework contribution to the asymmetric unit and connectivity of the structure in **8b** is similar to that in **8a** (Figure 3.18).

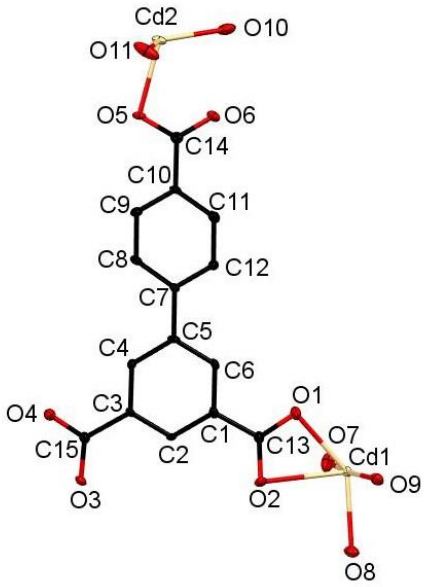

Figure 3.18 The asymmetric unit of $[Cd_3(bptc)_{1.8}(bpdc)_{0.2}(H_2O)_9][NO_3]_{0.2}\cdot 3.8H_2O$ **8b** with an ellipsoid probability of 40 %. Hydrogen atoms are removed for clarity.

The ligand in the asymmetric unit is modelled as a disordered bptc and bpdc ligand, with the O1-C13-O2 and O3-C15-O4 carboxylate groups displaying an occupancy of 95 %. This suggests that the bpdc ligand is disordered over the two available carboxylate positions, with a 5 % occupancy in each position giving a total bptc:bpdc ratio of 90:10. As in the case of **8a**, the crystal of **8b** displays lower bpdc content than the average of the batch it was selected from. The proposed rationale for this observation is similar to that for **8a**.

No crystallographic evidence for partial occupancy of the cadmium centres is observed in the structure of **8b**. Neither the guest solvent nor the nitrate counter-ion within the structure could be resolved and were treated with Platon SQUEEZE. The crystal structure is therefore found to have the composition $[Cd_3(bptc)_{1.8}(bpdc)_{0.2}(H_2O)_9][NO_3]_{0.2}\cdot 3.8H_2O$ **8b**.

In order to determine if any effects on the porosity of the structure resulted from the inclusion of the dicarboxylate bpdc ligand into the framework, gas adsorption measurements are required. Unfortunately due to the very low yields of the reactions, even after scaling up, material for reliable gas adsorption measurements could not be isolated.

3.4 Defect formation in $[Zn_4O(bptc)_{2-x}(bpdc)_x(H_2O)_2(DMF)][NO_3]_x$

$[Zn_4O(bptc)_2(H_2O)_2(DMF)]$ has been reported by Li and co-workers and is formed through the combination of $Zn(NO_3)_2{\cdot}6H_2O$ and H_3bptc in DMF.[15] The reaction is reported as occurring at 110 ^oC for 60 hours prior to being slowly cooled to room temperature, producing colourless block crystals in a yield of 36 %.

The framework structure reportedly contains four zinc atoms bridged by a co-ordinating oxygen to form Zn_4O aggregates which are linked together into a three dimensional framework by the bptc ligands (Figure 3.19). The bptc ligands coordinate through all six of their carboxylate oxygen atoms, each linking to six different zinc atoms.

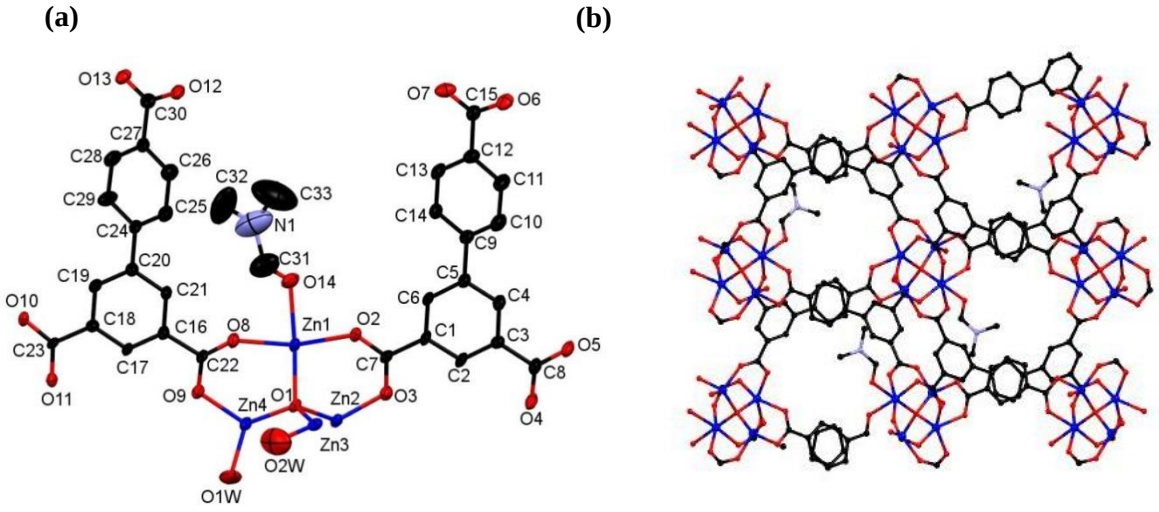

Figure 3.19 Part of the structure of $[Zn_4O(bptc)_2(H_2O)_2(DMF)]$ showing **(a)** the asymmetric unit with a calculated ellipsoid probability of 40 % and **(b)** the three-dimensional network viewed down the *b*-axis. Hydrogen atoms have been removed for clarity.[15]

The framework contains narrow channels running along the *b*-axis of the structure with dimensions of approximately 6.5 x 8 Å (measuring O···O distances across the pore). No gas adsorption data has been reported for this system detailing its porosity to date. The reported structure contains no guest solvent within the pores and has been shown to demonstrate high thermal stability, with the framework stable up to 350 ^oC.

Mixed-ligand systems containing the tricarboxylate bptc ligand and the reduced symmetry dicarboxylate ligand, bpdc, were prepared through the reaction of $Zn(NO_3)_2{\cdot}6H_2O$ with a mixture of H_3bptc and H_2bpdc. Three ratios of H_3bptc:H_2bpdc were employed, 4:1, 1:1 and 1:4. The reactions were carried out in DMF at 110 ^oC and cooled to room temperature at a rate of 0.02 ^oC/minute in a similar fashion to that of $[Zn_4O(bptc)_2(H_2O)_2(DMF)]$.[15] All products yielded colourless/white microcrystalline solids in yields of approximately 15 - 20 %.

The composition of the products was determined through ^{1}H NMR spectroscopy on acid digested samples of the dried MOFs, using a d_6-DMSO/DCl mixture. All spectra were found to contain both D_3bptc and D_2bpdc (Figure 3.20).

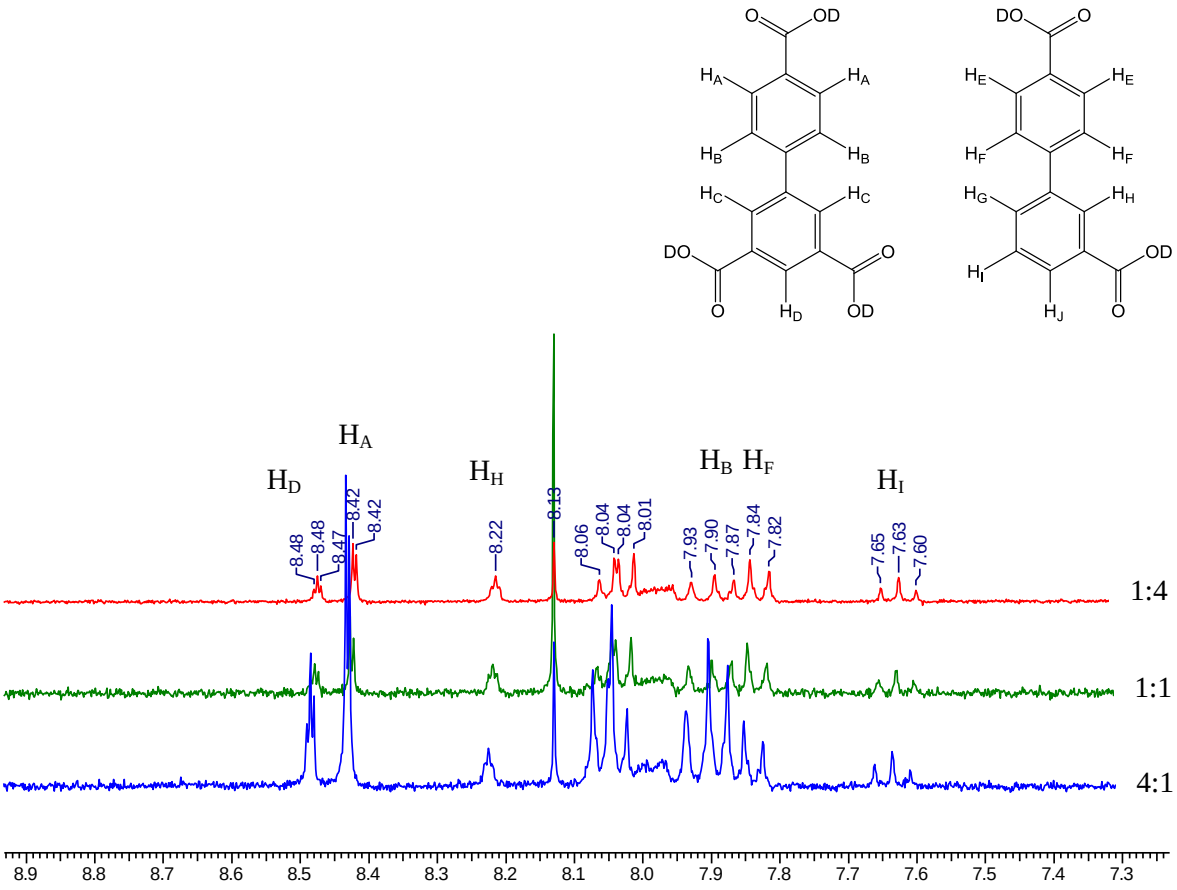

Figure 3.20 ^{1}H NMR spectra of acid digested products. The corresponding H_3bptc:H_2bpdc ratios used in the reaction mixtures are shown against each spectrum. Resonances at δ 7.9 – 8.06 ppm are overlapped protons H_C, H_E, H_G and H_J.

Resonances at δ 8.48 ppm, δ 8.42 ppm and δ 7.89 ppm correspond to the aromatic protons of D_3bptc. Resonances at δ 8.22 ppm, δ 7.83 and δ 7.63 ppm correspond to the aromatic protons of D_2bpdc. Resonances in the region δ 7.9 – 8.06 ppm are overlapped protons of D_3bptc and D_2bpdc (labelled H_C, H_E, H_G and H_J in Figure 3.20). The mixed-ligand products did not yield large enough crystals for ^{1}H NMR spectroscopy to be carried out on individual crystal samples. As the products appear homogenous through microscope observations the presence of both ligands in the ^{1}H NMR spectroscopy studies suggests the formation of mixed-ligand species.

The synthesis of each product was repeated twice and each batch was analysed by ^{1}H NMR spectroscopy. A study of the integrated resonances within each spectrum was conducted to determine the product compositions. The average percentage of D_2bpdc in each product is given in Figure 3.21. No obvious preferential inclusion of one ligand over the other was found in the product frameworks, suggesting that the composition of mixed-ligand products can be controlled through the reaction stoichiometry.

Error bars calculated from standard deviations in the bpdc content of products formed from the same H_3bptc:H_2bpdc ratios are also given in Figure 3.21. Compositional variation of 3-7 % bpdc content exists between repeat syntheses of reactions containing the same H_2bpdc concentration. The average value is used to define the composition of the three mixed-ligand products

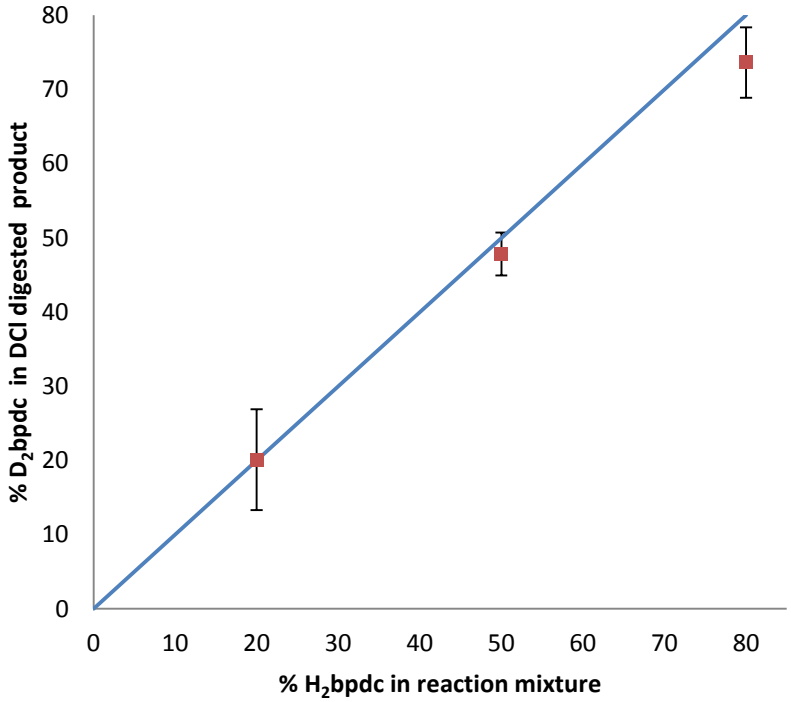

Figure 3.21 The average percentage inclusion of bpdc from ^{1}H NMR spectra between three batches of the mixed-ligand products. The standard deviation error bars are calculated from the three sets of data collected for each ligand ratio.

Due to the charge discrepancy between bptc^{3-} and bpdc^{2-} ligands, the inclusion of an anion is necessary to charge balance the product formula. As with the $[Cd_3(bptc)_{2-x}(bpdc)_x(H_2O)_9][NO_3]_x$ structures (see Section 3.3) the identity of the anion is possibly that of NO_3^-, originating from the zinc source. The product synthesis was attempted with $Zn(BF_4)_2$ as the zinc source to allow ^{19}F NMR spectroscopy to be used to confirm the presence of the BF_4^- anion in the products. However, the reaction did not yield products which could be analysed by powder X-ray diffraction or NMR spectroscopy techniques, and therefore the identity of the anion cannot be conclusively given. The product formulae given in Table 3.5 include the presence of the nitrate anion to achieve charge balance and should be read as a suggested composition. Any solvent present in the products are not included in these formulae.

Table 3.5 Percentage of H_2bpdc in the reaction mixture and resulting products, as determined from ^{1}H NMR spectra of individual crystal samples. The product formulae, minus any guest solvent, are given for each product.

% of H_2bpdc in reaction mixture	**Average % of bpdc in product**	**Product Formula**
20	20	$[Zn_4O(bptc)_{1.6}(bpdc)_{0.4}(H_2O)_2(DMF)][NO_3]_{0.4}$
50	48	$[Zn_4O(bptc)_{1.04}(bpdc)_{0.96}(H_2O)_2(DMF)][NO_3]_{0.96}$
80	68	$[Zn_4O(bptc)_{0.64}(bpdc)_{1.36}(H_2O)_2(DMF)][NO_3]_{1.36}$

The products were analysed by powder X-ray diffraction and compared to that of the powder XRD trace generated from the reported single crystal structure, $[Zn_4O(bptc)_2(H_2O)_2(DMF)]$ (Figure 3.22). Products containing 20 % and 48 % bpdc display PXRD patterns containing similar general features to that of the PXRD trace of $[Zn_4O(bptc)_2(H_2O)_2(DMF)]$. This suggests that these compounds contain similar framework topologies to that of the literature compound. Increasing amounts of amorphous product are observed with increasing bpdc content, as evidenced by increasing noise in the PXRD patterns and the presence of the broad peak at approximately 2θ 12°. The powder diffraction pattern of the product containing 68 % bpdc shows the structure to be amorphous.

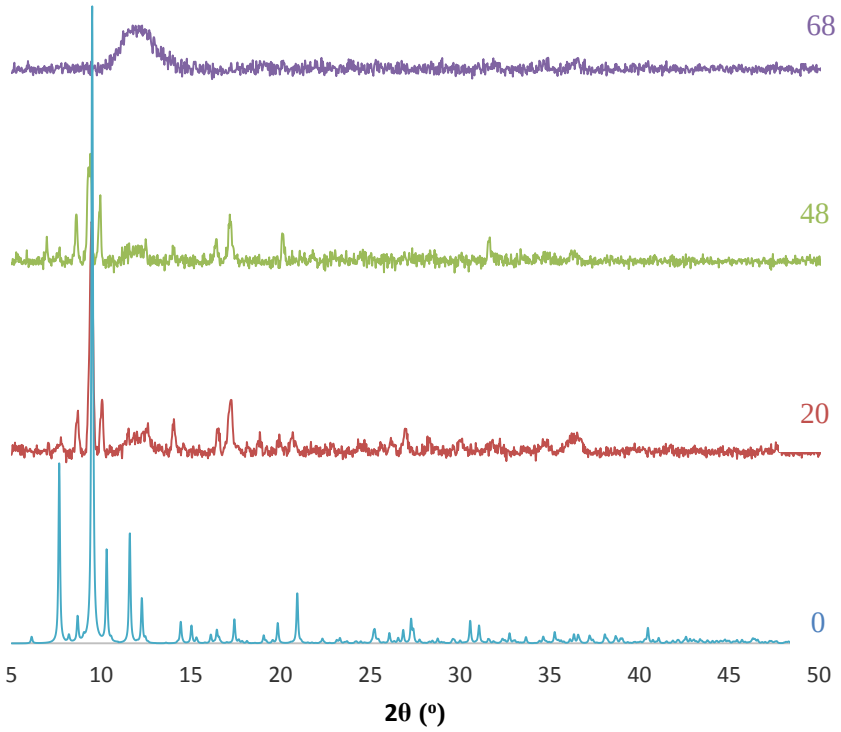

Figure 3.22 PXRD patterns of the compounds $[Zn_4O(bptc)_{2-x}(bpdc)_x(H_2O)_2(DMF)][NO_3]_x$ with the number shown against each powder pattern showing the % bpdc in the product.

Single crystal X-ray diffraction analysis was not possible for the mixed-ligand structures produced due to the small size of the crystals and the loss of crystallinity with increasing bpdc ligand content.

3.4.1 Gas adsorption studies of $[Zn_4O(bptc)_2(H_2O)_2(DMF)]$, and $[Zn_4O(bptc)_{2-x}(bpdc)_x(H_2O)_2(DMF)][NO_3]_x$ products

To determine the effect of the inclusion of the reduced symmetry ligand bpdc into the framework on the porosity of the mixed-ligand products, nitrogen gas sorption measurements were performed on $[Zn_4O(bptc)_2(H_2O)_2(DMF)]$, $[Zn_4O(bptc)_{1.04}(bpdc)_{0.96}(H_2O)_2(DMF)][NO_3]_{0.96}$ **9a** and $[Zn_4O(bptc)_{0.64}(bpdc)_{1.36}(H_2O)_2(DMF)][NO_3]_{1.36}$ **9b**. Samples were first activated to remove solvent molecules within the pores of the structures using an activation method which was chosen based upon data from the reported TGA of $[Zn_4O(bptc)_2(H_2O)_2(DMF)]$, which showed a structural stability of the framework up to temperatures of 350 ^oC. The activation method chosen involved a solvent exchange, washing the samples with $CHCl_3$ three times over three days, prior to heating at 120 ^oC for 1,000 minutes. The adsorption isotherms were recorded on activated samples at a pressure of 1 bar and at a temperature of 77 K.

Surface area calculations were completed using the Brunauer-Emmett Teller (BET) method. For the single ligand system, $[Zn_4O(bptc)_2(H_2O)_2(DMF)]$ the surface area was calculated to be 21.72 m^2g^{-1} from data points over a pressure region p/p_0 = 0.06 – 0.36. The nitrogen sorption isotherm displays similarities to a type II isotherm, with a gradual increase in adsorption and no limit at high p/p_0, indicating the compound is non-porous (Figure 3.23).

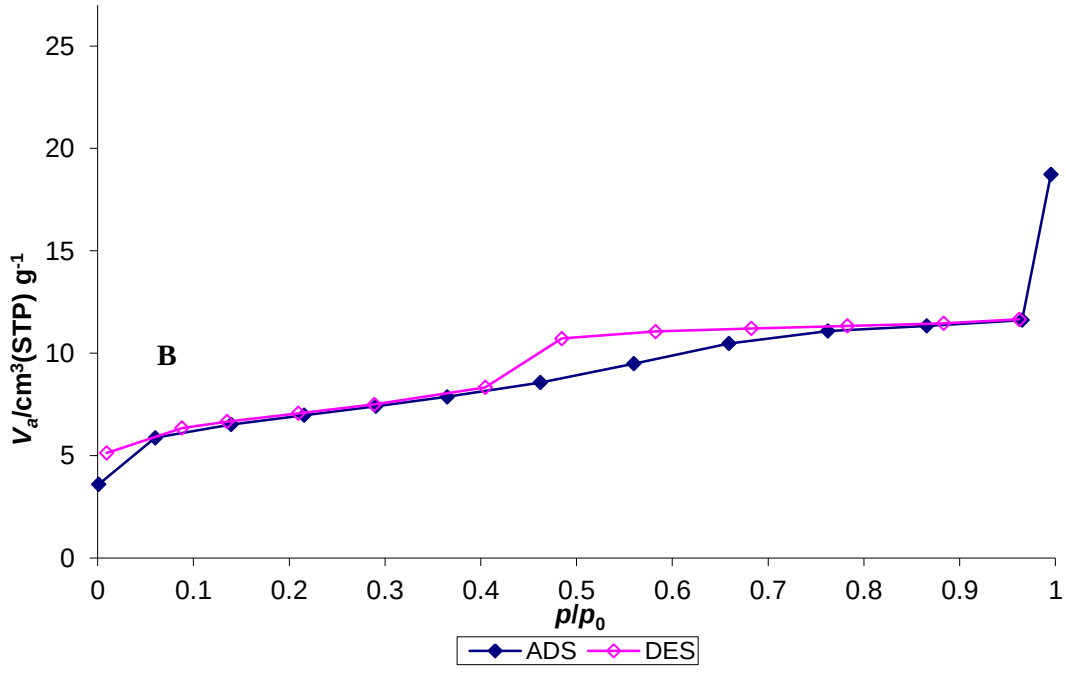

Figure 3.23 Gas sorption isotherm of $[Zn_4O(bptc)_2(H_2O)_2(DMF)]$. Adsorption and desorption branches can be identified through filled and non-filled symbols respectively.

The gradual increase in gas sorption is typical of monolayer gas formation on the surface of the material. Point **B** indicated in Figure 3.23, shows the point at which monolayer coverage is complete. After this, a gentle increase in adsorption of the gas indicates that further sorption occurs leading to multilayer formation, which continues until $p/p_0 = 1$ with a sharp increase between $p/p_0 = 0.9$-1. A small hysteresis is apparent in the desorption branch of the isotherm which can be characterised as a type H4 hysteresis loop (see Section 3.1.2). Type H4 hysteresis loops, as observed in this case, are typified by their lack of a limiting adsorption at high p/p_0. Such behaviour is caused by materials with slit-shaped pores or pores which are not completely filled with adsorbate.[17] This analysis fits with the low observed surface area and with the reported crystal structure which indicates the presence of small pores.

The nitrogen sorption of **9a** and **9b** were recorded using similar methods to that of $[Zn_4O(bptc)_2(H_2O)_2(DMF)]$ with a pressure of 1 bar and at a temperature of 77 K. For **9a** the surface area was calculated to be 255.6 $m^2\ g^{-1}$ from data points over a pressure region $p/p_0 = 0.08$–0.46 (Figure 3.24).

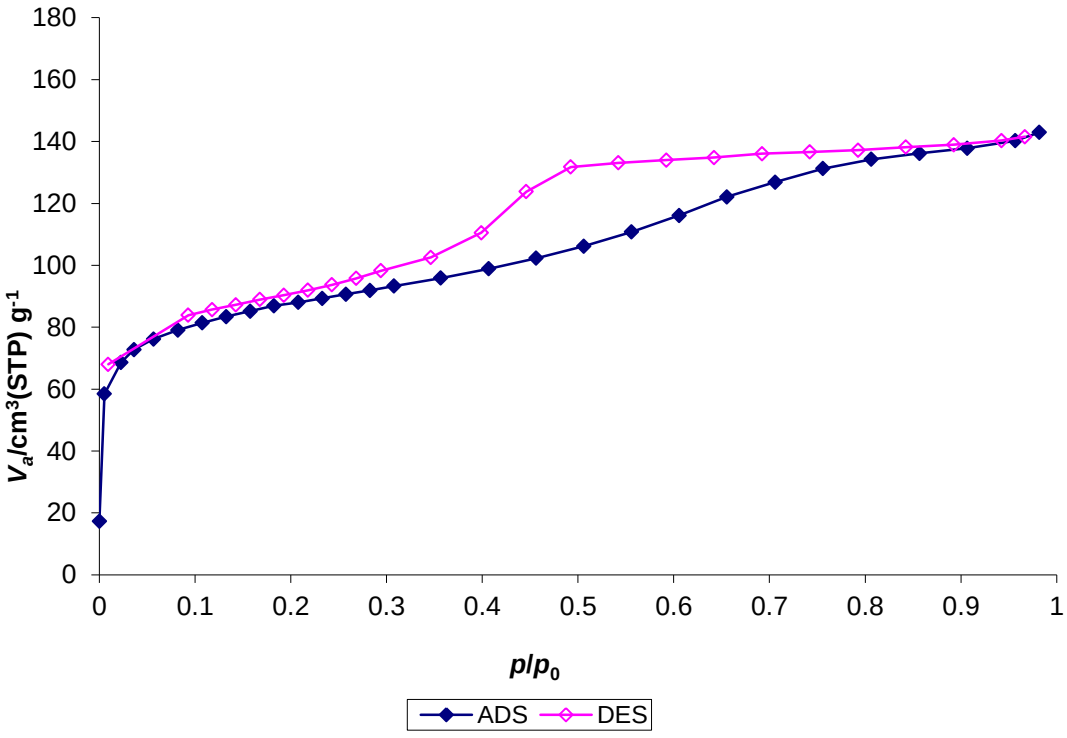

Figure 3.24 Gas sorption isotherm of $[Zn_4O(bptc)_{1.04}(bpdc)_{0.96}(H_2O)_2(DMF)][NO_3]_{0.96}$ **9a**. Adsorption and desorption branches can be identified through filled and non-filled symbols respectively.

The isotherm of **9a** shows an initial sharp increase in sorption is followed by a gradual increase, similarly to that of to that of $[Zn_4O(bptc)_2(H_2O)_2(DMF)]$, but has a lack of steep increase in adsorption as p/p_0 approaches 1, featuring instead a plateau. Overall, the isotherm can be described as a combination of type I and IV isotherms. The isotherm of **9a** also displays a pronounced

hysteresis loop which can be classified as type H2b hysteresis loop due to its plateau at high pressure and its gradual desorption branch (see Section 3.1.2). This hysteresis is indicative of interconnected pores of differing sizes present in the structures. These ink-bottle type pores can be explained through the formation of defect sites in the structure which result in larger, open cavities which are then interlinked by the smaller, intrinsic pores of the framework.

For **9b** the calculated surface area was 289 m^2 g^{-1} from data points over a pressure region p/p_0 = 0.11-0.45. The isotherm contains the same general features as described for **9a**, which can be described as a combination of type I and IV isotherms with hysteresis (Figure 3.25). The apparent porosity of **9b** suggests that although the material is amorphous, as shown through PXRD analysis, the material maintains a three dimensional, porous structure.

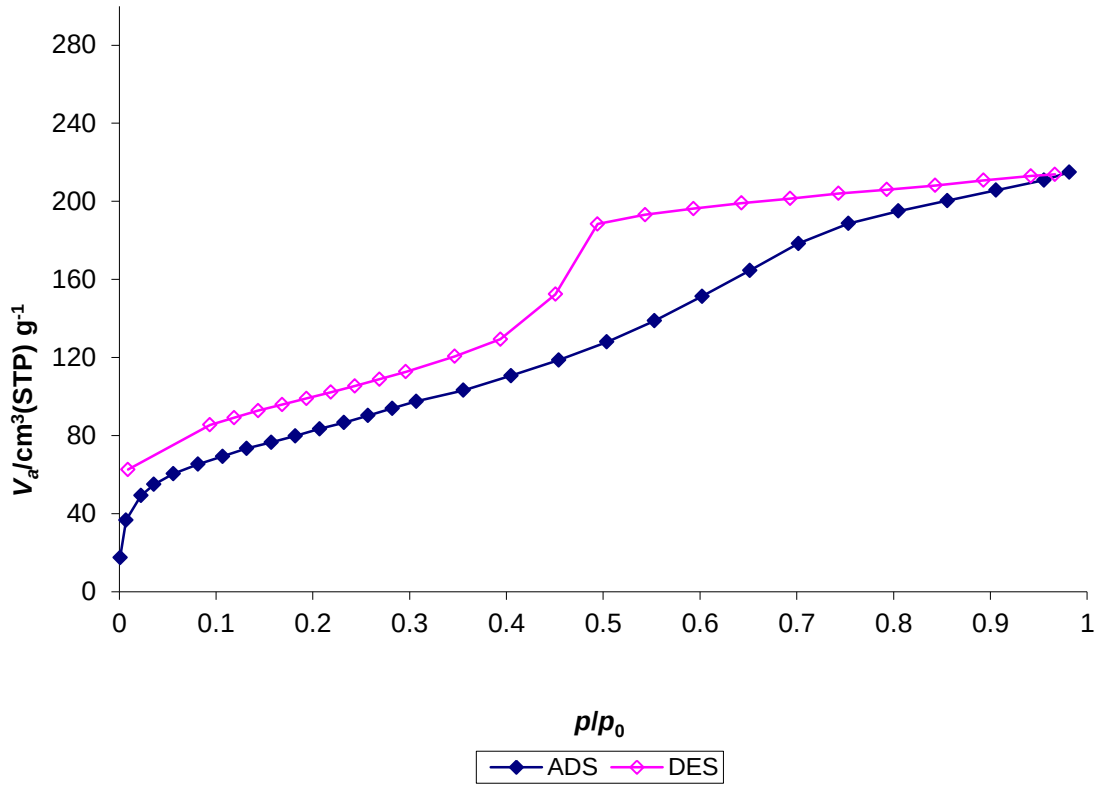

Figure 3.25 Gas sorption isotherm of $[Zn_4O(bptc)_{0.64}(bpdc)_{1.36}(H_2O)_2(DMF)][NO_3]_{1.36}$ **9b**.

The hysteresis loop in the isotherm of **9b** is similar to that of **9a** but continues throughout the desorption branch to very low pressures. Low pressure hysteresis can occur due to strong interactions between the adsorbed gas and the framework, allowing gas to be retained in the structure even during desorption at low pressure.[18] This is more commonly the case for adsorption studies with gases such as hydrogen, which can interact with metal sites in the framework.[19] Other cases of low pressure hysteresis have been shown to be, on occasion, an artefact of the adsorption process which can be removed through alteration of the equilibrium time during the gas adsorption

measurement.[20] These cases are observed when equilibrium times are low, but upon increasing the equilibrium time the low pressure hysteresis is removed.

In the case of **9b** it has not been possible to determine if the low pressure hysteresis is an artefact of low equilibrium times, as repeat syntheses of this material did not yield samples with either a large enough yield or matching framework structure to be studied under different equilibrium conditions.

Overall the gas adsorption investigations of $[Zn_4O(bptc)_2(H_2O)_2(DMF)]$, **9a** and **9b** show that the surface areas of the materials increase with increasing bpdc content within the framework (Table 3.6).

Table 3.6 Calculated surface areas of $[Zn_4O(bptc)_{2-x}(bpdc)_x(H_2O)_2(DMF)]$ structures in comparison to that of $[Zn_4O(bptc)_2(H_2O)_2(DMF)]$.

Structure	**Calculated Surface Area m_2 g^{-1}**
$[Zn_4O(bptc)(\mu_4\text{-}O)(H_2O)_2(DMF)]$	21.72
$[Zn_4O(bptc)_{1.04}(bpdc)_{0.96}(H_2O)_2(DMF)][NO_3]_{0.96}$ **9a**	255.6
$[Zn_4O(bptc)_{0.64}(bpdc)_{1.36}(H_2O)_2(DMF)][NO_3]_{1.36}$ **9b**	288.9

$[Zn_4O(bptc)_2(H_2O)_2(DMF)]$ was shown to be non-porous whilst the mixed-ligand systems display some porosity. Although the porosity of the mixed-ligand species is low in comparison to other reported MOFs this is the first report of a non-porous to porous transition in a MOF through defect engineering methods.

3.5 Conclusion and future work

The successful inclusion of the reduced symmetry ligand, bpdc into two frameworks containing the bptc ligand has been demonstrated and the mixed-ligand products $[Cd_3(bptc)_{2-x}(bpdc)_x(H_2O)_9][NO_3]_x \cdot nH_2O$ and $[Zn_4O(bptc)_{2-x}(bpdc)_x(H_2O)_2(DMF)][NO_3]_x$ have been characterised.

The $[Zn_4O(bptc)_{2-x}(bpdc)_x(H_2O)_2(DMF)][NO_3]_x$ mixed-ligand products show the inclusion of both bptc and bpdc ligands into the framework in similar ratios to those present in the reaction mixtures, suggesting compositional control can be achieved through the reaction stoichiometry. In contrast a clear ligand preference is observed in the mixed-ligand products of $[Cd_3(bptc)_{2-x}(bpdc)_x(H_2O)_9][NO_3]_x \cdot nH_2O$, with up to 40 % more bptc ligand in the framework than is available in the reaction mixture. Compositional variations between crystals from the same product were also found. In both $[Cd_3(bptc)_{2-x}(bpdc)_x(H_2O)_9][NO_3]_x \cdot nH_2O$ and $[Zn_4O(bptc)_{2-x}(bpdc)_x (H_2O)_2(DMF)][NO_3]_x$ inclusion of the bpdc ligand into the framework results in a decrease in crystallinity of the products.

The systematic formation of mixed-ligand MOFs has demonstrated that the pore structures of the frameworks can be altered and controlled through inclusion of reduced symmetry ligands. The $[Cd_3(bptc)_{1.54}(bpdc)_{0.46}(H_2O)_9][NO_3]_{0.46} \cdot 1.9H_2O$ **8a** structure shows clear crystallographic evidence for the presence of linker site vacancies within the pores. Future work could be completed to confirm the presence of uncoordinated metal sites in the $[Cd_3(bptc)_{2-x}(bpdc)_x(H_2O)_9][NO_3]_x$ frameworks. This could take the form of CO inclusion in the framework to monitor CO-Cd bond stretches through FTIR spectroscopy.

Gas adsorption measurements show that whilst the $[Zn_4O(bptc)_2(H_2O)_2(DMF)]$ structure is non-porous, structures of $[Zn_4O(bptc)_{1.04}(bpdc)_{0.96}(H_2O)_2(DMF)][NO_3]_{0.96}$ **9a** and $[Zn_4O(bptc)_{0.64}(bpdc)_{1.36}(H_2O)_2(DMF)][NO_3]_{1.36}$ **9b** are porous, demonstrating the first change from non-porous to porous behaviour achieved in a MOF through defect engineering. Analysis of the hysteresis in the isotherms of the mixed-ligand products suggests the presence of ink-bottle type pores consistent with the small, slit shaped pores being interlinked by larger cavities due to the presence of linker vacancies in the structures.

In summary, findings show the potential for new defect materials to have adapted pore geometries and surface areas which can be controlled through ligand ratios.

3.6 Experimental

3.6.1 General experimental details

The H_3bptc (4, 3', 5'-biphenyltricarboxylate)[21] and H_2bpdc (4, 3'-biphenyldicarboxylate)[22] compounds were synthesised using reported methods, all other starting materials and solvents were purchased from commercial sources and were used without further purification.

Powder X-ray diffraction (PXRD), single crystal X-ray diffraction data, ^{1}H NMR spectroscopy and TGA experiments were carried out in a similar manner to that detailed in Section 2.5.

3.6.2 Synthesis of $[Cd_3(bptc)_{2-x}(bpdc)_x(H_2O)_9][NO_3]_x$

$Cd(NO_3)_2{\cdot}4H_2O$ (0.304 mmol, 0.094 g) was combined with H_3bptc and H_2bpdc (a total carboxylic acid content of 0.105 mmol) in 3.2 ml DMF and 6.4 ml H_2O. The solution was placed in a sealed vial and sonicated for 15 minutes prior to being heated at 85 ^oC for 3 days. The reaction gave colourless crystals in yields of 10-20 % based on the total H_3bptc and H_2bpdc used (For example, the product $[Cd_3(bptc)_{1.6}(bpdc)_{0.4}(H_2O)_9][NO_3]_{0.4}{\cdot}3.8H_2O$ gave a yield of 0.021 g, 0.19 %).

3.6.3 Synthesis of $[Cd_3(bptc)_{1.7}(bpdc)_{0.3}(H_2O)_9][BF_4]_{0.3}$

$Cd(BF_4)_2$ was prepared by dissolving $CdCl_2$ (1.402 mmol, 0.257 g) in H_2O . $AgBF_4$ (1.48 mmol, 0.291 g) was added to the solution and stirred overnight in light sensitive conditions. The resulting precipitate was filtered under vacuum. The MOF synthesis was then completed by combining $Cd(BF_4)_2$ (0.342 mmol, 0.098 g) with H_3bptc (0.052 mmol, 0.0148 g) and H_2bpdc (0.052 mmol, 0.0126 g) in 3.2 ml DMF and 6.4 ml H_2O. The solution was placed in a sealed vial and sonicated for 15 minutes prior to being heated at 85 ^oC for 3 days.

3.6.4 Synthesis of $[Zn_4O(bptc)_{2-x}(bpdc)_x(H_2O)_2(DMF)]$

$Zn(NO_3)_2{\cdot}6H_2O$ (1.22 mmol,0.361 g) H_3bptc and H_2bpdc (a total carboxylic acid content of 0.540 mmol) were combined in a vial with 18 ml DMF. The vial was sealed and sonicated for 15 minutes. The vial was then heated to 110 ^oC for 60 hours and cooled to room temperature over 72 hours. The supernatant was then decanted and replaced with fresh DMF. The product was a white microcrystalline solid in yields of 15-20 % based on the total H_3bptc and H_2bpdc used (For example, the product $[Zn_4O(bptc)_{1.6}(bpdc)_{0.4}(H_2O)_2(DMF)][NO_3]_{0.4}$ gave a yield of 0.103 g, 18 %).

3.7 References

1. D. S. Sholl and R. P. Lively, *J. Phys. Chem. Lett.*, 2015, 6, 3437-3444
2. Z. Wang, J. Yu and R. Xu, *Chem. Soc. Rev.*, 2012, 41, 1729-1741
3. H. Furukawa, U. Muller and O. M. Yaghi, *Angew. Chem. Int. Ed.*, 2015, 54, 3417-3430
4. F. Vermoortele, B. Bueken, G. Le Bars, B. Van de Voorde, M. Vandichel, K. Houthoofd, A. Vimont, M. Daturi, M. Waroquier, V. Van Speybroeck, C. Kirschhock and D. E. De Vos, *J. Am. Chem. Soc.*, 2013, 135, 11465-11468
5. B. Van de Voorde, I. Stassen, B. Bueken, F. Vermoortele, D. De Vos, R. Ameloot, J.-C. Tan and T. D. Bennett, *J. Mater. Chem. A*, 2015, 3, 1737-1742
6. F. Vermoortele, R. Ameloot, L. Alaerts, R. Matthessen, B. Carlier, E. V. R. Fernandez, J. Gascon, F. Kapteijn and D. E. De Vos, *J. Mater. Chem.*, 2012, 22, 10313-10321
7. Y. P. Zhigang Hu, Kai Min Tan and Dan Zhao, *Cryst. Eng. Comm.*, 2015, 17, 7124-7129
8. Z. Fang, J. P. Dürholt, M. Kauer, W. Zhang, C. Lochenie, B. Jee, B. Albada, N. Metzler-Nolte, A. Pöppl, B. Weber, M. Muhler, Y. Wang, R. Schmid and R. A. Fischer, *J. Am. Chem. Soc.*, 2014, 136, 9627-9636
9. K. Kaneko. M. Thommes, A.V. Neimark, J. P. Olivier, and J. Rouquerol and K. Sing, *Pure Appl. Chem.*, 2015, 87, 1051-1069
10. C. Ji, Y. Li, Z. Guoa and H. Zheng, *Cryst. Eng. Comm.*, 2011, 13, 459-466
11. ACD/ilab, RSC national chemical database service http://ilab.cds.rsc.org, 2016
12. A. D. Burrows, L. C. Fisher, C. Richardson and S. P. Rigby, *Chem. Commun.*, 2011, 47, 3380-3382
13. G. C. Shearer, J. G. Vitillo, S. Bordiga, S. Svelle, U. Olsbye and K. P. Lillerud, *Chem. Mater.*, 2016, 28, 7190-7193
14. R. V. Honeychuck. and W. H. Hersh, *Inorg. Chem.*, 1989, 28, 2869-2886
15. C. Lv, J. Li, Z. Hou and M. Li, *Inorg. Chem. Commun.*, 2013, 36, 1-3
16. T. D. Bennett and A. K. Cheetham, *Acc. Chem. Res.*, 2014, 47, 1555-1562
17. M. Thommes, *Chem. Ing. Tech. Int. Ed.*, 2010, 82, 1059-1073
18. S. Xiang, J. Huang, L. Li, J. Zhang, L. Jiang, X. Kuang and C. Y. Su, *Inorg. Chem.*, 2011, 50, 1743-1748
19. P. M. Forster, B. D. Heiken, J. B. Parise, J. W. Yoon, S. H. Jhung, J. Chang and A. K. Cheetham, *J. Am. Chem. Soc.*, 2006, 128, 16846-16850
20. A. M. Silvestre-Albero, J. M. Juárez-Galán, J. Silvestre-Albero and F. Rodríguez-Reinoso, *J. Phys. Chem. C*, 2012, 116, 16652-16655
21. O. L. Antek, G. Wong-Foy, and Adam J. Matzger, *J. Am. Chem. Soc*, 2007, 15740-15741
22. J. R. Li and H. C. Zhou, *Angew. Chem. Int. Ed*, 2009, 48, 8465-8468

4. Photochromic and thermochromic metal-organic frameworks (MOFs)

4.1 Introduction

4.1.1 Host-guest MOFs

Much attention has been paid to the selective functionalisation of MOFs through alterations of the framework itself, by either post-synthetic modification of the organic ligands or variations to the metal sites within the framework.[1] However, the potential to functionalise the free pore volume is also available through the formation of host-guest materials.[2] Host-guest materials take advantage of the porous nature of MOFs by including guest species into the cavities of the framework to create new materials that may have altered properties to the guest-free analogue.[3]

Untreated, as-synthesised MOFs contain solvent molecules and/or unreacted starting materials within the pores of the structure. These materials can be removed from the pores through a process of activation to give a guest-free framework which has empty cavities (see Section 1.3). Early studies on guest-removal were intended to investigate the gas sorption properties of MOFs, and the resulting structures were probed for their ability to uptake gaseous species into the pores, such as hydrogen.[4]

Increasingly research is being conducted in which a range of molecules are being investigated as potential guests within porous frameworks, including organic dyes[5], proteins[6] and explosives.[7] These materials have been utilised for sensing or detection applications whereby the host framework is chosen for its selective inclusion of guest molecules. The luminescent MOF $[Mg_2(bdc)_2(bpno)]\cdot 2DMF$ (bdc = 1,4-benzenedicarboxylate and bpno = 4,4′-dipyridyl-*N*,*N*′-dioxide) has been used for the selective adsorption of liquid explosive molecules.[7] The MOF has a three-dimensional structure with one-dimensional channels running along the *a*-axis (Figure 4.1).

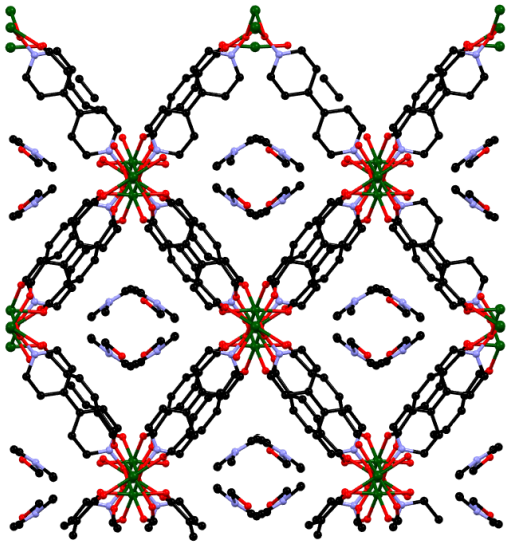

Figure 4.1 Part of the structure of $[Mg_2(bdc)_2(bpno)]\cdot 2DMF$ showing the three-dimensional network with porous channels occupied by DMF solvent. Hydrogen atoms have been removed for clarity.

Both the solvated $[Mg_2(bdc)_2(bpno)]\cdot 2DMF$ and desolvated $[Mg_2(bdc)_2(bpno)]$ structures exhibit blue luminescence when excited with light at a wavelength of 305 nm. Upon the inclusion of nitrobenzene, nitromethane or nitroethane into the pores of the MOF the luminescence is quenched (Figure 4.2). The guest molecules can be readily removed to form either the guest-free structure $[Mg_2(bdc)_2(bpno)]$ or the solvated $[Mg_2(bdc)_2(bpno)]\cdot 2DMF$ structure.

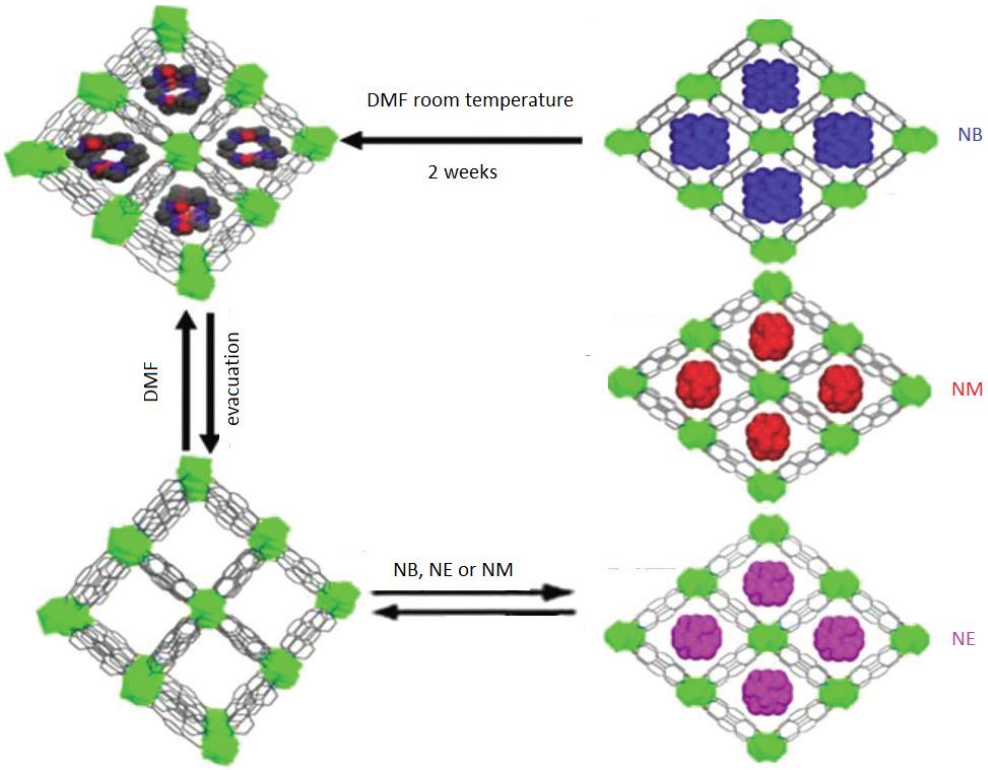

Figure 4.2 Schematic representations of the $[Mg_2(bdc)_2(bpno)]\cdot 2DMF$ three-dimensional framework and the reactions to form the desolvated form and host-guest complexes with nitrobenzene (NB), nitromethane (NM) and nitroethane (NE).[7]

As well as confining the guest species, many of these host-guest complexes allow new possible uses of the guest species to be accessed. The encapsulation of metal hydrides within the pores of MOFs has been shown to result in the formation of nanoscale metal hydride clusters in the framework. Nanoscale metal hydrides have altered properties compared to bulk metal hydride materials resulting in improved release of hydrogen.[4] The inclusion of $NaAlH_4$ into $[Cu_3(btc)_2]$, HKUST-1, and $[Mg_2(dobdc)]$, MOF-74, (dobdc = dioxidoterephthalate) was successfully achieved, forming nanocluster $NaAlH_4$ in the pores of the structures (Figure 4.3).[8,9]

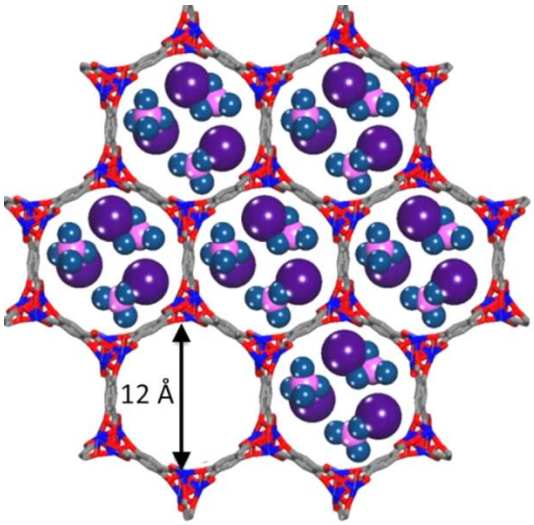

Figure 4.3 Schematic representation of $NaAlH_4$ clusters in the pores of MOF-74, $[Mg_2(dobdc)]$.[4]

Encapsulation of $NaAlH_4$ in the MOFs alters the reaction pathway of the dehydrogenation reaction, avoiding the production of Na_3AlH_6 which forms as a stable intermediate in the reaction of the bulk metal hydride and is rate limiting (Scheme 4.1). Dehydrogenation of the metal hydride clusters in HKUST-1 and MOF-74 to give NaH, Al and H_2 showed reduced activation energies by up to 60 $kJmol^{-1}$ compared to the bulk metal hydride material.[4]

$$NaAlH_4 \rightleftharpoons \tfrac{1}{3}\, Na_3AlH_6 + \tfrac{2}{3}\, Al + H_2 \rightleftharpoons NaH + Al + \tfrac{1}{2}\, H_2$$

Scheme 4.1 The two-step dehydrogenation of $NaAlH_4$.

Host-guest complexes can also give rise to emerging properties which are not native to either host or guest material.[10] Allendorf and co-workers reported the formation of TCNQ@HKUST-1 complex (TCNQ = tetracyanoquinodimethane).[11] Inclusion of TCNQ molecules into the HKUST-1 framework produces a charge transfer material that displays electrical conductivity of 0.1 S cm^{-1}. Neither HKUST-1 nor TCNQ display conductivity in isolation and it is thought that the binding of the TCNQ molecules to copper centres in the HKUST-1 framework forms a conductive channel through the MOF (Figure 4.4).

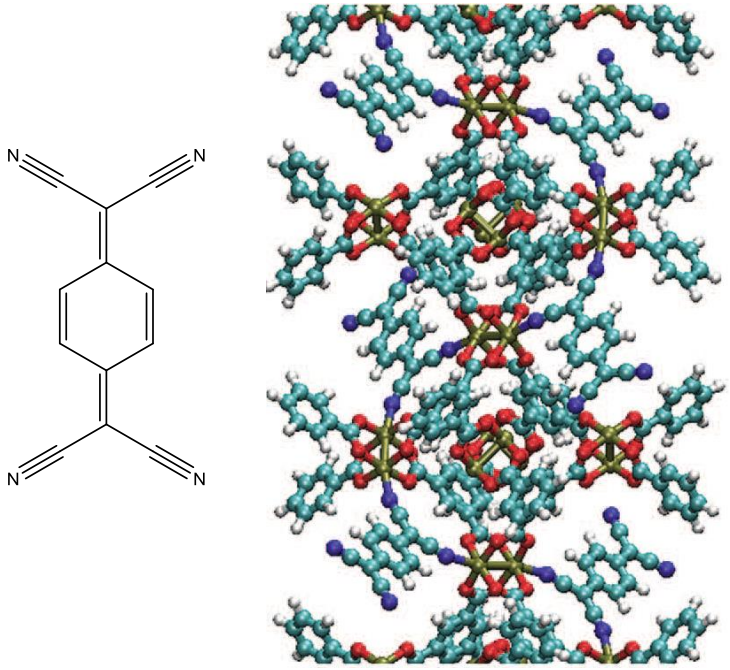

Figure 4.4 The structure of the TCNQ molecule and structural representation showing the possible configuration of TCNQ molecules in HKUST-1 forming a conductive channel.[11] Carbon atoms are shown in green, nitrogen in blue, oxygen in red, hydrogen in white and copper in yellow.

In addition to host-guest systems, the inclusion of some counter-ions into charged frameworks can result in emergent properties of the resulting MOF material. One class of MOFs which falls under this description is viologen-containing frameworks which have been studied for their thermochromic and photochromic properties.

4.1.2 Viologen species and their solution phase chemistry

Viologen (*N*,*N*'-disubstituted bipyridinium) species undergo reversible redox reactions which are accompanied by a distinct colour change. As such they were initially studied as redox indicators in biological systems but have more recently gained attention for their potential uses in electrochromic displays and photochemical applications.[12] The vast majority of studies of viologens have been in the solution phase.

Viologens exhibit three oxidation states, with accompanying dication V^{2+}, radical cation $V^{+\bullet}$ and neutral charges V^0 (Figure 4.5).

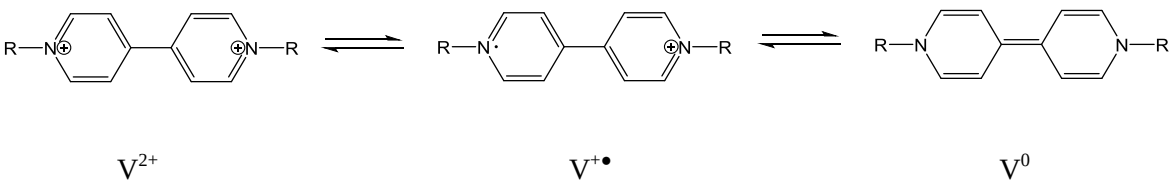

Figure 4.5 The oxidation states of viologen species where R is an alkyl or aryl substituent.

The first reduction step, from V^{2+} to $V^{+\bullet}$, is readily reversible and can be cycled multiple times. However, the second reduction step, from $V^{+\bullet}$ to V^0, has limited reversibility due to the insoluble nature of the V^0 product.[12] These reduction/oxidation steps have predominantly been studied through electrochemistry techniques, although chemically reduced reactions are also reported.[12, 13]

Each step is associated with a distinct colour change. For example, methyl viologen dichloride ($MVCl_2$) contains R = Me and is a yellow solid in its dication form, MV^{2+}. It can undergo a reduction to give the deep blue radical cation, $MV^{+\bullet}$. The neutral MV^0 compound of methyl viologen has been reported to be yellow/orange in a solution of acetonitrile and heptane.[13] Viologen radicals rapidly react with molecular oxygen to regenerate the dication species. As this reaction is accompanied by a colour change, the reaction has been proposed as a mechanism for the detection of dissolved oxygen in solutions in low concentrations.[14]

Viologen solutions have also been shown to be reduced from V^{2+} to $V^{+\bullet}$ through thermal or photosensitised methods.[15] This process has been demonstrated through heating or UV irradiation of viologens in alkaline aqueous or alcoholic solutions in the absence of air.[13]

Viologen species are generally stable, but in strongly alkaline solutions dealkylation can occur. An example of methyl viologen dealkylation is given in Figure 4.6.

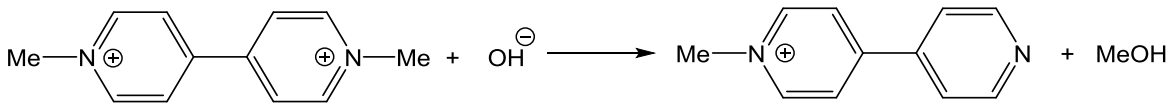

Figure 4.6 Dealkylation of methyl viologen in alkaline solution

In aqueous solution the formation of a V_2^{2+} dimer species can be observed. The dimer has a suggested sandwich structure, in which the π-clouds of the two monomers overlap.[14] Dimerisation occurs through a two-step process of conproportionation, in which the V^0 and V^{2+} species in solution undergo an electron transfer process forming the dimer (Scheme 4.2).[14]

$$V^{2+} \rightarrow V^0$$

$$V^{2+} + V^0 \rightarrow V_2^{2+}$$

Scheme 4.2 Two-step process to form the V_2^{2+} dimer.

For methyl viologen, the dimer is red and can undergo a disproportionation reaction to generate the radical cation monomers (Scheme 4.3).[14] As the radical cation monomer is blue, this equilibrium between monomer and dimer can cause the solution to appear violet.

$$V_2^{2+} \rightarrow 2V^{+\bullet}$$

Scheme 4.3 Disproportionation of the V_2^{2+} dimer to product radical cations.

Viologen compounds have been produced with a range of substituent groups on the nitrogen atoms and some general trends in the properties of the resulting compounds can be drawn. The substituent is known to affect the solubility of the cation radical complex, with alkyl substituents greater than five carbons in length forming an insoluble cation radical species which precipitates out of solution, reducing the reversibility of the V^{2+} to $V^{+\bullet}$ reaction.[12]

The redox reactions of viologens and their distinctive colour changes have made viologen species attractive in applications such as electrochromic devices, where the device exhibits a colour change in response to a voltage.

4.1.3 Viologen containing MOFs

While the study of the photochromic behaviour of viologens in solution is well documented, reports of solid state viologen photochromism are rarer. Crystal packing influences the success of viologen photochromism in the solid state, with geometric restraints making photoinduced electron transfer between donor and the viologen acceptor moieties difficult to achieve.[16]

Examples of both the inclusion of viologens as counter-ions in the pores of charged MOFs and as ligands, forming part of the backbone of the framework, have been reported. In both cases the inclusion of viologens into MOFs has been investigated with a view to forming new multifunctional materials which can undergo photo-induced electron transfer behaviours.

Fu and co-workers reported the inclusion of the viologen-based ligand cpbpy and the dicarboxylate ligand ip, into the cadmium MOF, $[Cd(cpbpy)(ip)]\cdot H_2O$ (cpbpy = N-(3-carboxyphenyl)-4,4-bipyridinium, ip = 1,3-benzenedicarboxylate).[17] The framework is formed from cadmium dimeric SBUs, linked through the cpbpy and ip linkers into two-dimensional layers (Figure 4.7).

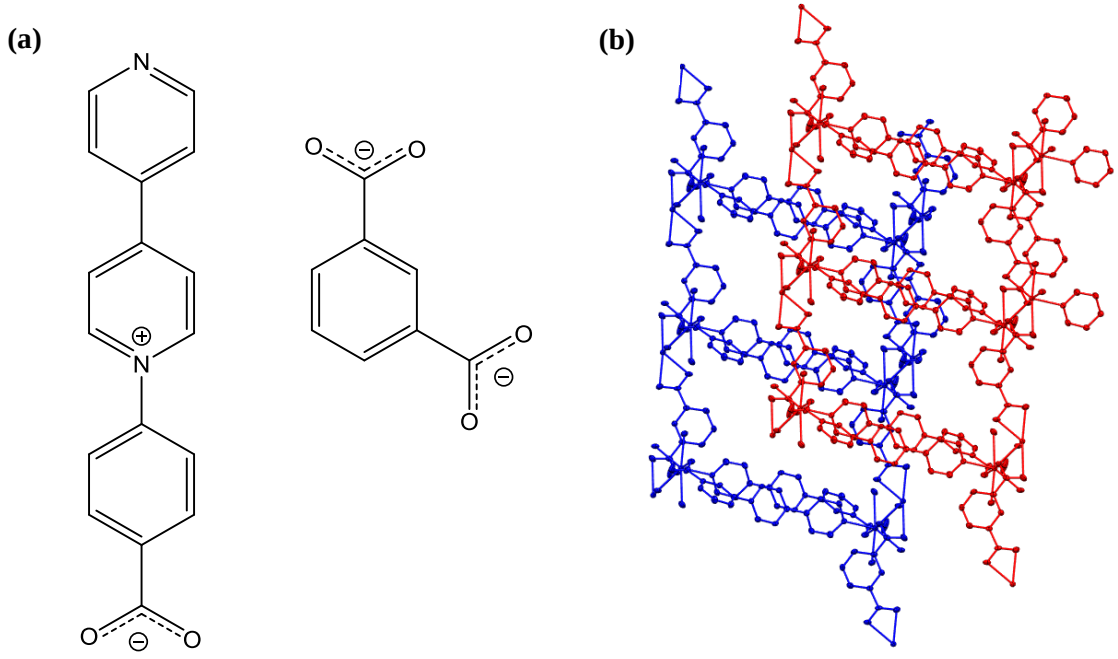

Figure 4.7 (a) The cpbpy and ip ligands and **(b)** part of the structure of [Cd(cpbpy)(ip)]·H_2O viewed down the *a*-axis showing the two-dimensional layers in blue and red.[17]

The crystals of [Cd(cpbpy)(ip)]·H_2O undergo a colour change from yellow to blue upon light irradiation, indicating the formation of the radical viologen species. Close packing of the layers within the crystal structure are expected to aid electron transfer between the ip ligand and the cpbpy ligand upon irradiation. The framework shows high thermal stability, maintaining its topology with heating up to 370 ^{o}C as monitored by powder X-ray diffraction. The photochromic behaviour and high thermal stability of [Cd(cpbpy)(ip)]·H_2O makes this material attractive to application in photochromic devices, which often suffer damage due to heat generation after repeated irradiation.

A MOF containing methyl viologen counter-ions has been reported with the formula [MV][$Zn_3(ip)_4$].[18] [MV][$Zn_3(ip)_4$] was formed through synthesis of $Zn(NO_3)_2$·$6H_2O$ with H_2ip and viologen diacetic acid dichloride, which undergoes hydrolysis during the synthesis to form methyl viologen (Figure 4.8).

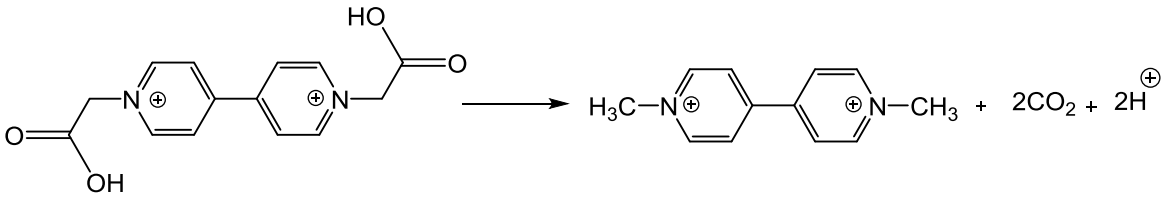

Figure 4.8 The formation of methyl viologen from viologen diacetic acid. The viologen diacetic acid is shown in its cationic form without the chloride counter ions.

The SBU of the framework is formed from three zinc atoms linked by eight carboxylate groups (Figure 4.9). The ip ligands link these trinuclear zinc SBUs to form two dimensional chains. The framework contains square channels running perpendicular to the two-dimensional chains in which methyl viologen cations are located (Figure 4.9). The reported dimensions of the square pores are 9.5 x 10.1 Å.

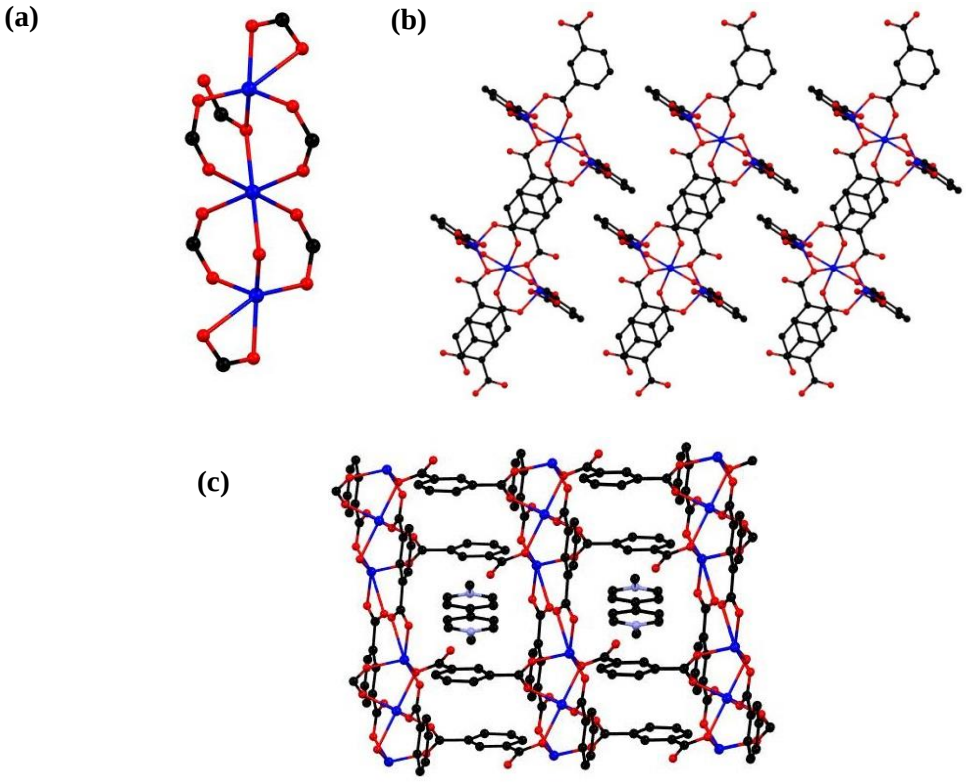

Figure 4.9 Part of the structure of [MV][$Zn_3(ip)_4$] showing **(a)** the $Zn_3(CO_2)_8$ SBU, **(b)** the two-dimensional chains viewed down the *b*-axis with counter-ions removed for clarity and **(c)** the square pores occupied by methyl viologen cations. Hydrogen atoms are omitted in all cases for clarity.[18]

The [MV][$Zn_3(ip)_4$] structure displays both photochromic and thermochromic behaviours, changing from yellow/orange to blue upon light irradiation or heating to above 120 ^oC. Close contact (3.256(5) Å) of the non-coordinating oxygen on the ip ligands to the nitrogen on the methyl viologen accounts for effective charge transfer between the framework and methyl viologen dication, reducing the viologen to its blue radical cation form. Once generated, the radical species is stable in air for several weeks forming a long-lived charge separated state. This is in contrast to the solution phase methyl viologen radical cation which rapidly oxidises to the colourless MV^{2+} state in air.

4.2 Aims and objectives

Following the reported formation of a photochromic and thermochromic material from the methyl viologen containing zinc-based framework, $[MV][Zn_3(ip)_4]$ an investigation into the formation of MOFs featuring viologen species as counter-ions was undertaken.

The investigation aimed to determine if viologen containing MOFs can be formed through direct synthesis with the viologen species, as an alternative to being generated *in situ* as demonstrated in the case of $[MV][Zn_3(ip)_4]$ where methyl viologen is generated from viologen diacetic acid dichloride. A number of anionic zinc frameworks were also chosen to be studied for their ability to include viologen counter-ions.

Firstly, the direct synthesis with methyl viologen diiodide was undertaken for the $[Zn_3(ip)_4]^{2-}$ system. An investigation into the reaction synthesis temperature and its effect on framework formation and viologen oxidation state was also undertaken. This method was then extended to other zinc-based frameworks, namely $[Zn_3(bdc)_4]^{2-}$, $[Zn(btc)]^-$ and $[Zn_3(bpdc)_4]^{2-}$ which were selected for their anionic charge and porous channels which may potentially include viologen cations. In all cases the radical formation and stability was investigated.

A comparison study with a different viologen species was also completed in which the frameworks $[Zn_3(ip)_4]^{2-}$,$[Zn_3(bdc)_4]^{2-}$ and $[Zn(btc)]^-$ were studied for their inclusion of ethyl viologen counter-ions.

In all systems the composition of the products and inclusion of viologen species into the framework was determined through ^1H NMR spectroscopy studies. The topology of the resulting frameworks was studied through powder X-ray diffraction and single crystal X-ray diffraction analyses and the formation of the radical cation species was examined through electron paramagnetic resonance spectroscopy.

4.3 Methyl viologen containing MOFs

4.3.1 Synthesis and characterisation of [MV][$Zn_3(ip)_4$]

The reported structure of [MV][$Zn_3(ip)_4$][18] (ip = isophthalic acid, MV = methyl viologen) contains methyl viologen counter-ions within the pores of the framework. The methyl viologen is formed *in situ* during the MOF synthesis from the hydrolysis of viologen diacetic acid dichloride (see Section 4.1.3).

Investigations into a possible new preparatory route for the [MV][$Zn_3(ip)_4$] structure were carried out to determine if the MOF could be synthesised directly with methyl viologen cations. Methyl viologen diiodide (MVI_2) was used as the viologen source, and the reaction with zinc nitrate and H_2ip was carried out in DMF. The reaction was completed on two batches each at a different temperature; 85 ^oC or 120 ^oC, for 48 hours. The reaction temperature of 85 ^oC was selected based upon the synthesis temperature of [MV][$Zn_3(ip)_4$] from viologen diacetic acid. The higher temperature of 120 ^oC was selected as heating [MV][$Zn_3(ip)_4$] above this temperature is reported to form methyl viologen radical cations. The effect of the reaction temperature on product formation and methyl viologen oxidation state was investigated.

The reaction carried out at 85 ^oC yielded a mixture of yellow and blue crystals while increasing the reaction temperature to 120 ^oC gave a product of blue crystals only. Powder X-ray diffraction analysis of the products were carried out and compared to the powder diffraction trace of [MV][$Zn_3(ip)_4$] (Figure 4.10).

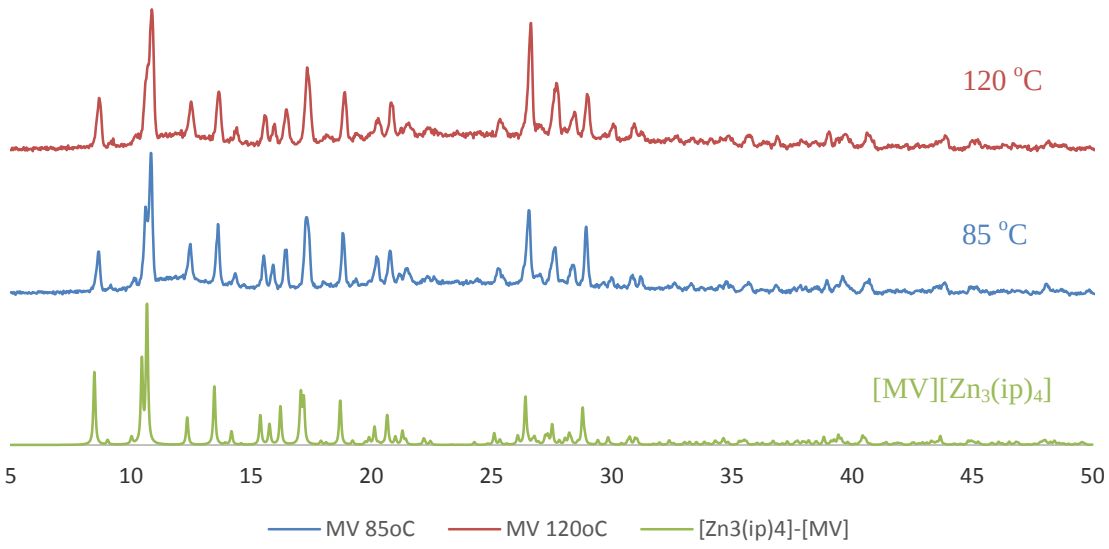

Figure 4.10 Powder X-ray diffraction pattern for [MV][$Zn_3(ip)_4$] calculated from the reported crystal structure and the products formed from reactions with MVI_2. Corresponding reaction temperatures for each product are given.

Similarities in the peak positions and relative intensities of the products to that of the reported $[MV][Zn_3(ip)_4]$ suggests that all species have similar framework topologies to one another. The presence of both yellow and blue crystals in the product formed at 85 ^oC is indicative of some crystals containing methyl viologen in their dicationic form (MV^{2+}) and others containing methyl viologen in the radical cationic form ($MV^{+\bullet}$), which is known to be blue. The homogeneous blue appearance of the product formed at 120 ^oC suggests that all crystals contain methyl viologen radical cations ($MV^{+\bullet}$). As both products give similar powder diffraction patterns to one another the state of the methyl viologen within the framework, MV^{2+} or $MV^{+\bullet}$, can be seen to have no effect on the overall MOF topology.

The blue colour of the product formed with a reaction temperature of 120 ^oC persists when the material is left in air at ambient temperature for several weeks. The appearance of the material was monitored under these conditions for 3 months and no change in the blue colour was observed during this time. This in contrast to the stability of the methyl viologen radical cations ($MV^{+\bullet}$) in solution, which rapidly oxidise to the dicationic state (MV^{2+}) in the presence of oxygen within minutes (see Section 4.1.2). A similar stability of the methyl viologen radical cation in the structure of $[MV][Zn_3(ip)_4]$ formed from the viologen diacetic acid was reported.

The composition of the products was investigated through ^1H NMR spectroscopy studies. The products were first washed to ensure any residual methyl viologen not within the pores of the MOF were removed. The washing involved decanting the crystals from their supernatant and replacing this with fresh DMF. This was repeated daily for three days. The MOFs were then digested in a d_6-DMSO/ DCl mixture prior to analysis by ^1H NMR spectroscopy. The digestion solution of both products was orange/yellow in colour, indicating the methyl viologen to be in its dicationic form.

Spectra from both products formed at 85 ^oC and 120 ^oC showed the presence of D_2ip and methyl viologen (Figure 4.11). The resonances at δ 7.61 ppm, δ 8.11 ppm and δ 8.42 ppm originate from the D_2ip whilst the resonances at δ 4.43 ppm, δ 8.73 ppm and δ 9.26 ppm are from the methyl viologen. The resonance at δ 7.91 ppm originates from the solvent DMF.

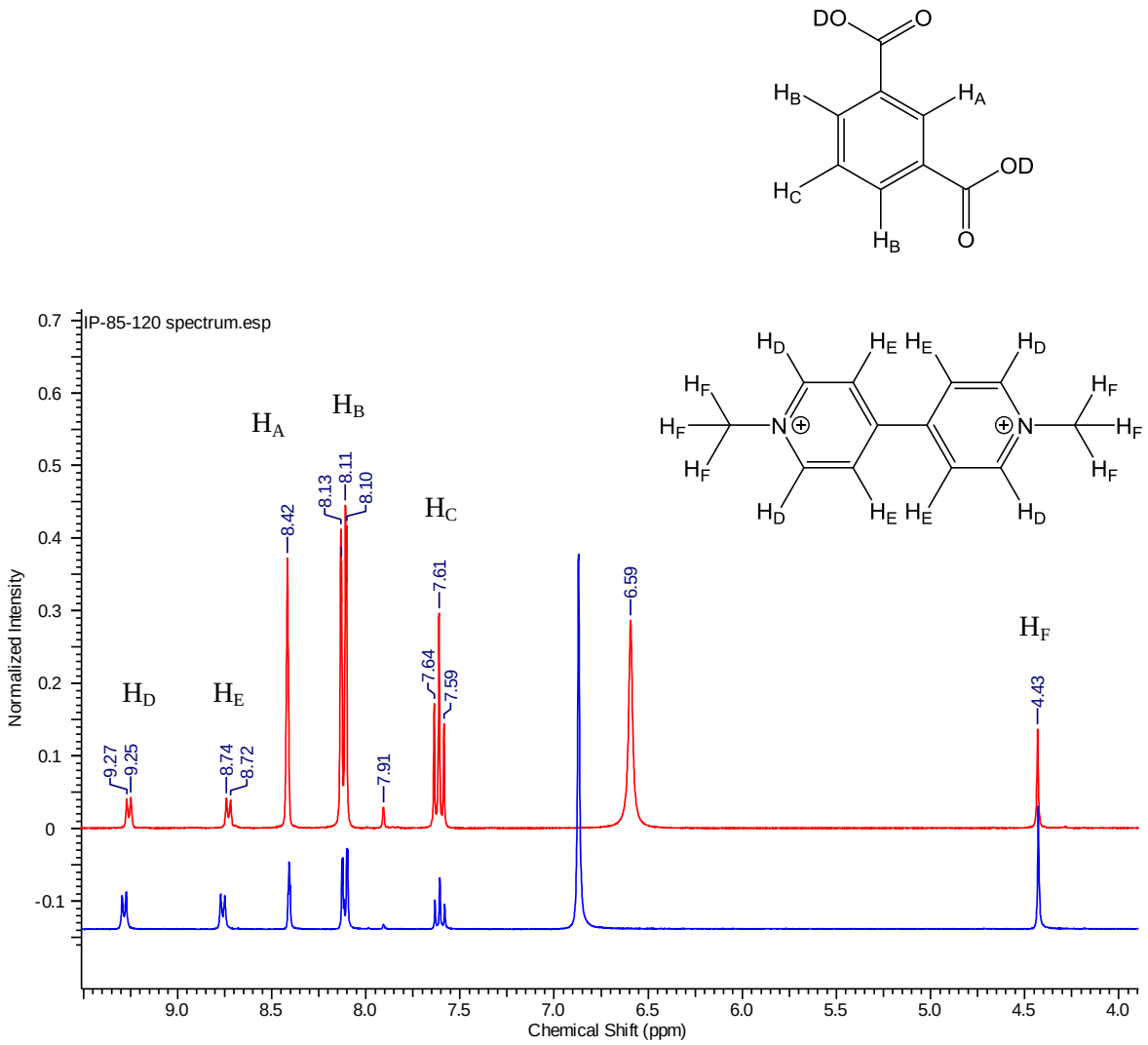

Figure 4.11 ^{1}H NMR spectra of digested samples of [MV][$Zn_3(ip)_4$] synthesised at 85 ^{o}C and 120 ^{o}C. The resonances at δ 6.8 ppm and δ 6.59 ppm in each sample respectively originate from water present in the samples.

Analysis of the integrated resonances within each ^{1}H NMR spectra allow the relative amounts of ip:viologen within each product to be identified. Both reactions were performed using a 1:1 ratio of H_2ip:MVI_2 in the reaction mixture and both reactions produced products which contain a D_2ip:MVI_2 ratio of 4:1. As the MOF has a framework formula of $[Zn_3(ip)_4]^{2-}$, one MV^{2+} is required for every four isophthalate ligands to charge balance the structure. In the case of the blue coloured product synthesised at 120 ^{o}C, the methyl viologen counter-ions are in their radical cation form. However, the reported structure of [MV][$Zn_3(ip)_4$][18] indicates that the reduction of MV^{2+} to $MV^{+\bullet}$ occurs through an electron transfer process from the framework to the methyl viologen cation. Therefore no change in formula is needed to charge balance the $MV^{+\bullet}$ containing structure. The overall formula for both products is therefore found to be [MV][$Zn_3(ip)_4$]. Thermogravimetric analysis of the product found no solvent to be present within the structure (see appendix A4.1.1).

4.3.2 Formation of $[MV]_{0.44}[HMVH]_{0.36}[NH_2(CH_3)_2]_{0.4}[Zn_3(bdc)_4]\cdot 2H_2O\cdot 1.2DMF$ by direct synthesis methods

Following the successful formation of $[MV][Zn_3(ip)_4]$ by direct synthesis with methyl viologen diiodide, other MOFs were investigated for the inclusion of methyl viologen cations. The framework $[Zn_3(bdc)_4]^{2-}$ was studied due to its anionic charge and porous channels.[19]

The reported synthesis for $[NH_2(CH_3)_2]_2[Zn_3(bdc)_4]\cdot DMF\cdot H_2O$[19] involves the reaction of zinc nitrate with H_2bdc in DMF. The addition of $[NH_2(CH_3)_2]Cl$ acts to template the final MOF structure. The synthesis with methyl viologen was carried out using similar reaction conditions but replacing $[NH_2(CH_3)_2]Cl$ with methyl viologen diiodide. The reaction was conducted at both 85 ^oC and 120 ^oC over 48 hours to determine the effect of reaction temperature on product formation and the methyl viologen form. The reactions yielded crystalline products of blue/yellow crystals and blue crystals respectively.

Powder X-ray diffraction analysis was carried out on both products, the results of which are shown alongside the powder diffraction pattern of $[NH_2(CH_3)_2]_2[Zn_3(bdc)_4]\cdot DMF\cdot H_2O$ in Figure 4.12.

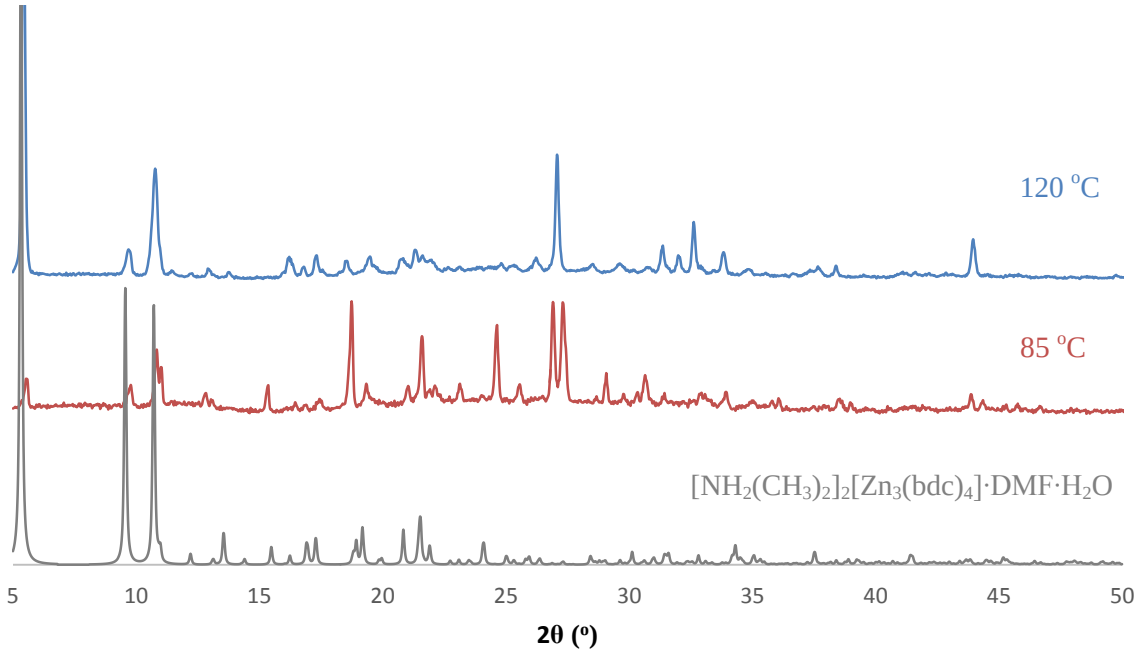

Figure 4.12 Powder X-ray diffraction patterns of $[NH_2(CH_3)_2]_2[Zn_3(bdc)_4]\cdot DMF\cdot H_2O$ (calculated from the reported crystal structure) and the experimental powder diffraction patterns. Corresponding reaction temperatures are given.

The diffraction patterns of both products have similar gross features to one another and contain some peaks at similar positions to those observed in the powder diffraction pattern of $[NH_2(CH_3)_2]_2[Zn_3(bdc)_4]\cdot DMF\cdot H_2O$. Additional peaks are also present in the experimental powder patterns compared to that of $[NH_2(CH_3)_2]_2[Zn_3(bdc)_4]\cdot DMF\cdot H_2O$. Possible explanations for this include structural differences between the reported and experimental structures or differences in the

counter-ion species which may also influence peak positions. The experimental products contain the larger and more rigid methyl viologen cations compared to the dimethyl ammonium cations of $[NH_2(CH_3)_2]_2[Zn_3(bdc)_4]\cdot DMF\cdot H_2O$. Differences in solvent inclusion may contribute to the differences in relative intensities of peaks between powder diffraction patterns.

^{1}H NMR spectroscopy was carried out on a digested sample of the blue product formed at 120 ^{o}C. The sample was dried at 120 ^{o}C for 15 minutes prior to being digested in a d_6-DMSO/DCl mixture. The digestion mixture was orange in colour, indicating the methyl viologen to be in its dicationic form. The ^{1}H NMR spectrum is shown in Figure 4.13.

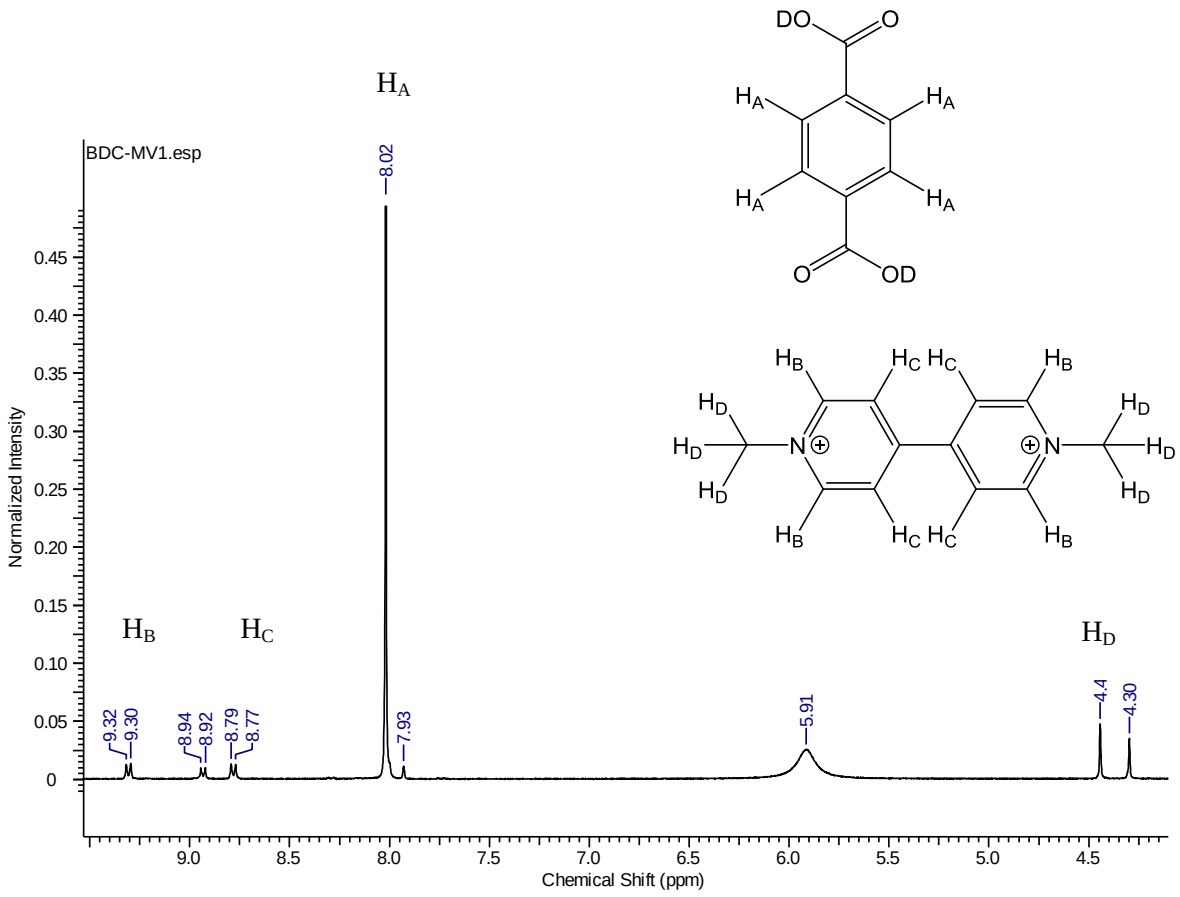

Figure 4.13 ^{1}H NMR spectra of the digested product. The structures of D_2bdc and methyl viologen are shown alongside the spectrum. The resonance at δ 7.93 ppm originates from DMF and δ 5.91 ppm originates from water.

The presence of both D_2bdc and methyl viologen were detected in the digestion mixture with the resonance at δ 8.02 ppm originating from the aromatic protons of D_2bdc and δ 9.31 ppm, δ 8.78 ppm and δ 4.44 ppm originating from the protons of methyl viologen. Additional resonances at δ 8.93 ppm, δ 8.01 ppm (shoulder) and δ 4.30 ppm are observed in the ^{1}H NMR spectrum suggesting the presence of a third organic species.

Due to the presence of the shoulder at δ 8.01 ppm on the D_2bdc resonance, the digestion was carried out a second time using a D_2O/DCl mixture. D_2bdc is insoluble in D_2O and the undissolved D_2bdc was removed by filtration following digestion (Figure 4.14). Resonances at δ 9.00 ppm, δ

8.48 ppm and δ 4.45 ppm originate from the methyl viologen and the resonance at δ 7.91 ppm corresponds to DMF. The resonances at δ 8.65 ppm, δ 7.93 ppm and δ 4.29 ppm correspond to the third organic species noted in the d_6-DMSO/DCl digestion spectrum as H_E, H_F and H_G.

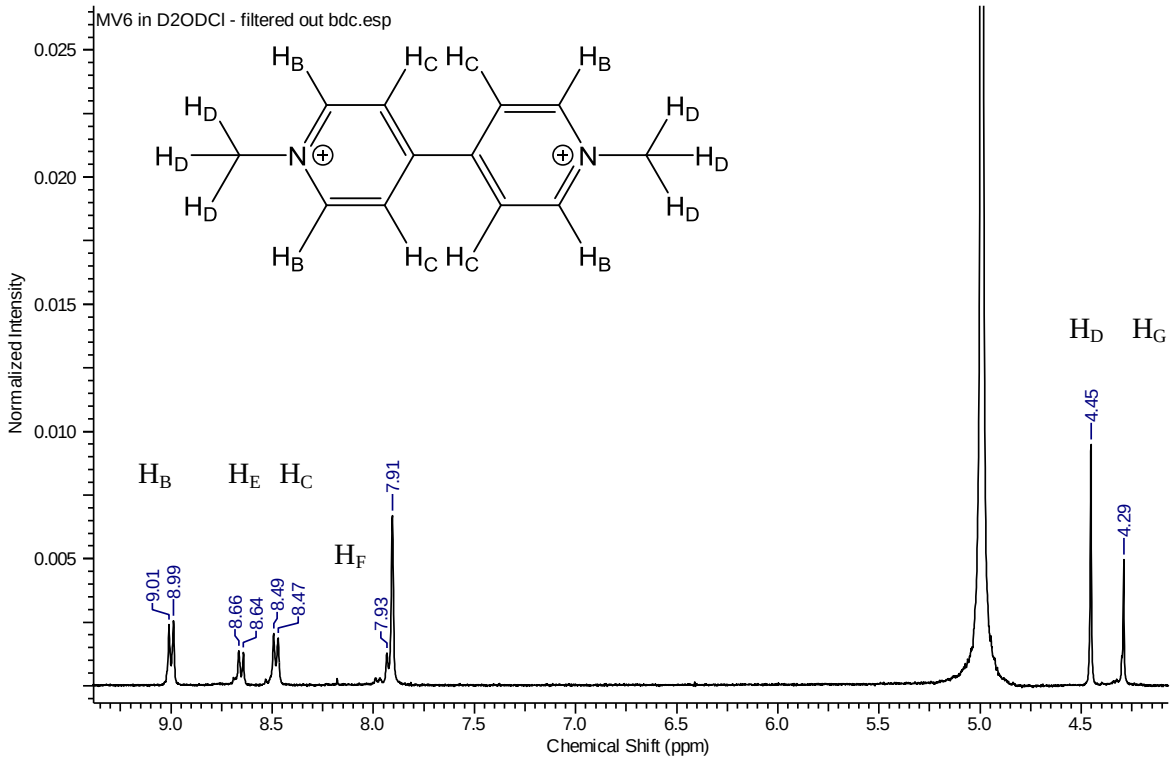

Figure 4.14 ^{1}H NMR spectra of the digested product in D_2O/DCl. The proton resonances are labelled, where H_B, H_C and H_D correspond to methyl viologen protons and H_E, H_F and H_G protons correspond to the unknown compound.

Further 2D ^{1}H NMR spectroscopy studies were carried out on the d_6-DMSO/DCl digestion sample to determine if the observed resonances belong to the same species. ^{1}H-^{1}H correlated spectroscopy (COSY) and nuclear overhauser effect spectroscopy (NOESY) were carried out on the digested sample.

The ^{1}H-^{1}H COSY spectrum is shown in Figure 4.15. The resonance from H_F is present as a shoulder on the D_2bdc H_A resonance. Cross peaks between protons of H_E and H_F can be observed, indicating that the protons corresponding to these resonances are connected through covalent bonds. Similar cross peaks are observed for the protons of H_B and H_C in methyl viologen.

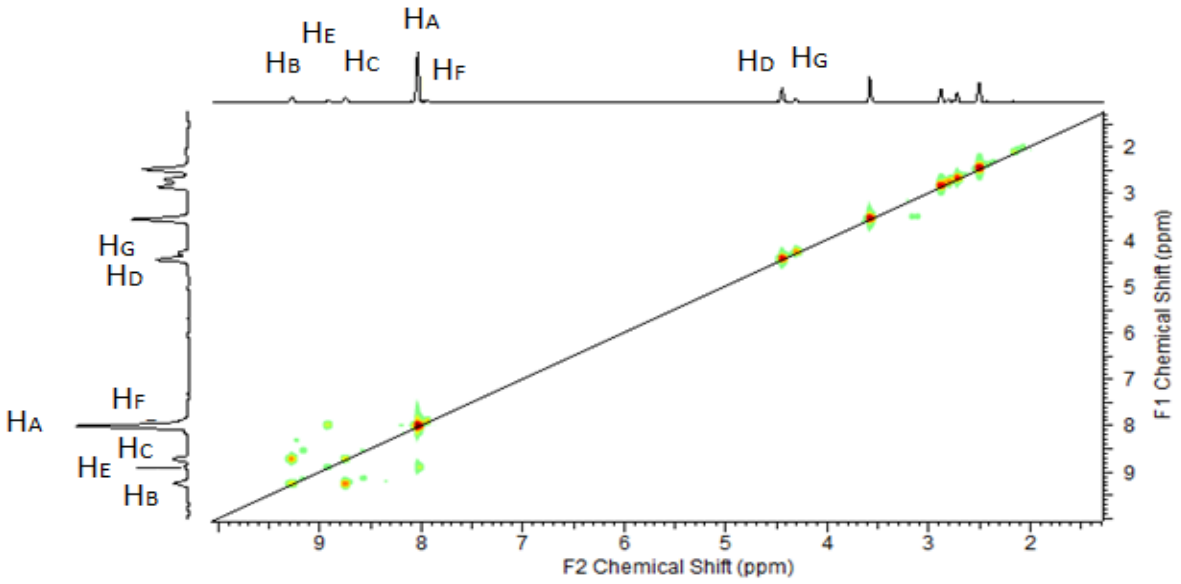

Figure 4.15 ^{1}H-^{1}H COSY spectrum of the digested product. The resonances belonging to H_2bdc (H_A), methyl viologen (H_B, H_C and H_D) and the further unidentified resonances (H_E, H_F, and H_G) are labelled.

The NOESY spectrum is shown in Figure 4.16. In this spectrum the protons from H_F are hidden completely beneath those of H_A in D_2bdc and are therefore not labelled. Cross-peaks can be observed between H_D and H_B, showing the H_D methyl protons on the viologen to be close in space to the aromatic H_B protons. A similar cross-peak is also observed between H_G and H_E of the unknown species suggesting a similar correlation is present between these protons.

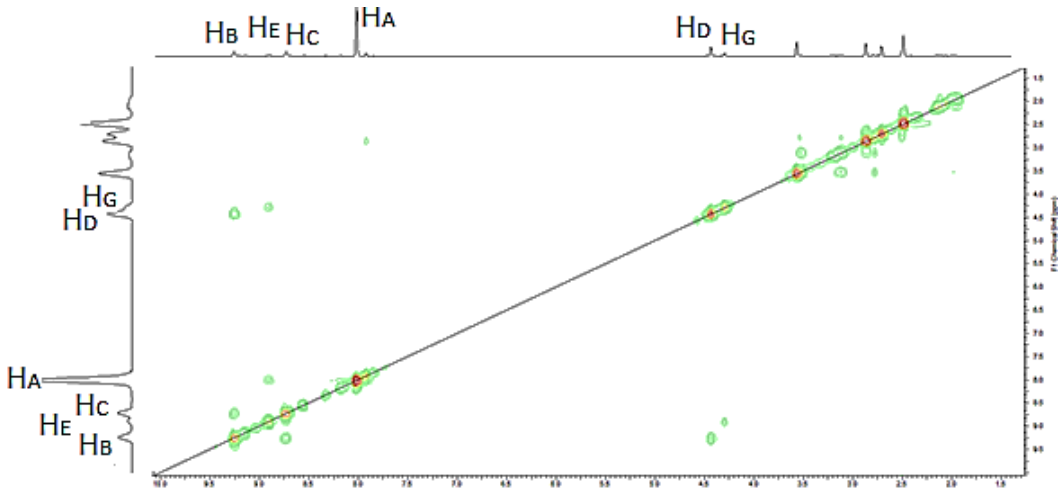

Figure 4.16 NOESY spectrum of the digested product. The resonances belonging to H_2bdc (H_A), methyl viologen (H_B, H_C and H_D) and the further unidentified resonances (H_E, and H_G) are labelled.

Overall, the ^{1}H NMR spectroscopy studies have illustrated that the unidentified resonances present in the digestion of the product correspond to two sets of protons in the aromatic region, and one set of protons in the aliphatic region. The aromatic protons are correlated to one another through covalent bonding, whilst the aliphatic protons are correlated to one set of aromatic protons through

space. This mirrors the proton resonances observed for the methyl viologen species, suggesting the unidentified compound has similar proton environments and symmetry.

A possible identity of the species found in the ^{1}H NMR spectroscopy studies of the product is the protonated $HMVH^{2+}$ species, the singly protonated species, HMV^+, is hypothesised to form when methyl viologen radicals are heated in acidic conditions. However, no spectral evidence for HMV^+ has been reported. (Figure 4.17).[20]

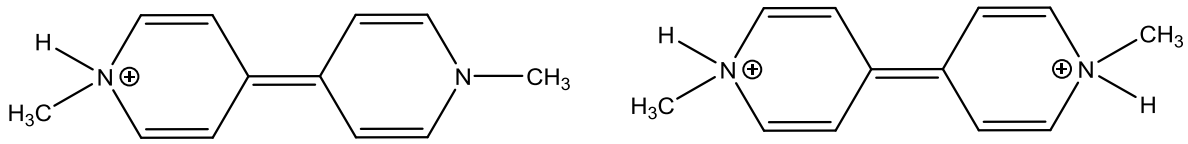

Figure 4.17 Proposed structure of the singly protonated HMV^+ and doubly protonated $HMVH^{2+}$.

The product formed from the reaction carried out at 120 ^{o}C is blue in colour, indicating that the methyl viologen undergoes a reduction during the formation of the MOF, producing the methyl viologen radical cation. Both H_2bdc and $Zn(NO_3)_2$ are acidic sources which may account for the formation of $HMVH^{2+}$ during the MOF synthesis. The symmetry and proton environments of $HMVH^{2+}$ correspond to the observed resonances in the ^{1}H NMR spectroscopy studies.

Analysis of the integrated ^{1}H NMR spectrum (refer to Figure 4.13) gives an approximate D_2bdc:MV^{2+}:$HMVH^{2+}$ ratio of 83:10:7 in the digestion mixture. As the $[Zn_3(bdc)_4]^{2-}$ framework contains four bdc ligands, this ratio gives an overall formula of $[MV]_{0.44}[HMVH]_{0.36}[NH_2(CH_3)_2]_{0.4}[Zn_3(bdc)_4]$, excluding any guest solvent present within the pores. In order to charge balance this formula $[NH_2(CH_3)_2]^+$ counter-ions are included. Spectroscopic evidence of the presence of $[NH_2(CH_3)_2]^+$ counter-ions was not available, as the ^{1}H NMR spectrum of $[NH_2(CH_3)_2]^+$ gives one singlet at a resonance of δ 2.8 ppm, and overlaps with that of the DMF in the product.

Thermogravimetric analysis of the product showed a percentage mass loss of 3.64 % at approximately 120 ^{o}C corresponding to a loss of 2 water molecules, and a percentage mass loss of 9.22 % at approximately 150 ^{o}C corresponding to a loss of 1.2 DMF molecules (see appendix A4.1.2). No mass loss is observed above 500 ^{o}C and the final percentage weight corresponds to 2.9 ZnO per unit formula. The formula is therefore determined to be $[MV]_{0.44}[HMVH]_{0.36}[NH_2(CH_3)_2]_{0.4}[Zn_3(bdc)_4]\cdot 2H_2O\cdot 1.2DMF$.

The stability of the methyl viologen radicals within $[MV]_{0.44}[HMVH]_{0.36}[NH_2(CH_3)_2]_{0.4}[Zn_3(bdc)_4]\cdot 2H_2O\cdot 1.2DMF$ was investigated. When synthesised, the crystals are blue in colour, however upon exposure to air, the crystals turn orange within 5-10 minutes indicating oxidation of the methyl

viologen radical cationic species to the methyl viologen dicationic species (Figure 4.18). This is in contrast to the [MV][Zn_3ip_4] system which, once in its radical form, is stable in air for weeks.[18]

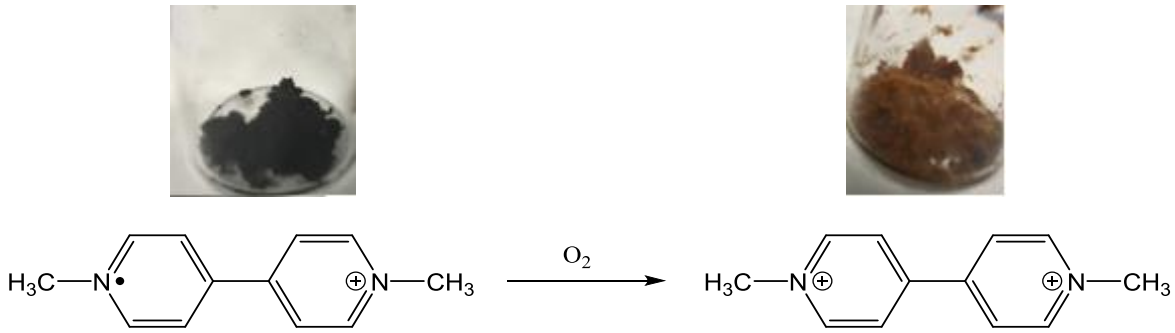

Figure 4.18 Images of the as-synthesised, blue crystals of $[MV]_{0.44}[HMVH]_{0.36}[NH_2(CH_3)_2]_{0.4}[Zn_3(bdc)_4]\cdot 2H_2O\cdot 1.2DMF$ which contain $MV^{+\bullet}$ and the orange crystals which form over time in air, containing MV^{2+}. The schematic representation of the oxidation of $MV^{+\bullet}$ is also shown.

Regeneration of the $MV^{+\bullet}$ species was achieved through heating of the orange crystals to a temperature of 120 °C in oxygen-free conditions or by UV light irradiation in the absence of oxygen. Under either of these conditions the orange crystals undergo a colour change to blue which is reversed upon exposure to air. UV irradiation was completed using a 125 W mercury lamp in an immersion well photochemical reactor producing light of λ = 365-366 nm. A colour change from orange to blue was observed after 2 hours (Figure 4.19).

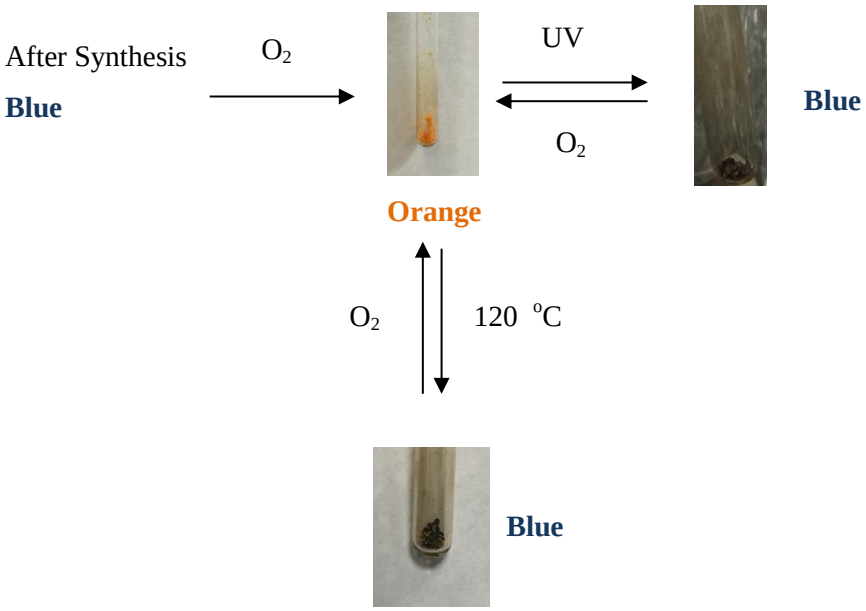

Figure 4.19 Thermochromic and photochromic behaviour of $[[MV]_{0.44}[HMVH]_{0.36}[NH_2(CH_3)_2]_{0.4}[Zn_3(bdc)_4]\cdot 2H_2O\cdot 1.2DMF$ shown in photographic images.

Electron paramagnetic resonance (EPR) spectroscopy was carried out on solid state samples of $[MV]_{0.44}[HMVH]_{0.36}[NH_2(CH_3)_2]_{0.4}[Zn_3(bdc)_4]\cdot 2H_2O\cdot 1.2DMF$ in both the blue and orange forms. The spectrum of the blue crystals (taken after synthesis and kept in oxygen free conditions) is shown in Figure 4.20. The signal at g = 1.99 is indicative of an organic radical species, confirming that the included methyl viologen counter-ions are in present as $MV^{+\bullet}$. Further details about the environment of the radical could not be obtained as the solid state of the sample prevents hyperfine detail from being achieved in the EPR spectrum.

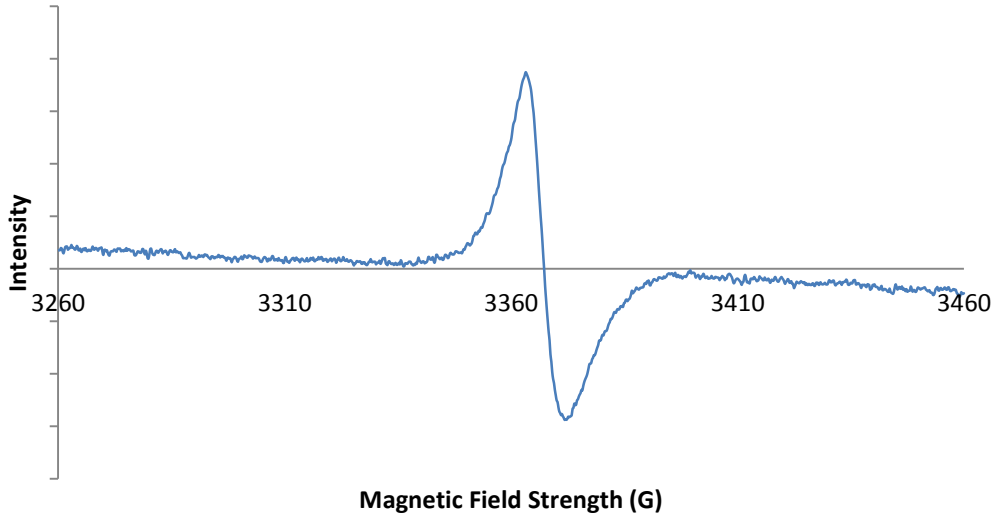

Figure 4.20 EPR spectrum of blue crystals of $[MV]_{0.44}[HMVH]_{0.36}[NH_2(CH_3)_2]_{0.4}[Zn_3(bdc)_4]\cdot 2H_2O\cdot 1.2DMF$.

The spectrum of the orange crystals, obtained after leaving blue $[MV]_{0.44}[HMVH]_{0.36}[NH_2(CH_3)_2]_{0.4}[Zn_3(bdc)_4]\cdot 2H_2O\cdot 1.2DMF$ crystals in air overnight, is shown in Figure 4.21. The absence of any signal in this spectrum indicates that no radical species is present, and the methyl viologen is in its dicationic, MV^{2+} state.

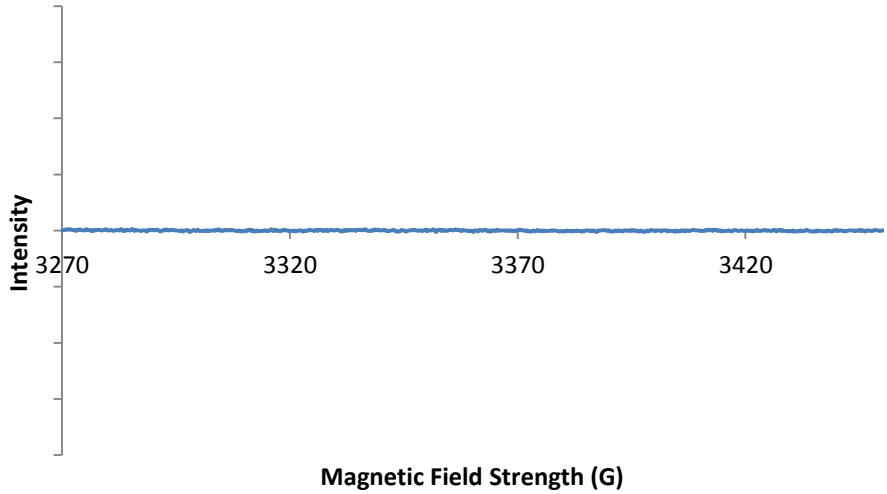

Figure 4.21 EPR spectrum of orange crystals of $[MV]_{0.44}[HMVH]_{0.36}[NH_2(CH_3)_2]_{0.4}[Zn_3(bdc)_4]\cdot 2H_2O\cdot 1.2DMF$.

Structure description of $[MV]_{0.44}[HMVH]_{0.36}[NH_2(CH_3)_2]_{0.4}[Zn_3(bdc)_4]\cdot 2H_2O\cdot 1.2DMF$, **9a**

A crystal of $[MV]_{0.44}[HMVH]_{0.36}[NH_2(CH_3)_2]_{0.4}[Zn_3(bdc)_4]\cdot 2H_2O\cdot 1.2DMF$, **9a** was suitable for single crystal X-ray diffraction analysis. The crystal was blue, indicating the methyl viologen was in its radical form, and the crystal was mounted in oil and kept under nitrogen during the data collection. Observations at the end of the data collection showed the crystal to still be blue in colour. The structure of **9a** is found to crystallise in the monoclinic space group *C*2/*c* (Table 4.1).

Table 4.1 Crystal data for $[MV]_{0.44}[HMVH]_{0.36}[NH_2(CH_3)_2]_{0.4}[Zn_3(bdc)_4]\cdot 2H_2O\cdot 1.2DMF$, **9a**

Identification code	**9a**
Empirical formula	$C_{47.5}H_{43.02}N_{3.7}O_{17.7}Zn_3$
Formula weight	1144.98
Temperature/K	150.00(10)
Crystal system	monoclinic
Space group	*C*2/*c*
a/Å	32.8285(7)
b/Å	9.6716(2)
c/Å	18.4076(4)
α/°	90
β/°	94.7250(19)
γ/°	90
Volume/Å^3	5824.6(2)
Z	4
ρ_{calc}g/cm^3	1.306
μ/mm^{-1}	2.005
F(000)	2342.0
Crystal size/mm^3	0.15 × 0.073 × 0.056
Radiation	Cu *K*α (λ = 1.54184)
2θ range for data collection/°	5.4 to 145.84
Index ranges	$-39 \leq h \leq 35$, $-11 \leq k \leq 11$, $-22 \leq l \leq 21$
Reflections collected	13234
Independent reflections	5656 [R_{int} = 0.0218, R_{sigma} = 0.0292]
Data/restraints/parameters	5656/126/375
Goodness-of-fit on F^2	1.068
Final *R* indexes [$I>=2\sigma(I)$]	R_1 = 0.0458, wR_2 = 0.1418
Final *R* indexes [all data]	R_1 = 0.0505, wR_2 = 0.1466
Largest diff. peak/hole / e Å^{-3}	1.27/-0.74

From the crystallographic analysis, the asymmetric unit of **9a** comprises of two zinc atoms, Zn1 at full occupancy and Zn2 with site occupancy of 50 %, one complete and two half bdc ligands. One DMF molecule with occupancy of 50 % and half of a $MV^{+\bullet}$/$HMVH^{2+}$ overlaid with one another with a combined site occupancy of 80 % are also present in the asymmetric unit (Figure 4.22).

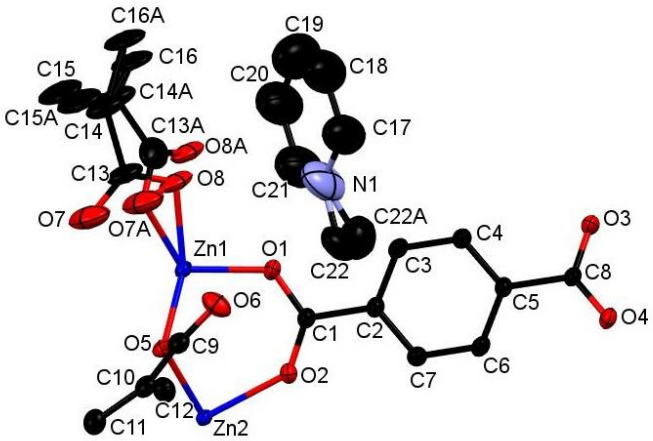

Figure 4.22 The asymmetric unit of **9a** with an ellipsoid probability of 40 %. Hydrogen atoms and the DMF molecule in the asymmetric unit have been omitted for clarity.

The half bdc ligand comprising of C13-C16 and O7-O8 is disordered over two positions within the asymmetric unit. This disorder was modelled by attributing the site occupancies of C13-C16 and O7-O8 to 75 % and C13A-C16A and O7A-O8A to 25 % based on electron density. Geometric restraints were also employed to O-C and C-C distances within the bdc moiety to assist a chemically sensible convergence.

The electron density of the $MV^{+\bullet}$/$HMVH^{2+}$ moieties is smeared; meaning that resolving the two species was not possible, with the exception of the methyl group attached to N1 which is disordered over two positions, C22 and C22A. This methyl group was modelled by attributing site occupancies of C22 and C22A to 44 % and 36 % respectively, informed by the ^{1}H NMR analysis. Due to the smearing of the electron density atomic displacement parameters and N-C and C-C distance restraints were required for the $MV^{+\bullet}$/$HMVH^{2+}$ moieties.

Zn1 lies on general position and displays a distorted tetrahedral geometry whilst Zn2 lies on an inversion centre and displays distorted octahedral geometry through symmetry generation. The SBU of the framework is formed from three zinc atoms and eight carboxylate groups (Figure 4.23).

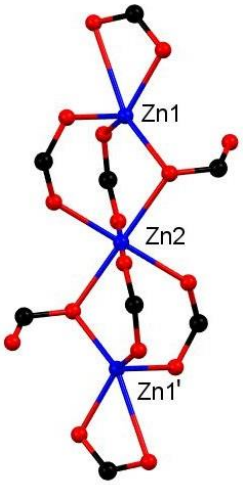

Figure 4.23 The SBU in **9a**. Primed labelled atoms are related to those in the asymmetric unit by the $^{3}/_{2}$-*x*,$^{3}/_{2}$-*y*,1-*z* symmetry operation. Only one disordered bdc component is shown for clarity.

The SBUs are linked together through bdc linkers forming a three-dimensional net. When viewed along the *b*-axis one dimensional channels can be observed which are occupied by DMF, methyl viologen cations and $HMVH^{2+}$ (Figure 4.24). Overall the topology of $[MV]_{0.44}[HMVH]_{0.36}[NH_2(CH_3)_2]_{0.4}[Zn_3(bdc)_4]\cdot 2H_2O\cdot 1.2DMF$ is comparable to that observed in $[NH_2(CH_3)_2]_2[Zn_3(bdc)_4]\cdot DMF\cdot H_2O$.

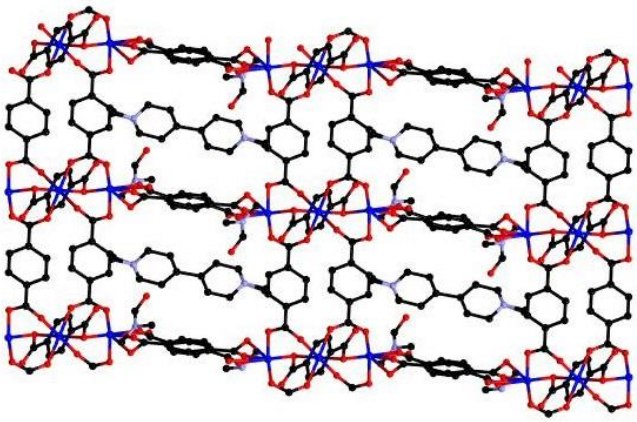

Figure 4.24 View of **9a** down the *b*-axis. Hydrogen atoms are omitted for clarity.

A comparison of the structures of $[MV]_{0.44}[HMVH]_{0.36}[NH_2(CH_3)_2]_{0.4}[Zn_3(bdc)_4]\cdot 2H_2O\cdot 1.2DMF$ and $[MV][Zn_3(ip)_4]$ shows a difference in the methyl viologen geometry. The methyl viologen present in $[MV][Zn_3(ip)_4]$ adopts a planar geometry (Figure 4.25). However, symmetry generation of the $MV^{+\bullet}/HMVH^{2+}$ in $[MV]_{0.44}[HMVH]_{0.36}[NH_2(CH_3)_2]_{0.4}[Zn_3(bdc)_4]\cdot 2H_2O\cdot 1.2DMF$ shows that the rings of the viologen(s) are twisted with respect to one another, with a plane normal to plane normal angle of 80^{o} (Figure 4.25).

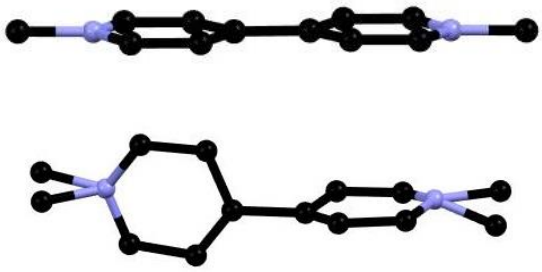

Figure 4.25 The planar methyl viologen in $[MV][Zn_3(ip)_4]$ (top) and the disordered $MV^{+\bullet}/HMVH^{2+}$ in $[MV]_{0.44}[HMVH]_{0.36}[NH_2(CH_3)_2]_{0.4}[Zn_3(bdc)_4]\cdot 2H_2O\cdot 1.2DMF$ **9a** (bottom) showing the twist in the rings relative to one another. Hydrogen atoms have been removed for clarity.

Methyl viologen moieties in the dication state are known to display a twisted geometry, but methyl viologen radical cations are usually planar in their geometry, allowing the stabilisation of the radical across both rings.[21] However, in **9a** we observe a radical species, identified through the blue colour and EPR spectroscopy analysis, and a twisted geometry of the two rings of methyl viologen in the single crystal structure. A possible explanation is that of steric interactions between the methyl viologen and the framework.

The pores in $[MV][Zn_3(ip)_4]$ are square channels in which the methyl viologen cations lie parallel to the ip ligands in the framework, pointing down the channels and stacking end-to-end (Figure 4.26). In **9a** the pores are narrower and rectangular in shape, and the methyl viologen cations stack with the rings parallel to one another in a face-to-face arrangement. The narrower pores of the $[Zn_3(bdc)_4]^{2-}$ framework and the stacking arrangement of the $MV^{+\bullet}/HMVH^{2+}$ cations make it conceivable that steric interactions may play a role in the observed ring twist.

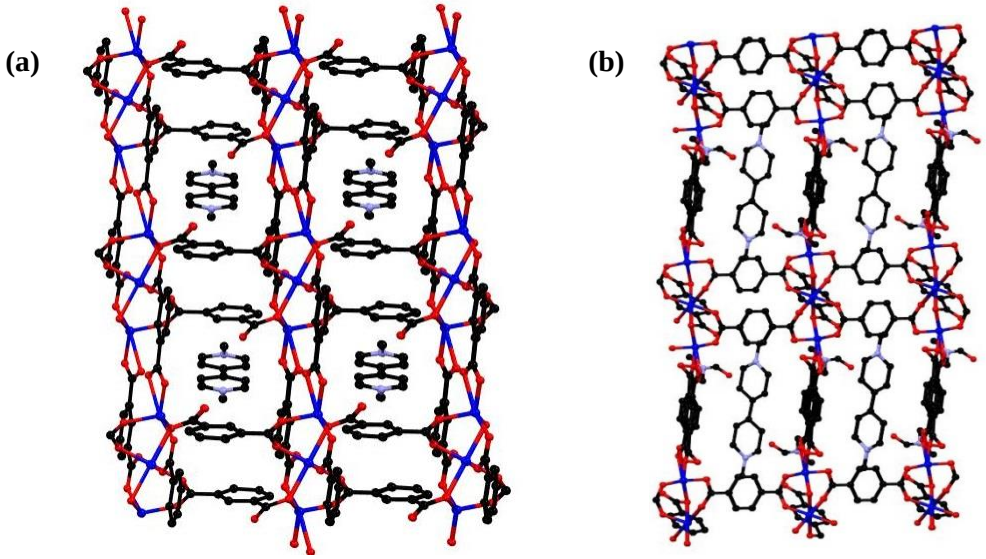

Figure 4.26 (a) The structure of $[MV][Zn_3(ip)_4]$ showing the one-dimensional channels occupied by methyl viologen and **(b)** the structure of **9a** showing the one-dimensional rectangular channels occupied by methyl viologen. All hydrogen atoms and solvent molecules have been omitted for clarity.

An un-coordinated oxygen atom from a carboxylate group on a bdc ligand is directed towards the nitrogen atom on the methyl viologen in **9a**, a similar arrangement to that observed in the $[MV][Zn_3(ip)_4]$ structure (Figure 4.27). The O···N distance is 3.635(9) Å, and within the expected value for a charge transfer donor-acceptor pair (less than 3.7 Å). The radical formation of the methyl viologen is therefore likely to occur due to electron transfer between the framework and the methyl viologen dication during the synthesis of the MOF.

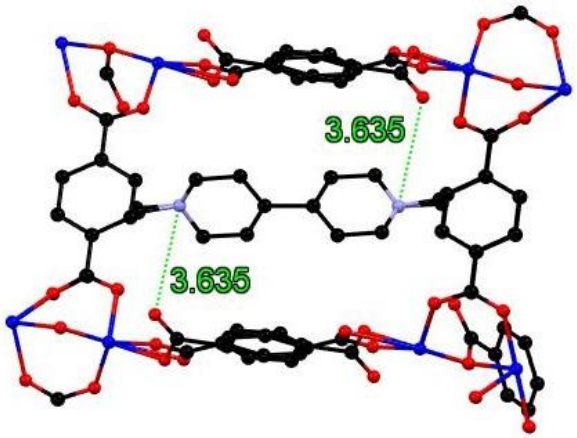

Figure 4.27 The O···N distance shown in Å between the un-coordinated oxygen of a carboxylate group on the bdc ligand and the nitrogen of the methyl viologen in **9a**. Hydrogen atoms and DMF solvent molecules have been omitted for clarity.

The powder X-ray diffraction pattern generated from the single crystal structure of **9a** shows some similarities in peak positions to that of the experimental PXRD trace (see appendix A4.2.1). The relative intensities of peaks common to both diffraction patterns are different, possibly due to differences in the solvent content between the single crystal model and the bulk sample.

4.3.3 Synthesis of $[MV]_{0.8}[NH_2(CH_3)_2]_{0.4}[Zn_3(bdc)_4]$ by *in situ* generation of methyl viologen

A second preparatory route for the viologen containing MOF was investigated with the aim of avoiding the formation of any by-products. In this synthesis viologen diacetic acid dichloride was used as the source of methyl viologen. As the methyl viologen is formed *in situ* during the MOF synthesis it was anticipated that the $HMVH^{2+}$ by-product may be prevented from forming within the timeframe of the reaction. The reaction was carried out in DMF at 85 ^oC and in DMF at 120 ^oC for 48 hours. The resulting products were orange and blue in colour respectively. PXRD traces of products from both reactions were compared to the powder diffraction pattern of $[MV]_{0.44}[HMVH]_{0.36}[NH_2(CH_3)_2]_{0.4}[Zn_3(bdc)_4]\cdot 2H_2O\cdot 1.2DMF$ (Figure 4.28).

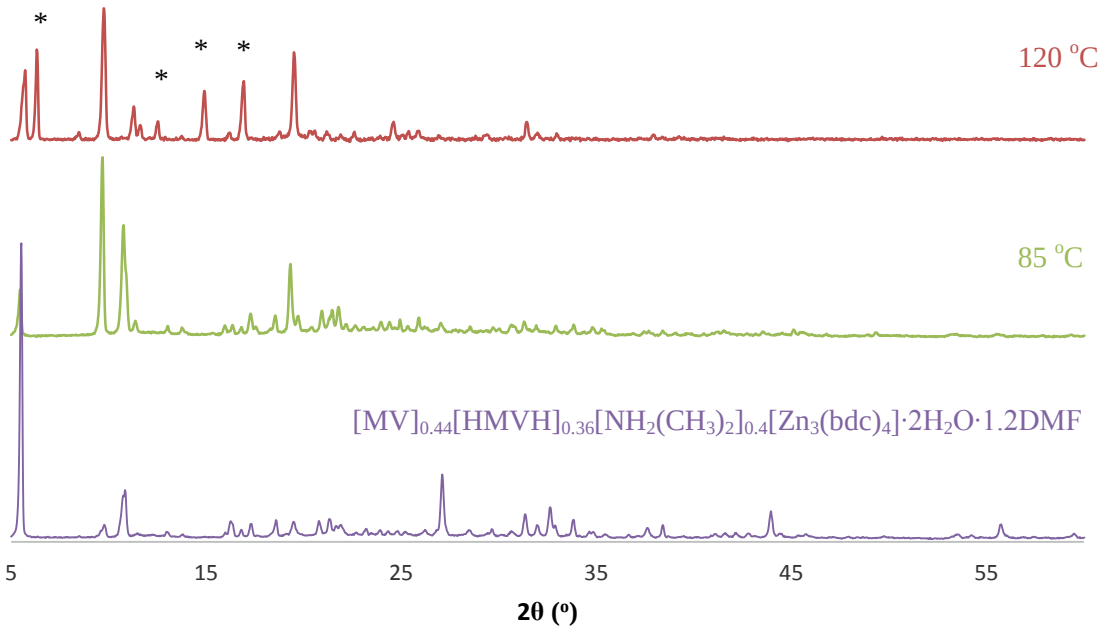

Figure 4.28 Powder X-ray diffraction patterns of products formed from the reaction of viologen diacetic acid dichloride with H_2bdc and zinc nitrate at 85 °C and 120 °C. The PXRD pattern of $[MV]_{0.44}[HMVH]_{0.36}[NH_2(CH_3)_2]_{0.4}[Zn_3(bdc)_4]\cdot 2H_2O\cdot 1.2DMF$ formed from the reaction with methyl viologen diiodide at 120 °C is also shown.

The product formed with viologen diacetic acid dichloride at 85 °C shows peaks in similar positions to those in $[MV]_{0.44}[HMVH]_{0.36}[NH_2(CH_3)_2]_{0.4}[Zn_3(bdc)_4]\cdot 2H_2O\cdot 1.2DMF$. The deviations in relative intensities of the peaks can be explained through possible orientation effects or differences in solvent inclusion between the two products. Whilst the product formed with viologen diacetic acid dichloride at 120 °C shows peaks that correspond with those in $[MV]_{0.44}[HMVH]_{0.36}[NH_2(CH_3)_2]_{0.4}[Zn_3(bdc)_4]\cdot 2H_2O\cdot 1.2DMF$, there are additional peaks present, labelled with * in Figure 4.28. This suggests possible structural differences or the presence of a second phase in this product.

^{1}H NMR spectroscopy analysis was carried out on the product formed at 85 °C. The sample was dried at 120 °C prior to being digested in a d_6-DMSO/DCl mixture. The spectrum is shown in Figure 4.29 and shows the presence of D_2bdc (δ 8.02 ppm) and methyl viologen (δ 9.33 ppm, δ 8.80 ppm and δ 4.45 ppm). No evidence for the formation of the $HMVH^{2+}$ species was found under these reaction conditions and the absence of the CH_2 proton resonance from viologen diacetic acid (which occurs at δ 5.76 ppm in d_6-DMSO/DCl) suggests that complete conversion to methyl viologen occurs during the reaction.

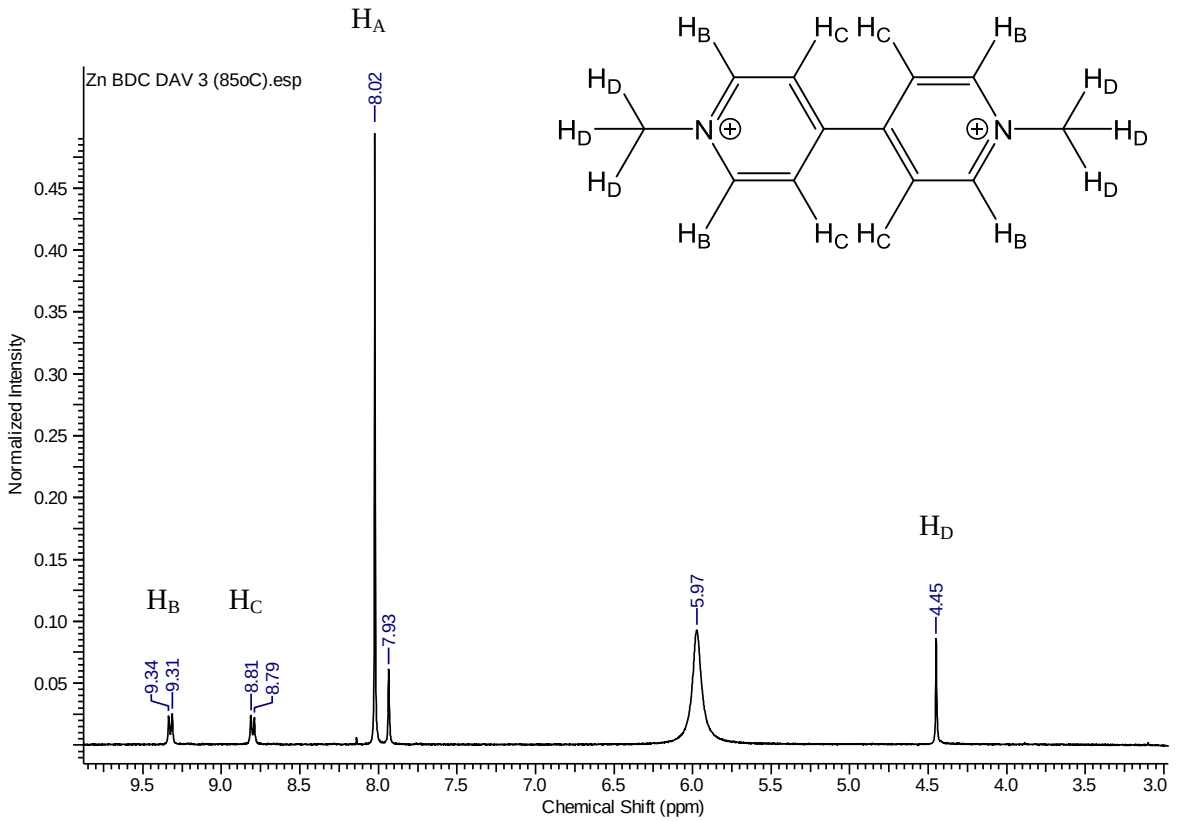

Figure 4.29 ^{1}H NMR spectrum of the product formed from the reaction at 85 ^{o}C. The resonance at δ 5.97 ppm originates from water present in the acidic digestion.

Analysis of the integrated resonances at δ 9.33 ppm and δ 8.02 ppm show a D_2bdc:MV ratio of 82.5:17.5, giving a product formula of $[MV]_{0.8}[NH_2(CH_3)_2]_{0.4}[Zn_3(bdc)_4]$ excluding solvent, where the dimethyl ammonium cations are present to charge balance the formula. A comparison to the product formed from the reaction with methyl viologen diiodide, $[MV]_{0.44}[HMVH]_{0.36}[NH_2(CH_3)_2]_{0.4}[Zn_3(bdc)_4]\cdot 2H_2O\cdot 1.2DMF$, shows a similar total viologen content; with 0.8 viologen moieties per unit formula.

It can therefore be concluded that the framework $[Zn_3(bdc)_4]^{2-}$can be formed with methyl viologen counter-ions either through the reaction of viologen diacetic acid dichloride or through direct synthesis with methyl viologen diiodide although some conversion of the methyl viologen to $HMVH^{2+}$ occurs under these latter conditions.

4.3.4 Synthesis and characterisation of $[MV]_{0.5}[Zn(btc)]\cdot DMF$

A third zinc-based framework, $[Zn(btc)]^-$ (btc = 1,3,5-benzenetricarboxylate) was investigated for its ability to include methyl viologen counter-ions within the pores. The framework was targeted for this investigation due to its anionic nature and rectangular one-dimensional channels.[22]

$[NH_2(CH_3)_2][Zn(btc)]\cdot DMF$ is reported as being synthesised by combining zinc acetate with 1,3,5-benzenetricarboxylic acid in DMF at 140 ^oC over 48 hours. The SBU contains two zinc atoms which are bridged by two bidentate carboxylate groups. Two further carboxylate groups co-ordinate in a unidentate manner to each zinc centre (Figure 4.30). The SBUs are linked together by the btc ligands to give an overall three-dimensional network which contains one-dimensional rectangular channels (Figure 4.30).

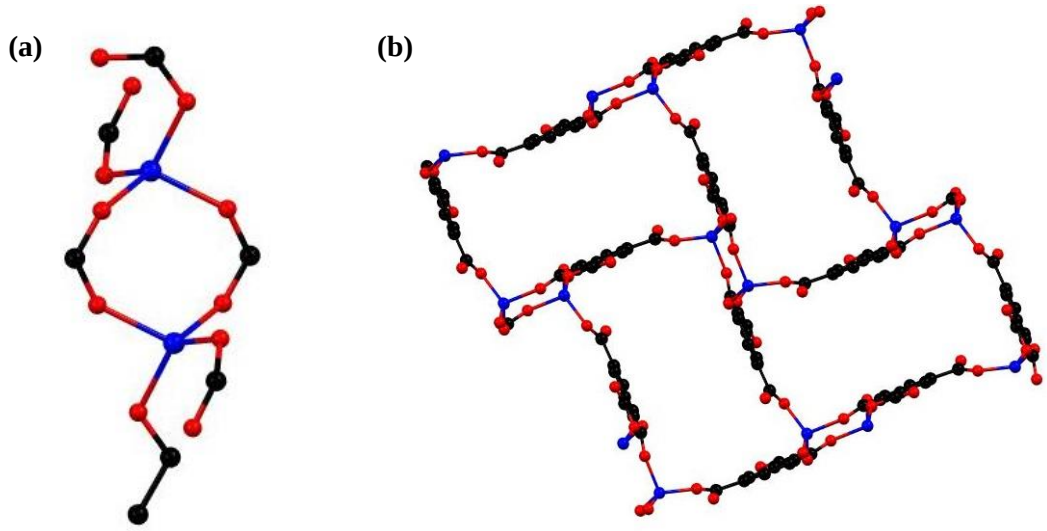

Figure 4.30 Part of the crystal structure of $[NH_2(CH_3)_2][Zn(btc)]\cdot DMF$ showing **(a)** the SBU and **(b)** the one dimensional channels of the network viewed along the *a*-axis. Hydrogen atoms and solvent/counter-ions have been removed for clarity.

The synthesis of the methyl viologen derivative of $[Zn(btc)]^-$ was carried out by combining zinc nitrate with 1,3,5-benzenetricarboxylic acid and methyl viologen diiodide in DMF at 120 ^oC over 48 hours. The reaction yielded blue crystals, suggesting the presence of methyl viologen in its radical cation form. The synthesis was also carried out using a similar method but heating at 85 ^oC for 48 hours and a microcrystalline, orange product was obtained, typically indicative of the structure containing methyl viologen in its dicationic form. Both products were analysed by powder X-ray diffraction and the resulting PXRD patterns are shown in Figure 4.31 alongside that for $[NH_2(CH_3)_2][Zn(btc)]\cdot DMF$.

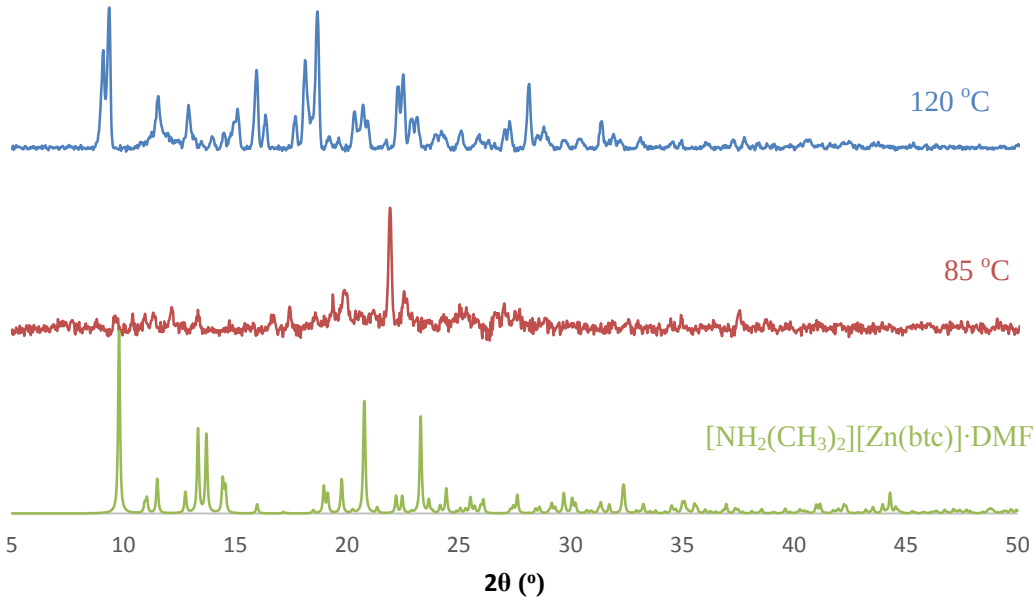

Figure 4.31 Powder X-ray diffraction patterns of the products formed from the reaction of $Zn(NO_3)_2$, H_3btc and MVI_2 at 85 °C and 120 °C. The powder diffraction trace for $[NH_2(CH_3)_2][Zn(btc)]\cdot DMF$ is also shown.

The microcrystalline product from the reaction carried out at 85 °C shows few peaks in the resulting powder diffraction pattern and high background noise, suggesting a poor crystallinity and no further analysis was undertaken on this product. The product from the reaction carried out at 120 °C has a powder diffraction pattern with multiple peaks and a comparison of this powder diffraction pattern to that of $[NH_2(CH_3)_2][Zn(btc)]\cdot DMF$ shows common peaks at 2θ values of 9.3°, 11.5°, 12.8° and 15.9°. However, distinct differences between the two powder diffraction patterns are clear, with multiple additional peaks in the experimental pattern suggesting structural differences between the two compounds.

^{1}H NMR spectroscopy analysis was carried out on an acid digested sample of the product formed at 120 °C. The digestion mixture was orange indicating the methyl viologen to be in its dicationic form. The sample was first dried at 120 °C for 15 minutes prior to being digested in a d_6-DMSO/DCl mixture. The resulting ^{1}H NMR spectrum is shown in Figure 4.32.

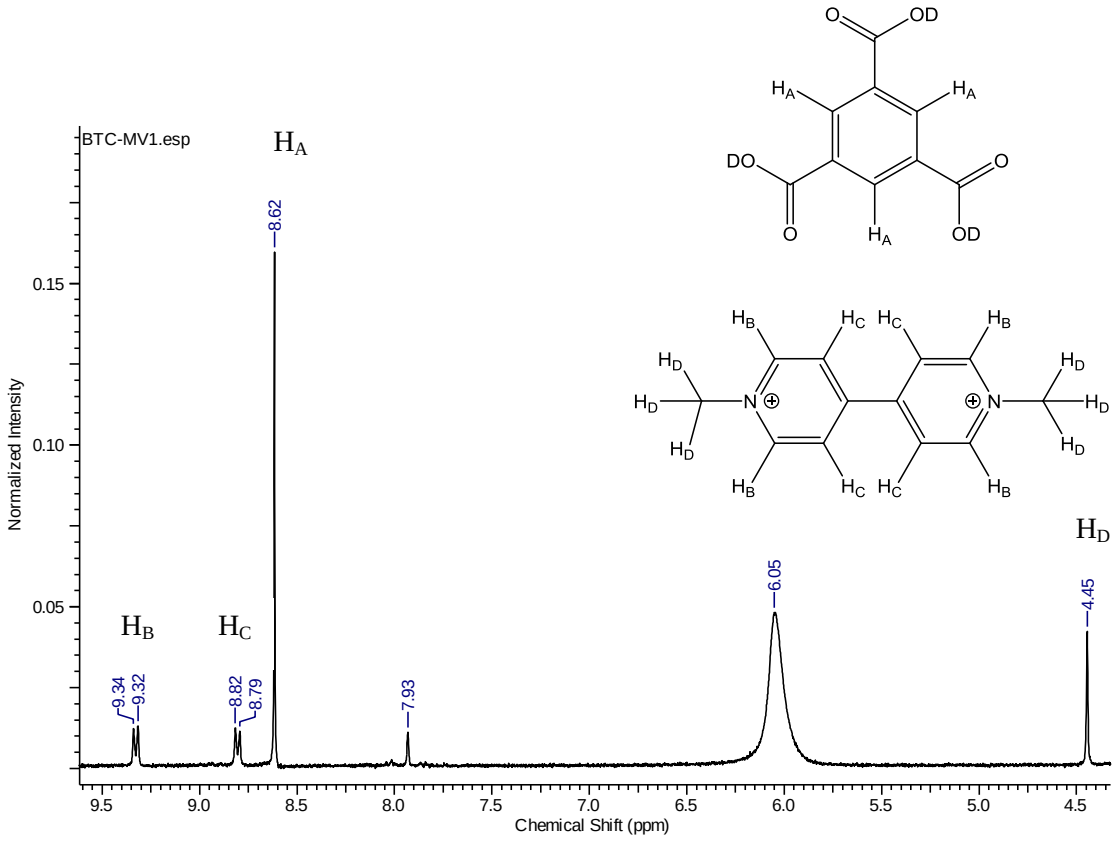

Figure 4.32 ^{1}H NMR spectrum of the acid digested product formed from the reaction of $Zn(NO_3)_2$, H_3btc and MVI_2 at 120 ^{o}C.

Both D_3btc and methyl viologen were found to be present in the digested mixture. The resonance at δ 8.62 ppm corresponds to the aromatic protons of the D_3btc compound, whilst resonances at δ 9.33 ppm, δ 8.81 ppm and δ 4.45 ppm correspond to the protons of methyl viologen. The resonances at δ 7.93 ppm and δ 6.05 ppm originate from residual DMF and water respectively. Analysis of the integrated resonances for D_3btc and methyl viologen show a H_3btc:MV ratio of 73:27 in the digestion mixture.

Structure description of $[MV]_{0.5}[Zn(btc)]\cdot DMF$ **9b**

A blue crystal of the product (**9b**) was suitable for single crystal X-ray diffraction analysis. The structure crystallised in the monoclinic space group $P2_1/n$ (Table 4.2).

Table 4.2 Crystal data for $[MV]_{0.5}[Zn(btc)]\cdot DMF$ **9b**

Identification code	**9b**
Empirical formula	$C_{36}H_{34}N_4O_{14}Zn_2$
Formula weight	877.41
Temperature/K	150.01(10)
Crystal system	monoclinic
Space group	$P2_1/n$
a/Å	9.6981(2)
b/Å	16.1078(5)
c/Å	11.5458(4)
α/°	90
β/°	90.923(3)
γ/°	90
Volume/Å^3	1803.41(9)
Z	2
ρ_{calc}g/cm^3	1.616
μ/mm^{-1}	2.305
F(000)	900.0
Crystal size/mm^3	0.08 × 0.03 × 0.025
Radiation	Cu$K\alpha$ (λ = 1.54184)
2θ range for data collection/°	9.426 to 146.132
Index ranges	$-6 \leq h \leq 11$, $-19 \leq k \leq 19$, $-14 \leq l \leq 14$
Reflections collected	7613
Independent reflections	3527 [R_{int} = 0.0382, R_{sigma} = 0.0515]
Data/restraints/parameters	3527/10/285
Goodness-of-fit on F^2	1.045
Final R indexes [I>=2σ (I)]	R_1 = 0.0430, wR_2 = 0.1085
Final R indexes [all data]	R_1 = 0.0559, wR_2 = 0.1157
Largest diff. peak/hole / e Å^{-3}	0.74/-0.55

The asymmetric unit comprises of one zinc atom, one btc ligand, one DMF solvent molecule disordered over two positions and half a methyl viologen (Figure 4.33).

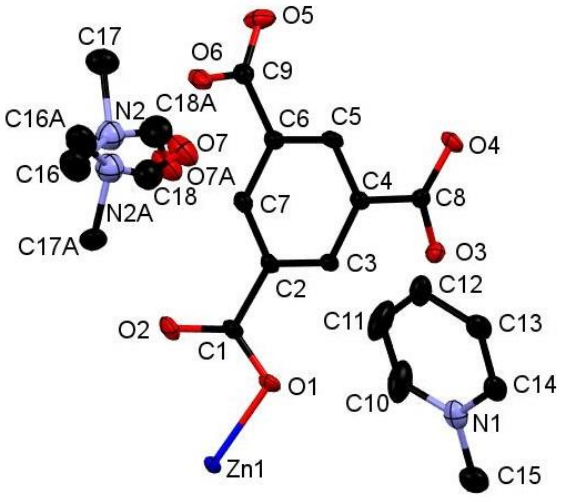

Figure 4.33 The asymmetric unit of **9b**. Ellipsoids have been calculated with an ellipsoid probability of 40 %. Hydrogen atoms have been omitted for clarity.

The half methyl viologen moiety within the asymmetric unit lies about an inversion centre, giving rise to symmetry generation of a full methyl viologen cation. Crystallographically the structure of **9b** is therefore attributed to $[MV]_{0.5}[Zn(btc)]\cdot DMF$. There is a discrepancy between this formula and the H_3btc:MV ratio of 73:27 found through ^{1}H NMR spectroscopy analysis. Further discussion of this will follow.

The disordered DMF in the asymmetric unit has site occupancies of 75 % for C16, C17, C18, N2, O7 and 25 % for C16A, C17A, C18A, N2A and O7A. Geometric restraints were applied to C-N and C-O bond distances to assist convergence. Atomic displacement parameter restraints of the smaller component were also employed.

The btc ligand co-ordinates through all three carboxylate groups to four different zinc atoms. Two of the carboxylate groups are monodentate, binding through O1 and O6, and the third carboxylate group binds to two zinc atoms through both O3 and O4 (Figure 4.34). There was no crystallographic evidence for the presence of hydrogen atoms on non-coordinating oxygens O2 and O5. The zinc atom is in a distorted tetrahedral co-ordination environment, co-ordinating to four carboxylate groups from four different btc ligands. The SBU is formed from dimeric zinc units bridged by two carboxylate groups (Figure 4.34).

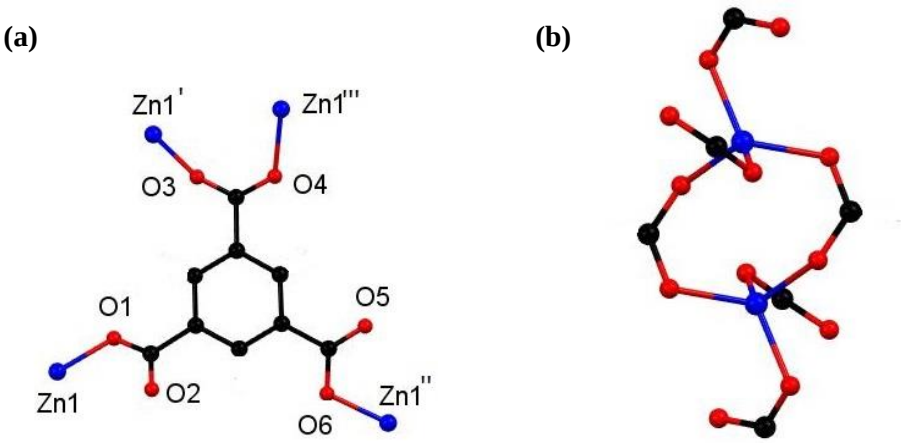

Figure 4.34 (a) The co-ordination environments of the btc ligand in **9b**, primed, double primed and triple primed atoms are related to those in the asymmetric unit by the $1 - x$, $1 - y$, $2 - z$, $½ + x$, $½ - y$, $z - ½$, and $1 + x$, y, z symmetry operations respectively. **(b)** The dimeric SBU.

The dimeric SBUs are linked together by the btc linkers to form a three-dimensional network containing channels along the *a*-axis (Figure 4.35). The channels are occupied by methyl viologen cations which lie in a near-perpendicular arrangement to the btc ligands of the framework. The methyl viologens stack down the channels, alternating between layers of DMF solvent molecules (Figure 4.35).

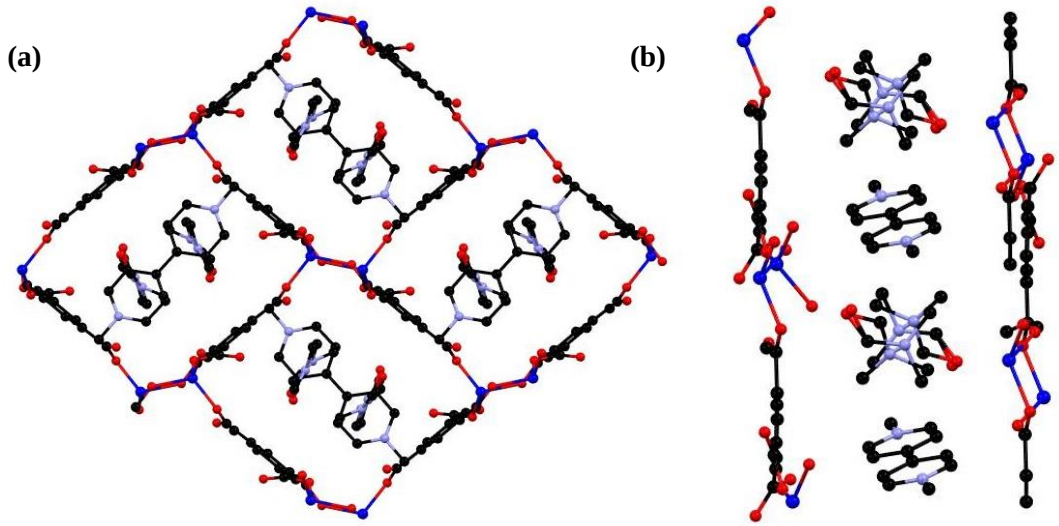

Figure 4.35 The one-dimensional pores in **9b** viewed down **(a)** the *a*-axis and **(b)** the *b*-axis. All hydrogen atoms have been omitted for clarity. The DMF molecules within the pores are disordered over two positions.

One non-coordinating oxygen atom from the btc ligand is directed towards the nitrogen atom of the methyl viologen (Figure 4.36). The O···N distance is 2.972(4) Å, indicating a charge transfer interaction between the framework and methyl viologen, in a similar manner to that observed in **9a**.

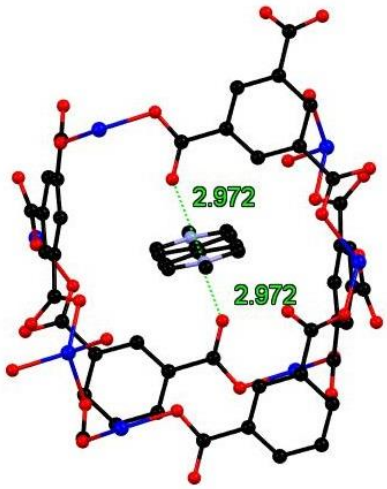

Figure 4.36 Part of the structure of **9b** showing the distance between the methyl viologen nitrogen atoms and un-coordinating oxygen atoms of btc. Hydrogen atoms are omitted for clarity.

The $[MV]_{0.5}[Zn(btc)]\cdot DMF$ structure displays a similar framework connectivity to that of $[NH_2(CH_3)_2][Zn(btc)]\cdot DMF$. Both systems crystallise in the monoclinic space group $P2_1/n$ but display some differences in their unit cell parameters (Table 4.3). This is consistent with the differences in powder diffraction patterns observed between the two species.

Table 4.3 Crystallographic data showing the unit cell parameters for $[MV]_{0.5}[Zn(btc)]\cdot DMF$ **9b** and $[NH_2(CH_3)_2][Zn(btc)]\cdot DMF$.

Identification code	**9b**	$[NH_2(CH_3)_2][Zn(btc)]\cdot DMF$
Empirical formula	$C_{36}H_{34}N_4O_{14}Zn_2$	$C_{28}H_{36}N_4O_{14}Zn_2$
Formula weight	877.41	391.67
Temperature/K	150.01(10)	188 K
Crystal system	monoclinic	monoclinic
Space group	$P2_1/n$	$P2_1/n$
a/Å	9.6981(2)	9.4550(6)
b/Å	16.1078(5)	16.0074(11)
c/Å	11.5458(4)	11.0347(7)
α/°	90	90
β/°	90.923(3)	98.4660(10)
γ/°	90	90
Volume/Å^3	1803.41(9)	1651.90(19)
Z	2	2

A clear difference between the two structures can be seen in the pore geometries; in $[NH_2(CH_3)_2][Zn(btc)]\cdot DMF$ rectangular pores are observed whilst in $[MV]_{0.5}[Zn(btc)]\cdot DMF$ the pores are closer to being square-shaped (Figure 4.37).

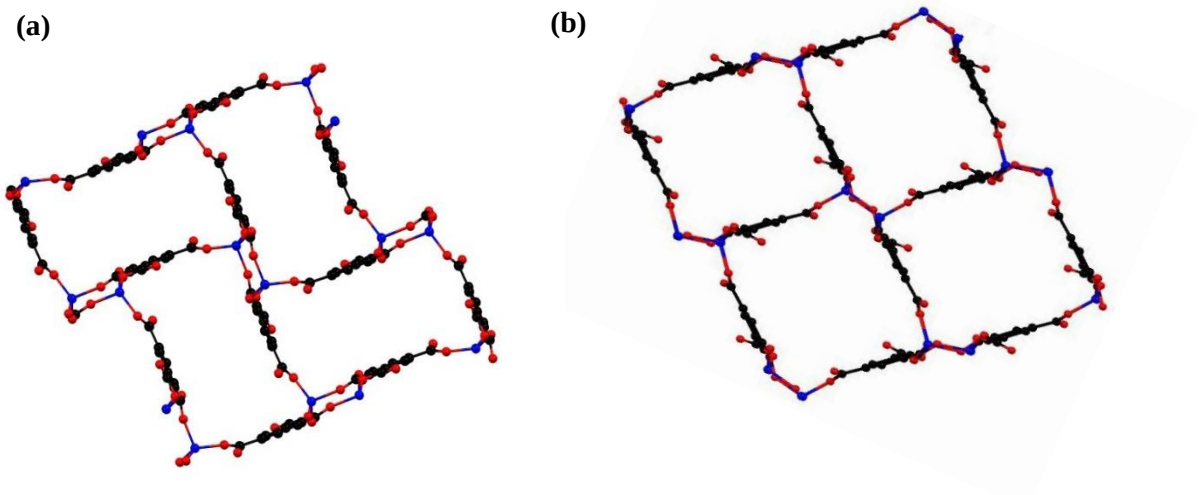

Figure 4.37 The pore structures of **(a)** $[NH_2(CH_3)_2][Zn(btc)]\cdot DMF$ and **(b)** $[MV]_{0.5}[Zn(btc)]\cdot DMF$ **9b**. All solvent molecules, counter-ions and hydrogen atoms have been omitted for clarity.

This difference in pore geometry can be explained through a compression of the Zn···Zn distances in the dimeric SBU of $[MV]_{0.5}[Zn(btc)]\cdot DMF$, **9b** compared to that of $[NH_2(CH_3)_2][Zn(btc)]\cdot DMF$. The Zn···Zn distance across the SBU of $[NH_2(CH_3)_2][Zn(btc)]\cdot DMF$ is 4.0133(7) Å, whilst in **9b** the zinc atoms are off-set and have a reduced Zn···Zn distance of 3.8250(7) Å (Figure 4.38).

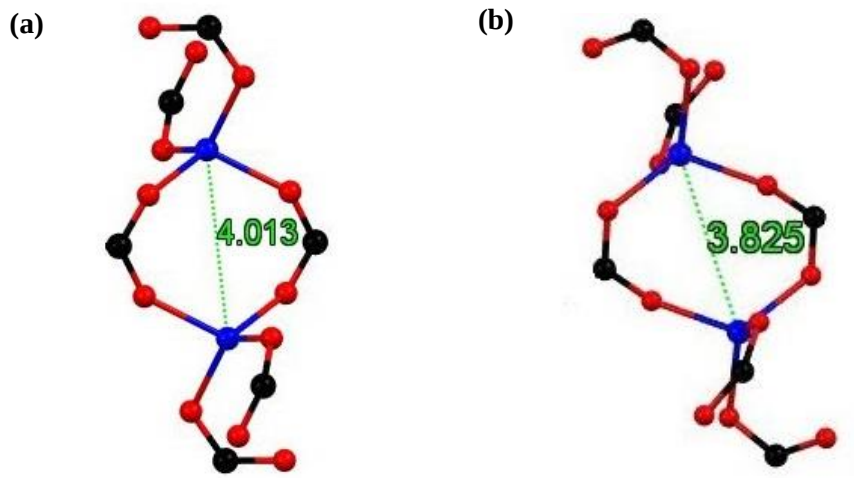

Figure 4.38 (a) The SBU of $[NH_2(CH_3)_2][Zn(btc)]\cdot DMF$[22] and **(b)** the SBU of **9b** showing the Zn···Zn distance in Å. Hydrogen atoms have been omitted for clarity.

The distortion of the dimer within **9b** allows the methyl viologen to reside within the pores of the framework. Without this compression the narrow, rectangular pores displayed by $[NH_2(CH_3)_2][Zn(btc)]\cdot DMF$ may not accommodate the methyl viologen cations.

The powder X-ray diffraction pattern generated from the single crystal structure of **9b** was compared to that of the experimental powder diffraction pattern of the bulk sample (Figure 4.39).

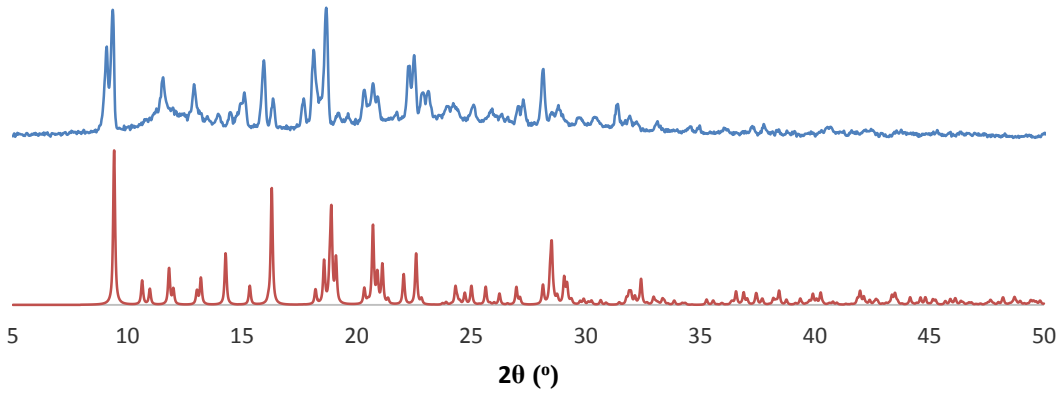

Figure 4.39 Powder X-ray diffraction patterns of **9b** generated from the single crystal structure (bottom) and the experimental powder diffraction pattern of the bulk sample (top).

There is a reasonable match of Bragg peaks for the two structures shown, however, the PXRD trace of the bulk sample shows additional peaks to that of **9b** at 2θ values of 9 °, 14 °, 16 °, 18 ° and 22°. This suggests a second species may be present in the bulk phase and supports the ^{1}H NMR spectroscopy analysis, which showed a discrepancy in the methyl viologen content between the bulk sample and crystallographic structure.

Thermogravimetric analysis of the bulk product found a percentage mass loss of 7.5 % at approximately 150 ^{o}C corresponding to 0.3 DMF molecules per unit formula (see appendix Figure A4.1.3). Crystallographically, **9b** was found to contain one DMF molecule per unit formula. This difference in solvent content between single crystal structure and analysis on the bulk material may be due to the impurity presence in the bulk phase.

The product was found to be blue in colour when synthesised at 120 ^{o}C, indicating the presence of methyl viologen radical cations within the structure. EPR spectroscopy was carried out on the bulk sample to confirm the presence of the radical species. The analysis was carried out on solid state samples of the product and the resulting spectrum is shown in Figure 4.40. The presence of the signal with a g=1.99 value is typical of an organic radical species, supporting the visual observations of a methyl viologen radical presence.

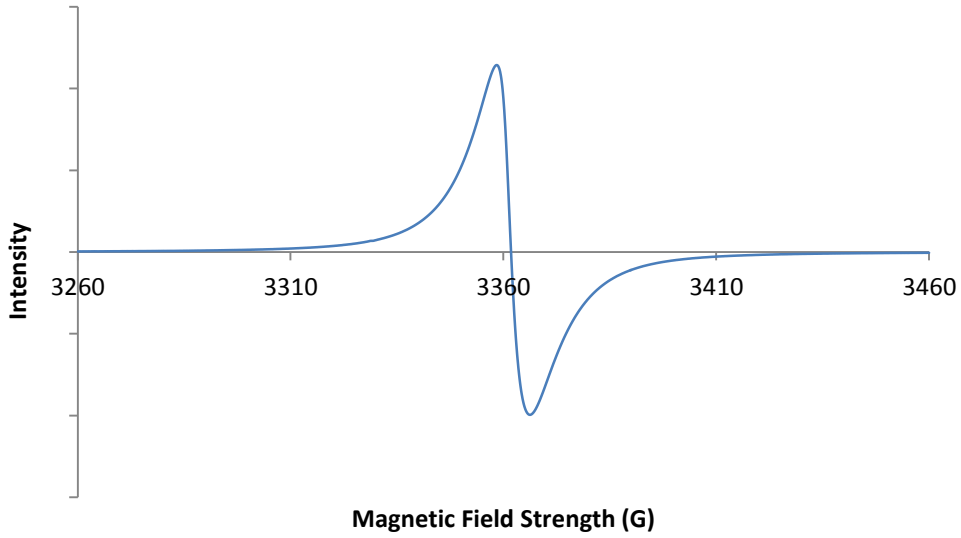

Figure 4.40 EPR Spectrum of the bulk sample, blue crystals.

The crystals were found to retain their blue colour when exposed to air for at least six weeks. Similar stability of the methyl viologen radical was reported in the [MV][$Zn_{3(}ip)_4$] structure.

4.3.5 Synthesis and characterisation of $[MV]_2[Zn_8(bpdc)_{10}]\cdot16DMF\cdot20H_2O$

The reported MOF $[NH_2(CH_3)_2]_2[Zn_3(bpdc)_4]\cdot5DMF$ (where bpdc = 4,4'-biphenyldicarboxylate)[23] displays the same SBU as that observed in $[NH_2(CH_3)_2]_2[Zn_3(bdc)_4]\cdot DMF\cdot H_2O$, which link together to form a three dimensional structure with porous channels. The bpdc ligands are extended in length between carboxylate groups in comparison to the bdc ligands, resulting in an interpenetrated structure (Figure 4.41).

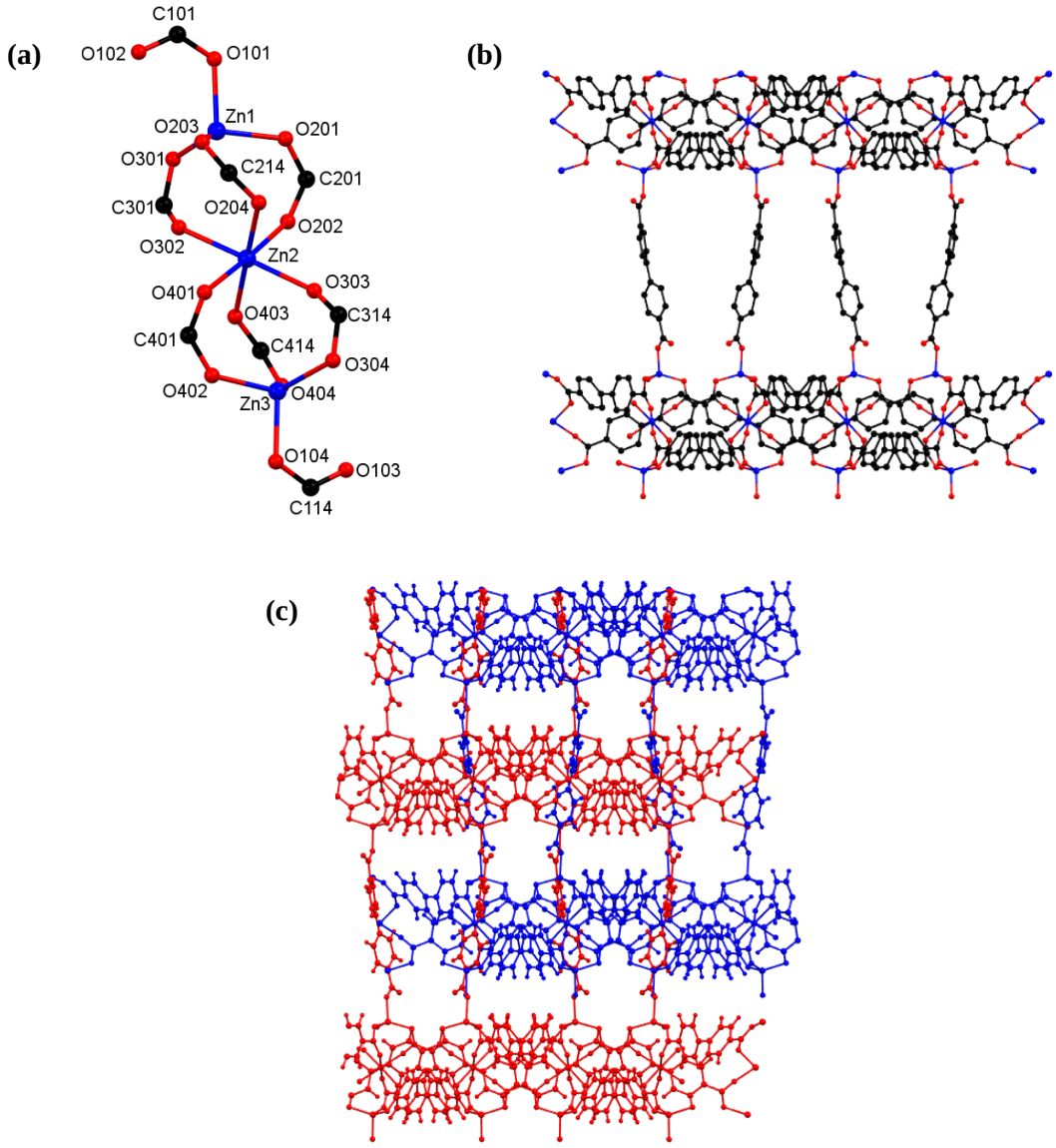

Figure 4.41 Part of the structure of $[NH_2(CH_3)_2]_2[Zn_3(bpdc)_4]\cdot5DMF$ showing **(a)** the SBU, **(b)** the porous one-dimensional channels of one net viewed down the *a*-axis and **(c)** the interpenetration of the structure, with one net coloured blue and one net shown in red. All hydrogen atoms, counter-ions and solvent molecules within the pores have been omitted for clarity.[23]

The framework is charge balanced by the presence of dimethyl ammonium cations within the pores. The study of an anionic zinc and bpdc containing framework with methyl viologen counter-ions was undertaken to investigate the effect of interpenetration of the framework on the inclusion of methyl viologen.

In this work the synthesis of the reported $[NH_2(CH_3)_2]_2[Zn_3(bpdc)_4]\cdot 5DMF$ structure was completed by combining $Zn(NO_3)_2\cdot 6H_2O$ with H_2bpdc and $[NH_2(CH_3)_2]Cl$ in DMF and heating at 120 ^oC for 48 hours. Confirmation of the formation of $[NH_2(CH_3)_2]_2[Zn_3(bpdc)_4]\cdot 5DMF$ was determined through powder X-ray diffraction analysis of the product (see appendix figure A4.2.2).

The methyl viologen containing MOF was then synthesised using a similar methodology, combining $Zn(NO_3)_2\cdot 6H_2O$ with H_2bpdc and MVI_2 in DMF and heating at 120 ^oC for 48 hours. The reaction was also carried out at 85 ^oC for comparison. The reactions yielded blue and orange/yellow crystalline products respectively. All products were analysed by powder X-ray diffraction and the resulting diffraction patterns are shown in Figure 4.42 offset against the powder diffraction trace of $[NH_2(CH_3)_2]_2[Zn_3(bpdc)_4]\cdot 5DMF$.

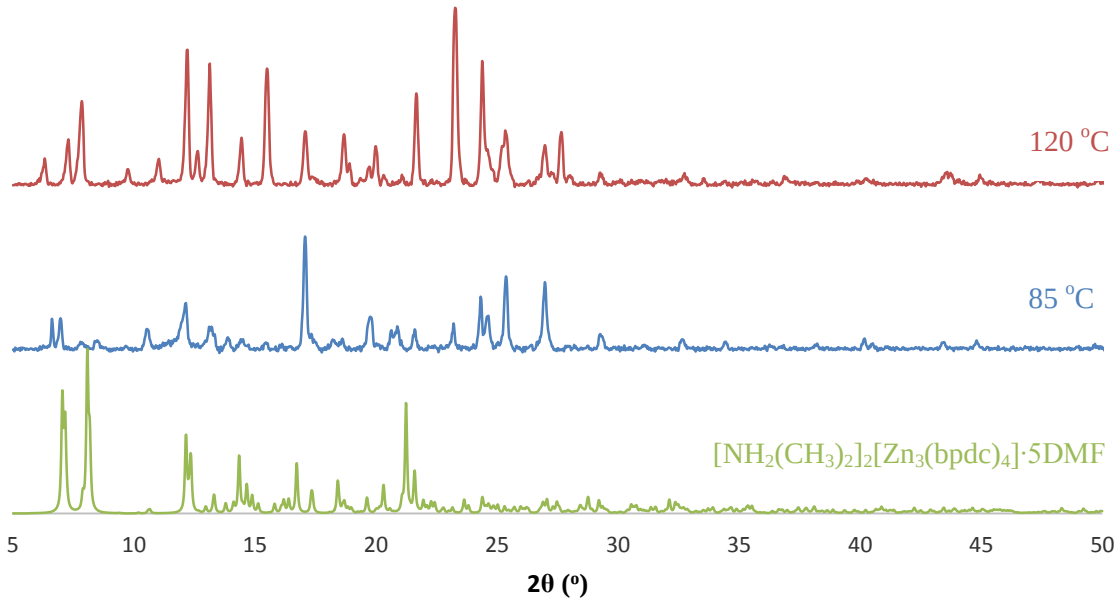

Figure 4.42 Powder X-ray diffraction patterns of $[NH_2(CH_3)_2]_2[Zn_3(bpdc)_4]\cdot 5DMF$ and the products from reaction with $Zn(NO_3)_2\cdot 6H_2O$ with H_2bpdc and MVI_2 at 120 ^oC and 85 ^oC.

Both products show significantly different powder X-ray diffraction patterns to that of $[NH_2(CH_3)_2]_2[Zn_3(bpdc)_4]\cdot 5DMF$. This indicates that the substitution of $[NH_2(CH_3)_2]Cl$ for MVI_2 in the reaction synthesis causes the formation of a structurally different product. The product formed from the reaction at 85 ^oC showed some similarities in peak positions to that of the product formed at 120 ^oC, but displayed reduced crystallinity, with increased background noise and lower signal intensity in the diffraction pattern. As a result, further analysis of the products was limited to that from the reaction conducted at 120 ^oC.

^1H NMR spectroscopy was conducted on an acid-digested sample of the product formed at 120 ^oC. The sample was prepared in a similar manner to those in Sections 4.3.2-4.3.4. The resulting ^1H

NMR spectrum shows clearly the presence of both D_2bpdc and methyl viologen in the acid digested product, with the assignment of resonances shown in Figure 4.43.

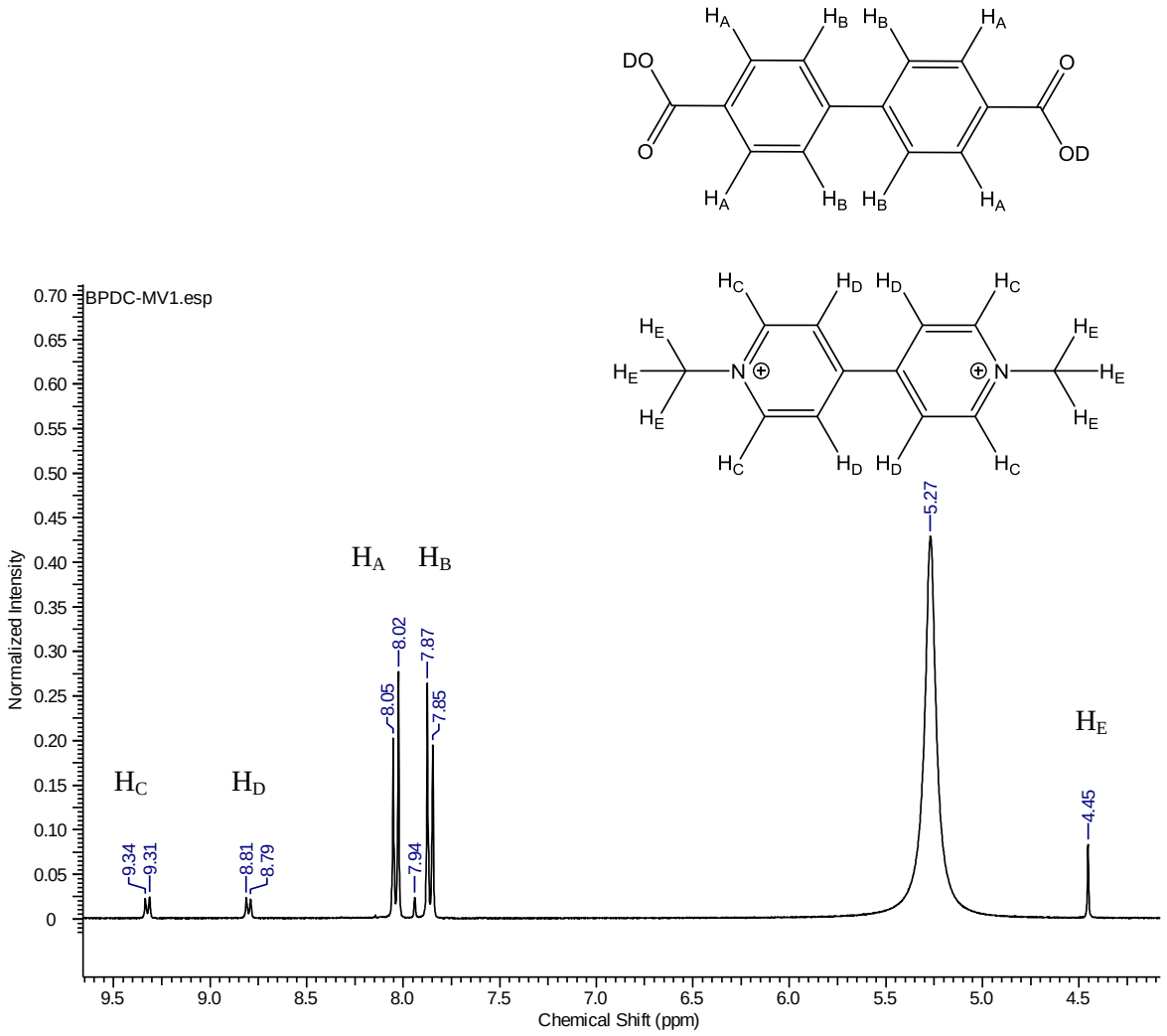

Figure 4.43 ^{1}H NMR spectrum of the acid digested product from reaction with $Zn(NO_3)_2{\cdot}6H_2O$ with H_2bpdc and MVI_2 at 120 ^{o}C.

Analysis of the integrated resonances at δ 8.04 ppm and δ 9.33 ppm allow the ratio of D_2bpdc:MV within the acid-digested product to be determined. This reveals a D_2bpdc:MV ratio of 88:12.

Structure description of $[MV]_2[Zn_8(bpdc)_{10}]\cdot 16DMF\cdot 20H_2O$ **9c**

A crystal of the product was found to be suitable for single crystal X-ray diffraction analysis. The crystal, **9c**, was blue in colour and was found to crystallise in the orthorhombic space group $Pca2_1$ (Table 4.4).

Table 4.4 Crystal data and structure refinement for $[MV]_2[Zn_8(bpdc)_{10}]\cdot 16DMF\cdot 20H_2O$ **9c.**

Identification code	**9c**
Empirical formula	$C_{212}H_{260}N_{20}O_{76}Zn_8$
Formula weight	4827.34
Temperature/K	150.00(10)
Crystal system	orthorhombic
Space group	$Pca2_1$
a/Å	36.4926(13)
b/Å	14.6058(4)
c/Å	45.4204(13)
α/°	90
β/°	90
γ/°	90
Volume/Å^3	24209.2(13)
Z	4
ρ_{calc} g/cm^3	1.324
μ/mm^{-1}	1.588
F(000)	10080.0
Crystal size/mm^3	0.129 × 0.067 × 0.016
Radiation	Cu$K\alpha$ (λ = 1.54184)
2θ range for data collection/°	6.052 to 136.502
Index ranges	$-43 \leq h \leq 17$, $-17 \leq k \leq 16$, $-53 \leq l \leq 54$
Reflections collected	52150
Independent reflections	32875 [R_{int} = 0.0508, R_{sigma} = 0.0940]
Data/restraints/parameters	32875/619/2700
Goodness-of-fit on F^2	1.050
Final R indexes [I>=2σ (I)]	R_1 = 0.0791, wR_2 = 0.2040
Final R indexes [all data]	R_1 = 0.0983, wR_2 = 0.2261
Largest diff. peak/hole / e Å^{-3}	1.29/-0.98
Flack parameter	0.48(3)

The asymmetric unit was found to contain eight zinc atoms, ten bpdc ligands, sixteen DMF solvent molecules and two methyl viologen cations (Figure 4.44). The water content could not be resolved in the crystal structure and was treated with PLATON SQUEEZE. A value of twenty water molecules per asymmetric unit was determined from the SQUEEZE analysis, giving a formula of $[MV]_2[Zn_8(bpdc)_{10}]\cdot 16DMF\cdot 20H_2O$ **9c**.

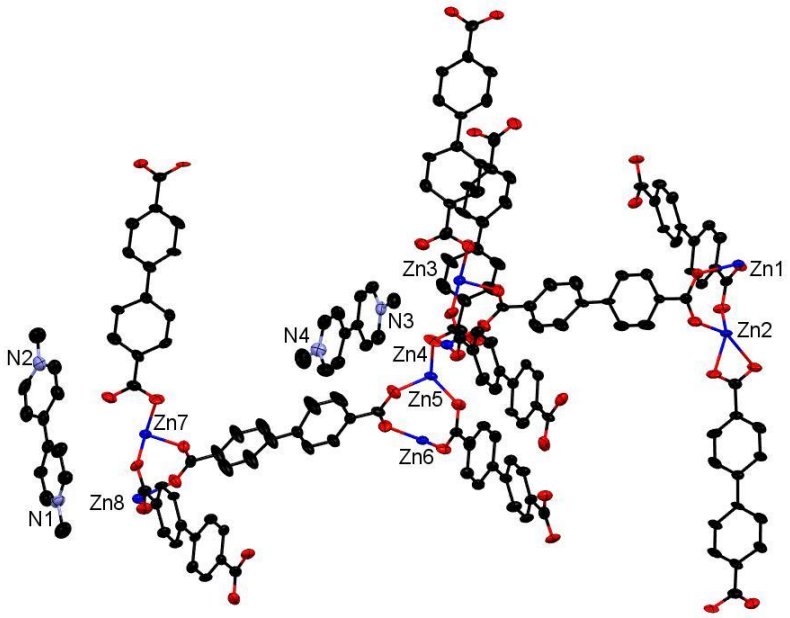

Figure 4.44 Asymmetric unit of **9c** with ellipsoid probabilities of 40 %. DMF molecules and hydrogen atoms have been omitted for clarity. Labelling of zinc and nitrogen atoms only is shown.

Four carbons (C6, C7 and C40 and C41) of two bpdc ligands displayed a smearing of the electron density and were modelled through the application of atomic displacement parameter restraints. Two co-ordination modes of the bpdc ligands are observed in the structure of **9c** and are shown in Figure 4.45.

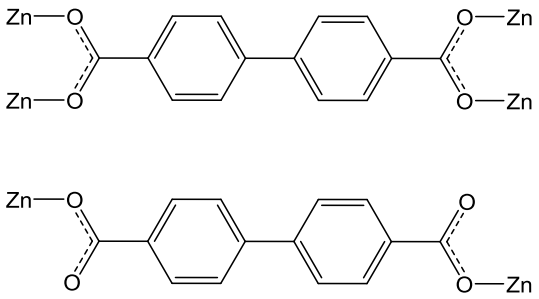

Figure 4.45 The two co-ordination modes of the bpdc ligand observed in the structure of **9c**.

Six of the ten bpdc ligands within the asymmetric unit co-ordinate to four different zinc atoms through all four oxygen atoms of the carboxylate groups, whilst the remaining four bpdc ligands co-ordinate through two oxygen atoms to two zinc atoms. There was no evidence for the presence of hydrogen atoms on the non-coordinated carboxylate oxygen atoms of these bpdc ligands (O6, O7, O13 O19, O28, O30, O38 and O49).

All zinc atoms in the asymmetric unit are four co-ordinate displaying distorted tetrahedral geometry. Pairs of zinc atoms are bridged by three bidentate carboxylate groups of bpdc ligands to form dimeric SBUs and are further co-ordinated by two axially bound monodentate carboxylate groups to give $Zn_2(CO_2)_5$ units. The Zn7/Zn8 containing SBU is given in Figure 4.46.

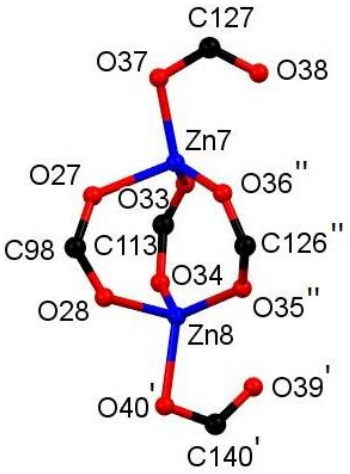

Figure 4.46 The $Zn_2(CO_2)_5$ SBU of **9c**. Hydrogen atoms are omitted for clarity. O37, O38 and C123 primed atoms and double primed atoms are related to those in the asymmetric unit by the ½ + *x*, – *y* – 1, *z* and *x*, *y* – 1, *z* symmetry operations respectively.

The SBUs are linked by bpdc linkers to form a three-dimensional network. Two networks are present forming an interpenetrated structure. Of the zinc atoms in the asymmetric unit, Zn1, Zn2, Zn5 and Zn6 form one network while Zn3, Zn4, Zn7 and Zn8 form the second network. The interpenetrated structure is shown in Figure 4.47.

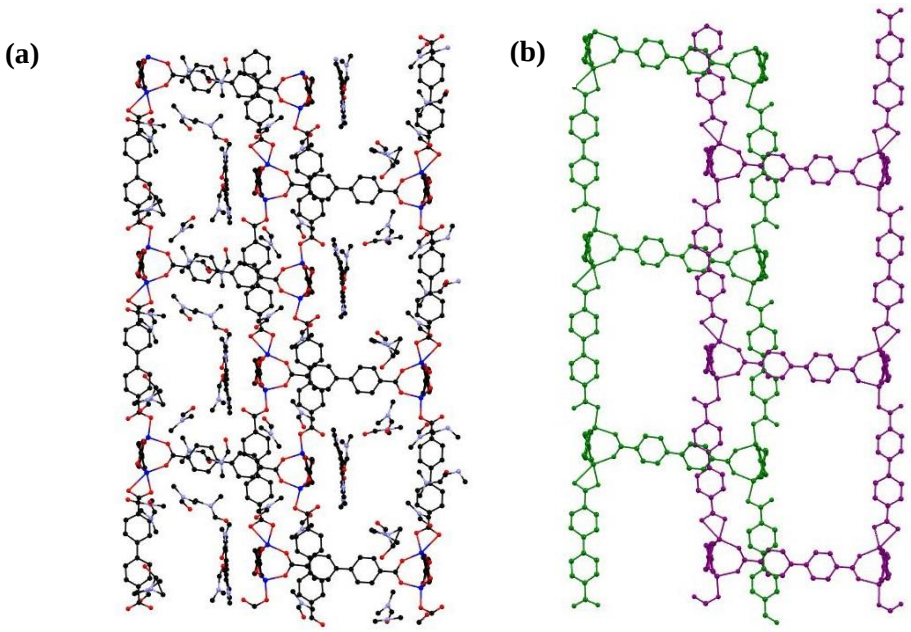

Figure 4.47 Interpenetrated structure of **9c** viewed down the *b*-axis showing **(a)** the solvent and methyl viologen within the pores and **(b)** nets shown in green and purple with solvent molecules/counter-ions removed. Hydrogen atoms are omitted for clarity.

The overall network contains one-dimensional channels down the *b*-axis which are occupied by DMF solvent molecules and methyl viologen cations. In a similar manner to **9b** the methyl viologen cations are near planar in their geometry and alternate with DMF molecules down the channels. As was observed in both **9a** and **9b**, uncoordinated oxygen atoms from the dicarboxylate ligands are directed towards the methyl viologen cations (Figure 4.48). Charge transfer between the framework and the methyl viologen is therefore likely to occur during the synthesis, forming the methyl viologen radical cation species and accounting for the observed blue colour of the product.

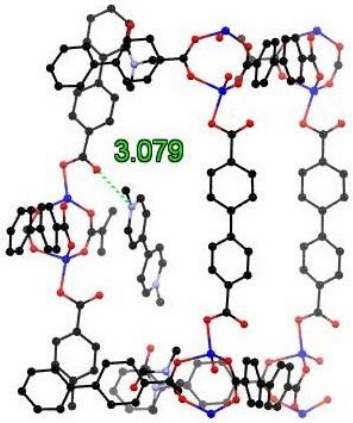

Figure 4.48 Part of the structure of **9c** showing the O···N distance between the bpdc ligand (O) and the methyl viologen (N). Hydrogen atoms are omitted for clarity.

A comparison of the powder diffraction pattern generated from the single crystal structure of **9c** to that of the bulk, show both diffraction patterns to contain Bragg peaks with largely similar positions to one another (see appendix A4.2.3). Differences in the relative intensities of the peaks between the experimental bulk collection and the powder diffraction trace generated from the single crystal data may be due to differences in solvent content between the two samples.

4.3.6 Comparison of radical stability in the methyl viologen containing MOFs

For $[MV][Zn_3(ip)_4]$, $[MV]_{0.44}[HMVH]_{0.36}[NH_2(CH_3)_2]_{0.4}[Zn_3(bdc)_4]\cdot 2H_2O\cdot 1.2DMF$ and $[MV]_{0.5}$ [Zn(btc)]·DMF significant differences in the stability of the methyl viologen radical cation are observed between frameworks. In $[MV]_{0.44}[HMVH]_{0.36}[NH_2(CH_3)_2]_{0.4}$ $[Zn_3(bdc)_4]\cdot 2H_2O\cdot 1.2DMF$ the $MV^{+\bullet}$ oxidises in air to the dication state within a few minutes. However, both $[MV][Zn_3(ip)_4]$ and $[MV]_{0.5}$ [Zn(btc)]·DMF systems display increased stability of the methyl viologen radical when exposed to air, with the radical persisting for multiple weeks.

Some explanations of this observed radical stability can be given through comparison of the single crystal structures. Both frameworks of $[MV][Zn_3(ip)_4]$ and $[MV]_{0.5}$[Zn(btc)]·DMF contain one-dimensional porous channels which are occupied with methyl viologen cations and solvent molecules. A model of voids within these structures calculated based on the contact surface shows that in $[MV][Zn_3(ip)_4]$ only small, isolated pockets remain unoccupied forming 1.6 % of the unit cell volume (Figure 4.49). This is supported by the reported thermogravimetric analysis of this compound, in which no mass loss corresponding to solvent within the pores of the structure is observed.[18] In the case of $[MV]_{0.5}$ [Zn(btc)]·DMF no unoccupied accessible pores are available (Figure 4.49). This means that the methyl viologen radical cations remain isolated from the external environment of the MOF, allowing them to persist in their radical state even when the MOF is exposed to air.

(a)

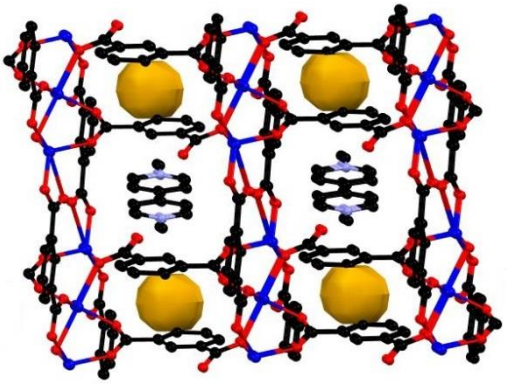

(b)

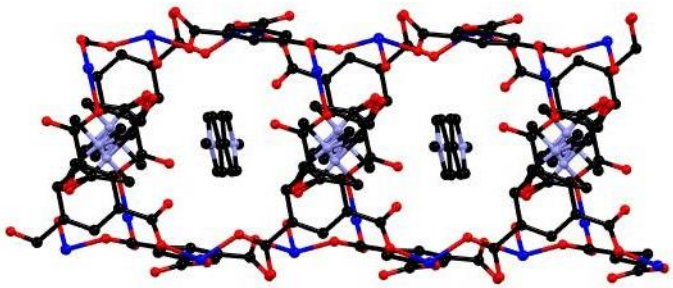

Figure 4.49 (a) Structure of $[MV][Zn_3(ip)_4]$ viewed down the *c*-axis showing voids in yellow calculated using the contact surface measurement and a probe radius of 1.2 Å and resulting in a void space of 1.6 % of the unit cell volume. **(b)** Structure of $[MV]_{0.5}$ [Zn(btc)]·DMF viewed along the *c*-axis. No accessible void space was present calculated using a probe radius of 1.2 Å.

The structure of $[MV]_{0.44}[HMVH]_{0.36}[NH_2(CH_3)_2]_{0.4}[Zn_3(bdc)_4]\cdot 2H_2O\cdot 1.2DMF$ also contains one-dimensional channels occupied by methyl viologen cations and solvent molecules. Void calculations show that in addition to this, two further pore types are observed making up a total of 11.8 % of the unit cell volume (Figure 4.50). Some of these 'voids' will contain DMF and water solvent molecules which were not resolved in the crystal structure but were found to be present through thermogravimetric analysis. The larger of the pores link together along the *b*-axis of the structure and form channels through which oxygen can readily migrate. This offers an explanation as to why the methyl viologen radical cations within the pores of the $[MV]_{0.44}[HMVH]_{0.36}[NH_2(CH_3)_2]_{0.4}[Zn_3(bdc)_4]\cdot 2H_2O\cdot 1.2DMF$ framework are so rapidly oxidised.

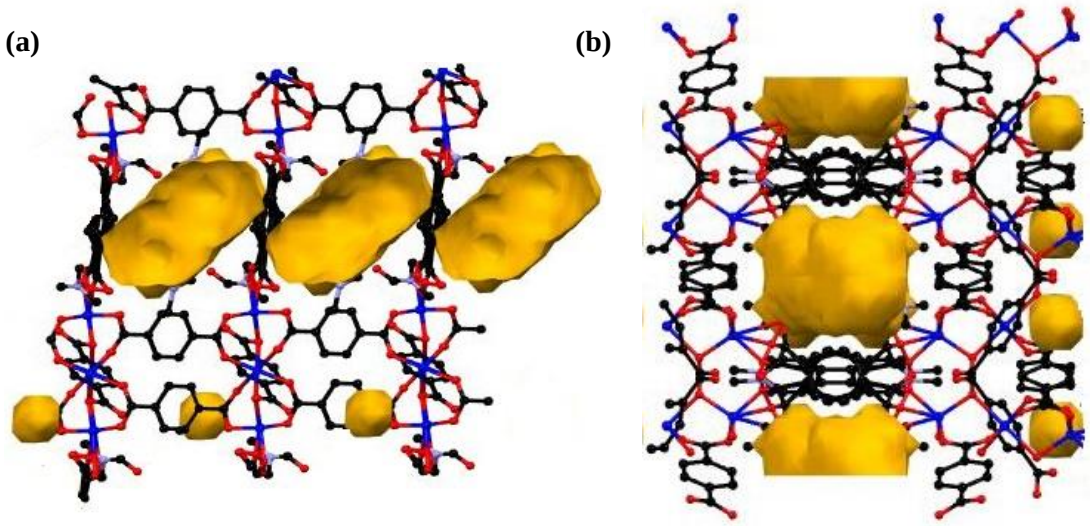

Figure 4.50 (a) Structure of $[MV]_{0.44}[HMVH]_{0.36}[NH_2(CH_3)_2]_{0.4}[Zn_3(bdc)_4]\cdot 2H_2O\cdot 1.2DMF$ viewed along the *c*-axis and **(b)** viewed down the *b*-axis showing the voids calculated using the contact surface measurement and a probe radius of 1.2 Å and resulting in a void space of 11.8 % of the unit cell volume.

4.4 Ethyl viologen containing MOFs

Following the successful inclusion of methyl viologen counter-ions in anionic zinc-carboxylate MOFs, the investigation was extended to include ethyl viologen counter-ions into similar frameworks. This aimed to determine if any differences in the product structure, radical formation or stability occurred with variation of the viologen species. Two systems were investigated with ethyl viologen as the cation, those based on the $[Zn_3(ip)_4]^{2-}$ and $[Zn_3(bdc)_4]^{2-}$ frameworks. These frameworks were selected as they displayed differences to one-another in their ability to stabilise the radical form of the methyl viologen species (see Section 4.3).

4.4.1 Synthesis and characterisation of $[EV][Zn_3(ip)_4]$

Following the successful formation of $[MV][Zn_3(ip)_4]$ a similar reaction was undertaken using ethyl viologen dibromide rather than methyl viologen diiodide in the reaction mixture. The reaction was carried out by combining zinc nitrate with H_2ip and ethyl viologen dibromide in DMF at 120 ^oC for 48 hours. The reaction temperature of 120 ^oC was chosen due to the success of these reaction conditions in forming the $[MV][Zn_3(ip)_4]$ complex (see Section 4.3.1). The synthesis yielded blue crystals.

Powder X-ray diffraction analysis of the product was compared to that for $[MV][Zn_3(ip)_4]$ (Figure 4.51). Both PXRD traces contain Bragg peaks with similar positions and relative intensities to one another suggesting frameworks of similar topology. Some differences between the powder diffraction patterns can be observed, including the loss of the peak at 2θ value of 10.5^o and the presence of additional peaks at 2θ value of 10.2^o and 10.8^o in the product formed with ethyl viologen cations. These differences may be due to different counter-ion and solvent inclusions between the two frameworks.

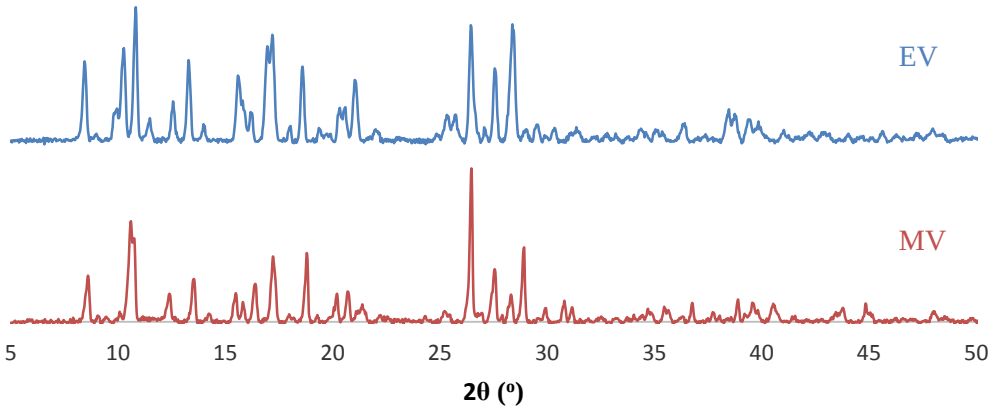

Figure 4.51 Powder diffraction patterns for $[MV][Zn_3(ip)_4]$ (bottom) and the product of the reaction with ethyl viologen (EV) (top).

The blue appearance of the crystalline product suggests the ethyl viologen is present in the radical cation state within the pores of the MOF. A comparable stability of the ethyl viologen radical cations in the framework is observed to that of the methyl viologen radical cation species within $[MV][Zn_3(ip)_4]$, with the blue colour persisting for more than four weeks when the product is exposed to air.

The crystals were washed using a similar method to that described in Section 4.3, and digested in a d_6-DMSO/DCl mixture, which was orange in colour. The resulting ^{1}H NMR spectrum shows the presence of both D_2ip and ethyl viologen (Figure 4.52). The resonance at δ 5.83 ppm originates from water in the sample, δ 2.87 ppm and δ 2.71 ppm originates from DMF and δ 2.07 ppm from residual acetone.

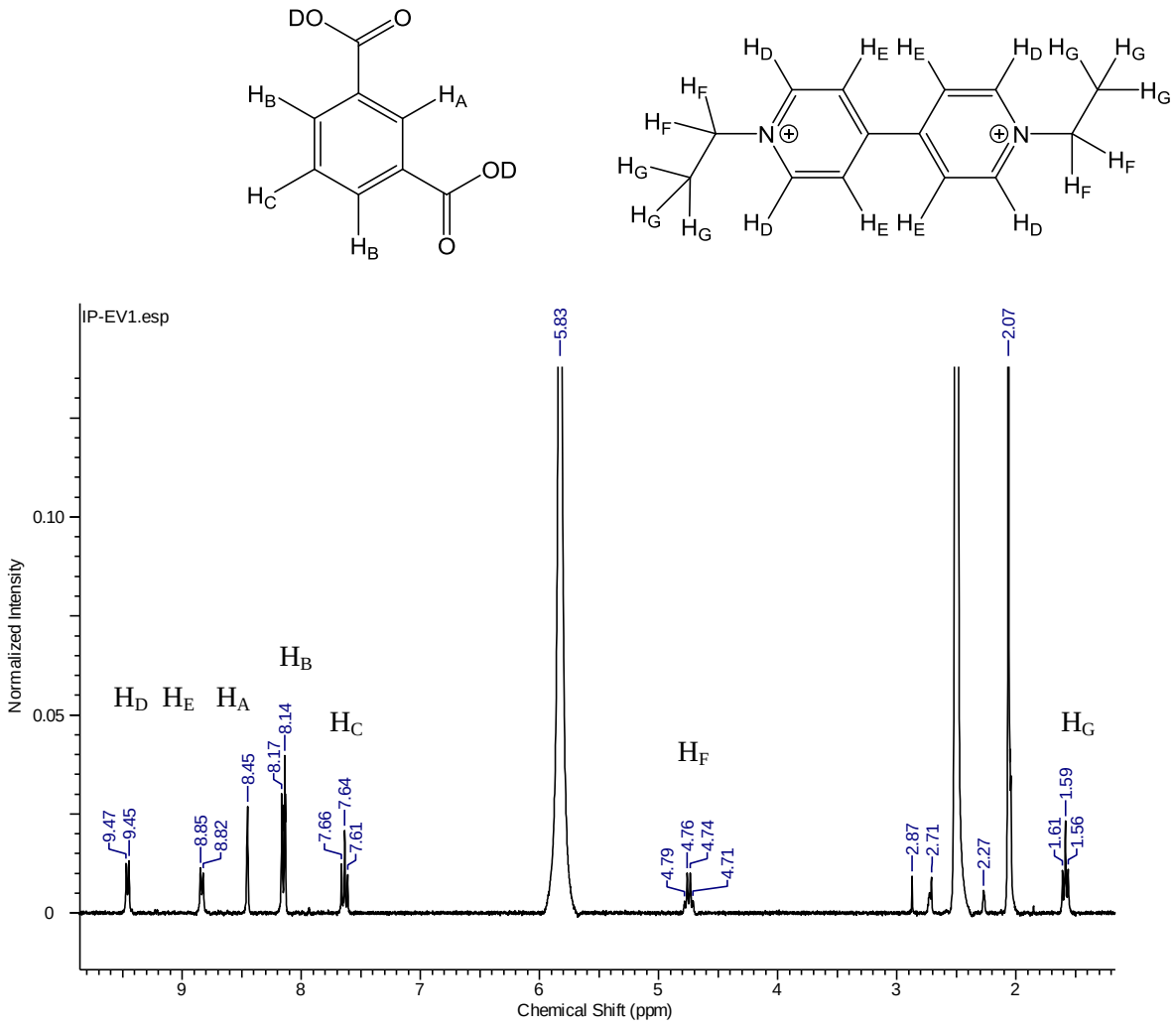

Figure 4.52 ^{1}H NMR spectrum of the acid digested product from the reaction of zinc nitrate with H_2ip and ethyl viologen dibromide

Analysis of the integrated resonances at δ 8.45 ppm and δ 9.46 ppm were used to determine the composition of the product. The ratio of D_2ip:EV in the digestion mixture was found to be 4:1. Thermogravimetric analysis of the product shows no mass loss associated with solvent in the

structure and thermal stability of the framework up to 400 ^{o}C (see appendix Figure A4.1.4). This is similar to the reported TGA of [MV][$Zn_3(ip)_4$]. The product formula can therefore be written as [EV][$Zn_3(ip)_4$], giving a charge balanced structure.

4.4.2 Synthesis and characterisation of $[EV]_{0.69}[HEVH]_{0.29}[NH_2(CH_3)_2]_{0.2}[Zn_3(bdc)_4]\cdot 0.9DMF\cdot 1.3H_2O$.

The direct synthesis of MVI_2 with zinc nitrate and H_2bdc gave rise to the complex $[MV]_{0.44}[HMVH]_{0.36}[NH_2(CH_3)_2]_{0.4}[Zn_3(bdc)_4]\cdot 2H_2O\cdot 1.2DMF$. The product contains both MV^{2+} and $HMVH^{2+}$ cationic species within the pores of the framework. A similar reaction was conducted with ethyl viologen bromide.

The synthesis was carried out by combining zinc nitrate with H_2bdc and $EVBr_2$ in DMF and heating at 120 ^oC for 48 hours. The reaction yielded blue crystals which rapidly turned orange upon exposure to air.

Powder X-ray diffraction analysis was completed on the product and compared to the powder diffraction trace obtained for $[MV]_{0.44}[HMVH]_{0.36}[NH_2(CH_3)_2]_{0.4}[Zn_3(bdc)_4]\cdot 2H_2O\cdot 1.2DMF$ (Figure 4.53). Both PXRD traces contain Bragg peaks with similar positions, suggesting frameworks of a similar topology have been formed. A difference in the relative intensities of peaks at 2θ values of 9.6^o, 10.6^o and 10.7^o may be due to differences in the counter-ions and solvent inclusion between the two structures.

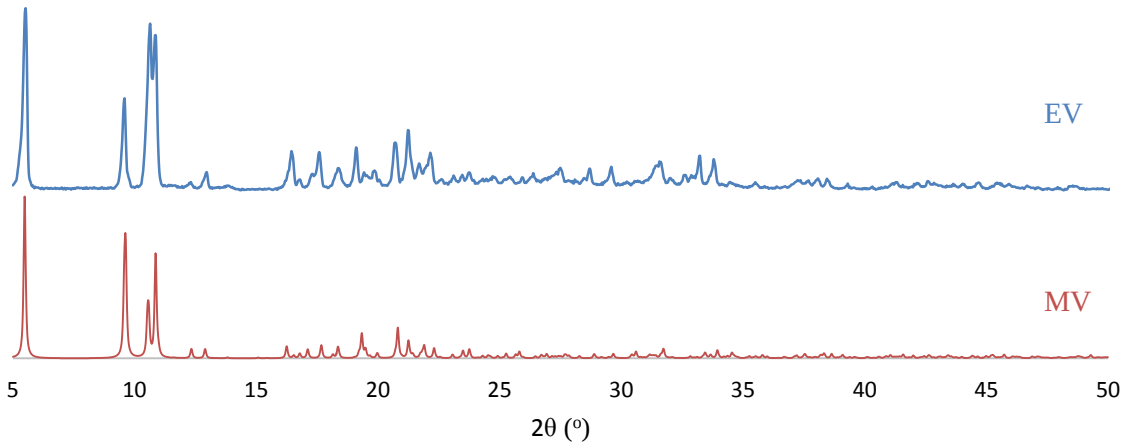

Figure 4.53 Powder X-ray diffraction patterns for the ethyl viologen containing product (top) and $[MV]_{0.44}[HMVH]_{0.36}[NH_2(CH_3)_2]_{0.4}[Zn_3(bdc)_4]\cdot 2H_2O\cdot 1.2DMF$ (bottom).

The product was washed in DMF following methods previously described, and digested using a d_6-DMSO/DCl mixture. The orange digestion solution was then analysed by ^1H NMR spectroscopy (Figure 4.54).

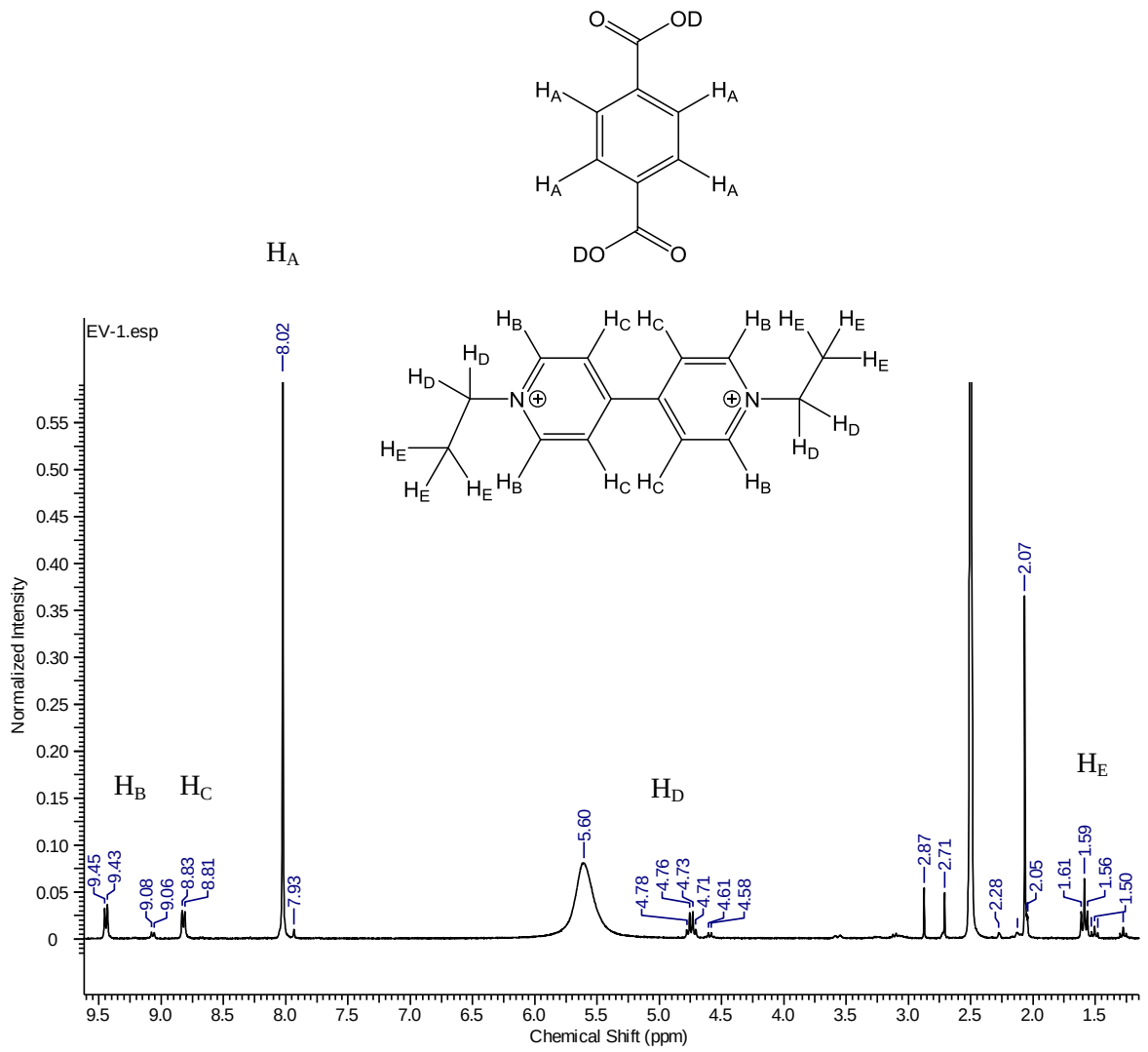

Figure 4.54 ^{1}H NMR spectrum of the acid digested product from the reaction of zinc nitrate with H_2bdc and ethyl viologen dibromide

The presence of both D_2bdc and ethyl viologen (EV) can be seen in the ^{1}H NMR spectrum of the digested product. Additional unassigned resonances at δ 9.07 ppm, δ 4.59 ppm and δ 1.50 ppm can be observed. This is similar to the ^{1}H NMR spectrum of the digested $[MV]_{0.44}[HMVH]_{0.36}[NH_2(CH_3)_2]_{0.4}[Zn_3(bdc)_4]\cdot 2H_2O\cdot 1.2DMF$ product, which contained resonances which were assigned to the $HMVH^{2+}$ species (see Section 4.3.2). It is therefore likely that a similar by-product is being formed in the reaction with ethyl viologen dibromide. This product will be referred to as $HEVH^{2+}$ and a hypothesised structure for this species is shown in Figure 4.55.

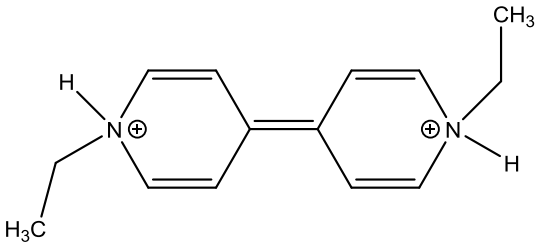

Figure 4.55 Possible structure of the $HEVH^{2+}$ species.

Analysis of the integrated resonances revealed a $D_2bdc:EV^{2+}:HEVH^{2+}$ ratio of 83:11:6, corresponding to 0.53 EV^{2+} and 0.26 $HEVH^{2+}$ per framework unit formula, $[Zn_3(bdc)_4]^{2-}$. Thermogravimetric analysis on a sample of the product showed a percentage mass loss of 2.5 % at 120 ^oC, equating to 1.3 water molecules, and a percentage mass loss of 7.7 % at approximately 150 ^oC equating to a loss of 0.9 DMF molecules per unit formula (see appendix Figure A4.1.5). No further mass loss was observed after 480 ^oC and the final mass of the sample is equivalent to three ZnO moieties per unit formula. The product therefore be assigned the formula $[EV]_{0.54}[HEVH]_{0.26}[NH(CH_3)_2]_{0.2}[Zn_3(bdc)_4]\cdot 0.9DMF\cdot 1.3H_2O$ with the dimethyl ammonium cations present to charge balance the formula solvent.

The crystals are blue when they are synthesised, which indicates the presence of the ethyl viologen in its radical cationic form. Upon exposure to air the crystals rapidly turn orange suggesting the radical viologen species is oxidised to its cationic form in a similar manner to that observed for $[MV]_{0.44}[HMVH]_{0.36}[NH_2(CH_3)_2]_{0.4}[Zn_3(bdc)_4]\cdot 2H_2O\cdot 1.2DMF$.

Structure description of $[EV]_{0.61}[HEVH]_{0.29}[NH(CH_3)_2]_{0.2}[Zn_3(bdc)_4]\cdot 1.4DMF\cdot 1.3H_2O$ **9d**

A crystal from the product with an average formula of $[EV]_{0.54}[HEVH]_{0.26}[NH(CH_3)_2]_{0.2}[Zn_3(bdc)_4]\cdot 0.9DMF\cdot 1.3H_2O$, **9d**, was suitable for single crystal X-ray diffraction analysis. The crystal was orange in colour when the data collection was completed, indicating the ethyl viologen within the crystal are in their dication state. Crystal data and structure refinement information for **9d** is given in Table 4.5.

Table 4.5 Crystal data for **9d**.

Identification code	**9d**
Empirical formula	$C_{48.2}H_{46.52}N_{3.4}O_{18.7}Zn_3$
Formula weight	1168.72
Temperature/K	150.15
Crystal system	monoclinic
Space group	*C*2/c
a/Å	32.6406(6)
b/Å	9.63384(16)
c/Å	18.4404(4)
α/°	90
β/°	102.534(2)
γ/°	90
Volume/Å^3	5660.48(19)
Z	4
ρ_{calc}g/cm^3	1.371
μ/mm^{-1}	2.085
F(000)	2396.0
Crystal size/mm^3	0.091 × 0.068 × 0.034
Radiation	Cu*K*α (λ = 1.54184)
2θ range for data collection/°	9.592 to 145.74
Index ranges	$-40 \leq h \leq 39$, $-11 \leq k \leq 11$, $-22 \leq l \leq 22$
Reflections collected	26374
Independent reflections	26374 [R_{int} = 0.0437, R_{sigma} = 0.0523]
Data/restraints/parameters	26374/153/463
Goodness-of-fit on F^2	1.031
Final *R* indexes [I>=2σ (I)]	R_1 = 0.0568, wR_2 = 0.1495
Final *R* indexes [all data]	R_1 = 0.0698, wR_2 = 0.1597
Largest diff. peak/hole / e Å^{-3}	0.71/-0.70

The asymmetric unit contains two crystallographically independent zinc atoms, Zn1 with site occupancy of 100 % and Zn2 site occupancy of 50 %. One full bdc ligand is present along with two half bdc ligands. Two solvent molecules of DMF and one H_2O molecule, each with a site occupancy of 35 % are also present along with half an ethyl viologen dication with attributed site occupancy of 45 % (Figure 4.56).

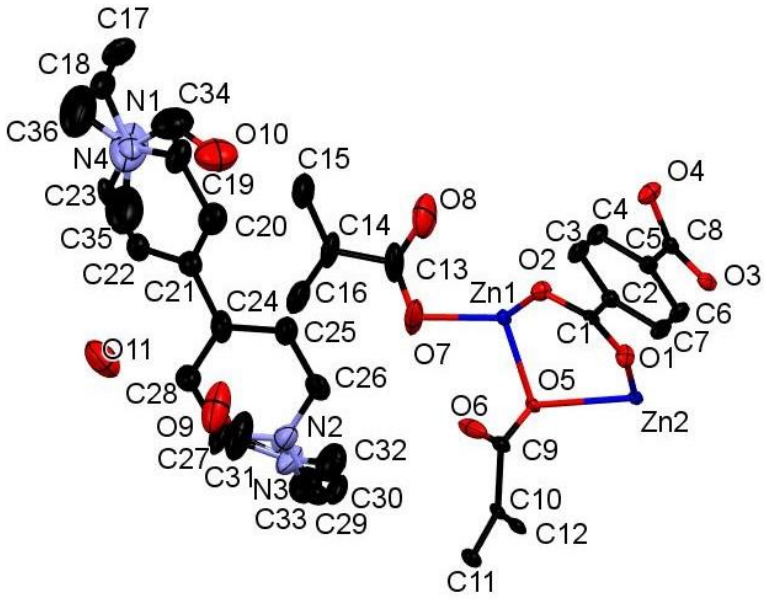

Figure 4.56 The asymmetric unit of .**9d.**

The SBU of the framework is similar to that observed in **9a** and **9c**, being formed from three zincs and eight carboxylates. The three-dimensional framework is formed through the linking of SBUs and contains one-dimensional channels down the *b*-axis occupied by DMF solvent molecules and viologen counter-ions (Figure 4.57). The framework topology of **9d** is similar that of **9a**.

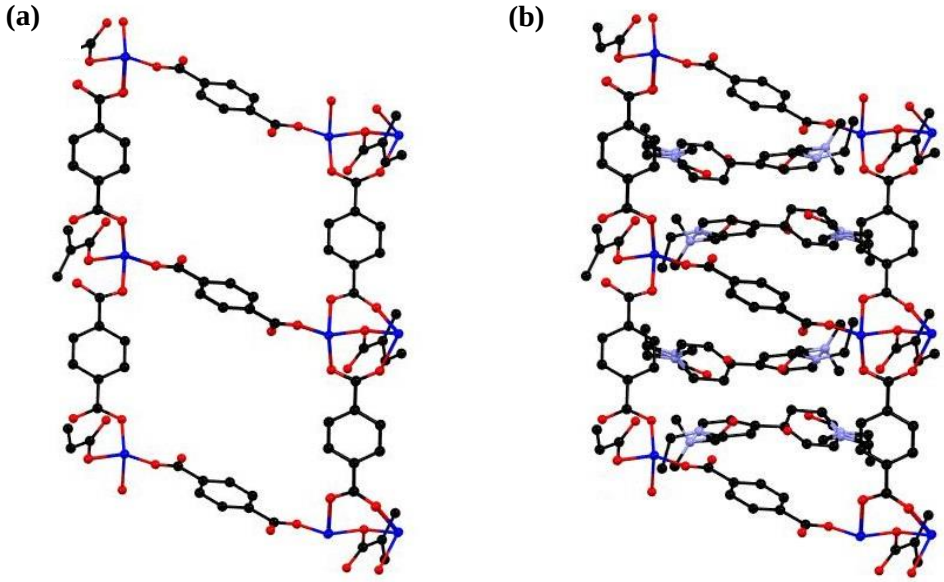

Figure 4.57 Part of the structure of **9d** showing **(a)** the porous framework viewed down the *b*-axis with cations and solvent omitted and **(b)** with DMF and EV^{2+}/$HEVH^{2+}$ occupying the pores. Hydrogen atoms are omitted

The viologen content of **9d** differs to that of the bulk sample as determined through ^{1}H NMR spectroscopic analysis. The bulk sample shows a total $EV^{2+/}HEVH^{2+}$ content of 0.79 per three zinc centres, whilst **9d** contains 0.9 viologen moieties per three zinc centres. This difference may be due to compositional variation between crystals in the sample. A ratio of 0.61 EV^{2+} to 0.29 $HEVH^{2+}$ can be assigned to **9d** by using the same relative ratios of $EV^{2+/}HEVH^{2+}$ found in the bulk sample.

A total solvent content of 1.4 DMF and 0.7 H_2O molecules per three zinc centres was refined crystallographically. Treatment with PLATON SQUEEZE revealed additional electron density in the pores of the framework, giving a total solvent content of 1.4 DMF and 1.3 H_2O molecules. The composition of **9d** is therefore determined to be $[EV]_{0.61}[HEVH]_{0.29}[NH(CH_3)_2]_{0.2}[Zn_3(bdc)_4]$ $\cdot 1.4DMF \cdot 1.3H_2O$.

The viologen moiety shows positional disorder, which required atomic displacement, planarity and distance restraints to achieve a chemically sensible convergence. The ^{1}H NMR spectroscopy analysis showed the presence of both $EV^{2+}/HEVH^{2+}$, which could not be resolved in the crystal structure due to smearing of the electron density.

The EV^{2+} moiety displays twisting of the two rings relative to one another, with a plane to plane angle of 52^{o}. A similar twisting was present in the viologen cation in **9a** and is discussed in Section 4.3.2. The position of the viologen counter-ions in the pores of the **9d** is comparable to that of **9a**, and displays O···N distances between the viologen and non-coordinating oxygen of the bdc ligand, within the range for charge transfer to occur.

4.5 Conclusion and future work

The successful formation of four zinc MOFs with methyl viologen cations has been successfully achieved through the direct synthesis with methyl viologen diiodide. In three of the systems investigated, $[MV][Zn_3(ip)_4]$, $[MV]_{0.44}[HMVH]_{0.36}[NH_2(CH_3)_2]_{0.4}[Zn_3(bdc)_4]\cdot 2H_2O\cdot 1.2DMF$ and $[MV]_{0.5}[Zn(btc)]\cdot DMF$ the MOFs were found to have a similar framework topology to the methyl viologen-free structures. The inclusion of methyl viologen diiodide in the synthesis with zinc nitrate and H_2bpdc yielded a new framework structure which has been characterised as $[MV]_2[Zn_8(bpdc)_{10}]\cdot 16DMF\cdot 20H_2O$. The structure is interpenetrated, indicating that inclusion of methyl viologen cations into the framework does not preclude the formation of interpenetrated MOFs.

In the case of the $[Zn_3(bdc)_4]^{2-}$ framework, direct synthesis with methyl viologen diiodide resulted in the formation of the protonated species $HMVH^{2+}$ which was included into the framework along with MV cations. The protonated species $HMVH^{2+}$ most likely forms over time under the reaction conditions employed in the synthesis of the MOF. The generation of this protonated viologen species was avoided by using an alternative synthesis in which the methyl viologen was formed *in situ* from viologen diacetic acid.

All MV containing MOFs produced crystalline products which were blue in colour when synthesised at a reaction temperature of 120 ^{o}C. The blue colour of the products suggests the formation of the methyl viologen species in its radical cation form and this was confirmed through EPR spectroscopy. Single crystal X-ray analysis of the products showed that, in all cases, the methyl viologen species are in close proximity to unco-ordinated oxygen atoms of the framework (less than 3.7 Å) allowing the frameworks to act as electron donors in the reduction of viologens from their dicationic to radical cationic states during the reaction procedure.

For the $[MV]_{0.44}[HMVH]_{0.36}[NH_2(CH_3)_2]_{0.4}[Zn_3(bdc)_4]\cdot 2H_2O\cdot 1.2DMF$ system the radical species was rapidly oxidised to its dicationic form on exposure to air, mimicking the behaviour of methyl viologen in the solution phase. Such materials may have applications in areas such as oxygen detection. However, for $[MV][Zn_3(ip)_4]$ and $[MV]_{0.5}[Zn(btc)]\cdot DMF$ the blue colour of the crystals persisted when exposed to air for multiple weeks. This demonstrates that these frameworks shield the radical species from oxidation in air, providing a route to long lived radical species. This has potential applications in the field of molecular electronics, in which nanoscale materials can behave as electronic components.[16]

Similar product formation and properties were observed when changing the cation from methyl viologen to ethyl viologen. Studies into the inclusion of ethyl viologen into $[Zn_3(ip)_4]^{2-}$ and $[Zn_3(bdc)_4]^{2-}$ frameworks were successful, forming the species $[EV][Zn_3(ip)_4]$ and $[EV]_{0.54}[HEVH]_{0.26}[NH(CH_3)_2]_{0.2}[Zn_3(bdc)_4]\cdot 0.9DMF\cdot 1.3H_2O$.

The photochromic behaviour exhibited by the materials detailed in this chapter has potential use in optoelectronics and as optical switches, due to their responsive behaviour to light stimulus.[16]

This work could be continued through further study of viologen containing MOFs by studying different viologen species as counter-ions. The study of viologens with bulkier substituents and the effect on framework formation may further our understanding of whether sterically hindered viologen counter-ions can be included into MOFs and the effect this has on framework topology. Further studies into the viologen radical cation stability in air can be explored, monitoring both the framework stability through powder X-ray diffraction methods and the viologen radical cation species stability through EPR spectroscopy studies.

4.6 Experimental

4.6.1 General experimental details

Methyl viologen diiodide[24], ethyl viologen dibromide[25] and diacetic viologen dichloride[26] compounds were synthesised using reported methods; all other starting materials and solvents were purchased from commercial sources and were used without further purification.

Powder X-ray diffraction (PXRD) patterns, single crystal X-ray diffraction data and ^{1}H NMR were conducted as detailed in Chapter 2. UV irradiation experiments were conducted using a Photochemical Reactor Ltd small quartz RQ125 Immersion Well reactor with a 125 W mercury, medium pressure lamp.

EPR spectroscopy was conducted by Dr Floriana Tuna at the National EPR facility, University of Manchester.

4.6.2 Synthesis of [MV][$Zn_3(ip)_4$]

$Zn(NO_3)_2{\cdot}6H_2O$ (0.502 mmol, 0.149 g), H_2ip (0.493 mmol, 0.082 g) and MVI_2 (0.502 mmol, 0.22 g) were combined in a vial with 7 ml anhydrous DMF and sealed. The reactants were sonicated for 15 minutes until dissolved and heated to 85 ^oC for 2 days. Orange and blue crystals were produced in a yield of 0.174 g, 34 % based on H_2ip. The reaction was repeated using the same procedure and altering the reaction temperature to 120 ^oC. Blue crystalline product was produced with a yield of 0.211 g, 41 % based on H_2ip.

4.6.3 Synthesis of $[MV]_{0.44}[HMVH]_{0.36}[NH_2(CH_3)_2]_{0.4}[Zn_3(bdc)_4]{\cdot}2H_2O{\cdot}1.2DMF$

$Zn(NO_3)_2{\cdot}6H_2O$ (0.0.498 mmol, 0.148 g), H_2bdc (0.498 mmol, 0.083 g) and MVI_2 (0.502 mmol, 0.22 g) were combined in a vial with 7 ml anhydrous DMF and sealed. The reactants were sonicated for 15 minutes until dissolved and heated to 85 ^oC for 2 days. Orange and blue crystals were produced in a combined yield of 0.236 g, 40 % based on H_2bdc. The reaction was repeated using the same procedure and altering the reaction temperature to 120 ^oC. Blue crystalline product was produced with a yield of 0.284 g, 48 % based on H_2bdc.

4.6.4 Synthesis of $[MV]_{0.8}[NH_2(CH_3)_2]_{0.4}[Zn_3(bdc)_4]$

$Zn(NO_3)_2{\cdot}6H_2O$ (0.502 mmol, 0.149 g), H_2bdc (0.481 mmol, 0.080 g) and viologen diacetic acid dichloride (0.631 mmol, 0.217 g) were combined in a vial with 7 ml anhydrous DMF and sealed. The reactants were sonicated for 15 minutes until dissolved and heated to 120 ^oC for 2 days. Blue crystals were produced in a yield of 0.244 g, 47 % based on H_2bdc.

4.6.5 Synthesis of $[MV]_{0.5}[Zn(btc)]{\cdot}DMF$

$Zn(NO_3)_2{\cdot}6H_2O$ (0.502 mmol, 0.149 g), H_3btc (0.501 mmol, 0.106 g) and MVI_2 (0.547 mmol, 0.24 g) were combined in a vial with 7 ml anhydrous DMF and sealed. The reactants were sonicated for 15 minutes until dissolved and heated to 85 ^oC for 2 days. Orange and blue crystals were produced in a yield of 0.075 g, 32 % based on H_3btc. The reaction was repeated using the same procedure

and altering the reaction temperature to 120 ^{o}C. Blue crystalline product was produced with a yield of 0.080 g, 38 % based on H_3btc.

4.6.6 Synthesis of $[MV]_2[Zn_8(bpdc)_{10}]\cdot 16DMF\cdot 20H_2O$

$Zn(NO_3)_2\cdot 6H_2O$ (0.253 mmol, 0.075 g), H_2bpdc (0.512 mmol, 0.124 g) and MVI_2 (0.251 mmol, 0.11 g) were combined in a vial with 7.5 ml anhydrous DMF and sealed. The reactants were sonicated for 15 minutes until dissolved and heated to 85 ^{o}C for 2 days. Blue crystals were produced in a yield of 0.280 g, 23 % based on $Zn(NO_3)_2\cdot 6H_2O$. The reaction was repeated using the same procedure and altering the reaction temperature to 120 ^{o}C. Blue crystalline product was produced with a yield of 0.311 g, 26 % based on $Zn(NO_3)_2\cdot 6H_2O$.

4.6.7 Synthesis of $[EV][Zn_3(ip)_4]$

$Zn(NO_3)_2\cdot 6H_2O$ (0.502 mmol, 0.149 g), H_2ip (0.498 mmol, 0.083 g) and EVI_2 (0.615 mmol, 0.23 g) were combined in a vial with 7 ml anhydrous DMF and sealed. The reactants were sonicated for 15 minutes until dissolved and heated to 120 ^{o}C for 2 days. Blue crystals were produced in a yield of 0.170 g, 37 % based on H_2ip.

4.6.8 Synthesis of $[EV]_{0.53}[HEVH]_{0.26}[NH(CH_3)_2]_{0.42}[Zn_3bdc_4]$

$Zn(NO_3)_2\cdot 6H_2O$ (0.502 mmol, 0.149 g), H_2bdc (0.501 mmol, 0.082 g) and EVI_2 (0.513 mmol, 0.192 g) were combined in a vial with 7 ml anhydrous DMF and sealed. The reactants were sonicated for 15 minutes until dissolved and heated to 120 ^{o}C for 2 days. Blue crystals were produced in a yield of 0.158 g, 30 %.

4.7 References

1. A. D. Burrows, C. G. Frost, M. F. Mahon and C. Richardson, *Angew. Chem. Int. Ed.*, 2008, 47, 8482-8486
2. M. Muller, A. Devaux, C. H. Yang, L. De Cola and R. A. Fischer, *Photochem. Photobio. Sci.*, 2010, 9, 846-853
3. M. J. Rosseinsky, *Microporous Mesoporous Mater.*, 2004, 73, 15-30
4. A. M. Ullman, J. W. Brown, M. E. Foster, F. Leonard, K. Leong, V. Stavila and M. D. Allendorf, *Inorg. Chem*, 2016, 55, 7233-7249
5. D. Y. Siberio-Perez, H. K. Chae, J. Kim, Y. Go, A. J. Matzger. M. Eddaoudi, M. O'Keeffe and O. M. Yaghi, *Nature*, 2004, 427, 523-527
6. Y. Chen, V. Lykourinou, C. Vetromile, T. Hoang, L. J. Ming, R. W. Larsen and S. Ma, *J. Am. Chem. Scoc.*, 2012, 134, 13188-13191
7. D. Liu, X. Liu, Y. Liu, Y. Yu, F. Chen and C. Wang, *Dalton Trans.*, 2014, 43, 15237-15244
8. J. L. Herberg, R. K. Bhakta, B. Jacobs, A. Highley, R. Behrens, Jr., N. W. Ockwig, J. A. Greathouse, and M. D. Allendorf, *J. Am. Chem. Soc*, 2009, 131, 13198–13199
9. R. K. Bhakta. V. Stavila, T. M. Alam, E. H. Majzoub, and M. D. Allendorf, *ACS Nano*, 2012, 6, 9807–9817
10. M. D. Allendorf, M. E. Foster, F. Leonard, V. Stavila, P. L. Feng, F. P. Doty, K. Leong, E. Y. Ma, S. R. Johnston and A. A. Talin, *J. Phys. Chem. Lett.*, 2015, 6, 1182-1195
11. A. Centrone, A. A. Talin, A. C. Ford, M. E. Foster, V. Stavila,, R. A. Kinney, P. Haney, V. Szalai, F. El Gabaly, H. P. Yoon, F. Léonard and M. D. Allendorf, *Science*, 2014, 343, 66-69
12. C. L. Bird and A. T. Kuhn, *Chem. Soc. Rev.*, 1981, 10, 49-82
13. M. Mohammad, *J. Org. Chem.*, 1987, 52, 2779–2782
14. P. M. S. Monk, *Dyes Pigm.*, 1998, 39, 125-128
15. A. Ledwith, A.S. Hopkins and M. F. Stam, *J. Chem. Soc. D*, 1970, 494-495
16. J. K. Sun and J. Zhang, *Dalton Trans*, 2015, 44, 19041-19055
17. Y. Tan, Z. Fu, Y. Zeng, H. Chen, S. Liao, J. Zhang and J. Dai, *J Mater. Chem.*, 2012, 22, 17452-17455
18. Y. Zeng, Z. Fu, H. Chen, C. Liu, S. Liao and J. Dai, *Chemical Commun.*, 2012, 48, 8114-8116
19. K. Cassar. A. D. Burrows, R. M. W. Friend, M. F. Mahon, S. P. Rigby and J. E. Warren, *Cryst. Eng. Comm.*, 2005, 548–550
20. Q. G. Mulazzani, M. Z. Hoffmann and M. Venturi, *Radiat. Phys. Chem.*, 1984, 23, 229-236
21. W. W. Porter and T. P. Vaid, *J. Org. Chem.* , 2005, 70, 5028-5035
22. L. Xie, S. Liu, B. Gao, C. Zhang, C. Sun, D. Li and Z. Su, *Chem. Commun.*, 2005, 2402-2404
23. S. A. Sapchenko, D. N. Dybtsev, D. G. Samsonenko and V. P. Fedin, *New J. Chem.*, 2010, 34, 2445-2450
24. L. Pescatori, A. Arduini, A. Pochini, A. Secchi, C. Massera and F. Ugozzoli, *Org. Biomol. Chem.*, 2009, 7, 3698-3708
25. L. Chu. Y. Xiao, Y. Sanakis and P. Liu, *J. Am. Chem. Soc*, 2009, 131, 9931–9933
26. Z. Fei, A. D. Phillips, W. Han Ang, R. Scopelliti, and P. J. Dyson, *Cryst. Growth Des.*, 2009, 9, 1966–1978

5. Tailoring the emission of mixed-lanthanide metal-organic frameworks (MOFs)

5.1 Introduction

5.1.1 Lanthanide MOFs

Lanthanide MOFs are those in which the metal source within the framework is an *f*-block, lanthanide element. Increasing numbers of lanthanide MOFs are being reported and these can often display different topologies and properties from those of transition metal MOFs. The 4*f* orbitals are contracted, and shielded by the 5*s* and 5*p* electrons resulting in minimal participation of the *f* orbitals with ligand bonding. A direct consequence of this is that metal-ligand interactions are ionic in nature. The larger ionic radii of lanthanide metals compared to transition metals, means that both high and variable co-ordination numbers are possible in the resulting frameworks and these typically range from 6-12. This has made the predictability and control of resulting structures difficult, however it does aid the formation of three-dimensional networks making MOF formation favourable.[1,2] A further consequence of high connectivity is that resulting structures are often condensed and microporous in nature.[1]

The $[Ln_2(CIP)_2(DMF)_{4-x}(H_2O)_x]\cdot nH_2O$ structures (CIP = 5-(4-carboxybenzylideneamino)-isophthalate, x = 0-2 and n = 3-7) are a series of isoreticular lanthanide MOFs with three-dimensional networks.[3] This framework has been formed using many different lanthanide metals (Ln = La, Ce, Pr, Sm, Eu, Gd, Tb. Dy, Ho), the products of which contain similar topologies to one another. The structure of the CIP ligand and the SBU of $[La_2(CIP)_2(DMF)_{4-x}(H_2O)_x]\cdot 4H_2O$ are shown in Figure 5.1. The SBU is formed from two lanthanum ions, six carboxylate groups and two oxygen atoms from co-ordinating DMF molecules.

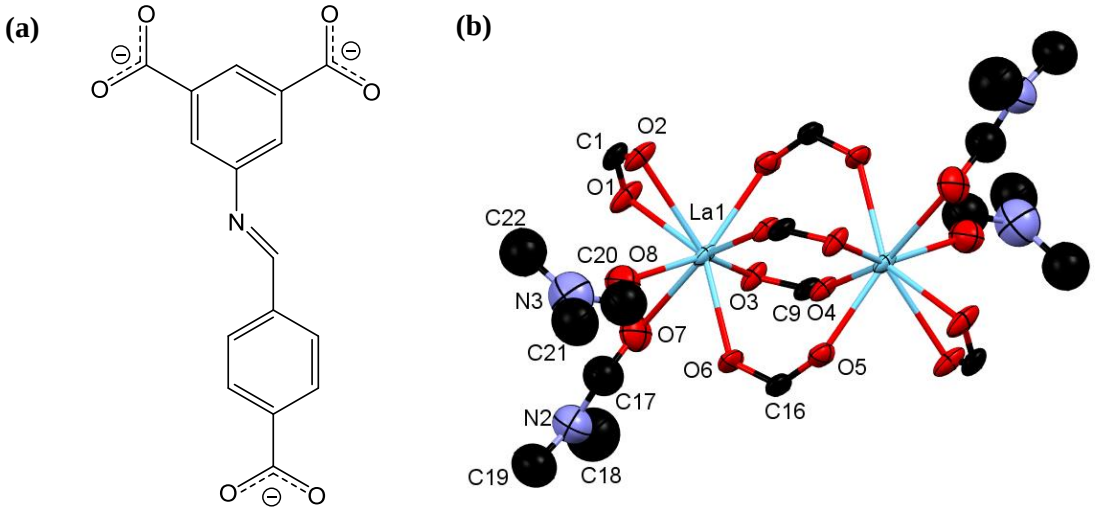

Figure 5.1 (a) The structure of the CIP ligand and **(b)** the SBU of $[La_2(CIP)_2(DMF)_{4-x}(H_2O)_x]\cdot 4H_2O$ with an ellipsoid probability of 40 %, hydrogen atoms have been removed for clarity. Atoms belonging to the asymmetric unit are labelled.[3]

The SBUs are linked together through the CIP ligands to form a three-dimensional network containing cavities reported to be 3-4 Å in diameter and connected through narrow passages 2 Å in diameter (Figure 5.2).

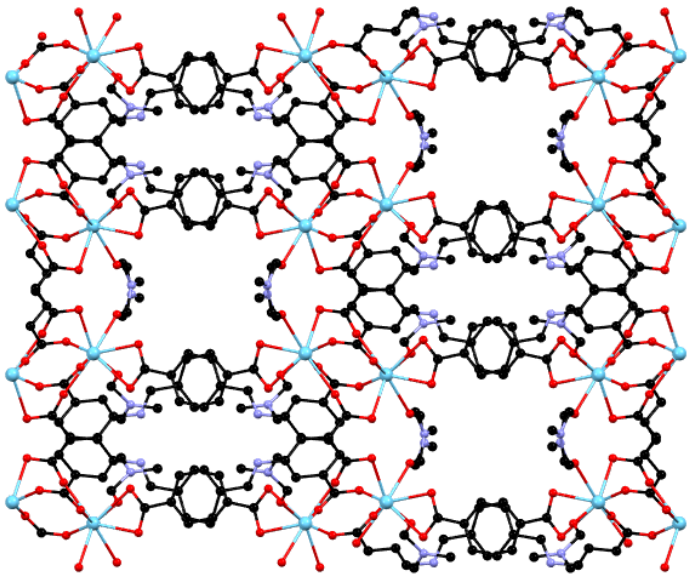

Figure 5.2 Part of the structure of $[La_2(CIP)_2(DMF)_{4-x}(H_2O)_x]\cdot 4H_2O$ viewed down the *c*-axis. Hydrogen atoms and guest solvent within the pores are removed for clarity.[3]

While the overall connectivity of the $[Ln_2(CIP)_2(DMF)_{4-x}(H_2O)_x]\cdot nH_2O$ structures are similar, changes to the unit cell parameters with different lanthanide centres are reported and are dependent upon the solvent ratio present in the framework.[4] A decrease in unit cell parameters of frameworks containing lanthanides of increasing atomic number is a commonly observed trend.[4] This is in line with the decrease in ionic radii of lanthanides across the series, due to an increase in nuclear charge and the poor shielding effect of the 4*f* electrons.

Many lanthanide MOFs display interpenetrated structures. An example is given in Figure 5.3, showing the interpenetrated structure of $[Er(bdc)_{1.5}(DMF)(H_2O)]$.[5] Reported thermogravimetric analysis on this structure shows no solvent guest molecules to be present in the framework.

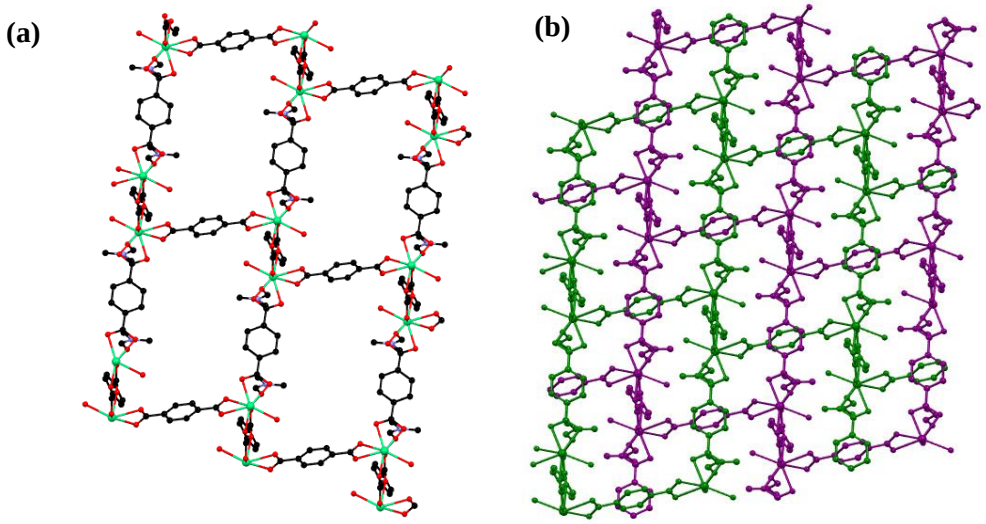

Figure 5.3 Part of the structure of $[Er(bdc)_{1.5}(DMF)(H_2O)]$ showing **(a)** one net with Er in green, C in black and O in red and **(b)** the two-fold interpenetrating nets in green and purple. In both cases the structure is viewed down the *b*-axis and hydrogen atoms are removed.

The structure contains a three-dimensional grid-like network with channels running in all three-dimensions. The channels are reported as being 11.3 x 14.7 Å in size and an overall two-fold interpenetration can be observed, resulting in a non-porous framework.

Controlling interpenetration in order to access structures with higher porosity has been highly studied in transition metal MOFs (see Section 1.1). Similar methods can be applied to lanthanide MOFs, as demonstrated by He and co-workers in the case of the interpenetrated $[Ln(bdc)_{1.5}(DMF)(H_2O)]$ (Ln = Er, Tm) structures.[5] In these studies three approaches were taken to control interpenetration. Firstly the co-ordinating solvent molecules were replaced with a rigid and bulky chelating ligand to form the structure of $[Ln_2(bdc)_3(phen)_2]\cdot 3H_2O$ (phen = phenanthroline). Secondly the bdc ligand was substituted with a benzenedicarboxylate ligand of increased steric bulk, tetramethyl benzenedicarbocxylate (tmbdc), forming $[Ln_2(tmbdc)_3(DMF)_2(H_2O)_2]\cdot 4H_2O$. Finally, a combination of the two methods was employed to form $[Ln_2(tmbdc)_3(phen)_2]\cdot 4DMF\cdot 2H_2O$. The structures of bdc, tmbdc and phen are given in Figure 5.4.

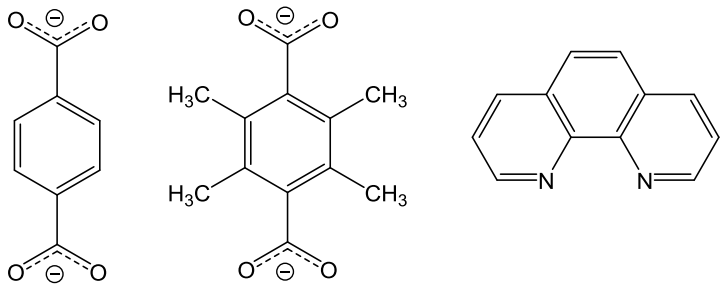

Figure 5.4 Structures of the1,4-benzenedicarbocxylate (bdc), tetramethyl-1,4-benzenedicarbocxylate (tmbdc) and phenanthroline (phen) ligands.

In all cases, the products were isostructural to the network in $[Ln(bdc)_{1.5}(DMF)(H_2O)]$, but did not display interpenetration.[5]

Although microporous structures are most common for lanthanide MOFs, frameworks with mesoporous cavities have also been reported. One of the earliest reports was that of $[Tb_{16}(tatb)_{16}(DMA)_{24}]\cdot 91DMA\cdot 108H_2O$, formed from the solvothermal reaction of triazine-1,3,5-tribenzoic acid (H_3tatb) and terbium nitrate.[6] The structure contains two types of cages with sizes of 3.9 nm and 4.7 nm in diameter respectively (Figure 5.5). Gas adsorption studies on the activated structure (see Section 1.4) found the surface area to be 1783 m^2g^{-1}.

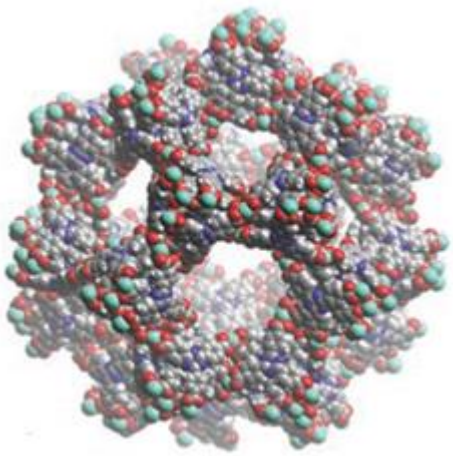

Figure 5.5 One of the mesoporous cages of $[Tb_{16}(tatb)_{16}(DMA)_{24}]\cdot 91DMA\cdot 108H_2O$. Carbon atoms are shown in grey, hydrogen in white, nitrogen in blue, oxygen in red and terbium in light blue.[6]

5.1.2 Lanthanide Luminescence

Lanthanide luminescence is well studied and has potential application in lighting and sensing applications.[7, 8] Therefore, reports of lanthanide MOFs have often focussed upon their luminescent properties.

The optical properties of lanthanide cations, Ln^{3+}, are governed by their electronic configurations, [Xe]4f^{n} (n=0-14).[9] Given the different electronic configuration of each lanthanide ion, and the numerous possible ways electrons can be distributed over the seven 4*f* orbitals, each lanthanide ion has a unique fingerprint emission spectrum (Figure 5.6).[1]

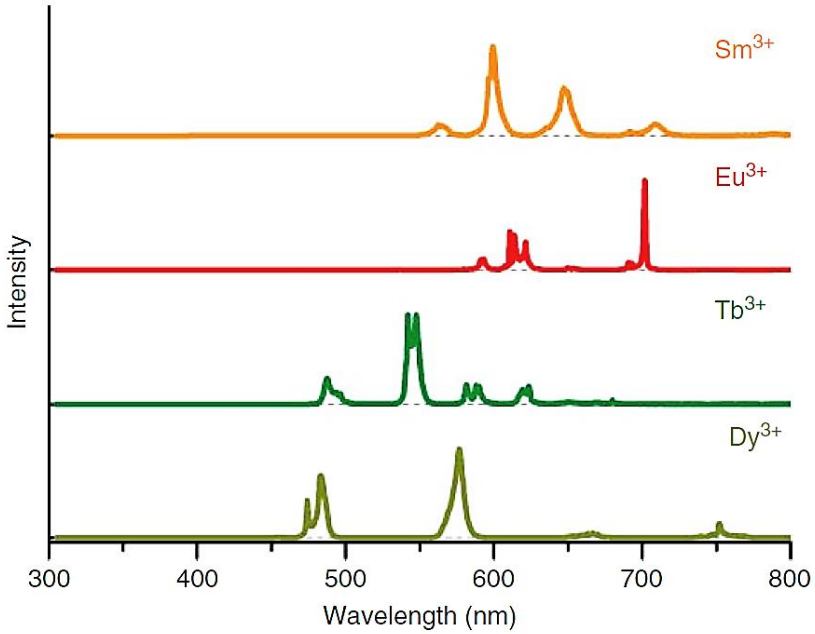

Figure 5.6 Emission spectra of the lanthanide ions Dy^{3+}, Tb^{3+}, Eu^{3+} and Sm^{3+}.[1]

The emission bands in the lanthanide spectra relate to *f-f* transitions relative to the ground state and arise in the UV, visible or NIR ranges. Many organic molecules, such as organic dyes, exhibit adsorption over a much broader range than lanthanide ions, due to the closely spaced vibrational levels present in organic molecules. Conversely, the emissions of the lanthanide ions are narrow and sharp as they involve transitions between 4*f* orbitals which are shielded by the occupied 5*p* orbitals.[10] As the *f*-orbitals minimally interact with the ligands, the emissions of lanthanide-containing compounds are generally independent of the co-ordination environment.

Lanthanides which emit in the visible region have distinctive associated colours, including red for Eu^{3+}, green for Tb^{3+}, yellow for Dy^{3+} and orange for Sm^{3+}. The *f-f* transitions are Laporte forbidden meaning direct absorption of the lanthanide ions is weak, limiting their use. Complexation with organic ligands is one route through which the weak adsorption of Ln^{3+} ions can be overcome. This process is referred to as sensitisation, in which the organic ligands act as antennae for exciting the

Ln^{3+} ions, first being excited themselves and then transferring their excitation energies to the lanthanide centre. (Figure 5.7).[9]

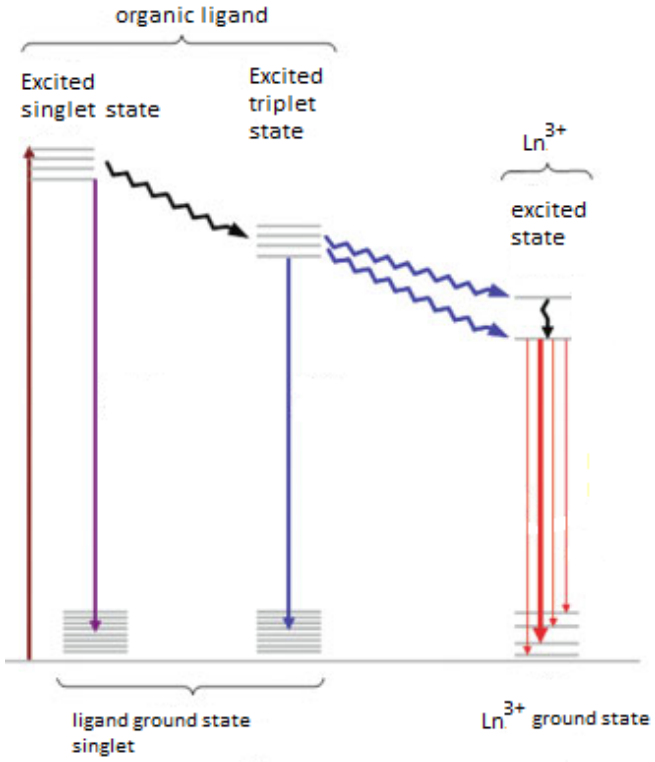

Figure 5.7 Schematic representation of sensitisation of luminescent lanthanide complexes with an organic antenna.[10]

This antenna effect occurs through absorption of a UV photon by the ligand, causing an electron to be promoted from the ground state to the excited singlet state. The electron in this excited state may then either return to the ground state through radiative emission, or cross to an excited triplet state changing its spin in the process. Deactivation of this excited triplet state may occur either through return to the ground state or through energy transfer to an excited state of the lanthanide ion, which is then followed by radiative emission to the lanthanide ground state.[10] This process is reliant upon the excited triplet state of the ligand being higher in energy than the excited state of the lanthanide ion.

In contrast to discrete molecular lanthanide complexes, lanthanide-MOFs have high thermal stability and their luminescence properties can be enhanced by organic ligands, with applications in light emitting devices.[8] The porosity of MOFs means that these materials also have the potential for other applications such as chemical sensing.[2] Structural alterations to lanthanide MOFs is a route to tailoring their emission properties. One such method of tailoring is that of ligand design to produce emission sensitisation through the antenna effect described above. This was demonstrated with the formation of the $[Ln_2(hfipbb)_3]$ frameworks, formed from the 4,4′-(hexafluoroisopropylidene)bis-benzoate ligand (hfipbb) (Figure 5.8).[11]

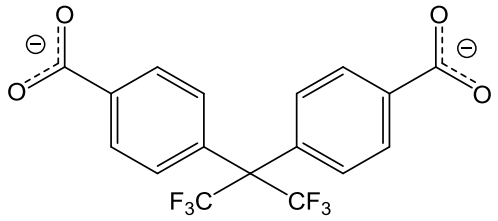

Figure 5.8 Structure of 4,4′-(hexafluoroisopropylidene)bis-benzoate, hfipbb.

The resulting MOFs display luminescence with colours of red, green and white emission for Ln = Eu, Tb and Gd respectively and blue/white emission for other lanthanides used, which is typical of the emission for the hfipbb ligand.[11]

A second route to property tailoring of lanthanide MOFs is the formation of mixed-lanthanide systems. Colour tuning can be affected by the Ln^{3+} ion type or concentration and can also be influenced by other factors such as the guest species within the structure.[12] Combining lanthanides, typically Eu^{3+} (red) and Tb^{3+} (green), within the same material is an approach which has proven effective in colour tuning MOF materials. Guo and co-workers successfully demonstrated this by forming $[Eu_{1-x}Tb_x(btc)(H_2O)]$ (where btc = 1,3,5-benzenetricarboxylate) structures with varying Eu:Tb ratios.[13] The structures show a change in the intensity of the Tb^{3+} emission, with alterations to the Eu:Tb ratio. As a result, the mixed-lanthanide structures range in colour from yellow/green to red.

5.1.3 Core-shell lanthanide MOFs: a route to tailoring luminescence properties

Mixed-lanthanide MOFs often have a random distribution of the lanthanide centres throughout the structure. This randomisation can lead to quenching of the colour emissions through energy transfer between emitter centres, making colour tuning difficult to achieve. One method to overcome this quenching is to form highly ordered, heterogeneous structures in which the different emitters (lanthanide types) are located within specific regions of the structure. This has been demonstrated through the formation of core-shell mixed-lanthanide systems based on the frameworks of $[Ln_2(mell)(H_2O)_8]\cdot H_2O$, mell = mellitate anion (Figure 5.9).[14]

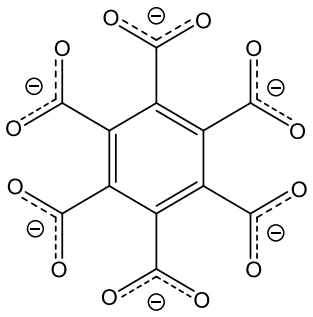

Figure 5.9 Structure of mellitate, mell.

In this study, a mixed-lanthanide system containing randomly distributed Eu^{3+}, Tb^{3+} and Gd^{3+} ions in a 1:1:1 ratio was synthesised. The resulting emission spectrum was dominated by Eu^{3+} emission (red) with much lower intensity Tb^{3+} (green) and ligand (blue) emissions. This is reported as being due to direct energy transfer between Tb^{3+} and Eu^{3+} centres which are in close proximity to one another in the framework, quenching the Tb^{3+} emission.

A comparison study was then carried out in which core-shell crystals of Gd@Tb@Eu ($[Gd_2(mell)(H_2O)_8]\cdot H_2O@[Tb_2(mell)(H_2O)_8]\cdot H_2O@[Eu_2(mell)(H_2O)_8]\cdot H_2O$) were formed through epitaxial growth of one lanthanide containing MOF onto the surface of another (see Section 1.5.2).[14] This process involves the synthesis of the inner core framework, $[Eu_2(mell)(H_2O)_8]\cdot H_2O$, the crystals of which are then placed in a solution containing the reactants needed to form the second shell, $[Tb_2(mell)(H_2O)_8]\cdot H_2O$. This second shell is deposited on the surface of the $[Eu_2(mell)(H_2O)_8]\cdot H_2O$ crystals during the reaction synthesis. The product of this reaction can be written as $[Tb_2(mell)(H_2O)_8]\cdot H_2O@[Eu_2(mell)(H_2O)_8]\cdot H_2O$. A final outer shell containing the gadolinium framework is formed through a similar method, giving the overall $[Gd_2(mell)(H_2O)_8]\cdot H_2O@[Tb_2(mell)(H_2O)_8]\cdot H_2O@[Eu_2(mell)(H_2O)_8]\cdot H_2O$ product.

Similar core-shell structures of Gd@Eu@Tb, Eu@Tb@Gd and Eu@Gd@Tb of the same framework topology were also formed in this manner. The resulting MOFs showed emission spectra which contained blue, green and red emissions of similar relative intensities to one another. Forming core-shell MOFs based on the framework of $[Ln_2(Mell)(H_2O)_8]\cdot H_2O$ is therefore an effective route to colour tuning the emission of the resulting materials, allowing control of energy transfer between emitting centres to be achieved.

5.2 Aims and objectives

While studies on lanthanides MOFs containing rigid linkers are common, there have been little reported on comparative systems with inherent linker flexibility. Thus the formation of lanthanide MOFs with the tetracarboxylate 5,5-oxydiisophthalate (odip) ligand were investigated, with a view to characterising the structure and topology of the resulting products. The odip ligand has a flexible ether bridging group between the benzene rings (Figure 5.10).

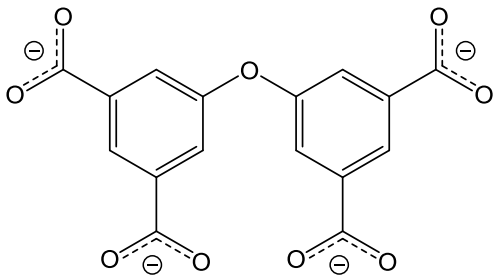

Figure 5.10 The structure of the 5,5-oxydiisophthalate, odip ligand.

The formation of lanthanide MOFs with odip were investigated using six lanthanides; Sm^{3+}, Eu^{3+}, Gd^{3+}, Tb^{3+}, Dy^{3+} and Er^{3+}. The resulting MOFs were structurally characterised through powder X-ray diffraction and single crystal X-ray diffraction methods. The luminescence properties of the products were analysed through fluorescence spectroscopy.

The possibility of tuning the emission of the lanthanide odip-containing frameworks was investigated through the synthesis of a series of isostructural, mixed-lanthanide materials. Firstly, an investigation into the mixed-lanthanide containing species formed through direct synthesis with Eu^{3+}, Tb^{3+} and Gd^{3+} ions was undertaken. This study aimed to investigate the possibility of emission tuning through randomly distributing lanthanide centres within the framework.

Secondly a study into the formation of core-shell structures was undertaken. The luminescence properties of the resulting structures were investigated to determine the effect of segregating different lanthanide centres on the emission of the MOF. The core shell structures were formed from Eu^{3+}, Tb^{3+} and Gd^{3+} containing shells and were studied through energy dispersive X-ray (EDX) spectroscopy and fluorescence spectroscopy.

Finally a comparison of the emission properties of the core-shell structures versus a physical mixture of single lanthanide systems containing Eu^{3+}, Tb^{3+} and Gd^{3+} ions, in order to assess the fluorescence of these two systems.

5.3 Synthesis and characterisation of $[Ln(Hodip)(H_2O)]\cdot nH_2O$

Lanthanide MOFs containing the tetracarboxylate ligand odip (5,5-oxydiisophthalate) were prepared through the reaction of a lanthanide nitrate with H_4odip in H_2O at 85 ^oC for 2 days. This reaction was conducted with the nitrates of Sm, Eu, Gd, Tb, Dy and Er. All reactions yielded colourless crystalline products.

Powder X-ray diffraction analyses were completed on all products and are shown in Figure 5.11. All of the powder diffraction patterns show Bragg peaks with similar positions to one another. There is some variation in the relative intensity of the peaks between products which may be due to differences in the solvent content of the products or orientation effects present during the data collection, as only small quantities of each product were available for analysis.

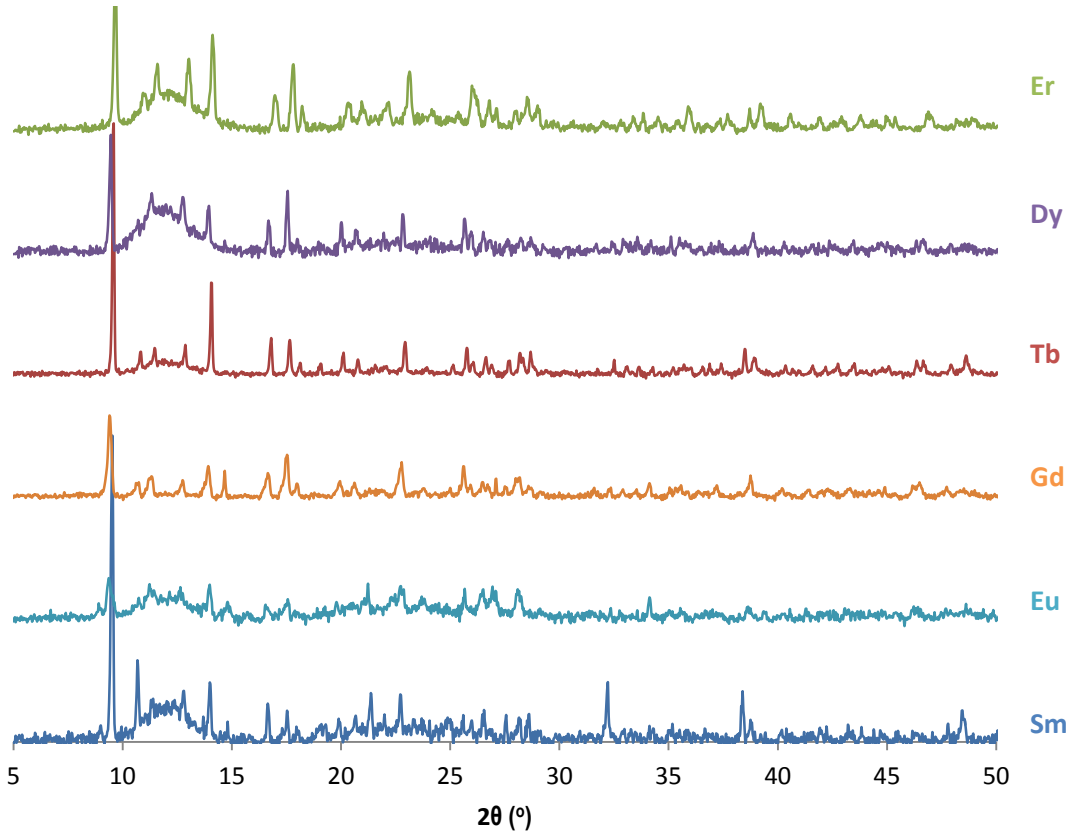

Figure 5.11 Powder X-ray diffraction patterns of products formed from the reaction of $Ln(NO_3)_3$ and H_4odip (Ln = Sm, Eu, Gd, Tb, Dy, Er).

The powder diffraction patterns of samples containing Sm, Eu, Dy and Er show the presence of a broad peak centred on a 2θ value of approximately 12^o. This is typical of an amorphous material, and suggests the presence of amorphous compounds within these products. The powder diffraction pattern of the product containing europium centres displays low peak intensity within the

diffraction pattern, suggesting the material has reduced crystallinity compared to the other products.

Crystals from the products containing Gd, Dy, Er, Sm and Tb were suitable for single crystal X-ray diffraction analysis.

Structure description of [Tb(Hodip)(H_2O)]·2H_2O **10a**

A colourless crystal of dimensions 0.079 × 0.054 × 0.029 mm^3 was selected from the product formed from the reaction with terbium nitrate and H_4odip, and analysed by single crystal X-ray diffraction. Associated data are presented in Table 5.1.

Table 5.1 Crystal data and structure refinement for [Tb(Hodip)(H_2O)]·2H_2O **10a**

Identification code	**10a**
Empirical formula	$C_{16}H_{13}O_{11}Tb$
Formula weight	556.18
Temperature/K	150.01(10)
Crystal system	monoclinic
Space group	$P2_1/n$
a/Å	9.8243(2)
b/Å	12.7350(3)
c/Å	13.9772(3)
α/°	90
β/°	93.8140(19)
γ/°	90
Volume/Å^3	1744.85(7)
Z	4
ρ_{calc}g/cm^3	2.117
μ/mm^{-1}	20.585
F(000)	1080.0
Crystal size/mm^3	0.079 × 0.054 × 0.029
Radiation	Cu$K\alpha$ (λ = 1.54184)
2θ range for data collection/°	9.404 to 145.672
Index ranges	$-11 \leq h \leq 12$, $-15 \leq k \leq 8$, $-17 \leq l \leq 17$
Reflections collected	7002
Independent reflections	3383 [R_{int} = 0.0304, R_{sigma} = 0.0431]
Data/restraints/parameters	3383/1/270
Goodness-of-fit on F^2	1.143
Final R indexes [I>=2σ (I)]	R_1 = 0.0382, wR_2 = 0.0789
Final R indexes [all data]	R_1 = 0.0460, wR_2 = 0.0824
Largest diff. peak/hole / e Å^{-3}	0.54/-0.56

The asymmetric unit of **10a** is formed from one terbium, one singly protonated Hodip ligand, one water molecule co-ordinating to the Tb centre and two free water solvent molecules, one of which is disordered over two positions (Figure 5.12).

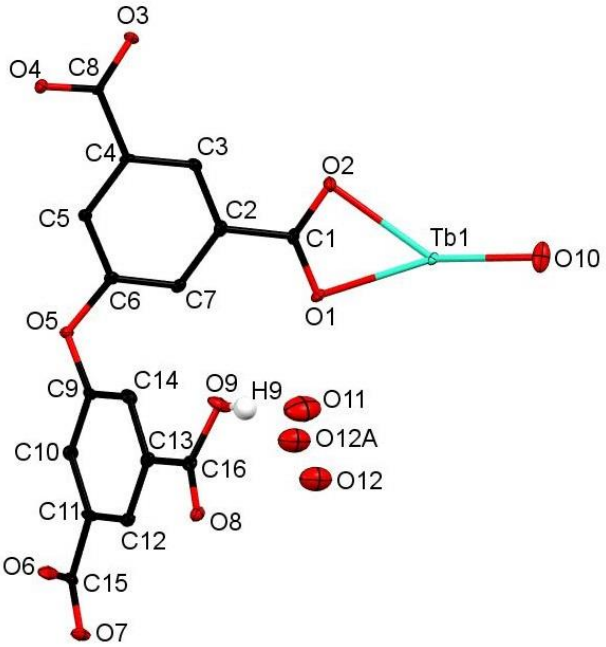

Figure 5.12 The asymmetric unit of [Tb(Hodip)(H_2O)]·2H_2O **10a** with an ellipsoid probability of 40 %. Hydrogen atoms, with the exception of H9, are removed for clarity.

The Hodip ligand present in the asymmetric unit co-ordinates to a total of six terbium atoms through seven of its carboxylate oxygen atoms. One carboxylate group remains protonated (O9). Five of the oxygen atoms (O3, O4, O6, O7 and O8) are monodentate, co-ordinating to five different terbium atoms, with the remaining carboxylate group (O1 and O2) co-ordinating to the same terbium centre through both oxygen atoms (Figure 5.13).

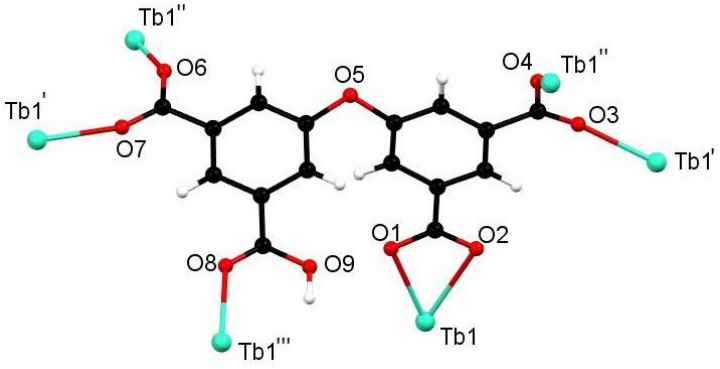

Figure 5.13 The co-ordination modes of Hodip displayed in [Tb(Hodip)(H_2O)]·2H_2O **10a**. Primed, double primed, triple primed and quadruple primed labelled atoms are related to those in the asymmetric unit by $x - 1, y, z$, $-x - ½, y - ½, ½ - z$, $x - ½, -y - ½, z - ½$ and $½ - x, ½ + y, ½ - z$ symmetry operations respectively.

The terbium is eight-coordinate, co-ordinating to six different Hodip ligands and one H_2O molecule (Figure 5.14).

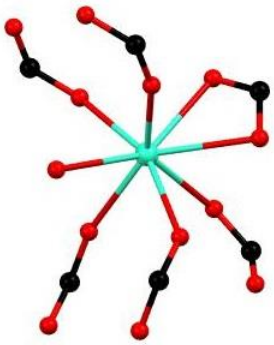

Figure 5.14 The terbium co-ordination in [Tb(Hodip)(H_2O)]·2H_2O **10a**.

The terbium centres are linked through the bridging carboxylate groups forming one-dimensional terbium chains in a zig-zag arrangement along the *a*-axis (Figure 5.15). These one-dimensional chains are linked together by the Hodip ligands to form a three-dimensional network (Figure 5.15).

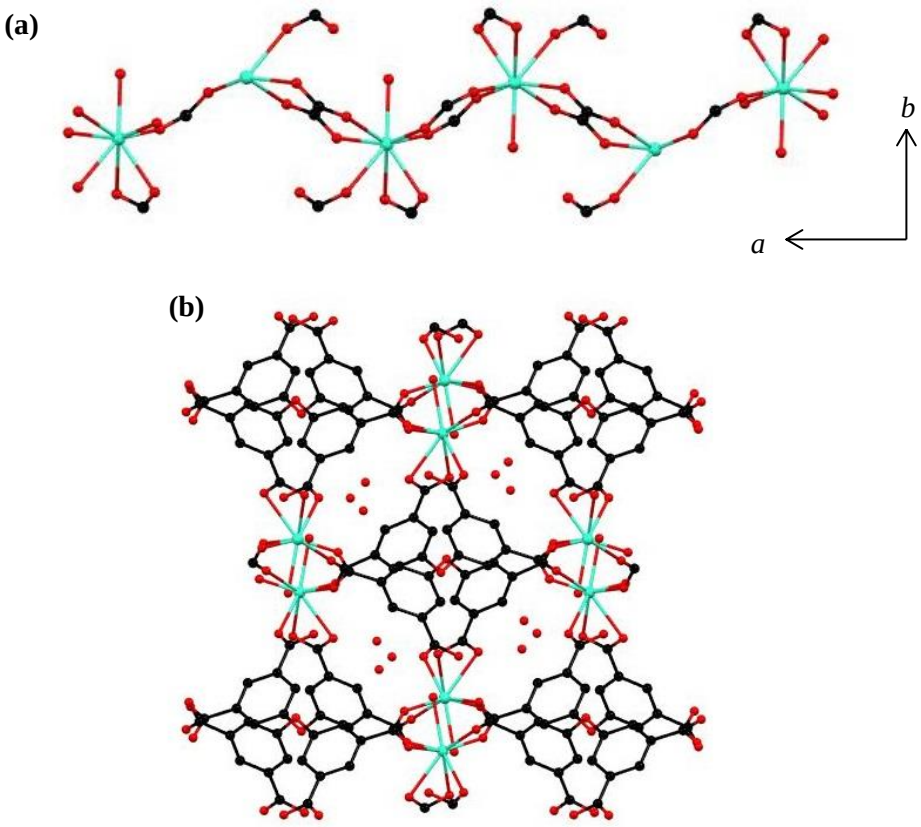

Figure 5.15 Part of the structure of [Tb(Hodip)(H_2O)]·2H_2O **10a** showing **(a)** the one-dimensional terbium chains linked by carboxylate groups and **(b)** the three-dimensional network viewed down the *a*-axis. Hydrogen atoms are removed for clarity.

The network contains small pores of 3.9 Å x 8.6 Å which are occupied by water molecules. The disordered solvent water molecule, O12/O12A have site occupancies of 80 % and 20 % respectively, based upon electron density. The hydrogen atoms relating to these water molecules could not be reliably located and were therefore omitted from the refinement. PLATON analysis revealed no additional solvent content and did not merit treatment with the SQUEEZE algorithm.

The powder diffraction pattern generated from the single crystal structure of **10a** was compared to the experimentally collected powder diffraction pattern of [Tb(Hodip)(H_2O)]·2H_2O (Figure 5.16). Both diffraction patterns contain Bragg peaks of similar position, but show differences in their relative intensities. This is possibly due to orientation effects present in the experimental diffraction pattern. Due to low yielding reactions, only a small amount of sample was able to be used for the powder diffraction data collection making orientation effects more likely. Other contributing factors to the difference in relative intensities of the two patterns could include differences in solvent content between the samples.

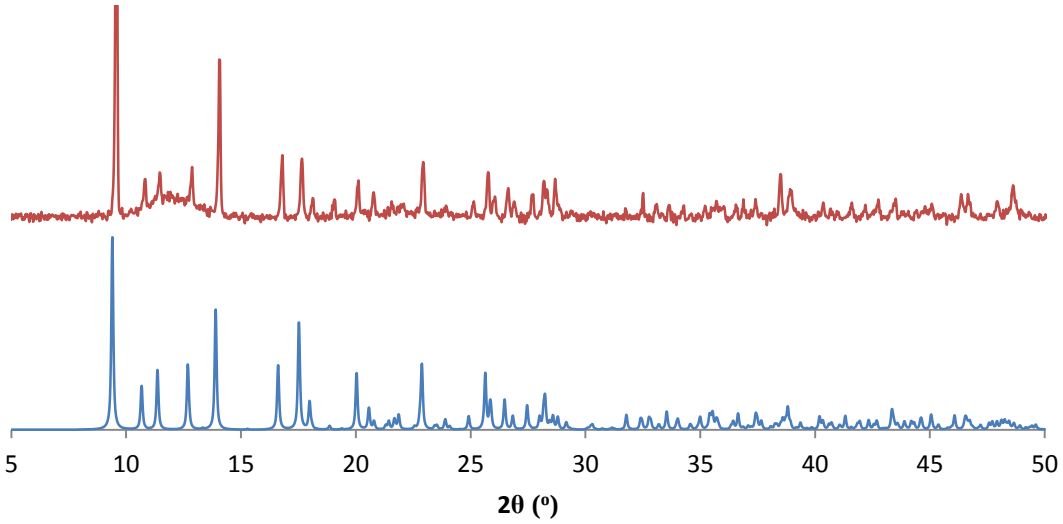

Figure 5.16 Powder X-ray diffraction patterns of [Tb(Hodip)(H_2O)]·2H_2O **10a** generated from single crystal structure (bottom) and collected experimentally (top).

Structure description of [Dy(Hodip)(H_2O)]·1.8H_2O **10b**, [Sm(Hodip)(H_2O)]·1.65H_2O **10c**, [Er(Hodip)(H_2O)]·1.8H_2O **10d** and [Gd(Hodip)(H_2O)]·2H_2O **10e**

Crystals from the products containing Dy, Sm, Er and Gd, were analysed by single crystal X-ray diffraction and showed the structures to be isostructural to that of [Tb(Hodip)(H_2O)]·2H_2O, **10a** and have comparative atom numbering. Crystal data for these structures are given in Table 5.2.

Table 5.2 Crystal data and structure refinement for [Dy(Hodip)(H_2O)]·1.8H_2O **10b**

Identification code	**10b**	**10c**	**10d**	**10e**
Empirical formula	$C_{16}H_{12.6}DyO_{11.8}$	$C_{16}H_{12.3}O_{11.65}Sm$	$C_{16}H_{12.6}ErO_{11.8}$	$C_{16}H_{13}GdO_{11}$
Formula weight	556.16	541.31	560.92	554.51
Temperature/K	150.00(10)	150.00(10)	150.01(10)	150.00(10)
Crystal system	monoclinic	monoclinic	monoclinic	monoclinic
Space group	$P2_1/n$	$P2_1/n$	$P2_1/n$	$P2_1/n$
a/Å	9.8077(2)	9.92621(12)	9.76631(17)	9.8450(5)
b/Å	12.7197(3)	12.74029(16)	12.7056(2)	12.7548(6)
c/Å	13.9411(4)	13.9980(2)	13.9075(2)	13.9951(8)
α/°	90	90	90	90
β/°	93.756(2)	93.8694(12)	93.7181(16)	93.753(5)
γ/°	90	90	90	90
Volume/Å^3	1735.42(8)	1766.19(4)	1722.10(5)	1753.62(16)
Z	4	4	4	4
ρ_{calc}g/cm^3	2.129	2.036	2.163	2.100
μ/mm^{-1}	23.679	25.589	9.694	25.113
F(000)	1076.0	1054.0	1084.0	1076.0
Crystal size/mm^3	0.056 × 0.032 × 0.025	0.079 × 0.058 × 0.042	0.111 × 0.046 × 0.019	0.078 × 0.019 × 0.015
Radiation	Cu$K\alpha$ (λ = 1.54184)	Cu$K\alpha$ (λ = 1.54184)	Cu$K\alpha$ (λ = 1.54184)	Cu$K\alpha$ (λ = 1.54184)
2θ range for data collection/°	9.422 to 145.704	9.396 to 145.918	9.438 to 145.298	9.39 to 145.7
Index ranges	-10 ≤ h ≤ 12, -15 ≤ k ≤ 9, -16 ≤ l ≤ 17	-12 ≤ h ≤ 12, -15 ≤ k ≤ 15, -16 ≤ l ≤ 17	-9 ≤ h ≤ 11, -15 ≤ k ≤ 9, -16 ≤ l ≤ 16	-12 ≤ h ≤ 10, -15 ≤ k ≤ 15, -17 ≤ l ≤ 17
Reflections collected	6659	26509	5971	5691
Independent reflections	3377 [R_{int} = 0.0324, R_{sigma} = 0.0458]	3504 [R_{int} = 0.0294, R_{sigma} = 0.0163]	3336 [R_{int} = 0.0252, R_{sigma} = 0.0377]	5691 [R_{int} = 0.0252, R_{sigma} = 0.0458]
Data/restraints/parameters	3377/0/278	3504/1/270	3336/0/276	5691/6/279
Goodness-of-fit on F^2	1.014	1.069	1.060	0.893
Final R indexes [I>=2σ(I)]	R_1 = 0.0299, wR_2 = 0.0610	R_1 = 0.0219, wR_2 = 0.0531	R_1 = 0.0311, wR_2 = 0.0749	R_1 = 0.0282, wR_2 = 0.0695
Final R indexes [all data]	R_1 = 0.0407, wR_2 = 0.0652	R_1 = 0.0241, wR_2 = 0.0542	R_1 = 0.0378, wR_2 = 0.0792	R_1 = 0.0419, wR_2 = 0.0718
Largest diff. peak/hole / e Å^{-3}	0.62/-0.52	0.46/-0.72	0.66/-0.64	0.83/-0.60

The structures of **10b**-**10e** contain two water molecules per asymmetric unit, one of which is disordered over two positions. The occupancies of these solvent molecules differ between structures. The asymmetric unit of dysprosium-containing structure, **10b**, contains O11 with a site occupancy of 80 % based on electron density whilst the O12/O12A disordered water molecule was modelled with a site occupancy to 75 % and 25 % respectively. A total of 1.8 solvent water

molecules are therefore present per dysprosium giving a formula of $[Dy(Hodip)(H_2O)]\cdot 1.8H_2O$ **10b**.

The samarium-containing structure contains O11 with a site occupancy of 65 % and O12 which is disordered over two sites; O12 and O12A with site occupancies of 65 % and 35 % respectively. The structure therefore contains a total solvent content of 1.65 water molecules per samarium giving a formula of $[Sm(Hodip)(H_2O)]\cdot 1.65H_2O$ **10c**.

The water molecules in the structure of **10d** have site occupancy factors of 80 % and 20 % to O11 and O11A respectively and 100 % for O12 giving the product formula of $[Er(Hodip)(H_2O)]\cdot 1.8H_2O$ **10d**.

The structure of **10e** was found to contain a twin component which was located at 180° around the 1,0,0 reciprocal direction. The twin fractions were modelled with a ratio of 75:25. The disordered water molecule of O12 and O12A has site occupancies of 80 % and 20 % respectively.

In all cases, the hydrogen atoms pertaining to the water molecules could be reliably located and so were not included within the refinement.

$[Eu(Hodip)(H_2O)]\cdot nH_2O$

Unfortunately, crystals of the Eu containing product were unsuitable for single crystal X-ray diffraction analysis due to their small size. However, the powder X-ray diffraction data suggests the product is isoreticular to the frameworks of Gd, Dy, Er, Sm and Tb products. The structure is therefore defined as $[Eu(Hodip)(H_2O)]\cdot nH_2O$, in which the value of n in the solvent content is not known.

5.3.1 Fluorescence spectroscopy studies of H_4odip and [Ln(Hodip)(H_2O)]·nH_2O, Ln = Tb, Eu, Gd

Fluorescence studies were conducted on samples of [Tb(Hodip)(H_2O)]·2H_2O and [Eu(Hodip)(H_2O)]·nH_2O due to the characteristic emission of Tb^{3+} (green) and Eu^{3+} (red) in the visible region. The fluorescence of [Gd(Hodip)(H_2O)]·2H_2O was also investigated, as Gd^{3+}-containing compounds are often dominated by ligand emission, as the lowest excited (emitting) level in Gd^{3+} often lies above the excited triplet level of organic ligands.[15]

In preparation, the excitation and emission spectra of H_4odip were recorded and are shown in Figure 5.17. The excitation spectrum, produced with a λ_{ex} = 420 nm, shows a broad band centred around 370 nm due to absorption of the ligand. The emission spectrum was recorded using an excitation wavelength equivalent to the excitation maximum; λ_{ex} = 370 nm. A broad emission band centred at 420 nm can be observed, arising from the π-π* transitions within the organic compound giving the compound overall blue emission.

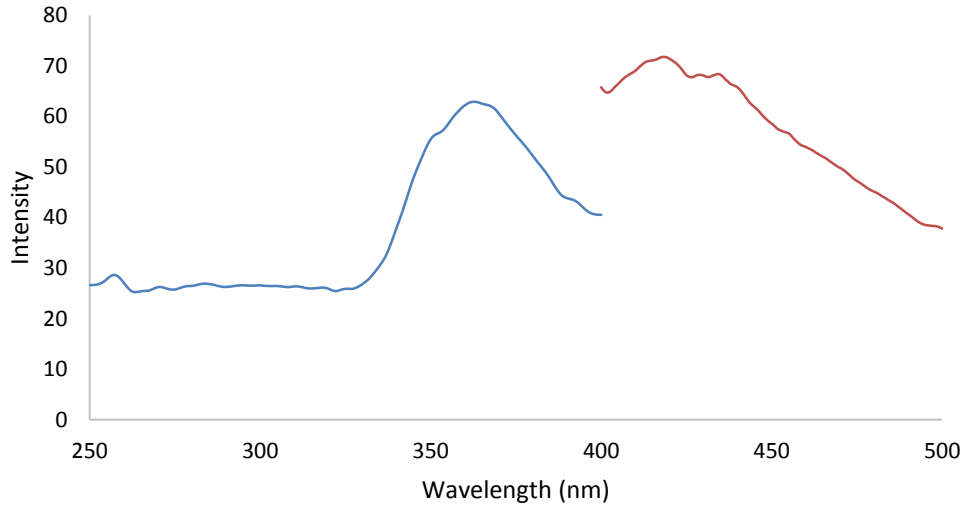

Figure 5.17 The solid state excitation and emission spectrum of H_4odip. The emission spectrum is shown in red and the excitation spectrum in blue.

Emission spectra for the lanthanide MOFs with Hodip ligands were recorded around the ligand excitation maximum (370 nm) at room temperature to determine if any ligand sensitisation of the lanthanide centres occurs within these compounds.

[Tb(Hodip)(H_2O)]·2H_2O

The excitation and emission spectra of [Tb(Hodip)(H_2O)]·2H_2O are shown in Figure 5.18.

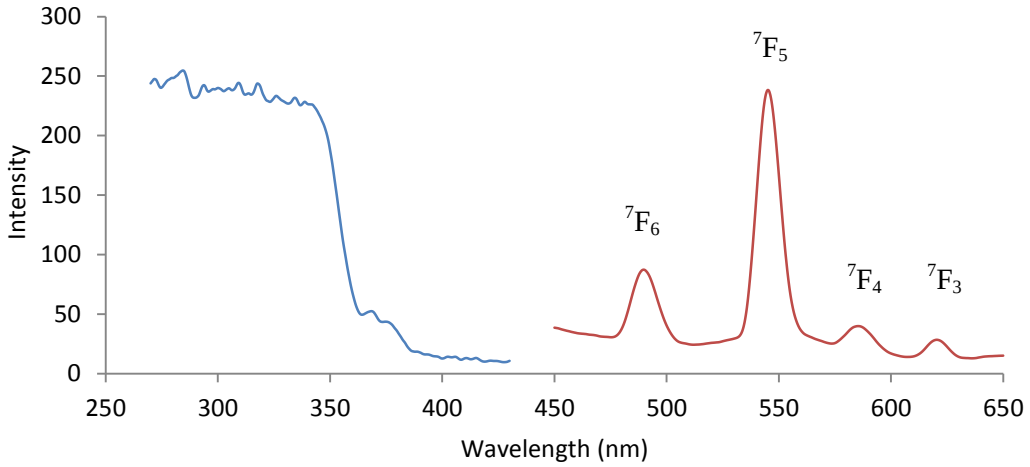

Figure 5.18 The solid state excitation and emission spectrum of [Tb(Hodip)(H_2O)]·2H_2O, with corresponding term symbols for each transition (all of which originate from $^5D_4$). The emission spectrum is shown in red and the excitation spectrum in blue.

The emission spectrum shows four peaks at 480 nm, 545 nm, 580 nm and 620 nm which correspond to the $^5D_4$ -$^7F_6$, $^5D_4$-$^7F_5$, $^5D_4$-$^7F_4$ and $^5D_4$ -$^7F_3$ transitions between energy level states of Tb^{3+} respectively.[1] Overall the emission of [Tb(Hodip)(H_2O)]·2H_2O is observed in the green region of the visible spectrum which is characteristic of Tb^{3+}.

The excitation spectrum was recorded using a λ_{ex} = 545 nm and is dominated by a band at approximately 270-340 nm. The high intensity and broad nature of the band is suggestive of ligand to metal charge transfer (LMCT). Similar bands have been observed in the excitation spectra of other lanthanide materials, but are not present in the spectrum of the terbium salt only.[16] The LMCT band suggests that ligand sensitisation of the Tb^{3+} centre may be occuring.[17]

The excitation and emission spectra of [Eu(Hodip)(H_2O)]·nH_2O and [Gd(Hodip)(H_2O)]·2H_2O are shown in Figure 5.19 and were found to emit red and blue light respectively.

The emission spectra of both of these products are dominated by a broad band at 370 nm typical of H_4odip. The spectrum of [Eu(Hodip)(H_2O)]·nH_2O also shows three peaks; 594 nm, 615 nm and 693 nm, corresponding to $^5D_0$-$^7F_1$, $^5D_0$-7F_2 and $^5D_0$-$^7F_4$ transitions of the energy states in Eu^{3+}.[1] The Eu^{3+} transitions are overlapped by the broad emission band which is indicative of luminescence sensitisation of the Eu^{3+} centres by the ligand.[18] The spectrum of [Gd(Hodip)(H_2O)]·2H_2O shows only the H_4odip emission, indicating no ligand sensitisation is occurring, possibly due to the high energy of the Gd^{3+} excited states.[15]

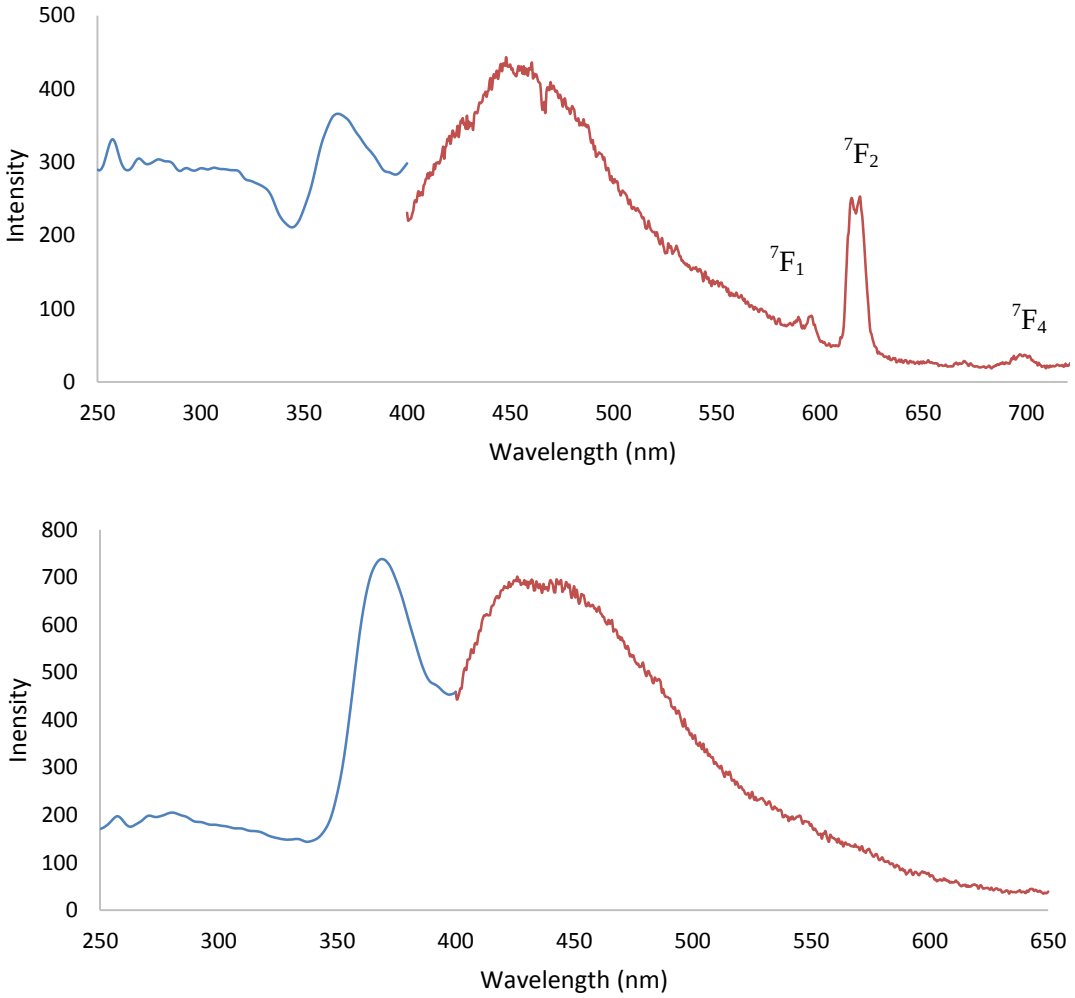

Figure 5.19 The solid state excitation and emission spectrum of [Eu(Hodip)(H_2O)]·nH_2O with corresponding term symbols for each transition, all of which originate from $^5D_0$ (top), and [Gd(Hodip)(H_2O)]·2H_2O (bottom). The emission spectra are shown in red and the excitation spectra in blue.

The excitation spectra (λ_{ex} = 615 nm and λ_{ex} = 370 nm respectively) show similar features to that of [Tb(Hodip)(H_2O)]·2H_2O, with a broad band at 250-240 nm thought to be due to LMCT. The band at 370 nm is typical of H_4odip.

As the fluorescence studies on [Tb(Hodip)(H_2O)]·2H_2O, [Eu(Hodip)(H_2O)]·nH_2O and [Gd(Hodip)(H_2O)]·2H_2O show, these compounds emit green, red and blue light respectively. The potential therefore exists to produce compounds which have colour tuned emission by combining these lanthanide metals to produce mixed-lanthanide frameworks.

5.4 Investigation of the mixed-lanthanide species $[Gd_{0.17}Tb_{0.19}Eu_{0.64}(Hodip)(H_2O)]$

A targeted synthesis to produce a mixed-metal MOF with the [Ln(Hodip)(H_2O)] framework and containing a mixture of Gd^{3+}, Tb^{3+} and Eu^{3+} ions was carried out by combining the nitrates of gadolinium, terbium and europium in a 1:1:1 ratio with H_4odip in H_2O and heating to 85 ^oC for 2 days. The reaction yielded a colourless crystalline product, which was analysed by powder X-ray diffraction. This is shown in Figure 5.20 alongside the powder diffraction pattern of $[Tb(Hodip)(H_2O)]\cdot 2H_2O$.

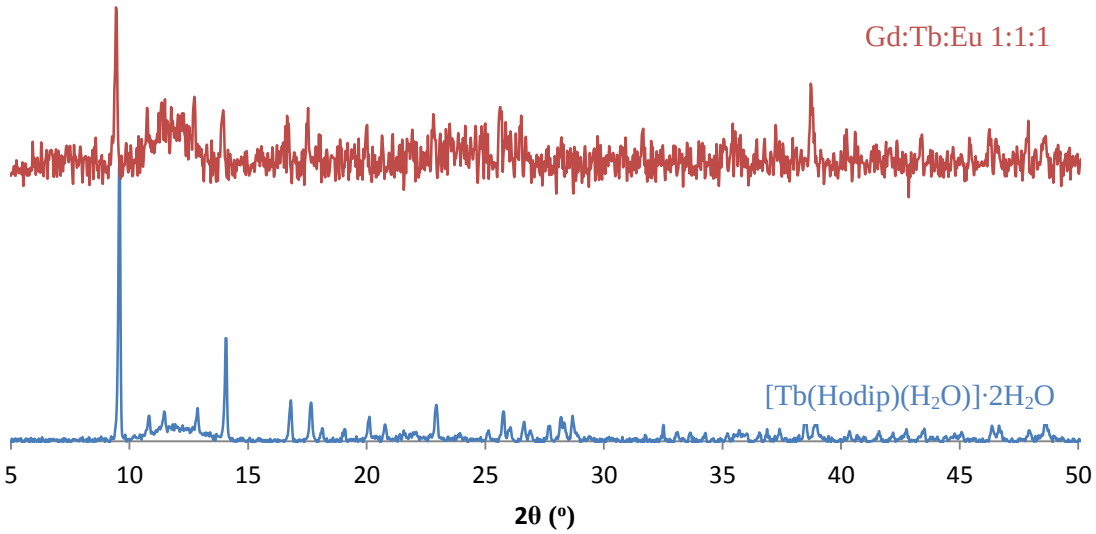

Figure 5.20 Powder diffraction patterns of $[Tb(Hodip)(H_2O)]\cdot 2H_2O$ (bottom) and the product formed from the synthesis of a 1:1:1 mixture of $Gd(NO_3)_3$, $Tb(NO_3)_3$ and $Eu(NO_3)_3$ with H_4odip (top).

The powder X-ray diffraction pattern of the mixed-lanthanide product shows the product to be largely amorphous. However, there is some evidence for the presence of a crystalline product isostructural to that of $[Tb(Hodip)(H_2O)]\cdot 2H_2O$ with peaks evident at 2θ values of 9.4º, 14.0º, 16.5º and 17.5º.

The presence of Gd^{3+}, Tb^{3+} and Eu^{3+} in the product was confirmed by EDX spectroscopy. Scanning electron microscope (SEM) images of the sample show that the product is not homogeneous, with some crystals appearing darker than others (Figure 5.21).

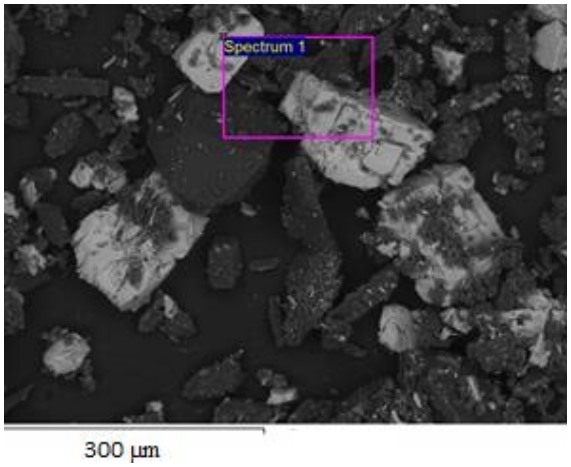

Figure 5.21 SEM image of the product formed from the synthesis of a 1:1:1 mixture of $Gd(NO_3)_3{\cdot}6H_2O$, $Tb(NO_3)_3.5H_2O$ and $Eu(NO_3)_3.xH_2O$ with H_4odip.

The darker regions correspond to materials which contain lighter elements, and EDX analysis identifies these as an organic material which is, most likely, H_4odip. The lighter regions are due to the collision of the electron beam with atoms containing larger nuclei, emitting more electrons and therefore making the image appear brighter. These crystals contain heavier elements, and EDX analysis shows the presence of europium, gadolinium and terbium ions. Due to the combination of the Gd^{3+}, Tb^{3+} and Eu^{3+} ions during the synthetic procedure, the crystals are likely to have randomly distributed lanthanide ions within their structure. Five of the light-coloured crystals were analysed by EDX spectroscopy to determine the percentage of europium, gadolinium and terbium present in the crystal, normalised to equal a total of 100 %. The results are shown graphically in Figure 5.22.

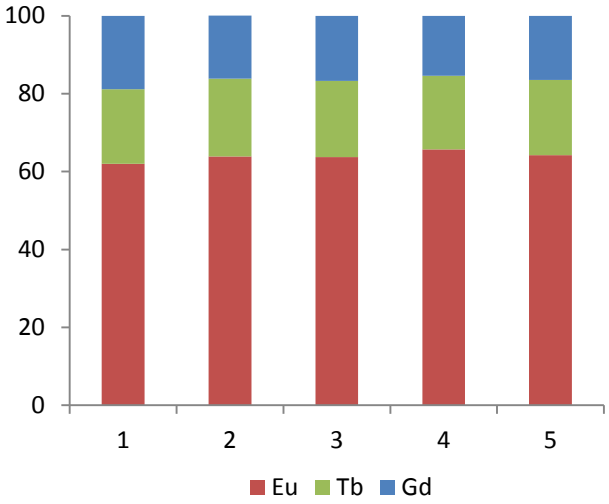

Crystal	% Eu	% Tb	% Gd
1	62.0	19.3	18.7
2	63.9	19.9	16.2
3	63.7	19.5	16.8
4	65.7	18.9	15.4
5	64.2	19.4	16.4

Figure 5.22 The percentage of europium, terbium and gadolinium present in five crystals of the product as determined through EDX spectroscopy.

A clear preferential inclusion of europium in the product can be seen, with an average of 64 % Eu^{3+} across the five crystals analysed. The remaining lanthanide composition is formed from an average of 19.3 % Tb^{3+} and 16.7 % Gd^{3+}. The composition of the product can therefore be proposed as $[Gd_{0.17}Tb_{0.19}Eu_{0.64}(Hodip)(H_2O)]$, omitting any guest solvent molecules which may be present. All five crystals analysed were seen to contain similar lanthanide ion ratios to one another. This infers that little compositional variation is present between crystals produced through this method.

5.4.1 Fluorescence spectroscopy studies of $[Gd_{0.17}Tb_{0.19}Eu_{0.64}(Hodip)(H_2O)]$

Visual observations of the $[Gd_{0.17}Tb_{0.19}Eu_{0.64}(Hodip)(H_2O)]$ product under a UV lamp showed the product to be red when illuminated with light of λ = 254 nm. Solid state emission spectra were therefore recorded at room temperature through excitation at this wavelength (λ_{ex} = 254 nm) and at excitation of H_4odip (λ_{ex} = 370 nm) and are shown in Figure 5.23.

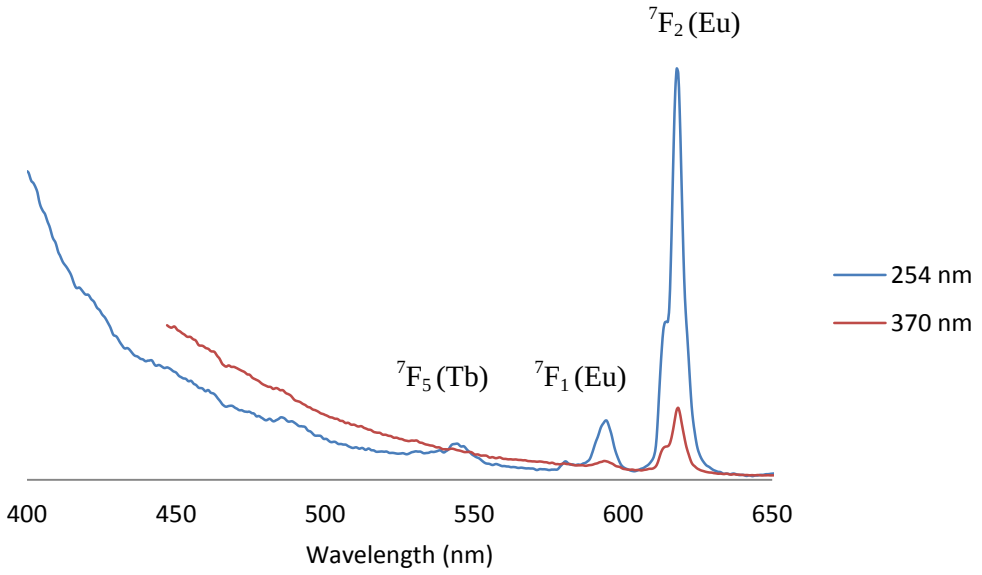

Figure 5.23 Solid state emission spectra of $[Gd_{0.17}Tb_{0.19}Eu_{0.64}(Hodip)(H_2O)]$. Corresponding term symbols for each transition are given (The Tb transitions originate from $^5D_4$ and the Eu transitions originate from $^5D_0$).

Both emission spectra are comparable to one another and are dominated by high intensity emission bands of Eu^{3+} at 594 nm and 618 nm. Some evidence of Tb^{3+} emission is present, with a band at 545 nm, and the tail of the broad ligand emission band can also be observed (400 – 500 nm), suggestive of sensitisation of the Ln^{3+} luminescence. Variation between the intensity of the two emission spectra is a result of different excitation wavelengths being used, as the fluorescence intensity is directly proportional to the intensity of the incident radiation, which is itself a function of wavelength.[14]

The solid state excitation spectra were recorded through excitation of the ligand (442 nm), Tb^{3+} (545 nm) and Eu^{3+} (618 nm) and are shown in Figure 5.24.

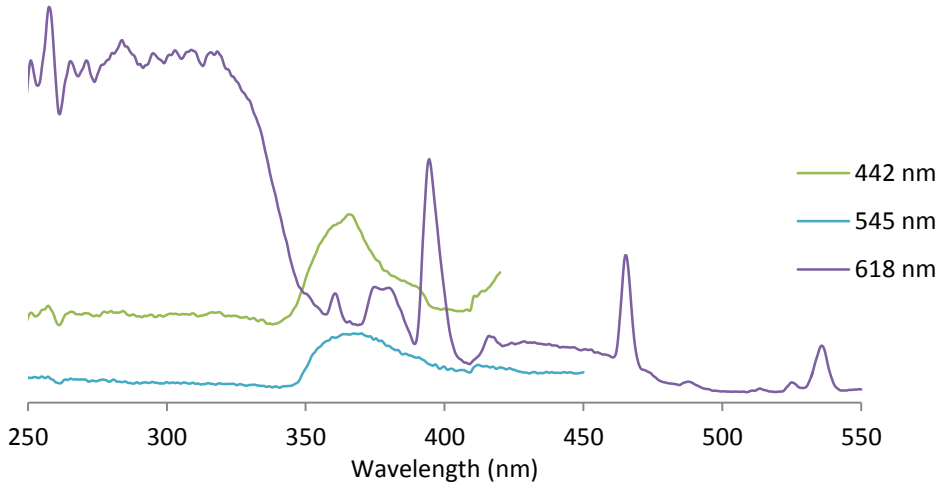

Figure 5.24 Solid state excitation spectra of $[Gd_{0.17}Tb_{0.19}Eu_{0.64}(Hodip)(H_2O)]$.

Excitation of Eu^{3+} (618 nm) shows a strong, broad band at 250 - 350 nm possibly due to LMCT and sharper bands at 361 nm, 377 nm, 394 nm and 465 nm which arise from Eu^{3+} transitions. The excitation of Tb^{3+} (545 nm) and the H_4odip (442 nm) have similar features to one another. Both show a broad band at 250-340 nm with a lower intensity to that of the analogous band in the Eu^{3+} excitation spectra, and a band at 370 nm characteristic of H_4odip.

Overall, the solid state emission and excitation spectra of the mixed-metal framework $[Gd_{0.17}Tb_{0.19}Eu_{0.64}(Hodip)(H_2O)]$ shows a dominance by Eu^{3+}, which confirms the visual observations of the sample under UV irradiation (appearing red in colour). This may be due to the increased concentration of europium within the sample in comparison to terbium and gadolinium content, but may also be influenced by quenching of the terbium fluorescence by the europium centres.[14] Metal to metal energy transfer is known to occur between Tb^{3+} and Eu^{3+} ions in close proximity to one another. Electrons in the excited state of the Tb^{3+} are transferred to lower lying Eu^{3+} states, resulting in a quenching of Tb^{3+} transitions and a predominance of the Eu^{3+} transitions. A quenching of the Tb^{3+} emission through this electron transfer process was reported for the mixed-lanthanide system $[Ln_2(mell)(H_2O)_8]\cdot H_2O$, which showed an overall red emission (see Section 5.1.3).[14]

5.5 Investigation of mixed-lanthanide core-shell species

As stated earlier (section 5.1.3) the formation of core-shell lanthanide MOFs has been demonstrated to prevent energy transfer between lanthanide ions within a mixed-metal system.[14] Hence, a similar method was undertaken, based on the frameworks [Ln(Hodip)(H_2O)], forming core-shell analogues. The structures were formed through growth of one lanthanide containing MOF onto the surface of a MOF with similar topology but, with the former containing an alternative lanthanide metal. Three out of a possible six core-shell MOF permutations were synthesised and are given below with any guest solvent omitted from the formulae.

[Gd(Hodip)(H_2O)]@[Tb(Hodip)(H_2O)]@[Eu(Hodip)(H_2O)] (referred to as Gd@Tb@Eu)

[Tb(Hodip)(H_2O)]@[Eu(Hodip)(H_2O)]@[Gd(Hodip)(H_2O)] (referred to as Tb@Eu@Gd)

[Eu(Hodip)(H_2O)]@[Gd(Hodip)(H_2O)]@[Tb(Hodip)(H_2O)] (referred to as Eu@Gd@Tb)

Each material contains three shells, one containing each of europium, terbium or gadolinium centres. Overall, the three materials differ in the shell ordering.

For the Gd@Tb@Eu compound, crystals of [Eu(Hodip)(H_2O)] were first synthesised through the reaction of $Eu(NO_3)_3$ (which was prepared *in situ* from Eu_2O_3) with H_4odip in H_2O at 85 ^oC for 2 days. The resulting crystals were decanted from the supernatant and placed in fresh H_2O three times over three days to remove any unreacted reagents. The [Eu(Hodip)(H_2O)]·nH_2O crystals were then placed in a H_2O solution containing dissolved $Tb(NO_3)3{\cdot}5H_2O$ and H_4odip and heated to 85 ^oC for 2 days to form the first core-shell material [Tb(Hodip)(H_2O)]@[Eu(Hodip)(H_2O)]. This product was washed with H_2O in a similar manner to that for [Eu(Hodip)(H_2O)], to remove any unreacted reagents. These crystals were then placed in a H_2O solution containing dissolved $Gd(NO_3)_3{\cdot}6H_2O$ and H_4odip and heated to 85 ^oC for 2 days to form the final core-shell structure [Gd(Hodip)(H_2O)]@[Tb(Hodip)(H_2O)]@ [Eu(Hodip)(H_2O)] (Gd@Tb@Eu). The other two core-shell materials, Tb@Eu@Gd and Eu@Gd@Tb, were prepared using a similar method but varying the order of the lanthanide shells. All reactions gave colourless crystals.

The three products were analysed by powder X-ray diffraction and compared to the diffraction pattern of [Tb(Hodip)(H_2O)]·$2H_2O$ (Figure 5.25).

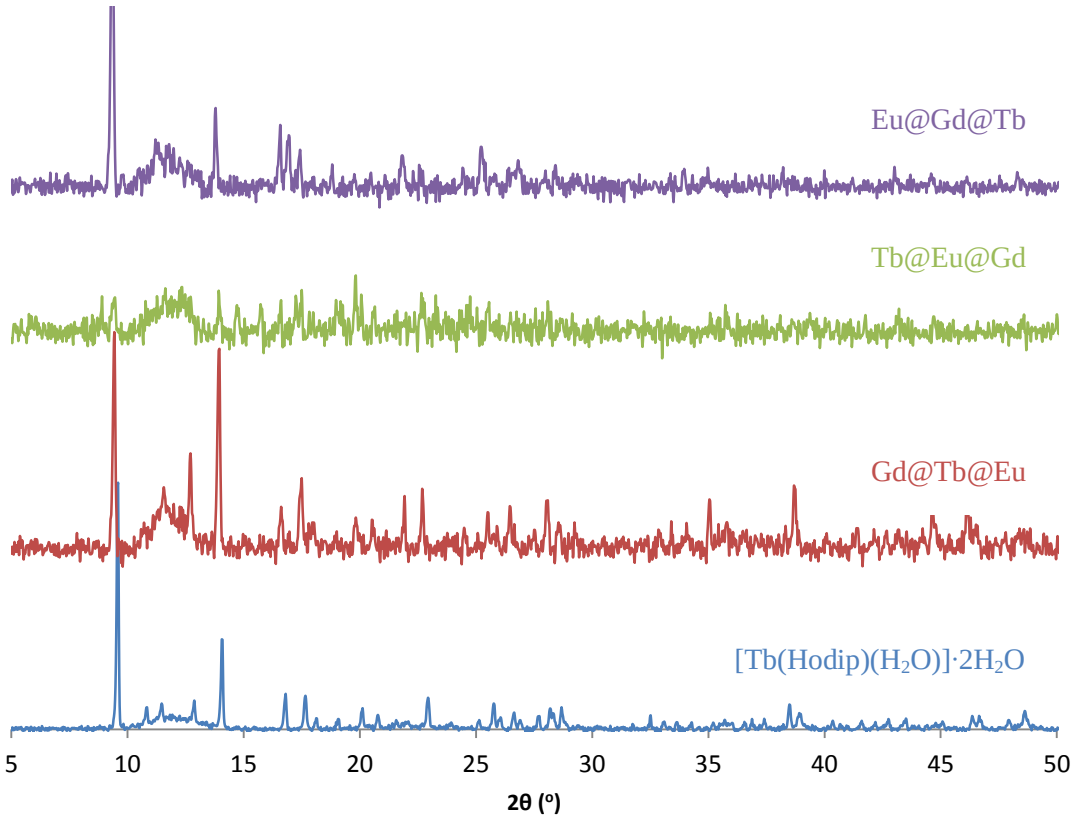

Figure 5.25 Powder X-ray diffraction patterns of the core-shell products Gd@Tb@Eu, Tb@Eu@Gd and Eu@Gd@Tb and the single lanthanide system [Tb(Hodip)(H_2O)]·2H_2O.

The presence of a broad peak centred on 2θ 11° in the core shell products is indicative of the presence of amorphous content. The Tb@Eu@Gd sample also shows low intensity of the crystalline peaks present, indicating a lower crystallinity than the other core-shell products.

A comparison of the diffraction patterns of the core-shell products to that of [Tb(Hodip)(H_2O)]·2H_2O show similar Bragg peak positions, suggesting the formation of products which are isoreticular to [Tb(Hodip)(H_2O)]·2H_2O, although this is more difficult to ascertain for the Tb@Eu@Gd product due to its low crystallinity.

All products formed through core-shell formation were analysed by energy dispersive X-ray (EDX) spectroscopy. SEM images of each product are shown in Figure 5.26 and each contains crystals which were both dark and light in appearance.

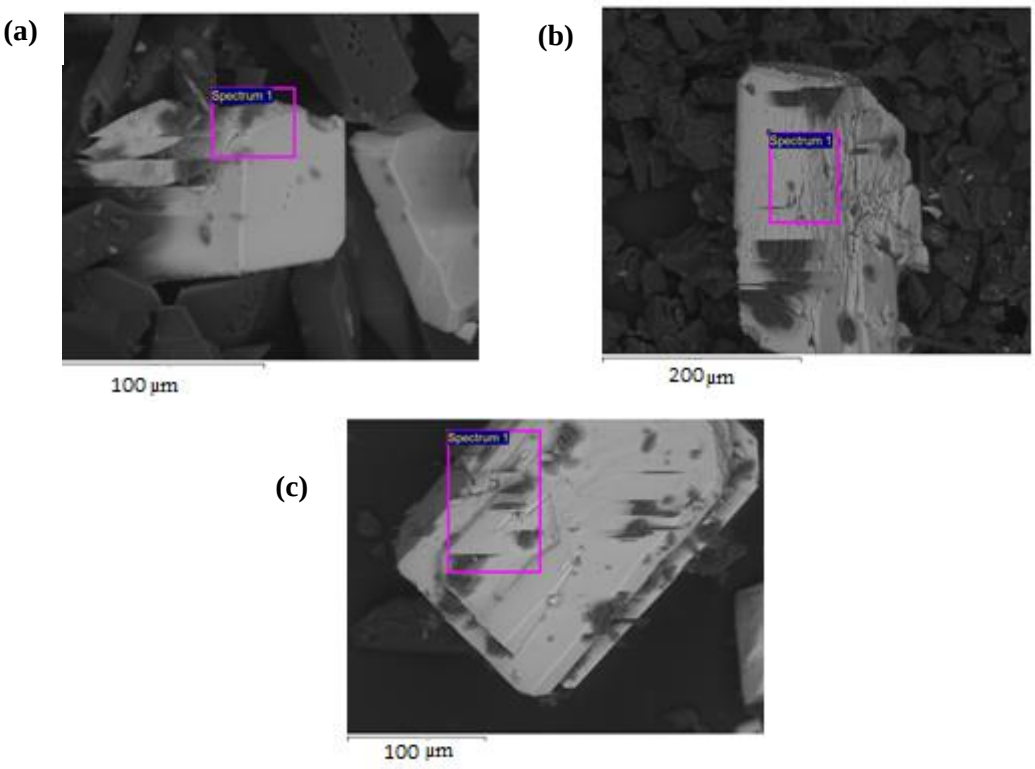

Figure 5.26 SEM images of **(a)** Tb@Eu@Gd **(b)** Eu@Gd@Tb and **(c)** Gd@Tb@Eu.

EDX spectroscopy was carried out on each product, with either four or five crystals being analysed for their gadolinium, europium and terbium content. EDX spectroscopy is a surface analysis technique, and was used to investigate any evidence of core-shell structure formation. A graphical representation of the results for each product is shown in Figure 5.27.

(a)

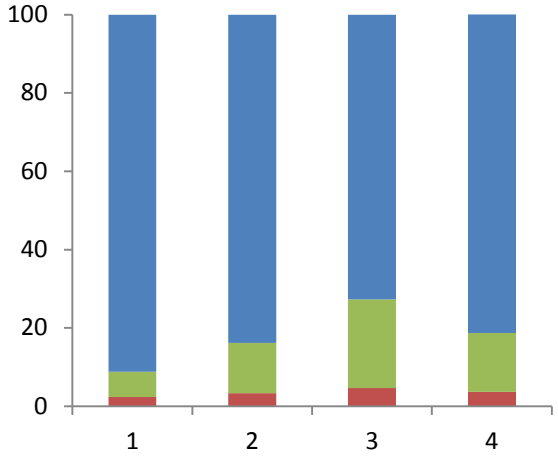

Crystal	% Eu	% Tb	% Gd
1	2.4	6.5	91.1
2	3.4	12.8	83.8
3	4.7	22.6	72.7
4	3.7	15.1	81.2

(b)

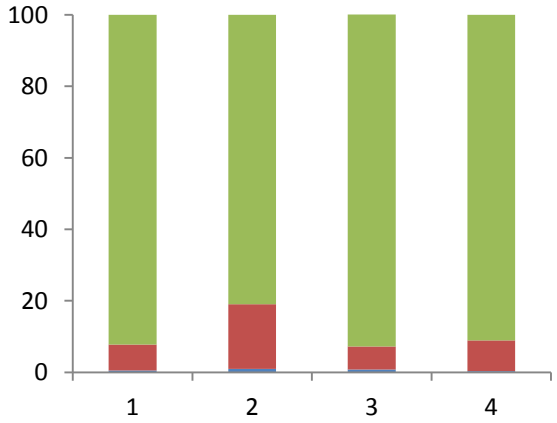

Crystal	% Eu	% Tb	% Gd
1	7.2	92.2	0.6
2	18.1	80.9	1.0
3	6.4	92.8	0.8
4	8.6	91.1	0.3

(c)

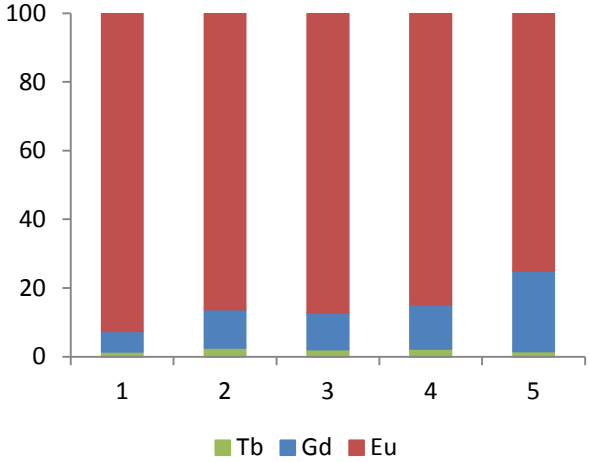

Crystal	% Eu	% Tb	% Gd
1	92.6	1.4	6.0
2	86.3	2.6	11.1
3	87.3	2.1	10.6
4	84.7	2.3	13.0
5	75.1	1.5	23.4

Figure 5.27 The percentage of Eu, Tb and Gd observed in crystals of **(a)** Gd@Tb@Eu **(b)** Tb@Eu@Gd and **(c)** Eu@Gd@Tb as by EDX analysis.

The presence of europium, terbium and gadolinium in each of the three products was observed. In each product the crystals analysed show broadly similar percentages of europium, terbium and gadolinium as one another, suggesting little compositional variation is occurring within each

sample. However, a drastic variation in the amount of europium, terbium and gadolinium between products are evident. This can be explained through a comparison of the lanthanide concentrations and the core-shell composition of each product.

For the Tb@Eu@Gd product (Figure 5.27 **(b)**) EDX analysis shows an average of 89 % Tb, 10 % Eu and 1 % Gd across the four crystals studied. Given that the EDX analysis is a surface analysis technique and the outermost layer of this product contains $[Tb(Hodip)(H_2O)]\cdot 2H_2O$, the high terbium content in comparison to europium and gadolinium content is supportive of the formation of a core-shell product. The synthetic procedure necessarily means that the innermost core of the product is $[Gd(Hodip)(H_2O)]\cdot 2H_2O$, and EDX analysis shows gadolinium to be the lowest content lanthanide of the three analysed. The EDX analysis can therefore be seen as supporting evidence for the formation of the core-shell structure Tb@Eu@Gd.

Similar support for the formation of core-shell structures Eu@Gd@Tb and Gd@Tb@Eu can be found in the EDX analysis. Crystals of the product Eu@Gd@Tb show a high europium content (85.2 %) corresponding to the outermost layer, followed by gadolinium (12.8 %) and finally terbium (2.0 %) which corresponds to the innermost core-layer. Crystals of the product Gd@Tb@Eu show the highest lanthanide content for gadolinium (82.2 %) which forms the outer layer of the product. This is followed by terbium (14.2 %) and europium (3.6 %) which makes up the inner layer of the product.

All products show a similar level of the lanthanides from corresponding layers in the products. For example, each product contains 82-89 % of the lanthanide forming the outermost layer, 10-14 % of the lanthanide from the middle layer and 1-4% of the lanthanide from the innermost core-layer.

5.5.1 Fluorescence spectroscopy of core-shell products

The solid state emission and excitation spectra were recorded for the Gd@Tb@Eu, Tb@Eu@Gd and Eu@Gd@Tb core-shell products at room temperature. For each product, emission spectra were recorded by excitation of the ligand at 370 nm and at 254 nm.

Gd@Tb@Eu

Visual observations under a UV lamp (254 nm) show the Gd@Tb@Eu compound to be pale yellow. The emission spectra are shown in Figure 5.28.

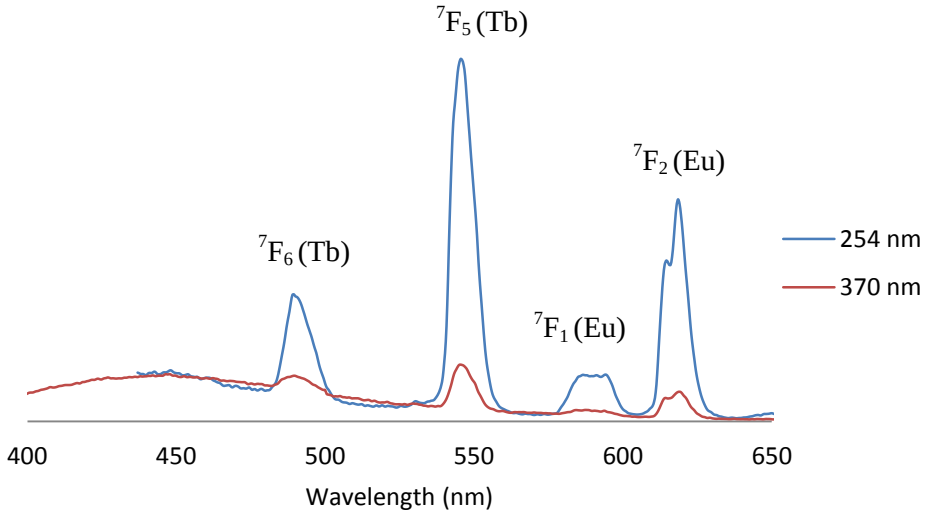

Figure 5.28 Emission spectra of [Gd(Hodip)(H_2O)]@[Tb(Hodip)(H_2O)]@[Eu(Hodip)(H_2O)] when excited with λ_{ex} = 254 nm and λ_{ex} = 370 nm. Corresponding term symbols for each transition are given (The Tb transitions originate from $^5D_4$ and the Eu transitions originate from $^5D_0$).

Both emission spectra show the presence of peaks corresponding to the energy states of Tb^{3+} (490 nm and 545 nm) and Eu^{3+} transitions (590 nm and 618 nm). The highest intensity peaks are those of the Tb^{3+} transitions, possibly due to the europium being confined to the inner-core of the crystals. This is in contrast to the doped mixed-lanthanide system which displayed emission spectra dominated by Eu^{3+}. A broad band at 400-500 nm is also present originating from H_4odip.

The excitation spectrum was recorded through excitation of the ligand (442 nm), Tb^{3+} (545 nm) and Eu^{3+} (618 nm) (Figure 5.29).

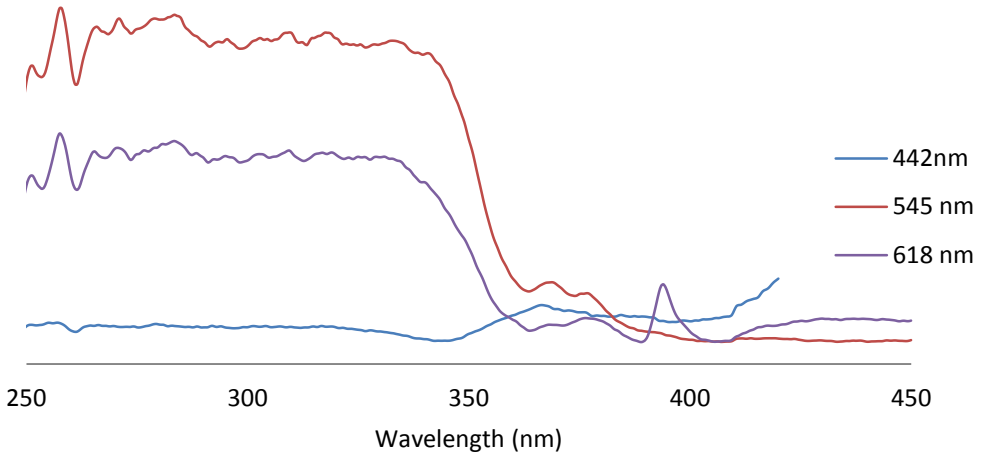

Figure 5.29 Excitation spectra of [Gd(Hodip)(H_2O)]@[Tb(Hodip)(H_2O)]@[Eu(Hodip)(H_2O)] when excited with λ_{ex} = 442 nm, 545 nm and 618 nm.

Excitation of both Eu^{3+} and Tb^{3+} give spectra which contain a broad, high intensity band from 250 - 340 nm. This band, also present in the spectra of the individual [Eu(Hodip)(H_2O)]·nH_2O and [Tb(Hodip)(H_2O)]·2H_2O compounds (Section 5.3) is thought to arise from charge transfer from the ligand to the metal centres. In this case, these bands are high in intensity for both Eu^{3+} (λ_{ex} = 618 nm) and Tb^{3+} (λ_{ex} = 545 nm) excitation, demonstrating that excitation of the core-shell compound between 250 nm - 340 nm will result in emission in both the green (terbium) and red (europium) regions. The band arising from excitation of Tb^{3+} has the highest intensity of the two, supporting the visual observations of an overall pale yellow appearance of the compound under UV excitation. Bands associated with H_4odip (370 nm) and Eu^{3+} (394 nm) are also present at a lower intensity.

Tb@Eu@Gd

Visual observations showed that when irradiated with UV light (254 nm) the Tb@Eu@Gd compound was pale yellow in appearance. Solid state emission and excitation spectra are comparative to that of Gd@Tb@Eu with emissions corresponding to H_4odip (380-480 nm), Tb^{3+} transitions (490 nm, 545 nm) and Eu^{3+} transitions (587 nm and 618 nm) as shown in Figure 5.30. As with the Gd@Tb@Eu material, the high intensity of the Tb^{3+} transitions is indicative of the core-shell ordering in the material. A higher intensity of Eu^{3+} transitions is observed in the Tb@Eu@Gd compound compared to that in the Gd@Tb@Eu material, again most likely due to the change in ordering of the lanthanide shells between the two materials.

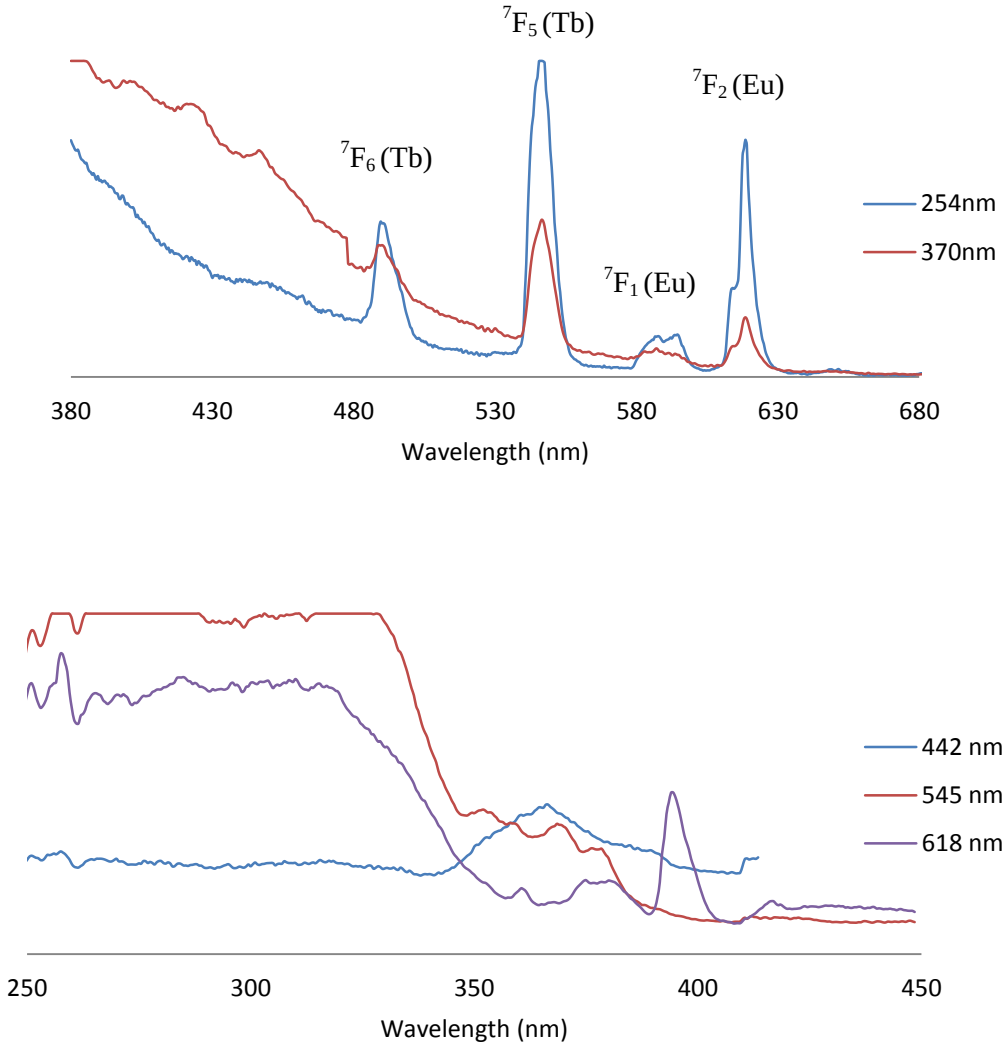

Figure 5.30 Emission spectra (top) and excitation spectra (bottom) of [Tb(Hodip)(H_2O)]@[Eu(Hodip)(H_2O)] @[Gd(Hodip)(H_2O)]. Corresponding term symbols for each transition are given (The Tb transitions originate from $^5D_4$ and the Eu transitions originate from $^5D_0$).

The excitation of both Eu^{3+} (λ_{ex} = 618 nm) and Tb^{3+} (λ_{ex} = 545 nm) show the presence of a LMCT band from 250 nm - 340 nm. Excitation of H_4odip (λ_{ex} = 442 nm) is dominated by the H_4odip band at 370 nm.

Overall, the two mixed-lanthanide core-shell structures Gd@Tb@Eu and Tb@Eu@Gd show high emission contributions from Eu^{3+} and Tb^{3+} centres. Some changes in relative intensities of the Eu^{3+} and Tb^{3+} emissions can be seen between the two core-shell materials. This demonstrates that segregation of the lanthanide species to single domains within the core-shell crystal and the subsequent ordering of the shells allows some degree of control over the emission of the resulting material.

Eu@Gd@Tb

In contrast to the previous two core-shell compounds discussed, the visual observations of Eu@Gd@Tb show the compound to appear purple when illuminated with UV light (254 nm). The emission spectra are shown in Figure 5.31.

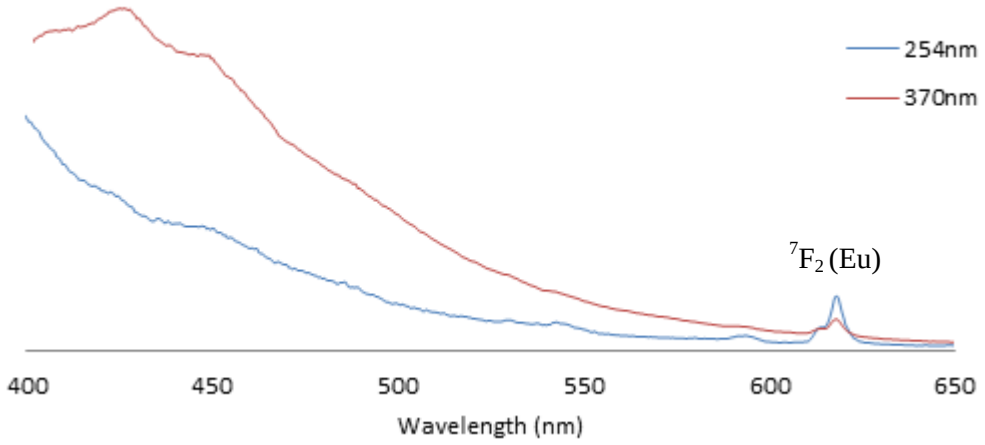

Figure 5.31 Emission spectra of [Eu(Hodip)(H_2O)]@[Gd(Hodip)(H_2O)]@[Tb(Hodip)(H_2O)] when excited with λ_{ex} = 254 nm and λ_{ex} = 370 nm. Corresponding term symbols for each transition are given which originate from $^5D_0$.

The emission spectra show a broad band from the ligand (400-500 nm) and peaks associated with the Eu^{3+} transitions (593 nm, 618 nm) which accounts for the purple appearance of the compound when irradiated with UV light. No Tb^{3+} transitions are observed in the emission spectra, possibly due to the Tb^{3+} centres being confined to the innermost shell of the structure. This lack of Tb^{3+} transitions is unlikely to be due to energy transfer from Tb^{3+} to Eu^{3+} due to the separation of the lanthanide ions in layered domains, which is supported by EDX analysis.

The excitation spectra recorded at excitation of the ligand (442 nm) and Eu^{3+} (618 nm) are shown in Figure 5.32.

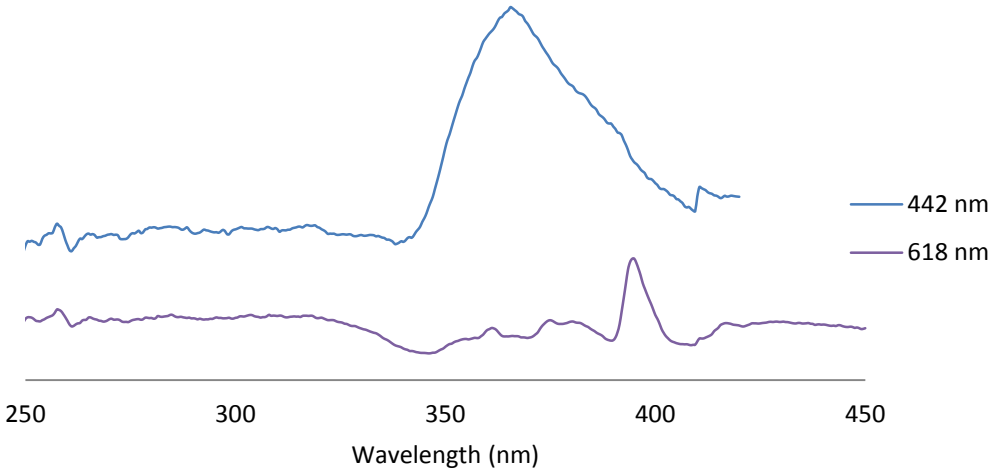

Figure 5.32 Excitation spectra of [Eu(Hodip)(H_2O)]@[Gd(Hodip)(H_2O)]@[Tb(Hodip)(H_2O)].

Excitation of the ligand (442 nm) shows a band characteristic of the ligand at 370 nm. The excitation of the Eu^{3+} shows bands from the ligand (370 nm) and Eu^{3+} (394 nm).

The predominance of the ligand and europium transitions to the detriment of the terbium in the Eu@Gd@Tb system is not observed in the other core-shell materials (Tb@Eu@Gd and Gd@Tb@Eu) and is possible evidence for the order of the layers in these systems influencing the fluorescence properties of the material. Alteration of layer ordering and thickness may therefore be a potential route to optical property tailoring of core-shell lanthanide MOFs.

5.5.2 A comparison of the core-shell structures to a physical mixture of [Tb(Hodip)(H_2O)]·2H_2O, [Eu(Hodip)(H_2O)]·nH_2O and [Gd(Hodip)(H_2O)]·2H_2O

Physical blending of lanthanide containing compounds in order to produce colour tuneable materials has been demonstrated in multiple systems. Therefore the optical properties of a physical mixture of the [Tb(Hodip)(H_2O)]·2H_2O, [Eu(Hodip)(H_2O)]·nH_2O and [Gd(Hodip)(H_2O)]·2H_2O compounds were investigated and compared to that of the mixed-lanthanide core-shell MOFs. The [Tb(Hodip)(H_2O)]·2H_2O, [Eu(Hodip)(H_2O)]·nH_2O and [Gd(Hodip)(H_2O)]·2H_2O MOFs were combined together 1:1:1 ratio post-synthesis. EDX analysis of the physical mixture is shown in Figure 5.33 showing [Tb(Hodip)(H_2O)] in green, [Eu(Hodip)(H_2O)] in red and [Gd(Hodip)(H_2O)] in blue.

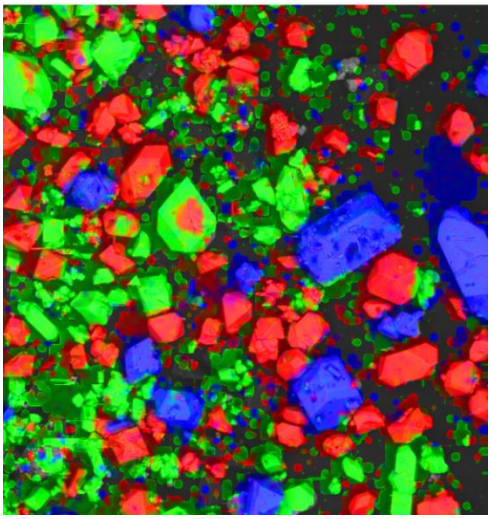

Figure 5.33 Scanning electron microscope (SEM) image of physical mixture of [Tb(Hodip)(H_2O)]·2H_2O (green), [Eu(Hodip)(H_2O)]·nH_2O (red) and [Gd(Hodip)(H_2O)]·2H_2O (blue) as identified by EDX analysis.

Observations of the mixture under UV irradiation showed the sample to appear green with blue and red speckles, indicative of its heterogeneous nature. The solid state emission spectrum of the mixture was collected at room temperature and is shown in Figure 5.34.

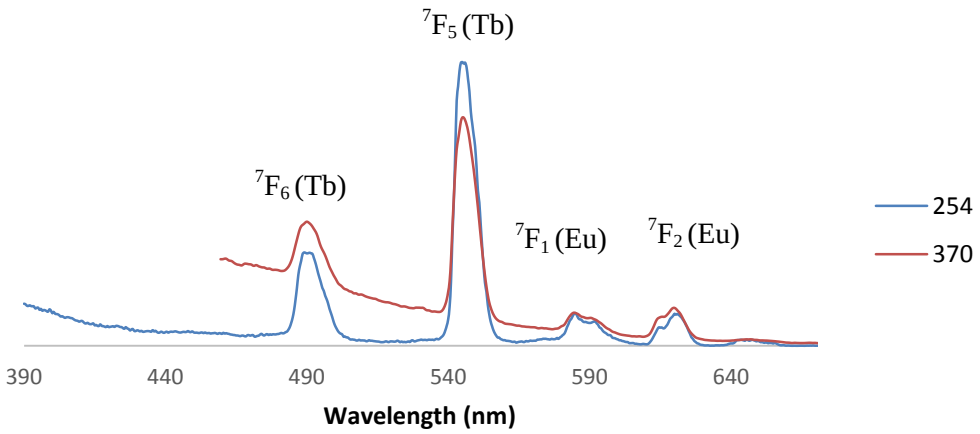

Figure 5.34 Emission spectra of physical mixture of [Tb(Hodip)(H_2O)]·$2H_2O$, [Eu (Hodip)(H_2O)]·nH_2O and [Gd(Hodip)(H_2O)]·$2H_2O$. The Tb transitions originate from $^5D_4$ and the Eu transitions originate from $^5D_0$.

Both spectra show similar features with bands at 490 nm, 545 nm corresponding to Tb^{3+}, 587 nm and 618 nm corresponding to Eu^{3+} and the tail end of the broad ligand peak at 390 – 470 nm typical of H_4odip. The highest intensity transitions are those of the Tb^{3+}, supporting the visual green colour of the mixture. The excitation spectra recorded at excitation of H_4odip (442 nm) and Eu^{3+} (618 nm) are shown in Figure 5.35.

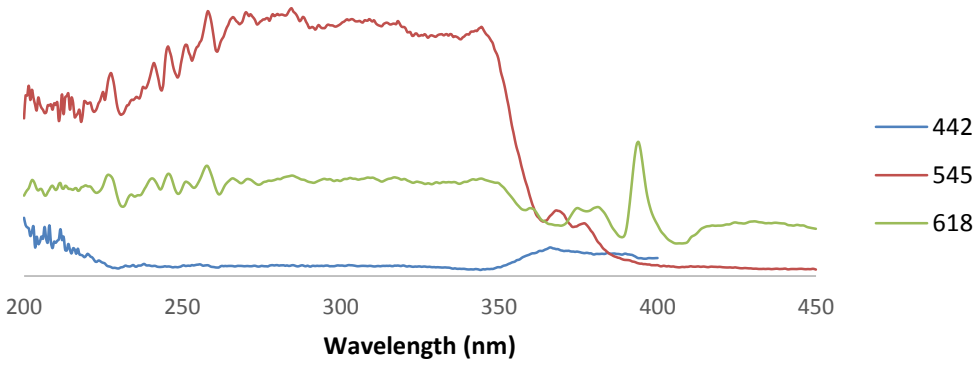

Figure 5.35 Excitation spectra of physical mixture of [Tb(Hodip)(H_2O)]·$2H_2O$, [Eu(Hodip)(H_2O)]·nH_2O and [Gd(Hodip)(H_2O)]·$2H_2O$.

A broad, high intensity band is present from 250-350 nm along with bands associated with H_4odip (370 nm) and Tb^{3+} (394 nm). Both the emission and excitation spectra are similar to Tb@Eu@Gd and Gd@Tb@Eu core-shell structures, confirming that these mixed-lanthanide MOFs behave in a similar way to the combined single lanthanide systems. However, in contrast to the heterogeneous appearance of the physical mixture the core-shell materials exhibit uniform emission across the sample. This is of particular interest in applications such as light emitting devices which require uniform emission in order to produce an evenly dispersed and stable material.[19]

5.6 Conclusions and future work

The formation of a series of lanthanide MOFs of the form $[Ln(Hodip)(H_2O)]\cdot nH_2O$ (Ln = Sm, Eu, Gd, Tb, Dy and Er) has been successfully achieved. The products all display powder diffraction patterns with similar peak positions, and single crystal structures with similar topologies confirming the formation of isoreticular products.

The successful formation of a mixed-lanthanide system of similar topology to the single metal systems was achieved through direct synthesis methods. Combining a 1:1:1 ratio of europium, terbium and gadolinium nitrates in the reaction mixture formed the $[Gd_{0.17}Tb_{0.19}Eu_{0.64}(Hodip)(H_2O)]\cdot nH_2O$ system, whose structure and composition was confirmed by powder X-ray diffraction and EDX spectroscopy analysis. The product shows a preferential inclusion of the Eu^{3+} centres into the product, making up 64 % of the total lanthanide content of the structure. Fluorescence spectroscopic studies of the mixed-lanthanide system show an emission spectrum which is dominated by Eu^{3+} transitions, with the additional presence of lower intensity Tb^{3+} and ligand transitions. The mixed-lanthanide compound therefore appears red upon excitation with UV light. Both the higher concentration of europium in the compound, and potential energy transfer from Tb^{3+} to Eu^{3+} within the crystal could be contributing factors to this predominance of europium emission.

The post-synthetic formation of three of a possible six core-shell mixed-lanthanide systems based around the $[Ln(Hodip)(H_2O)]\cdot nH_2O$ structure were investigated, and successfully produced three products; $[Gd(Hodip)(H_2O)]$@$[Tb(Hodip)(H_2O)]$@$[Eu(Hodip)(H_2O)]$, $[Tb(Hodip)(H_2O)]$@$[Eu(Hodip)(H_2O)]$@$[Gd(Hodip)(H_2O)]$ and $[Eu(Hodip)(H_2O)]$@$[Gd(Hodip)(H_2O)]$@$[Tb(Hodip)(H_2O)]$. The products were confirmed to be core-shell systems through EDX spectroscopic analysis, which revealed the presence of all three lanthanide species in each system, with decreasing concentration of the metals from the outermost layer to the innermost layer.

Fluorescence spectroscopic studies of both $[Gd(Hodip)(H_2O)]$@$[Tb(Hodip)(H_2O)]$@$[Eu(Hodip)(H_2O)]$ and $[Tb(Hodip)(H_2O)]$@$[Eu(Hodip)(H_2O)]$@$[Gd(Hodip)(H_2O)]$ show emission spectra with Tb^{3+}, Eu^{3+} and ligand transitions present. In these systems, the Tb^{3+} transitions are the most intense. These systems also show that excitation over a broad wavelength (250-350 nm) results in high intensity emission of both green (Tb) and red (Eu) light. This is a usual and desirable property for lanthanide systems, as the material maintains its emission properties with changing excitation source making it more versatile in potential applications. A comparison of these emission spectra to that of a physical mixture of the single lanthanide systems $[Tb(Hodip)(H_2O)]\cdot 2H_2O$, $[Eu(Hodip)(H_2O)]\cdot nH_2O$ and $[Gd(Hodip)(H_2O)]\cdot 2H_2O$ show similar optical properties, demonstrating how core-shell systems can behave as a combination of the individual crystals.

The [Eu(Hodip)(H_2O)]@[Gd(Hodip)(H_2O)]@[Tb(Hodip)(H_2O)] system however shows an emission spectrum with only Eu^{3+} and ligand transitions present. As the Tb^{3+} and Eu^{3+} layers are separated by the Gd^{3+} layer, quenching of the Tb^{3+} transitions through metal to metal energy transfer cannot be occurring. The ordering of the core-shell layers and possibly their thickness may therefore be influencing the optical properties of the resulting material. This is potentially a further route to emission colour tailoring of lanthanide MOFs. Further syntheses of these core-shell materials and subsequent fluorescence spectroscopy would help to further understand the fluorescence observed. An investigation into the effect of reaction time on layer thickness would also be beneficial, as a potential route to composition and emission control in the core-shell structures.

A study into the ability of the [Ln(Hodip)(H_2O)]·nH_2O systems to undergo post-synthetic exchange of the metal centres should be undertaken. This work would rule out the possibility of lanthanide ion exchange occurring in the post-synthetic reactions, forming not core-shell structures but randomly distributed mixed-metal systems. This work would further support the fluorescence spectroscopy observations presented in this chapter.

5.7 Experimental

5.7.1 General experimental details

H_4odip was synthesised using reported methods.[20] $Eu(NO_3)_3$ was generated *in situ*.[21] All other starting materials and solvents were purchased from commercial sources and were used without further purification.

Powder X-ray diffraction (PXRD) patterns and single crystal X-ray diffraction data were collected using similar sample preparation and methods outlined in Section 2.5.

The UV excited luminescence was studied at room temperature using a LS 55 luminescence spectrometer with a R928 photomultiplier and a Xenon discharge lamp. Samples were decanted from solution and dried at 120 ^oC for 30 minutes prior to being ground with a pestle and mortar.

SEM and EDX spectroscopy analysis was conducted by Philip Fletcher on a JEOL 6480LV SEM with an Oxford Instrument EDX system with X-Act silicon drift detector.

5.7.2 Synthesis of $[Ln_2(Hodip)(H_2O)]\cdot nH_2O$

Synthetic methods to produce all products were similar. The synthesis of $[Tb_2(Hodip)(H_2O)]\cdot 2H_2O$ is detailed here. $Tb(NO_3)_3\cdot 5H_2O$ (0.3 mmol, 0.129 g) and H_4odip (0.3 mmol, 0.105g) were placed in a glass vial and dissolved in 15 ml H_2O. The vial was sealed and heated to 85 ^oC for 2 days. Colourless, needle crystals were produced with a yield of 0.054 g, 25 % based on H_4odip.

5.7.3 Synthesis of $[Gd_{0.17}Tb_{0.19}Eu_{0.64}(Hodip)(H_2O)]\cdot nH_2O$

Eu_2O_3 (0.099 mmol, 0.035 g) was dissolved in 15ml H_2O. Whilst stirring, HNO_3 (1M solution) was added dropwise until the pH of the solution was neutral. $Tb(NO_3)_3\cdot 5H_2O$ (0.098 mmol, 0.043 g) and $Gd(NO_3)_3\cdot 6H_2O$ (0.13 mmol, 0.062 g) were added to the solution along with H_4odip (0.303 mmol, 0.105g). The vial was sealed and heated to 85 ^oC for 2 days. Colourless, needle crystals were produced with a yield of 0.041 g, 27 % based on H_4odip.

5.7.4 Synthesis of core-shell species

The core-shell MOFs were synthesised using a similar method. The detailed synthesis of $[Gd(Hodip)(H_2O)]@[Tb(Hodip)(H_2O)]@[Eu(Hodip)(H_2O)]$ is provided here. Eu_2O_3 (0.298 mmol, 0.105 g) was dissolved in 15 ml H_2O. Whilst stirring, HNO_3 (1M solution) was added dropwise until the pH of the solution was neutral. H_4odip (0.303 mmol, 0.105g) was added to the solution and stirred until dissolved. The solution was placed in a sealed vial and heated to 85 ^oC for 2 days. Colourless, needle crystals were produced which were washed with H_2O through a process of decanting the supernatant and replacing with fresh H_2O. This was repeated three times over three days. The crystals were then placed in a dissolved solution of $Tb(NO_3)_3\cdot 5H_2O$ (0.296 mmol, 0.129 g) and H_4odip (0.303 mmol, 0.105g) in 15 ml H_2O heated to 85 ^oC for 2 days. Colourless crystals were produced and washed as previously described. These crystals were then placed in a dissolved

solution of $Gd(NO_3)_3 \cdot 5H_2O$ (0.292 mmol, 0.132 g) and H_4odip (0.303 mmol, 0.105g) in 15 ml H_2O heated to 85 ^oC for 2 days. The colourless crystals produced were the core-shell product [Gd(Hodip)(H_2O)]@[Tb(Hodip)(H_2O)]@[Eu(Hodip)(H_2O)].

For the synthesis of [Tb(Hodip)(H_2O)]@[Eu(Hodip)(H_2O)]@[Gd(Hodip)(H_2O)] the inner shell of [Gd(Hodip)(H_2O)] was first synthesised using the method detailed above. A solution of 15 ml H2O containing dissolved Eu_2O_3 (0.302 mmol, 0.106 g) and HNO_3 (1M solution) was added dropwise until the pH of the solution was neutral. The crystals of [Gd(Hodip)(H_2O)] were added to the solution and it was placed in a sealed vial and heated to 85 ^oC for 2 days. The resulting crystals were then placed in a dissolved solution of $Tb(NO_3)_3 \cdot 5H_2O$ (0.340 mmol, 0.147 g) and H_4odip (0.303 mmol, 0.105g) in 15 ml H_2O heated to 85 ^oC for 2 days. Colourless crystals of the core-shell product [Tb(Hodip)(H_2O)]@[Eu(Hodip)(H_2O)]@[Gd(Hodip)(H_2O)] were formed and washed as previously described.

The synthesis of [Eu(Hodip)(H_2O)]@[Gd(Hodip)(H_2O)]@[Tb(Hodip)(H_2O)] was carried out in a similar manner, but altering the ordering of the layers.

5.8 References

1. K. Müller-Buschbaum, *The Chemistry of Metal–Organic Frameworks: Synthesis, Characterization, and Applications*, Wiley-VCH Verlag GmbH & Co. KGaA, Weinheim, Germany, 2016
2. D.M.P Mingos, *Lanthanide Metal-Organic Frameworks*, Springer-Verlag Berlin Heidelberg, 2015
3. C. G. Efthymiou, E. J. Kyprianidou, C. J. Milios, M. J. Manos and A. J. Tasiopoulos, *J. Mater.Chem. A*, 2013, 1, 5061-5069
4. M. Gustafsson, A. Bartoszewicz, B. n. Martín-Matute, J. Sun, J. Grins, T. Zhao, Z. Li, G. Zhu and X. Zou, *Chem.Mater.*, 2010, 22, 3316-3322
5. H. He, D. Yuan, H. Ma, D. Sun, G. Zhang and H. C. Zhou, *Inorg. Chem.*, 2010, 49, 7605-7607
6. Y. K. Park, S. B. Choi, H. Kim, K. Kim, B. H. Won, K. Choi, J. S. Choi, W. S. Ahn, N. Won, S. Kim, D. H. Jung, S. H. Choi, G. H. Kim, S. S. Cha, Y. H. Jhon, J. K. Yang and J. Kim, *Angew. Chem. Int. Ed.*, 2007, 46, 8230-8233
7. L. V. Meyer, F. Schonfeld and K. Muller-Buschbaum, *Chem.Commun.*, 2014, 50, 8093-8108
8. Y. Chen and S. Ma, *Rev. Inorg. Chem.*, 2012, 32, 81-100
9. M. H. V. Werts, *Science Progress* 2005, 88, 101-131
10. R. C. Leif, L. M. Vallarino, M. C. Becker and S. Yang, *Cytometry. Part A*, 2006, 69, 767-778
11. A. de. Andres, F. Gándara, B. Gómez-Lor, E. Gutiérrez-Puebla, M. Iglesias, M. A. Monge, D. M. Proserpio, and N. Snejko, *Cryst. Growth Des.*, 2008, 8, 378–380
12. Y. Cui, Y. Yue, G. Qian and B. Chen, *Chem. Rev.*, 2012, 112, 1126-1162
13. H. Guo, Y. Zhu, S. Qiu, J. A. Lercher and H. Zhang, *Adv. Mater.*, 2010, 22, 4190-4192
14. L. L. da Luz, B. F. Lucena Viana, G. C. Oliveira. da Silva, C. C. Gatto, A. M. Fontes, M. Malta, I. T. Weber, M. O. Rodrigues and S. A. Júnior, *Cryst. Eng. Comm*, 2014, 16, 6914-6918
15. S. Lis, *Acta Physica Polonica A*, 1993, 84, 1003-1010
16. L. P. V. Zolin , V. Kudryashova , V. Tsaryuk , J. Legendziewicz , P. Gawryszewska and R. Szostak, *J. Alloys Compd.* 2002, 341, 376–380
17. S. Su, W. Chen, C. Qin, S. Song, Z. Guo, G. Li, X. Song, M. Zhu, S. Wang, Z. Hao and H. Zhang, *Cryst. Growth Des.*, 2012, 12, 1808-1815
18. D. B. Ambili. Raj, S. Biju, M. L. P. Reddy and B. M. Kariuki, *Inorg. Chem*, 2006, 45, 10651-10660
19. J. Wu, H. Zhang and S. Du, *J. Mater. Chem. C*, 2016, 4, 3364-3374
20. Y. Peng, G. Li, J. Hua, Z. Shi and S. Feng, *Cryst. Eng. Comm.*, 2015, 17, 3162-3170
21. H. Wang, R. Wang, X. Sun, R. Yan and Y. Li, *Mater. Res. Bull.*, 2005, 40, 911-919

Appendix

A2 Chapter 2 Appendix Information

A2.1 Powder X-ray Diffraction Analysis

A comparison of the predicted PXRD patterns from the single crystal x-ray diffraction structures to the experimental traces collected on bulk samples are given below.

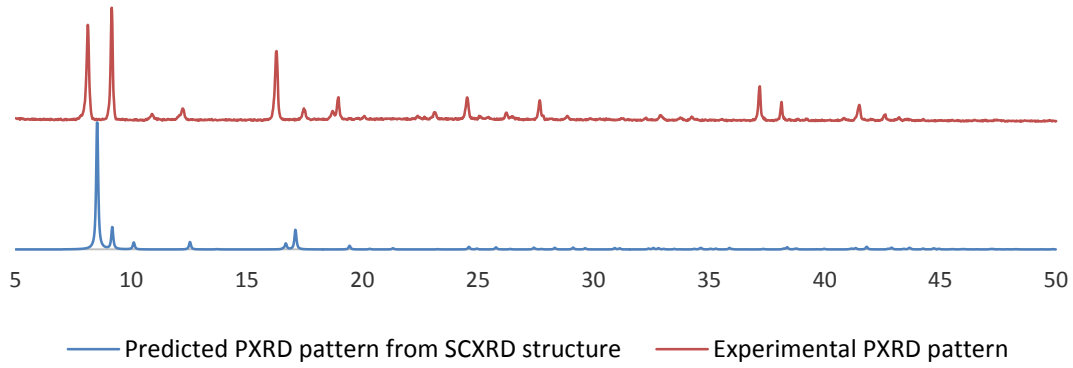

Figure A2.1.1 Predicted and experimental PXRD patterns of $[Zn_2(bdc)_{0.3}(bdc\text{-}Br)_{1.7}(dabco)]\cdot n$DMF **1d**.

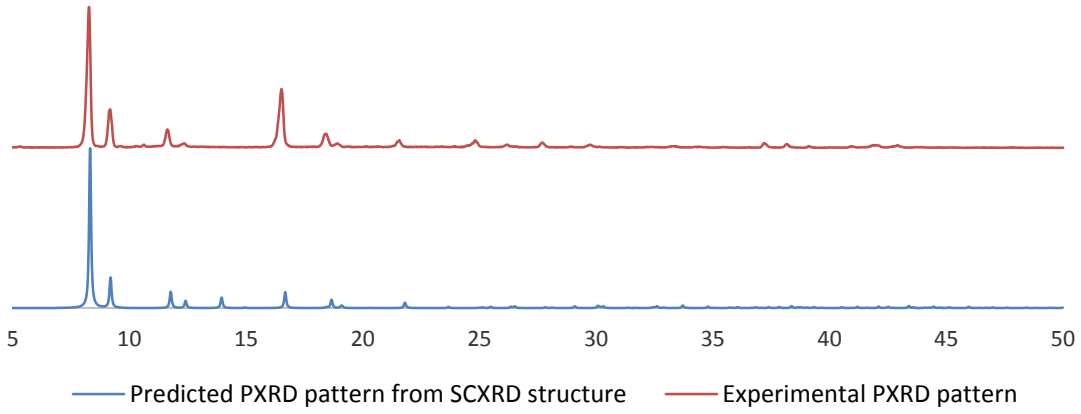

Figure A2.1.2 Predicted and experimental PXRD patterns of $[Zn_2(bdc)_{1.2}(bdc\text{-}NO_2)_{0.8}(dabco)]\cdot n$DMF **3a**.

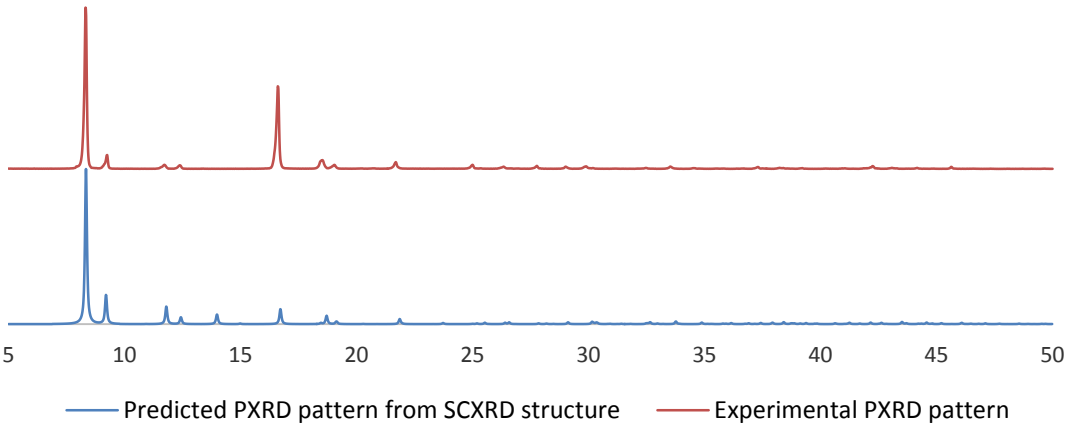

Figure A2.1.3 Predicted and experimental PXRD patterns of $[Zn_2(bdc)_{1.6}(bdc\text{-}NH_2)_{0.4}(dabco)]\cdot n$DMF **4a**.

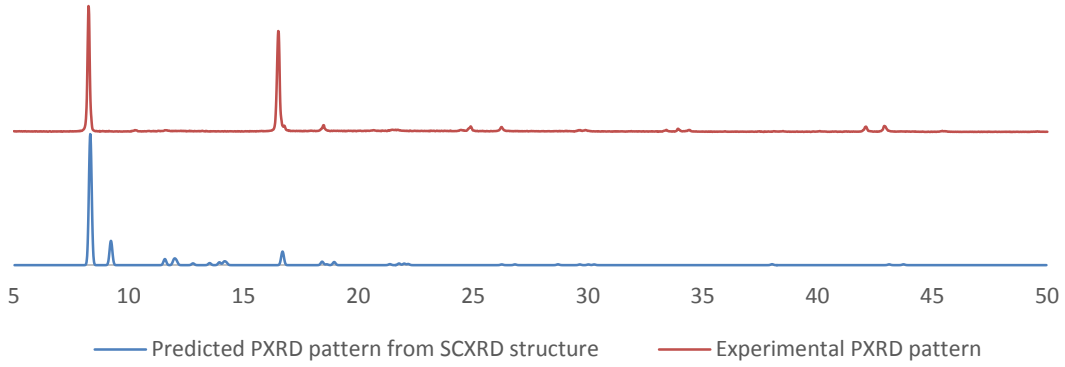

Figure A2.1.4 Predicted and experimental PXRD patterns of $[Zn_2(bdc)_{0.2}(bdc\text{-}NH_2)_{1.8}(dabco)]\cdot n$DMF **4b**.

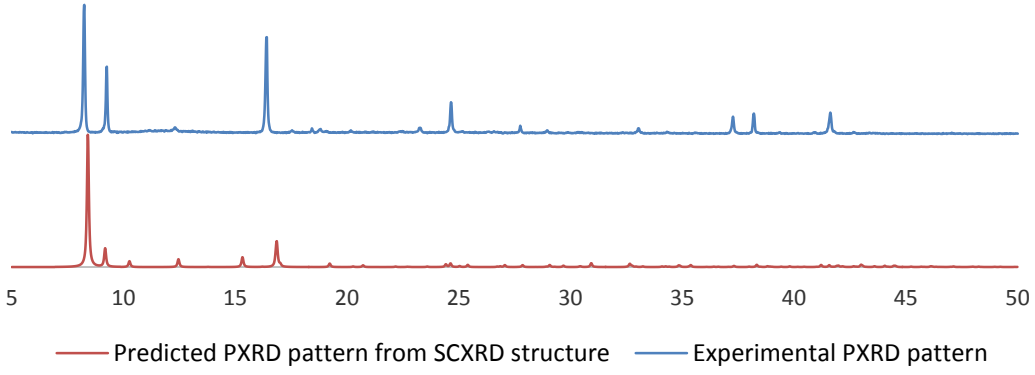

Figure A2.1.5 Predicted and experimental PXRD patterns of $[Zn_2(bdc\text{-}Br)_{1.4}(bdc\text{-}I)_{0.6}(dabco)]\cdot n$DMF **5a**.

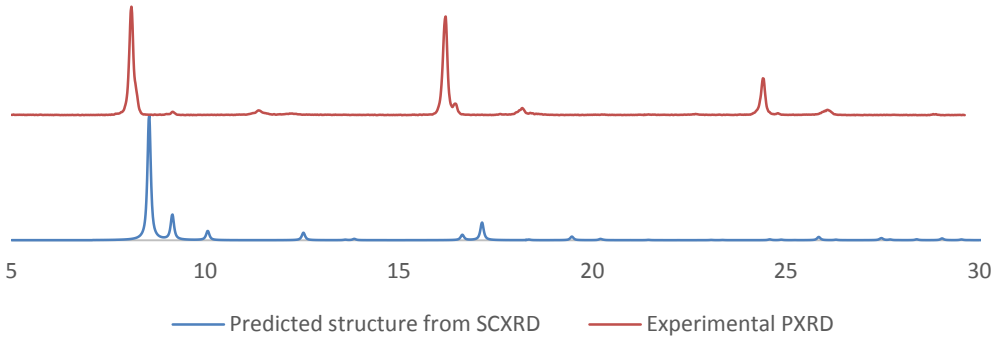

Figure A2.1.6 Predicted and experimental PXRD patterns of $[Zn_2(bdc\text{-}NO_2)_{1.4}(bdc\text{-}NH_2)_{0.6}(dabco)]\cdot n$DMF **6a**.

The predicted powder X-ray diffraction pattern from the single crystal data does not show a good match to the experimental powder diffraction pattern for **6a**. This is similar to the effect observed for **1c** and **1d** which was found to be due to temperature differences between the experimental and simulated powder patterns (see Section 2.2.1). A similar effect is therefore assumed to be at play in the case of **6a**.

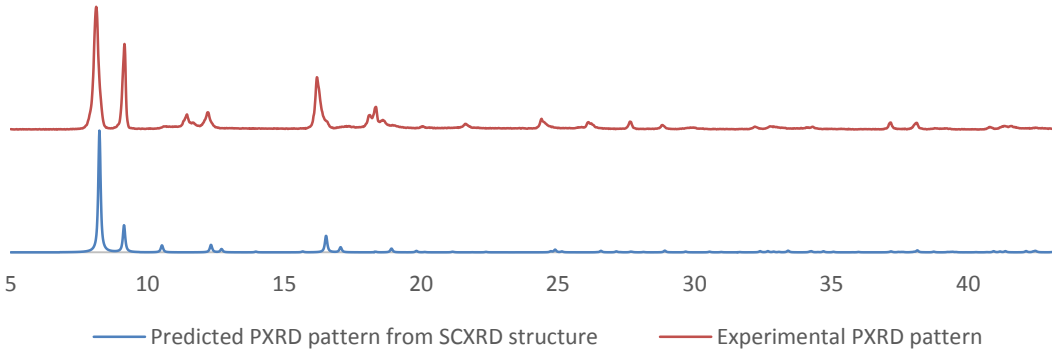

Figure A2.1.7 Predicted and experimental PXRD patterns of $[Zn_2(bdc)_{1.01}(ndc)_{0.99}(dabco)]\cdot 2.3$DMF **7a**

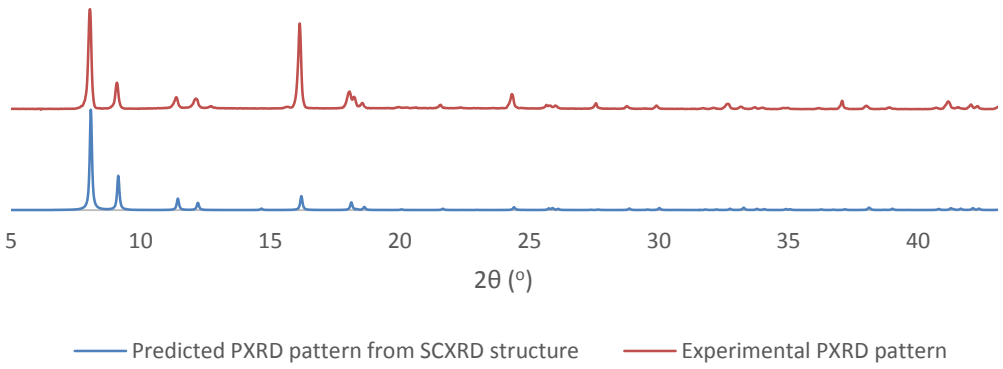

Figure A2.1.8 Predicted and experimental PXRD patterns of $[Zn_2(bdc)_{0.23}(1,4\text{-ndc})_{1.77}(dabco)]\cdot 1.6DMF$ **7b**.

A2.2 Thermogravimetric Analysis

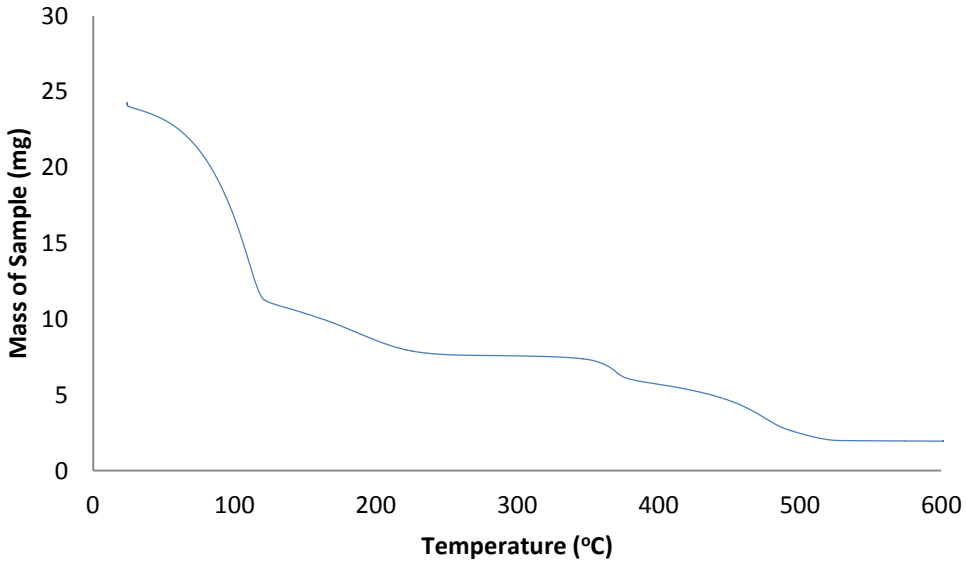

Figure A2.2.1 TGA of $[Zn_2(bdc)_{1.2}(bdc\text{-}NO_2)_{0.8}(dabco)]\cdot 2.5DMF$ **3a**.

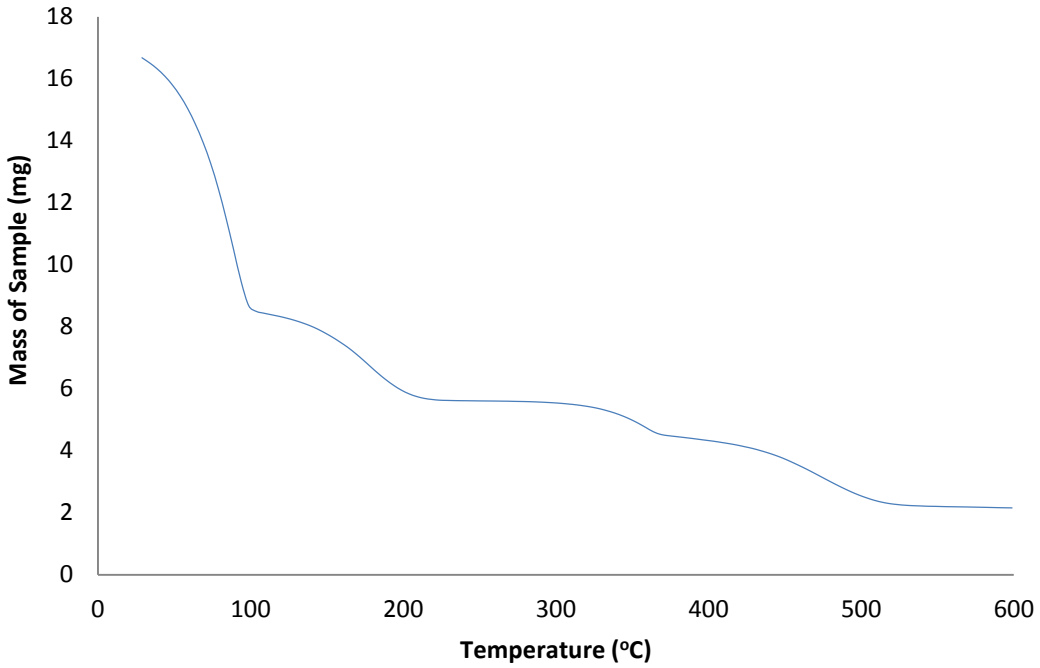

Figure A2.2.2 TGA of $[Zn_2(bdc)_{1.6}(bdc\text{-}NH_2)_{0.4}(dabco)]\cdot 2.6DMF$ **4a**.

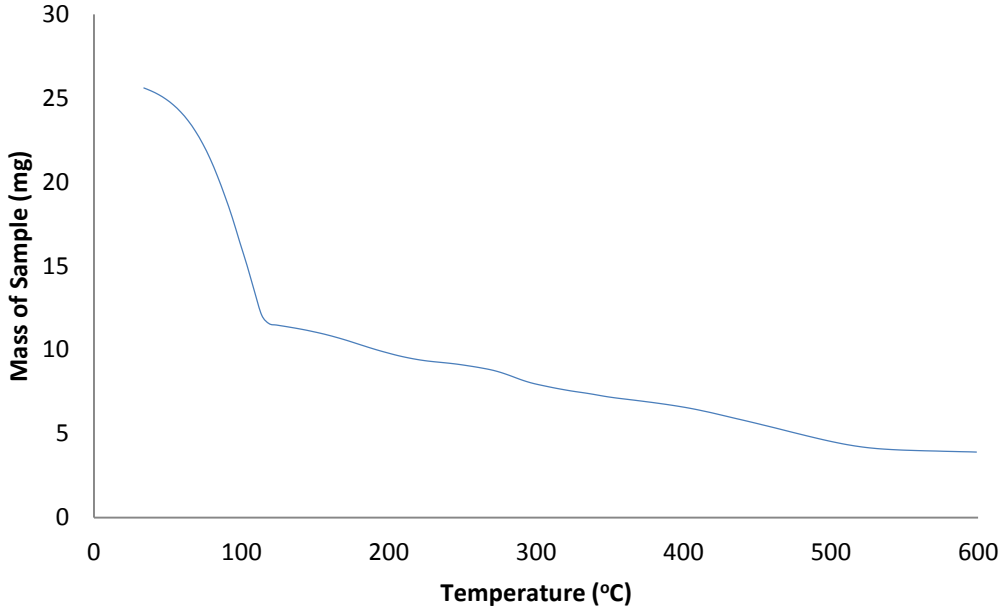

Figure A2.2.3 TGA of $[Zn_2(bdc)_{0.2}(bdc\text{-}NH_2)_{1.8}(dabco)]\cdot 1.5DMF$ **4b**.

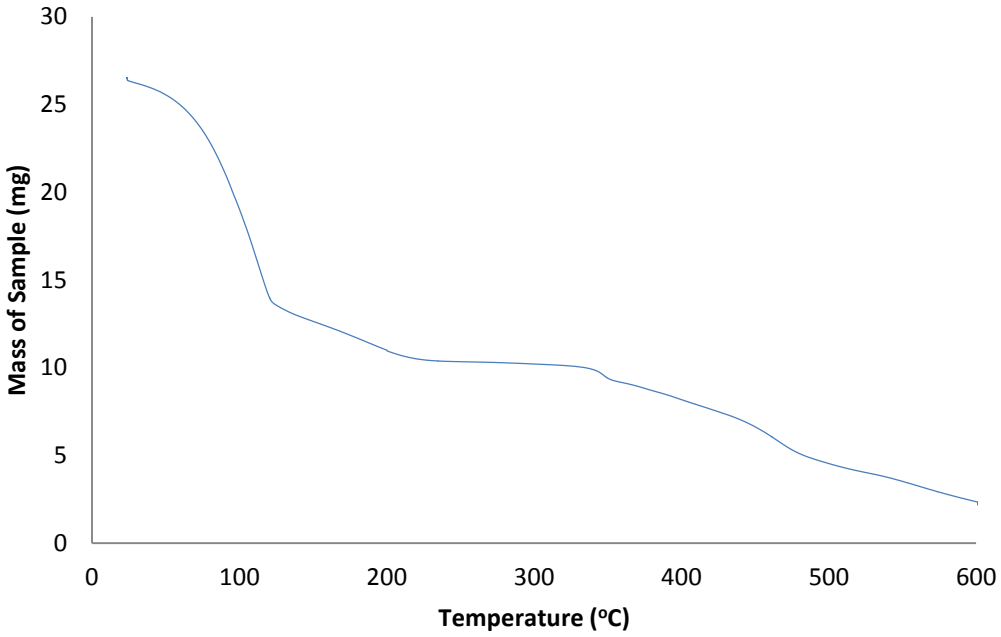

Figure A2.2.4 TGA of $[Zn_2(bdc\text{-}Br)_{1.4}(bdc\text{-}I)_{0.6}(dabco)]\cdot 2.6DMF$ **5a**.

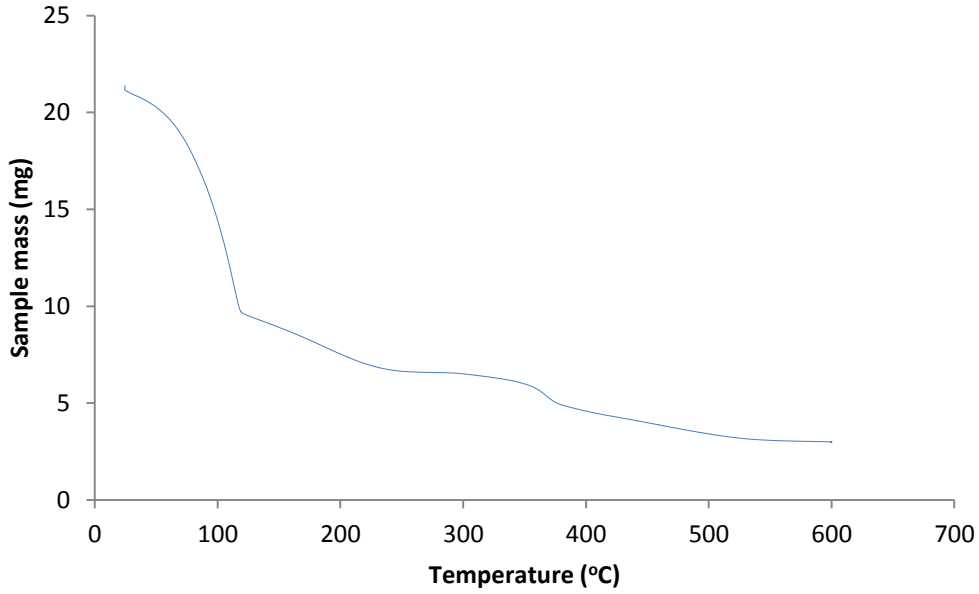

Figure A2.2.5 TGA of $[Zn_2(bdc\text{-}NO_2)_{0.12}(bdc\text{-}NH_2)_{0.88}(dabco)]\cdot 1.5DMF$ **6a**.

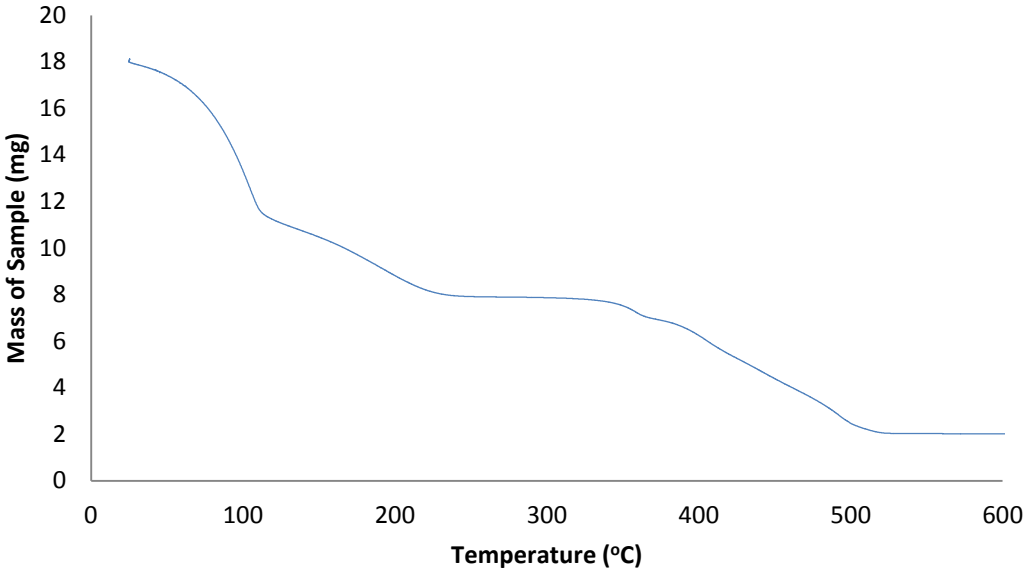

Figure A2.2.6 TGA of $[Zn_2(bdc)_{1.01}(1,4\text{-ndc})_{0.99}(dabco)]\cdot 2.3DMF$ **7a**.

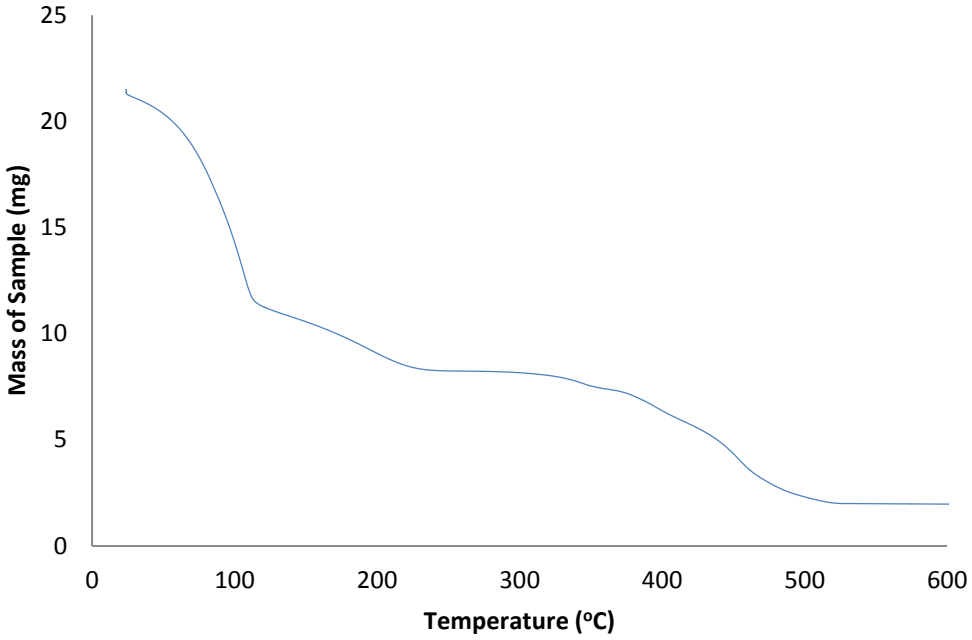

Figure A2.2.7 TGA of $[Zn_2(bdc)_{0.2}(ndc)_{1.8}(dabco)]\cdot 1.6DMF$ **7b**.

A2.3 Stability Analysis

The stabilities of the compounds $[Zn_2(bdc)(bdc\text{-}Br)(dabco)]\cdot DMF$ **1a**, $[Zn_2(bdc)_{1.48}(bdc\text{-}I)_{0.52}(dabco)]\cdot n DMF$ **2a**, $[Zn_2(bdc)_{1.2}(bdc\text{-}NO_2)_{0.8}(dabco)]\cdot 2.5DMF$ **3a**, $[Zn_2(bdc)_{1.16}(bdc\text{-}NH_2)_{0.84}(dabco)]\cdot n DMF$ **4c** and $[Zn_2(bdc\text{-}Br)_{1.4}(bdc\text{-}I)_{0.6}(dabco)]\cdot 2.6DMF$ **5a** and $[Zn_2(bdc\text{-}Br)_2(dabco)]$ to air were assessed by PXRD, with diffraction patterns recorded on samples over the course of several weeks.

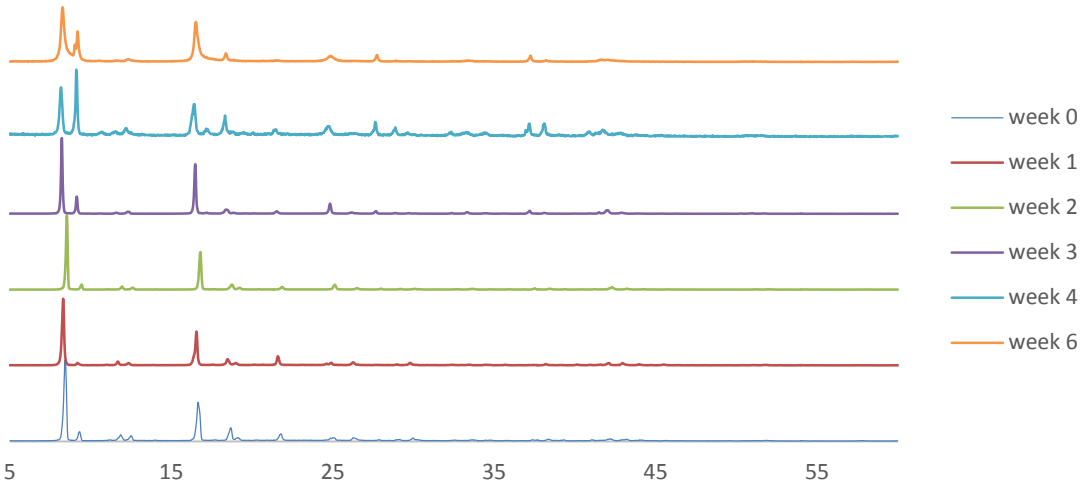

Figure A2.3.1 PXRD patterns of $[Zn_2(bdc)(bdc\text{-}Br)(dabco)]\cdot DMF$ **1a** left in air over a period of six weeks.

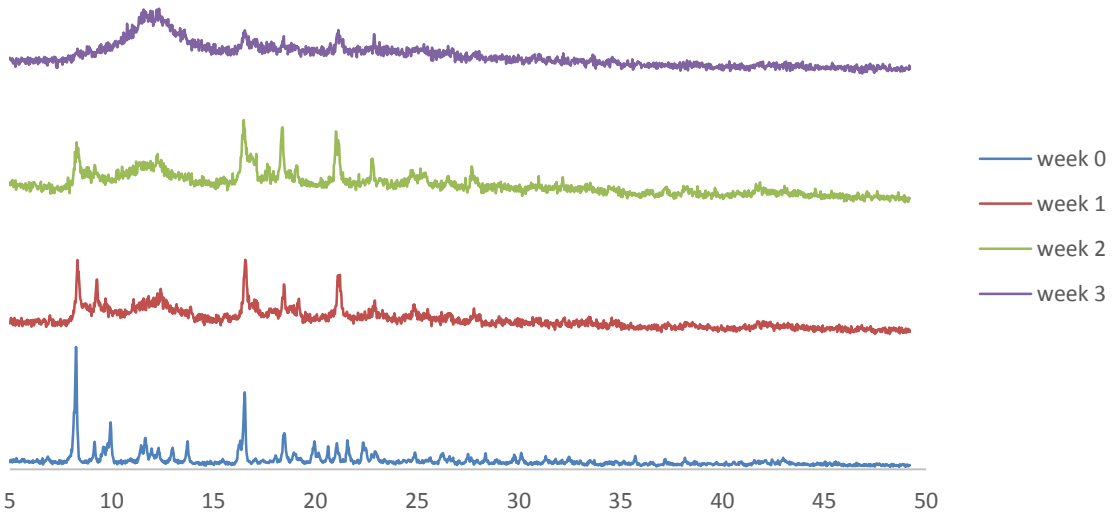

Figure A2.3.2 PXRD patterns of $[Zn_2(bdc)_{1.48}(bdc\text{-}I)_{0.52}(dabco)]\cdot n$DMF **2a** left in air over a period of three weeks.

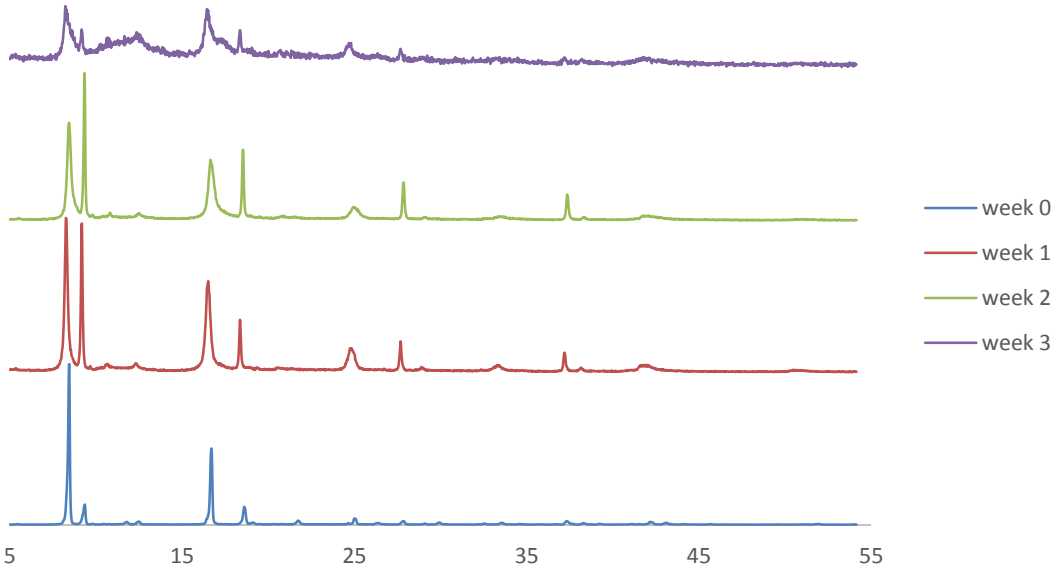

Figure A2.3.3 PXRD patterns of $[Zn_2(bdc)_{1.2}(bdc\text{-}NO_2)_{0.8}(dabco)]\cdot 2.5DMF$ **3a** left in air over a period of 3 weeks.

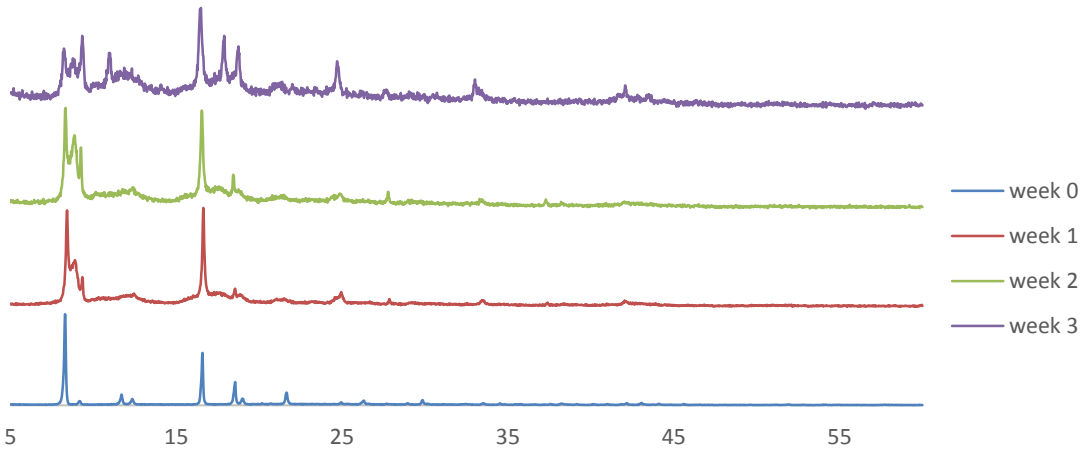

Figure A2.3.4 PXRD patterns of $[Zn_2(bdc)_{1.16}(bdc\text{-}NH_2)_{0.84}(dabco)]\cdot n$DMF **4c** left in air over a period of 3 weeks.

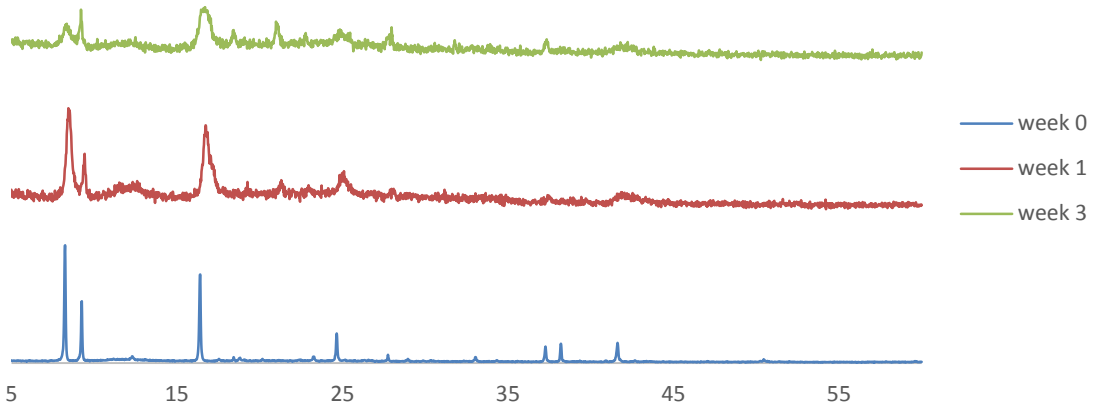

Figure A2.3.5 PXRD patterns of $[Zn_2(bdc\text{-}Br)_{1.4}(bdc\text{-}I)_{0.6}(dabco)]\cdot 2.6DMF$ **5a** left in air over a period of 3 weeks.

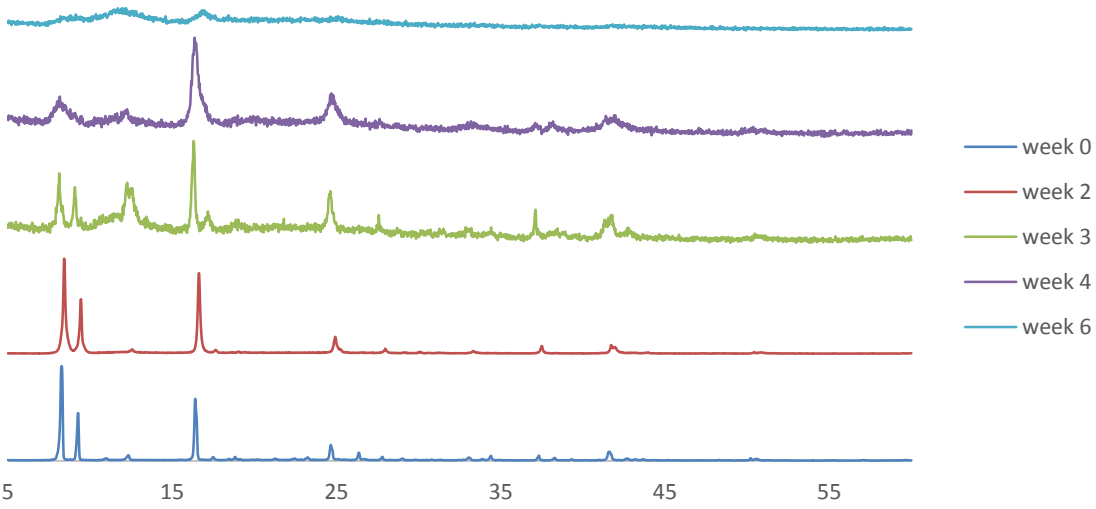

Figure A2.3.6 PXRD patterns of $[Zn_2(bdc\text{-}Br)_2(dabco)]$ left in air over a period of 6 weeks.

A3 Chapter 3 Appendix Information

A3.1 Thermogravimetric Analysis

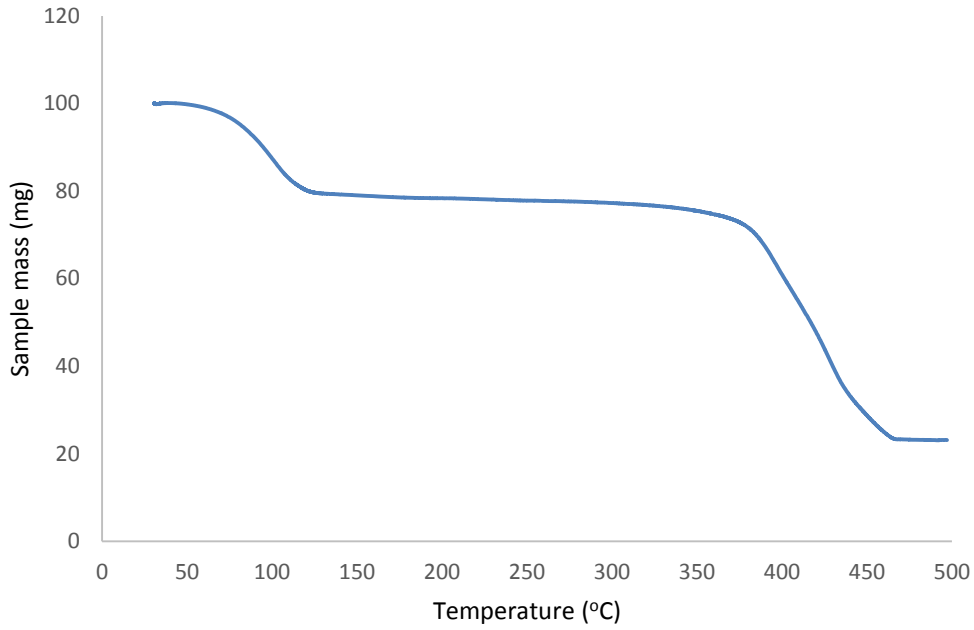

Figure A3.1.1 TGA of $[Cd_3(bptc)_{1.54}(bpdc)_{0.46}(H_2O)_9][NO_3]_{0.46}\cdot 1.9H_2O$ **8a**.

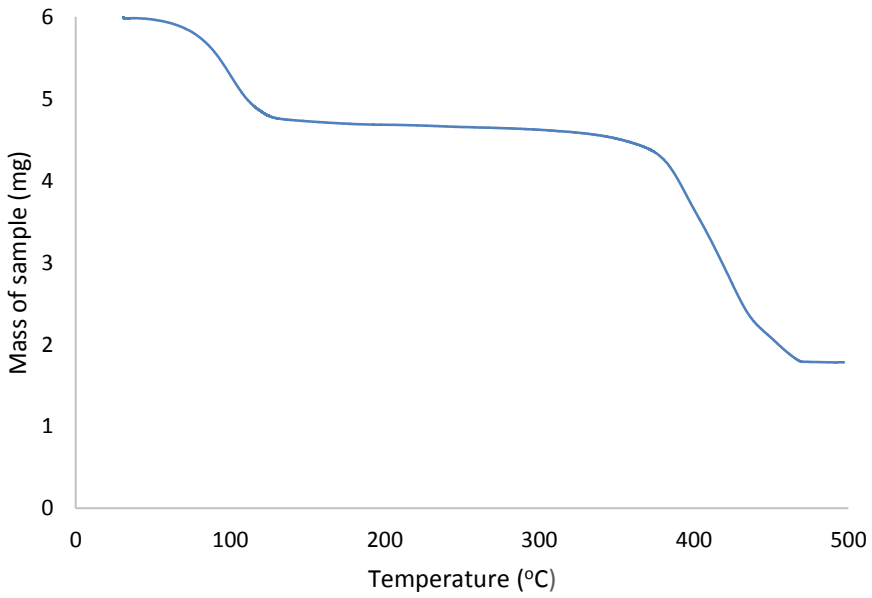

Figure A3.1.2 TGA of $[Cd_3(bptc)_{1.8}(bpdc)_{0.2}(H_2O)_9][NO_3]_{0.2}\cdot 3.8H_2O$ **8b**.

A3.2 PXRD Analysis

A comparison of the predicted PXRD patterns from the single crystal x-ray diffraction structures to the experimental traces collected on bulk samples are given below.

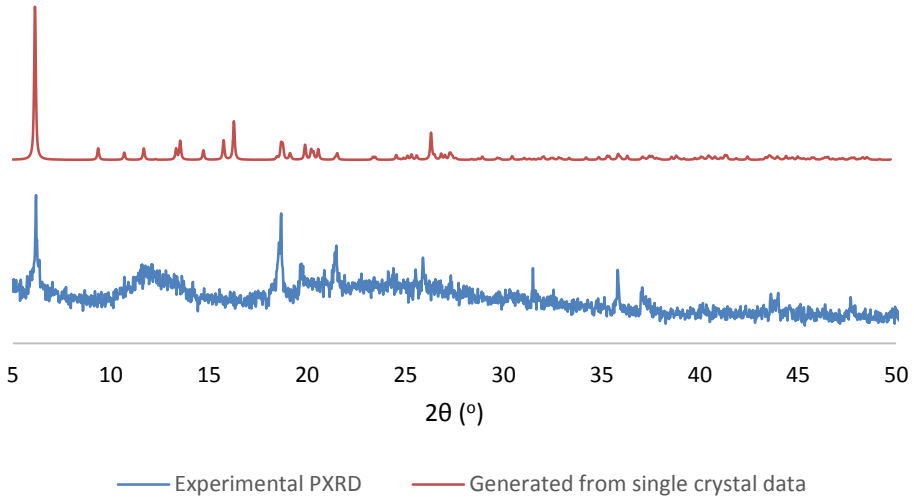

Figure A3.2.1 Predicted and experimental PXRD patterns of $[Cd_3(bptc)_{1.54}(bpdc)_{0.46}(H_2O)_9][NO_3]_{0.46}\cdot 1.9H_2O$ **8a**.

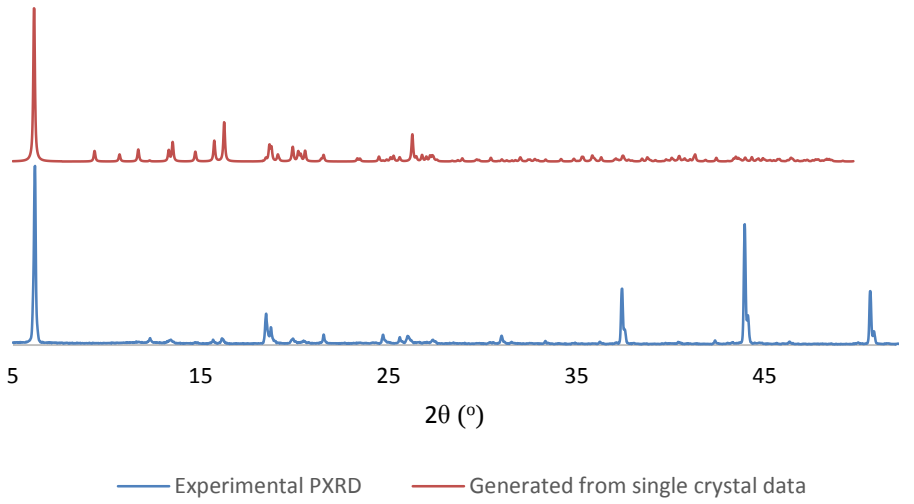

Figure A3.2.2 Predicted and experimental PXRD patterns of $[Cd_3(bptc)_{1.8}(bpdc)_{0.2}(H_2O)_9][NO_3]_{3.4}\cdot 3.8H_2O$ **8b**.

A4 Chapter 4 Appendix Information

A4.1 Thermogravimetric Analysis

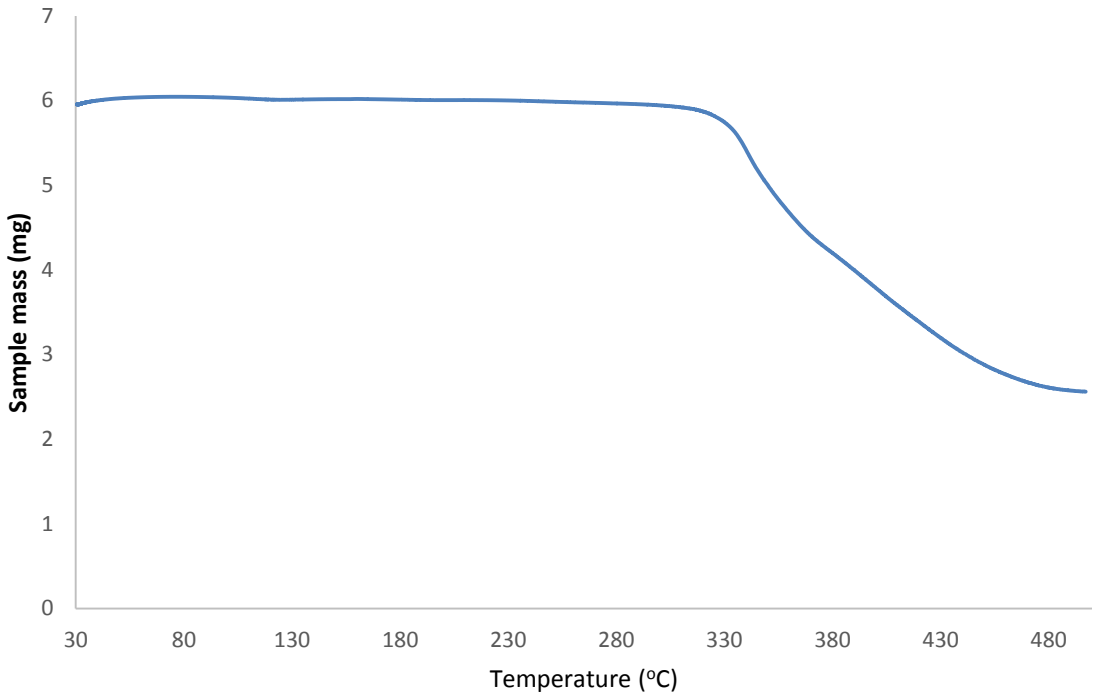

Figure A4.1.1 TGA of $[MV][Zn_3(ip)_4]$.

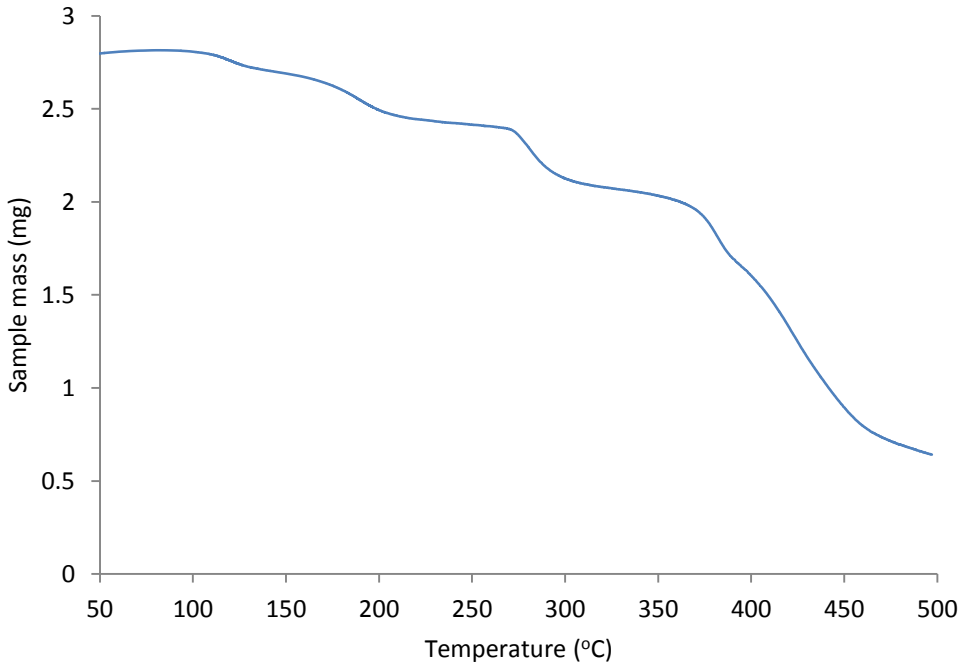

Figure A4.1.2 TGA of $[MV]_{0.44}[HMVH]_{0.36}[NH_2(CH_3)_2]_{0.4}[Zn_3(bdc)_4]\cdot 2H_2O\cdot 1.2DMF$.

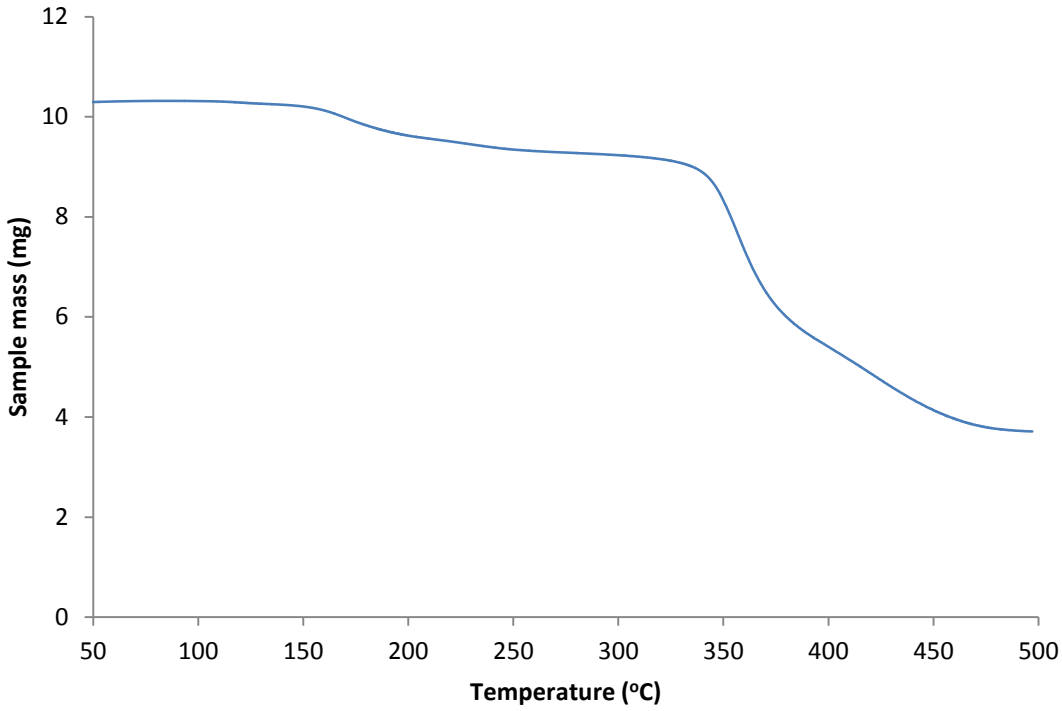

Figure A4.1.3 TGA of $[MV]_{0.5}[Zn(btc)]\cdot DMF$.

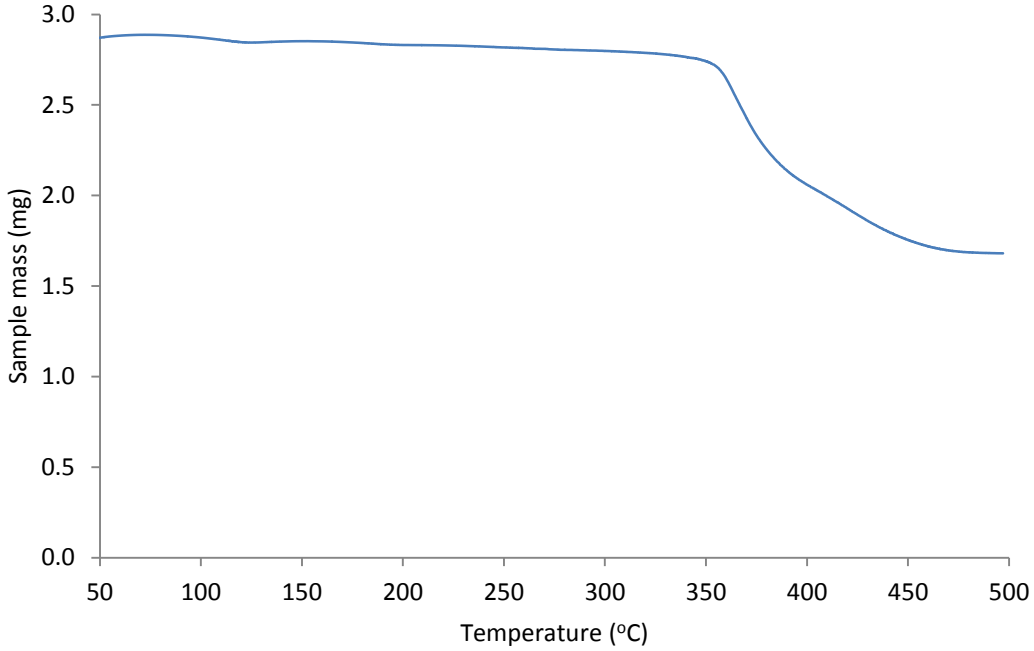

Figure A4.1.4 TGA of $[EV][Zn_3(ip)_4]$.

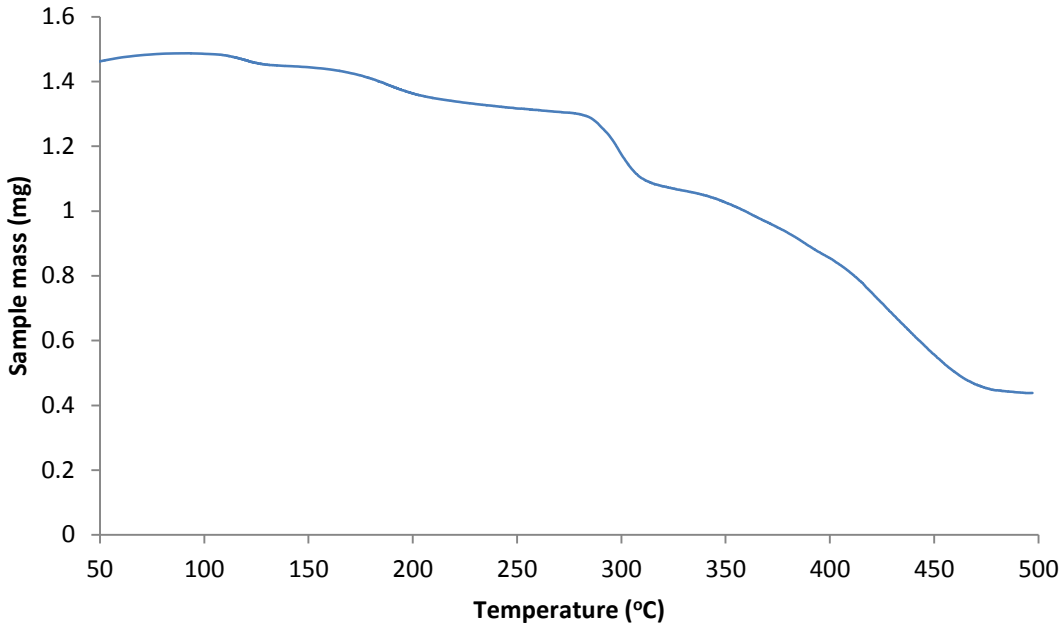

Figure A4.1.5 TGA of $[EV]_{0.69}[HEVH]_{0.29}[NH(CH_3)_2]_{0.2}[Zn_3(bdc)_4]$ ·0.9DMF·1.3H_2O.

A4.2 PXRD Analysis

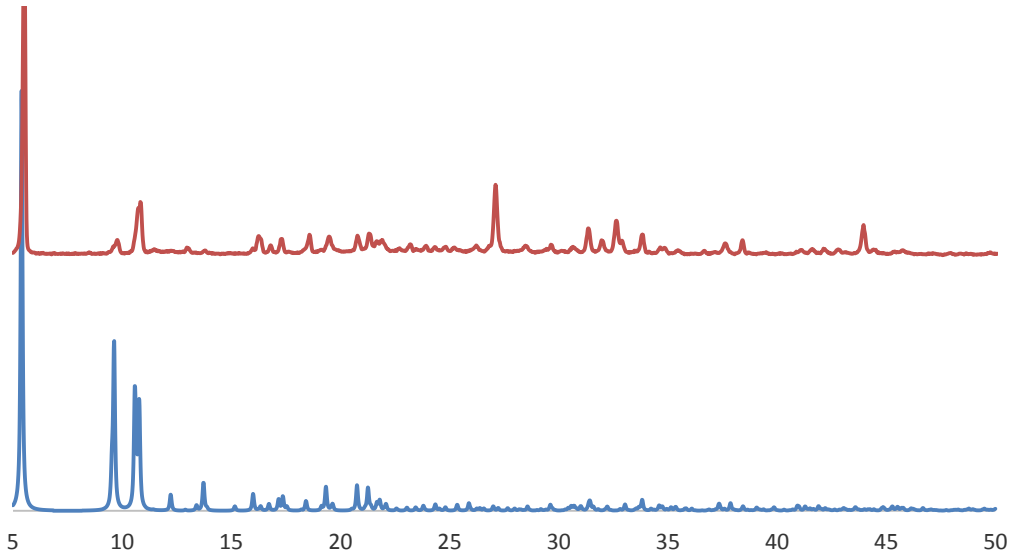

Figure A4.2.1 Predicted (bottom) and experimental (top) PXRD patterns of $[MV]_{0.44}[HMVH]_{0.36}[NH_2(CH_3)_2]_{0.4}[Zn_3(bdc)_4]\cdot 2H_2O\cdot 1.2DMF$ **9a**.

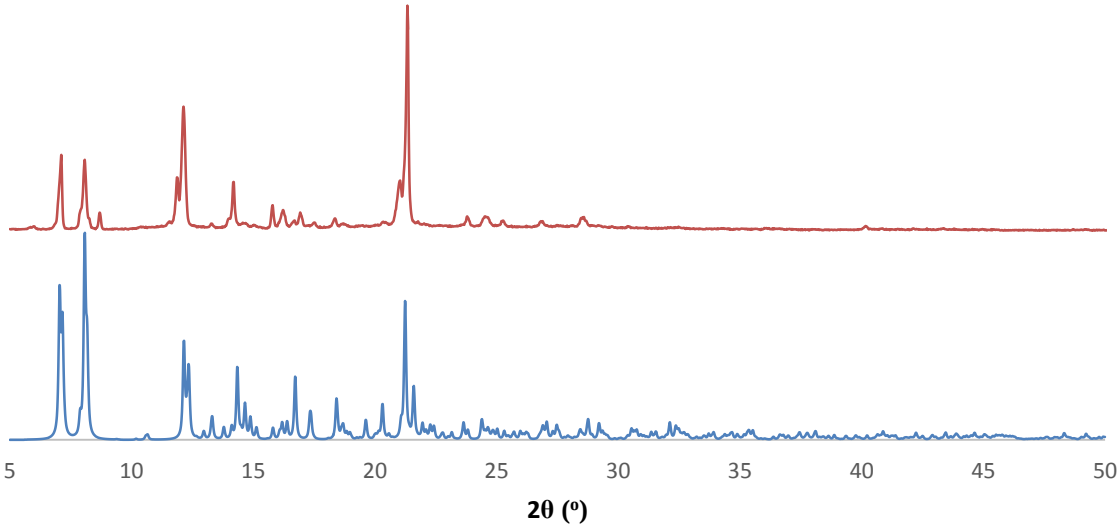

Figure A4.2.2 Predicted (bottom) and experimental (top) PXRD patterns of $[NH_2(CH_3)_2]_2[Zn_3(bpdc)_4]$ ·5DMF .

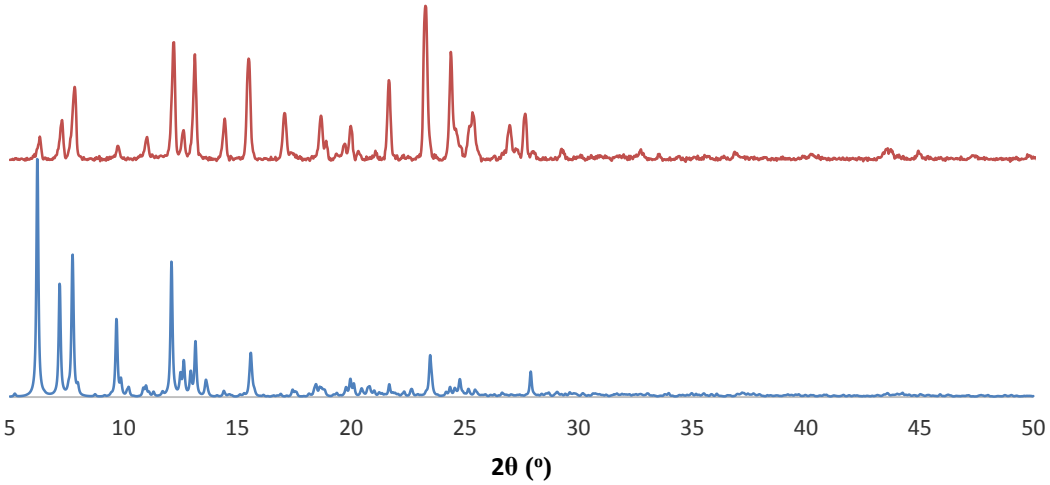

Figure A4.2.3 Predicted (bottom) and experimental (top) PXRD patterns of $[MV]_2[Zn_8(bpdc)_{10}]$ ·16DMF·20H_2O **9c**.